Report Title: AOI [3]: Smart Refractory Sensor Systems for Wireless Monitoring of Temperature, Health, and Degradation of Slagging Gasifiers

Type of Report: Final Scientific/Technical

Reporting Period Start Date: October 1, 2013

Reporting Period End Date: March 30, 2018

Principal Author(s): Debangsu Bhattacharyya, David Graham, Vinod Kulathumani, Edward M. Sabolsky

Date Report was Issued: May 2018

DOE Award Number: DE-FE0012383

Name and Address of Submitting Organization:

West Virginia University Research Corporation
86 Chestnut Ridge Road
PO Box 6845
Morgantown, WV 26506-6845
Telephone: 304-293-3998
Fax: 304-293-7435

ABSTRACT:

The objective of the work was to develop refractory "smart bricks", which would contain embedded temperature, strain/stress, and spallation sensors throughout the volume of high-chromia (-Cr_2O_3) refractory brick. The proposed work included work to interconnect the sensors to the reactor exterior, where the sensor signals may be processed by low-power electronics and transmitted wirelessly to a central processing hub. The data processing and wireless transmitter hardware was specifically designed to be isolated (with low power consumption) and to be adaptable to future implementation of energy-harvesting strategies for extended life. Finally, the collected data was incorporated into a model to estimate refractory degradation, a technique that could help monitor the health of the refractory in real-time. The long-term goal of this program was to demonstrate high-temperature, wireless sensor arrays for *in situ* three-dimensional (3-D) refractory monitoring or mapping for slagging gasification systems. The research was in collaboration with HarbisonWalker International (HWI) Technology Center in West Mifflin, PA. HWI is a leading developer and manufacturer of ceramic refractory products for high-temperature applications.

The work completed focused on the following areas: *1)* Investigation of the chemical stability, microstructural evolution, grain growth kinetics, degree of homogeneity (quantitative image analysis), and electrical properties of refractory oxide-silicide composites at temperatures between 750-1450ºC; *2)* Fabrication of silicide-alumina composite and oxide thermocouples and thermistor preforms and the development of techniques to embed them into high-chromia refractory bricks to form "smart bricks"; *3)* Utilization of commercial off-the-shelf discrete components to prototype circuits for interfacing between smart brick sensors and the wireless sensor network. The prototypes were then used to design an integrated circuit for thermistor, thermocouple, and capacitive-based smart brick sensor interfacing; *4)* Interfacing of the smart bricks with embedded sensors with wireless motes thus yielding a complete signal chain. This end-to-end data collection system was tested on a furnace heated to 1350 °C; *5)* Development of a slag penetration model and a nonlinear unknown input filter for the data from the embedded sensors for estimating temperature and extent of slag penetration.

TABLE OF CONTENTS:

FIGURES LIST:

Task 1 Figures

None

Task 2 Figures

Figure 2.13 XRD patterns of the (60-40) vol% (a) $MoSi_2$-ZrO_2, (b) WSi_2-ZrO_2, (c) $ZrSi_2$-ZrO_2, (d) $TaSi_2$-ZrO_2, (e) $NbSi_2$-ZrO_2, (f) $CrSi_2$-ZrO_2, and (g) $TiSi_2$-ZrO_2 composite samples after sintering under argon.

Figure 2.14 XRD patterns of the $CrSi_2$-Cr_2O_3 composite samples sintered at 1400°C for 2 hours: (a) (20-80), (30-70) and (40-60) vol% $CrSi_2$-Cr_2O_3, (b) (50-50), (55-45) and (60-40) vol% $CrSi_2$-Cr_2O_3, (c) (65-35), (70-30), (80-20) and (90-10) vol% $CrSi_2$-Cr_2O_3.

Figure 2.15 XRD patterns of the (a) pure $MoSi_2$, and (b) pure WSi_2 samples after sintering at 1600°C for 2 h, and short- and long-term annealing at 1400°C for 24-48 h.

Figure 2.16 XRD patterns of the (a) (60-40) vol% $MoSi_2$-Al_2O_3, and (b) (60-40) vol% WSi_2-Al_2O_3 composite samples after sintering at 1600°C for 2 h, and short- and long-term annealing at 1400°C for 24-48 h.

Figure 2.17 XRD patterns of the (a) (60-40) vol% $MoSi_2$-ZrO_2 and (b) (60-40) vol% WSi_2-ZrO_2 composite samples after sintering at 1600°C for 2 h, and short- and long-term annealing at 1400°C for 24-48 h.

Figure 2.18 X-ray diffraction patterns of the (a) (60-40) vol% $NbSi_2$-Al_2O_3 and (b) (60-40) vol% $NbSi_2$-ZrO_2 composites after annealing at 1400°C for 24, 48 and 96 hours.

Figure 2.19 X-ray diffraction patterns of the (a) (60-40) vol% $TaSi_2$-Al_2O_3 and (b) (60-40) vol% $TaSi_2$-ZrO_2 composites after annealing at 1400°C for 24, 48 and 96 hours.

Figure 2.20 XRD patterns of the (a) (50-50) vol% $CrSi_2$-Cr_2O_3, (b) (55-45) vol% $CrSi_2$-Cr_2O_3, and (c) (60-40) vol% $CrSi_2$-Cr_2O_3 composite samples after sintering at 1400°C for 2 hours, and also after annealing at 1400°C for 24, 48 and 96 hours.

Figure 2.21 Rietveld refinement fitting profiles obtained by MAUD software for (a) commercial $MoSi_2$ precursor powder, (b) pure $MoSi_2$ sample after sintering, (c) pure $MoSi_2$ sample after short-term (24 hrs) annealing, and (d) pure $MoSi_2$ sample after long-term (48 hrs) annealing.

Figure 2.22 Rietveld refinement fitting profiles obtained by MAUD software for (60-40) vol% $MoSi_2$-Al_2O_3 composite samples after (a) sintering, (b) short-term (24 hrs) annealing, and (c) after long-term (48 hrs) annealing.

Figure 2.23 Changes in the volume fraction of the secondary Nb_5Si_3 phase within the (60-40) vol% $NbSi_2$-Al_2O_3 and $NbSi_2$-ZrO_2 composites as a function of annealing time at 1400°C based on the Rietveld refinement results.

Figure 2.24 SEM micrographs of the fine polished (a-b) 60 vol% $MoSi_2$-40 vol% Al_2O_3, and (c-d) 60 vol% WSi_2-40 vol% Al_2O_3 composites sintered at 1600°C for 2 h.

Figure 2.25 SEM micrographs of the fine polished (a-b) 60 vol% $MoSi_2$-40 vol% Y_2O_3, and (c-d) 60 vol% WSi_2-40 vol% Y_2O_3 composites sintered at 1600°C for 2 h.

Figure 2.26 SEM micrographs of the fine polished (a-b) 60 vol% $MoSi_2$-40 vol% ZrO_2, and (c-d) 60 vol% WSi_2-40 vol% ZrO_2 composites sintered at 1600°C for 2 h.

Figure 2.27 SEM micrographs of the fine polished (a-b) 20 vol% $MoSi_2$-80 vol% Cr_2O_3, and (c-d) 20 vol% WSi_2-80 vol% Cr_2O_3 composites sintered at 1400°C for 2 h.

Figure 2.28 SEM micrographs (a-b-c-d) of the (60-40) vol% WSi_2-Al_2O_3 composite samples sintered at 1600°C for 2h after fine polishing and then chemical etching in 1:1:1 HCl:HNO_3:H_2O (volumetric ratio) acid mixture for 1-2 minutes.

Figure 2.29 SEM micrographs (a-b-c-d) of the (60-40) vol% $MoSi_2$-coarseAl_2O_3 composite samples sintered at 1600°C for 2h after fine polishing and then chemical etching in 2.0 M HCl acid solution for 1-2 minutes.

Figure 2.30 SEM micrographs (a-b) of the (60-40) vol% $MoSi_2$-coarseAl_2O_3 composite samples sintered at 1600°C for 2h after fine polishing and then chemical etching in 1:1:1 HCl:HNO_3:H_2O (volumetric ratio) acid mixture for 1-2 minutes.

Figure 2.31 Low-magnification backscattered SEM microstructures of the (a) $NbSi_2$-Al_2O_3, (b) $NbSi_2$-ZrO_2, (c) $TaSi_2$-Al_2O_3, and (d) $TaSi_2$-ZrO_2 composites with the addition of 40 vol% Al_2O_3 and ZrO_2 particles after sintering at 1600°C for 2 h in argon.

Figure 2.32 High magnification backscattered SEM microstructures of the (a) $NbSi_2$-Al_2O_3, (b) $NbSi_2$-ZrO_2, (c) $TaSi_2$-Al_2O_3, and (d) $TaSi_2$-ZrO_2 composites with the addition of 40 vol% Al_2O_3 and ZrO_2 particles after sintering at 1600°C for 2 h in argon.

Figure 2.33 (a) SEM micrograph of the pure $CrSi_2$ sample sintered at 1400°C for 2h, and its EDS analysis results for the (b) bright and (c) gray regions.

Figure 2.34 (a-b) SEM micrographs of the (20-80) vol% $CrSi_2$-Cr_2O_3 composite sample sintered at 1400°C for 2h, and its EDS analysis results for the (c) brighter and (d) gray regions.

Figure 2.35 (a-b) SEM micrographs of the (30-70) vol% $CrSi_2$-Cr_2O_3 composite sample sintered at 1400°C for 2h.

Figure 2.36 (a-b) SEM micrographs of the (40-60) vol% $CrSi_2$-Cr_2O_3 composite sample sintered at 1400°C for 2h, and its EDS analysis for the (c) bright and (d) dark regions.

Figure 2.37 (a) SEM micrograph of the (50-50) vol% $CrSi_2$-Cr_2O_3 composite sample sintered at 1400°C for 2h, and its EDS analysis results for the (b) bright and (c) dark regions.

Figure 2.38 (a-b) SEM micrographs of the (55-45) vol% $CrSi_2$-Cr_2O_3 composite sample sintered at 1400°C for 2h, and its EDS analysis results for the (c) brighter and (d) gray regions.

Figure 2.39 (a) SEM micrograph of the (60-40) vol% $CrSi_2$-Cr_2O_3 composite sample sintered at 1400°C for 2h, and (b) its EDS analysis results for the bright region.

Figure 2.40 (a) SEM micrograph of the (70-30) vol% $CrSi_2$-Cr_2O_3 composite sample sintered at 1400°C for 2h, and its EDS analysis results for the (b) bright and (c) gray regions.

Figure 2.41 (a-b) SEM micrographs of the (90-10) vol% $CrSi_2$-Cr_2O_3 composite sample sintered at 1400°C for 2h, and its EDS analysis results for the (c) bright and (d) gray regions.

Figure 2.42 SEM micrographs of (a-b) pure $MoSi_2$, and (c-d) (60-40) vol% $MoSi_2$-Al_2O_3 composite samples after annealing at 1400°C for 24 hrs with two different magnifications.

Figure 2.43 SEM micrographs of (a-b) pure $MoSi_2$, and (c-d) (60-40) vol% $MoSi_2$-Al_2O_3 composite samples after long-term annealing at 1400°C for 48 hours.

Figure 2.44 SEM micrographs of **a-b)** (60-40) vol% $MoSi_2$-coarseAl_2O_3 composite sample after long-term annealing at 1400°C for 48 hours [*Samples were chemically etched in 2.0 M HCl*].

Figure 2.45 SEM micrographs of (a-b) (60-40) vol% $MoSi_2$-ZrO_2 composite sample after long-term annealing at 1400°C for 48 hours [*Samples were chemically etched in 2.0 M HCl*].

Figure 2.46 SEM micrographs of **a-b)** (60-40) vol% WSi_2-Al_2O_3 composite sample after long-term annealing at 1400°C for 48 hours [*WSi_2-Al_2O_3 sample shown in Figure 2.46a was chemically etched in 1:1:1 HCl:HNO_3:H_2O*].

Figure 2.47 SEM micrographs of (a-b) (60-40) vol% WSi_2-coarseAl_2O_3, and (c-d) (60-40) vol% WSi_2-ZrO_2 composite samples after long-term annealing at 1400°C for 48 hours [*WSi_2-coarseAl_2O_3 sample shown in Figure 2.47a and all WSi_2-ZrO_2 samples were chemically etched in 1:1:1 HCl:HNO_3:H_2O*].

Figure 2.48 Grain growth kinetics of (a) $MoSi_2$, and (b) WSi_2 as a function of annealing time at 1400°C [*0 hour indicates the pre-sintered samples*].

Figure 2.49 Original cross-sectional SEM microstructures of the metal silicide-refractory oxide composites and their converted binary images showing individual metal silicide grains as black regions (on the right side): (a) (60-40) vol% WSi_2-ZrO_2, (b) (60-40) vol% WSi_2-Y_2O_3, and (c) (60-40) vol% $MoSi_2$-Al_2O_3.

Figure 2.50 The D index values calculated for three different metal silicide-refractory oxide composites' SEM microstructures as a function of total number of lines analyzed (2N) by using the proposed method.

Figure 2.51 The electrical conductivity of the (a) $MoSi_2$-based and (b) WSi_2-based composites and pure metal disilicides ($MoSi_2$, WSi_2) as a function of temperature (Electrical conductivity data is presented on the logarithmic scale).

Figure 2.52 (a) X-ray diffraction patterns and (b) electrical conductivity results of the $NbSi_2$, Nb_5Si_3 and $TaSi_2$ samples sintered at 1600°C.

Figure 2.53 Electrical conductivity of the (60-40) vol% $NbSi_2$- and $TaSi_2$-oxide composites as a function of temperature (Electrical conductivity data is presented on the logarithmic scale).

Figure 2.54 Electrical conductivity results of the (a) (50-50) vol% $CrSi_2$-Cr_2O_3, (b) (55-45) vol% $CrSi_2$-Cr_2O_3, and (c) (60-40) vol% $CrSi_2$-Cr_2O_3 composite samples sintered at 1400°C for 2 hours, as a function of temperature (100°-1000°C).

Figure 2.55 Electrical conductivity results of the (a) (50-50) vol% $CrSi_2$-Cr_2O_3, (b) (55-45) vol% $CrSi_2$-Cr_2O_3, and (c) (60-40) vol% $CrSi_2$-Cr_2O_3 composite samples after sintering at 1400°C for 2 h, and then annealing at 1400°C for 24-48 h, as a function of temperature (100°-1000°C).

Figure 2.56 Coefficients of thermal expansion (CTEs) of the (a) 25 vol% $MoSi_2$-75 vol% Al_2O_3, (b) 50 vol% $MoSi_2$-50 vol% Al_2O_3, (c) 60 vol% $MoSi_2$-40 vol% Al_2O_3, and (d) 75 vol% $MoSi_2$-25 vol% Al_2O_3 composite samples sintered at 1600°C for 2 h.

Figure 2.57 Coefficients of thermal expansion (CTEs) of the (a) 25 vol% WSi_2-75 vol% Al_2O_3, (b) 50 vol% WSi_2-50 vol% Al_2O_3, and (c) 60 vol% WSi_2-40 vol% Al_2O_3 composite samples sintered at 1600°C for 2 h.

Figure 2.58 Coefficients of thermal expansion (CTEs) of the (a) $MoSi_2$-Al_2O_3 composite samples, and (b) WSi_2-Al_2O_3 composite samples sintered at 1600°C for 2 h as a function of the $MoSi_2$ and WSi_2 volume percentages.

Figure 2.59 Comparison of the oxidation-induced mass changes (mg/cm^2) of the (a) $NbSi_2$-based composites with $NbSi_2$ and Nb_5Si_3, and (b) $TaSi_2$-based composites with $TaSi_2$, all sintered at 1600°C in argon, as a function of the oxidation temperature.

Figure 2.60 Mass change per unit surface area of the as-sintered (a) $MoSi_2$ and 30-70 vol% $MoSi_2$-Al_2O_3, and (b) WSi_2 and 30-70 vol% WSi_2-Al_2O_3 samples as a function of oxidation temperature in ambient air ("w/o" term refers to non-preoxidized or as-sintered samples).

Task 3 Figures

Fig. 3.1. Optical pictures of various thermocouple designs with various leg thicknesses.

Fig. 3.2. Optical picture of the first thermistor sensor embedded with alumina (with the Pt electrical connection shown).

Fig. 3.3. Resistance versus temperature of thermistor with composition 40 vol% Al_2O_3-60 vol% $MoSi_2$. Inset shows the photograph of thermistor.

Figure 3.4. Performance analysis of thermistors [90-10] vol% $TaSi_2$-Al_2O_3 and [90-10] vol% $NbSi_2$-Al_2O_3.

Figure 3.5. Performance analysis of thermistors [90-10] vol% $ZrSi_2$-Al_2O_3; [90-10] vol% WSi_2-Al_2O_3 and 90-10] vol% $MoSi_2$-Al_2O_3.

Figure 3.6. Resistance vs Temperature of four $MoSi_2$-Al_2O_3 thermostats with compositions (a) [50-50]vol% $MoSi_2$-Al_2O_3 (b) [60-40]vol% $MoSi_2$-Al_2O_3 (c) [75-25]vol% $MoSi_2$-Al_2O_3 (d) [90-10]vol% $MoSi_2$-Al_2O_3.

Fig. 3.7. Thermal processed strain sensors. (a) 60vol% $MoSi_2$-40vol% Al_2O_3; (b) 60vol% WSi_2-40 vol% Al_2O_3; (c)75 vol% $ZrSi_2$-25 vol% Al_2O_3.

Fig. 3.8. Section view of basic fixturing and test specimen for equibiaxial testing.

Fig. 3.9. The response of the strain sensor with composition 60vol% $MoSi_2$-40vol% Al_2O_3 as a function of applied force and the inset shows the photograph of the sensor.

Fig. 3.10. The response of the strain sensor with composition 60vol% $MoSi_2$-40vol% Al_2O_3 as a function of time.

Figure 3.11 (a) XPS wide range survey spectra and (b) high-resolution XPS spectra (Mo3d, Si2p, Al2p, O1s) of the various $MoSi_2$-Al_2O_3 composites after sintering at 1500°C for 2 h.

Figure 3.12 (a) XPS wide range survey spectra and (b) high-resolution XPS spectra (W4f, Si2p, Al2p, O1s) of the various WSi_2-Al_2O_3 composites after sintering at 1500°C for 2 h.

Figure 3.13 (a) XRD patterns of the [50-50] and [90-10] $MoSi_2$-Al_2O_3 composites after sintering at 1500°C for 2 h; (b-c) Rietveld refinement results of the [50-50] and [90-10] $MoSi_2$-Al_2O_3 composites, respectively [solid red lines = fitting curves; black dots = experimental XRD data].

Figure 3.14 SEM micrographs of the (a) [50-50], (b) [60-40], (c) [75-25] and (d) [90-10] $MoSi_2$-Al_2O_3 composites after sintering at 1500°C for 2 h.

Figure 3.15 SEM micrographs of the (a) [50-50], (b) [60-40], (c) [75-25] and (d) [90-10] WSi_2-Al_2O_3 composites after sintering at 1500°C for 2 h.

Figure 3.16 Optical photograph and SEM micrographs (alumina substrate, left leg, right leg, junction) of the [75-25] $MoSi_2$-Al_2O_3//Pt thermocouple screen printed on an alumina substrate and then sintered at 1500ºC for 2 h.

Figure 3.17 (a-c) Thermoelectric voltages (E) and (b-d) effective Seebeck coefficients (S) measured for the various $MoSi_2$-Al_2O_3//Pt and WSi_2-Al_2O_3//Pt thermocouples as a function of temperature difference.

Figure 3.18 Estimated Seebeck coefficients (S) of the various $MoSi_2$-Al_2O_3 and WSi_2-Al_2O_3 composites as a function of temperature difference (S_{Pt} is also presented).

Figure 3.19 (a) Thermoelectric voltages (E) and (b) effective Seebeck coefficients (S) measured for the $MoSi_2$//WSi_2 and various $MoSi_2$-Al_2O_3//WSi_2-Al_2O_3 thermocouples as a function of temperature difference.

Figure 3.20 Comparison of the estimated (*dashed lines*) and measured effective (*solid lines*) Seebeck coefficients of the various $MoSi_2$-Al_2O_3//WSi_2-Al_2O_3 (*abbreviated as MA//WA*) composite thermocouples as a function of temperature difference.

Figure 3.21 Thermoelectric performance of the [90-10] $MoSi_2$-Al_2O_3//[90-10] WSi_2-Al_2O_3 long composite thermocouple (22.9 cm length, 0.6 cm width) up to 1350°C, as a function of cold- and hot-junction temperature and time.

Figure 3.22. Nine inch long thermocouples.

Figure 3.23. Performance of various silicide long length thermocouples.

Figure. 3.24. Fabrication of Long Thermocouples (8” x 2” x 600 μm) using stencil lithography by using stencils as shadow masks for direct surface patterning without resist process.

Figure 3.25. Long Thermistors (8” x 1.5” x 600 μm) fabricated through stencil writing. (a) Thermistor pre-forms laminated in between alumina substrates before sintering (b) Sensor preforms sintered at 1500 °C, 2h in argon atmosphere.

Figure 3.26. Long Thermocouple: [75-25] vol. % $MoSi_2$-Al_2O_3// [75-25] vol. % $MoSi_2$-Al_2O_3 fabricated through stencil writing. (a) Schematic showing long thermocouple fabricated via stencil lithography (b) Sensor preforms sintered at 1500 ºC, 2h in argon atmosphere.

Figure 3.27. Performance analysis of [75-25] vol. % $MoSi_2$-Al_2O_3// [75-25] vol. % WSi_2-Al_2O_3 thermocouple fabricated through stencil lithography and laminated in between two 80/20 vol. % coarse/fine alumina laminated substrates. The thermocouple was tested at 1350 °C isothermally for 5h in 1st cycle and for 10h in 2nd cycle in argon atmosphere.

Figure 3.28. Fabrication of [75-25] $MoSi_2$-Al_2O_3//[75-25] WSi_2-Al_2O_3 thermocouple embedded in alumina substrates. The Various components used are numbered as (1) (80-20) vol% coarse vs

fine alumina substrate (2) [75-25] vol% $MoSi_2$-Al_2O_3 (3) (80-20) vol% coarse vs fine alumina filler material used to shape the sensor design (4) [75-25] vol% WSi_2-Al_2O_3 (5) (80-20) vol% coarse vs fine alumina substrate.

Figure 3.29. Photograph of [75-25] $MoSi_2$-Al_2O_3// [75-25] WSi_2-Al_2O_3 thermocouple (with full filler material as indicated by design I) embedded in alumina substrates.

Figure 3.30. Fabrication of [75-25] $MoSi_2$-Al_2O_3//WSi_2-Al_2O_3 thermocouple embedded in alumina substrates. The various components used are: (1) (80-20) vol% coarse vs fine alumina substrate (2) [75-25] vol% $MoSi_2$-Al_2O_3 (3) (80-20) vol% coarse vs fine alumina strip used as center filler (4) [75-25] vol% WSi_2-Al_2O_3 (5) (80-20) vol% coarse vs fine alumina substrate.

Figure 3.31. Photograph of [75-25] $MoSi_2$-Al_2O_3//[75-25] WSi_2-Al_2O_3 thermocouple (with center filler material) embedded in alumina substrates.

Figure 3.32. Fabrication of [75-25] $MoSi_2$-Al_2O_3// [75-25] WSi_2-Al_2O_3 thermocouple embedded in alumina substrates without filler material. The various components (1) (80-20) vol% coarse vs fine alumina substrate (2) [75-25] vol% $MoSi_2$-Al_2O_3 (3) [75-25] vol% WSi_2-Al_2O_3 (4) (80-20) vol% coarse vs fine alumina substrate.

Figure 3.34. Photograph of [75-25] $MoSi_2$-Al_2O_3//[75-25] WSi_2-Al_2O_3 thermocouples embedded in alumina substrates and sintered at 1550 °C , 2h in argon.

Figure 3.35 (a) Post-test photograph of [75-25] vol% $MoSi_2$-Al_2O_3//WSi_2-Al_2O_3 thermocouple sintered at 1550 °C for 2 hours in argon atmosphere. The thermocouple is embedded within 80/20 composite alumina substrate (b) Photograph of high temperature thermoelectric characterization facility for testing thermocouples/thermistors in argon atmospheres (c) Cold junction arrangement to test long thermocouples preforms.

Figure 3.36. Thermoelectric voltage of [75-25] vol% $MoSi_2$-Al_2O_3 //WSi_2-Al_2O_3 thermocouple embedded in 80/20 alumina substrate and sintered at 1550 °C, 2 h and the preform was tested isothermally at 1350 °C, 10 h in argon atmosphere.

Figure 3.37. Post-oxidation test photograph of [75-25] vol. % $MoSi_2$-Al_2O_3//WSi_2-Al_2O_3 thermocouple sintered at 1600 °C for 2 hours in argon atmosphere. The thermocouple is embedded within 80/20 composite alumina substrate.

Figure 3.38. Oxidation study of the thermocouple with configuration [90-10] vol.% $MoSi_2$-Al_2O_3//WSi_2-Al_2O_3. The oxidation study was conducted as (a) Run1: 100% argon (b) 1% O_2 balance argon and (c) Run3: 5% O_2 balance argon.

Figure 3.39. Photograph of [75-25] vol% WSi_2-Al_2O_3 thermistor green preforms embedded in fine alumina (SA: 8.6 m^2/g) substrates (length 8 ¾" and thickness ~650 μm).

Figure 3.40. Photograph of [75-25] vol% WSi_2-Al_2O_3 thermistors embedded in fine alumina and sintered at 1600 °C for 5h in argon atmosphere.

Figure 3.41. Temperature dependent resistance of [75-25] vol.% WSi_2-Al_2O_3 thermistor sintered at 1600 °C, 2h and tested at 1350 °C for 10h in argon atmosphere.

Figure 3.42. Post-test photograph of [75-25] vol% WSi_2-Al_2O_3 thermistor tested at 1350 °C, 10h.

Figure 3.43. X-ray diffraction pattern for the La_2NiO_4 (LNO) calcined at 1200°C and matched with matching K_2NiO_4 crystal structure (JCPDF #01-089-3460).

Figure 3.44 Images showing LNO thermistors: a) green, b) sintered, and c) sintered imaged on a light box to highlight embedded sensor material.

Figure 3.45 Resistance and temperature profile of LNO based thermistor co-sintered inside YSZ at 1350°C and tested to 1350°C. The thermistor material consisted of 100 vol% LNO core and 50:50 vol% LNO:YSZ intermediate layer inside YSZ shell.

Figure 3.46 SEM images and graphic depiction of thermistors' construction showing the following thermistors: a). LNO (as-received) thermistor in YSZ sintered at 1350°C, and b). LNO-1000 thermistor in YSZ sintered at 1450°C.

Figure 3.47 Resistance and temperature profile LNO-1000 based thermistor co-sintered inside YSZ at 1450°C and tested for 100 hrs at 1400°C. This graph illustrates continuous decrease in resistance from 22.38 to 20.00 ohms during the high temperature hold (10.63% change).

Task 4 Figures

Fig. 4.1. [60-40] vol% $MoSi_2$-Al_2O_3 thermistors screen printed on and laminated with Al_2O_3. The dimension of the thermistor is given on the right side.

Fig. 4.2. Chromia brick showing the embedded sensor.

Fig. 4.3. The schematic showing experimental set up used for the cup corrosion test.

Fig. 4.4. Performance analysis of [60-40] vol% $MoSi_2$-Al_2O_3 temperature sensor for 250 h.

Fig. 4.5. The resistivity of the thermistor increased with increase in temperature up to 1350°C then it decreased exhibiting a typical PTC thermistor characteristics.

Fig. 4.5. Photographs of green body of smart bricks embedded with sintered preforms of long thermistors/thermocouple sensors, slip casted at HWI (HarbisonWalker International).

Fig. 4.6. Optical micrograph of the cross sectional interface of the smart brick embedded with [35-65] vol. % $MoSi_2$-Al_2O_3 long thermistor.

Fig. 4.7. (a) Smart brick with embedded with TC : 34-79D[75-25] vol. % $MoSi_2$-Al_2O_3 (coarse Al_2O_3) // 34-79E[75-25] vol. % WSi_2-Al_2O_3 (coarse Al_2O_3) sintered at 1500 ºC, 2h in Argon; **(b)** Silver wire leads, connected to sensor using silver epoxy and Ag/Cu ink; **(c)** Thermoelectric testing arrangement of thermocouple embedded smart brick in an atmosphere controlled chamber furnace. The K-type thermocouple reads the cold junction temperature.

Fig. 4.8. Photographs of tape casted long temperature sensors (1) Thermistor tapes laser cut and placed on composite alumina substrates with lid before lamination (2) Laminated sensor preforms before firing (3) Sensor preforms sintered at 1550 °C in argon.

Figure 4.9. Phase diagram of CaO-Fe_2O_3-Al_2O_3/SiO_2

Fig. 4.10. Photographs of three slag compositions prepare (a) Illinois #6 (b) Pocahontas (c) Lignite coal.

Fig. 4.11. Photographs of three slag compositions melted in chromia refractory crucibles (a) Illinois #6 (b) Pocahontas (c) Lignite coal.

Fig. 4.12. Images of a profile of a brick used in slag experiments and an internal cavity of the brick containing melted slag after heat treatment.

Fig. 4.13. The optical micrograph showing the penetration of the slag. The marked (white dash lines) portion show the penetration of slag.

Fig. 4.14. (a) Photograph of Cr_2O_3 refractory cup embedded with thermocouples for static cup corrosion test (b) screen printed thermocouples lamented with alumina tape.

Fig. 4.15: Optical and Scanning Electron Microscopy(SEM) images showing: (a) fracture surface of Cr_2O_3 refractory cup after 5 hours of slag corrosion test performed at 1500 °C; (b) slag particles in the refractory; (c) Cr_2O_3 grains without slag.

Fig. 4.16. Optical and Scanning Electron Microscopy(SEM) images showing: (a) fracture surface of chromia refractory cup after 10 hours of slag corrosion test performed at 1500 °C; (1)-(7)SEM microstructure analysis of slag penetration inside the refractory.

Fig. 4.17. (a) Photographs of smart bricks embedded with long temperature sensors sintered 1550 °C in argon. (b) Photograph of the interface exposing the sensor leads out. (c) Lignite coal slag samples prepared for slag test (d) Photo graph of the smart brick surface polished and wired using Pt wire, Pt mesh and Pt ink.

Fig. 4.18. Post Test Analysis of Smart Refractory Brick Embedded with [75-25] vol% WSi_2-Al_2O_3 Thermistor at 1350 °C in Argon Atmosphere

Fig. 4.19. Static cup and corrosion test results of [75-25] WSi_2-Al_2O_3 thermistor embedded in chromia refractory tested with and without slag at 1350 °C in argon atmosphere.

Fig. 4.20. Small bricks with embedded LNO-based thermistors.

Fig. 4.21. Slagging experiments with a brick containing LNO based sensor. The sensor consists of 70:30 vol% LNO-1000: YSZ core and 50:50 vol% LNO-1000: YSZ intermediate layer inside YSZ shell. The thermal cycle for each run was 25°C to 1400°C with 10 hrs hold at 1400°C and slag was added at room temperature before Run 3.

Fig. 4.22. Resistance versus temperature curves for brick cycled two times without slag and once with slag. The graph highlights the difference in resistance measured during heating (darker color) and cooling ramps**.**

Fig. 4.23. Remnants of resolidified slag inside brick cavity after Run 3.

Fig. 4.24. Thermal cycling of LNO-1000 based sensor embedded in a high-chromia brick. The sensor was sintered at 1450°C and tested between 800°C and 1400°C showing significant change in resistance between cycles at low temperature.

Fig. 4.25. Resistance and temperature profile of LNO-1000 based sensor embedded in a high-chromia brick. This data was generated using the same brick shown in Fig. 4.24 after the electrodes were reapplied with extra 70:30 LNO(coarse):YSZ ink.

Fig. 4.26. Resistance and temperature profile of the La_2NiO_4 (LNO-1400) based thermistor co-sintered inside YSZ and embedded in high-chromia brick at 1450°C and tested to 1350°C. During testing, the leads were placed outside hot zone of the furnace and were only exposed to 132°C maximum temperature.

Fig. 4.27. Resistance and temperature profile of the La_2NiO_4 (LNO-1400) based thermistor co-sintered inside YSZ and embedded in high-chromia brick at 1450°C and tested to 1350°C. During testing, the leads were placed outside hot zone of the furnace and were only exposed to 132°C maximum temperature.

Fig. 4.28. Resistance and temperature profile of the La_2NiO_4 (LNO-1400) based thermistor co-sintered inside YSZ and embedded in high-chromia brick at 1450°C and tested at 1350°C, 1300°C, 1250°C, and 1200°C, each with six hour hold.

Task 5 Figures

Figure 5.1- Wireless sensor network architecture for refractory monitoring.

Figure 5.2- Circuit to measure resistance based upon a Wheatstone bridge.

Figure 5.3- Output of the resistance-based sensor interface circuit, showing accuracy >95%.

Figure 5.4- Schematic of a circuit to measure and amplify the output of thermocouple-based sensors.

Figure 5.5- Output of the thermocouple amplifier circuit after being transmitted wirelessly over a wireless sensor network. The accuracy is >95%.

Figure 5.6- Die photograph of the integrated circuit prototype.

Figure 5.7- Wheatstone-bridge integrated circuit performance.

Figure 5.8- Thermocouple amplifier integrated circuit schematic.

Figure 5.9- Thermocouple amplifier integrated circuit performance.

Figure 5.10- Cold-junction compensator integrated circuit schematic and measured performance.

Figure 5.11- Schematic of cold-junction compensation being added to the thermocouple amplifier.

Figure 5.12- Thermocouple amplifier output without cold-junction compensation (left) and thermocouple amplifier output with cold-junction compensation (right).

Figure 5.13- Schematic of circuit for interfacing with capacitive-based sensors.

Figure 5.14- Capacitive-based sensor interfacing integrated circuit performance.

Figure 5.15- (a) Resistive-based sensor interface circuit implemented on our reconfigurable analog architecture. (b) Measured output across a 100K temperature range.

Figure 5.16- Floating Gate current source used to generate bias current on RAMP.

Figure 5. 17- Temperature dependence of an FG transistor from 0-120 °C ambient temperature. Vcg node is swept at every 10°C. A constant Vcg is usually chosen for the design.

Figure 5. 18- Temperature compensation topology (blue) and multiple FGs within the FPAA.

Figure 5. 19- (a) Temperature compensation performance over a range of programming biases. (b) Synthesized comparator circuit performance using a programmed reference value plotted against temperature for a compensated and uncompensated FG current bias.

Figure 5. 20- Energy-harvesting circuitry.

Figure 5. 21- Energy-harvesting system powering a TelosB wireless sensor node.

Figure 5. 22- Schematic and simulated results of the single-clock charge pump for a custom energy-harvesting system.

Figure 5. 23- Linear model based algorithm for the base station /controller side.

Figure 5. 24- Finalized design of wireless sensing node (left) and it interfaced with an embedded thermistor within a furnace brick.

Figure 5.25- Sensing circuit output voltage over experimental furnace run with a temperature hold at 1200°C for 10 hours.

Figure 5.26- Output voltage and temperature versus thermistor resistance.

Figure 5.27- Percentage of packets received at the base station as a function of network size and source data transmission frequency (room temperature; no furnace).

Figure 5.28- Percentage of packets received at the base station as a function of network size and source data transmission frequency (outside furnace at 1400°C, inside an enclosed chamber).

Figure 5.29- Percentage of packets saved as a function of preset threshold T.

Figure 5.30- Actual error at the sensors as a function of the preset threshold T.

Figure 5.31- Impact of 5% data drops on the accuracy of the linear model based scheme.

Task 6 Figures

Fig. 6.1. Schematic of the smart brick with layouts of thermistor.

Fig. 6.2. Schematic of the smart brick with layouts of the IDC

Task 7 Figures

TABLES LIST:
Task 1 Tables

None

Task 2 Tables

Task 3 Tables

Task 4 Tables

None

Task 5 Tables

None

Task 6 Tables

Task 7 Tables

EXECUTIVE SUMMARY:

The objective of the work was to develop refractory "smart bricks", which would contain embedded temperature, strain/stress, and spallation sensors throughout the volume of high-chromia (-Cr_2O_3) refractory brick. The proposed work included work to interconnect the sensors to the reactor exterior, where the sensor signals may be processed by low-power electronics and transmitted wirelessly to a central processing hub. The collected data was incorporated into a model to estimate refractory degradation, a technique that could help monitor the health of the refractory in real-time. The long-term goal of this program was to demonstrate high-temperature, wireless sensor arrays for *in situ* three-dimensional (3-D) refractory monitoring or mapping for slagging gasification systems. The research was in collaboration with HarbisonWalker International (HWI) Technology Center in West Mifflin, PA. HWI is a leading developer and manufacturer of ceramic refractory products for high-temperature applications.

The achievements of the program can be best summarized reviewing each task in order. Task 1 was a project management task that possessed no technical milestones/deliverables. In the case of Task 2, all processing conditions such as ball-milling parameters, pellet pressing pressure and sintering temperature were initially studied and optimized using various silicide-oxide composite compositions. The various silicide-oxide composites displayed high electrical conductivity at high temperatures up to 1000°C, and electrical percolation was achieved even at relatively low metal silicide contents (20-30 vol%). The high-temperature annealing and oxidation studies/measurements also proved that the addition of 40-70 vol% refractory oxide phase could highly reduce the grain growth rates and also oxidation-induced mass gain in the pest oxidation temperature regime, and thus, significantly enhance their oxidation resistance. Therefore, as a result of the studies completed in this task, various silicide-oxide composite compositions showed promising results for high-temperature solid-state sensing applications based on their high chemical and thermal stability, reduced grain growth rates, improved oxidation resistance and high electrical conductivities in a wide temperature range.

In Tasks 3 and 4, the compositions developed in the previous task were used to form sensor preforms to embed into the refractory during the consolidation process. Initial work investigated methods to screenprint or cast ribbons of the composite material directly into the high-chromia refractory composition. Unfortunately, the conductive composites were shown to react with chromia to form unwanted resistive compositions. Therefore, screenprinting and casted ribbons were then deposited between two alumina tapes, and these materials were co-fired to form the sensor preform. This process was shown to be successful, and a portfolio of thermistor, spallation, strain, and thermocouple sensor compositions were formed and tested to 1400ºC in argon for >24 h. Interestingly, silicide/oxide thermocouple architectures were formed for the first time in literature, where their performance were above that of precious metal thermocouples. Thermistor, spallation and thermocouple sensor preforms were then embedded into high-chromia bricks and densified. The smart bricks were tested to 1350ºC for >250 h in argon, but it was found that sensor's performance degraded over time. It was found that silicide oxidation and Pt reaction at the interconnection location was causing the bricks to fail over extended testing. In order to continue development, a conductive oxide composition was used to replace the silicide/oxide compositions at the end of the program. This composition does not form unwanted oxides and does not react with the Pt interconnect wires (but has limited temperature operation range to

1400ºC, unlike the silicides). Full-size smart bricks were fabricated using the oxide composition for complete system testing in Task 7.

In Task 5, the electrical sensing outputs from the smart refractory for temperature and strain measurements were interfaced with an embedded processor and a wireless sensor network was designed for collecting the data at a processing unit for further data analysis. To ensure scalability in terms of number of sensors, efficient network protocols and model based data reduction schemes were designed that reduced the possibility of collisions and data loss during wireless data transfer. For ease of operations, the system parameters can be reconfigured wirelessly post-deployment and the output can be visualized on an intuitive graphical interface.

In Task 6, a rigorous, first-principles, dynamic model of the smart refractory brick was developed. The thermal model was developed by considering properties of the pristine smart refractory bricks as well as that of the slag-infiltrated brick. Using in-house experimental data and data from the open literature, correlations have been developed for thermal conductivity, heat capacity, and dielectric constant for the pristine and the slag-infiltrated brick. Models of embedded sensors namely thermistor, thermocouple, resistive circuit, strain gauge, and an interdigital capacitor, were developed by considering spatially distributed temperature-dependent electric properties of the sensor material. The sensitivities of embedded sensors to temperature changes as well as extent of slag penetration were studied. Traditional Kalman filters (TKF) was implemented for estimating the temperature profile of the refractory brick with simulated measurements from these sensors. Satisfactory estimates of the temperature profile for pristine and slag-infiltrated bricks are found. Because TKF is found to result in poor estimation of the slag penetration length, Extended Kalman filters (EKF) have been implemented for estimating the slag penetration length. It yields superior estimates even though the rate of change of the capacitance becomes higher when slag reaches the sensor. Unscented Kalman filter (UKF) was also studied in this task. Both additive and non-additive process noises are considered. The multi-scale EKF was developed to estimate temperature and slag penetration depth simultaneously using measurements from embedded thermistors and IDCs. Two different multi-scale dual Kalman filter algorithms are compared. In addition, measurements that arrive late have been utilized in KF-estimation frame work. Based on the estimator performance, a series of sensitivity studies were conducted. A sequence measurement out-of-sequence (OOSM) algorithm is proved to be able to take use of the out-of-sequence measurements and provide good estimates in a wide range of the data arrival rate. The study showed the promise of a model-based approach for estimating the temperature profile and the slag penetration profile in the gasifier wall by using ‘smart’ refractory bricks.

In Task 7, the entire system was combined for a demonstration of temperature monitoring of a high-temperature furnace. Smart bricks which contained a thermistor design using the conductive oxide composite composition was tested to 1400ºC in air. The low power electronics and wireless mote technology was used to read the temperature real-time from the interior of the smart brick. This demonstration shows the full implementation of the technology and the potential for application into harsh-environment systems, such as slagging gassifiers. Future work will include full demonstration in a reactor at HWI, and potentially other commercial partners in various energy, chemical and manufacturing industries.

REPORT DETAILS:

Overall Objectives:
The specific project objectives are as follows:

1) Investigate chemical stability, thermomechanical properties, and electrical properties of refractory oxide-silicide composites at temperatures between 750-1450ºC;
2) Define processes to pattern and embed the oxide-silicide composites within high-chromia refractory materials to incorporate temperature and strain/stress sensors into refractory bricks;
3) Develop methods to interface the electrical sensing outputs from the smart refractory with an embedded processor and to design a wireless sensor network to efficiently collect the data at a processing unit for further data analysis;
4) Develop algorithms for model-based estimation of temperature profile in the refractory, slag penetration depth, spallation thickness, and resultant health by using the data from the wireless sensor network.

The subsections that will follow will be organized by Task, and the required report content (Introduction, Experimental Methods, Results and Discussion, and Conclusions) will be included with each distinct subsection defined by these tasks. The tasks for this work were as follows:

Task 1: Project Management and Planning.
Task 2: Fabrication and Characterization of Oxide-Silicide Composites.
Task 3: Sensor Patterning and Embedding.
Task 4: Static and Dynamic Sensor Testing of Smart Refractory Specimens.
Task 5: Data Ex-Filtration Using a Wireless Sensor Network.
Task 6: Model-Based Estimation of Temperature Profile and Extent of Refractory Degradation.
Task 7: Full Wireless Concept Demonstration.

Task 1: Project Management and Planning

1.1 Introduction:

As dictated by the original solicitation, the following was the objective of this task:

"This task shall include all work elements required to maintain and revise the Project Management Plan, and to manage and report on activities in accordance with the plan. It shall also include the necessary activities to ensure coordination and planning of the project with DOE/NETL and other project participants. These shall include, but are not limited to, the submission and approval of required NEPA documentation."

1.2 Experimental Methods:

None

1.3 Results and Discussion:

None

1.4 Conclusions:

As required by the contact, all review meetings, peer-review meetings, and associated documentation (which includes written quarterly reports and the final report) were delivered to DOE in timely manner. The team also completed additional meetings set by the project manager and industrial partner in order to keep close communication between all parties, and to insure proper planning of all tasks, milestones, and deliverables.

Task 2: Fabrication and Characterization of Oxide-Silicide Composites

2.1 Introduction:

The objective of this task was to investigate chemical stability, thermomechanical properties, and electrical properties of refractory oxide-silicide composites at temperatures between 750-1450ºC. These composites are needed for forming the conductive, but stable, interconnects and sensor lines running through the microstructure of the refractory brick. Composite mixtures of refractory materials (Cr_2O_3, Al_2O_3, and ZrO_2) with various silicides (starting with $MoSi_2$, WSi_2, $(Mo,Al)Si_2$. Ti_5Si_3, $CrSi_2$) will be synthesized. Microstructure, chemistry, phase development, thermal expansion, and electrical performance will be characterized as a function of compositions and processing. The specific subtasks were as follows:

Subtask 2.1 Synthesis of Composite Compositions- Typical mixed-oxide processes will be utilized to fabricate the desired oxide-silicide mixtures in-house. Silicide loadings ranging between 20-50 vol% will be investigated. SEM and image analysis will be completed on the powders to characterize mixture mixedness and powder characteristics.

Subtask 2.2 Thermal Processing of Composite Compositions. - Samples will be pressed into bars specimens, and thermal processing matrix in various atmospheres (air, inert, reducing/syngas atmosphere) will be completed up to 1500ºC. XRD will used to better understand phase stability of the composites within oxygen partial pressures. SEM will be used to assess the microstructure and grain morphology after thermal processing at 1000-1500°C (in the various atmospheres).

Subtask 2.3 Composite Material Testing and Characterization.- The following testing and characterization will be completed on the refractory material and composites: 1) Electrical conductivity at 500-1450ºC; 2) static corrosion cup tests with simulated slag; 3) CTE and four-point bending tests; 4) XRD to understand phase stability at various oxygen partial pressures; 5) SEM/EDS to characterize microstructure of composite and passivation layers; 6) other tests as may be required for the modeling work to fully characterize the material.

2.2 Experimental Methods:

2.2.1 Synthesis of composite powder compositions

Commercial $MoSi_2$ (99.5% metals basis), *WSi2 (99.5% metals basis), NbSi2 (99.85% metals basis), TaSi2, CrSi2 (99+% metals basis), ZrSi2 (99.5% metals basis), TiSi2 (99.5% metals basis), Cr2O3 (98+%), Y2O3 (99.9%) and ZrO2 (99+%) powders, all purchased from Alfa Aesar (Tewksbury, MA, USA), were used as starting powders. In addition, fine Al2O3 (99.8%, 8.6 m2/g SSA) and coarse Al2O3 (99.6%, 1.2 m2/g SSA) starting powders used were purchased from Almatis (Leetsdale, PA, USA). Prior to the processing of the composites, phase and microstructure analysis of the starting powders were completed by X-ray* diffraction (XRD, Panalytical X'Pert Pro, Westborough, MA, USA) and field emission scanning electron microscopy (FE-SEM, Hitachi S-4700F, Tokyo, Japan), respectively. The amounts of the metal silicide powders in composite compositions were all determined based on volume. The silicide-oxide volume percentages ranged from 20-80 to 90-10 vol% for different composite systems. The composite powder compositions were then synthesized by a ball-milling procedure in isopropanol to restrict any major oxidation

of the silicides before thermal processing. The composite powders were milled for 15 h followed by 24 h drying while mixing within a beaker. Care has been taken to produce a homogenous mixture of the components without segregation during drying.

2.2.2 Thermal processing and characterization of composites

The composite powders produced in the previous section were uniaxially pressed into pellets having dimensions of 1 cm diameter and 2 mm thickness by using a stainless steel die under the pressure of 13.8 MPa. In addition, pure metal silicide pellets (without addition of oxide particles) were prepared for an understanding of their properties and an effective comparison with the oxide-silicide composites. All composite samples and pure metal silicides were then placed in an alumina crucible and fired in a tube furnace in flowing (10-50 sccm) argon gas to a temperature of 1400°-1600°C. The samples were all held for 2 hours at the maximum temperature and subsequently cooled to room temperature at a rate of 3°C/min. After sintering of the composites was completed, several pellets of each composition were further annealed at 1400°C for 24, 48 and 96 hours, respectively, in order to investigate and understand their thermal stability, microstructural evolution and grain growth kinetics at high temperatures.

Characterization studies were performed regarding their densification or sintering behavior, phase development, chemical and thermal stability, microstructure/grain growth and quantitative image analysis. Densities of the sintered composite samples were measured by employing the Archimedes principle using ethanol (0.789 g/cm^3) as the immersion liquid. The volume fractions of the secondary phases formed after sintering were not included in the theoretical density calculations. Phase analyses of the composite samples were performed both after sintering and annealing by X-ray diffraction (XRD, Panalytical X'Pert Pro, Westborough, MA, USA) with CuKα radiation source. Additionally, quantitative phase analysis studies via Rietveld method were performed by using the MAUD software [2.1] to determine the volume percentages of secondary phases formed after sintering and annealing. Sample preparation for microstructural analyses was carried out by cutting of the samples with a diamond saw, and then fine polishing with SiC sanding papers (600-1200 grits) and diamond paste (0.5 μm). Chemical etching was also utilized by soaking the samples in 2 M HCl or 1:1:1 HCl:HNO_3:H_2O acid solutions for 2 min. Afterwards, field emission scanning electron microscopy (FE-SEM, Hitachi S-4700F, Tokyo, Japan) was used to examine the microstructures of composite samples, and also to study the grain growth of the metal silicides. Average grain size of the metal silicides were determined from their SEM micrographs by using the ImageJ software [2.2].

Additionally, it is known that distribution of metal silicide particles as conductive particles within refractory oxides and uniform mixing is very important in order to achieve better electrical conductivity and thus performance of silicide/oxide composites [2.3]. Therefore, it is crucial to study the distribution of different composites, and particularly the distribution of metal silicide particles within a ceramic oxide matrix by performing image analysis studies via ImageJ software. With this purpose, quantitative image analysis studies on different composite microstructures were performed to develop a new method for determining of degree of distribution (homogeneity or mixedness) of silicide grains within a refractory oxide matrix. The proposed quantitative image analysis method based upon the free-path spacing (average distance between neighboring particles) is optimized for the quantification of the distribution in composite materials. Therefore, multiple straight lines are drawn both horizontally and vertically on a cross-sectional microstructure of a composite, which is already converted to a binary image by using ImageJ software. The free-path spacing data between all the neighboring particles are recorded as profile

plots as a function of distance, and measured by processing the data in the Microsoft Excel. Then the arithmetic mean of the free-path spacing on each line are first individually calculated. This step is followed by calculating the arithmetic mean ($\bar{X}$) and standard deviation (s) of the all free-path spacing values obtained for total number of lines analyzed. Since the mean free-path spacing values are different for each line, and the standard deviation value is also depending on the mean value in that case, the coefficient of variation (C_V) is selected to be used for determining the degree of distribution or homogeneity of the composites. Therefore, C_V is utilized as the distribution (D) index in this microstructural quantitative image analysis method, and thus presented as:

$$D\ index = C_V = \frac{s}{\bar{X}}$$

Since all the free-path spacing and their arithmetic mean values on each line are the same, this index exhibits a zero value for a perfectly homogeneous composite material. But the D index diverges from zero and then tends to increase up to one and/or above one, if the particles are agglomerated at a certain level. Therefore, this method and its outcome, the D index, can be efficiently used to quantify the degree of distribution and to compare the distribution levels of different composite samples.

2.2.3 Composite material testing at high-temperatures

For electrical measurements, a high temperature test rig was made using a high purity 4-bore alumina tube and platinum connection leads. The rectangular bar samples with average dimensions of 20×4×4 mm were prepared from the large cylindrical pellets for a standard measurement (ASTM B193-16) [2.4] and then, they connected to the test rig and the entire system was sealed in a tube furnace. Electrical resistance of the sintered composite samples was measured with a digital multimeter (Keithley 2100, Tektronix, Beaverton, OR, USA) by the DC four-probe method. A B-type of thermocouple was also used to monitor the temperature. The electrical measurements were conducted at temperatures up to 900°-1000°C in argon atmosphere to avoid material degradation. The resistance data was acquired as a function of time and temperature by LabView and Keithley programs, and lastly, the electrical resistivity/conductivity were calculated by using the specific sample dimensions. The coefficients of thermal expansion (CTE) of the silicide-oxide composites were also measured by using a horizontal pushrod dilatometer (Netzsch, Burlington, MA, USA) up to 1000°C.

For the oxidation studies, very small rectangular pellets having 0.1–0.3 cm^2 surface area were prepared via cutting and polishing processes, and their dimensions (width × length × height) were measured before oxidation tests for their surface area calculations. The high-temperature oxidation studies of the silicide-oxide composite samples were conducted using a thermogravimetric analyzer (TGA, Pyris 1, PerkinElmer, Shelton, CT) in flowing ambient air (20 ml/min). The samples were heated from 50°C to 800°C with a heating rate of 10°C/min, and the mass changes (mg/cm^2) were calculated using the recorded mass changes and the calculated specific sample surface areas.

2.3 Results and Discussion:

2.3.1 Subtask 2.1 - Synthesis of composite powder compositions

This section reports the (i) initial phase and microstructural characterization of the starting powders, and (ii) characterization of the silicide-oxide composite powder compositions.

2.3.1.1 Phase and microstructural analysis of starting powders

Phase and microstructural analysis of the starting metal silicide and refractory oxide ceramic powders were initially performed to get important knowledge about the selected precursor powders. X-ray diffraction (XRD) patterns of the starting metal silicide powders are presented in Figure 2.1. Some impurities such as molybdenum metal (Mo), silicon metal (Si) and silicon dioxide (SiO_2) in quartz form were found in the starting $MoSi_2$ powder. XRD result of the WSi_2 powder also implied the existence of SiO_2 in quartz form as an impurity, in addition to the major

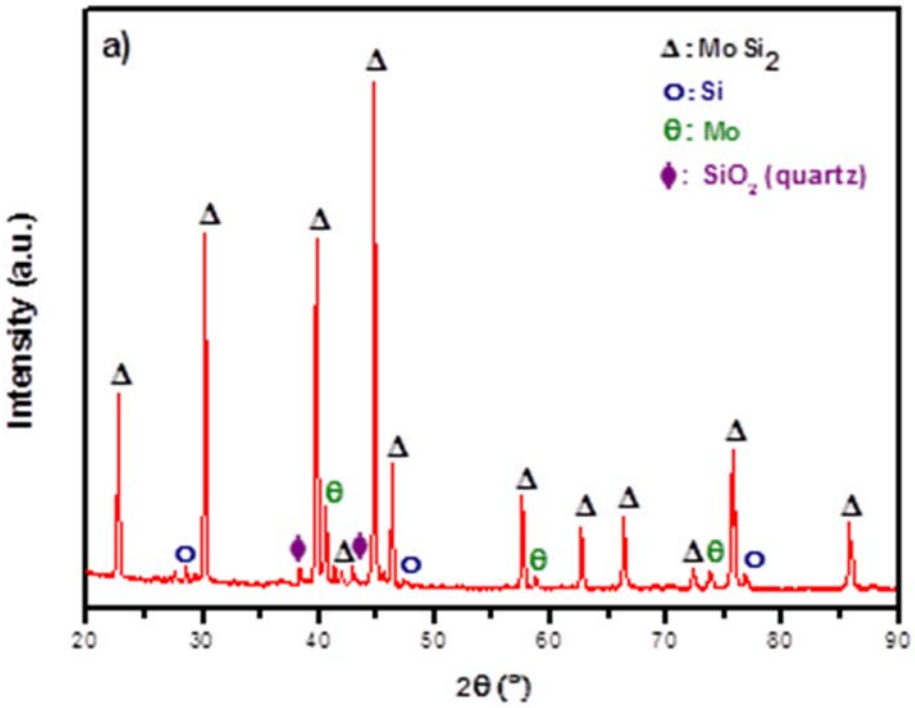

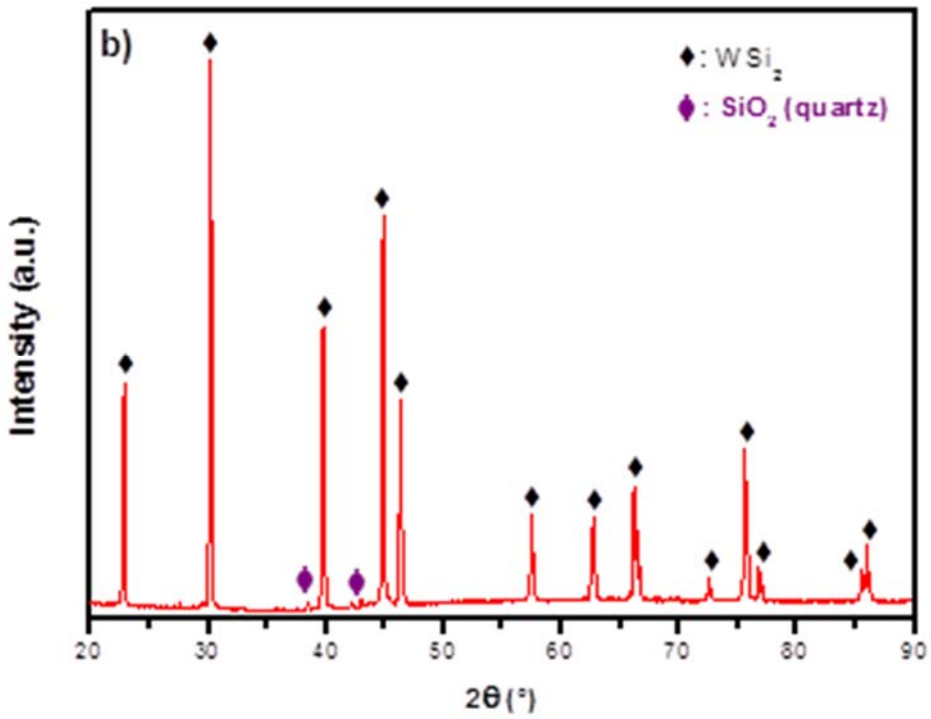

Figure 2.1. XRD patterns of the starting metal silicide powders: (a) $MoSi_2$, (b) WSi_2, (c) $TaSi_2$, (d) $NbSi_2$, (e) $CrSi_2$, and (f) $TiSi_2$.

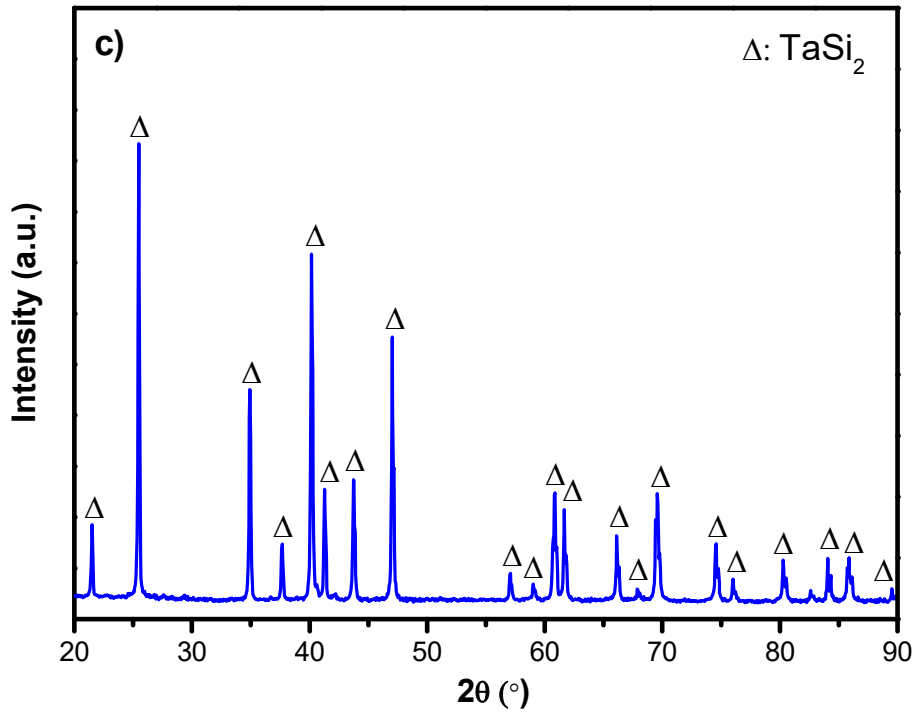

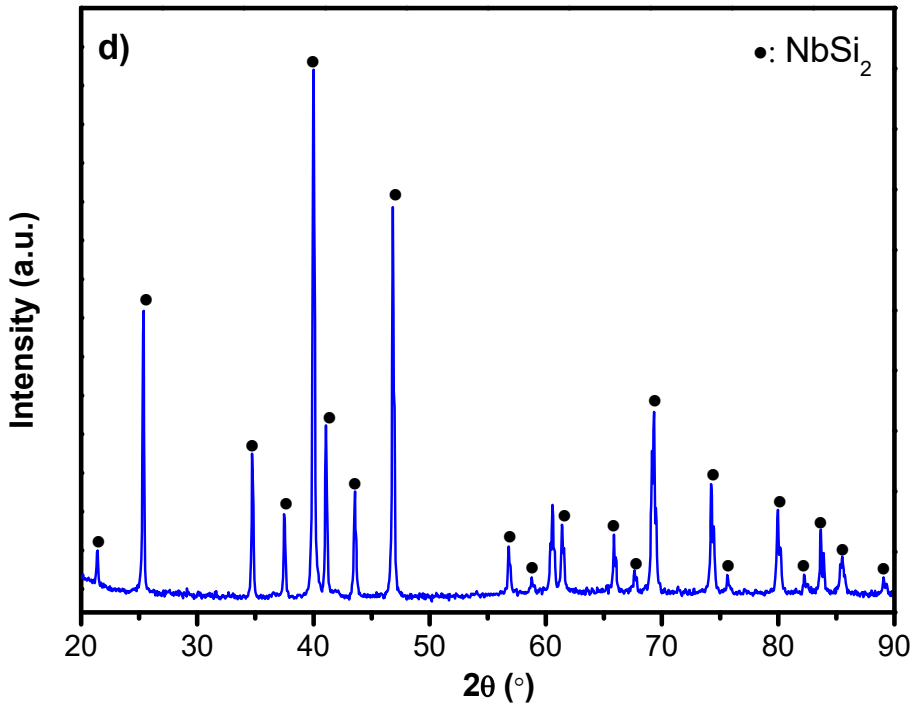

Figure 2.1. (continued) XRD patterns of the starting metal silicide powders: (a) $MoSi_2$, (b) WSi_2, (c) $TaSi_2$, (d) $NbSi_2$, (e) $CrSi_2$, and (f) $TiSi_2$.

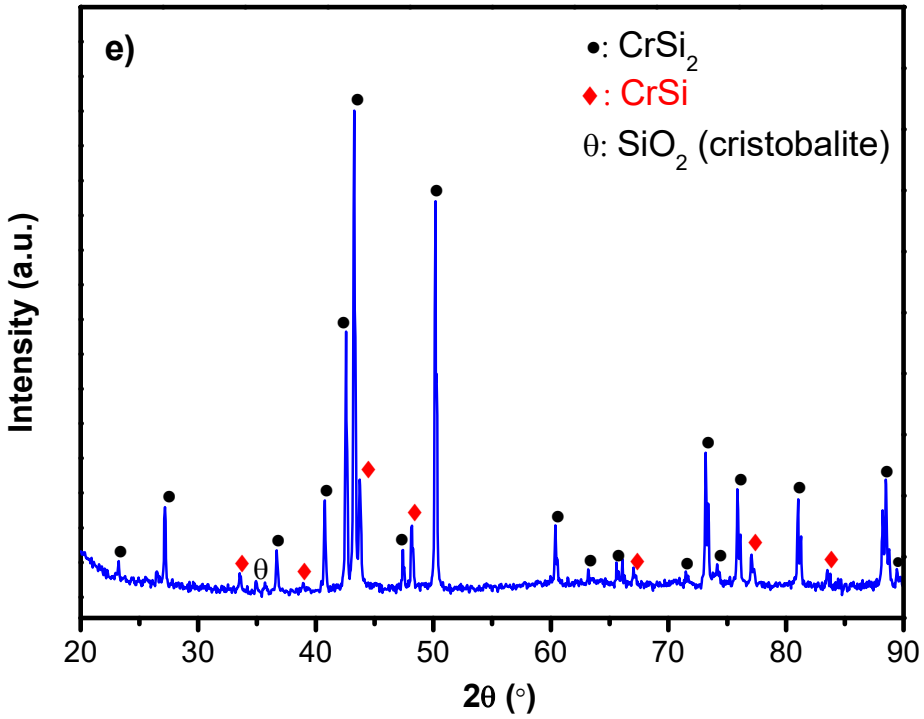

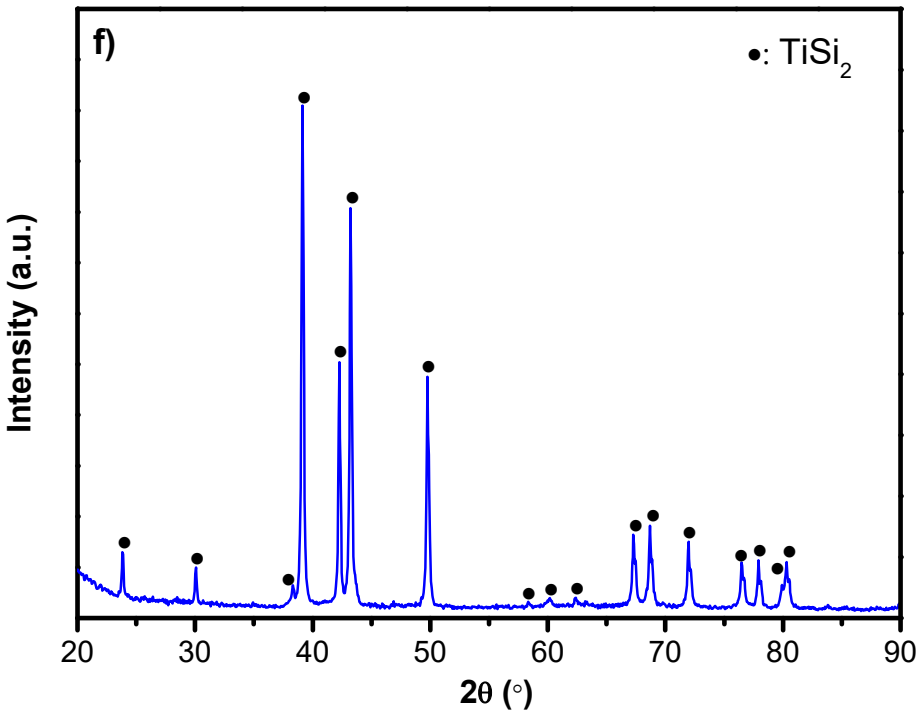

Figure 2.1. (continued) XRD patterns of the starting metal silicide powders: (a) $MoSi_2$, (b) WSi_2, (c) $TaSi_2$, (d) $NbSi_2$, (e) $CrSi_2$, and (f) $TiSi_2$.

WSi_2 peaks. The XRD results clearly indicated that the $TaSi_2$, $NbSi_2$, and $TiSi_2$ precursor powders do not contain any impurities. On the other hand, some impurities such as SiO_2 in the cristobalite form and also CrSi were found in the starting $CrSi_2$ powder. In addition, Figure 2.2 shows the XRD patterns of the starting refractory oxide ceramic powders. The XRD results indicated that the alumina, yttria and chromium oxide powders do not contain any impurities. Similarly, presence of any impurities was not identified for the monoclinic-structured zirconia powder. However, it is important to note that it contains 2% HfO_2 as stated by the vendor company (Alfa Aesar) in the related technical document.

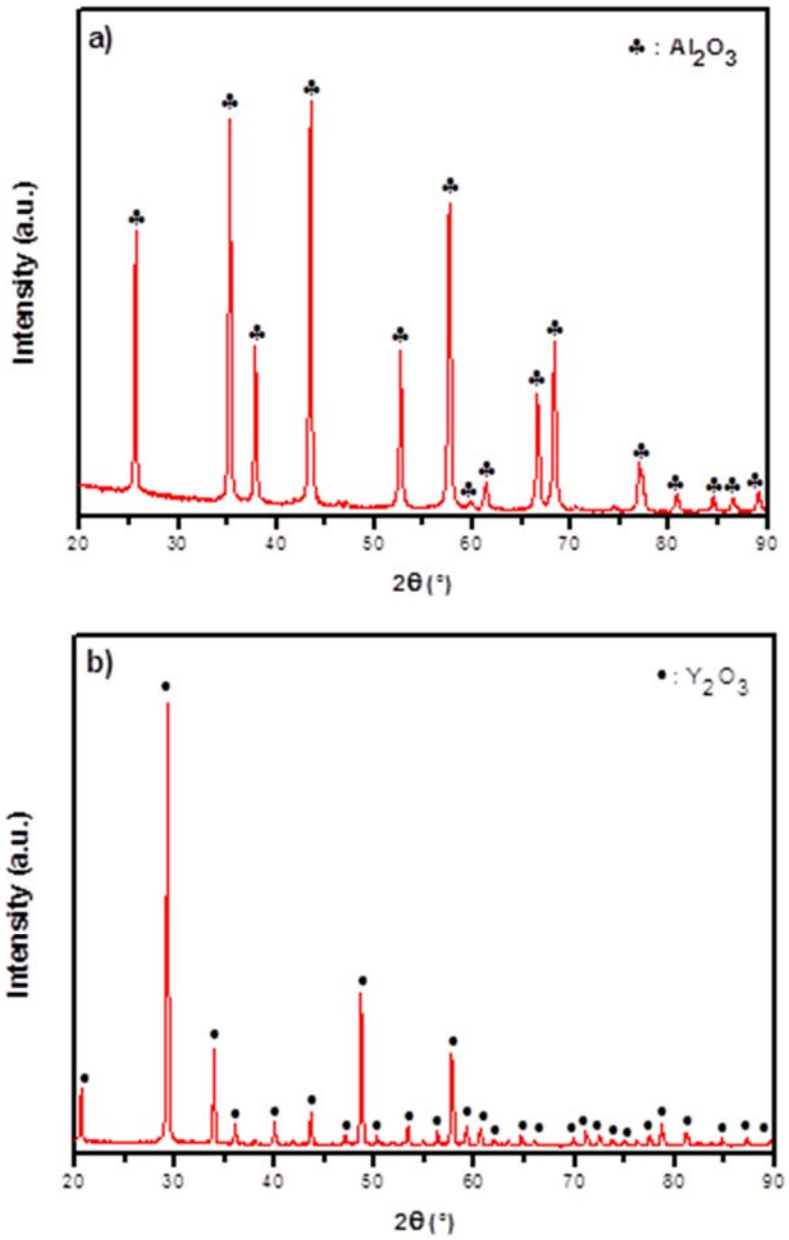

Figure 2.2. XRD patterns of the starting refractory oxide ceramic powders: (a) Al_2O_3, (b) Y_2O_3, (c) Cr_2O_3, and (d) ZrO_2.

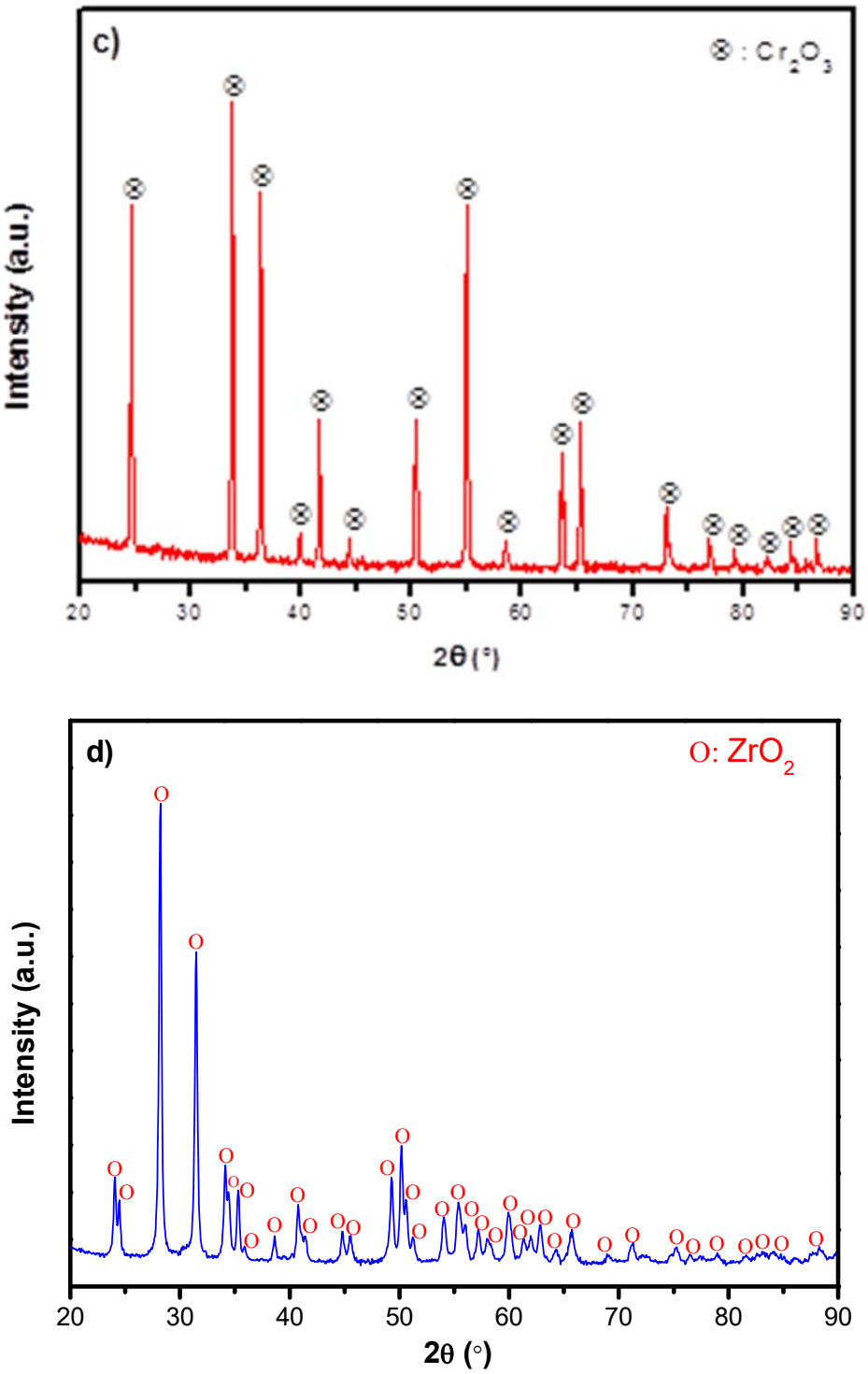

Figure 2.2. (continued) XRD patterns of the starting refractory oxide ceramic powders: (a) Al_2O_3, (b) Y_2O_3, (c) Cr_2O_3, and (d) ZrO_2.

After the completion of the phase analyses, microstructures of the starting powders were also characterized by Scanning electron microscopy (SEM). The chromia powders from HWI (Accrox 5891 and G5099) and commercially available Alfa Aesar (Cat. #: 12286) are shown in the SEM micrograph in Figure 2.3. The micrographs presented that the original chromia has a spherical morphology for all powders. The Accrox 5891 has a size in the range of 2-10 µm, where the other two precursor powders are much finer. Their average diameters are roughly in the range of 0.5-1.0 µm, which was later confirmed with a laser diffraction technique.

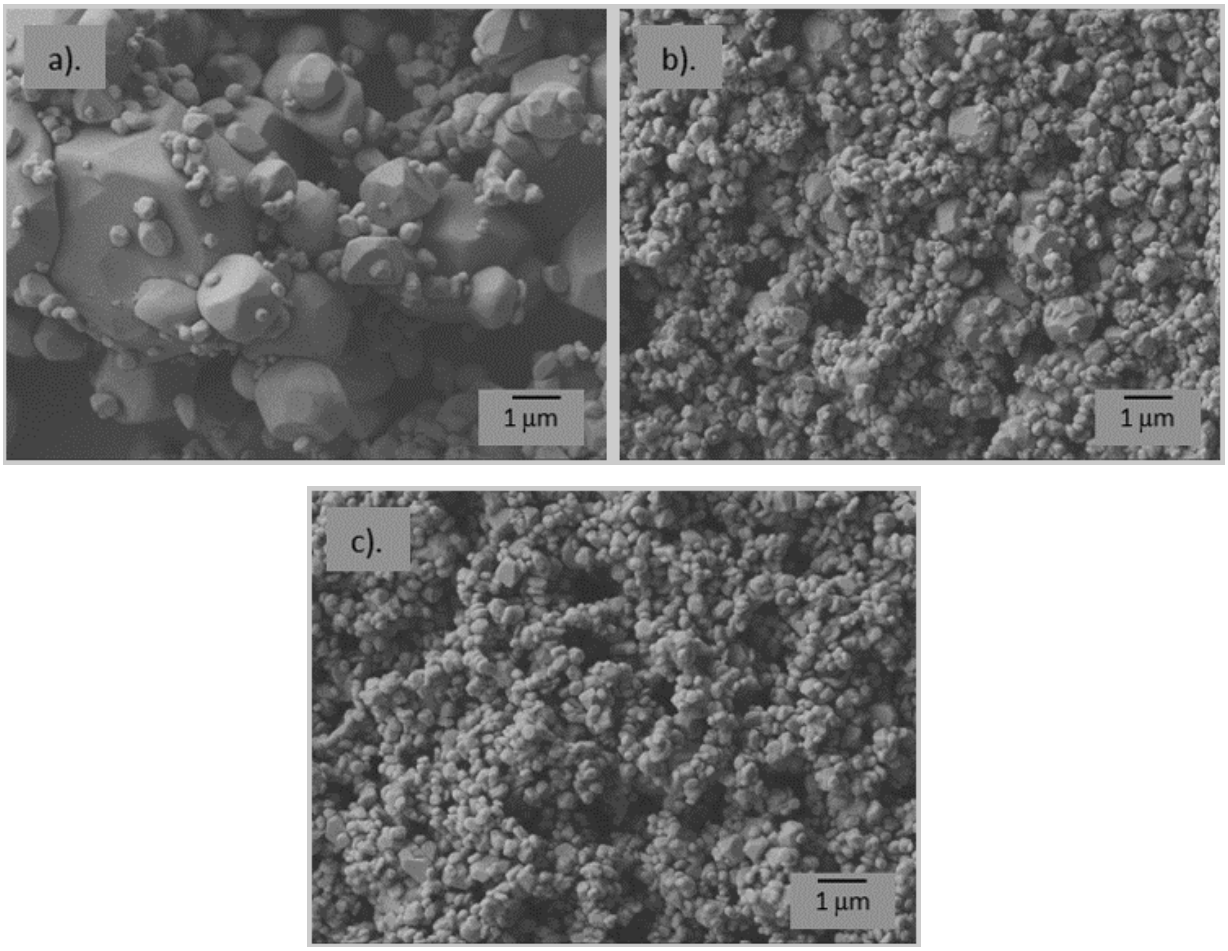

Figure 2.3. SEM micrographs of the starting HWI chromia powders (a) Accrox 5891, (b) Accrox G5099, and (c) commercial chromia powder from Alfa Aesar (#12286).

In Figure 2.4 (a-b-c-d), scanning electron microscope (SEM) micrographs of the $MoSi_2$, WSi_2, Al_2O_3 and Y_2O_3 precursor powders are presented. SEM micrographs demonstrated that the average particle size of the $MoSi_2$ and WSi_2 particles were approximately 5 µm and 7 µm, respectively. It was determined that Al_2O_3 particles have 0.4 µm average particle size and equiaxed shape, while the average particle size of Y_2O_3 particles is 3 µm. As a result of the SEM analyses, it can be noted that $MoSi_2$, WSi_2, and Y_2O_3 powders are composed of micron-sized particles.

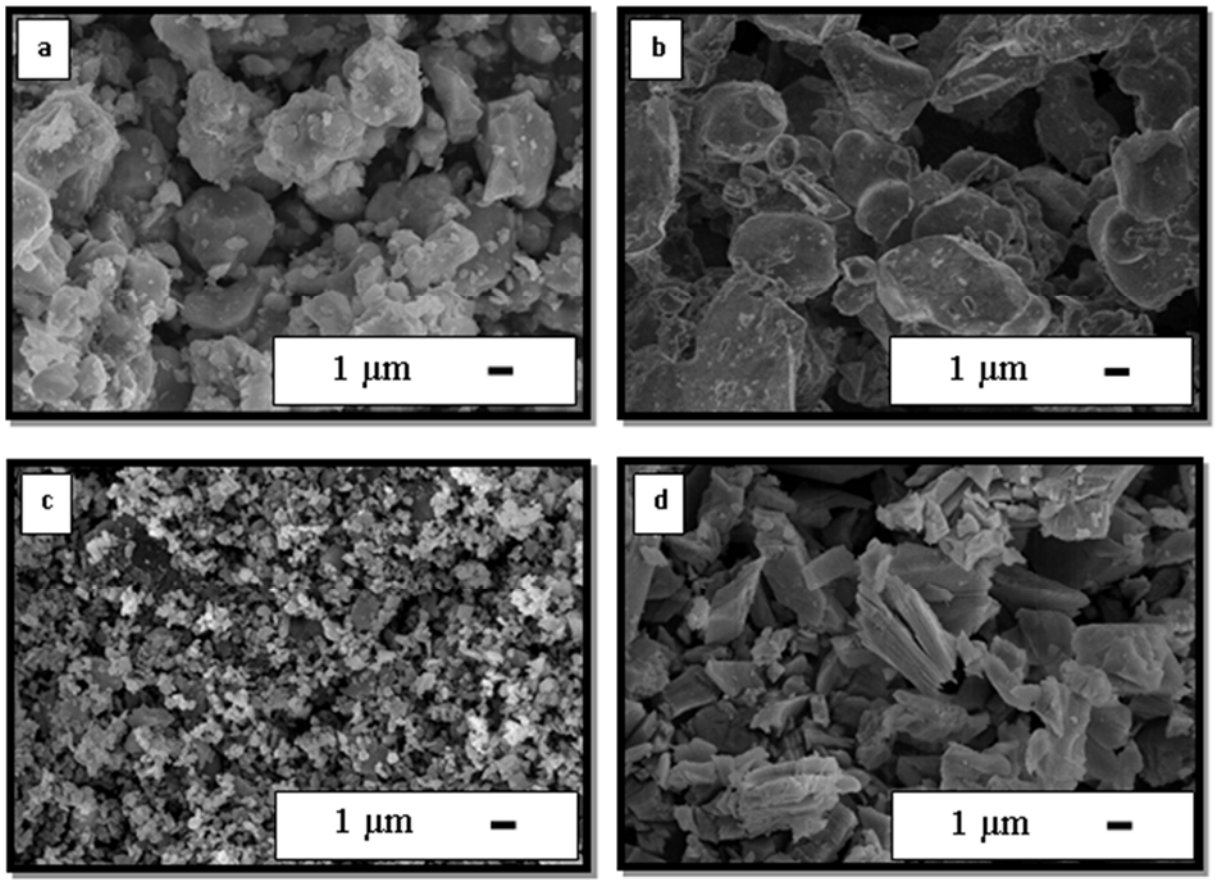

Figure 2.4. SEM micrographs of the commercial starting (a) $MoSi_2$, (b) WSi_2, (c) Al_2O_3, and (d) Y_2O_3 powders.

2.3.1.2 Microstructral analysis of composite powder compositions

Figure 2.5 (a-b-c) presents the SEM microstructures of (60-40) vol% $MoSi_2$-Al_2O_3, (60-40) vol% $MoSi_2$-Y_2O_3, and (60-40) vol% $MoSi_2$-ZrO_2 composite powders prepared via ball-milling for 15 h. These results clearly indicated that the distribution of the $MoSi_2$ particles is more homogeneous in Y_2O_3 and ZrO_2 matrix than their distribution in Al_2O_3 matrix. This can be explained by considering average particle size of the precursor powders. The average particle size of $MoSi_2$, Y_2O_3, and ZrO_2 precursor powders were 5 µm, 3 µm, and 12 µm, respectively. Also it is demonstrated that soft agglomerates of micron-sized ZrO_2 precursor particles were broken apart into ~1-2 micron-sized particles during ball balling process. Therefore, highly homogeneous distribution was obtained by ball-milling for (60-40) vol% $MoSi_2$-Y_2O_3 and (60-40) vol% $MoSi_2$-ZrO_2 composite powders due to similar micron-sized particle size of $MoSi_2$ with Y_2O_3 and ZrO_2. In the case of the $MoSi_2$-Al_2O_3 composite powders, distribution of silicide particles was not homogeneous due to submicron-sized (around 0.4 µm) fine Al_2O_3 particles and their initial agglomeration during ball-milling process.

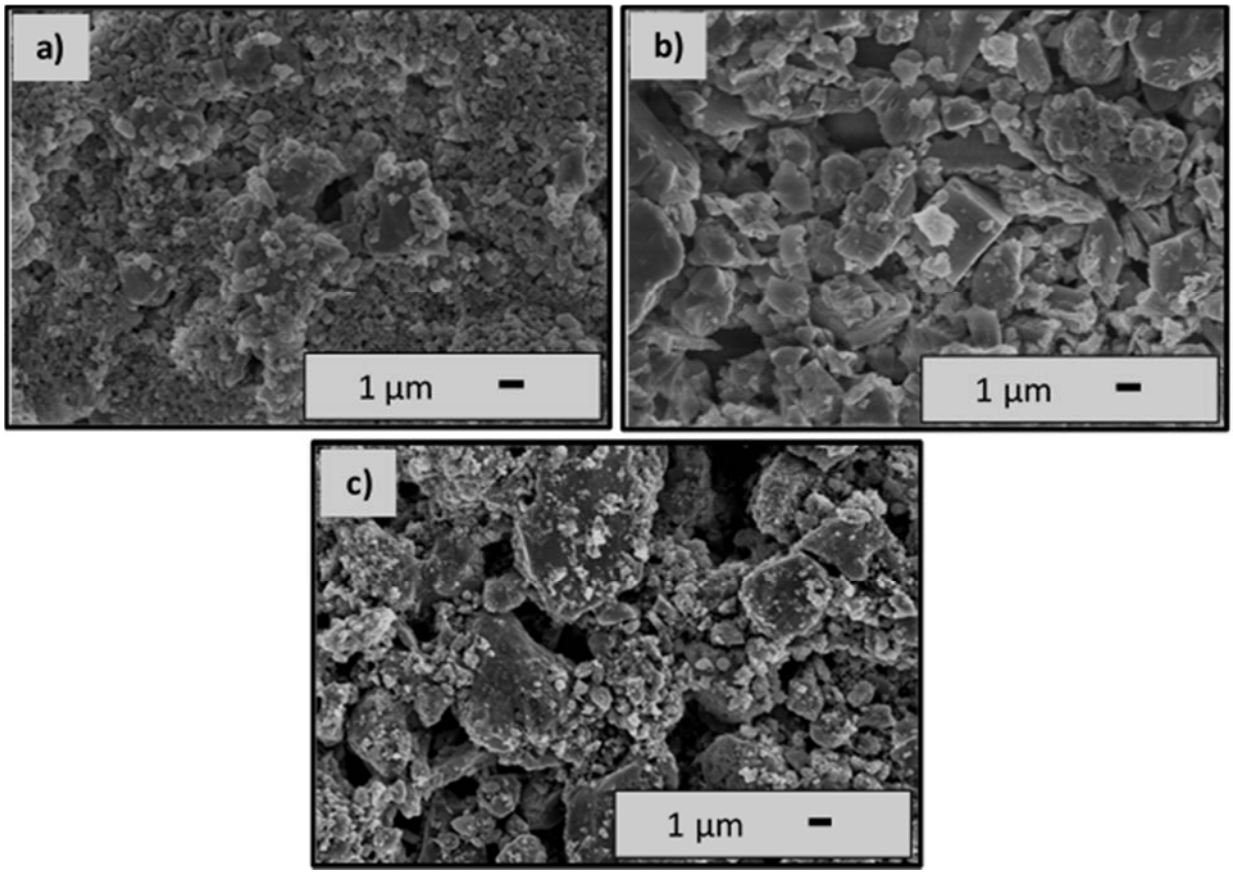

Figure 2.5. SEM micrographs of the (a) (60-40) vol% $MoSi_2$-Al_2O_3, (b) (60-40) vol% $MoSi_2$-Y_2O_3, and (c) (60-40) vol% $MoSi_2$-ZrO_2 composite powders prepared via ball-milling for 15 h.

Figure 2.6 (a-b-c) shows the SEM microstructures of (60-40) vol% WSi_2-Al_2O_3, (60-40) vol% WSi_2-Y_2O_3, and (60-40) vol% WSi_2-ZrO_2 composite powders prepared via ball-milling for 15 h. Similar to the $MoSi_2$-based composites, these results clearly presented that distribution of the WSi_2 particles is more homogeneous in Y_2O_3 and ZrO_2 matrix than their distribution in Al_2O_3 matrix based on average size of the precursor powders. The average size of WSi_2 particles (~7 µm) was similar with average size of the Y_2O_3 particles (precursor powder) and ZrO_2 particles (after ball-milling), which resulted in more homogeneous distribution than that of the WSi_2-Al_2O_3 composite powders. As a result, highly homogeneous distribution was obtained by ball-milling for (60-40) vol% WSi_2-Y_2O_3 and (60-40) vol% WSi_2-ZrO_2 composite powders. However, the distribution of silicide particles was not homogeneous for the WSi_2-Al_2O_3 composite powders like the $MoSi_2$-Al_2O_3 powders. These results can be considered as an indication of obtaining more homogeneous distribution for $MoSi_2$-Y_2O_3, $MoSi_2$-ZrO_2, WSi_2-Y_2O_3, and WSi_2-ZrO_2 after sintering at high temperature under argon atmosphere. It is important to note that this knowledge is very important, since the initial distribution of the particles after ball-milling is known to have a significant influence on the sintering or densification kinetics, which can result in different physical properties such as electrical percolation and thermal properties.

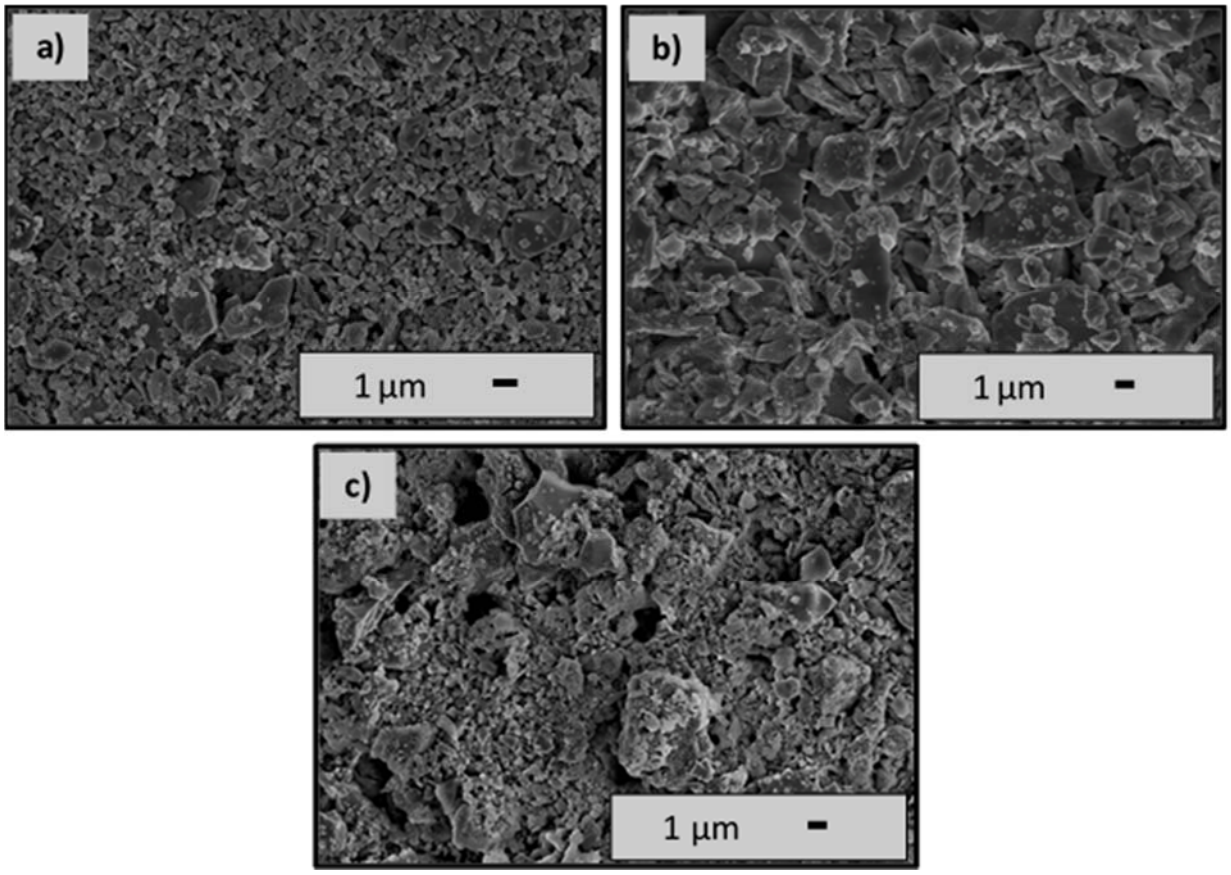

Figure 2.6. SEM micrographs of the (a) (60-40) vol% WSi_2-Al_2O_3, (b) (60-40) vol% WSi_2-Y_2O_3, and (c) (60-40) vol% WSi_2-ZrO_2 composite powders prepared via ball-milling for 15 h.

2.3.2 Subtask 2.2 - Thermal processing and characterization of composite compositions

This section reports the (i) densification and sintering behavior (kinetics), (ii) phase development, chemical and thermal stability, (iii) microstructural evolution, and (iv) quantitative image analysis of the various silicide-oxide composite compositions.

2.3.2.1 Densification behavior of the composites

Density of the samples was measured using Archimedes principle in ethanol. The relative density of the metal silicide-refractory oxide composites as a function of sintering temperature is presented in Figure 2.7 (a-d). The data presents the densification behavior of the $MoSi_2$-, WSi_2- and $ZrSi_2$-based composites with the addition of 20 vol% alumina, yttria, zirconia and chromia particles. It is evident that the relative densities significantly increased with increasing sintering temperature from 1200°C to 1600°C. The zirconia-based samples reached almost full densification at 1500°C, regardless of the type of silicide addition. In addition, ZrO_2-$ZrSi_2$ composite showed lowest relative densities at all temperatures with respect to other zirconia-based composites. The alumina-based samples showed 86-89% relative density values at 1500°C, which further improved to 91-98% levels when the sintering temperature is increased to 1600°C. Among the silicides used, $MoSi_2$ showed the higher relative density (98%) compared to WSi_2 (91%) and $ZrSi_2$ (92%) as presented. The yttria-based composite samples displayed a maximum density of 97, 90 and 75%,

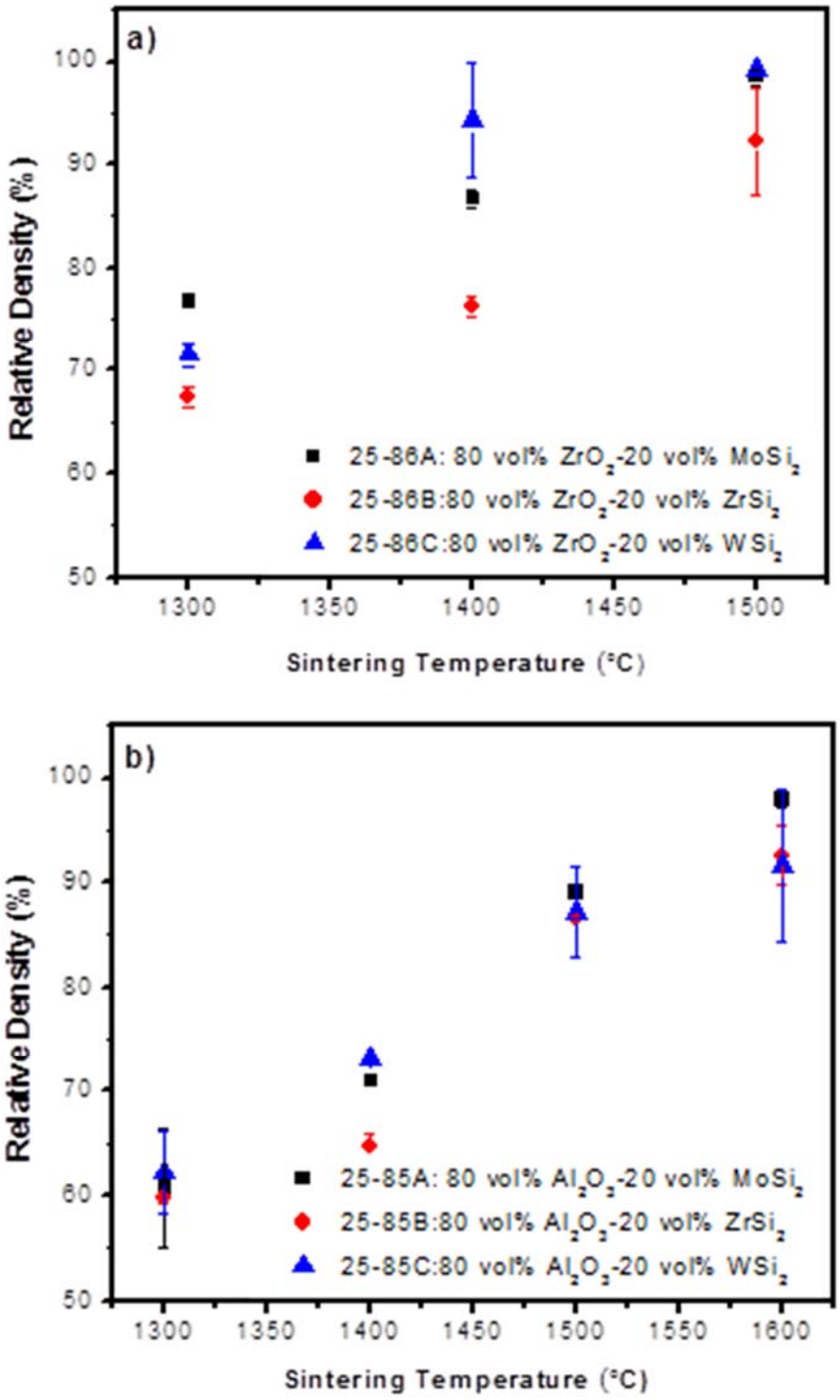

Figure 2.7. Relative density of the 20-80 vol% (a) silicide-zirconia, (b) silicide-alumina, (c) silicide-yttria, and (d) silicide-chromia composite compositions as a function of sintering temperature (Silicides: $MoSi_2$, WSi_2, $ZrSi_2$).

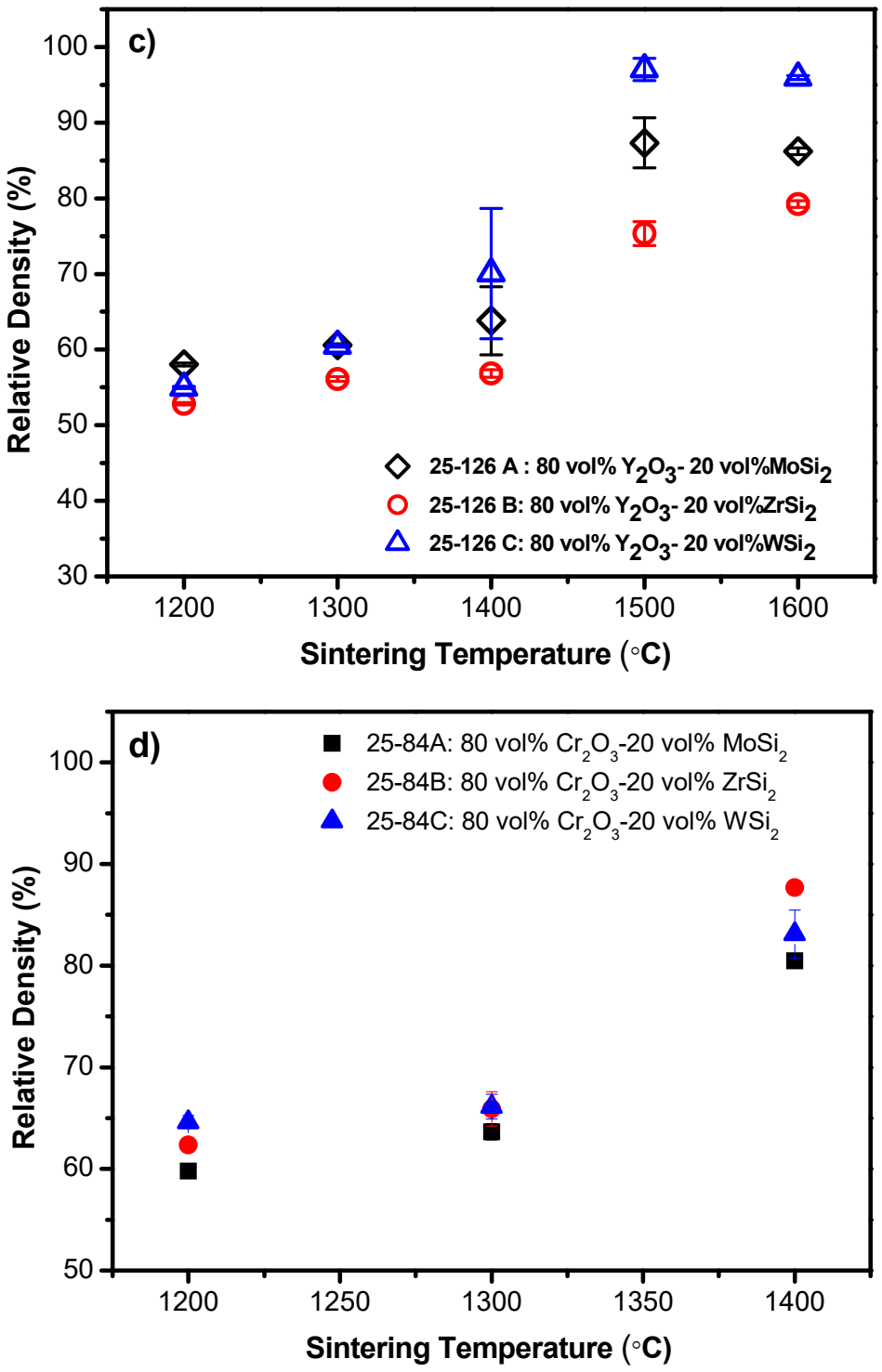

Figure 2.7. (continued) Relative density of the 20-80 vol% (a) silicide-zirconia, (b) silicide-alumina, (c) silicide-yttria, and (d) silicide-chromia composite compositions as a function of sintering temperature (Silicides: $MoSi_2$, WSi_2, $ZrSi_2$).

respectively, at 1500°C. When the temperature was further increased to 1600°C, the WSi_2-Y_2O_3 composite sample did not show a significant change. However, the $MoSi_2$-Y_2O_3 composite sample showed 6% decrease, while the $ZrSi_2$-Y_2O_3 composite sample displayed around 4% increase in the relative density. The decrease in relative density observed for the $MoSi_2$-Y_2O_3 composite sample may be due to potential decomposition of the $MoSi_2$ phase into MoO_3 and SiO_2 at higher temperatures. Figure 2.7d shows the density of chromia-based composite samples as a function sintering temperature. The relative densities were in the range of 80-87%, even though the sintering temperature was increased to 1400°C. Among the Cr_2O_3-based composite compositions, $ZrSi_2$-Cr_2O_3 composite sample showed highest density of 87.7% after sintering at 1400°C, which was followed by WSi_2-Cr_2O_3 (83.1%) and $MoSi_2$-Cr_2O_3 (80.4%). The results clearly indicated that the chromia-silicide composite samples require relatively higher sintering temperature to achieve better densification.

In addition, densification studies were conducted to determine the effect of high-temperature annealing on the densification behavior of the composites. The relative density of the composites after sintering at 1600°C for 2 h and then annealing at 1400°C for 24 and 48 h is presented in Table 2.1. These results showed that $MoSi_2$-Al_2O_3, $MoSi_2$-ZrO_2, and WSi_2-Al_2O_3 composites have higher relative densities (> 84.9%) after long-term annealing at 1400°C for 48 h in comparison to other composites and pure silicides. Also it can be clearly seen that the relative density of the $MoSi_2$-Al_2O_3, WSi_2-Al_2O_3, and WSi_2-coarseAl_2O_3 composites slightly decreased after long-term

Table 2.1. The relative density of the $MoSi_2$- and WSi_2-based composites and pure metal silicides after sintering at 1600°C for 2 h and then annealing at 1400°C for 24 and 48 h.

Composite samples	Relative Density (%)		
	After sintering at 1600°C-2h	After annealing at 1400°C-24h	After annealing at 1400°C-48h
Pure $MoSi_2$	83.45	84.22	80.53
(60-40) vol% $MoSi_2$-Al_2O_3	85.17	85.86	84.94
(60-40) vol% $MoSi_2$-coarseAl_2O_3	77.70	76.69	78.94
(60-40) vol% $MoSi_2$-ZrO_2	84.43	84.63	88.69
Pure WSi_2	81.69	81.58	80.15
(60-40) vol% WSi_2-Al_2O_3	88.59	88.83	87.04
(60-40) vol% WSi_2-coarseAl_2O_3	79.78	80.20	77.61
(60-40) vol% WSi_2-ZrO_2	85.00	84.93	-

annealing at 1400°C. Pure $MoSi_2$ and pure WSi_2 exhibited a similar trend with these composites, since their relative densities decreased in the percentage ranging from 1.4 to 3.7. Among all other composites, a significant decrease in the relative density was observed for WSi_2-coarse Al_2O_3 composite after annealing at 1400°C for 48 h. This decrease and low density for this composite may be explained by effect of coarse Al_2O_3 precursor powder and grain coarsening during annealing. On the other hand, the relative density of the $MoSi_2$-coarseAl_2O_3 and $MoSi_2$-ZrO_2 composites increased after long-term annealing. All these changes may be interrelated with precursor powder characteristics, grain coarsening and secondary phase formation during annealing process.

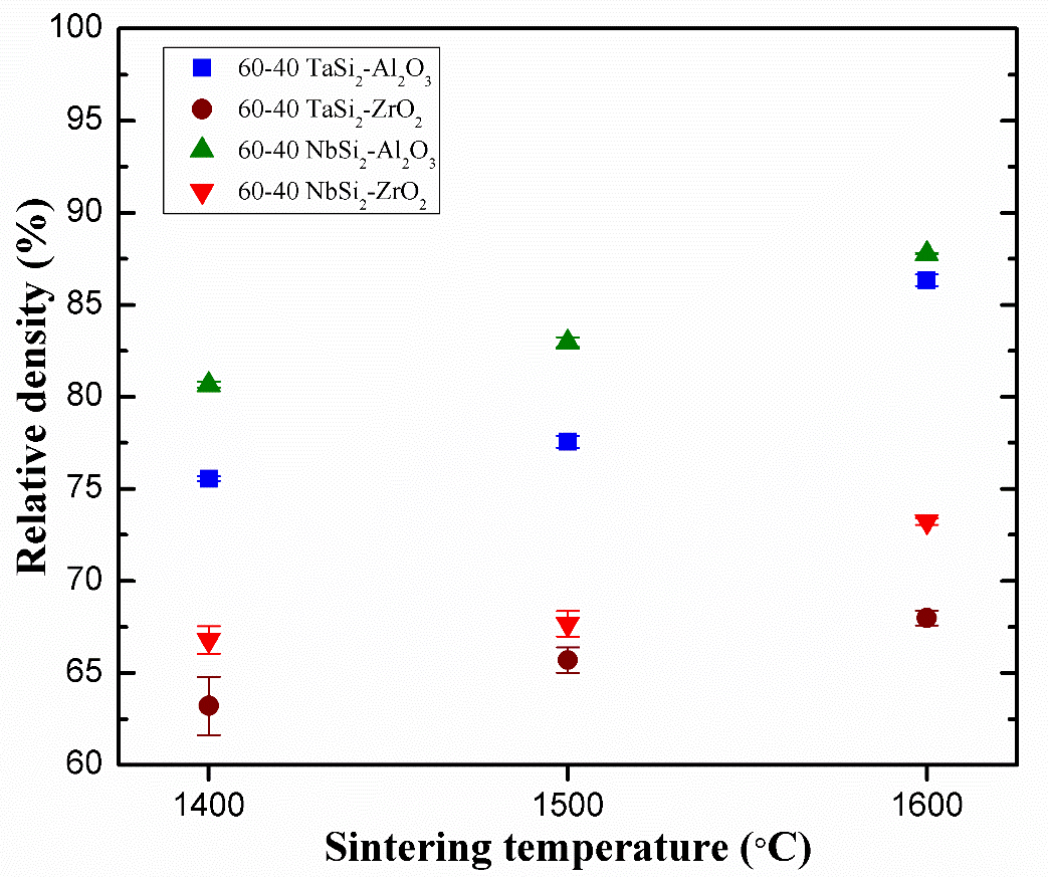

Figure 2.8. Densification behavior of the (60-40) vol% $NbSi_2$- and $TaSi_2$-based composites with addition of alumina and zirconia as a function of temperature (1400°-1600°C).

The densification studies were also performed on the $NbSi_2$- and $TaSi_2$-based composites fabricated via addition of alumina and zirconia particles, based on the 60-40 metal silicide-refractory oxide volume percentages. The sintering temperature ranged from 1400°C to 1600°C in argon atmosphere. Figure 2.8 presents the relative densities of the $NbSi_2$- and $TaSi_2$-based composites as a function of sintering temperature. The results showed that $NbSi_2$-Al_2O_3 and $TaSi_2$-Al_2O_3 composites have significantly higher relative densities than $NbSi_2$-ZrO_2 and $TaSi_2$-ZrO_2 composites at 1400°-1600°C. The $NbSi_2$-Al_2O_3 composite exhibited higher relative density (80.7%) at 1400°C, which then increased to 87.8% with increasing sintering temperature to

1600°C. In addition, $NbSi_2$-Al_2O_3 and $TaSi_2$-Al_2O_3 composites displayed similar relative densities (86.3-87.8%) at 1600°C. On the other hand, the relative densities of the $NbSi_2$-ZrO_2 and $TaSi_2$-ZrO_2 composites were found to be substantially lower, mostly less than 67.7% at 1400°C and 1500°C. The increase in their relative densities ranged from 2.3 to 5.5% with increasing sintering temperature from 1500° to 1600°C. These results demonstrated that fine alumina particles (0.4 μm) have the ability to fill voids between larger micron-sized metal silicide particles, enhancing particle packing and densification during sintering. The relatively low densities of the $NbSi_2$-ZrO_2 and $TaSi_2$-ZrO_2 composites at 1400°-1500°C could be explained by insufficient thermal energy for sintering and possible formation of microcracks due to the ZrO_2 monoclinic-tetragonal phase transition at around 1170°C, respectively. Based on the results discussed above, it was found that significantly higher densities could be obtained by sintering at 1600°C.

Additionally, their apparent densities and porosities were calculated to investigate their densification more efficiently as a function of composition and increasing sintering temperature. The apparent densities of these composites are listed in the Table 2.2. At the 30-70 volume percentages, the apparent density of the $NbSi_2$-Al_2O_3 and $TaSi_2$-Al_2O_3 composites increased with increasing sintering temperature from 1400° to 1500°C, but then decreased to the lower values at 1600°C. A similar trend was also observed for the $NbSi_2$-Al_2O_3, $TaSi_2$-Al_2O_3 and $TaSi_2$-ZrO_2 composites, which have 60-40 volume percentages. The decreased apparent densities for these composites, particularly from 1500° to 1600°C, could be attributed to the decreased porosity levels and enhanced densification at high sintering temperature. On the other hand, no significant changes were observed in the apparent densities of all $NbSi_2$-ZrO_2 and 30-70 $TaSi_2$-ZrO_2 composites at

Table 2.2. Apparent density of the $NbSi_2$- and $TaSi_2$-based composites with the addition of Al_2O_3 and ZrO_2 particles, as function of the sintering temperature.

Composite	Apparent density (g/cm^3)		
	1400°C	1500°C	1600°C
30-70 $NbSi_2$-Al_2O_3	4.41	4.49	4.25
60-40 $NbSi_2$-Al_2O_3	4.81	5.04	4.98
30-70 $NbSi_2$-ZrO_2	5.74	5.84	5.83
60-40 $NbSi_2$-ZrO_2	5.74	5.75	5.75
30-70 $TaSi_2$-Al_2O_3	5.38	5.53	5.28
60-40 $TaSi_2$-Al_2O_3	6.85	7.02	6.66
30-70 $TaSi_2$-ZrO_2	6.78	6.92	6.88
60-40 $TaSi_2$-ZrO_2	7.64	7.94	7.60

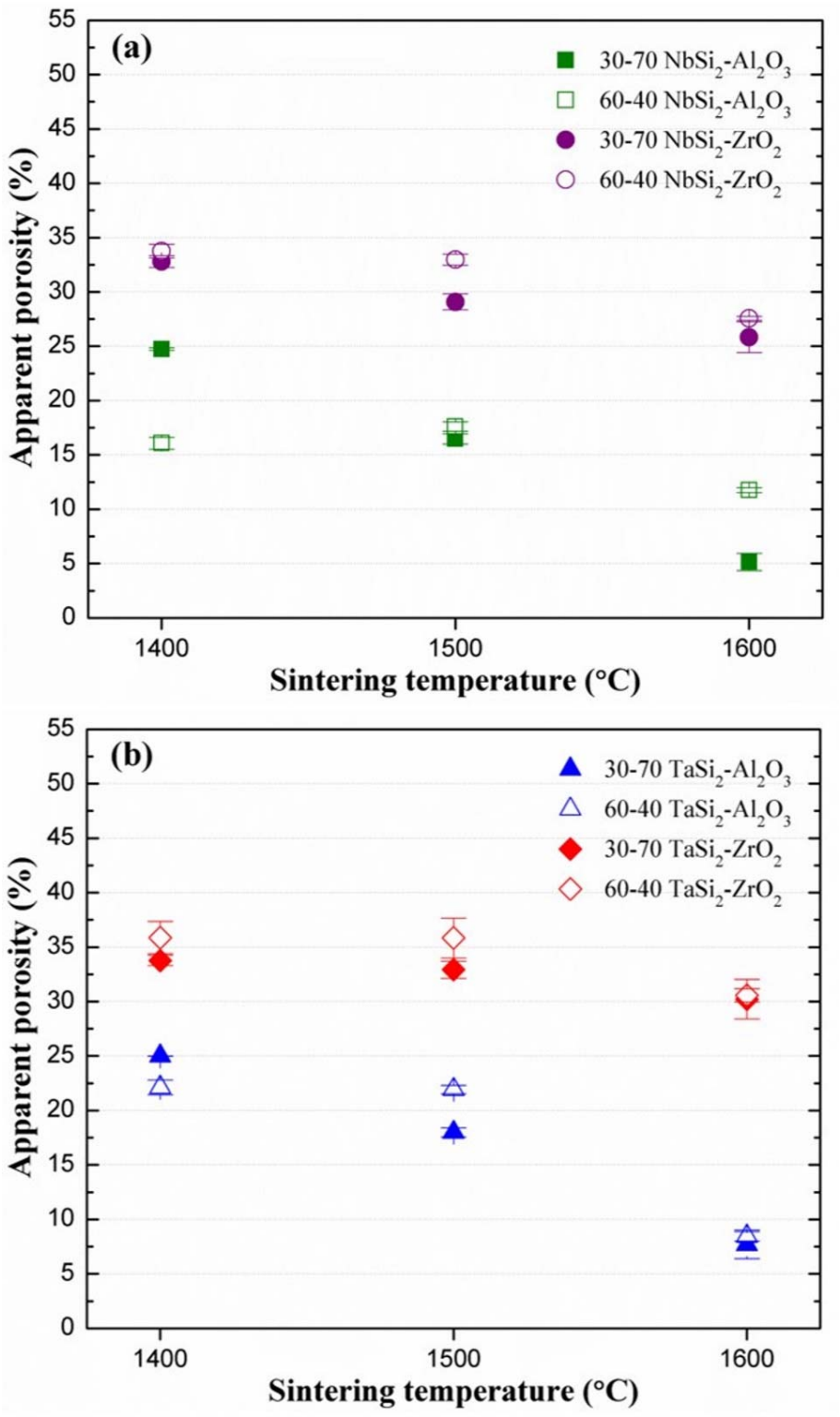

Figure 2.9. Apparent porosity levels (%) of the (a) $NbSi_2$-based, and (b) $TaSi_2$-based composites with the addition of the Al_2O_3 and ZrO_2 particles, as a function of sintering temperature.

1500°-1600°C. Their apparent porosity levels are presented as percentages (%) in the Figure 2.9 as a function of sintering temperature. At 1400°C, the apparent porosity levels were found to be above 22.1% for all the composites except for the 60-40 $NbSi_2$-Al_2O_3, since it revealed ~16.1% porosity at the same temperature. With increasing sintering temperature from 1400°C to 1500°C, significant reductions in the porosity levels ranging from 3.73 to 8.27% were achieved for the $NbSi_2$-Al_2O_3, $NbSi_2$-ZrO_2 and $TaSi_2$-Al_2O_3 composites all having 30-70 volume percentages. However, only a 0.19-0.79% decrease was observed at the same temperature range for the same compositions, but all having the 60-40 volume percentages. The apparent porosity levels were also reduced for all the composites by 2.70-13.5% with increasing sintering temperature from 1500°C to 1600°C, but this decrease was drastic (10.3-13.5%) only for the 30-70 $NbSi_2$-Al_2O_3, 30-70 $TaSi_2$-Al_2O_3 and 60-40 $TaSi_2$-Al_2O_3 composites. The lowest porosity levels were achieved (5.15-7.70%) for the $NbSi_2$-Al_2O_3 and $TaSi_2$-Al_2O_3 composites both with 30-70 volume percentages at 1600°C. It can also be clearly seen that porosity levels of the silicide-alumina composites were significantly lower than that of the silicide-zirconia composites in all cases. The silicide-zirconia composites displayed porosity levels higher than 25.8% even at 1600°C. In brief, these results demonstrated that the particle packing and densification kinetics were highly improved by lowering the metal silicide content (60 to 30 vol%) and/or increasing the refractory oxide (40 to 70 vol%) content within these composite systems. It is apparent that the particle packing was substantially enhanced with the addition of 70 vol% alumina particles to the $NbSi_2$ and $TaSi_2$, which acted as reinforcement particles in these cases. This could be related to the initial agglomeration of the fine alumina particles (~0.4 μm) and high metal silicide/alumina particle size ratios ($NbSi_2/Al_2O_3 \approx 3.5$; $TaSi_2/Al_2O_3 \approx 16.0$). Since the local densification kinetics were also more favored with the existence of agglomerated alumina grains and related single-phase grain boundary regions, the combination of all these parameters significantly enhanced the densification of the $NbSi_2$-Al_2O_3 and $TaSi_2$-Al_2O_3 composites not only at the 30-70 volume percentages, but also at the 60-40. These results were also found to be highly consistent with the previously reported results on the $MoSi_2$- and WSi_2-oxide composites. On the other hand, significantly high porosity levels and low densification for the silicide-zirconia composites at all sintering temperatures could be correlated to lower metal silicide/zirconia particle size ratios ($NbSi_2/ZrO_2 \approx 0.1$; $TaSi_2/ZrO_2 \approx 0.5$) and insufficient sintering kinetics for the ZrO_2 having the higher melting point. That could be also interrelated with the microcracks that may form within these composite microstructures due to reversible monoclinic-tetragonal phase transformation of zirconia near 1170°C.

2.3.2.2 Phase development and chemical/thermal stability of the composites

After sintering of the composite compositions, their phase development and high-temperature chemical and thermal stability were studied. Figure 2.10 presents the XRD patterns of the silicide-alumina composites after sintering under argon atmosphere. The phases identified for the $MoSi_2$-Al_2O_3 composite sample were $MoSi_2$, Al_2O_3, and SiO_2 in quartz form (Figure 2.10a). It is important to note that impurity existed in the precursor $MoSi_2$ powder was the main reason of SiO_2 phase. It is also demonstrated that the $MoSi_2$ did not react with Al_2O_3 at 1600°C, indicated its chemical stability. The phases identified for the WSi_2-Al_2O_3 composite sample were WSi_2, Al_2O_3, and W_5Si_3 (Figure 2.10b). It should be also noted that a different form of W-Si was formed as W_5Si_3. Similarly to the $MoSi_2$-Al_2O_3 composite system, it is demonstrated that WSi_2 did not react with Al_2O_3 at 1600°C. Figure 2.10c shows the XRD results of 80 vol% Al_2O_3-20 vol% $ZrSi_2$ sintered at 1300°, 1400° and 1500°C for 2 h. The phases identified were Al_2O_3, $ZrSi_2$ and SiO_2. Si phase existing within the $ZrSi_2$ may be reacted with residual oxygen to form SiO_2. Another plausible explanation is that SiO_2 may already be present in the starting powder. Figure 2.10d displays the XRD result

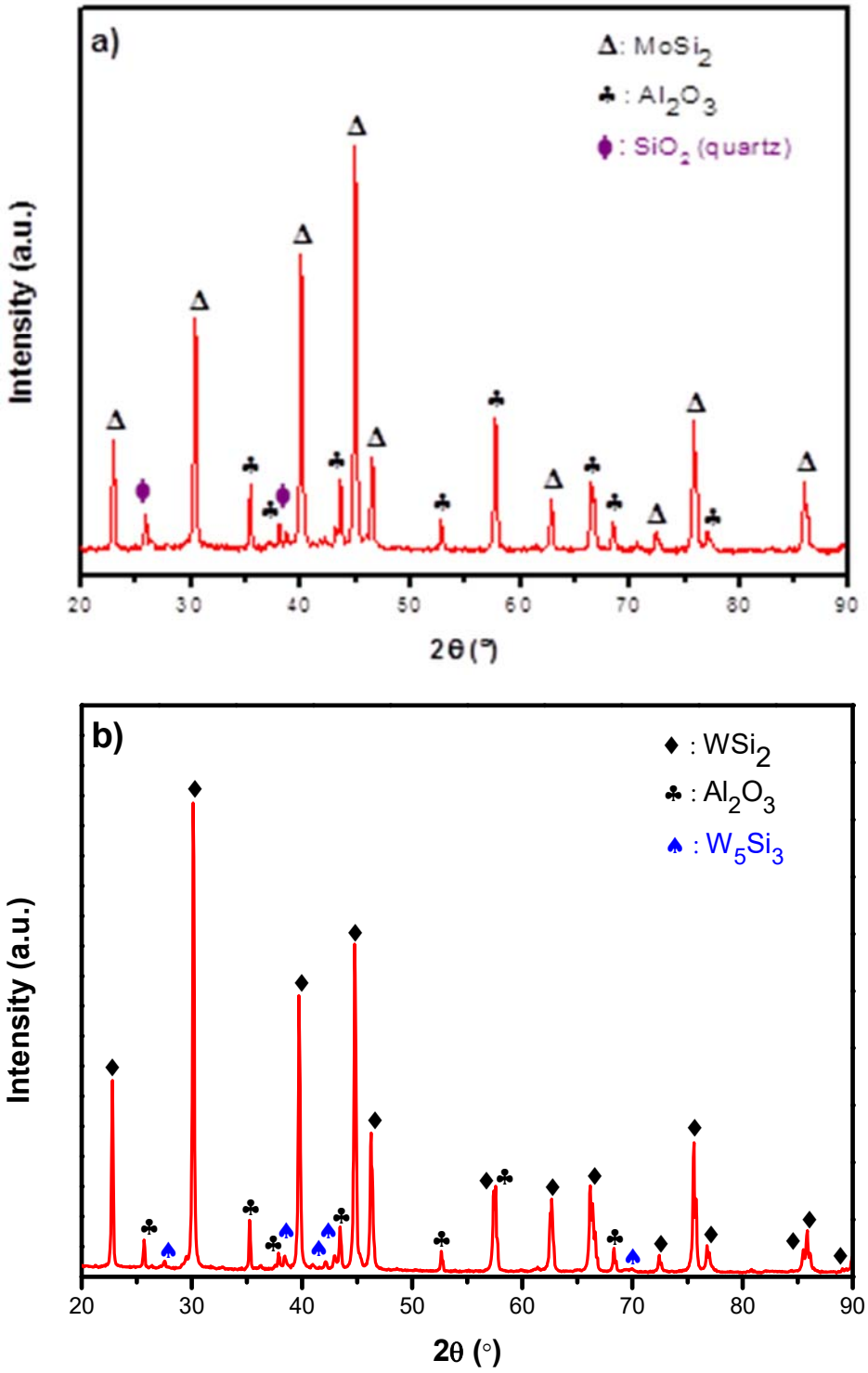

Figure 2.10. XRD patterns of the (a) (60-40) vol% $MoSi_2$-Al_2O_3, (b) (60-40) vol% WSi_2-Al_2O_3, (c) (20-80) vol% $ZrSi_2$-Al_2O_3, (d) (60-40) vol% $TaSi_2$-Al_2O_3, (e) (60-40) vol% $NbSi_2$-Al_2O_3, and (f) (60-40) vol% $CrSi_2$-Al_2O_3 composite samples after sintering under argon.

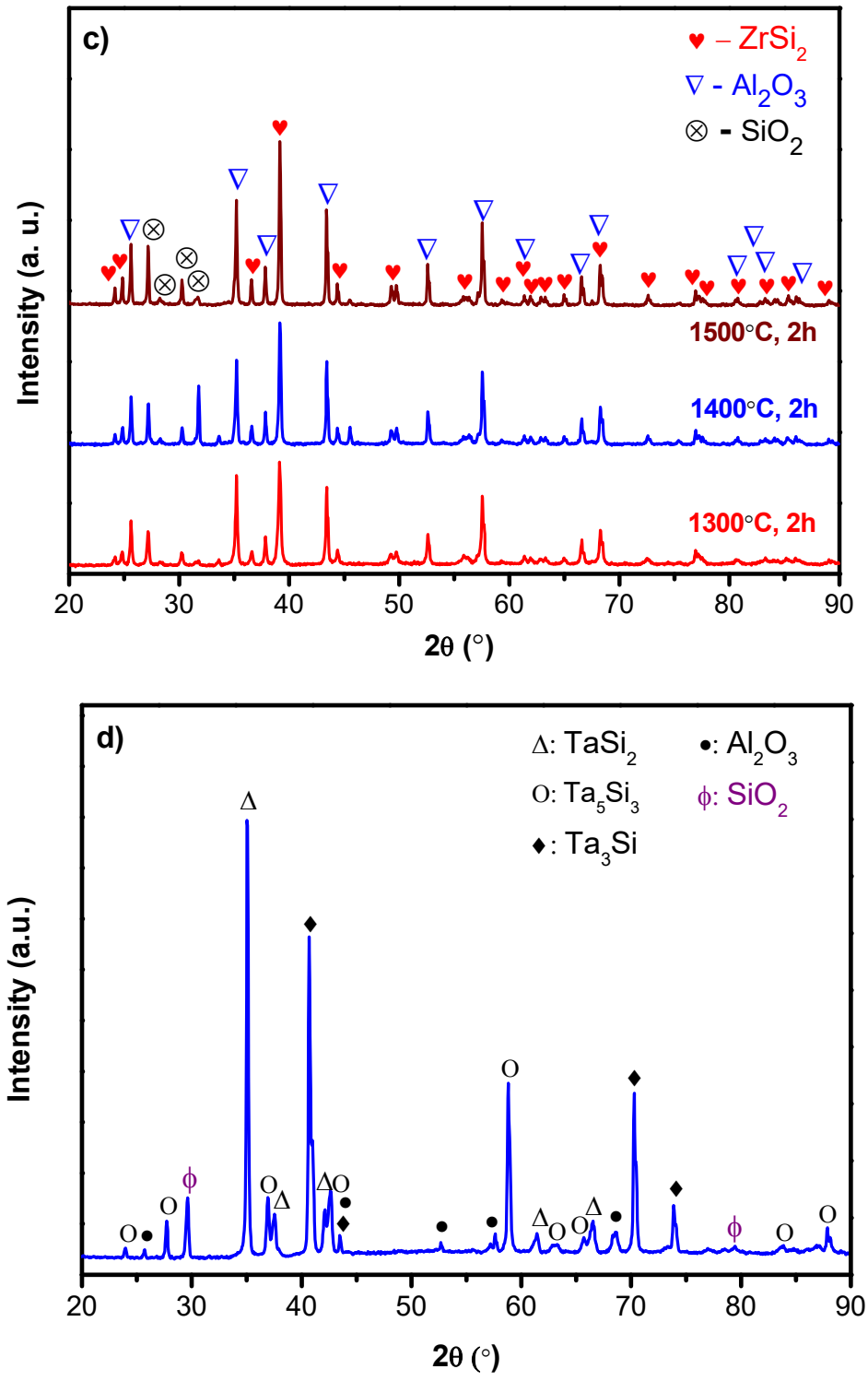

Figure 2.10. (continued) XRD patterns of the (a) (60-40) vol% $MoSi_2$-Al_2O_3, (b) (60-40) vol% WSi_2-Al_2O_3, (c) (20-80) vol% $ZrSi_2$-Al_2O_3, (d) (60-40) vol% $TaSi_2$-Al_2O_3, (e) (60-40) vol% $NbSi_2$-Al_2O_3, and (f) (60-40) vol% $CrSi_2$-Al_2O_3 composite samples after sintering under argon.

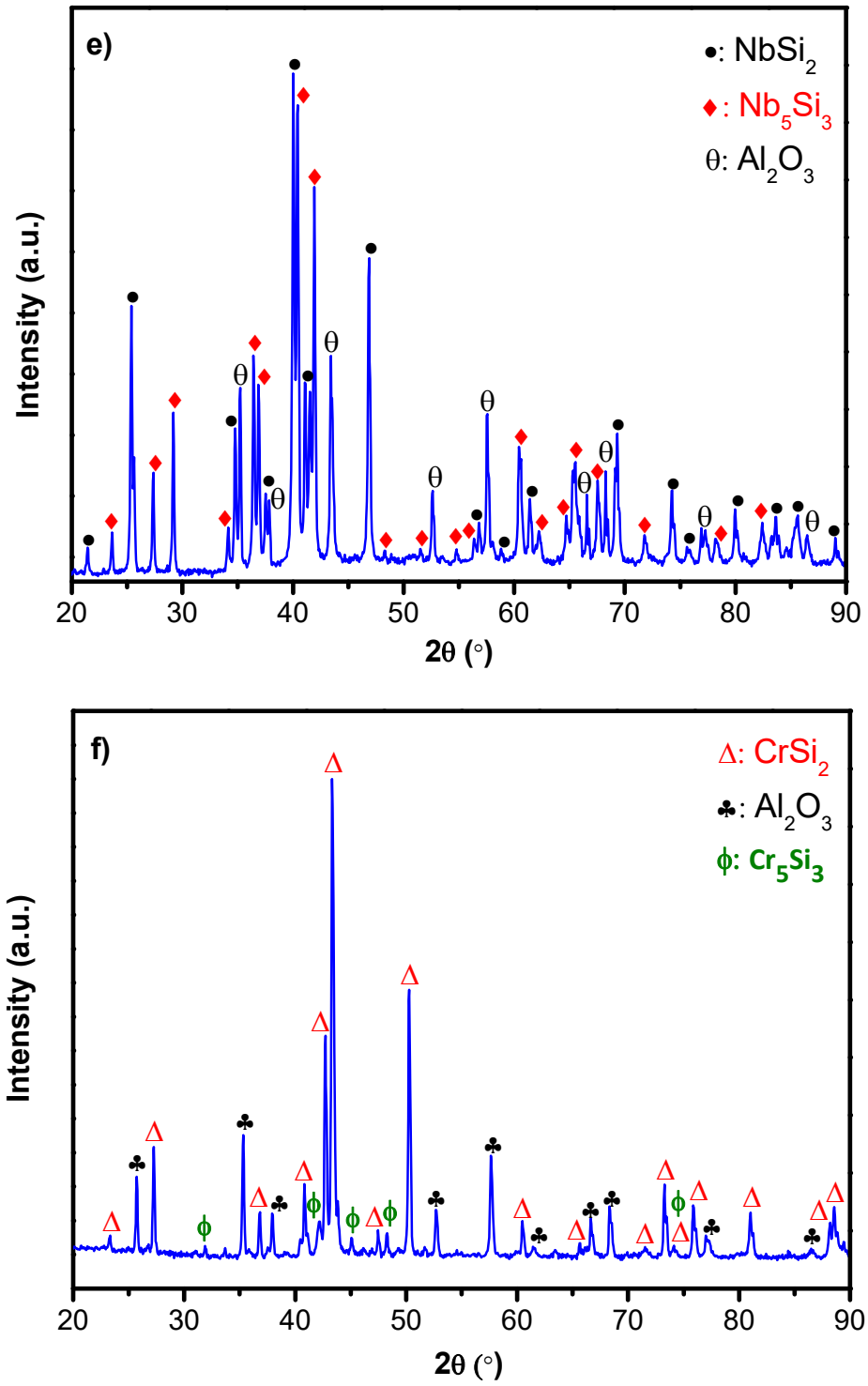

Figure 2.10. (continued) XRD patterns of the (a) (60-40) vol% $MoSi_2$-Al_2O_3, (b) (60-40) vol% WSi_2-Al_2O_3, (c) (20-80) vol% $ZrSi_2$-Al_2O_3, (d) (60-40) vol% $TaSi_2$-Al_2O_3, (e) (60-40) vol% $NbSi_2$-Al_2O_3, and (f) (60-40) vol% $CrSi_2$-Al_2O_3 composite samples after sintering under argon.

of 60 vol% $TaSi_2$-40 vol% Al_2O_3 composite sintered at 1600°C for 2 h. It is shown that $TaSi_2$ partially reacted with Al_2O_3 to form different silicide forms of tantalum (Ta_5Si_3 and Ta_3Si) and also SiO_2. Figure 2.10e presents the XRD result of the 60 vol% $NbSi_2$-40 vol% Al_2O_3 composite sintered at 1600°C for 2 h. The phases identified for $NbSi_2$-Al_2O_3 sample were $NbSi_2$, Nb_5Si_3, and Al_2O_3. It is important to state that a different form of Nb-Si was formed as Nb_5Si_3 as similar to the WSi_2-Al_2O_3 and $TaSi_2$-Al_2O_3 composite systems. Also, the XRD pattern of the 60 vol% $CrSi_2$-40 vol% Al_2O_3 composite sample sintered at 1400°C for 2h is shown in Figure 2.10f. Similarly to these composite systems, a different type of Cr-Si was formed as Cr_5Si_3, while there was no reaction between $CrSi_2$ and Al_2O_3, and also no formation of any undesired phases. As a review of these XRD results, it can be stated that different forms of metal silicides such as Ta_5Si_3, Ta_3Si, Nb_5Si_3, and Cr_5Si_3 were found to be formed during sintering at high temperatures.

In addition to the silicide-alumina composite compositions, silicide-yttria composite samples were studied by XRD. Figure 2.11 presents the XRD patterns of the silicide-yttria composites after sintering under argon atmosphere. The $MoSi_2$, $Y_5Mo_2O_{12}$, Y_2O_3, SiO_2 (quartz), Mo_3Si, and Mo_3O phases were identified for the (60-40) vol% $MoSi_2$-Y_2O_3 composite sample sintered at 1600°C. XRD results clearly proved that $MoSi_2$ decomposed to Mo_3Si and Mo_3O. It is also demonstrated that $Y_5Mo_2O_{12}$ phase was formed as a result of the reaction between $MoSi_2$ and Y_2O_3. As shown in the Figure 2.11b, the WSi_2, Y_2SiO_5, WO_2, and SiO_2 (stishovite) phases were identified for the (60-40) vol% WSi_2-Y_2O_3 composite sample sintered at 1600°C for 2 h. XRD results indicated that a portion of WSi_2 decomposed to WO_2 and SiO_2. It is also demonstrated that Y_2SiO_5 phase was formed as a result of the reaction between SiO_2 and Y_2O_3. As a result, it is demonstrated that $MoSi_2$ and WSi_2 did not react with Al_2O_3, while they decomposed and then reacted in Y_2O_3 ceramic matrix at 1600°C. In addition to that, phase changes were evaluated in the $TaSi_2$-Y_2O_3, $NbSi_2$-Y_2O_3, $CrSi_2$-Y_2O_3, and $TiSi_2$-Y_2O_3 composite systems. Figure 2.11(c-d) present the XRD results of the 60 vol% $TaSi_2$-40 vol% Y_2O_3 and 60 vol% $NbSi_2$-40 vol% Y_2O_3 composite samples sintered at 1600°C for 2 h, respectively. The phases identified for the $TaSi_2$-Y_2O_3 composite after sintering were $TaSi_2$, Y_2SiO_5, $Y_{10}Ta_4O_{25}$, and Ta_2O_5. This result clearly indicated that $TaSi_2$ firstly decomposed to Ta_2O_5 and SiO_2, and reacted with Y_2O_3 which resulted in the formation of Y_2SiO_5 and $Y_{10}Ta_4O_{25}$ secondary phases. On the other hand, $NbSi_2$, Nb_5Si_3, Y_2SiO_5, Y_2O_3, and SiO_2 (quartz) phases were identified for the $NbSi_2$-Y_2O_3 composite sample sintered at 1600°C. Similar to the WSi_2-Y_2O_3 and $TaSi_2$-Y_2O_3 composite systems, Y_2SiO_5 phase was formed as a result of the reaction between SiO_2 and Y_2O_3. It is also important to state that Nb_5Si_3 phase was formed as a different form of Nb-Si similar to the $NbSi_2$-Al_2O_3 composite system. Figure 2.11e shows the XRD result of the 60 vol% $CrSi_2$-40 vol% Y_2O_3 composite sample sintered at 1400°C for 2 h. In addition to the expected $CrSi_2$ and Y_2O_3 phases, Y_2SiO_5 phase was identified similar to the WSi_2-Y_2O_3, $TaSi_2$-Y_2O_3 and $NbSi_2$-Y_2O_3 composite systems. It was formed due to the reaction of Y_2O_3 and SiO_2 existed directly in the commercial $CrSi_2$ precursor powder. In addition, the XRD pattern of the 60 vol% $TiSi_2$-40 vol% Y_2O_3 composite sample sintered at 1400°C is shown in Figure 2.11f. The phases identified were $TiSi_2$, TiO_2 in rutile form, $Y_2Si_2O_7$, Y_2O_3, and SiO_2 in cristobalite form. This result clearly indicates that $TiSi_2$ decomposed to TiO_2 and SiO_2 phases, and reacted with Y_2O_3. $Y_2Si_2O_7$ phase was hereby formed as a result of that reaction during high temperature sintering at 1400°C for 2 h.

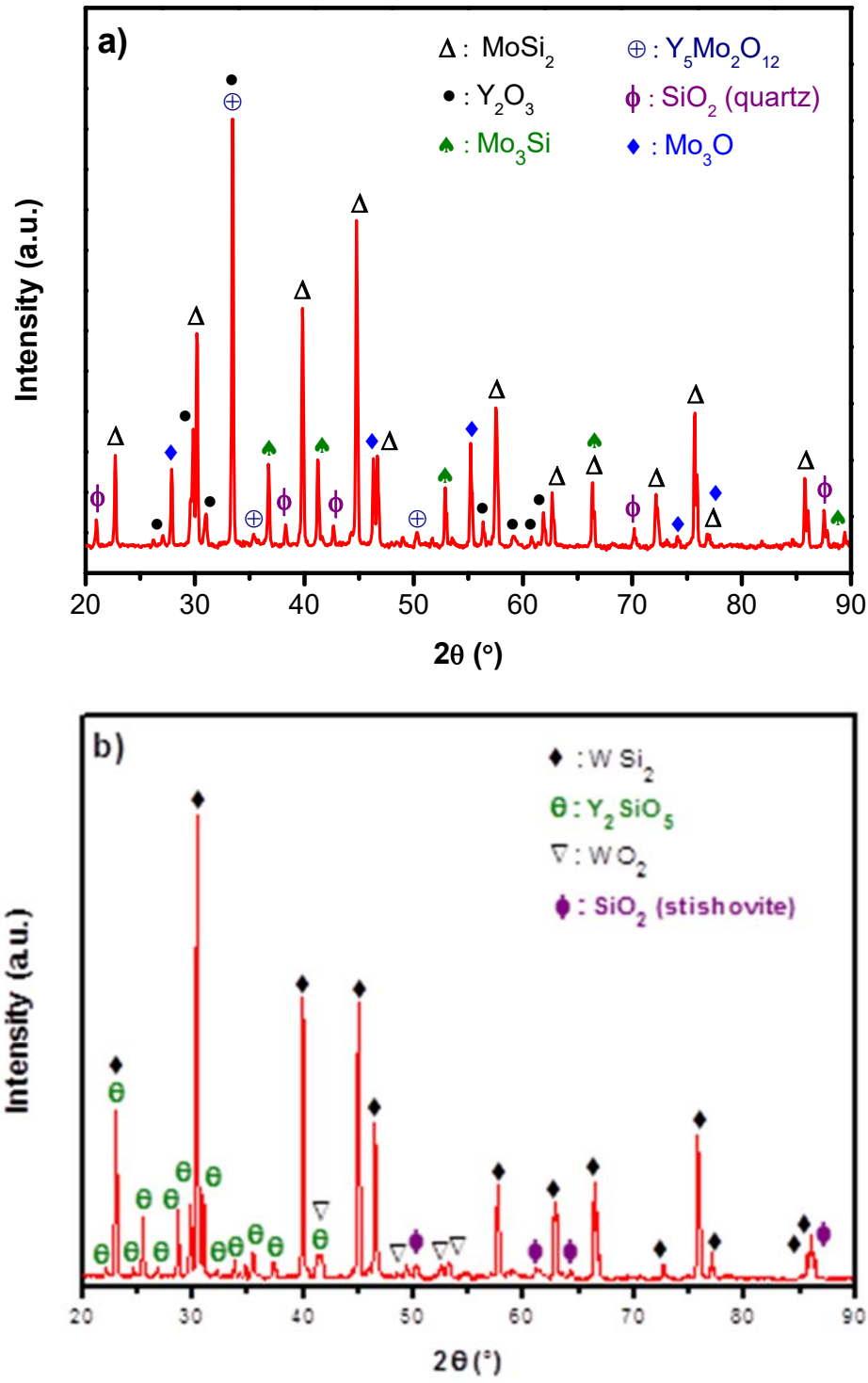

Figure 2.11. XRD patterns of the (a) (60-40) vol% $MoSi_2$-Y_2O_3, (b) (60-40) vol% WSi_2-Y_2O_3, (c) (60-40) vol% $TaSi_2$-Y_2O_3, (d) (60-40) vol% $NbSi_2$-Y_2O_3, (e) (60-40) vol% $CrSi_2$-Y_2O_3, and (f) (60-40) vol% $TiSi_2$-Y_2O_3 composite samples after sintering under argon.

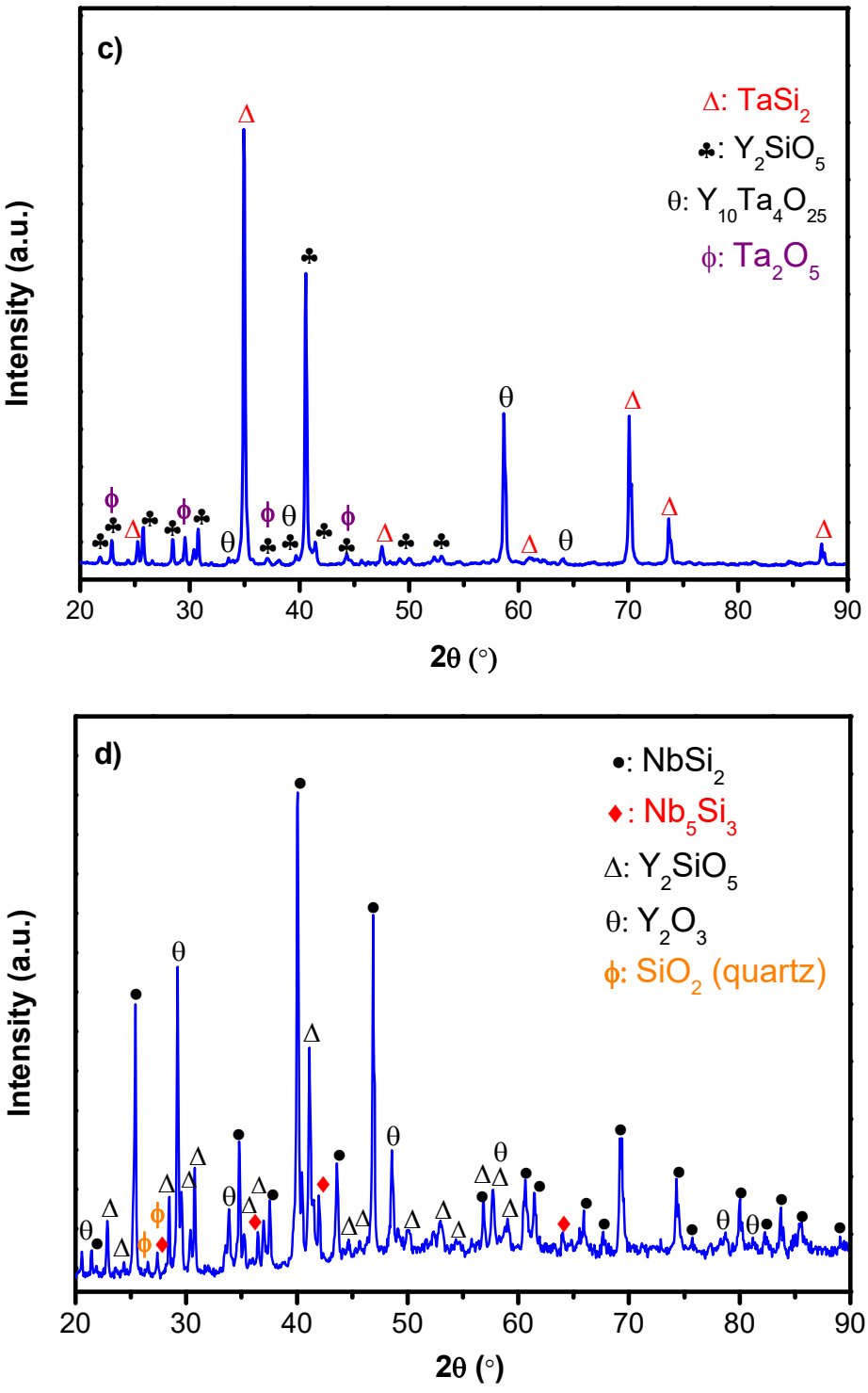

Figure 2.11. (continued) XRD patterns of the (a) (60-40) vol% $MoSi_2$-Y_2O_3, (b) (60-40) vol% WSi_2-Y_2O_3, (c) (60-40) vol% $TaSi_2$-Y_2O_3, (d) (60-40) vol% $NbSi_2$-Y_2O_3, (e) (60-40) vol% $CrSi_2$-Y_2O_3, and (f) (60-40) vol% $TiSi_2$-Y_2O_3 composite samples after sintering under argon.

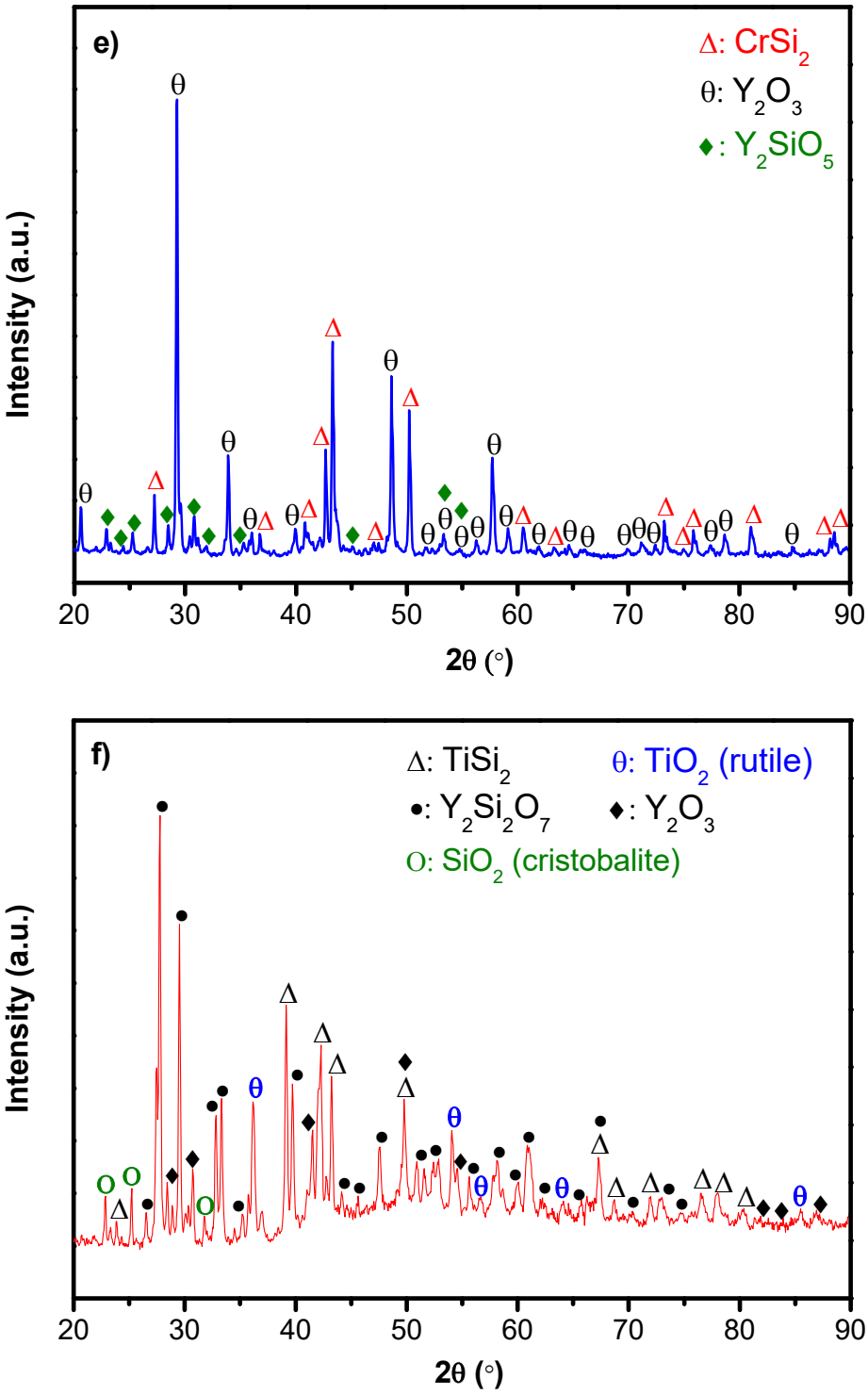

Figure 2.11. (continued) XRD patterns of the (a) (60-40) vol% $MoSi_2$-Y_2O_3, (b) (60-40) vol% WSi_2-Y_2O_3, (c) (60-40) vol% $TaSi_2$-Y_2O_3, (d) (60-40) vol% $NbSi_2$-Y_2O_3, (e) (60-40) vol% $CrSi_2$-Y_2O_3, and (f) (60-40) vol% $TiSi_2$-Y_2O_3 composite samples after sintering under argon.

After completion of the phase analyses of the silicide-alumina and silicide-yttria composite compositions, further XRD studies were performed on silicide-chromia and silicide-zirconia samples to understand the phase development and chemical stability. Figure 2.12 presents the XRD patterns of the (20-80) vol% silicide-chromia composites after sintering under argon atmosphere. It is clearly evident that Cr_2O_3 partially reacted with $MoSi_2$ at 1400°C to form unwanted phases such as Cr_3Mo and SiO_2 in cristobalite form. In addition to that, it is important to note that existence of SiO_2 is also due to the SiO_2 impurity in the precursor $MoSi_2$ powder. Similarly, an additional phase, SiO_2 is detected in the case of Cr_2O_3 samples with WSi_2 and $ZrSi_2$ as evident in the Figure 2.12(b-c). It is demonstrated that WSi_2 partially reacted with Cr_2O_3 to form W_3O and SiO_2, while $ZrSi_2$ did not react with Cr_2O_3. XRD results pointed to the fact that at 1400°C, Cr_2O_3 reacted with the silicides to form unwanted phases such as Cr_3Mo, SiO_2, and W_3O, which prevented the full densification of all Cr_2O_3 samples and adversely affected their chemical stability at high temperatures. The following composite systems investigated for phase changes and reactions were $TaSi_2$-Cr_2O_3, $NbSi_2$-Cr_2O_3, $CrSi_2$-Cr_2O_3, and $TiSi_2$-Cr_2O_3. Figure 2.12(d-e) show the XRD results of the 20 vol% $TaSi_2$-80 vol% Cr_2O_3 and 20 vol% $NbSi_2$-80 vol% Cr_2O_3 composite samples sintered at 1400°C for 2 h, respectively. The phases identified for the sintered $TaSi_2$-Cr_2O_3 composite sample were Cr_2O_3, Ta_2O_5, TaO_2, $CrTaO_4$, and Cr. This result clearly indicates that $TaSi_2$ highly reacted with Cr_2O_3 which resulted in the formation of unwanted tantalum oxide and chromium tantalum oxide additional phases at 1400°C. It can be also stated that $NbSi_2$ highly reacted with Cr_2O_3 to form $CrNbO_4$ and CrNbSi secondary phases. The other unwanted phases

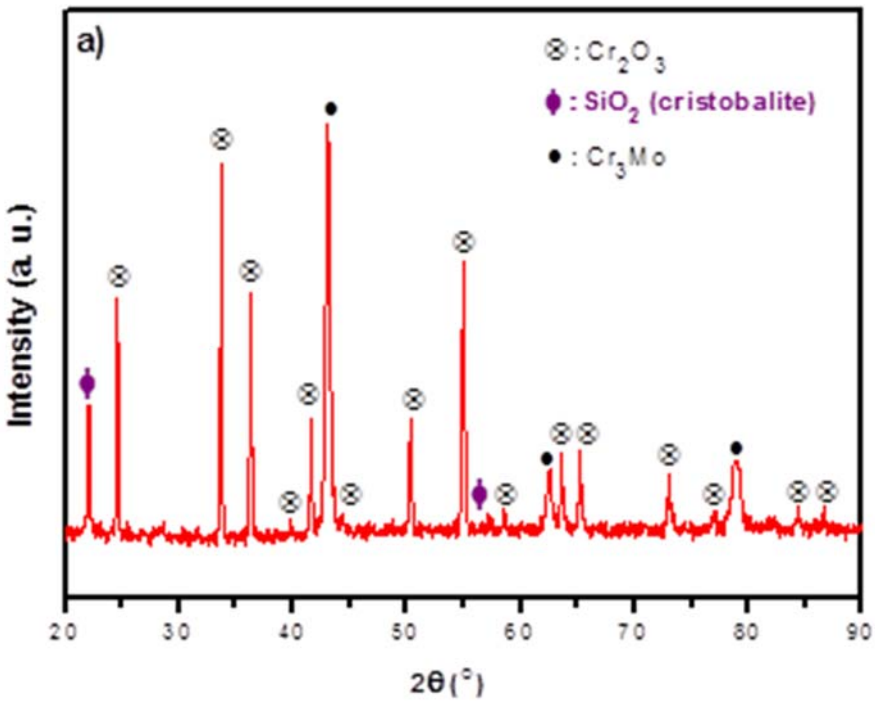

Figure 2.12. XRD patterns of the (20-80) vol% (a) $MoSi_2$-Cr_2O_3, (b) $ZrSi_2$-Cr_2O_3, (c) WSi_2-Cr_2O_3, (d) $TaSi_2$-Cr_2O_3, (e) $NbSi_2$-Cr_2O_3, (f) $CrSi_2$-Cr_2O_3, and (g) $TiSi_2$-Cr_2O_3 composite samples after sintering under argon at 1400°C.

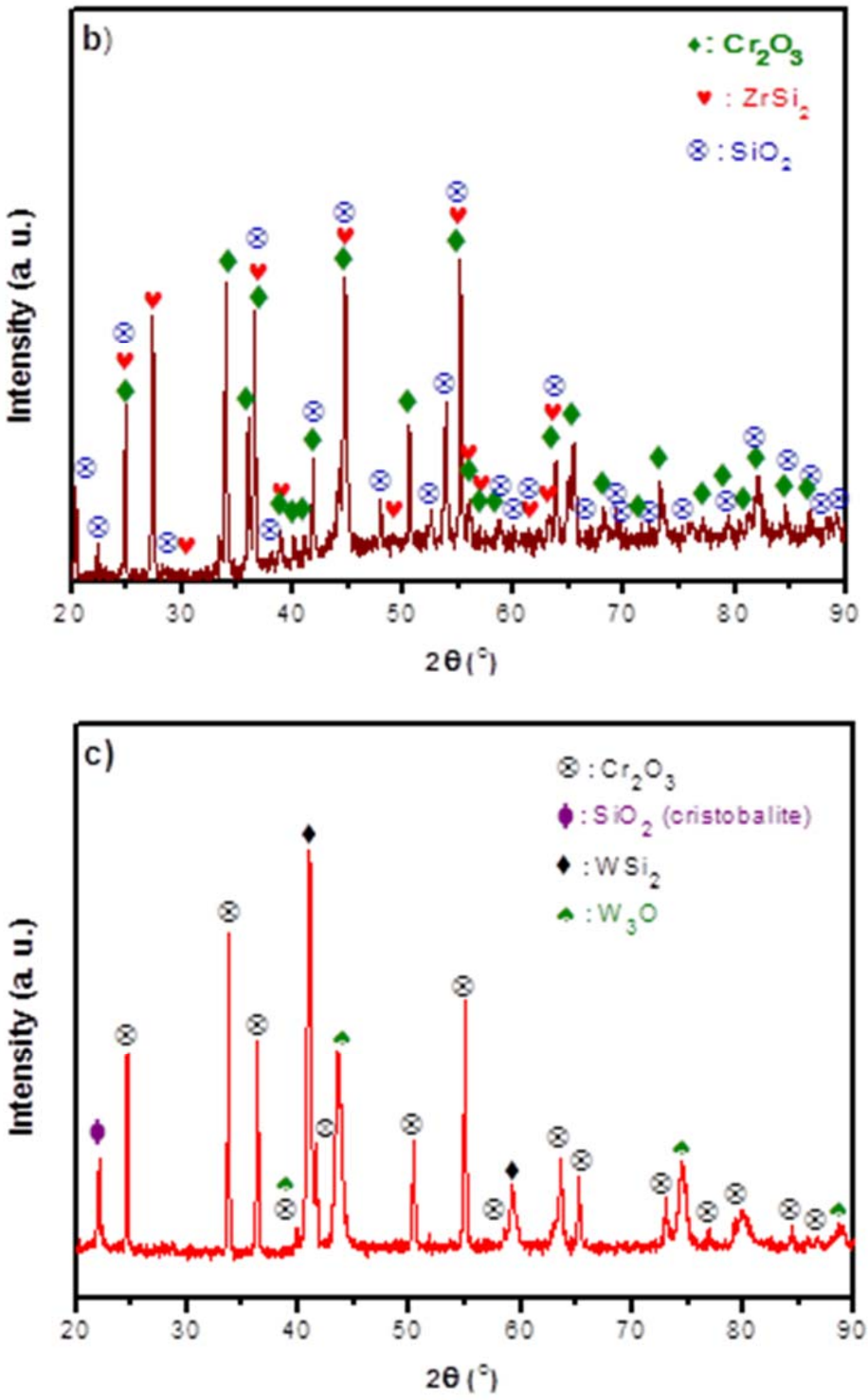

Figure 2.12. (continued) XRD patterns of the (20-80) vol% (a) $MoSi_2$-Cr_2O_3, (b) $ZrSi_2$-Cr_2O_3, (c) WSi_2-Cr_2O_3, (d) $TaSi_2$-Cr_2O_3, (e) $NbSi_2$-Cr_2O_3, (f) $CrSi_2$-Cr_2O_3, and (g) $TiSi_2$-Cr_2O_3 composite samples after sintering under argon at 1400°C.

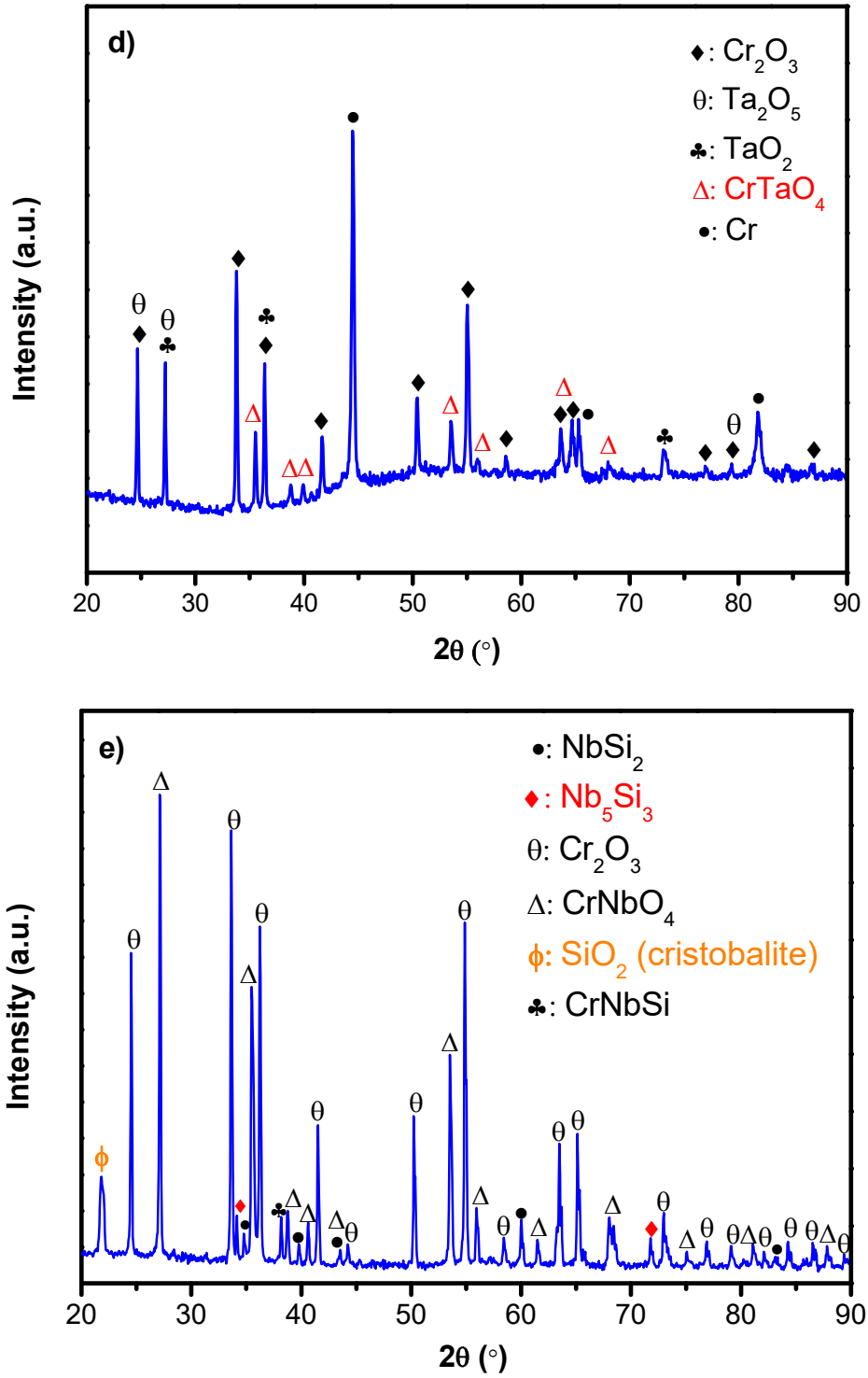

Figure 2.12. (continued) XRD patterns of the (20-80) vol% (a) $MoSi_2$-Cr_2O_3, (b) $ZrSi_2$-Cr_2O_3, (c) WSi_2-Cr_2O_3, (d) $TaSi_2$-Cr_2O_3, (e) $NbSi_2$-Cr_2O_3, (f) $CrSi_2$-Cr_2O_3, and (g) $TiSi_2$-Cr_2O_3 composite samples after sintering under argon at 1400°C.

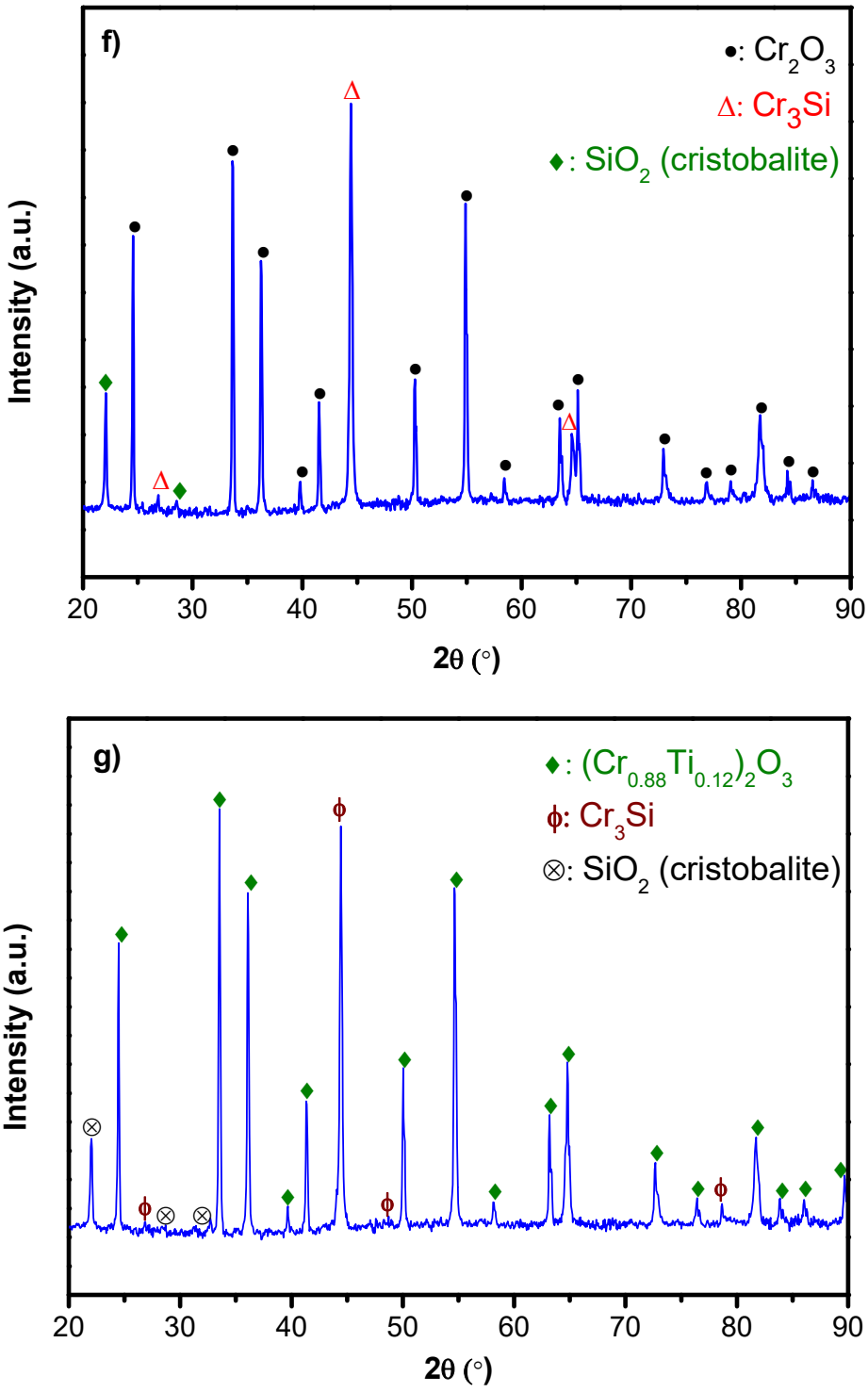

Figure 2.12. (continued) XRD patterns of the (20-80) vol% (a) $MoSi_2$-Cr_2O_3, (b) $ZrSi_2$-Cr_2O_3, (c) WSi_2-Cr_2O_3, (d) $TaSi_2$-Cr_2O_3, (e) $NbSi_2$-Cr_2O_3, (f) $CrSi_2$-Cr_2O_3, and (g) $TiSi_2$-Cr_2O_3 composite samples after sintering under argon at 1400°C.

identified after sintering were Nb_5Si_3 and SiO_2 in cristobalite form, which also proved the decomposition of $NbSi_2$ and its reaction with Cr_2O_3. Figure 2.12(f-g) present the XRD results of the 20 vol% $CrSi_2$-80 vol% Cr_2O_3 and 20 vol% $TiSi_2$-80 vol% Cr_2O_3 composite samples sintered at 1400°C for 2 h, respectively. It can be noted that similar to the other composite systems $CrSi_2$ partially reacted with Cr_2O_3 to form a different form of Cr-Si as Cr_3Si at 1400°C. In addition to that, it is important to state that existence of SiO_2 in cristobalite form is a result of the SiO_2 impurity in the precursor $CrSi_2$ powder. Figure 2.12g shows the XRD result of the 20 vol% $TiSi_2$-80 vol% Cr_2O_3 composite samples sintered at 1400°C for 2 h. This result clearly indicates that Cr_2O_3 completely reacted with $TiSi_2$ to form an additional phase (solid solution) $(Cr_{0.88}Ti_{0.12})_2O_3$. It is also important to state that $TiSi_2$ decomposed, highly reacted with Cr_2O_3 and then formed Cr_3Si and SiO_2 (cristobalite) phases. As a review of all metal silicides-Cr_2O_3 composite systems, it can be clearly concluded that all metal silicides partially or completely reacted with Cr_2O_3 phase at 1400°C.

In addition, zirconium oxide (ZrO_2) refractory oxide powder was used as an alternative particularly for the Y_2O_3 and Cr_2O_3 in the development of new and thermally stable composite compositions. Phase changes and potential reactions were firstly investigated in $MoSi_2$-ZrO_2, WSi_2-ZrO_2, and $ZrSi_2$-ZrO_2 composite systems. Figure 2.13(a-b-c) present the XRD results of the 60 vol% $MoSi_2$-40 vol% ZrO_2, 60 vol% WSi_2-40 vol% ZrO_2, and 60 vol% $ZrSi_2$-40 vol% ZrO_2, respectively. The phases identified for the $MoSi_2$-ZrO_2 composite sample sintered at 1600°C for 2 h were $MoSi_2$, ZrO_2, and Mo_5Si_3. It is important to note that a different form of Mo-Si was formed during sintering. This result clearly shows that $MoSi_2$ does not react with ZrO_2 at 1600°C. As shown in the Figure 2.13b, WSi_2, ZrO_2, and W_5Si_3 phases were identified after sintering of WSi_2-ZrO_2 composite sample at 1600°C. It can be stated that WSi_2 similarly does not react with ZrO_2, and does show almost the same behavior with $MoSi_2$-ZrO_2 and WSi_2-Al_2O_3 composite systems. Figure 2.13c presents the XRD result of the 60 vol% $ZrSi_2$-40 vol% ZrO_2 composite sample sintered at 1500°C due to its lower melting temperature (1620°C). The phases identified were only $ZrSi_2$ and ZrO_2. This result clearly proves that $ZrSi_2$ does not react with ZrO_2 at 1500°C, which also indicates that $ZrSi_2$-ZrO_2 composite system is thermally stable up to this temperature. Based on the XRD results of these three composite systems, it can be concluded that zirconium oxide can be a promising alternative to the reactive Y_2O_3 and Cr_2O_3. Lastly, phase changes were evaluated in $TaSi_2$-ZrO_2, $NbSi_2$-ZrO_2, $CrSi_2$-ZrO_2, and $TiSi_2$-ZrO_2 composite systems. Figure 2.13(d-e) show the XRD result of the 60 vol% $TaSi_2$-40 vol% ZrO_2 and 60 vol% $NbSi_2$-40 vol% ZrO_2 composites sintered at 1600°C for 2 h, respectively. The phases identified for $TaSi_2$-ZrO_2 composite system were Ta_5Si_3, ZrO_2, and SiO_2 (quartz). This result indicates that $TaSi_2$ partially reacted with ZrO_2 to form Ta_5Si_3 and SiO_2 in quartz form. Figure 2.13e presents the XRD result of the 60 vol% $NbSi_2$-40 vol% ZrO_2 composites sintered at 1600°C. It can be stated that a different type of Nb-Si (Nb_5Si_3) and SiO_2 in quartz form were formed, which showed that $NbSi_2$ partially reacted with ZrO_2 at 1600°C. Also XRD results of the 60 vol% $CrSi_2$-40 vol% ZrO_2 and 60 vol% $TiSi_2$-40 vol% ZrO_2 composites sintered at 1400°C are shown in Figure 2.7 (f-g). It is important to note that $CrSi_2$ did not react with ZrO_2 which can be stated as a proof of its thermal stability up to 1400°C. Lastly, Figure 2.13g presents the XRD result of the 60 vol% $TiSi_2$-40 vol% ZrO_2 sintered at 1400°C. Although $TiSi_2$ and ZrO_2 phases were obtained after sintering as expected, TiO_2 in rutile form and SiO_2 in cristobalite form were formed at 1400°C as a result of the partial decomposition of $TiSi_2$ phase.

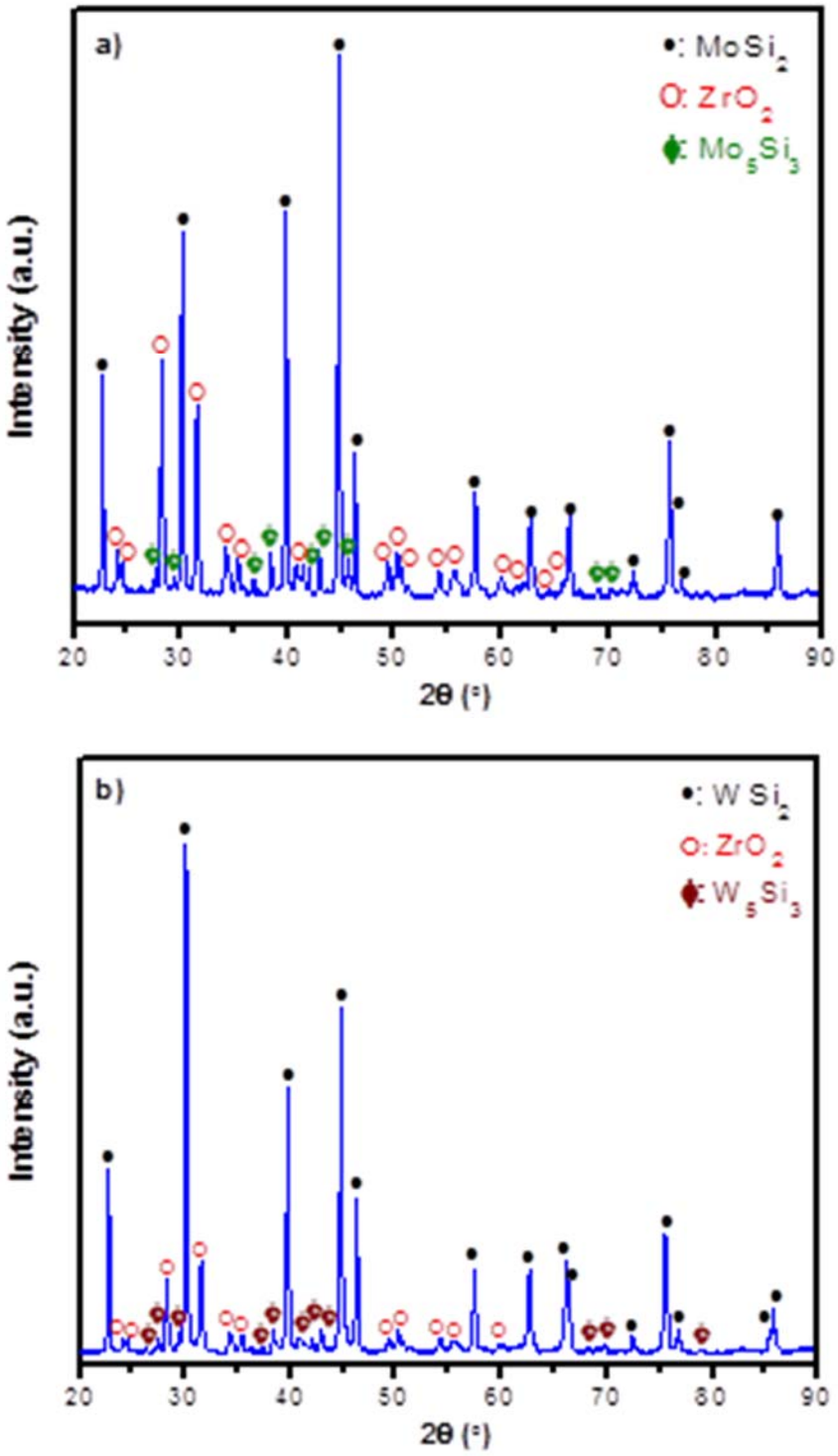

Figure 2.13. XRD patterns of the (60-40) vol% (a) $MoSi_2$-ZrO_2, (b) WSi_2-ZrO_2, (c) $ZrSi_2$-ZrO_2, (d) $TaSi_2$-ZrO_2, (e) $NbSi_2$-ZrO_2, (f) $CrSi_2$-ZrO_2, and (g) $TiSi_2$-ZrO_2 composite samples after sintering under argon.

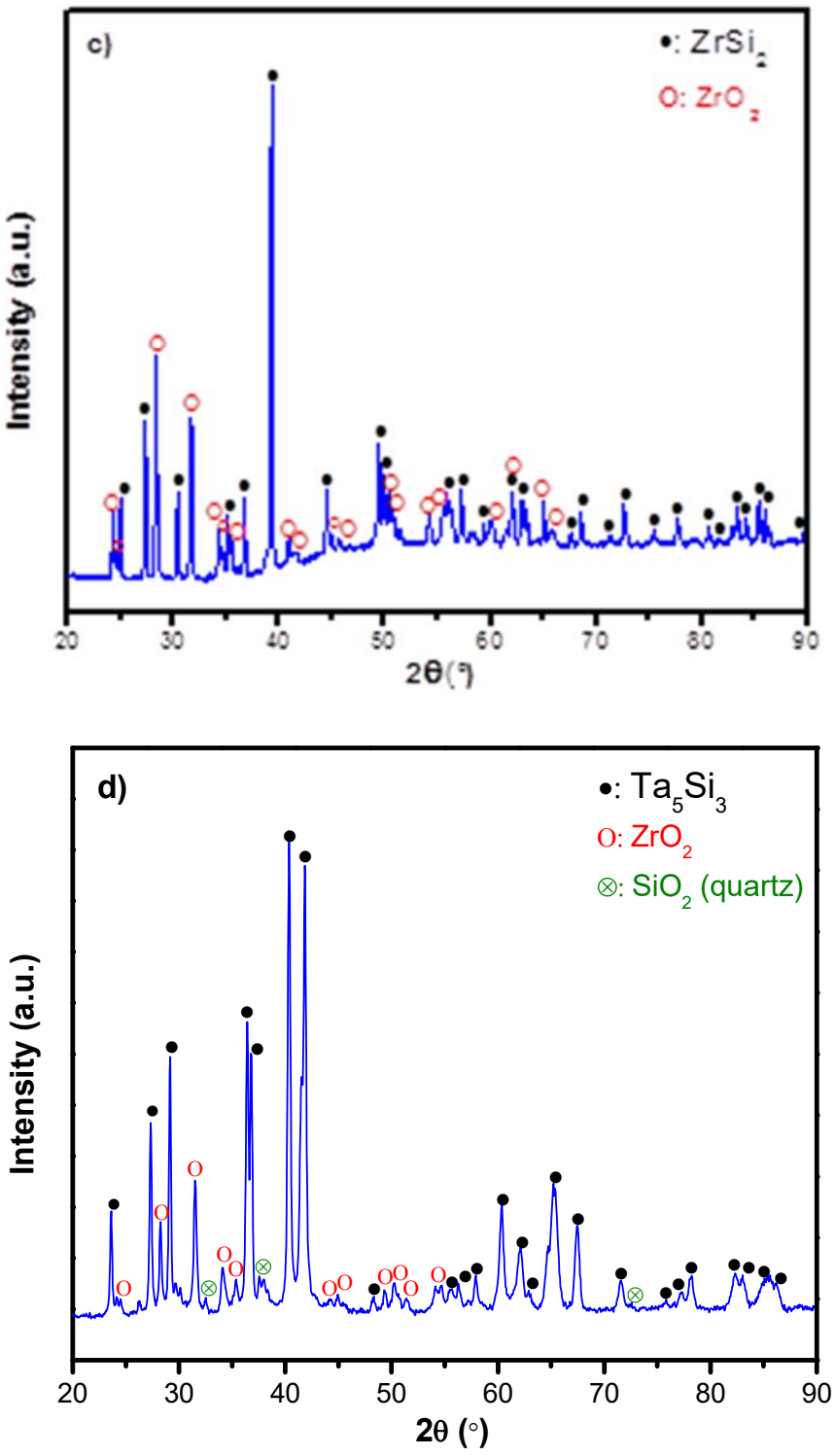

Figure 2.13. (continued) XRD patterns of the (60-40) vol% (a) $MoSi_2$-ZrO_2, (b) WSi_2-ZrO_2, (c) $ZrSi_2$-ZrO_2, (d) $TaSi_2$-ZrO_2, (e) $NbSi_2$-ZrO_2, (f) $CrSi_2$-ZrO_2, and (g) $TiSi_2$-ZrO_2 composite samples after sintering under argon.

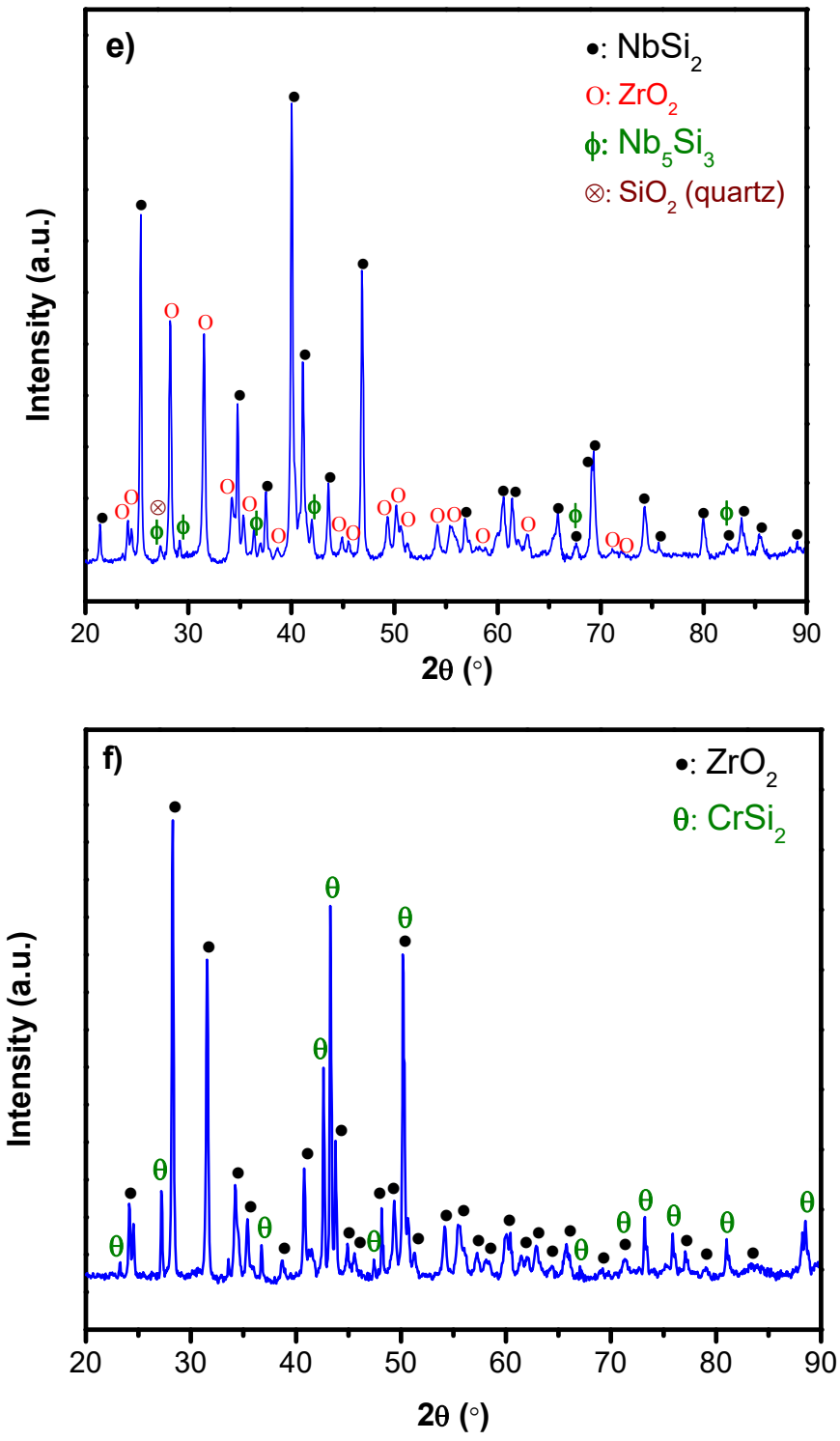

Figure 2.13. (continued) XRD patterns of the (60-40) vol% (a) $MoSi_2$-ZrO_2, (b) WSi_2-ZrO_2, (c) $ZrSi_2$-ZrO_2, (d) $TaSi_2$-ZrO_2, (e) $NbSi_2$-ZrO_2, (f) $CrSi_2$-ZrO_2, and (g) $TiSi_2$-ZrO_2 composite samples after sintering under argon.

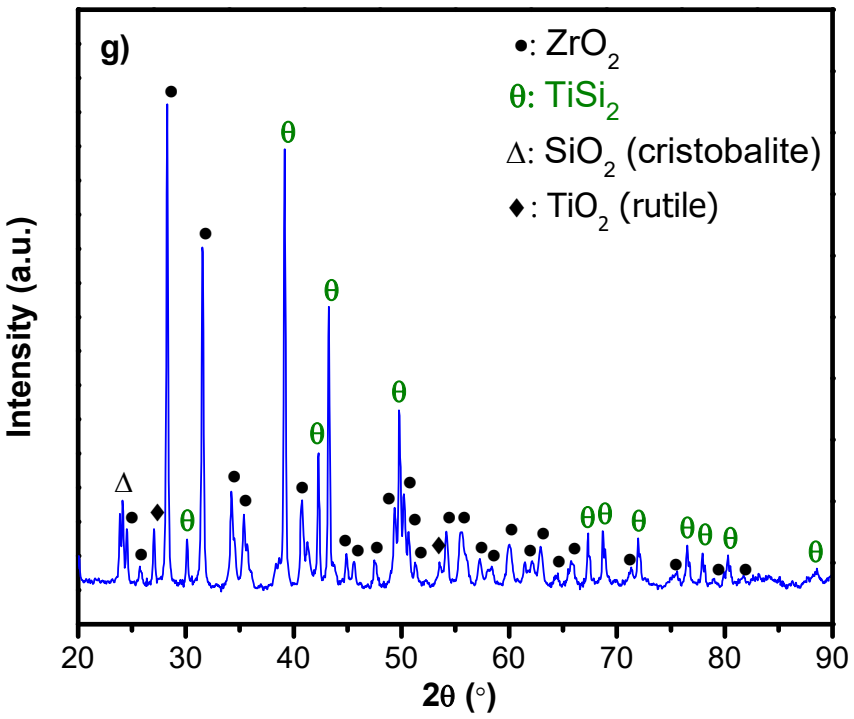

Figure 2.13. (continued) XRD patterns of the (60-40) vol% (a) $MoSi_2$-ZrO_2, (b) WSi_2-ZrO_2, (c) $ZrSi_2$-ZrO_2, (d) $TaSi_2$-ZrO_2, (e) $NbSi_2$-ZrO_2, (f) $CrSi_2$-ZrO_2, and (g) $TiSi_2$-ZrO_2 composite samples after sintering under argon.

X-Ray diffraction (XRD) experiments were also performed to evaluate the phases formed during high temperature sintering of $CrSi_2$-Cr_2O_3 composites having different metal silicide volume percentages ranging from 20 to 90 vol%. Figure 2.14a presents the XRD results of the (20-80) vol% $CrSi_2$-Cr_2O_3, (30-70) vol% $CrSi_2$-Cr_2O_3 and (40-60) vol% $CrSi_2$-Cr_2O_3 composite samples sintered at 1400°C for 2h. It is shown for (20-80) and (30-70) vol% $CrSi_2$-Cr_2O_3 composite that $CrSi_2$ and CrSi phases existing in the commercial metal silicide powder reacted with Cr_2O_3 to form SiO_2, and Cr metal and/or $Cr_{0.91}Si_{0.09}$ as major phases. Since the Cr metal and $Cr_{0.91}Si_{0.09}$ phases have very close identical XRD peaks, it is difficult to differentiate them without further experiments. However, theoretical calculations based on the Cr-Si phase diagram indicate that Cr metal can be likely obtained due to formation of SiO_2 and large shift to the left side on the phase diagram. In addition, it can be clearly seen that Cr_2O_3 and CrSi phases still exist after sintering at 1400°C. For (40-60) vol% $CrSi_2$-Cr_2O_3 composite, it can be clearly seen that Cr_2O_3 almost completely reacted with chromium silicide, and hereby formed $Cr_{0.91}Si_{0.09}$ and SiO_2 in cristobalite form. It is important to note that there is no any information for this chromium silicide phase, therefore it is important to study this composition further. Figure 2.14b shows the XRD results of the (50-50) vol% $CrSi_2$-Cr_2O_3, (55-45) vol% $CrSi_2$-Cr_2O_3 and (60-40) vol% $CrSi_2$-Cr_2O_3 composite samples sintered at 1400°C for 2h. For (50-50) vol% $CrSi_2$-Cr_2O_3 composite, it is determined that $CrSi_2$ and CrSi completely reacted with Cr_2O_3, and formed Cr_3Si as a single conductive silicide phase in the composite system. The other phase formed is SiO_2 in cristobalite form as expected, since there is no remaining Cr_2O_3 phase in the system. A similar XRD pattern can be also seen for the (55-45) vol% $CrSi_2$-Cr_2O_3 composite sample, since the major phases were

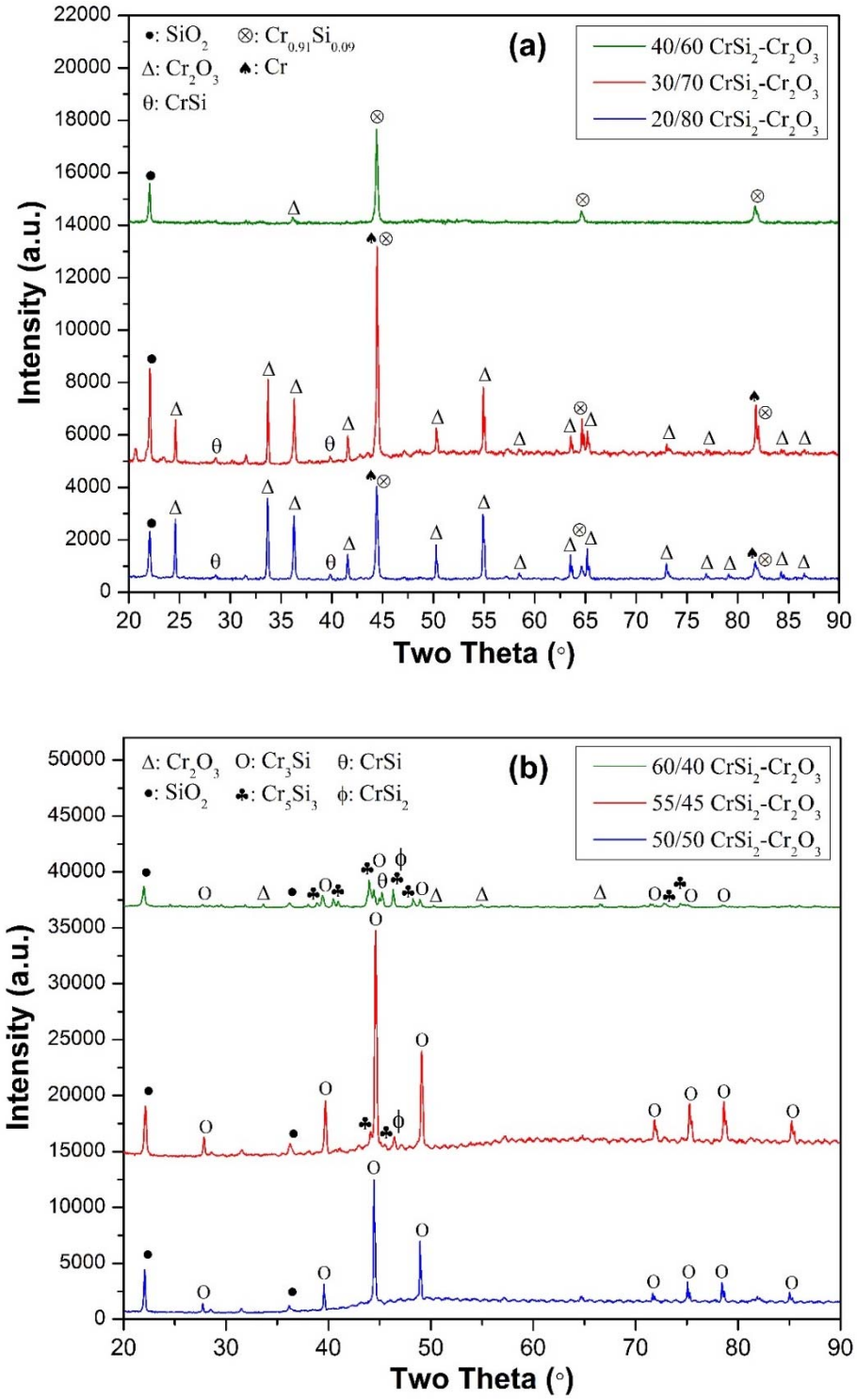

Figure 2.14. XRD patterns of the $CrSi_2$-Cr_2O_3 composite samples sintered at 1400°C for 2 hours: (a) (20-80), (30-70) and (40-60) vol% $CrSi_2$-Cr_2O_3, (b) (50-50), (55-45) and (60-40) vol% $CrSi_2$-Cr_2O_3, (c) (65-35), (70-30), (80-20) and (90-10) vol% $CrSi_2$-Cr_2O_3.

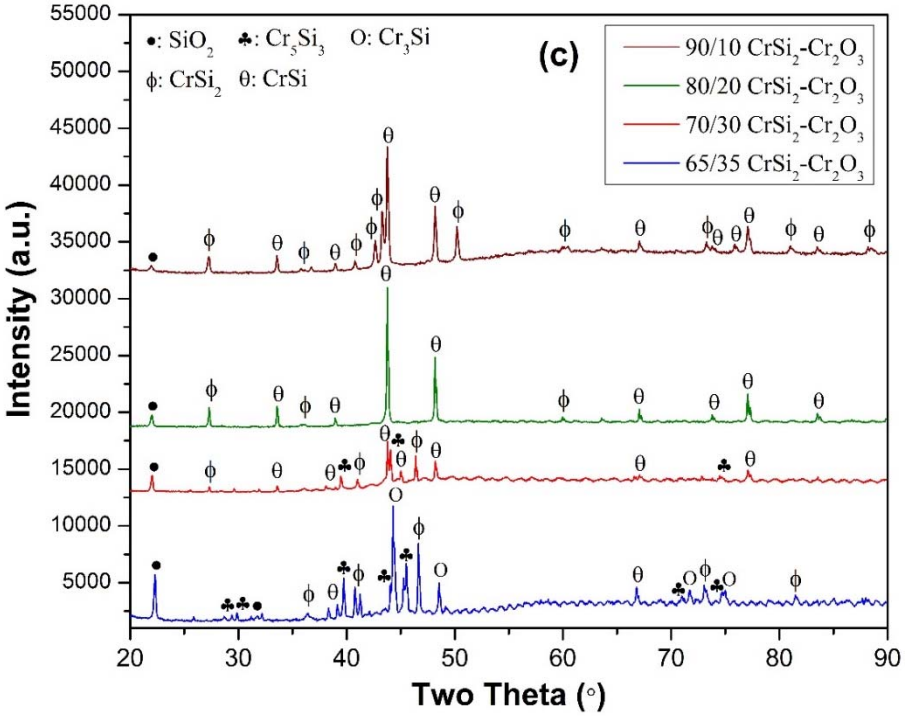

Figure 2.14. (continued) XRD patterns of the $CrSi_2$-Cr_2O_3 composite samples sintered at 1400°C for 2 hours: (a) (20-80), (30-70) and (40-60) vol% $CrSi_2$-Cr_2O_3, (b) (50-50), (55-45) and (60-40) vol% $CrSi_2$-Cr_2O_3, (c) (65-35), (70-30), (80-20) and (90-10) vol% $CrSi_2$-Cr_2O_3.

obtained as Cr_3Si and SiO_2 in cristobalite form. But the existence of $CrSi_2$ phase in the (55-45) vol% $CrSi_2$-Cr_2O_3 composite system indicated that the reaction between chromium silicide and chromium oxide was not completed. Also, it is found that Cr_5Si_3 silicide phase was formed as a result of the reaction. The XRD result of the (60-40) vol% $CrSi_2$-Cr_2O_3 composite presents that chromium silicide partially reacted with chromium oxide to form Cr_5Si_3, Cr_3Si and SiO_2 in cristobalite form. The other phases observed are Cr_2O_3, CrSi and $CrSi_2$ in the system after sintering at 1400°C. It is important to note that both Cr_5Si_3 and Cr_3Si phases are major conductive phases in the (60-40) vol% $CrSi_2$-Cr_2O_3, while the major conductive phase is Cr_3Si for the (50-50) and (55-45) vol% $CrSi_2$-Cr_2O_3 composites. Figure 2.14c shows the XRD results of the (65-35) vol% $CrSi_2$-Cr_2O_3, (70-30) vol% $CrSi_2$-Cr_2O_3, (80-20) vol% $CrSi_2$-Cr_2O_3 and (90-10) vol% $CrSi_2$-Cr_2O_3 composite samples sintered at 1400°C for 2h. The phases obtained for the (65-35) vol% $CrSi_2$-Cr_2O_3 composite are Cr_3Si, Cr_5Si_3, $CrSi_2$, CrSi and SiO_2 in cristobalite form, which indicates that the chromium silicide partially reacted with Cr_2O_3. Although the major conductive phases are Cr_3Si and Cr_5Si_3, there are still certain amount of remaining $CrSi_2$ and CrSi low-temperature phases in the system. The XRD result of the (70-30) vol% $CrSi_2$-Cr_2O_3 composite sample sintered at 1400°C for 2h is also presented for comparison. The major silicide phases obtained for (70-30) vol% $CrSi_2$-Cr_2O_3 are CrSi and Cr_5Si_3 as expected in this region based on the Cr-Si phase diagram. But it is important to state that $CrSi_2$ still exist as a minor silicide phase. For (80-20) vol% $CrSi_2$-Cr_2O_3 composite, the major silicide phase was obtained as CrSi due to a slight reaction between $CrSi_2$ and Cr_2O_3 to form CrSi and SiO_2. In the (90-10) vol% $CrSi_2$-Cr_2O_3 composite system, there

is no any significant changes observed compared to the initial phases, since the major phases are still CrSi and $CrSi_2$. But it is important to note that SiO_2 in cristobalite form was obtained as a result of the reaction between chromium silicide and low amount of Cr_2O_3. As a result of these XRD results of the $CrSi_2$-Cr_2O_3 composites, it can be clearly concluded that different type of conductive chromium silicide phases (Cr_3Si, Cr_5Si_3, CrSi etc.) obtained after sintering, depending on the metal silicide and chromium oxide fractions in the initial composite composition. Based on these results and also literature review on the chromium silicides, (50-50), (55-45) and (60-40) vol% $CrSi_2$-Cr_2O_3 composites were selected for further stability and post-characterization (electrical conductivity) studies, since the major conductive phases are Cr_3Si and Cr_5Si_3 both having higher melting points and electrical conductivities compared to other chromium silicide phases such as CrSi and $CrSi_2$.

Furthermore, selected silicide and silicide-oxide composite samples were further annealed at high temperature, and their thermal stabilities were investigated by XRD. For a short- and long-term thermal stability studies, six different composites and two pure metal silicides were firstly sintered at 1600°C for 2 h and then annealed at 1400°C for 24 and 48 h. The main purpose of this study was to study thermal stability of the composites by investigating the phase changes and formation of secondary phases at 1400°C. Therefore, X-ray diffraction (XRD) experiments were performed to evaluate the phases formed during high temperature sintering and then annealing. These XRD results are presented in comparison with the XRD results previously reported after sintering and annealing processes. Figure 2.15(a-b) shows the XRD results of pure $MoSi_2$ and pure WSi_2 samples after sintering and annealing processes at high temperatures, respectively. It is found that

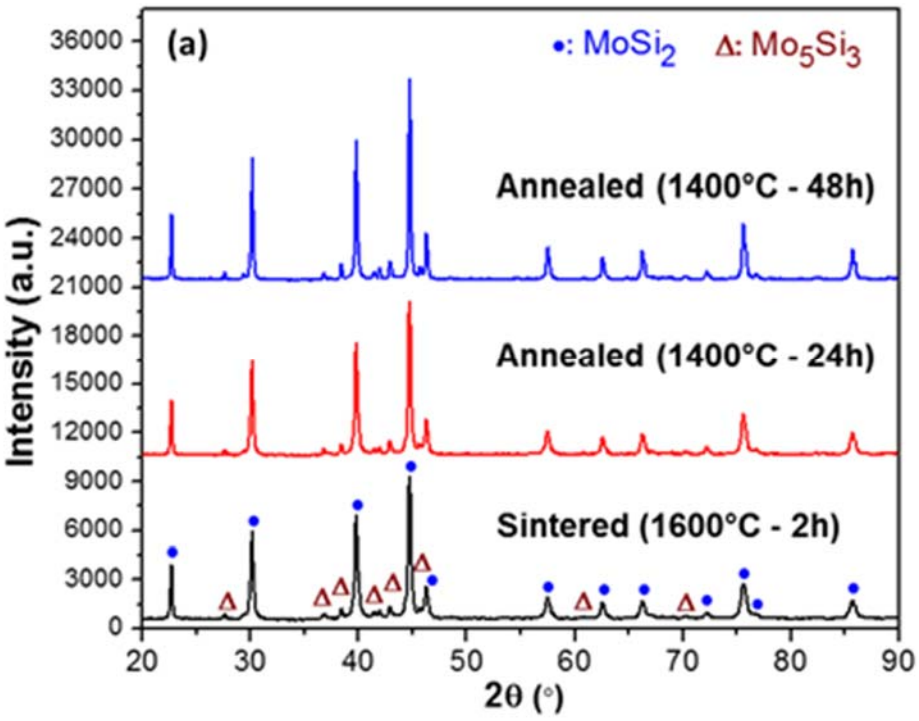

Figure 2.15. XRD patterns of the (a) pure $MoSi_2$, and (b) pure WSi_2 samples after sintering at 1600°C for 2 h, and short- and long-term annealing at 1400°C for 24-48 h.

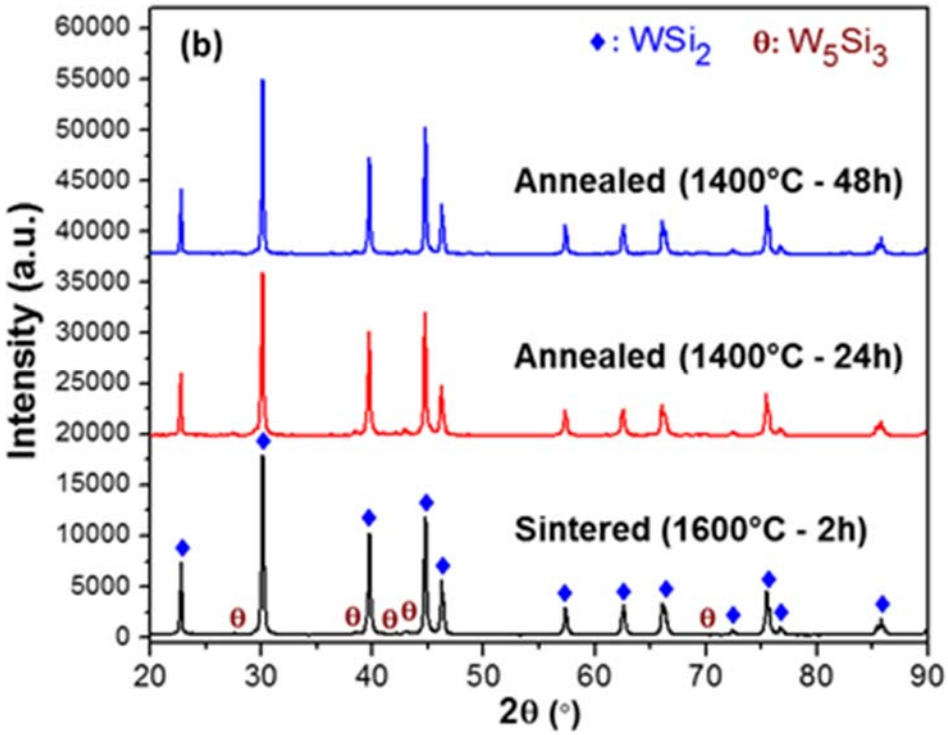

Figure 2.15. (continued) XRD patterns of the (a) pure $MoSi_2$, and (b) pure WSi_2 samples after sintering at 1600°C for 2 h, and short- and long-term annealing at 1400°C for 24-48 h.

Mo_5Si_3 and W_5Si_3 secondary phases as 5-3 silicides were firstly formed after sintering at 1600°C for 2 h. Although the XRD patterns for pure $MoSi_2$ and WSi_2 are all similar after sintering and annealing processes, it is observed that the peak intensities of the Mo_5Si_3 and W_5Si_3 phases slightly increased after short- and long-term annealing at 1400°C as shown in Figure 2.15(a-b). This result indicates that the amount of the secondary phases formed increased with increasing annealing time at 1400°C. Lastly, it is important to note that these results will be used as a reference data for the thermal stability studies at high temperatures. XRD results of the (60-40) vol% $MoSi_2$-Al_2O_3 and (60-40) vol% WSi_2-Al_2O_3 composites after sintering and annealing processes are presented in the Figure 2.16(a-b). The phases identified for $MoSi_2$-Al_2O_3 composite both after short- and long-term annealing at 1400°C were $MoSi_2$, Al_2O_3, and Mo_5Si_3, which indicates that only 5-3 silicide phase was formed as similar to the pure $MoSi_2$ sample discussed above. It is also determined that the relative intensities of the Mo_5Si_3 peaks at 2Θ degrees ranging from 38.68 to 42.85 slightly increased with increasing annealing time at 1400°C. This result clearly indicates that the amount of the Mo_5Si_3 secondary phase increased during annealing at 1400°C. In the Figure 2.16b, similar XRD results can be seen for the (60-40) vol% WSi_2-Al_2O_3 composite both after sintering and annealing processes. Although there is a slight formation of W_5Si_3 secondary phase, it is observed that secondary phase formation within WSi_2-Al_2O_3 composite was less than that within $MoSi_2$-Al_2O_3 composite during annealing at 1400°C. This result may be related with less interaction between WSi_2 and Al_2O_3, and their higher stability at 1400°C both for short- and long-term in comparison to the $MoSi_2$-Al_2O_3 composite. However, it can be clearly concluded that $MoSi_2$-Al_2O_3

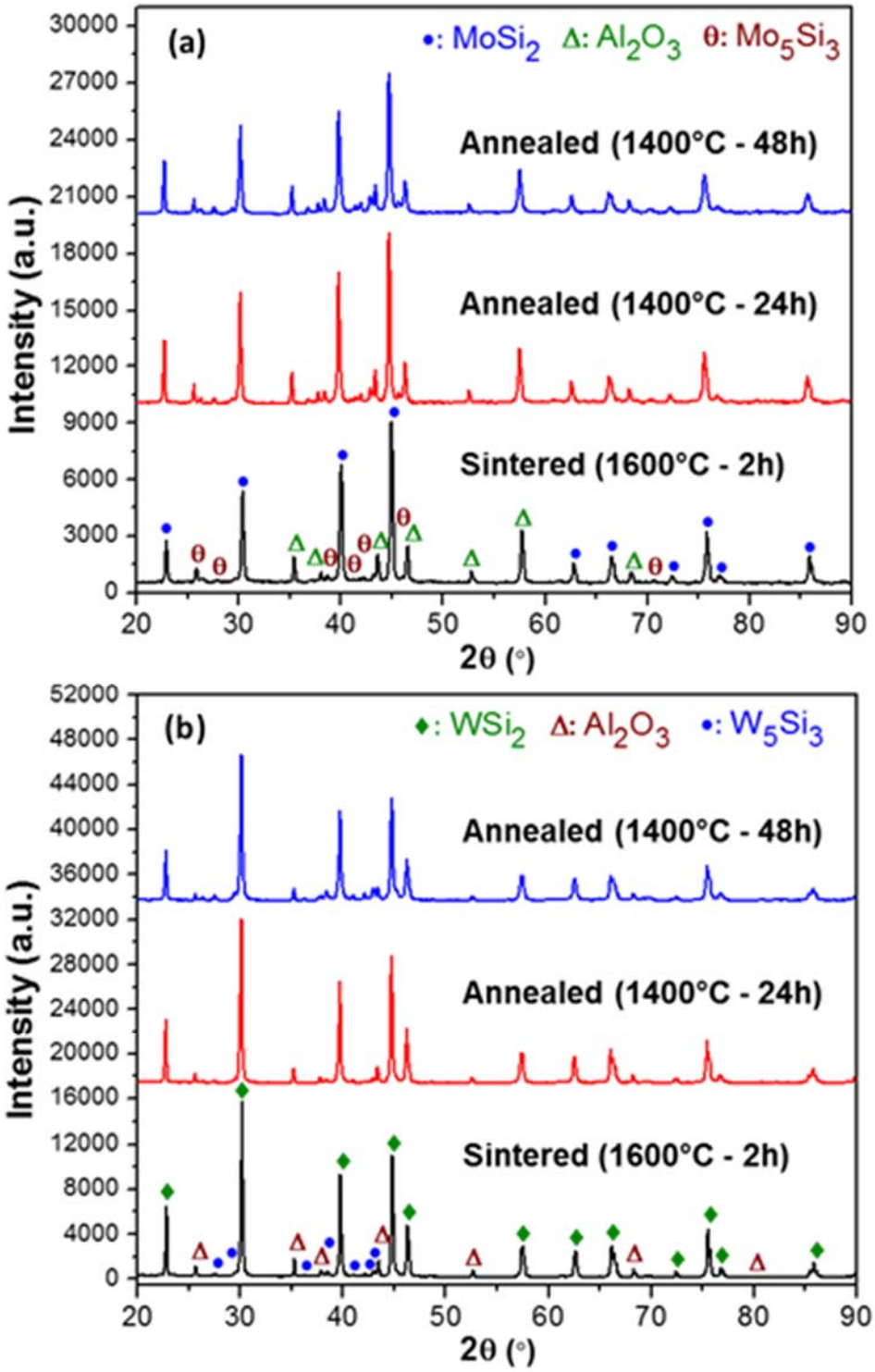

Figure 2.16. XRD patterns of the (a) (60-40) vol% $MoSi_2$-Al_2O_3, and (b) (60-40) vol% WSi_2-Al_2O_3 composite samples after sintering at 1600°C for 2 h, and short- and long-term annealing at 1400°C for 24-48 h.

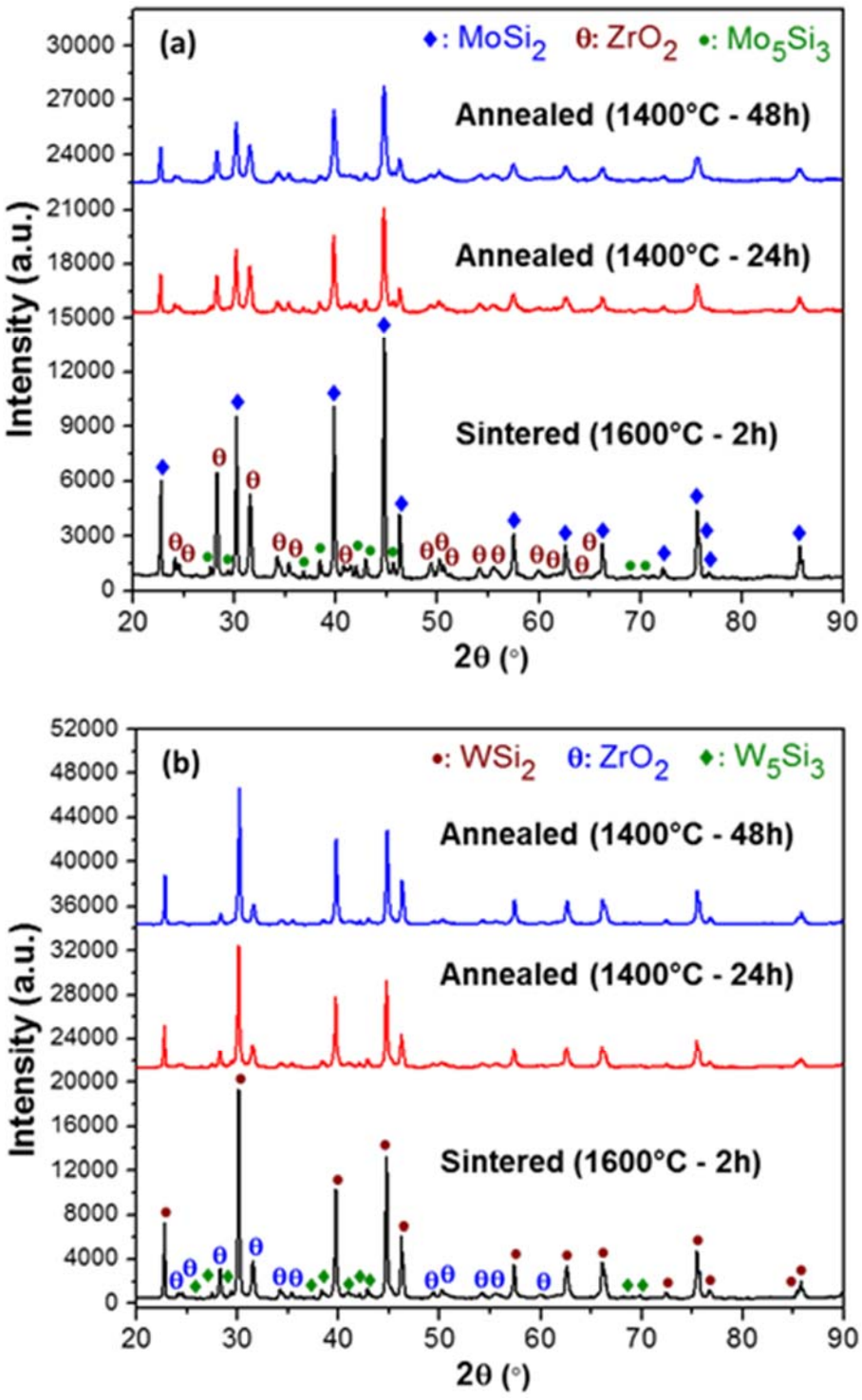

Figure 2.17. XRD patterns of the (a) (60-40) vol% $MoSi_2$-ZrO_2 and (b) (60-40) vol% WSi_2-ZrO_2 composite samples after sintering at 1600°C for 2 h, and short- and long-term annealing at 1400°C for 24-48 h.

and WSi_2-Al_2O_3 composites are very stable thermally at 1400°C both for short-term (24 h) and long-term (48 h). These results also indicate that WSi_2 is more stable by itself at high temperatures compared to the $MoSi_2$. In addition, the XRD results of the (60-40) vol% $MoSi_2$-ZrO_2 and (60-40) vol% WSi_2-ZrO_2 composites after sintering and annealing processes are presented in the Figure 2.17(a-b). The phases identified for $MoSi_2$-ZrO_2 composite after sintering (1600°C), and short- and long-term annealing (1400°C) were $MoSi_2$, Mo_5Si_3, and ZrO_2, which proves that there is only a formation of 5-3 silicide as a secondary phase similar to the $MoSi_2$-Al_2O_3 composites. In addition, it is determined that the relative intensities of the Mo_5Si_3 peaks slightly increased after short-term (24 h) annealing at 1400°C, but its formation did not proceed during long-term (48 h) annealing. Similar to the WSi_2-Al_2O_3 composite system, it is found that W_5Si_3 secondary phase were formed within WSi_2-ZrO_2 composite system after short-term annealing at 1400°C, since the peak intensities of the W_5Si_3 phases slightly increased as shown in the Figure 2.17b. But no change was observed in the relative intensities of these peaks, which indicated that the formation of W_5Si_3 did not continue after 24 h. These results clearly prove that the $MoSi_2$-ZrO_2 and WSi_2-ZrO_2 composites are highly stable thermally at 1400°C up to 48 h.

Figure 2.18a presents the XRD patterns of the (60-40) vol% $NbSi_2$-Al_2O_3 composites annealed at 1400°C for 24, 48 and 96 hours. The phases identified for all XRD patterns were $NbSi_2$, Nb_5Si_3 and Al_2O_3. The results clearly showed that the peak intensities of secondary Nb_5Si_3 phase relatively increased as a function of annealing time at 1400°C, which is an indication of its increased volume fraction within $NbSi_2$-Al_2O_3 composite over time. The XRD patterns of the annealed (60-40) vol% $NbSi_2$-ZrO_2 composites are shown in the Figure 2.18b. Similar to the $NbSi_2$-Al_2O_3 composite system, Nb_5Si_3 was identified as secondary phases after annealing at 1400°C up to 96 hours. A significant increase in the Nb_5Si_3 peak intensities can be seen with increasing annealing time, particularly after annealing at 1400°C for 96 hours. Therefore, it is clear that the general trend for the $NbSi_2$-based composites was the increased peak intensities for secondary Nb_5Si_3 phase as an indication of its increased volume fraction over time which may highly influence the physical properties of these composites. In addition to the niobium silicide-based composites, phase analysis studies were also performed on the tantalum silicide-based composites after thermal annealing. Figure 2.19a shows the XRD patterns of the (60-40) vol% $TaSi_2$-Al_2O_3 composites annealed at 1400°C for 24, 48 and 96 hours. $TaSi_2$, Ta_5Si_3 and Al_2O_3 phases were identified for all the annealed composite samples. The results demonstrated that the peak intensities of the secondary 5-3 metal silicide phase (Ta_5Si_3) slightly increased with increasing annealing time from 24 to 96 hours. Similar to the $NbSi_2$-based composites, this can be considered as an indication of the increased volume fraction of the secondary 5-3 metal silicide phase within the composite system. The XRD patterns of the (60-40) vol% $TaSi_2$-ZrO_2 composites annealed at 1400°C up to 96 hours are presented in the Figure 2.19b. Similar to the $TaSi_2$-Al_2O_3 composite system, secondary Ta_5Si_3 phase formation and its increased peak intensities were clearly observed. However, Ta_5Si_3 peaks were more intense for the $TaSi_2$-ZrO_2 composite system even just after annealing for 24 hours. This result may be an indication of relatively high volume fraction of Ta_5Si_3 secondary phase within the $TaSi_2$-ZrO_2 composites in comparison to the $TaSi_2$-Al_2O_3 composites. As a review, it is crucial to understand the effect of these secondary 5-3 metal silicide phases on the physical properties of the composites due to their potentially increased volume fractions over time at high temperatures.

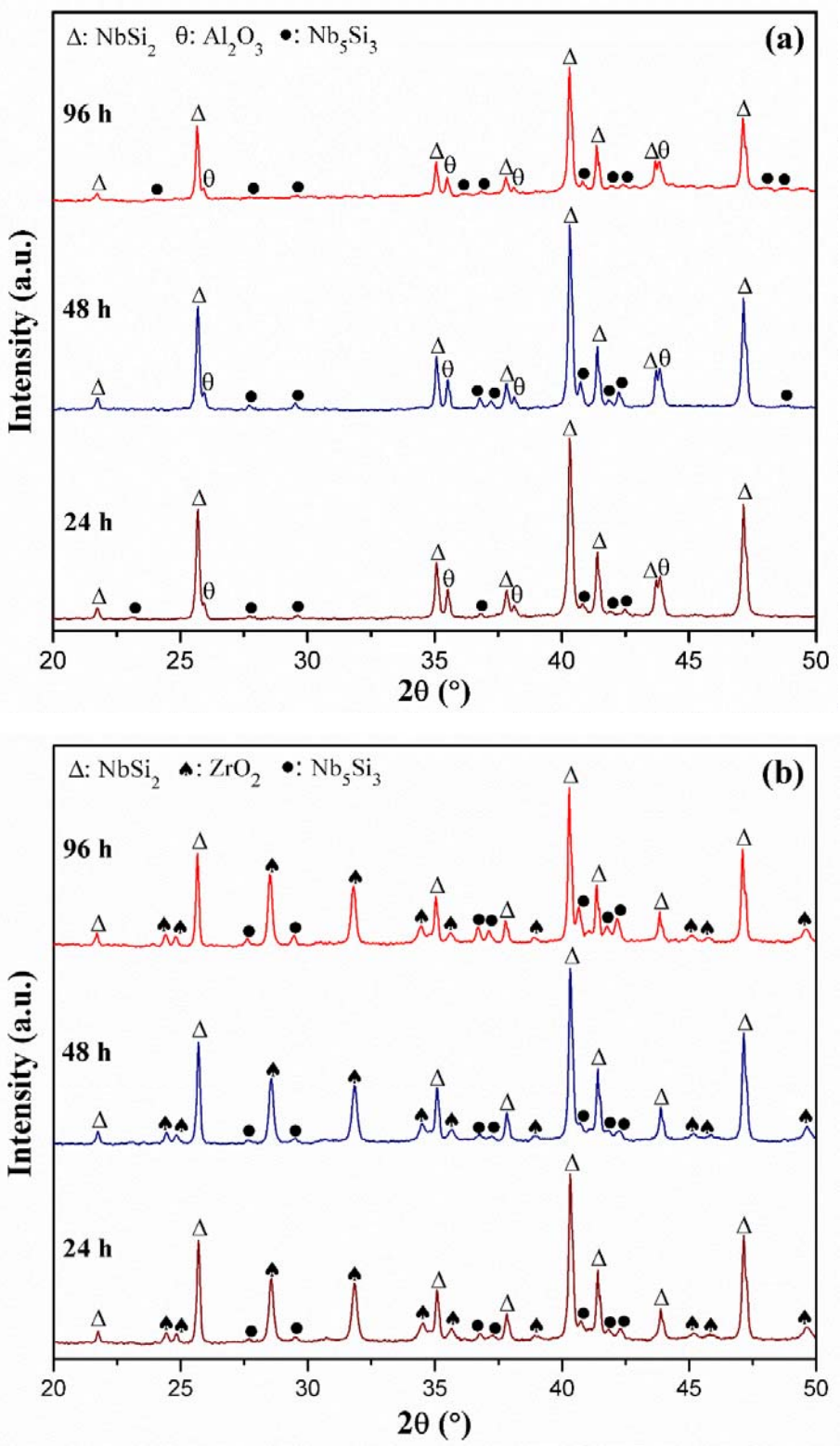

Figure 2.18. X-ray diffraction patterns of the (a) (60-40) vol% $NbSi_2$-Al_2O_3 and (b) (60-40) vol% $NbSi_2$-ZrO_2 composites after annealing at 1400°C for 24, 48 and 96 hours.

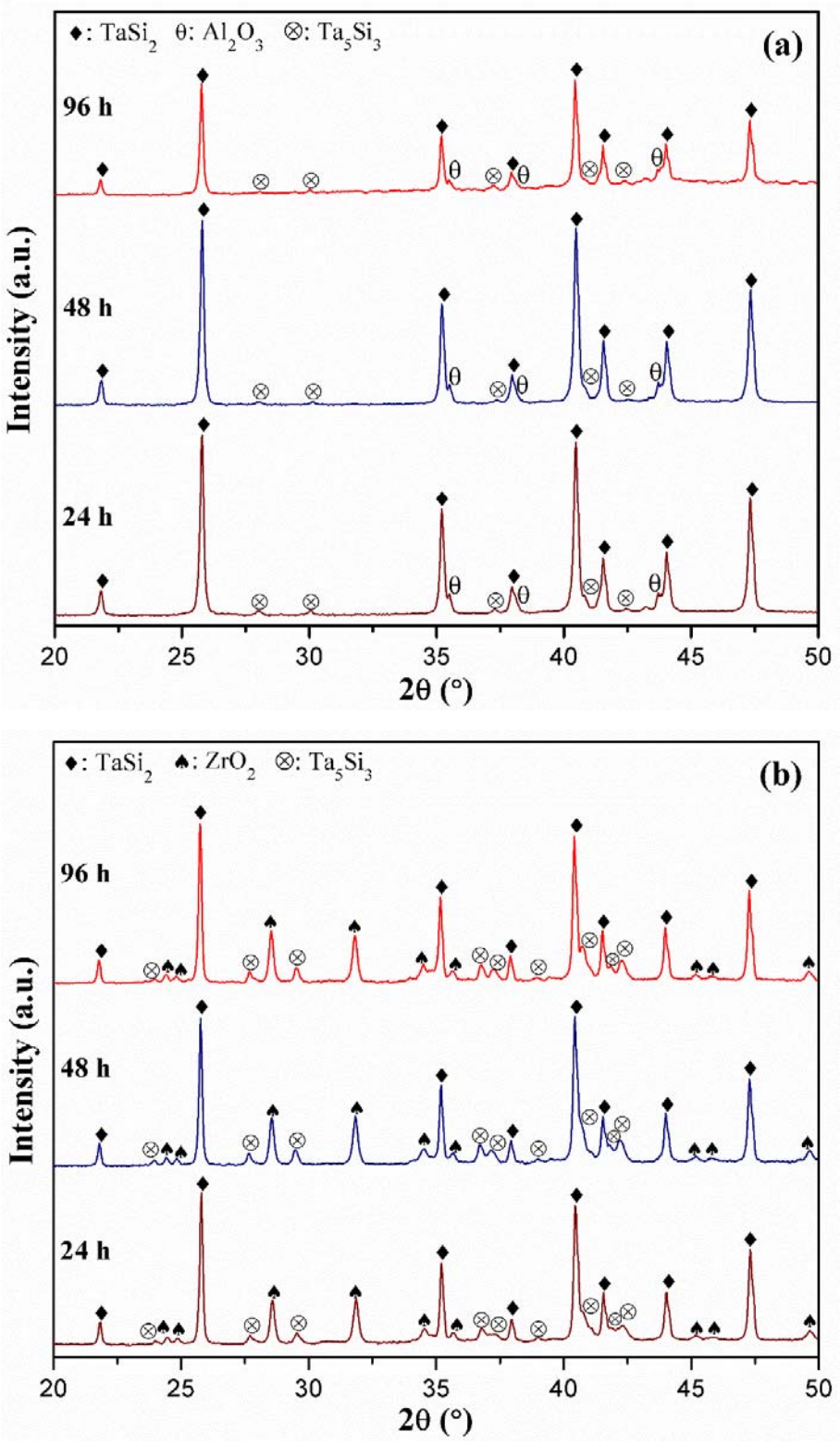

Figure 2.19. X-ray diffraction patterns of the (a) (60-40) vol% $TaSi_2$-Al_2O_3 and (b) (60-40) vol% $TaSi_2$-ZrO_2 composites after annealing at 1400°C for 24, 48 and 96 hours.

XRD experiments were also performed to evaluate the phase (thermal) stability of the selected $CrSi_2$-Cr_2O_3 compositions after annealing at 1400°C, particularly for 96 hours. The XRD results after sintering and annealing for 24, 48 and 96 hours of the (50-50) vol% $CrSi_2$-Cr_2O_3 composite are presented in the Figure 2.20a. No phase changes was observed after annealing up to 96 hours, since the major phases were all identified as Cr_3Si and SiO_2 in cristobalite form. In addition, the major change was a significant increase in the peak intensities of silica phase after annealing at 1400°C for 24 hours, but then, a slight decrease was observed after 96 hours. The increase in the SiO_2 cristobalite peak intensities may be related with its further crystallization, since alpha cristobalite phase can transform into β-cristobalite, which is known as a metastable phase between 270°C and 1470°C. Therefore, the results demonstrated that the (50-50) vol% $CrSi_2$-Cr_2O_3 composite exhibited high thermal stability for short- and long-term at 1400°C. Figure 2.20b presents the XRD results of the (55-45) vol% $CrSi_2$-Cr_2O_3 composite samples after sintering and annealing processes. It is important to note that a certain amount of $CrSi_2$ phase was remained in the system after sintering at 1400°C; and thus, it further reacted with the other phases (Cr_3Si, SiO_2 and Cr_5Si_3) during annealing. Therefore, a significant decrease in the peak intensities of the Cr_3Si phase and an increase in the peak intensities of the Cr_5Si_3 phase can be clearly observed after annealing at 1400°C for 24 hours. However, no further change was observed after 48 and 96 hours annealing, indicating the high phase and thermal stability of the (55-45) vol% $CrSi_2$-Cr_2O_3 composite particularly after 48 hours annealing at high-temperature. In addition to the (50-50) and (55-45) vol% $CrSi_2$-Cr_2O_3 composites, the XRD results of the (60-40) vol% $CrSi_2$-Cr_2O_3 composite samples were also discussed after sintering and annealing based on the Figure 2.20c. It was found that remained CrSi, $CrSi_2$ and Cr_2O_3 in the system after sintering further reacted to form more Cr_3Si, Cr_5Si_3 and SiO_2 with annealing at 1400°C for 24 hours. But it is important to state that

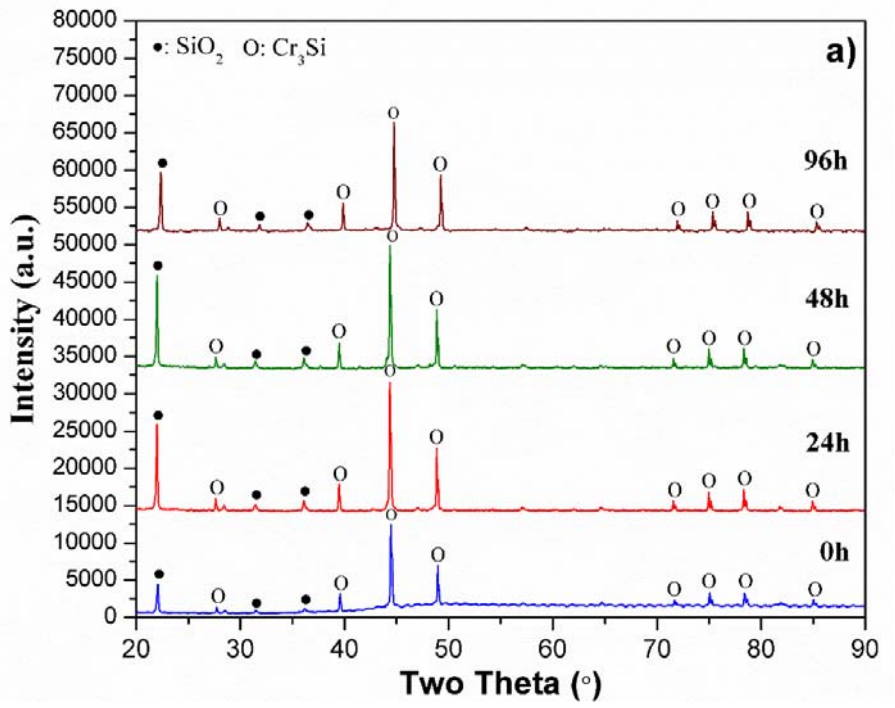

Figure 2.20. XRD patterns of the (a) (50-50) vol% $CrSi_2$-Cr_2O_3, (b) (55-45) vol% $CrSi_2$-Cr_2O_3, and (c) (60-40) vol% $CrSi_2$-Cr_2O_3 composite samples after sintering at 1400°C for 2 hours, and also after annealing at 1400°C for 24, 48 and 96 hours.

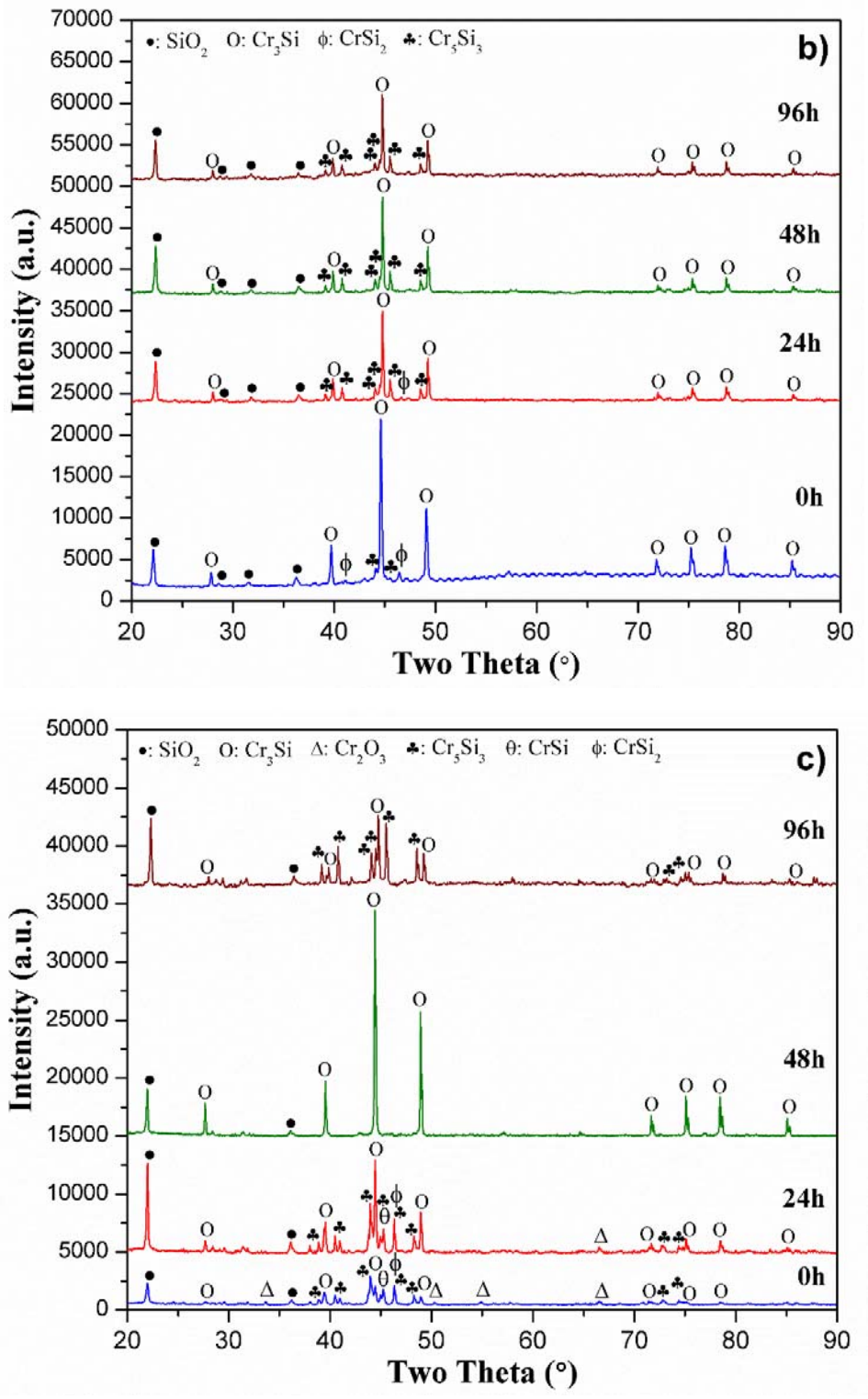

Figure 2.20. (continued) XRD patterns of the (a) (50-50) vol% $CrSi_2$-Cr_2O_3, (b) (55-45) vol% $CrSi_2$-Cr_2O_3, and (c) (60-40) vol% $CrSi_2$-Cr_2O_3 composite samples after sintering at 1400°C for 2 hours, and also after annealing at 1400°C for 24, 48 and 96 hours.

Cr_2O_3 and CrSi low-intensity peaks were still observed after 24 hours annealing period. Therefore, solid-state reactions slightly continued with further annealing at 1400°C for 48 hours, and only Cr_3Si and SiO_2 in cristobalite form were obtained after that. However, the formation of Cr_5Si_3 phase was clearly observed after annealing at 1400°C for 96 hours, indicating a substantial decrease in the amount of Cr_3Si phase in the system. As a result, the major silicide phases were obtained as Cr_5Si_3 and Cr_3Si for this composite after long-term annealing. As a review of the XRD results discussed above, it can be concluded that the (50-50), (55-45) and (60-40) vol% $CrSi_2$-Cr_2O_3 composites are not perfectly stable after sintering at 1400°C for 2 hours mainly due to remaining reactive phases with low melting points and/or further crystallization of the cristobalite SiO_2 phase at high temperature. Therefore, it is important to point out that these $CrSi_2$-Cr_2O_3 composites are promising materials for high temperature electrical applications, but they may need to be pre-annealed before use for achieving high thermal stability.

Lastly, in order to determine the fractions of secondary phases formed and investigate the thermal stability of the composites for long-term in detail, quantitative phase analysis studies on pure $MoSi_2$ and (60-40) vol% $MoSi_2$-Al_2O_3 composite were performed. In the quantitative phase analysis studies based on the Rietveld refinement technique, MAUD (Materials Analysis Using Diffraction) software [2.1], which is developed by Luca Lutterotti from the University of Trento, was used. The main goal of the Rietveld method is basically to minimize the residual function using a non-linear least squares algorithm, and therefore to refine the XRD spectrum by adjusting the diffraction intensity, line broadening (shape of the peaks), and positions of the peaks. In order to proceed quantitative phase analysis studies, crystallographic information files (CIFs) corresponding to Mo, $MoSi_2$, Mo_5Si_3, and Al_2O_3 were found by using the Crystallography Open Database system (*http://www.crystallography.net/cod*) [2.5]. Figure 2.21(a-d) presents the Rietveld refinement graphs of pure $MoSi_2$ precursor powder and pure $MoSi_2$ samples after sintering and annealing processes. These graphs indicate how the reference patterns/peaks fit to the corresponding XRD pattern, since it is very important to obtain reasonable error values and good fitting for accurate quantitative phase analysis data. It is known that the goodness of fit (sig = R_{wp}/R_{exp}) should be less than two, and Chi-square (X^2) indicating the accuracy of the Rietveld refinement should be less than four. For pure $MoSi_2$ precursor powder, the quantitative phase analysis results showed that weight percentages (wt.%) of Mo, $MoSi_2$, and Mo_5Si_3 are 62.90, 26.38 and 10.72, respectively (Figure 2.21a). This result clearly proves that the major phase in the commercial $MoSi_2$ powder is molybdenum metal. The sig and Chi-square values representing the reliability of the Rietveld refinement were obtained as 1.437 and 2.066, respectively. For pure $MoSi_2$ sample sintered at 1600°C for 2 hrs, the weight percentages of $MoSi_2$ and Mo_5Si_3 were determined as 76.42 and 23.58, respectively. Based on this result, it can be clearly stated that 62.90 wt.% molybdenum metal existing in the precursor powder completely transformed into $MoSi_2$ and Mo_5Si_3 phases, since the weight percentages of both phases highly increased after sintering process. For this sample, the sig and Chi-square values were obtained as 1.410 and 1.987, respectively. After short-term annealing at 1400°C, quantitative phase analysis results showed that weight percentages of $MoSi_2$ and Mo_5Si_3 are 71.76 and 28.24, respectively (Figure 2.21c). In this case, the sig and Chi-square values were also obtained as 1.457 and 2.125, respectively. Based on this result, it can be clearly stated that the weight percentage of $MoSi_2$ decreased from 76.42 to 71.76, while the weight percentage of Mo_5Si_3 as a secondary phase increased from 23.58 to 28.24 after short-term annealing at 1400°C. As also presented in the Figure 2.21d for pure $MoSi_2$ sample annealed at 1400°C for 48 hours, the weight percentages of $MoSi_2$ and Mo_5Si_3 were determined as 61.73 and 38.27, respectively. For this sample, sig and Chi-square values indicating reliability

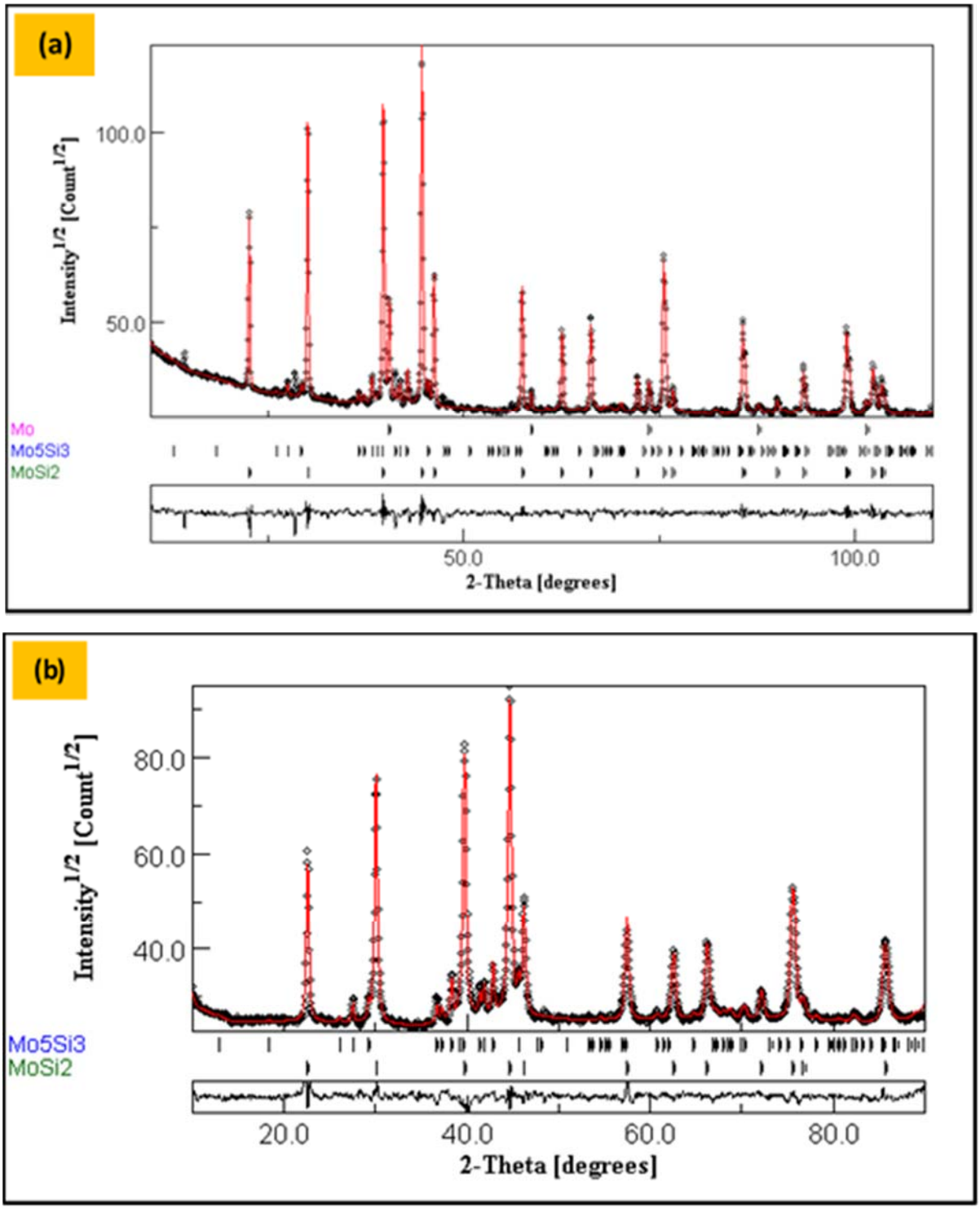

Figure 2.21. Rietveld refinement fitting profiles obtained by MAUD software for (a) commercial $MoSi_2$ precursor powder, (b) pure $MoSi_2$ sample after sintering, (c) pure $MoSi_2$ sample after short-term (24 hrs) annealing, and (d) pure $MoSi_2$ sample after long-term (48 hrs) annealing.

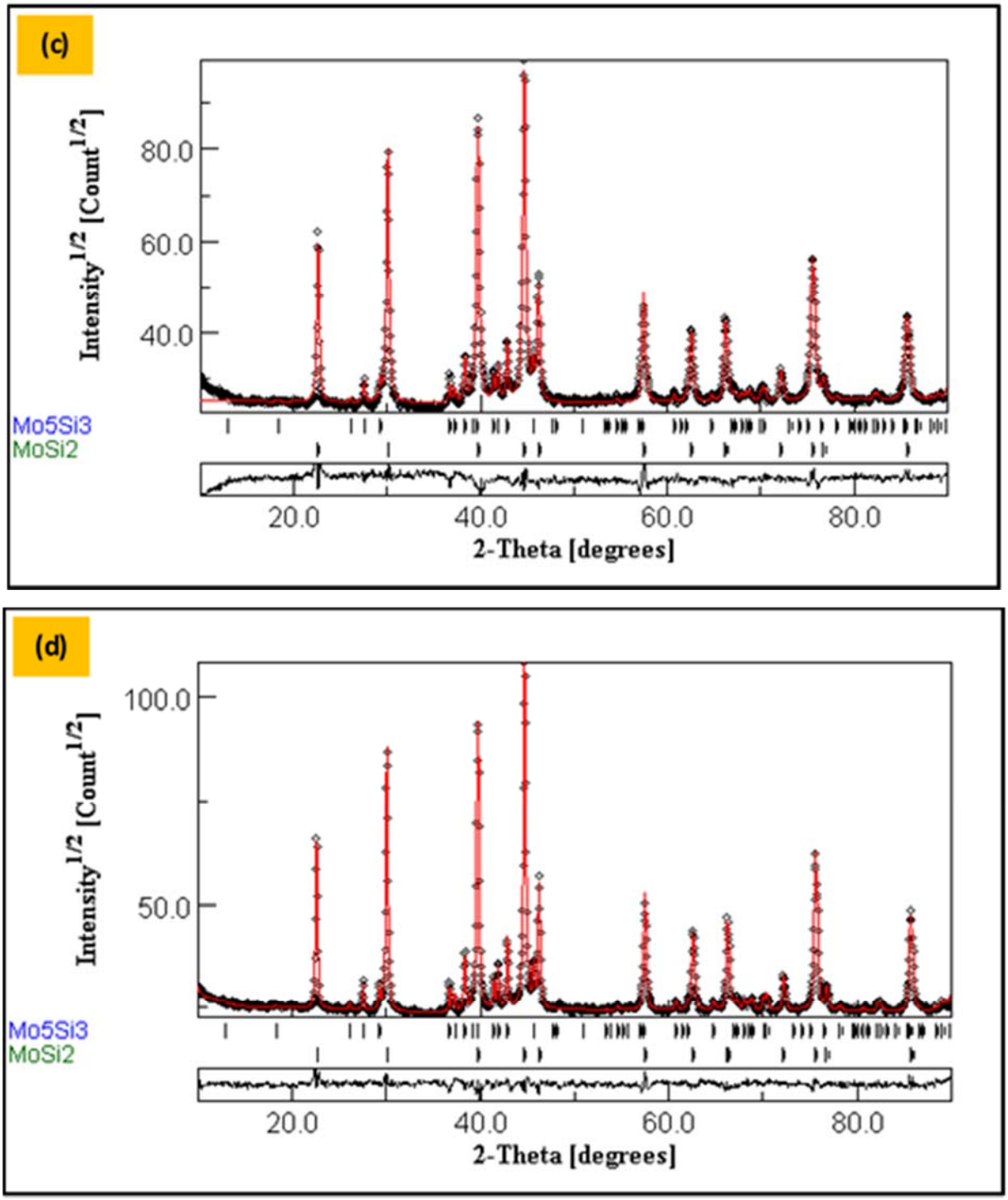

Figure 2.21. (continued) Rietveld refinement fitting profiles obtained by MAUD software for (a) commercial $MoSi_2$ precursor powder, (b) pure $MoSi_2$ sample after sintering, (c) pure $MoSi_2$ sample after short-term (24 hrs) annealing, and (d) pure $MoSi_2$ sample after long-term (48 hrs) annealing.

of the Rietveld refinement were achieved as 1.282 and 1.644, respectively. As a review of the quantitative phase analysis results obtained for pure $MoSi_2$ samples by Rietveld refinement method, it is important to note that commercial $MoSi_2$ precursor powder contains 62.90 wt.% molybdenum metal, which completely transformed into $MoSi_2$ and Mo_5Si_3 phases during sintering at 1600°C. In addition, it is found that the weight percentage of Mo_5Si_3 secondary phase increased from 23.58 to 38.27 during annealing at 1400°C up to 48 hours. Due to high fraction of Mo_5Si_3 formed, it is crucial to understand the effect of Mo_5Si_3 on physical properties of the composites, particularly on their high temperature electrical conductivities. Therefore, further studies are needed for better understanding of the role of Mo_5Si_3 in metal silicide/refractory oxide composite systems, which would fundamentally contribute to the academic literature.

In addition to the pure $MoSi_2$ samples, quantitative phase analysis studies were also performed on (60-40) vol% $MoSi_2$-Al_2O_3 composite samples after sintering and annealing processes. Figure 2.22(a-c) presents the Rietveld refinement graphs of $MoSi_2$-Al_2O_3 composite samples after sintering, short-term and long-term annealing processes, respectively. For the (60-40) vol% $MoSi_2$-Al_2O_3 composite sample sintered at 1600°C, the quantitative phase analysis results showed that weight percentages of $MoSi_2$, Mo_5Si_3 and Al_2O_3 are 63.32, 0.46 and 36.22 respectively (Figure 2.22a). This result clearly proves that the major silicide phase in the $MoSi_2$-Al_2O_3 composite after sintering is $MoSi_2$ with 63.32 wt.%. But still it is important to note that there is a slight formation of Mo_5Si_3 secondary phase. For this sample, the sig and Chi-square values indicating the reliability

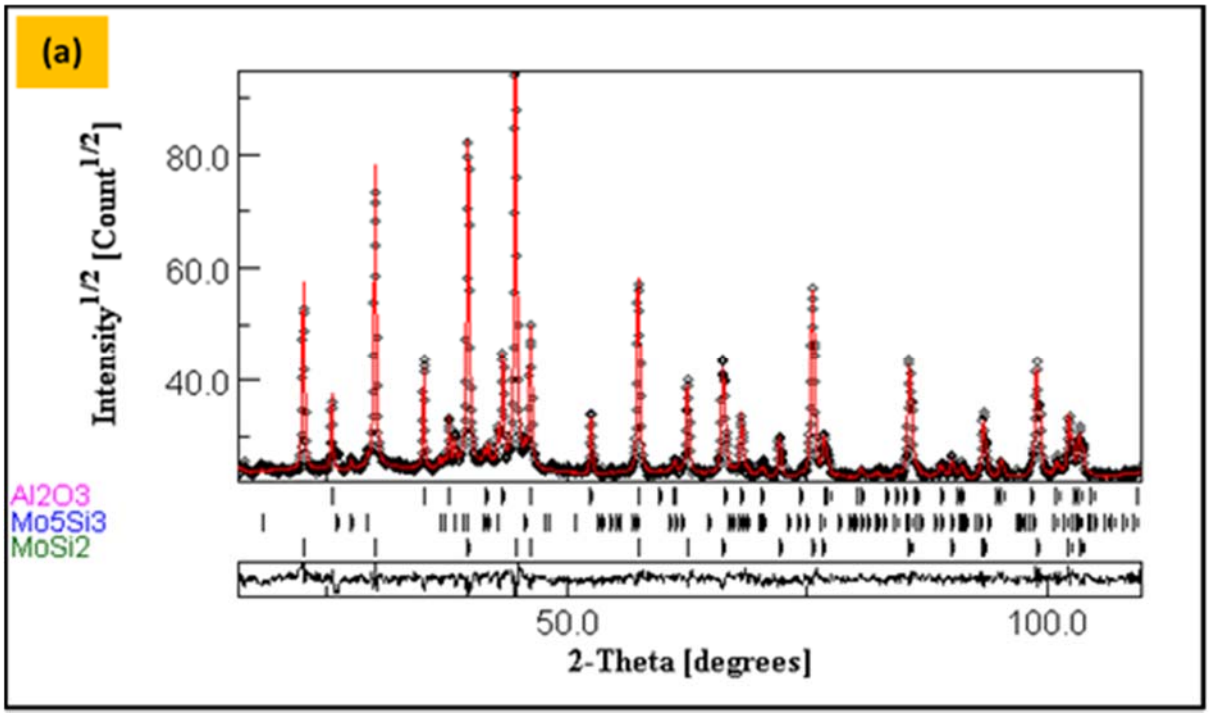

Figure 2.22. Rietveld refinement fitting profiles obtained by MAUD software for (60-40) vol% $MoSi_2$-Al_2O_3 composite samples after (a) sintering, (b) short-term (24 hrs) annealing, and (c) after long-term (48 hrs) annealing.

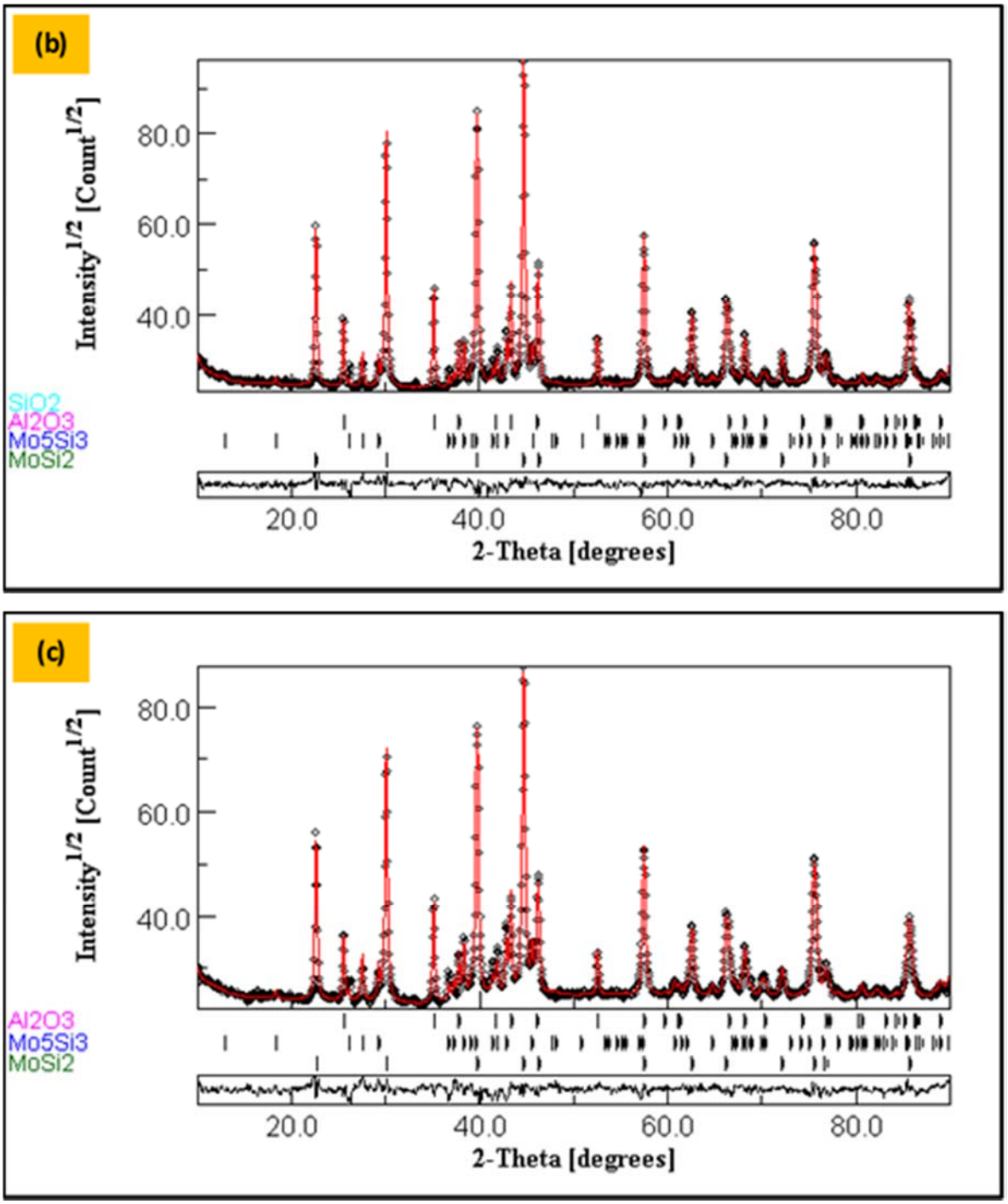

Figure 2.22. (continued) Rietveld refinement fitting profiles obtained by MAUD software for (60-40) vol% $MoSi_2$-Al_2O_3 composite samples after (a) sintering, (b) short-term (24 hrs) annealing, and (c) after long-term (48 hrs) annealing.

of the Rietveld refinement were obtained as 1.340 and 1.796, respectively. After short-term annealing at 1400°C, the quantitative phase analysis results showed that the weight percentage of $MoSi_2$ phase slightly decreased from 63.32 to 60.15 wt.%, while weight percentage of Mo_5Si_3

secondary phase increased from 0.46 to 3.53 wt.%. Also the results showed that the weight percentage of Al_2O_3 phase is 36.32 wt.% after short-term annealing at 1400°C. Here the sig and Chi-square values were achieved as 1.325 and 1.756, respectively. For the (60-40) vol% $MoSi_2$-Al_2O_3 composite sample annealed at 1400°C for 48 hours, the quantitative phase analysis results showed that the weight percentages of $MoSi_2$, Mo_5Si_3 and Al_2O_3 phases are 59.19, 5.64 and 35.17, respectively. Therefore, it is important to note that the weight percentage of Mo_5Si_3 secondary phase slightly increased from 3.53 to 5.64 wt.% with an additional 24 hours annealing at 1400°C. For this sample, the sig and Chi-square values were also obtained as 1.384 and 1.914, respectively. As a result of the quantitative phase analysis studies performed via Rietveld refinement method, it is found that the commercial $MoSi_2$ powder contains 62.90 wt.% molybdenum metal as a major phase. During sintering at 1600°C for 2 hours, the molybdenum metal completely transformed into $MoSi_2$ and Mo_5Si_3 phases. Furthermore, it is determined that the weight percentage of Mo_5Si_3 phase highly increased from 23.58 to 38.27 wt.% during annealing at 1400°C for 48 hours. This result indicates that the formation of Mo_5Si_3 phase and its effect on the physical properties (electrical, thermal, etc.) need to be investigated in detail for better understanding of the silicide/oxide composite systems. In the case of $MoSi_2$-Al_2O_3 composite system, it is clearly presented that there is a slight formation of Mo_5Si_3 secondary phase during sintering and annealing processes, which may affect the physical properties of the composites.

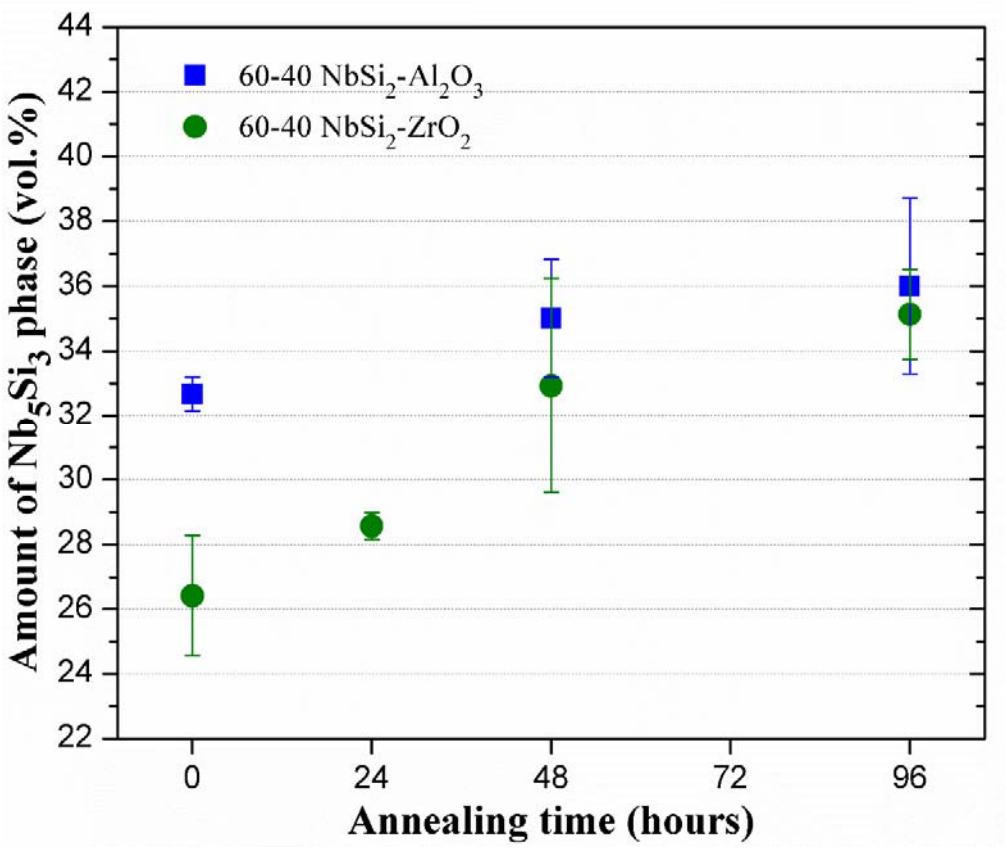

Figure 2.23. Changes in the volume fraction of the secondary Nb_5Si_3 phase within the (60-40) vol% $NbSi_2$-Al_2O_3 and $NbSi_2$-ZrO_2 composites as a function of annealing time at 1400°C based on the Rietveld refinement results.

The quantitative phase analysis studies on $NbSi_2$-Al_2O_3 and $NbSi_2$-ZrO_2 composites were also performed in order to investigate the fractions of secondary Nb_5Si_3 phase within these composite materials, which may highly influence their physical properties. In order to proceed quantitative phase analyses studies, crystallographic information files (CIFs) corresponding to $NbSi_2$, Nb_5Si_3, Al_2O_3 and ZrO_2 were found by using the Crystallography Open Database (COD). However, $TaSi_2$-based composite samples were not analyzed by Rietveld method, since a CIF file corresponding to Ta_5Si_3 phase could not be found on the database. The sig and Rwp values representing the quality of the Rietveld refinement and fitting were found as 1.48-2.06 and 1.86-4.47 for all the XRD patterns, respectively. Figure 2.23 presents the changes in the Nb_5Si_3 volume fraction within the (60-40) vol% $NbSi_2$-Al_2O_3 and $NbSi_2$-ZrO_2 composites as a function of annealing time at 1400°C. "0" annealing time was used to indicate the composite samples after sintering as the beginning point. The results for the $NbSi_2$-Al_2O_3 composites clearly showed that Nb_5Si_3 fraction increased from 32.7 to 36.0 vol% with increasing annealing time from 24 to 96 hours. This increase was from 26.4 to 35.1 vol% for the $NbSi_2$-ZrO_2 composites. In comparison of these composite systems, the Nb_5Si_3 fraction was significantly higher within $NbSi_2$-Al_2O_3 composite after sintering at 1600°C. However, the level of increase in the Nb_5Si_3 volume fraction was significantly higher for the $NbSi_2$-ZrO_2 composites (8.7 vol% after 96 hrs) in comparison to the $NbSi_2$-Al_2O_3 composites (3.3 vol% after 96 hrs). These results clearly demonstrated that the $NbSi_2$-Al_2O_3 composite is more thermally stable with less increase in the secondary phase volume fraction during thermal annealing.

2.3.2.3 Microstructures and grain growth behavior of the composites

This section reports the (i) microstructral characterization of the silicide-oxide composites after sintering processes, and (ii) microstructral evolution and grain growth kinetics after high-temperature annealing processes.

2.3.2.3.1 Microstructural analysis of the composites after sintering

Due to the polishing difficulty of two phase systems including softer and harder materials, a new polishing protocol has been developed for the silicide-oxide composites and their SEM studies. The prepared composite samples were firstly polished by 600 grits SiC abrasive paper for 5-10 minutes followed by cleaning of the sample surface by ultrasonication in distilled water and/or ethanol for 15 minutes. In the second step, those samples were fine polished by 1200 grits SiC abrasive paper for 5-10 minutes again followed by cleaning of the sample surface by ultrasonication in distilled water and/or ethanol for 15 minutes. Then those samples were lastly polished by using 0.5 μm diamond paste for 10 minutes, and the polishing was completed by final cleaning of the polished sample surface with ultrasonication in both distilled water and ethanol for 15 minutes each. Figure 2.24(a-d) present the SEM microstructures of 60 vol% $MoSi_2$-40 vol% Al_2O_3 and 60 vol% WSi_2-40 vol% Al_2O_3 composite samples sintered at 1600°C for 2 h. It can be clearly seen that there are some non-homogeneous regions mainly composed of fine alumina grains within the microstructures of $MoSi_2$-Al_2O_3 and WSi_2-Al_2O_3 composites. However it is important to note that distribution of metal silicides within Al_2O_3 refractory oxide matrix is more homogeneous for WSi_2-Al_2O_3 composites in comparison with $MoSi_2$-Al_2O_3 composites. Since the densities of 60 vol% $MoSi_2$-40 vol% Al_2O_3 and 60 vol% WSi_2-40 vol% Al_2O_3 composite samples

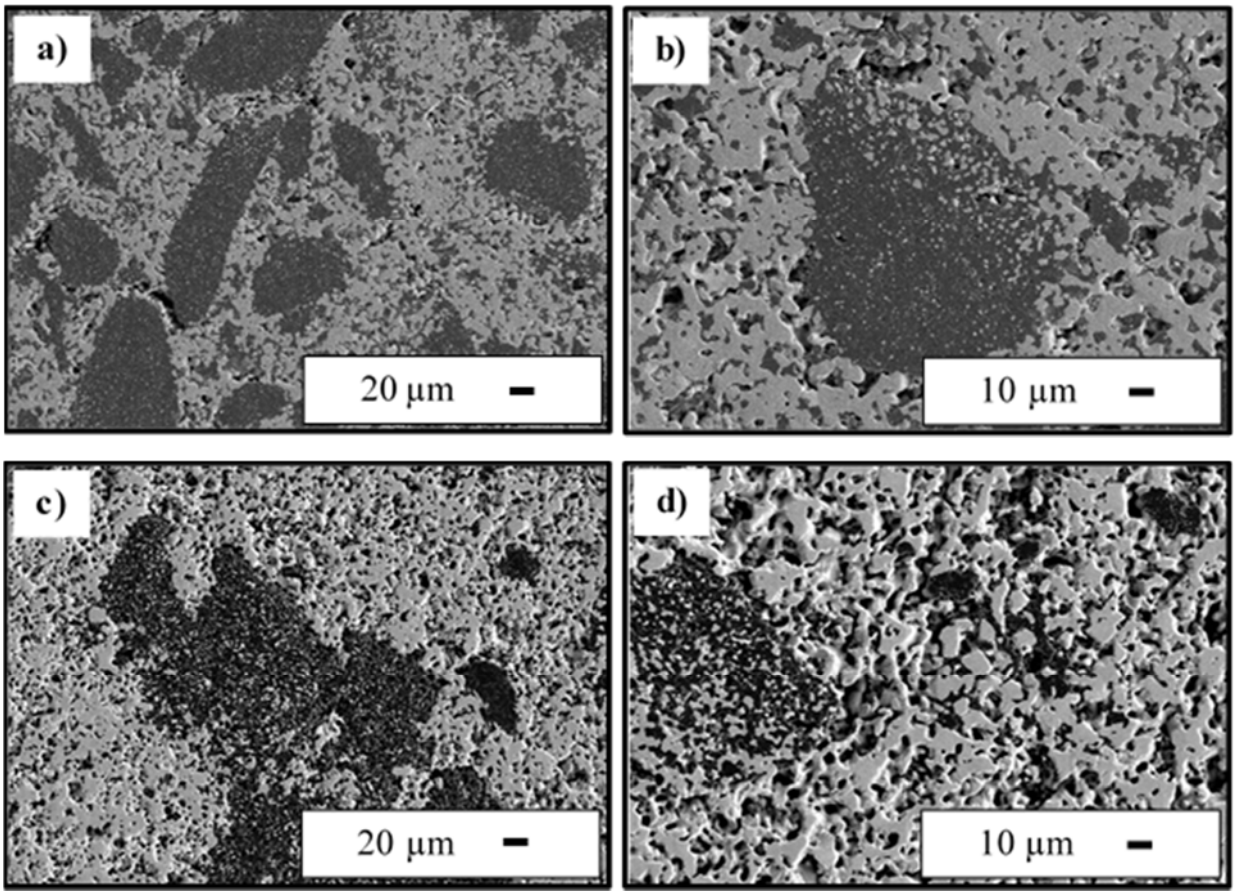

Figure 2.24. SEM micrographs of the fine polished (a-b) 60 vol% $MoSi_2$-40 vol% Al_2O_3, and (c-d) 60 vol% WSi_2-40 vol% Al_2O_3 composites sintered at 1600°C for 2 h.

sintered at 1600°C were 87.97 and 95.48%, respectively, it can be concluded that increasing density is related with more homogeneous distribution of WSi_2 within Al_2O_3 matrix. Figure 2.25 (a-d) show the SEM microstructures of 60 vol% $MoSi_2$-40 vol% Y_2O_3 and 60 vol% WSi_2-40 vol% Y_2O_3 composite samples sintered at 1600°C for 2 h. The results clearly indicate that homogeneous distribution of metal silicides within Y_2O_3 refractory oxide matrix was achieved for both $MoSi_2$-Y_2O_3 and WSi_2-Y_2O_3 composites. Although it is hard to distinguish different phases existed in $MoSi_2$-Y_2O_3 composite system due to slight difference between the atomic number of Mo and Y, three different phases can be identified indicating $MoSi_2$, Y_2O_3 (darker regions) and $Y_5Mo_2O_{12}$ (brighter regions). In the WSi_2-Y_2O_3 composite system, two phases showing WSi_2 (bright regions) and Y_2SiO_5 (dark regions) were clearly identified (Figure 2.25c-d). However, decomposition of metal silicides, formation of undesired secondary phases and hereby their lower densities (~ 83-84%) can be stated as main problems regarding to the Y_2O_3-based composites.

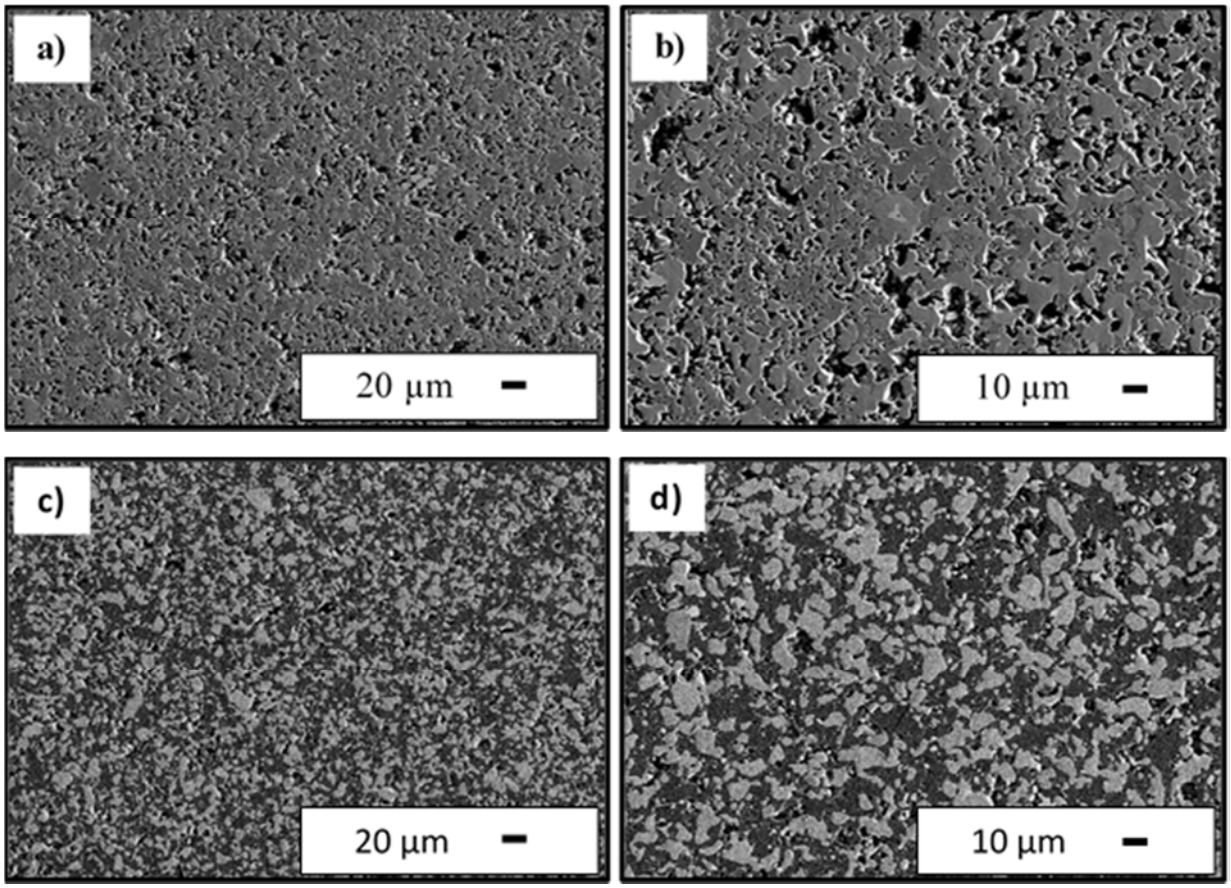

Figure 2.25. SEM micrographs of the fine polished (a-b) 60 vol% $MoSi_2$-40 vol% Y_2O_3, and (c-d) 60 vol% WSi_2-40 vol% Y_2O_3 composites sintered at 1600°C for 2 h.

Figure 2.26 (a-d) present the SEM microstructures of 60 vol% $MoSi_2$-40 vol% ZrO_2 and 60 vol% WSi_2-40 vol% ZrO_2 composite samples sintered at 1600°C for 2 h. It can be clearly seen that both $MoSi_2$ and WSi_2 grains were well distributed within ZrO_2 refractory oxide matrix particularly in comparison to the $MoSi_2$-Al_2O_3 and WSi_2-Al_2O_3 composites. Since there were no reaction between these metal silicides and ZrO_2, only two phases indicating metal silicides (bright regions) and ZrO_2 (dark regions) can be seen in micrographs. It was hard to distinguish $MoSi_2$ and ZrO_2 grains due to slight difference between atomic number of Mo and Zr. Although the densities of the 60 vol% $MoSi_2$-40 vol% ZrO_2 and 60 vol% WSi_2-40 vol% ZrO_2 composite samples sintered at 1600°C were 87.82 and 84.57%, respectively, ZrO_2-based composites have higher homogeneity and well distribution of metal silicides. Figure 2.27 (a-d) present the SEM microstructures of 20 vol% $MoSi_2$-80 vol% Cr_2O_3 and 20 vol% WSi_2-80 vol% Cr_2O_3 composite samples sintered at 1400°C for 2 h. Since metal silicides partially reacted with Cr_2O_3 to form secondary phases, more than two phases are seen in all micrographs. In $MoSi_2$-Cr_2O_3 composite system, three phases indicating $MoSi_2$ (brighter regions), Cr_3Mo, and Cr_2O_3 (darker regions) were clearly identified. On the other hand, four different phases showing the presence of WSi_2, W_3O (brighter regions), Cr_2O_3, and SiO_2 (darker regions) were determined. Therefore these reactions between metal silicides and Cr_2O_3 at 1400°C were found to be as a main problem in the Cr_2O_3-based composites.

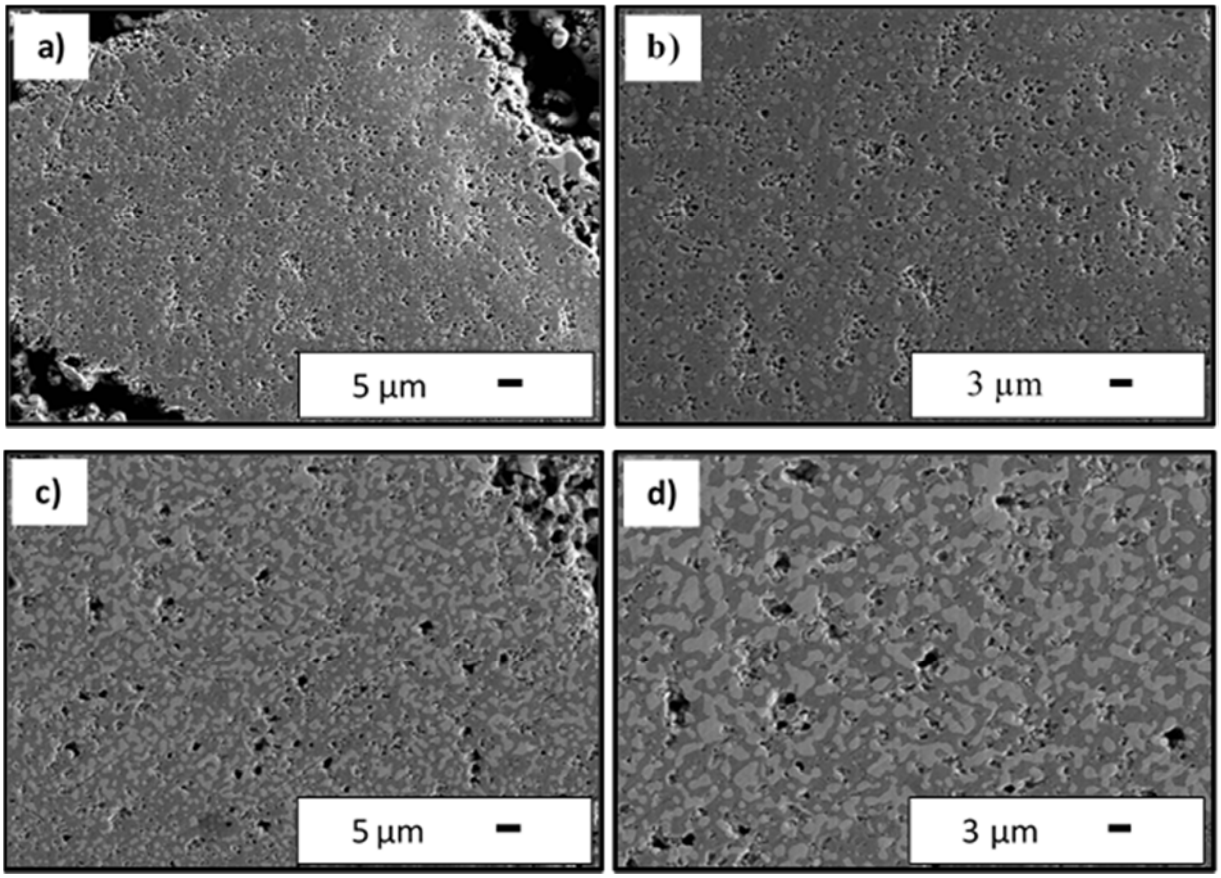

Figure 2.26. SEM micrographs of the fine polished (a-b) 60 vol% $MoSi_2$-40 vol% ZrO_2, and (c-d) 60 vol% WSi_2-40 vol% ZrO_2 composites sintered at 1600°C for 2 h.

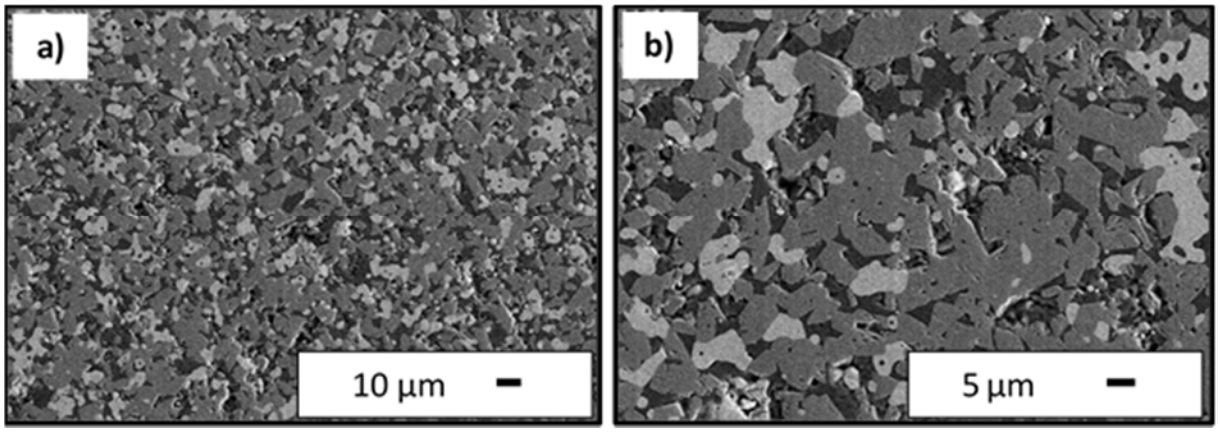

Figure 2.27. SEM micrographs of the fine polished (a-b) 20 vol% $MoSi_2$-80 vol% Cr_2O_3, and (c-d) 20 vol% WSi_2-80 vol% Cr_2O_3 composites sintered at 1400°C for 2 h.

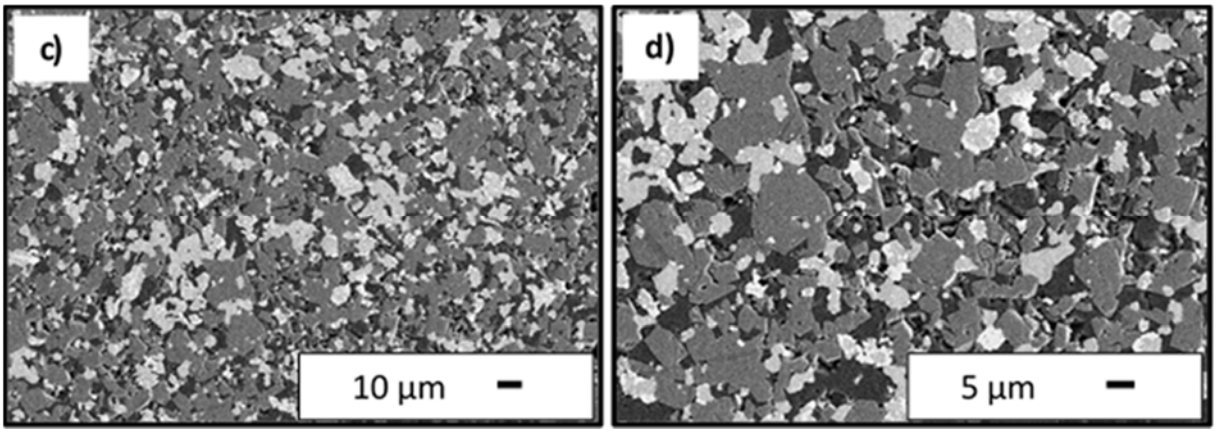

Figure 2.27. (continued) SEM micrographs of the fine polished (a-b) 20 vol% $MoSi_2$-80 vol% Cr_2O_3, and (c-d) 20 vol% WSi_2-80 vol% Cr_2O_3 composites sintered at 1400°C for 2 h.

Based on the results of thermal etching and related composite microstructures, some other composite samples were additionally chemically etched by soaking for 1-2 minutes in different acid solutions in order to bring out more contrast between different phases and to understand these composites' microstructure better. Figure 2.28 (a-d) shows the SEM microstructures of (60-40) vol% WSi_2-Al_2O_3 composite samples after fine polishing and then chemical etching in 1:1:1 HCl:HNO_3:H_2O (volumetric ratio) acid mixture for 1-2 minutes. These results showed that grain boundaries of agglomerated Al_2O_3 grains were exposed more clearly, and more contrast between silicide and oxide grains were formed by chemical etching. By this way, dark areas or spots corresponding to Al_2O_3 grains were obtained as also shown in the microstructures (Figure 2.28a-b). In the previous reports, it was noted that fine polished, unetched SEM microstructure of (60-40) vol% WSi_2-Al_2O_3 composite showed only two phases which are WSi_2 and Al_2O_3. But here it was found that there are three different phases corresponding to bright, gray, and dark regions in

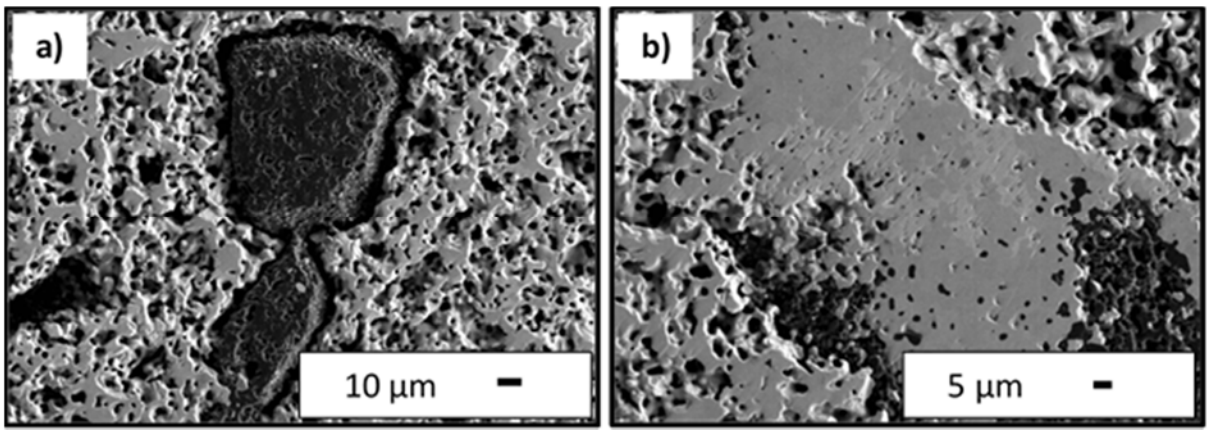

Figure 2.28. SEM micrographs (a-b-c-d) of the (60-40) vol% WSi_2-Al_2O_3 composite samples sintered at 1600°C for 2h after fine polishing and then chemical etching in 1:1:1 HCl:HNO_3:H_2O (volumetric ratio) acid mixture for 1-2 minutes.

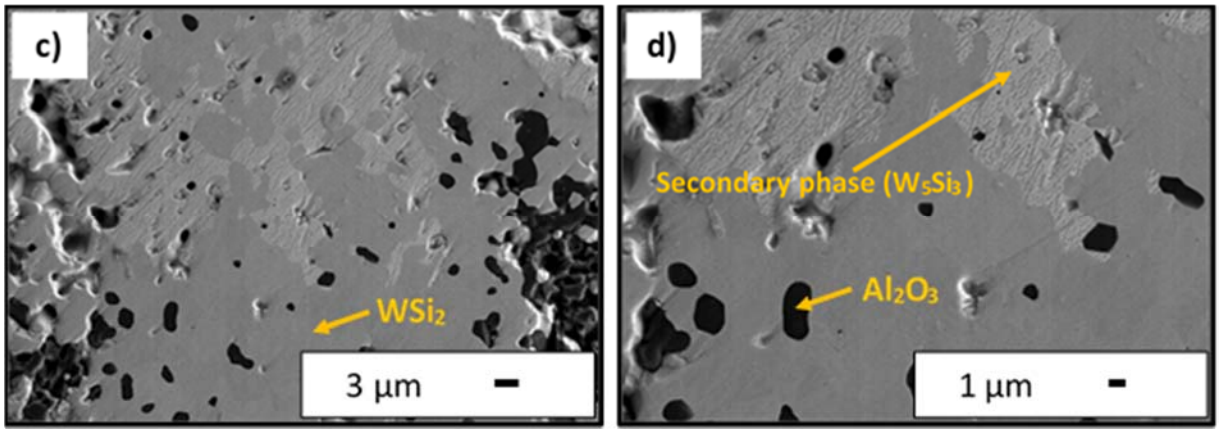

Figure 2.28. (continued) SEM micrographs (a-b-c-d) of the (60-40) vol% WSi_2-Al_2O_3 composite samples sintered at 1600°C for 2h after fine polishing and then chemical etching in 1:1:1 HCl:HNO_3:H_2O (volumetric ratio) acid mixture for 1-2 minutes.

these microstructures. Based on the XRD result, it can be concluded that the third phase (bright regions) existing in the microstructure is W_5Si_3 formed during sintering at 1600°C for 2 h. Also it can be seen that the formation of this phase started particularly at the grain boundaries of Al_2O_3 (dark regions).

Figure 2.29(a-d) presents the SEM microstructures of (60-40) vol% $MoSi_2$-coarseAl_2O_3 composite samples after fine polishing and then chemical etching in 2.0 M HCl acid solution for 1-2 minutes. These results showed that HCl acid solution damaged Al_2O_3 grains (dark regions) to a certain extent in some regions that were not well-polished. Therefore, it was not possible to get any information regarding this composite's microstructure from such regions. In the case of well-polished and then chemically etched samples/regions in HCl, the results clearly showed the existence of three different phases and formation of a secondary phase by starting from the grain boundaries of Al_2O_3 (Figure 2.29b-c-d). It can be stated that this information has a crucial role in understanding of their microstructure and interaction of different phases at high temperatures. Similarly the dark areas or spots corresponding to Al_2O_3 grains were obtained as also shown in the microstructures. In the previous reports, it was stated that fine polished, unetched SEM microstructure of (60-40) vol% $MoSi_2$-Al_2O_3 composite showed only two phases which are $MoSi_2$ and Al_2O_3. But here it was found that there are three different phases corresponding to bright, gray, and dark regions in these microstructures. Based on the XRD result of (60-40) vol% $MoSi_2$-Al_2O_3 composites, it can be concluded that the third phase (bright regions) existing in the microstructure is Mo_5Si_3 formed during sintering at 1600°C for 2 h. Also, (60-40) vol% $MoSi_2$-coarseAl_2O_3 composite samples were etched in 1:1:1 HCl:HNO_3:H_2O acid mixture for 1-2 minutes. In comparison to the samples etched in HCl, more contrast between those three phases was obtained (Figure 2.30a-b). Similarly, formation of a secondary phase can be seen in these microstructures by starting from dark regions or spots corresponding to Al_2O_3 grain boundaries. As a result, it is important to note that chemical etching can be used efficiently by selecting suitable acid solutions or mixtures in order to investigate different composites' microstructures and also to understand them better.

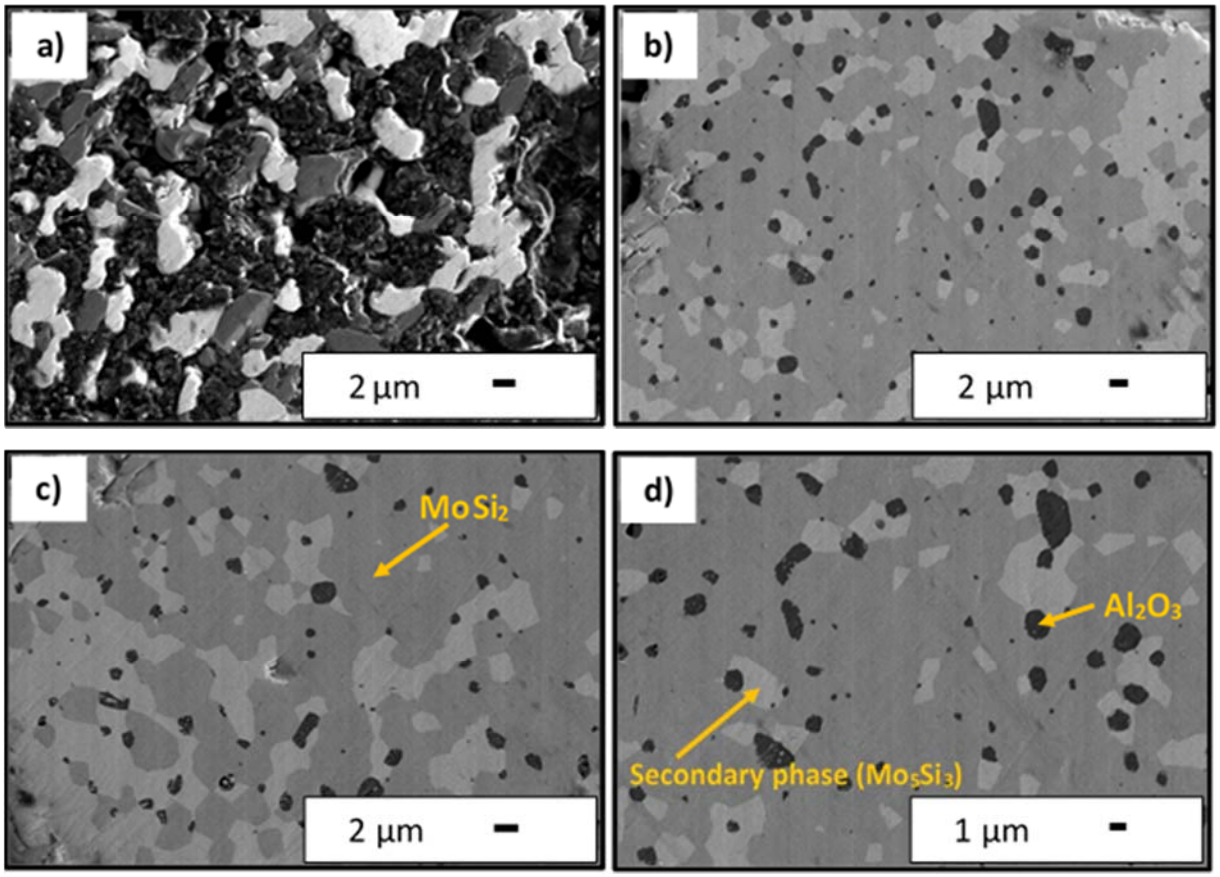

Figure 2.29. SEM micrographs (a-b-c-d) of the (60-40) vol% $MoSi_2$-coarseAl_2O_3 composite samples sintered at 1600°C for 2h after fine polishing and then chemical etching in 2.0 M HCl acid solution for 1-2 minutes.

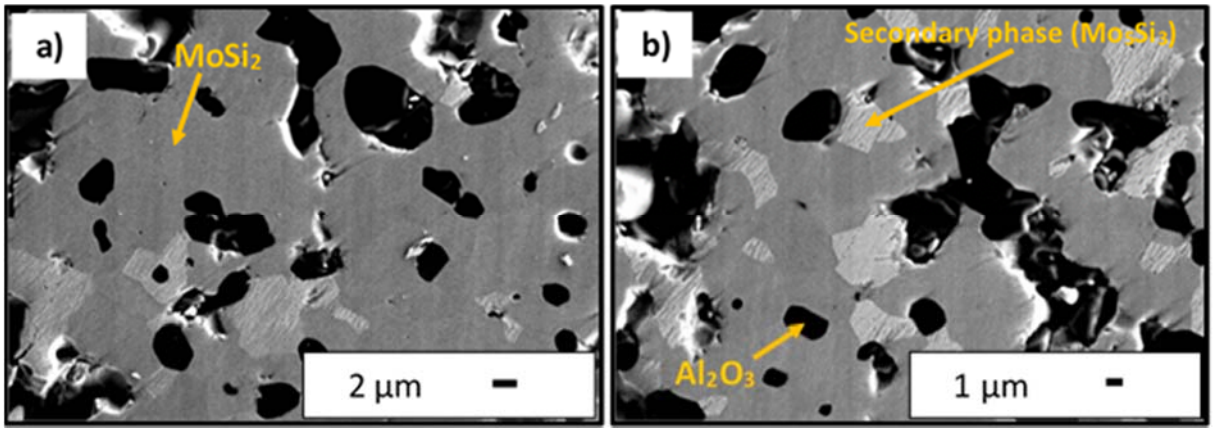

Figure 2.30. SEM micrographs (a-b) of the (60-40) vol% $MoSi_2$-coarseAl_2O_3 composite samples sintered at 1600°C for 2h after fine polishing and then chemical etching in 1:1:1 HCl:HNO_3:H_2O (volumetric ratio) acid mixture for 1-2 minutes.

Figure 2.31 presents the backscattered SEM microstructures of these composites with the addition of 40 vol% refractory oxide after sintering at 1600°C for 2 h in argon at relatively low magnifications. In the $NbSi_2$-Al_2O_3 microstructure, gray and dark regions refer to the $NbSi_2$ and Al_2O_3 grains, respectively (Fig. 2.31a). It was observed that the micron-sized niobium silicide grains were homogeneously distributed between the insulating alumina grains. However, three different phases can be clearly seen within the microstructure of the as-sintered $NbSi_2$-ZrO_2 composite, where the bright, gray and dark regions indicate Nb_5Si_3, ZrO_2 and $NbSi_2$ grains, respectively (Fig. 2.31b). It was found that the intermediate Nb_5Si_3 grains (bright regions) were formed mostly around the $NbSi_2$ grains (dark regions), which resulted in the formation of different interfaces ($NbSi_2$-Nb_5Si_3 and Nb_5Si_3-ZrO_2) and $NbSi_2$-ZrO_2-Nb_5Si_3 triple phase boundaries. Additionally, it should be noted that the Nb_5Si_3 grains and their formation from the $NbSi_2$ grain boundaries could positively affect the percolation and electrical properties within the composite. The SEM microstructure of the $TaSi_2$-Al_2O_3 displayed only two phases with a homogeneous distribution at low magnification (Fig. 2.31c). Similar results were also observed for the microstructure of the $TaSi_2$-ZrO_2 composite (Fig. 2.31d). In the $TaSi_2$-based composites, the gray and dark regions refer to the $TaSi_2$ and refractory oxide (Al_2O_3, ZrO_2) grains, respectively. As a review, all these composites generally exhibited homogeneous distribution of the conductive metal silicide phases within the insulating oxides, which could positively affect the electrical percolation and reduce the critical percolation concentration.

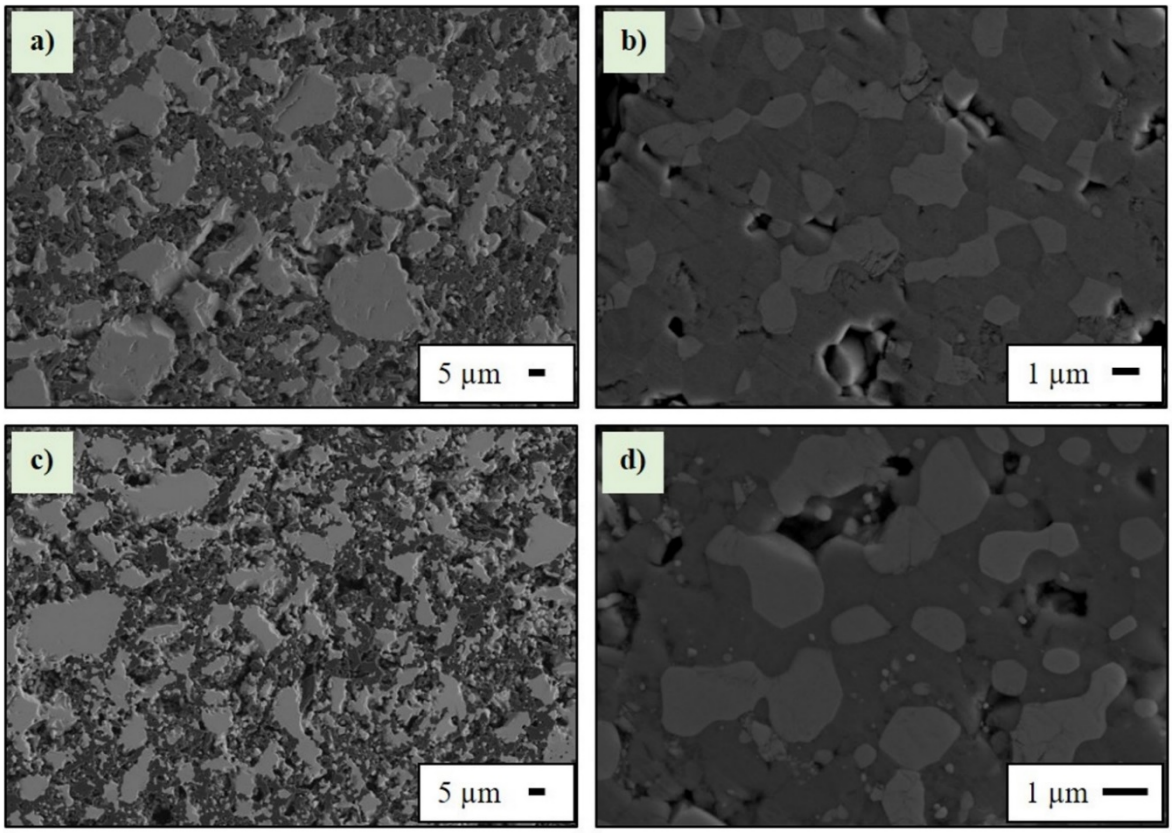

Figure 2.31. Low-magnification backscattered SEM microstructures of the (a) $NbSi_2$-Al_2O_3, (b) $NbSi_2$-ZrO_2, (c) $TaSi_2$-Al_2O_3, and (d) $TaSi_2$-ZrO_2 composites with the addition of 40 vol% Al_2O_3 and ZrO_2 particles after sintering at 1600°C for 2 h in argon.

In addition, microstructures of these composites were examined at higher magnifications to better characterize the 5-3 metal silicide secondary phase formation. Figure 2.32 shows the high magnification backscattered SEM microstructures of the $NbSi_2$- and $TaSi_2$-based composites with the addition of 40 vol% refractory oxides after sintering at 1600°C. For the $NbSi_2$-based composites, intermediate Nb_5Si_3 phases formed during high-temperature sintering can be observed in the bright regions as presented on the microstructures. Similarly, the intermediate Ta_5Si_3 phases were also detected for the $TaSi_2$-based composites at high magnifications as shown in Fig. 2.32(c-d). The presence of the 5-3 metal silicide phases was additionally identified by utilizing energy dispersive spectroscopy (EDS) on the related regions of the microstructures. The average weight percentages of niobium (Nb) and silicon (Si) elements in the bright microstructural areas of the $NbSi_2$-based composites were measured as 82.3 and 17.7 wt%, respectively. For the $TaSi_2$-based composites, the EDS quantification results revealed 91.0 wt% of tantalum (Ta) and 9.0 wt% of Si elements for the related bright regions. These results clearly demonstrated the formation of these intermediate phases in 5-3 stoichiometry, as supported with the previously reported XRD results. Furthermore, it could be proposed based on these results that the 5-3 metal silicide phases started to form at the metal disilicide-oxide grain boundaries, and then continued to grow towards the metal disilicide grains. This formation could be attributed to the reaction of the metal disilicides with the entrapped or grain boundary diffused oxygen from environmental sources at high-temperatures. These results hereby demonstrated that the intermediate 5-3 silicide phase formation was predominantly controlled by high-temperature oxidation reactions of the metal disilicides.

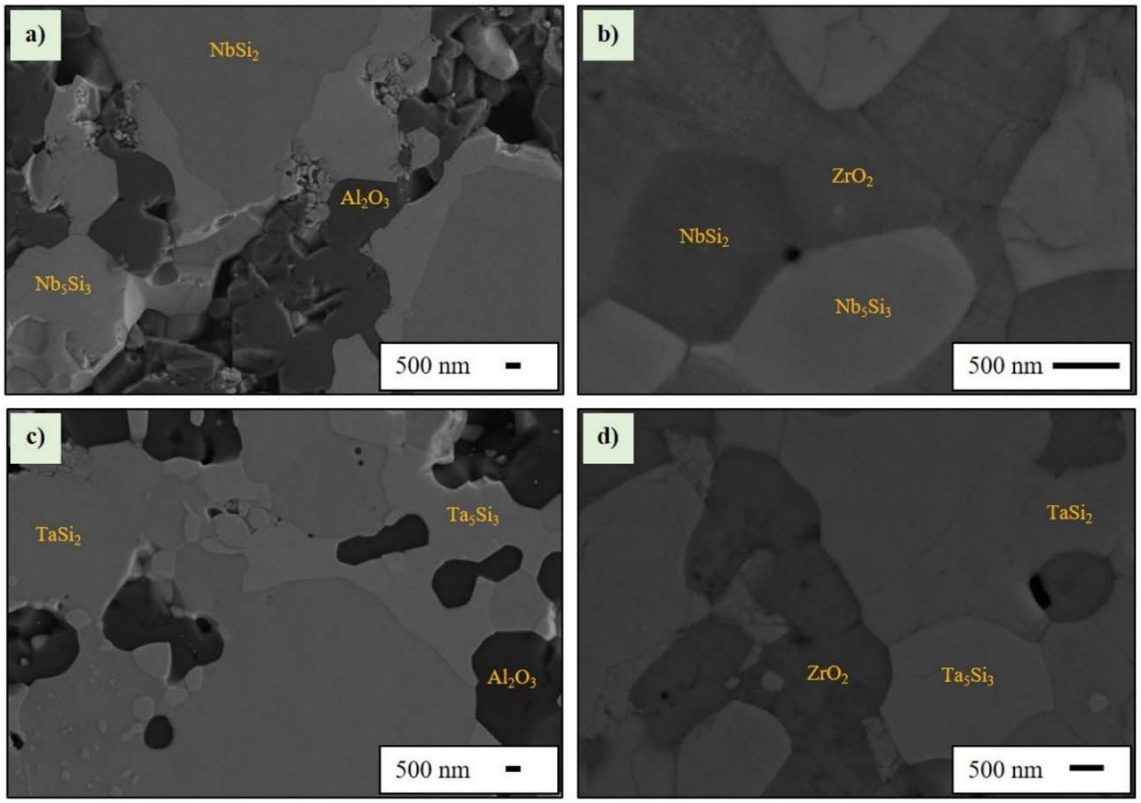

Figure 2.32. High magnification backscattered SEM microstructures of the (a) $NbSi_2$-Al_2O_3, (b) $NbSi_2$-ZrO_2, (c) $TaSi_2$-Al_2O_3, and (d) $TaSi_2$-ZrO_2 composites with the addition of 40 vol% Al_2O_3 and ZrO_2 particles after sintering at 1600°C for 2 h in argon.

This also resulted in the reduction of the volume percentages of the metal disilicides; and thus, the increase in the amount of the 5-3 metal silicide phases within these composite systems as a function of increasing temperature and hold time. This correlates well with the previously reported XRD/Rietveld results.

In addition to the $MoSi_2$-, WSi_2-, $NbSi_2$- and $TaSi_2$-based composites, the microstructures of various $CrSi_2$-Cr_2O_3 composites were characterized by SEM/EDS techniques. Figure 2.33(a) presents the SEM microstructures of the pure $CrSi_2$ sample sintered at 1400°C. The results demonstrated the existence of three different phases observed as bright, gray and dark regions in the microstructures. To understand the phases existing in the microstructure, the EDS analyses were also performed. The EDS analysis taken from the bright region (Figure 2.33b) revealed that the weight percentages of Cr, Si and O were 66.9, 31.8 and 1.3 wt.%, respectively. However, the weight percentage of Cr element decreased from 66.9 to 51.5 wt.% in the gray region (Figure 2.33c), while the weight percentage of Si element increased from 31.8 to 48.5 wt.%. In addition, gold (Au) and palladium (Pd) elements were detected in the EDS analyses due to initial Au-Pd sputter coating for these studies. These results clearly demonstrated that the bright and gray regions represent the CrSi and $CrSi_2$ phases, respectively. Therefore, it was also found that the dark region indicates a small amount of the SiO_2 phase. It is important to point out that these results highly support the XRD/Rietveld data, since they also displayed that the phases identified for the sintered pure $CrSi_2$ sample were $CrSi_2$ and CrSi. Due to a small amount of SiO_2 phase in the system, it could not be detected by XRD analysis, similar to the $MoSi_2$- and WSi_2-based composites.

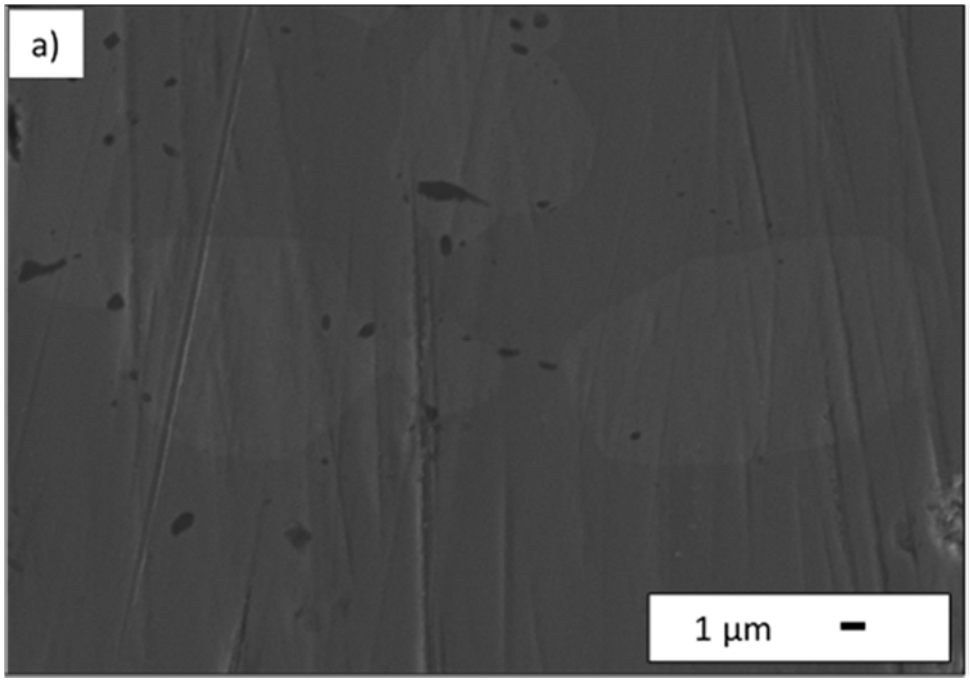

Figure 2.33. (a) SEM micrograph of the pure $CrSi_2$ sample sintered at 1400°C for 2h, and its EDS analysis results for the (b) bright and (c) gray regions.

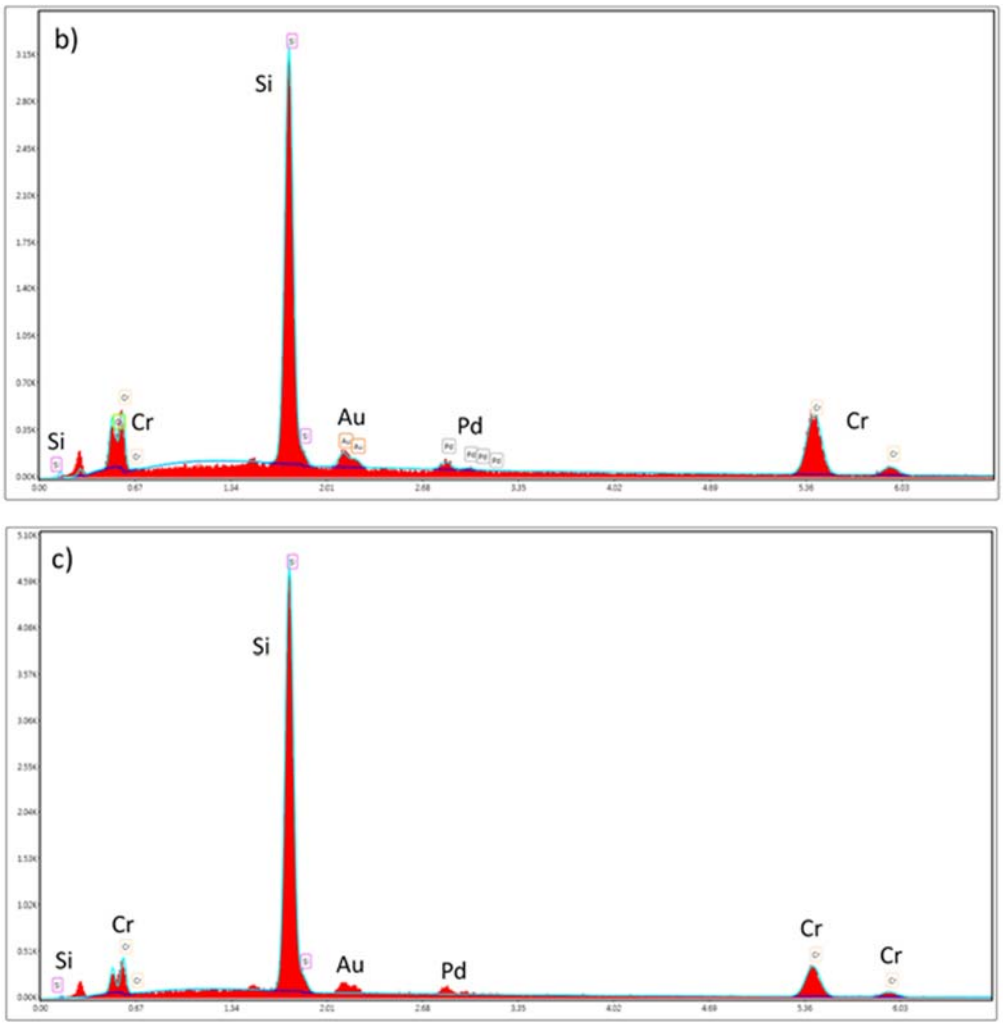

Figure 2.33. (continued) (a) SEM micrograph of the pure $CrSi_2$ sample sintered at 1400°C for 2h, and its EDS analysis results for the (b) bright and (c) gray regions.

The SEM microstructures of the (20-80) vol% $CrSi_2$-Cr_2O_3 composite sample sintered at 1400°C for 2h are presented in the Figure 2.34(a-b). It can be clearly seen that (20-80) vol% $CrSi_2$-Cr_2O_3 composite is composed of three different phases represented by brighter, gray and darker regions in its microstructures. In the Figure 2.34b, these three phases and related grain boundaries can be clearly seen. However, small needle-like particles were also observed mostly on the surface of other grains. It was previously reported for the (20-80) vol% $CrSi_2$-Cr_2O_3 composite based on the XRD results that $CrSi_2$ and CrSi phases existing in the commercial metal silicide powder reacted with Cr_2O_3 to form SiO_2, and Cr metal and/or $Cr_{0.91}Si_{0.09}$ as major phases. Since Cr metal and $Cr_{0.91}Si_{0.09}$ phases have very close identical XRD peaks, it was difficult to differentiate them without further experiments. Therefore, to understand its microstructure and existing phases better, a detailed EDS analyses were carried out for this composite. The EDS analysis taken from the brighter region of the (20-80) vol% $CrSi_2$-Cr_2O_3 composite demonstrated that the weight percentages of Cr, Si and O elements were 98.1, 0.5 and 1.4 wt.%, respectively (Figure 2.34c). The weight percentages of Cr and O elements in the gray region were determined as 81.0 and 19.0

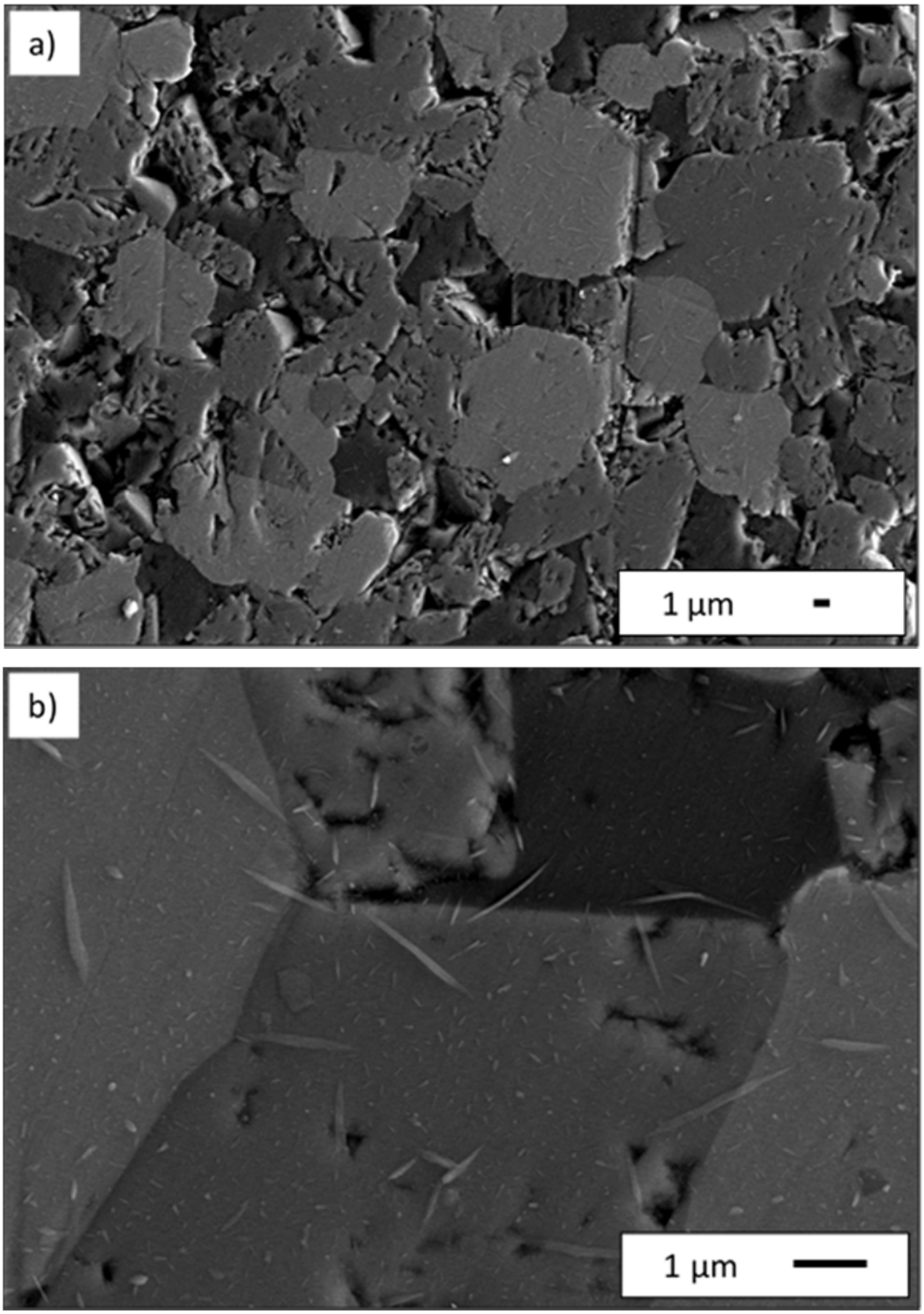

Figure 2.34. (a-b) SEM micrographs of the (20-80) vol% $CrSi_2$-Cr_2O_3 composite sample sintered at 1400°C for 2h, and its EDS analysis results for the (c) brighter and (d) gray regions.

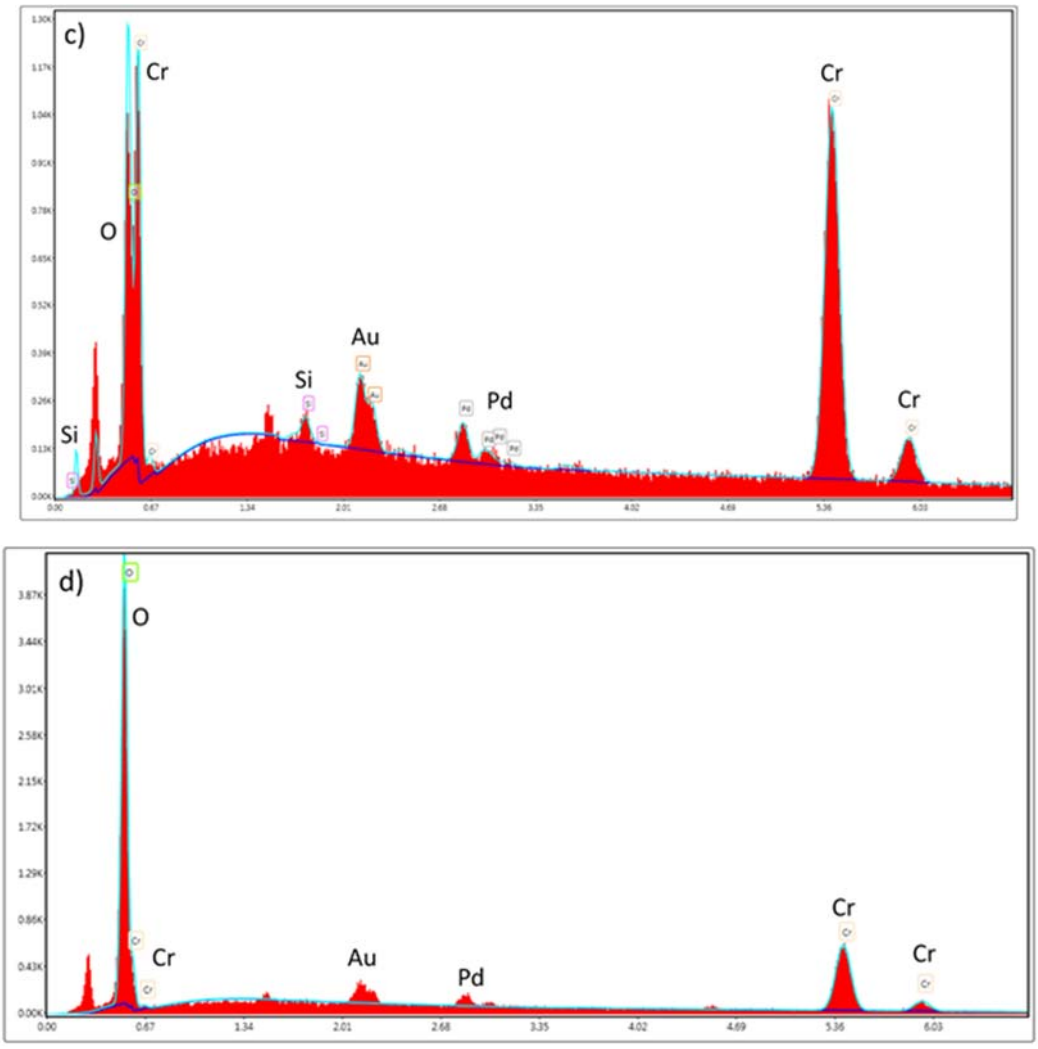

Figure 2.34. (continued) (a-b) SEM micrographs of the (20-80) vol% $CrSi_2$-Cr_2O_3 composite sample sintered at 1400°C for 2h, and its EDS analysis results for the (c) brighter and (d) gray regions.

wt.%, respectively (Figure 2.34d). There results presented that brighter region highly indicates metallic Cr phase, while gray regions may refer to a mixture of metallic Cr and remaining and/or unreacted Cr_2O_3 phases based on the weight percentages obtained by EDS analyses. These results were found to be in correlation with the theoretical calculations based on the Cr-Si phase diagram, which also indicated that Cr metal can be likely obtained due to formation of SiO_2 and large shift to the left side on the Cr-Si phase diagram. In addition, the XRD results showed that Cr_2O_3 and CrSi phases still exist after sintering at 1400°C. This result also demonstrates that $CrSi_2$ phase completely reacted with Cr_2O_3 to form Cr and SiO_2, while CrSi partially reacted with Cr_2O_3 and resulted in SiO_2, Cr with unreacted CrSi and Cr_2O_3 phases in the system. Figure 2.35(a-b) present the SEM microstructures of the (30-70) vol% $CrSi_2$-Cr_2O_3 composite sample sintered at 1400°C for 2 h. The results showed that (30-70) vol% $CrSi_2$-Cr_2O_3 composite is composed of two different phases observed in the brighter, gray and darker regions in these microstructures. In addition, an

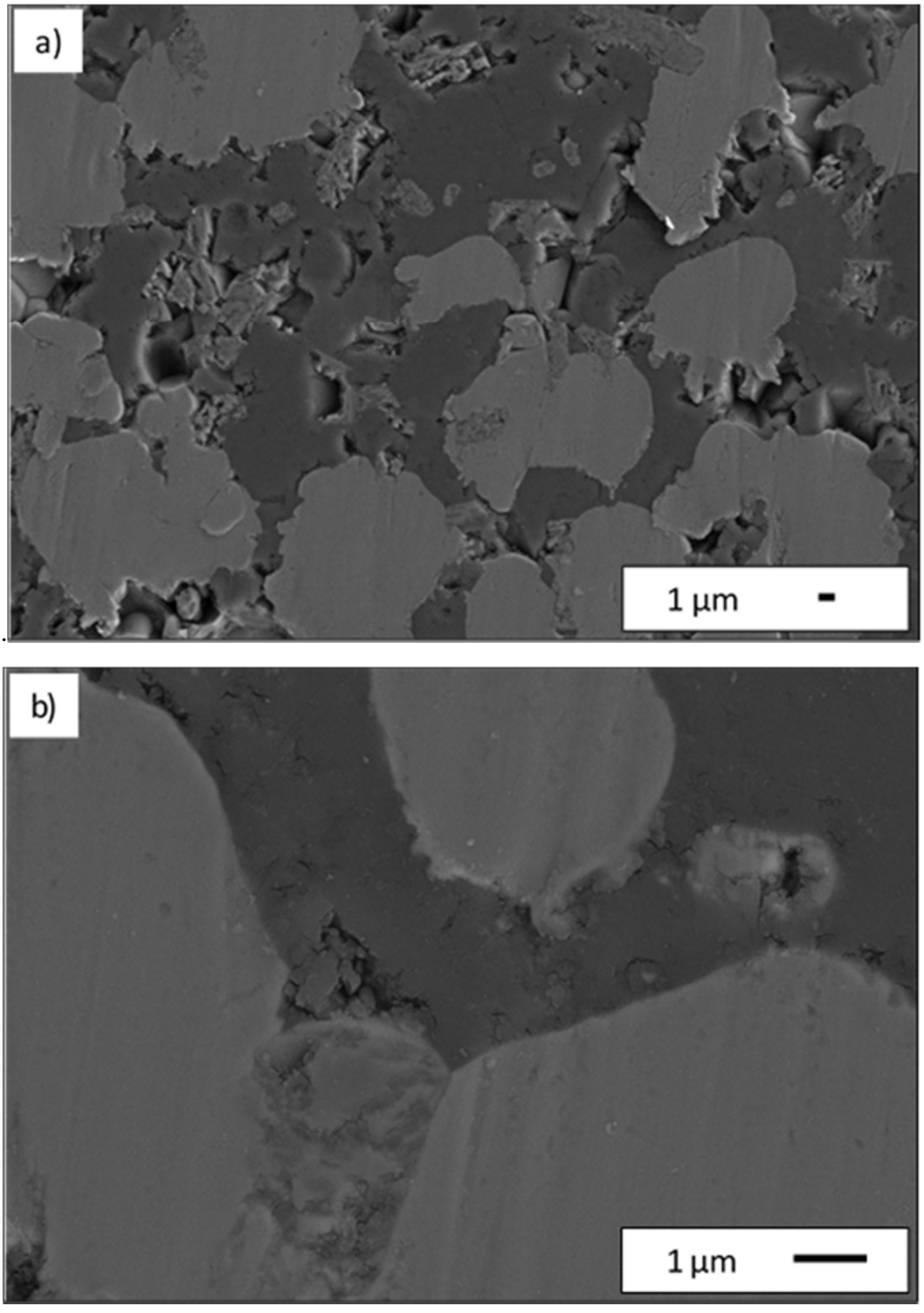

Figure 2.35. (a-b) SEM micrographs of the (30-70) vol% $CrSi_2$-Cr_2O_3 composite sample sintered at 1400°C for 2h.

intermediate phase (gray region) was observed between two grains (bright regions) as clearly presented in the Figure 2.35b. Similar to the (20-80) vol% $CrSi_2$-Cr_2O_3 composite system, the XRD results proved that $CrSi_2$ and CrSi reacted with Cr_2O_3 to form SiO_2 and metallic Cr phases. There was also unreacted Cr_2O_3 and a small amount of CrSi in the system after sintering. The EDS results demonstrated that the bright region (98.7 wt% Cr + 1.3 wt% O) highly indicates the metallic Cr phase with a small amount of unreacted Cr_2O_3 phase. In the gray region observed between two grains (Figure 2.35b), it was found that the weight percentage of Cr element decreased from 98.7 to 81.5 wt.%, but the weight percentage of O increased from 1.3 to 18.5 wt.%. There results similarly showed that brighter region highly indicates metallic Cr phase, while gray regions may refer both metallic Cr and remaining and/or unreacted Cr_2O_3 phases based on the weight percentages obtained by EDS analyses. Therefore, it is important to point out that there is no significant difference between (20-80) and (30-70) vol% $CrSi_2$-Cr_2O_3 composites based on the XRD and SEM/EDS results. The only change could be the increased fraction of Cr and SiO_2 phases, and decreased fraction of unreacted Cr_2O_3 phase with increasing starting silicide fraction from 20 to 30 vol%.

Figure 2.36(a-b) shows the SEM microstructures of the (40-60) vol% $CrSi_2$-Cr_2O_3 composite sample sintered at 1400°C for 2h. The results demonstrated that two phases (bright and dark regions) exist within this composite system. For the (40-60) vol% $CrSi_2$-Cr_2O_3 composite, these results are in correlation with the previously reported XRD data, since it proved that Cr_2O_3 almost

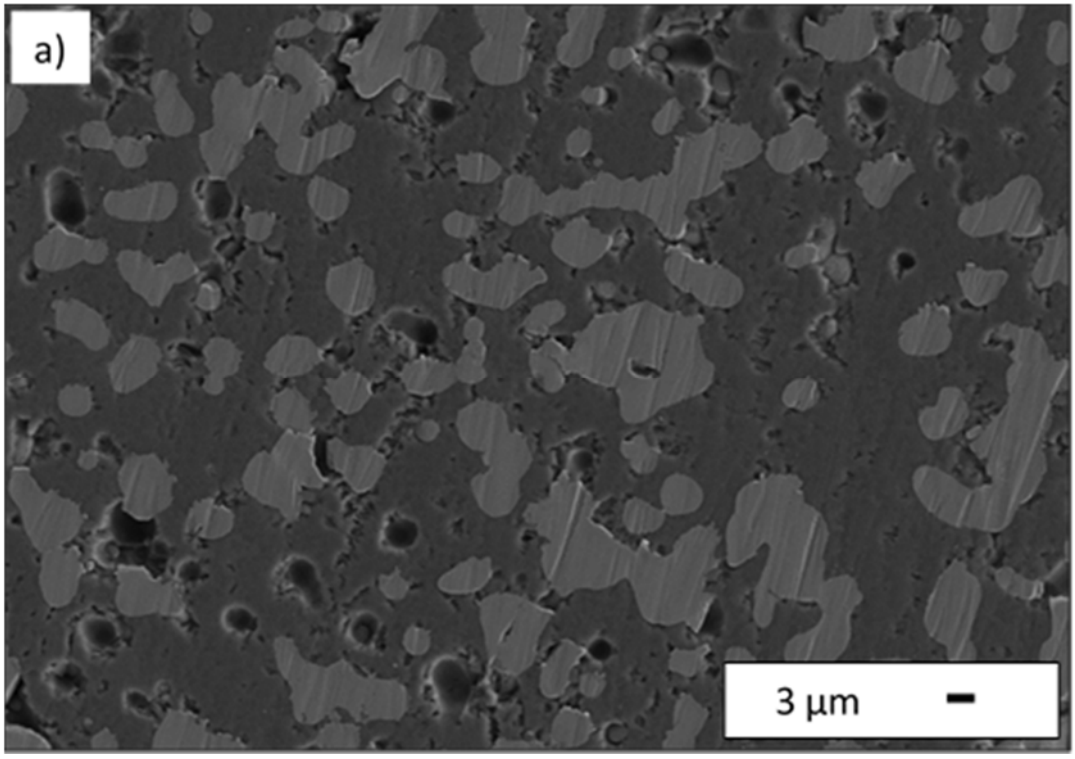

Figure 2.36. (a-b) SEM micrographs of the (40-60) vol% $CrSi_2$-Cr_2O_3 composite sample sintered at 1400°C for 2h, and its EDS analysis for the (c) bright and (d) dark regions.

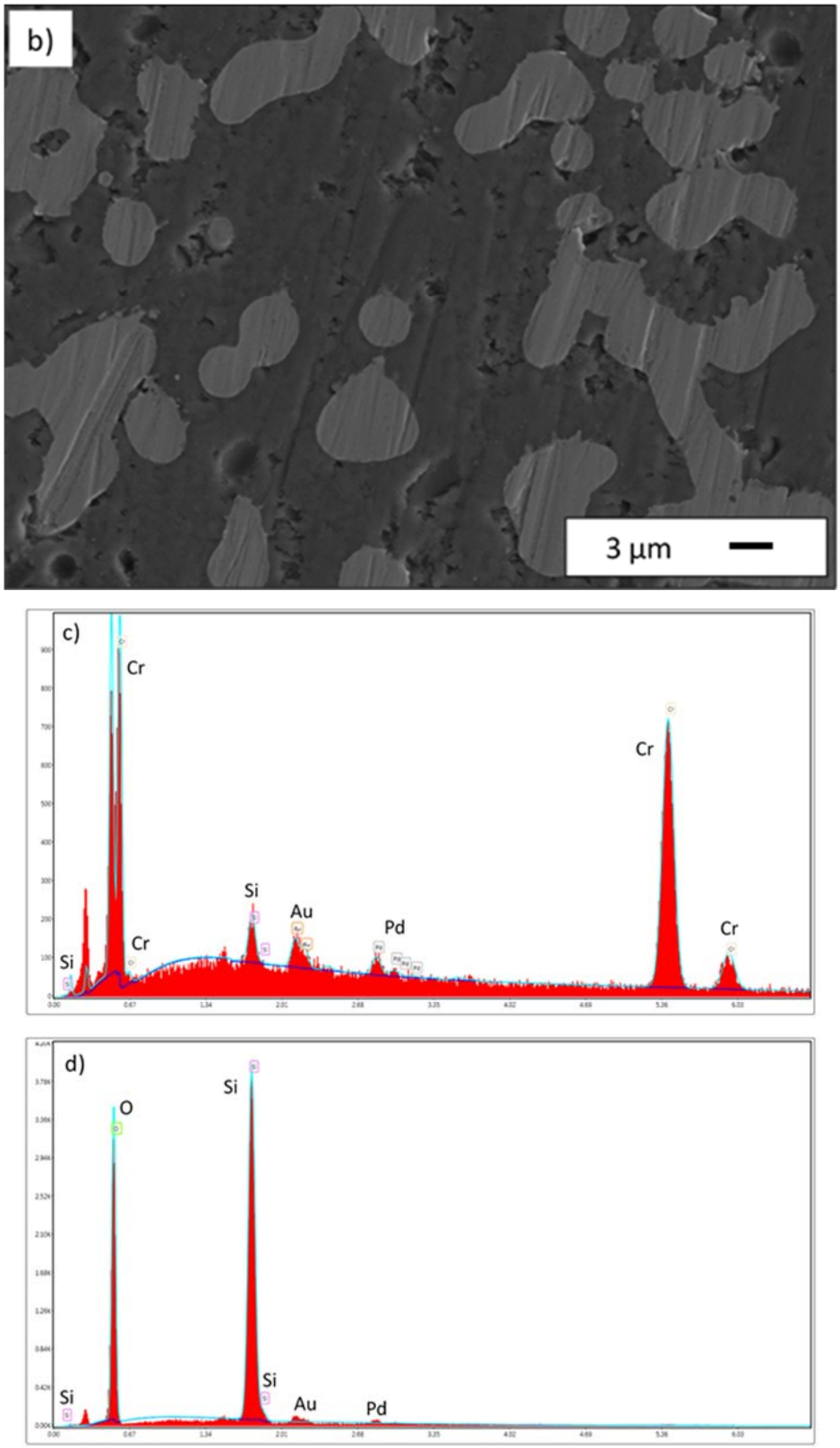

Figure 2.36. (continued) (a-b) SEM micrographs of the (40-60) vol% $CrSi_2$-Cr_2O_3 composite sample sintered at 1400°C for 2h, and its EDS analysis for the (c) bright and (d) dark regions.

completely reacted with chromium silicide phases, and hereby formed $Cr_{0.91}Si_{0.09}$ and SiO_2 in cristobalite form. For a better understanding, an extensive EDS analysis was performed on this composite sample for both bright and dark regions. The results revealed that 98.6 wt.% Cr and 1.4 wt.% Si elements exist in the bright region (Figure 2.36c), indicating the formation of a new chromium silicide phase. The best candidate was found as $Cr_{0.91}Si_{0.09}$ for this phase based on the XRD and EDS results. Figure 2.36d presents the EDS analysis taken from the dark region of the microstructure. The weight percentages of Si and O elements were measured as 56.3 and 43.7 wt.%, respectively. This result indicated the formation of SiO_2 phase in the (40-60) vol% $CrSi_2$-Cr_2O_3 composite system, supporting its XRD data. SEM microstructure of the (50-50) vol% $CrSi_2$-Cr_2O_3 composite sample sintered at 1400°C for 2 h is presented in the Figure 2.37a. It can be clearly seen that there are only two phases existing in this composite represented by bright and dark regions. For the (50-50) vol% $CrSi_2$-Cr_2O_3 composite, it was previously determined by the XRD results that $CrSi_2$ and CrSi completely reacted with Cr_2O_3, and formed Cr_3Si as a single conductive silicide phase in the composite system. The other phase formed was SiO_2 in cristobalite form as expected, since there was no unreacted Cr_2O_3 phase in the system after sintering. The EDS analysis for the bright region (Figure 2.37b) demonstrated that the weight percentages of Cr, Si and O elements are 86.8, 11.8 and 1.4 wt.%, respectively. This result indicated the existence of Cr_3Si (major phase) and a small amount of SiO_2 phase in the bright regions. In the dark region (Figure 2.37c), only Si and O elements were detected by EDS, supporting the formation of SiO_2 phase as a result of the reaction between chromium silicides and chromium oxide. Therefore, it is found that the major chromium silicide phase changed from $Cr_{0.91}Si_{0.09}$ to Cr_3Si with increasing the starting chromium silicide fraction from 40 to 50 vol% in the composite system.

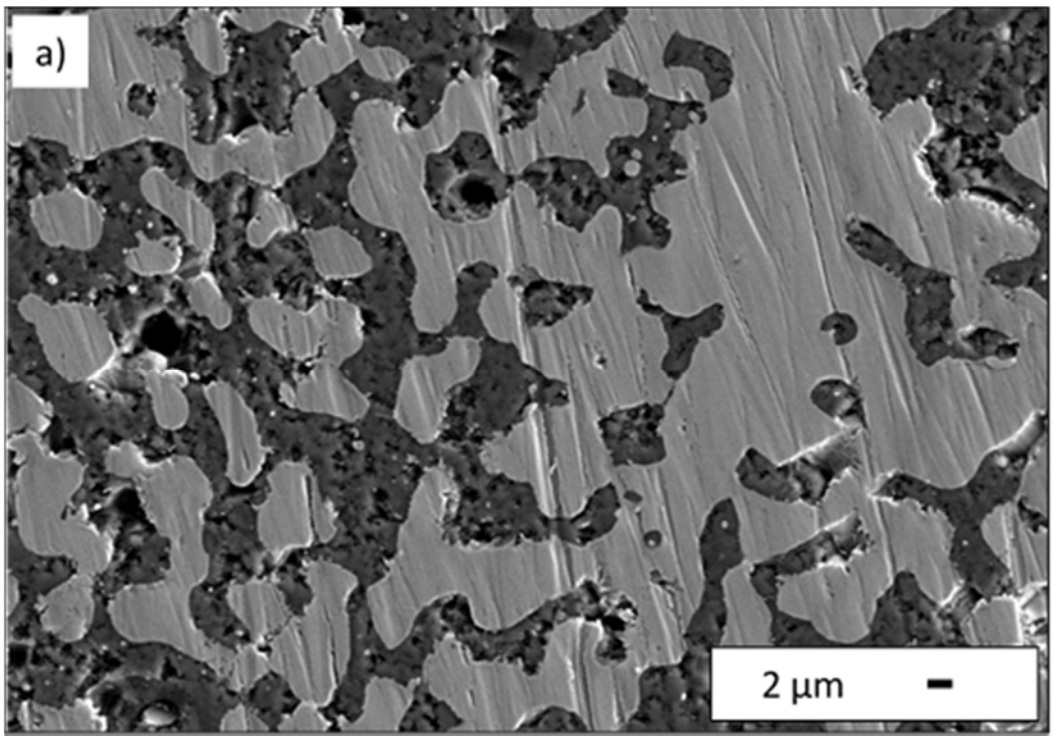

Figure 2.37. (a) SEM micrograph of the (50-50) vol% $CrSi_2$-Cr_2O_3 composite sample sintered at 1400°C for 2h, and its EDS analysis results for the (b) bright and (c) dark regions.

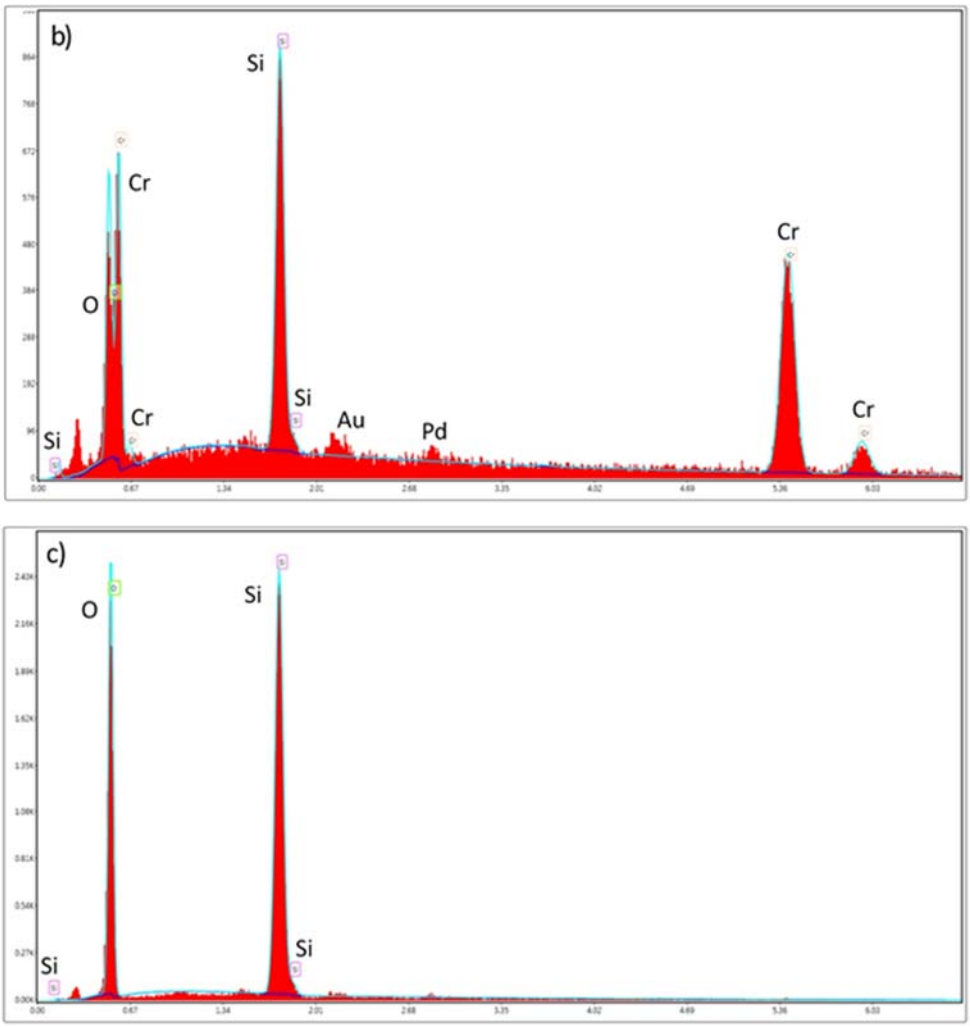

Figure 2.37. (continued) (a) SEM micrograph of the (50-50) vol% $CrSi_2$-Cr_2O_3 composite sample sintered at 1400°C for 2h, and its EDS analysis results for the (b) bright and (c) dark regions.

Figure 2.38(a-b) present the SEM microstructures of the (55-45) vol% $CrSi_2$-Cr_2O_3 sintered at 1400°C for 2h. It can be clearly seen that the conductive phase (Cr-silicides) is very homogeneously distributed within the insulating phase. As seen in the Figure 2.38b, the bright regions are composed of two different phases represented by brighter and gray regions. The major phases were determined by XRD data as Cr_3Si and SiO_2 in cristobalite form. But the existence of $CrSi_2$ phase in the (55-45) vol% $CrSi_2$-Cr_2O_3 composite system indicated that the reaction between chromium silicide and chromium oxide was not completed. Also, it is found that Cr_5Si_3 silicide phase was formed as a result of the reaction during sintering. For a better understanding of this composite system, a detailed EDS analyses were also performed. The EDS analysis taken from the brighter region (Figure 2.38c) revealed that the weight percentages of Cr, Si and O are 85.3, 13.3 and 1.4 wt.%, respectively. This result proved that the brighter region refers to Cr_3Si (major phase) with a very small amount of SiO_2, supporting the XRD data. In the gray region (Figure 2.38d), weight percentages of the Cr, Si and O elements were measured as 76.8, 21.9 and 1.3 wt.%, respectively. This result demonstrated the existence of Cr_5Si_3 and SiO_2 phases in the gray region.

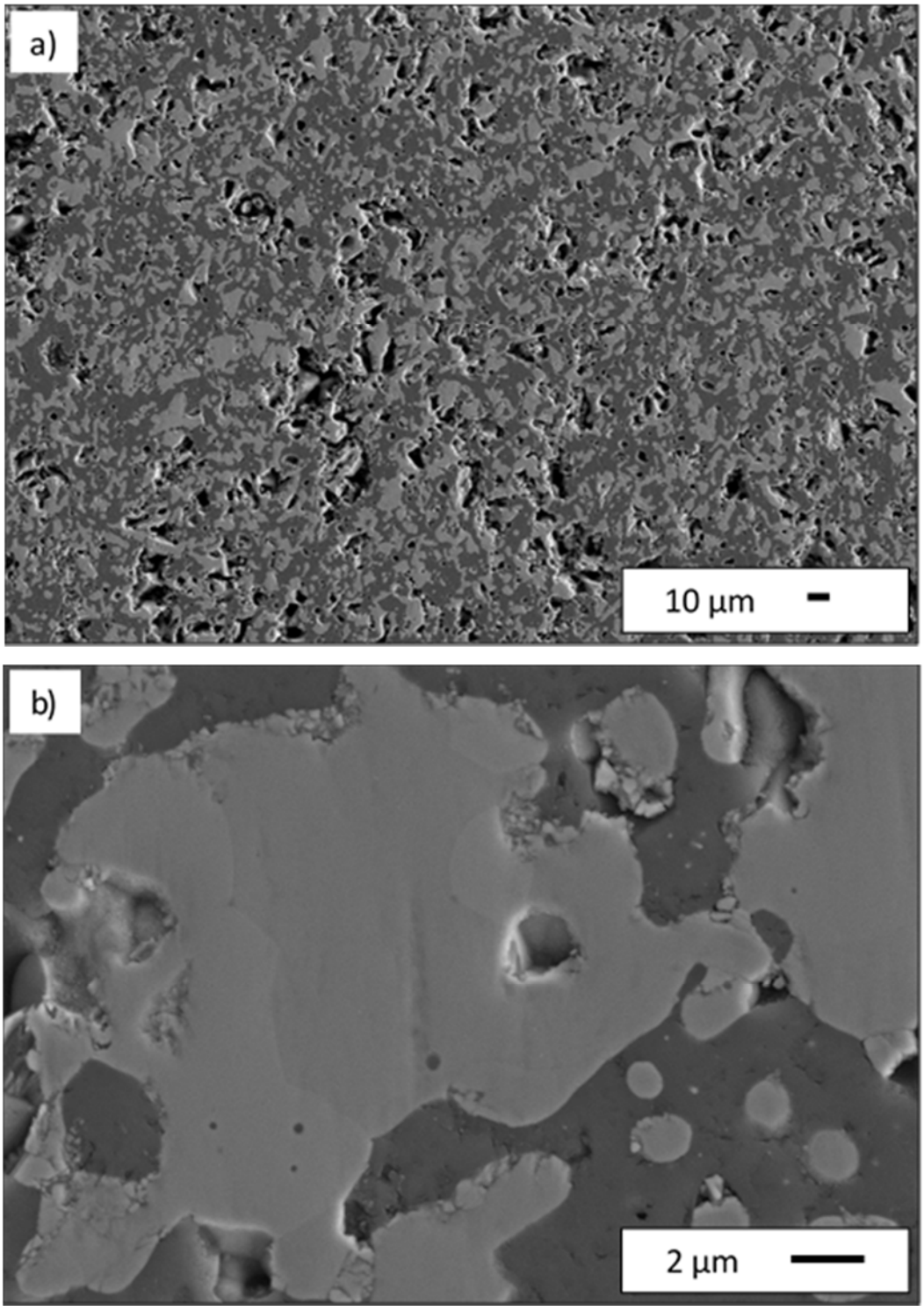

Figure 2.38. (a-b) SEM micrographs of the (55-45) vol% $CrSi_2$-Cr_2O_3 composite sample sintered at 1400°C for 2h, and its EDS analysis results for the (c) brighter and (d) gray regions.

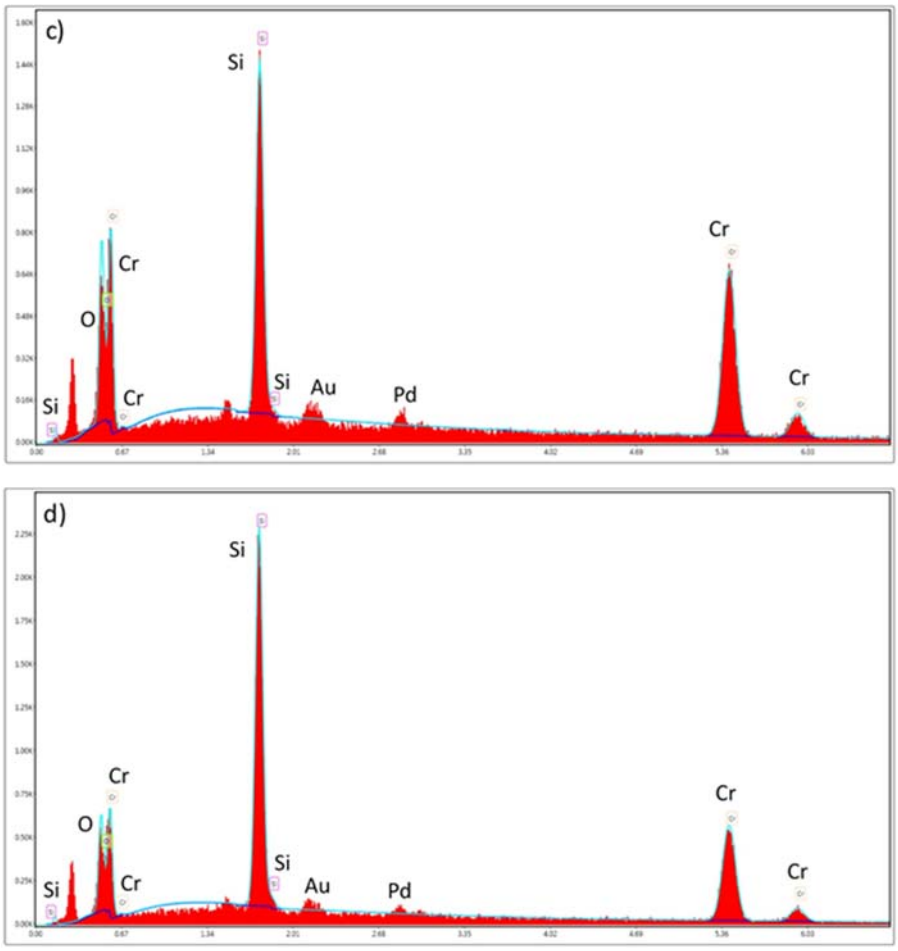

Figure 2.38. (continued) (a-b) SEM micrographs of the (55-45) vol% $CrSi_2$-Cr_2O_3 composite sample sintered at 1400°C for 2h, and its EDS analysis results for the (c) brighter and (d) gray regions.

Therefore, it is clear that the bright regions in the Figure 2.38a are composed of Cr_3Si and Cr_5Si_3 as major conductive chromium silicide phases. Lastly, the EDS analysis results presented that the dark region indicates SiO_2 phase formed during sintering. Figure 2.39(a) shows the SEM microstructures of the (60-40) vol% $CrSi_2$-Cr_2O_3 sintered at 1400°C for 2h. A homogeneous distribution of chromium silicide phases within the insulating phase can be clearly seen. The XRD result of the (60-40) vol% $CrSi_2$-Cr_2O_3 composite demonstrated that chromium silicide partially reacted with chromium oxide to form Cr_5Si_3, Cr_3Si and SiO_2 in cristobalite form. The other phases observed were Cr_2O_3, CrSi and $CrSi_2$ in the system after sintering. However, only two phases represented by bright and dark regions were observed in the microstructures, probably due to the polishing difficulty and also very small amounts of unreacted Cr_2O_3, CrSi and $CrSi_2$ phases. The EDS analysis results (Figure 2.39b) revealed that the weight percentages of Cr, Si and O elements are 76.3, 22.2 and 1.5 wt.%, respectively. This result clearly proved that the bright region refers to Cr_5Si_3 phase, which is the major conductive phase in (60-40) vol% $CrSi_2$-Cr_2O_3 composite system. In addition, the dark region was found to be indicated to the SiO_2 phase formed based on the EDS data obtained.

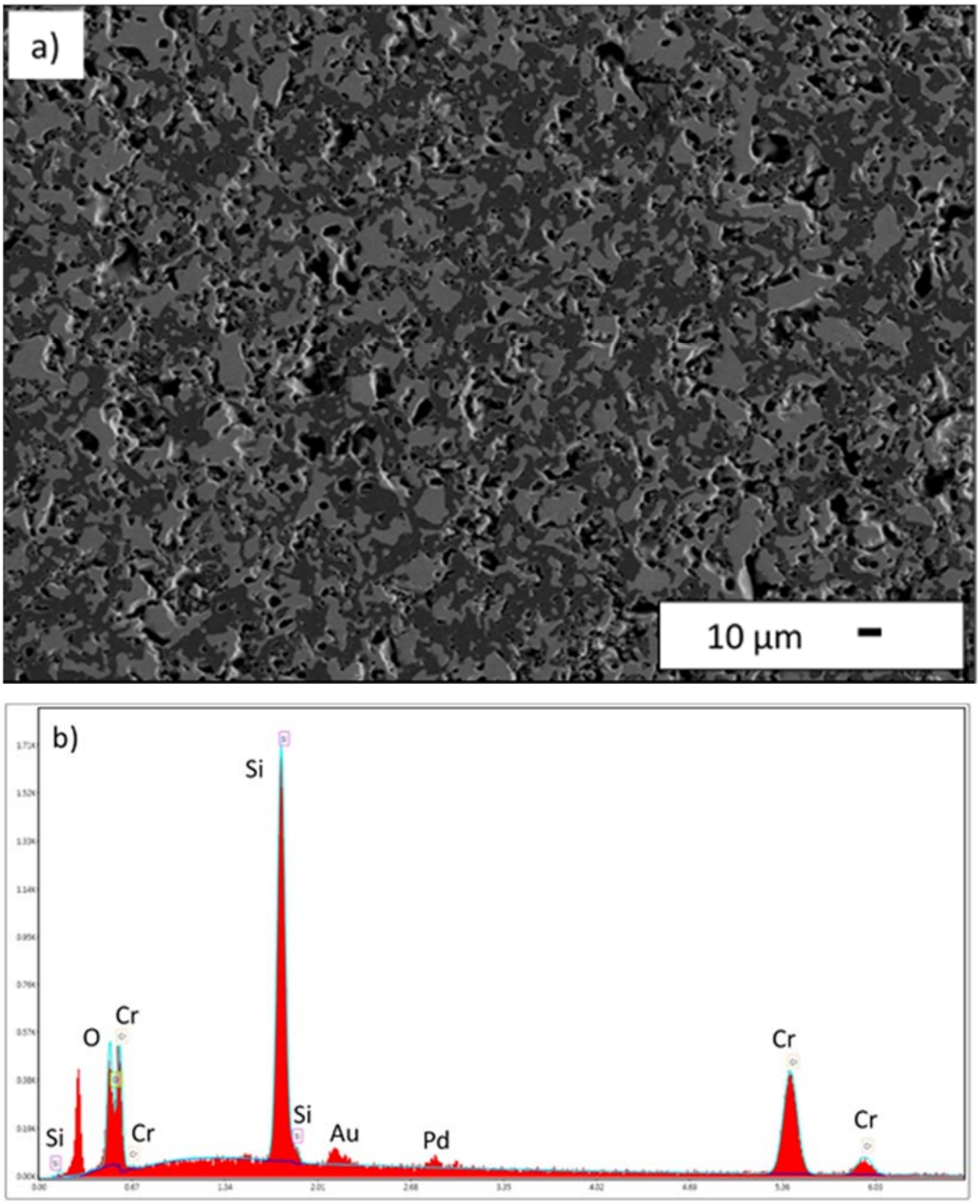

Figure 2.39. (a) SEM micrograph of the (60-40) vol% $CrSi_2$-Cr_2O_3 composite sample sintered at 1400°C for 2h, and (b) its EDS analysis results for the bright region.

SEM microstructure of the (70-30) vol% $CrSi_2$-Cr_2O_3 composite sample sintered at 1400°C for 2h are presented in the Figure 2.40(a). The results showed that there are three different phases existing in the composite system represented by brighter, gray and dark regions in the microstructure. The major silicide phases obtained for the (70-30) vol% $CrSi_2$-Cr_2O_3 were CrSi and Cr_5Si_3 based on the XRD data. But it is important to state that $CrSi_2$ and SiO_2 phases still existed as minor phases. Figure 2.40(b-c) show the EDS analysis results of the bright and gray regions, respectively. The weight percentages of the Cr, Si and O elements were 75.8, 22.9 and 1.3 wt.%, respectively. This

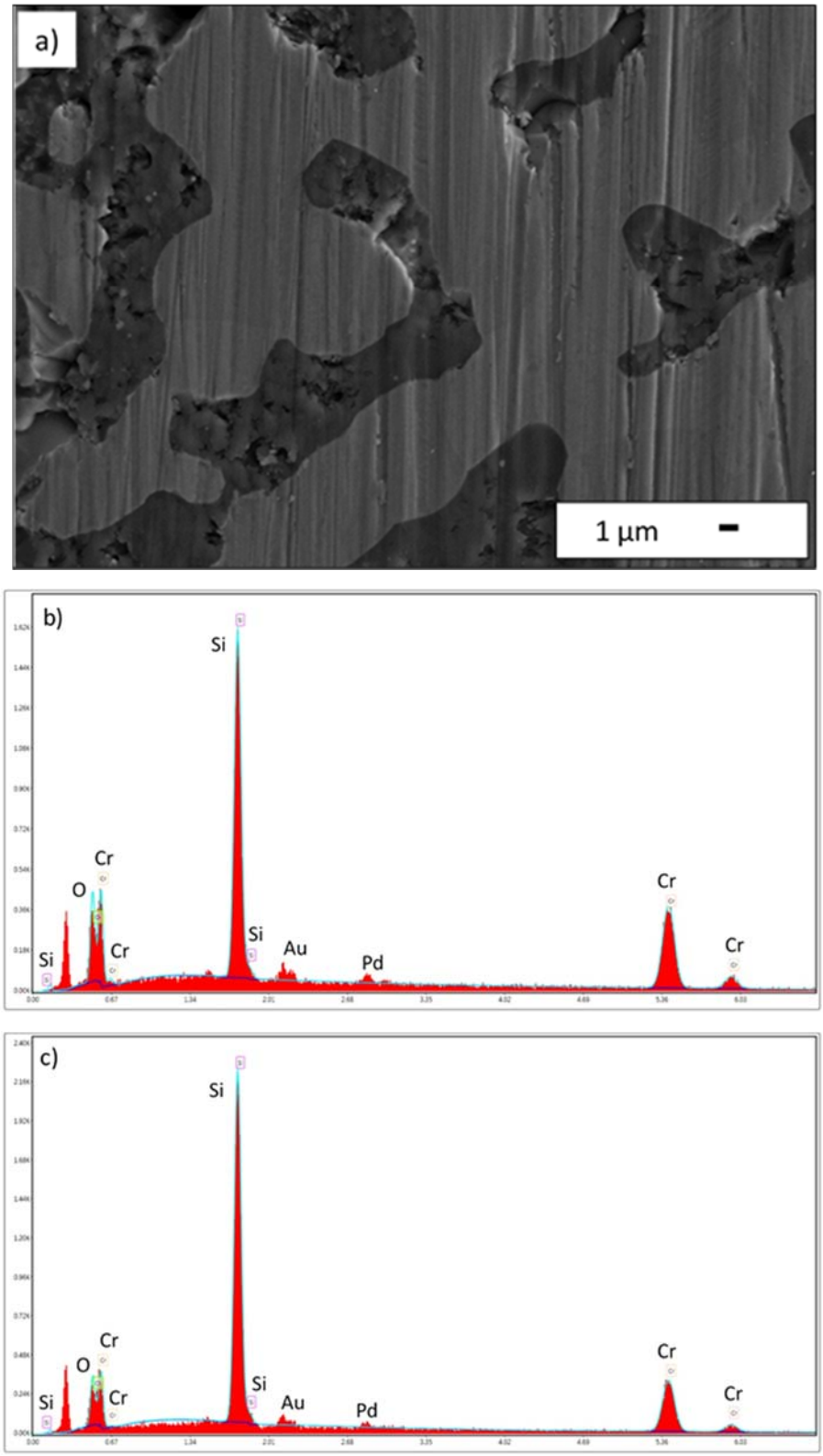

Figure 2.40. (a) SEM micrograph of the (70-30) vol% $CrSi_2$-Cr_2O_3 composite sample sintered at 1400°C for 2h, and its EDS analysis results for the (b) bright and (c) gray regions.

result showed that the bright region corresponds to Cr_5Si_3 phase with a small amount of silica phase. In addition, 66.7 wt.% Cr, 32.0 wt.% Si and 1.3 wt.% O results obtained in the gray region proved the existence of unreacted CrSi phase with a small amount of silica. However, the $CrSi_2$ phase could not be detected by EDS analysis due to its very small amount remained after sintering. Lastly, the EDS analysis results presented that the dark region indicates the SiO_2 phase formed during sintering. Figure 2.41(a-b) present the SEM microstructures of the (90-10) vol% $CrSi_2$-Cr_2O_3 composite sample sintered at 1400°C for 2h. It can be seen that there are three different phases existing in the composite system (bright, gray and dark regions). These phases and their grain boundaries were clearly observed in the Figure 2.41b. Based on the previous XRD data, there was no any significant changes observed compared to the initial phases, since the major phases were still CrSi and $CrSi_2$. But it is important to note that SiO_2 in cristobalite form was obtained as a result of the reaction between chromium silicides and small amount of Cr_2O_3. The EDS results for the bright and gray regions are presented in the Figure 2.41(c-d), respectively. It was found that the bright region corresponds to CrSi phase with a small amount of silica, while the gray region refers to $CrSi_2$ phase. In addition to these results, it was demonstrated that the dark region indicates to a small amount of silica grain boundary phase.

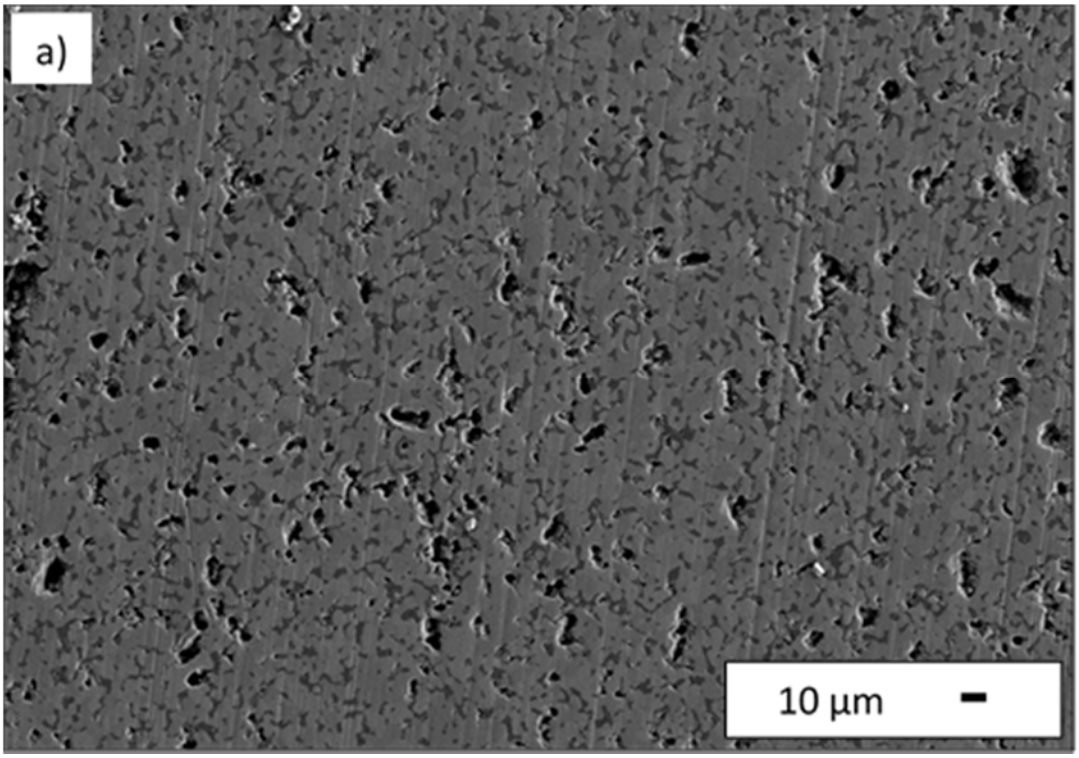

Figure 2.41. (a-b) SEM micrographs of the (90-10) vol% $CrSi_2$-Cr_2O_3 composite sample sintered at 1400°C for 2h, and its EDS analysis results for the (c) bright and (d) gray regions.

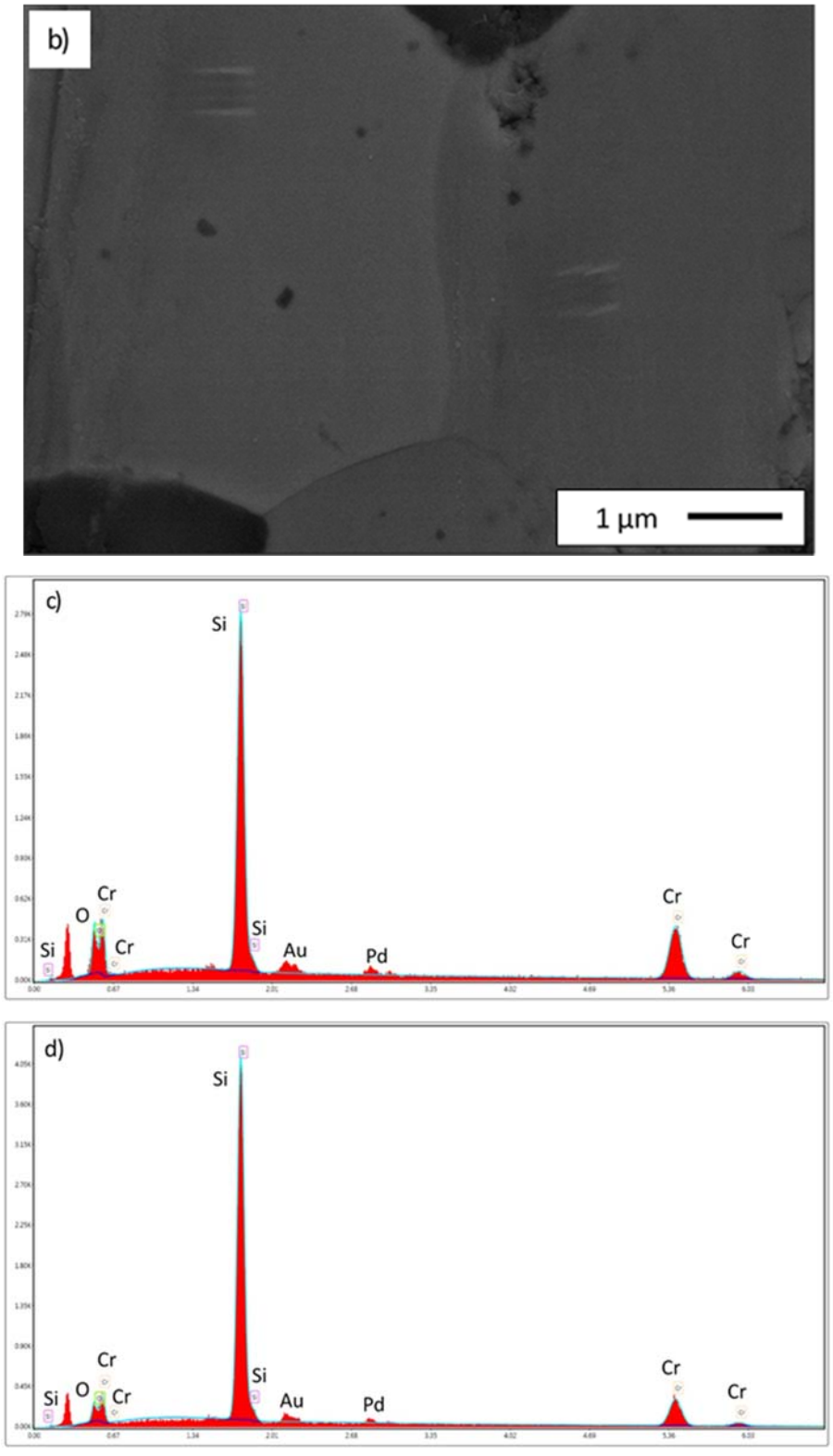

Figure 2.41. (continued) (a-b) SEM micrographs of the (90-10) vol% $CrSi_2$-Cr_2O_3 composite sample sintered at 1400°C for 2h, and its EDS analysis results for the (c) bright and (d) gray regions.

2.3.2.3.2 Microstructral evolution and grain growth kinetics after annealing

In order to perform short-term grain growth studies, six different composites and two pure metal silicides were firstly sintered at 1600°C for 2 h and then annealed at 1400°C for 24 h. The main purpose of this study was to study grain growth of the metal silicides within different composite systems by performing SEM studies, and also measuring silicide grain sizes (coarsening) before/after sintering and annealing processes. By this way, the effect of refractory oxide matrix phases on grain growth kinetics of the composites and particularly metal silicides was examined. Therefore, SEM microstructure studies were primarily performed to investigate microstructural evolution of the composites during high temperature sintering and then short-term annealing. Figure 2.42(a-d) presents the SEM microstructures of pure $MoSi_2$ and (60-40) vol% $MoSi_2$-Al_2O_3 composite samples at different magnifications after annealing at 1400°C for 24 hrs, respectively. For pure $MoSi_2$ sample, individual $MoSi_2$ grains can be clearly seen in Figure 2.42(a-b). The average $MoSi_2$ grain size for pure $MoSi_2$ was measured by image analysis approximately as 15.3 µm after short-term annealing at 1400°C for 24 hrs. For (60-40) vol% $MoSi_2$-Al_2O_3 composite system, Figure 2.42c shows the general SEM microstructure presenting the size and distribution of $MoSi_2$, Al_2O_3, and also Mo_5Si_3 (secondary phase) grains within this composite system. Since individual $MoSi_2$ grains can be also seen for $MoSi_2$-Al_2O_3 composite in Figure 2.42d, their average grain size was similarly measured approximately as 5.6 µm. As a result of these SEM studies and grain size measurements, it is clearly found that grain growth rate in pure $MoSi_2$ is quite higher than its rate in $MoSi_2$-Al_2O_3 composite system, since $MoSi_2$ grain coarsening in pure $MoSi_2$ system is almost three times higher than that in composite system. This result showed that the refractory Al_2O_3 grains retard $MoSi_2$ grain growth due to the pinning effect of Al_2O_3 grains on metal silicide grain growth as a main mechanism in the composite systems. This result is directly related to the pinning effect of the refractory oxide phases on silicide grain growth, which may provide a great advantage for long-term performance of such composite systems.

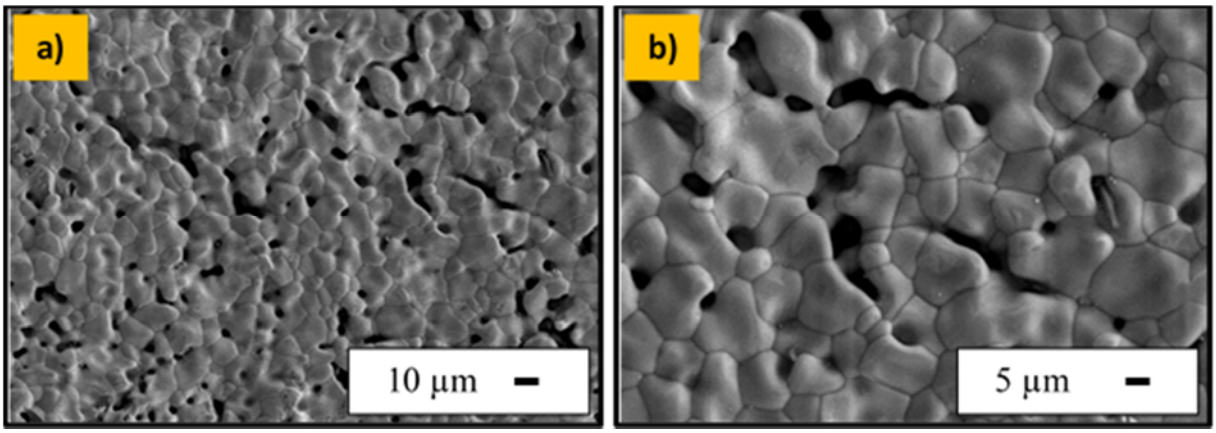

Figure 2.42 SEM micrographs of (a-b) pure $MoSi_2$, and (c-d) (60-40) vol% $MoSi_2$-Al_2O_3 composite samples after annealing at 1400°C for 24 hrs with two different magnifications.

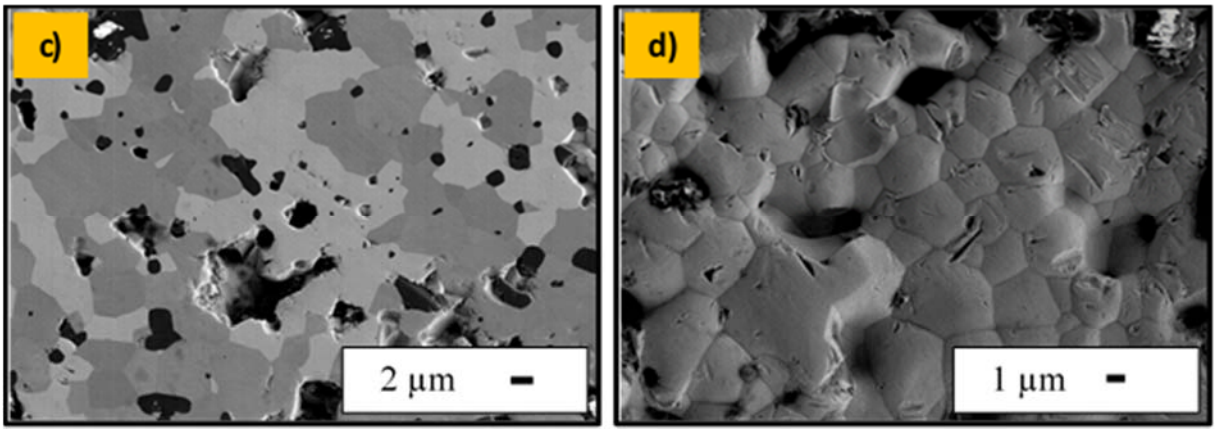

Figure 2.42. (continued) SEM micrographs of (a-b) pure $MoSi_2$, and (c-d) (60-40) vol% $MoSi_2$-Al_2O_3 composite samples after annealing at 1400°C for 24 hrs with two different magnifications.

Figure 2.43(a-d) presents the SEM microstructures of pure $MoSi_2$ and (60-40) vol% $MoSi_2$-Al_2O_3 composite samples at different magnifications after long-term annealing at 1400°C for 48 hours, respectively. For pure $MoSi_2$, individual $MoSi_2$ and Mo_5Si_3 grains can be clearly seen as gray and bright regions, respectively, in Figure 2.43(a-b). The average grain size of $MoSi_2$ grains was measured by image analysis software approximately as 12.7 µm after long-term annealing at 1400°C. But it is important to note that further microstructural analysis is needed for better measurement of $MoSi_2$ grain size from a better microstructure covering more number of $MoSi_2$ grains. For (60-40) vol% $MoSi_2$-Al_2O_3 composite sample, Figure 2.43(c-d) show the general SEM microstructures presenting the size and distribution of $MoSi_2$, Al_2O_3, and also Mo_5Si_3 (secondary phase) grains within this composite system. Since individual $MoSi_2$ grains can be seen in certain

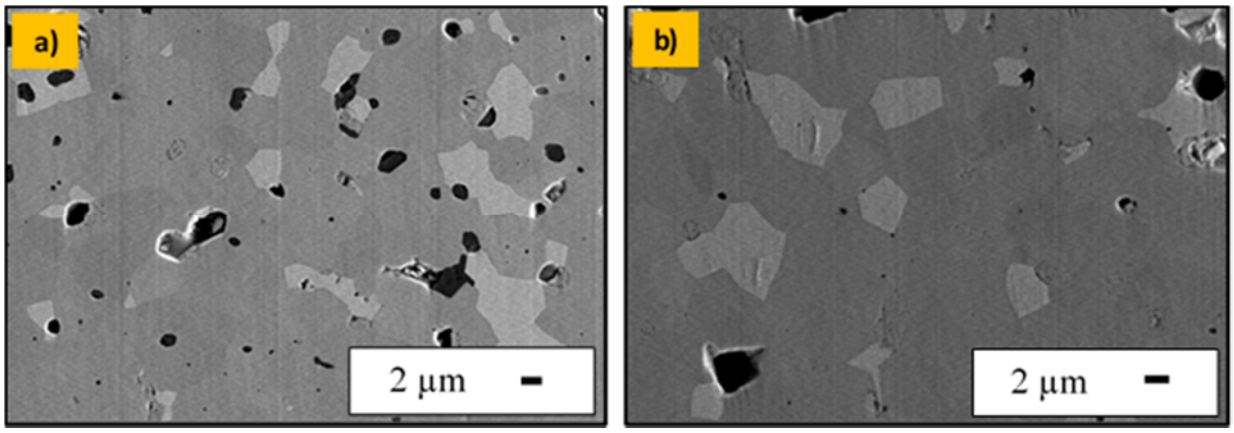

Figure 2.43. SEM micrographs of (a-b) pure $MoSi_2$, and (c-d) (60-40) vol% $MoSi_2$-Al_2O_3 composite samples after long-term annealing at 1400°C for 48 hours.

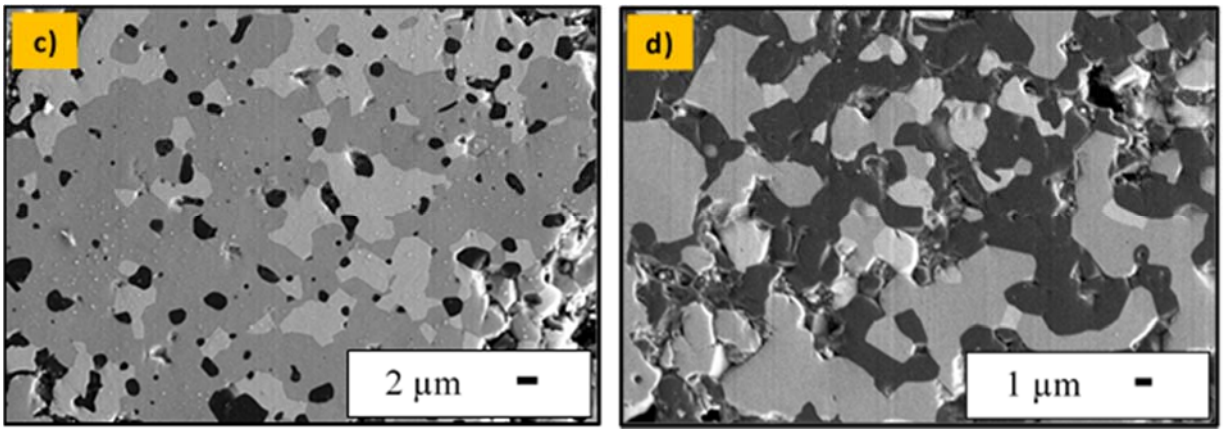

Figure 2.43. (continued) SEM micrographs of (a-b) pure $MoSi_2$, and (c-d) (60-40) vol% $MoSi_2$-Al_2O_3 composite samples after long-term annealing at 1400°C for 48 hours.

gray regions for $MoSi_2$-Al_2O_3 composite in Figure 2.43c, their average grain size was measured approximately as 5.2 µm after annealing at 1400°C for 48 hours. In addition to that, the formation for Mo_5Si_3 (bright regions) as a secondary phase is observed at the regions between $MoSi_2$ (gray) and Al_2O_3 (dark) grains. As a result of these SEM studies and grain size measurements after long-term annealing studies, it is clearly found that grain growth rate of $MoSi_2$ is higher than its rate in $MoSi_2$-Al_2O_3 composite system. This result indicated that the refractory Al_2O_3 grains successfully retard the grain growth due to the pinning effect of these grains on metal silicide grains as a main mechanism. Figure 2.44(a-b) shows the SEM microstructures of (60-40) vol% $MoSi_2$-coarseAl_2O_3 composite sample at different magnifications after long-term annealing at 1400°C for 48 hours. $MoSi_2$ and coarse Al_2O_3 grains can be seen in the gray and dark regions, respectively. The average grain size of $MoSi_2$ grains was measured approximately as 5.3 µm after long-term annealing at

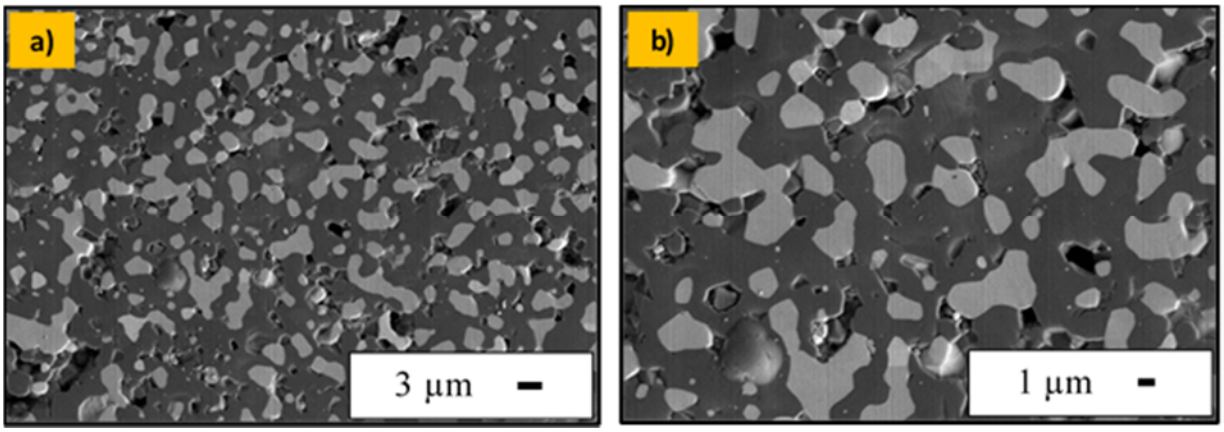

Figure 2.44. SEM micrographs of **a-b)** (60-40) vol% $MoSi_2$-coarseAl_2O_3 composite sample after long-term annealing at 1400°C for 48 hours [*Samples were chemically etched in 2.0 M HCl*].

1400°C. Therefore, it can be stated that the overall $MoSi_2$ grain growth rate is slightly higher in $MoSi_2$-coarseAl_2O_3 composite system than that in $MoSi_2$-Al_2O_3 composite. But the key point is that the $MoSi_2$ grain growth is highly retarded by refractory Al_2O_3 phase in these composite systems, which could provide a great advantage for their long-term use.

In the Figure 2.45(a-b), the SEM microstructures of (60-40) vol% $MoSi_2$-ZrO_2 composite sample are presented at different magnifications after long-term annealing at 1400°C for 48 hours. Due to the close atomic number of molybdenum and zirconium elements, there is only a slight difference in contrast between $MoSi_2$ and ZrO_2 grains in these microstructures. It is important to note that the darker regions indicate ZrO_2 grains, while other gray regions present $MoSi_2$ grains as shown in the Figure 2.45(a-b). The average grain size of $MoSi_2$ grains were determined as 6.0 µm after long-term annealing at 1400°C. As a result of the long-term annealing and grain growth studies on pure $MoSi_2$ and $MoSi_2$-based composites, it is found that the overall grain growth rate of $MoSi_2$ is relatively higher for $MoSi_2$-ZrO_2 composite system in comparison to the $MoSi_2$-Al_2O_3 and $MoSi_2$-coarseAl_2O_3 composites. However, all refractory ceramic oxides (Al_2O_3 and ZrO_2) successfully retarded the grain growth of $MoSi_2$ as a result of the pinning effect, since the average grain size of $MoSi_2$ grains increased from 4.2 to 12.7 µm after sintering and long-term annealing processes. But the average grain size of $MoSi_2$ grains were in the range of 5.2 and 6.0 µm for the metal silicide/refractory oxide composites after all those processes.

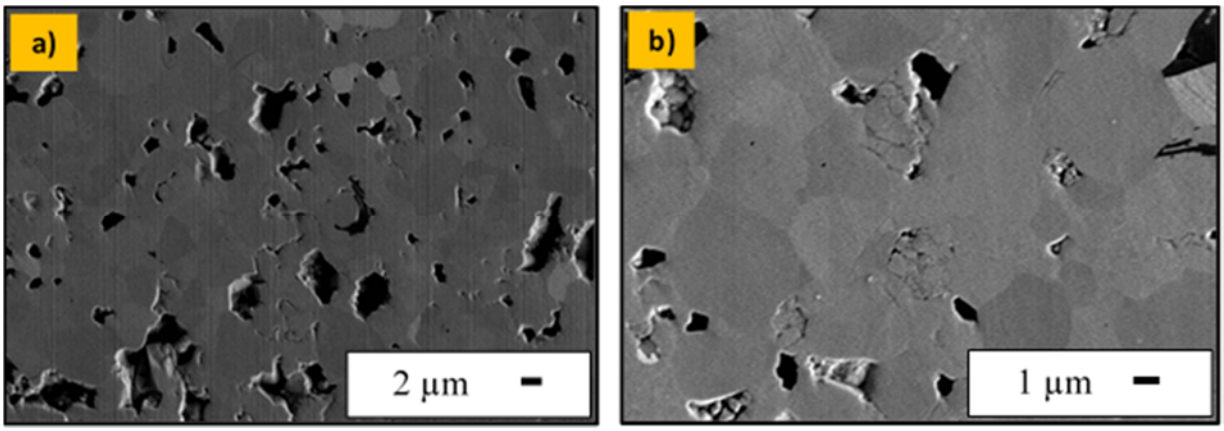

Figure 2.45. SEM micrographs of (a-b) (60-40) vol% $MoSi_2$-ZrO_2 composite sample after long-term annealing at 1400°C for 48 hours [*Samples were chemically etched in 2.0 M HCl*].

In addition to the pure $MoSi_2$ and $MoSi_2$-based composites, pure WSi_2 and WSi_2-based composites were also studied as a part of the microstructure and grain growth studies. Due to the difficulty of fine polishing of pure WSi_2 sample, individual WSi_2 grains were not observed, and therefore those results were not presented here. Further studies are needed for the development of a new polishing procedure specifically for WSi_2 material. Figure 2.46(a-b) presents the SEM microstructures of (60-40) vol% WSi_2-Al_2O_3 composite samples at different magnifications after long-term annealing at 1400°C for 48 hours. The formation of W_5Si_3 as a secondary phase can be clearly seen as bright regions in the Figure 2.46a. As a main point of this study, the average grain size of WSi_2 grains was measured by image analysis software approximately as 6.4 µm after long-term annealing at

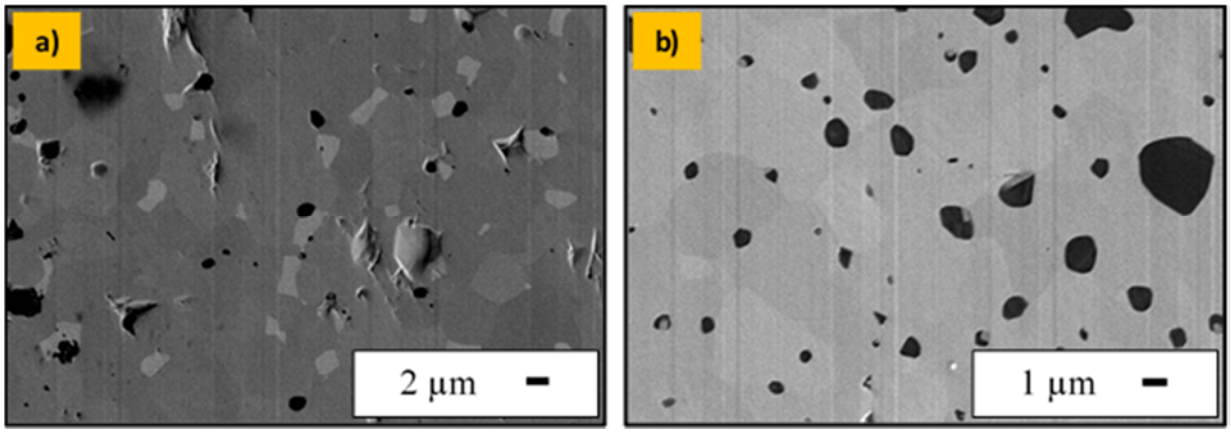

Figure 2.46. SEM micrographs of **a-b)** (60-40) vol% WSi_2-Al_2O_3 composite sample after long-term annealing at 1400°C for 48 hours [*WSi_2-Al_2O_3 sample shown in Figure 2.46a was chemically etched in 1:1:1 HCl:HNO_3:H_2O*].

1400°C. Therefore, it can be stated that the average grain size of WSi_2 increased from 5.3 to 6.4 µm within WSi_2-Al_2O_3 composite system after sintering and long-term annealing processes. The grain growth rate of WSi_2 for this composite system is found very similar to the grain growth rate of $MoSi_2$ for all $MoSi_2$-based composites.

Figure 2.47(a-d) shows the SEM microstructures of (60-40) vol% WSi_2-coarseAl_2O_3 and (60-40) vol% WSi_2-ZrO_2 composite samples at different magnifications after long-term annealing at 1400°C for 48 hours, respectively. Although there is a slight difference in contrast, individual WSi_2 (gray regions) and W_5Si_3 (bright regions) grains can be clearly seen for WSi_2-coarseAl_2O_3 composite in the Figure 2.47a. In addition to that, individual WSi_2 grains and their distribution within coarse Al_2O_3 grains are presented in the Figure 2.47b. The average grain size of WSi_2 grains was measured approximately as 6.3 µm after long-term annealing at 1400°C. As a result of this data, it is important to note that the average WSi_2 grain size increased from 5.3 to 6.3 µm after sintering and long-term annealing processes, which is quite similar to the result obtained for WSi_2-Al_2O_3 composite system. In the Figure 2.47(c-d), the SEM microstructures of (60-40) vol% WSi_2-ZrO_2 composite samples after long-term annealing are presented. Individual WSi_2 (gray regions) and W_5Si_3 (bright regions) grains can be observed in these microstructures. The average grain size of WSi_2 grains was measured approximately as 6.4 µm, which is almost same with the data obtained for WSi_2-Al_2O_3 and WSi_2-coarseAl_2O_3 composites after long-term annealing at 1400°C. As a result of these studies, it is found that all refractory oxides retarded the grain growth of WSi_2 by pinning effect of a secondary phase. However, further studies are still needed for determination of the grain growth kinetics of pure WSi_2 after sintering, short-term and long-term annealing studies, and its comparison with the WSi_2-based composites.

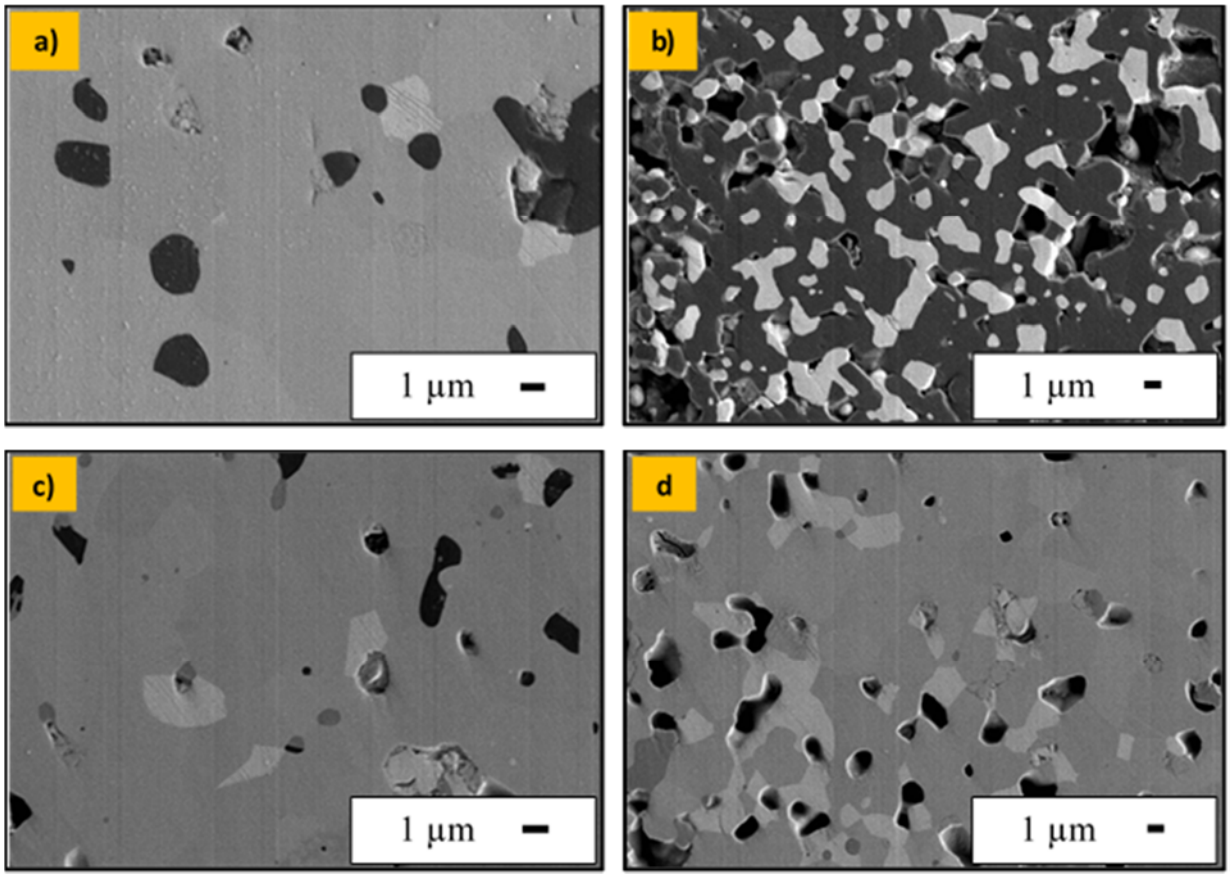

Figure 2.47. SEM micrographs of (a-b) (60-40) vol% WSi_2-coarseAl_2O_3, and (c-d) (60-40) vol% WSi_2-ZrO_2 composite samples after long-term annealing at 1400°C for 48 hours [*WSi_2-coarseAl_2O_3 sample shown in Figure 2.47a and all WSi_2-ZrO_2 samples were chemically etched in 1:1:1 HCl:HNO_3:H_2O*].

As a review of the sintering, annealing and grain growth studies performed, it can be pointed out that refractory oxides can successfully retard the grain growth of metal silicides at high temperatures (1400°C) for both short- and long-term. Figure 2.48a presents the changes in the grain growth of $MoSi_2$ grains as a function of sintering and annealing processes. It is clear that the overall $MoSi_2$ grain growth rates for $MoSi_2$-Al_2O_3 and $MoSi_2$-coarseAl_2O_3 composite systems are quite similar, since the average $MoSi_2$ grain size increased from 4.2 to 5.2-5.3 µm in both cases. However, the overall $MoSi_2$ grain growth rate is found relatively higher for $MoSi_2$-ZrO_2 composite system in comparison to the other $MoSi_2$-based composites, since the average $MoSi_2$ grain size increased up to 6.0 µm after sintering and long-term annealing processes. In case of pure $MoSi_2$, overall $MoSi_2$ grain growth rate is extremely high, because their average grain size increased approximately up to 12.7 µm after sintering and long-term annealing processes. These results clearly prove that the grain growth rate of $MoSi_2$ can be highly affected by the existence of refractory oxides in the system. In case of WSi_2-based composites, it is determined that the overall WSi_2 grain growth rate is quite similar for WSi_2-Al_2O_3, WSi_2-coarseAl_2O_3 and WSi_2-ZrO_2 composite systems, since the average grain size of WSi_2 increased from 5.3 to 6.3-6.4 µm in all cases after sintering and long-term annealing processes (Figure 2.48b).

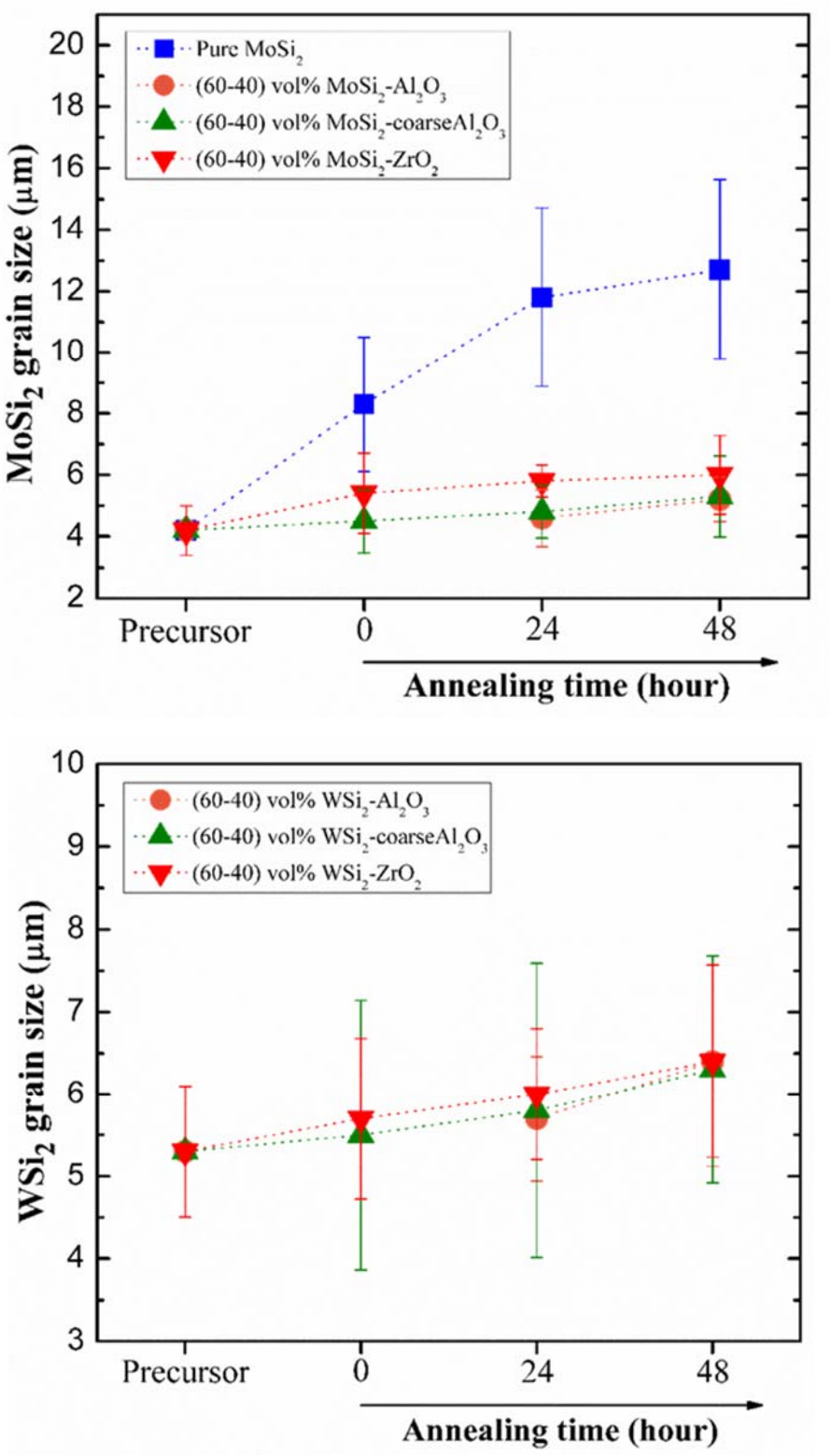

Figure 2.48. Grain growth kinetics of (a) $MoSi_2$, and (b) WSi_2 as a function of annealing time at 1400°C [*0 hour indicates the pre-sintered samples*].

2.3.2.4 Quantitative image analysis and homogeneity levels of the composites

It is known that distribution of metal silicide particles as conductive particles within refractory oxides and uniform mixing is very important in order to achieve better electrical conductivity and thus performance of silicide/oxide composites. Therefore it is crucial to study the distribution of different composites, and particularly the distribution of metal silicide particles within a ceramic matrix by performing image analysis studies via ImageJ software. Based on the literature survey on image analysis for distribution, it is found that quadrat-based method is mostly used technique among all other techniques such as nearest-neighborhood distance method, k-function, Monte-Carlo method, mean free path, radial distribution function, polygonal methods, and local area fraction due to its simplicity [2.3, 2.6, 2.7]. The main principle of the quadrat-based method is to divide the microstructure image to a number of equal square areas called as quadrats, and then to determine the number of particles in each quadrat. Then, Skewness index (third moment of the central deviation) needs to be calculated in order to obtain an index indicating the distribution. Since an increase in the skewness means an increase in particle clustering and a decrease in distribution or mixedness, there is no any reference value in this method to compare the calculated skewness index in order to get a percentage value corresponding to degree of distribution (homogeneity) or mixedness of a composite. The other problem of this method is known as determination of the optimum quadrat size, which increases the error margin on skewness index and hereby distribution. Therefore, image analysis studies on different composite microstructures were performed via ImageJ to develop a new technique for determining of degree of distribution (homogeneity) of silicide grains within a refractory oxide matrix.

In order to investigate the efficiency and accuracy of the quantitative image analysis method developed, it was applied to the microstructures of the composites. Figure 2.49 shows the original cross-sectional SEM microstructures of the metal silicide-refractory oxide composites and also their converted binary images composed of individual metal silicide grains as black regions. (60-40) vol% WSi_2-ZrO_2, (60-40) vol% WSi_2-Y_2O_3 and (60-40) vol% $MoSi_2$-Al_2O_3 composite compositions are selected for this study, since they all represent different degrees of distribution of metal silicide grains within a refractory oxide matrix. To quantify the homogeneity of these composites via D index, the free-path spacing and their arithmetic mean values were measured on a total of 40 lines that was drawn both in the horizontal and vertical direction. Also it is important to note that the free-path spacing and all calculated values were measured in microns after setting the scale. The calculated D index values for three different metal silicide-refractory oxide composites as a function of total number of lines are presented in the Figure 2.50. The measured D index values for (60-40) vol% WSi_2-ZrO_2 composite range from 0.189 to 0.142 with increasing total number of lines analyzed from 2 to 40. For high accuracy, its D index is accepted as 0.142 based on the results obtained with 40 lines, since the arithmetic mean ($\bar{X}$) and standard deviation (s) of the all free-path spacing values are found as 1.043 and 0.148 μm, respectively. These results demonstrate that the D index of (60-40) vol% WSi_2-ZrO_2 composite slightly diverges from zero, and thus the distribution of the WSi_2 grains within ZrO_2 ceramic matrix is highly homogeneous. For the (60-40) vol% WSi_2-Y_2O_3 composite, the arithmetic mean and standard deviation of the all free-path spacing values obtained on 40 lines was measured as 4.817 and 1.651 μm, respectively. The D index value for WSi_2-Y_2O_3 composite was found as 0.343, which represents a moderate level of homogeneity and distribution of WSi_2 grains within Y_2O_3 ceramic matrix due to agglomeration at certain regions. In comparison of WSi_2-ZrO_2 and WSi_2-Y_2O_3 composites, it is clear that the D index increases from 0.142 to 0.343 due to particle agglomeration. It can also be seen that the D index values for these two composites are highly stable after 8 lines were analyzed,

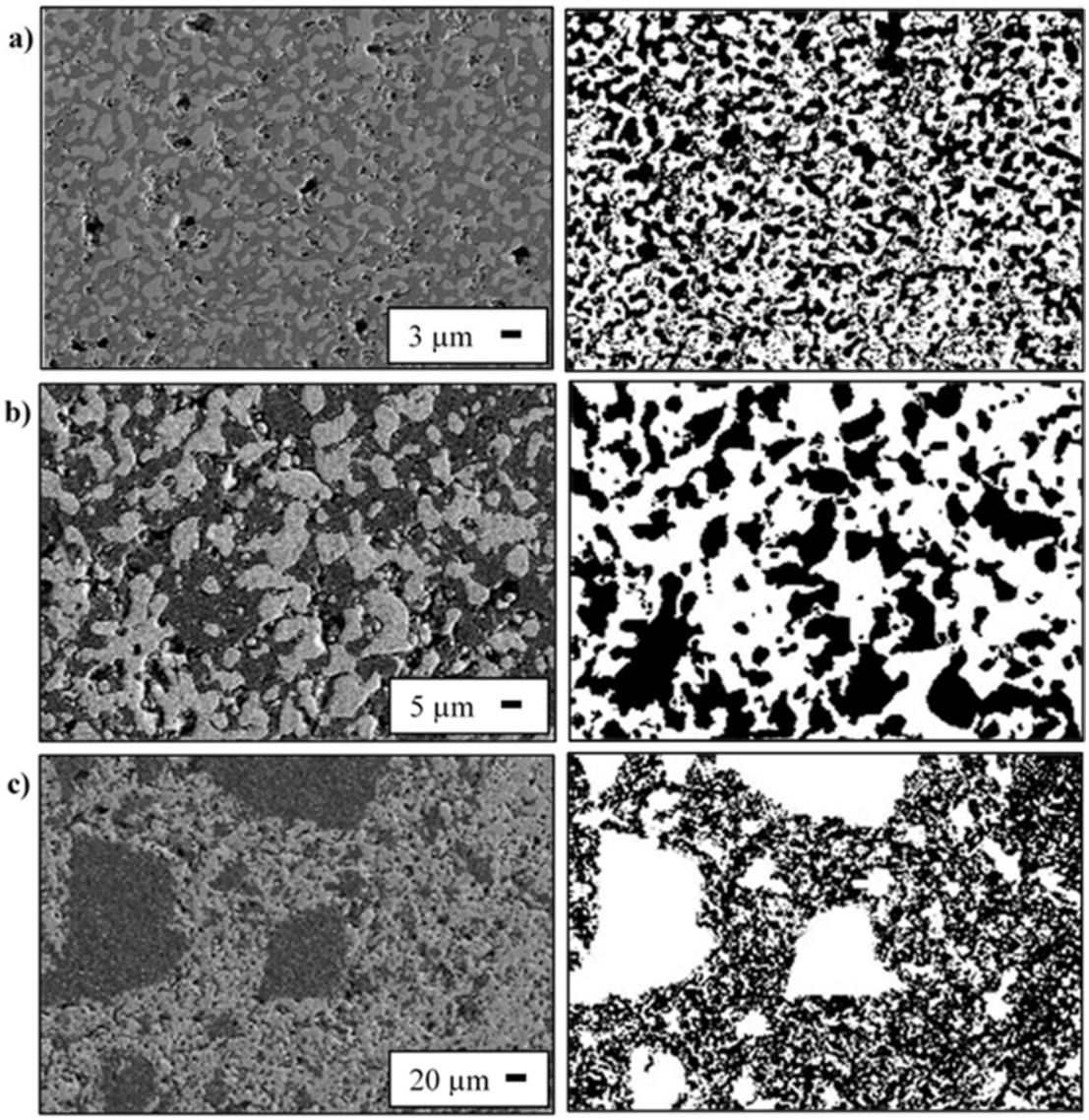

Figure 2.49. Original cross-sectional SEM microstructures of the metal silicide-refractory oxide composites and their converted binary images showing individual metal silicide grains as black regions (on the right side): (a) (60-40) vol% WSi_2-ZrO_2, (b) (60-40) vol% WSi_2-Y_2O_3, and (c) (60-40) vol% $MoSi_2$-Al_2O_3.

which proves that accurate results for these kinds of microstructures can be simply achieved by analyzing several lines on both axes. On the other hand, it was demonstrated that the D index values for (60-40) vol% $MoSi_2$-Al_2O_3 composite range from 0.444 to 0.557 with increasing total number of lines. However, its D index is considered as 0.557 based on the results obtained with 40 lines. Since the standard deviation (4.423 µm) is relatively high compared to its arithmetic mean (7.935 µm) due to high variations in the free-path spacing values, the $MoSi_2$-Al_2O_3 composite exhibits a low level of homogeneity. These results are found to be directly related with particle agglomeration and also poor distribution of $MoSi_2$ grains within Al_2O_3 matrix. Therefore, it can be clearly seen that the D index values are not stable until 28 lines are analyzed (Figure 2.50).

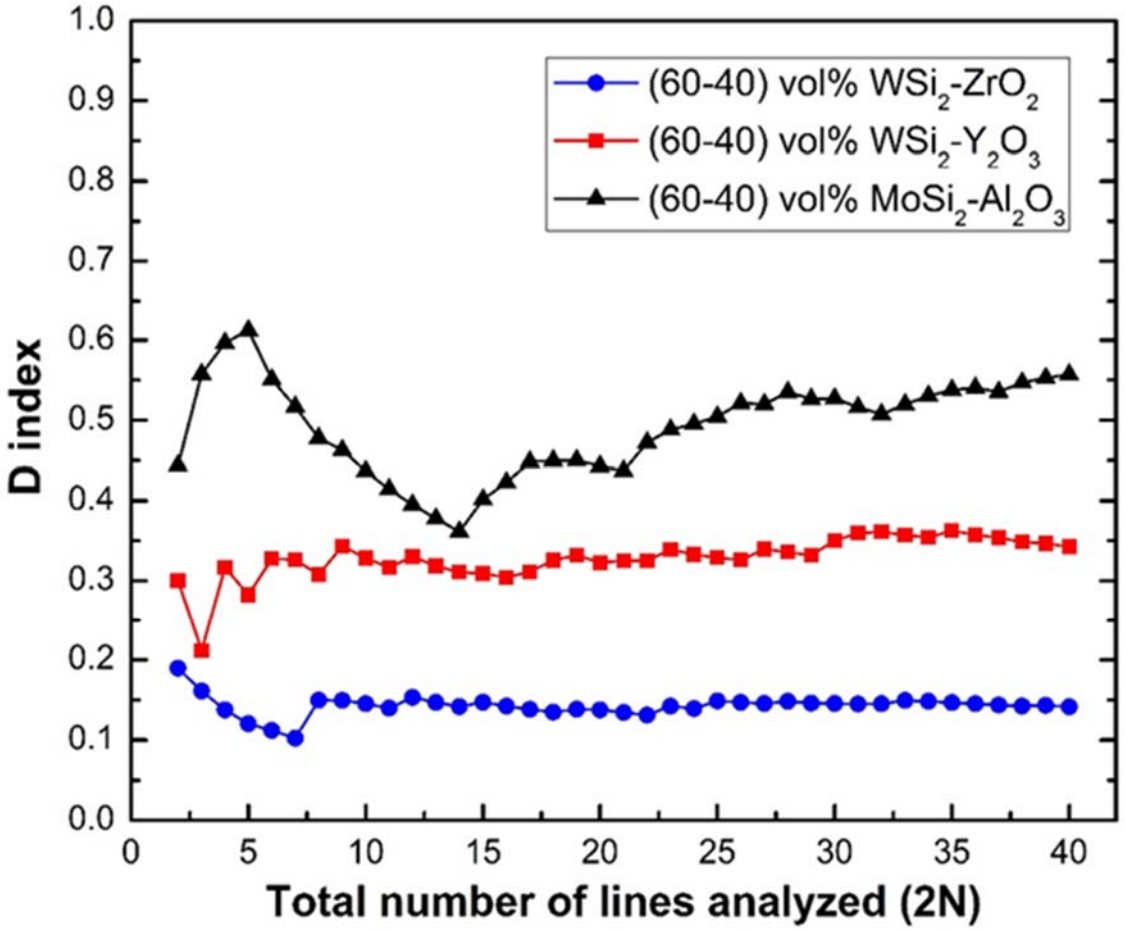

Figure 2.50. The D index values calculated for three different metal silicide-refractory oxide composites' SEM microstructures as a function of total number of lines analyzed (2N) by using the proposed method.

As a review of the data obtained by quantitative image analysis method developed, the D index values measured for metal silicide-refractory oxide composite microstructures increase from 0.142 to 0.557 depending on the free-path spacing, coefficient of variation, and degree of distribution. It was found that the (60-40) vol% WSi_2-ZrO_2 composite have high homogeneity, while (60-40) vol% WSi_2-Y_2O_3 and (60-40) vol% $MoSi_2$-Al_2O_3 composites exhibited moderate and low level of homogeneity, respectively. It was also shown that more accurate results for the composite microstructures having high or moderate level of homogeneity can be obtained by analyzing several lines (≤ 10), while there is a need to analyze more lines (≥ 28) for that having low or very low level of homogeneity. These results clearly indicate that the proposed microstructural quantitative image analysis method works very accurately on different kinds of composite microstructures by considering the coefficient of variation and related D index value as a measure of the degree of distribution.

2.3.3 Subtask 2.3 - Composite material testing and characterization

This section reports the (i) electrical conductivity measurements, (ii) thermal expansion coefficient measurements, and (iii) high-temperature (pest) oxidation experiments/behavior of the silicide-oxide composites as a function of processing, composition and temperature.

2.3.3.1 4-point DC electrical conductivity measurements of the composites

The electrical conductivity measurements of the composite samples were performed using a 4-probe DC conductivity method. A high temperature test rig was made using a high purity 4-bore alumina tube and platinum connection leads. An S-type thermocouple is used to monitor the temperature. The rectangular bar samples with dimension 20 x 4 x 4 mm were connected to the test rig and the entire system was sealed in a tube furnace. The experiments were conducted in Argon atmosphere to avoid material degradation. LabView and Keithley programs were used to acquire temperature and electrical resistance data automatically. Then electrical resistivity and electrical conductivity data were calculated by using specific sample dimensions.

The high-temperature electrical conductivity of the $MoSi_2$- and WSi_2-based composites reinforced by alumina and zirconia particles is shown as a function of temperature in the Figure 2.51. It is known that these composites are metallic conductors above a critical percolation limit [2.8], and thus, their electrical conductivity was shown to decrease with increasing temperature as expected. It is also important to note that the electrical conductivity data was achieved only at the temperatures above 400°C for all the 60-40 composites (except for 20-80 $MoSi_2$-fine.Al_2O_3), because of the very low resistance below this temperature which resulted in highly inaccurate measurements using the current digital multimeter. For the given sample dimensions, the upper limit for the electrical conductivity was near 3550 S/cm. Additionally, four-point electrical connections made by Pt wire and ink were lost at 820°-900°C, which inhibited the electrical conductivity measurements above that temperatures. This may be associated with the local reaction between Pt and metal disilicides to form platinum silicide (PtSi) phase having low melting-point on the sample surface [2.9, 2.10]. Therefore, the exponential fitting was applied to some of the results (60-40 $MoSi_2$-coarse.Al_2O_3, WSi_2-fine.Al_2O_3, WSi_2-ZrO_2) in order to extrapolate the electrical conductivity data from 820° to 900°C for a better data comparison (adjusted R-square values: 0.932-0.968). Furthermore, the electrical conductivity data could not be obtained at 20 vol% metal silicide fraction, except for the 20-80 $MoSi_2$-fine.Al_2O_3 composite. Since the main conduction mechanism within these composites is the formation of three-dimensional continuous percolating network, it is found that the certain percolation threshold could not be exceeded for other 20-80 composites. The electrical conductivity of the 20-80 $MoSi_2$-fine.Al_2O_3 was measured as 8.83 and 8.05 S/cm at the temperatures of 900°C and 1000°C, respectively (Figure 2.51a). This level of electrical conductivity, for instance 46.58 S/cm at around 110°C, was significantly higher than that for a similar 20-80 $MoSi_2$-Al_2O_3 composite (0.01 S/cm at around 50°C) reported by Kobel et al. [2.11]. The difference in the percolation concentration of 20-80 composites was found to be highly related to their relative densities, since the relative density of the 20-80 $MoSi_2$-fine.Al_2O_3 composite (97.92%) was substantially greater than that of the other composites (72.89-92.62%). Therefore, it is clear that densification of the composites should be highly improved to fabricate electroconductive ceramic composites even at low volume percentages of conductive phase by decreasing the critical percolation concentration.

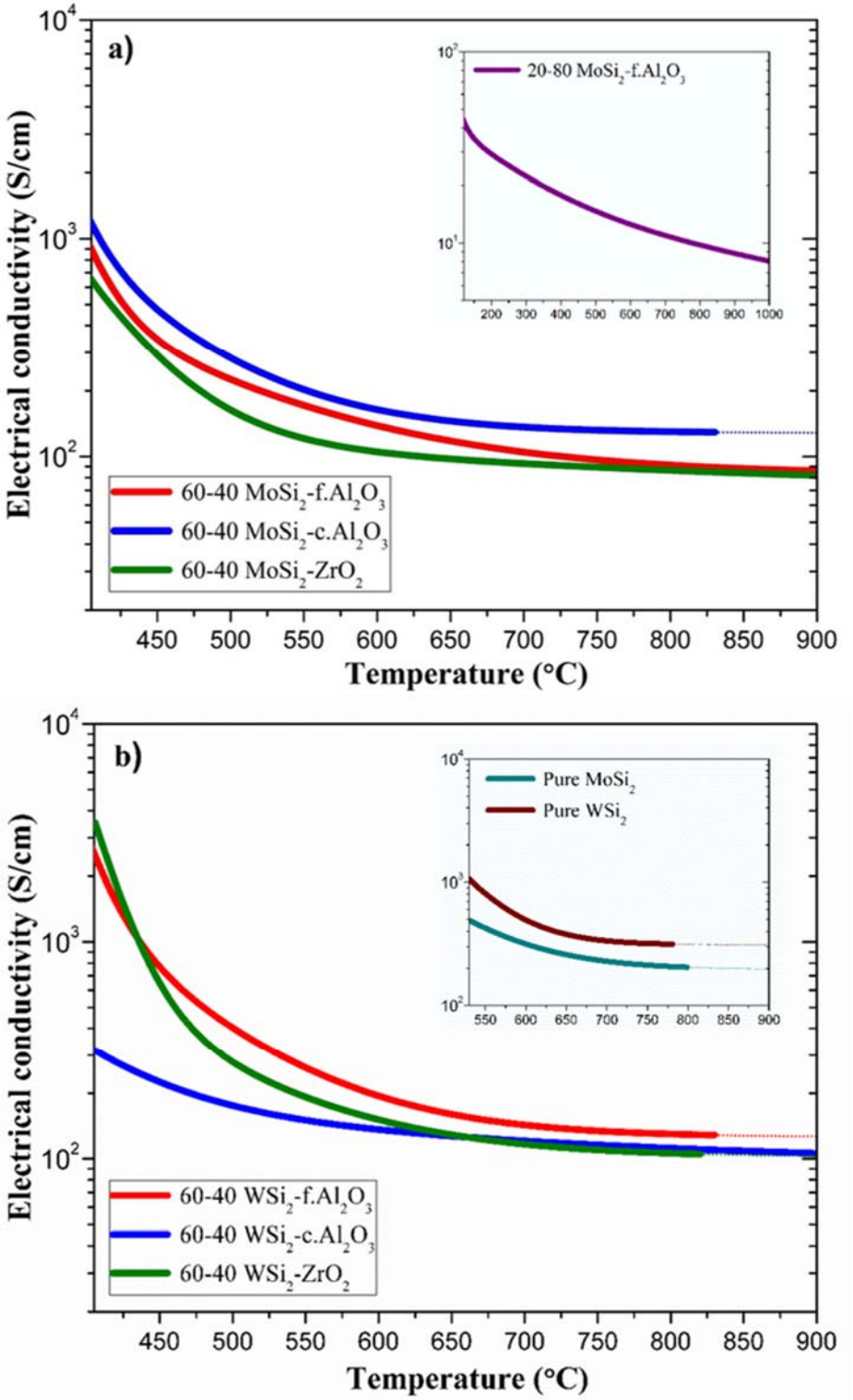

Figure 2.51. The electrical conductivity of the (a) $MoSi_2$-based and (b) WSi_2-based composites and pure metal disilicides ($MoSi_2$, WSi_2) as a function of temperature (Electrical conductivity data is presented on the logarithmic scale).

In the 60-40 $MoSi_2$-based composites, $MoSi_2$-coarse.Al_2O_3 composite displayed significantly higher electrical conductivity (128.4 S/cm) than the others (81.9-86.0 S/cm) at 900°C, as presented in the Figure 2.51a. The relative density of the $MoSi_2$-coarse.Al_2O_3 (77.7%) was lower than that of the $MoSi_2$-c.Al_2O_3 and $MoSi_2$-ZrO_2 (~87.9%). It displayed a higher electrical performance that could be correlated with the more homogeneous distribution of conductive silicide particles within insulating oxide phase, since it is well known that the electrical properties are highly influenced by distribution of particles or homogeneity of microstructure as well as particle size/morphology and density/porosity. On the other hand, the 60-40 WSi_2-fine.Al_2O_3 showed substantially higher electrical conductivity (126.6 S/cm) than other WSi_2-based composites (102.8-105.9 S/cm) as seen in the Figure 2.51b, due to its relatively high relative density (88.6%). No significant effect of conductive to insulating particle size ratio was observed. Therefore, this result may be also related to the amount of secondary W_5Si_3 phase within the composite system, since its content in the WSi_2-fine.Al_2O_3 (6.9 vol%) after sintering was significantly lower than that in the WSi_2-coarse.Al_2O_3 and WSi_2-ZrO_2 composites (18.5-21.8 vol%). However, there is no data reported in the literature regarding to the intrinsic electrical properties of W_5Si_3 phase. Among all the 60-40 vol% silicide-oxide composites, it is determined that the $MoSi_2$-coarse.Al_2O_3 and WSi_2-fine.Al_2O_3 revealed similar, but the highest electrical conductivities at 900°C. Besides, electrical conductivities of the pure $MoSi_2$ and WSi_2 samples are presented as a function of temperature in the Figure 2.51b. It can be clearly seen that the WSi_2 showed higher electrical conductivity (310.5 S/cm) than the $MoSi_2$ (197.6 S/cm) at 900°C based on the extrapolated data (dotted lines above 780°-800°C) using exponential fitting (adjusted R-square values: 0.932-0.974). Similarly, significantly high intrinsic electrical conductivity of the WSi_2 compared to the $MoSi_2$ was reported on thin films by Gottlieb et al. [2.8]. This also improved the electrical conductivity of the WSi_2-based composites. As a review of these results, these composites displayed promising electrical properties at high-temperatures, which were affected by their relative density, distribution level of particles (homogeneity), intrinsic conductivity of conductive phase, particle size/morphology and perhaps fraction of secondary 5-3 silicide phase.

Before discussing the electrical properties of the other silicide-oxide composite samples, it is important to review the XRD results of the sintered metal silicides ($NbSi_2$, $TaSi_2$ and Nb_5Si_3) and their electrical conductivities as a function of temperature. Figure 2.52a presents the XRD patterns of the $NbSi_2$, Nb_5Si_3 and $TaSi_2$ samples after sintering at 1600°C for 2 h under argon. The results showed that sintered $NbSi_2$ sample contains not only $NbSi_2$ phase, but also secondary Nb_5Si_3 phase. However, only Nb_5Si_3 and SiO_2 phases were observed for the Nb_5Si_3 sample after sintering at 1600°C. In addition to the niobium silicides, the results for the sintered $TaSi_2$ sample displayed that it contains $TaSi_2$ and Ta_5Si_3 phases, similar to the sintered $NbSi_2$ sample. The electrical conductivity results of these samples are shown in Figure 2.52b as a function of temperature (400°-900°C). The electrical conductivity of the sintered $NbSi_2$ sample decreased from 972.2 to 42.3 S/cm with increasing temperature from 400°C to 900°C. The sintered $TaSi_2$ sample also exhibited a similar trend, since its electrical conductivity decreased from 1285.4 to 41.5 S/cm with increasing temperature from 460° to 900°C. On the other hand, sintered Nb_5Si_3 sample revealed more linear trend in electrical conductivity compared to the other samples as clearly seen in the Figure 2.52b. The electrical conductivity of the sintered Nb_5Si_3 sample linearly decreased from 268.4 to 152.1 S/cm with increasing temperature. The results clearly proved that the sintered Nb_5Si_3 has significantly higher electrical conductivity at high-temperatures compared to the sintered $NbSi_2$ and $TaSi_2$ samples. In addition, it is clear that the sintered $NbSi_2$ and $TaSi_2$ samples have very similar electrical conductivities at around 900°C. This knowledge on the sintered niobium silicide

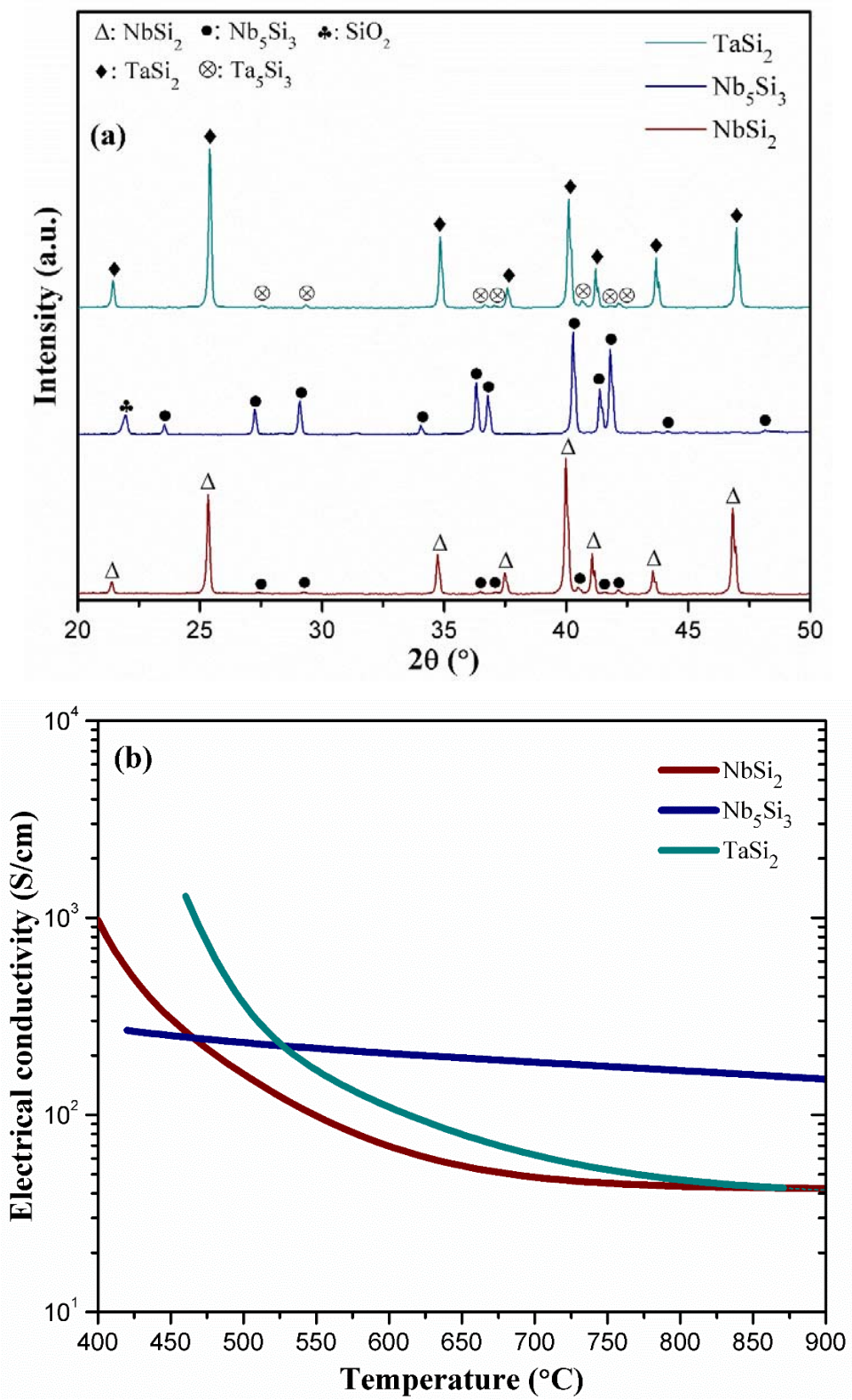

Figure 2.52. (a) X-ray diffraction patterns and (b) electrical conductivity results of the $NbSi_2$, Nb_5Si_3 and $TaSi_2$ samples sintered at 1600°C.

and tantalum silicide samples is very crucial for understanding the electrical properties of the $NbSi_2$- and $TaSi_2$-based composites better. Figure 2.53 presents the electrical conductivities of the $NbSi_2$- and $TaSi_2$-based composites sintered at 1600°C. The results showed that the electrical conductivity of the (60-40) vol% $NbSi_2$-Al_2O_3 composite decreased from 1057.5 to 107.3 S/cm with increasing temperature from 445°C to 900°C. (60-40) vol% $NbSi_2$-ZrO_2 composite displayed a very similar trend, since its electrical conductivity decreased from 2030.8 to 111.3 S/cm with increasing temperature from 440°C to 900°C. These high electrical conductivity values were found to be highly related to the high volume percentages of the Nb_5Si_3 phase and its higher intrinsic electrical conductivity. In comparison to the $NbSi_2$-based composites, (60-40) vol% $TaSi_2$-Al_2O_3 composite exhibited relatively low electrical conductivity at high-temperatures. Its electrical conductivity decreased from 643.4 to 87.3 S/cm with increasing temperature from 420°C to 900°C. It can be clearly seen that (60-40) vol% $TaSi_2$-ZrO_2 composite revealed substantially lower electrical conductivity values at high-temperatures compared to all other composite samples, since its electrical conductivity was measured as 25.9 S/cm at 900°C. This may be directly related to the higher porosity levels, amount of secondary Ta_5Si_3 phase and potential microcracks within this composite system.

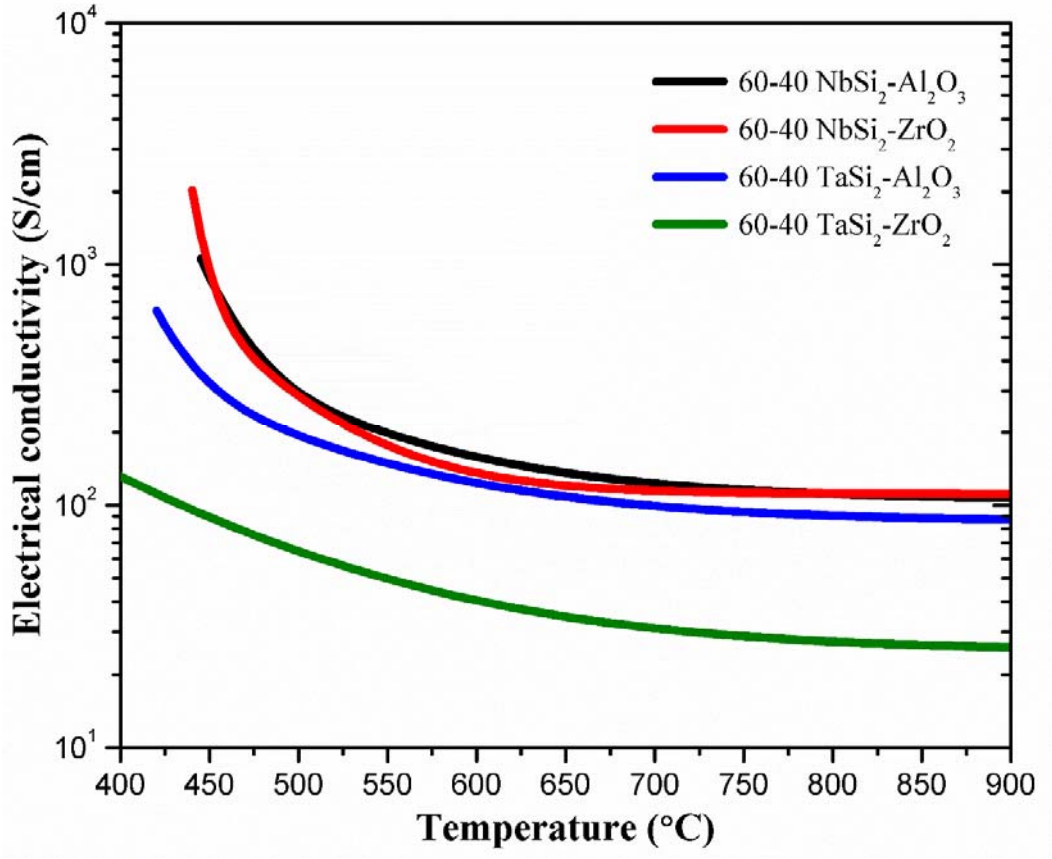

Figure 2.53. Electrical conductivity of the (60-40) vol% $NbSi_2$- and $TaSi_2$-oxide composites as a function of temperature (Electrical conductivity data is presented on the logarithmic scale).

In order to investigate the electrical properties of the $CrSi_2$-Cr_2O_3 composites at high temperatures, their electrical conductivities were also measured as a function of temperature (100°-1000°C). Figure 2.54a presents the electrical conductivity result of the (50-50) vol% $CrSi_2$-Cr_2O_3 composite sintered at 1400°C for 2 hours. It is found that its electrical conductivity decreased from 90.5 to 41.8 S/cm with increasing temperature from 105°C to 988°C. The electrical conductivity of the (50-50) vol% $CrSi_2$-Cr_2O_3 composite can be directly related with the major conductive phase, Cr_3Si and its distribution within SiO_2 phase. The electrical conductivity of the (55-45) vol% $CrSi_2$-Cr_2O_3 composite sintered at 1400°C is shown in the Figure 2.54b. Its electrical conductivity is determined as 213.3 S/cm at 1010°C, while it is 503.7 S/cm at 355°C. At around 988°C, the electrical conductivities of the (50-50) and (55-45) vol% $CrSi_2$-Cr_2O_3 composites were found as 41.8 and 214.6 S/cm, respectively. Therefore, it can be clearly stated that the high temperature electrical conductivity drastically increased with 5 vol% increase in the initial chromium silicide volume percentage, which can be explained by increased amount of Cr_3Si and formation of Cr_5Si_3 in the composite system. Figure 2.54c presents the electrical conductivity of the (60-40) vol% $CrSi_2$-Cr_2O_3 composite sintered at 1400°C as a function of temperature. The electrical conductivity of the (60-40) vol% $CrSi_2$-Cr_2O_3 composite decreased from 1521.3 to 119.2 S/cm with increasing temperature from 333°C to 986°C. This result is directly related with the major conductive phases that are Cr_5Si_3 and Cr_3Si. But it is important to note that the high temperature electrical conductivity highly decreased from 214.6 to 119.2 S/cm with 5 vol% increase in the initial chromium silicide content. This result can be explained by decreased amount of Cr_3Si, and remained CrSi and $CrSi_2$ phases after sintering. This result may indicate relatively low electrical

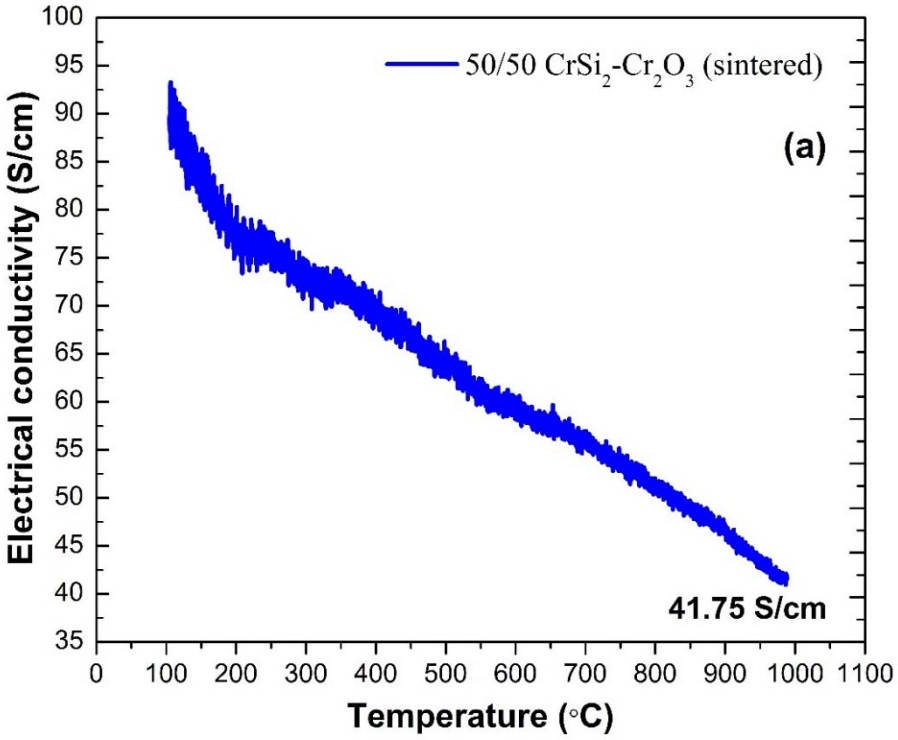

Figure 2.54. Electrical conductivity results of the (a) (50-50) vol% $CrSi_2$-Cr_2O_3, (b) (55-45) vol% $CrSi_2$-Cr_2O_3, and (c) (60-40) vol% $CrSi_2$-Cr_2O_3 composite samples sintered at 1400°C for 2 hours, as a function of temperature (100°-1000°C).

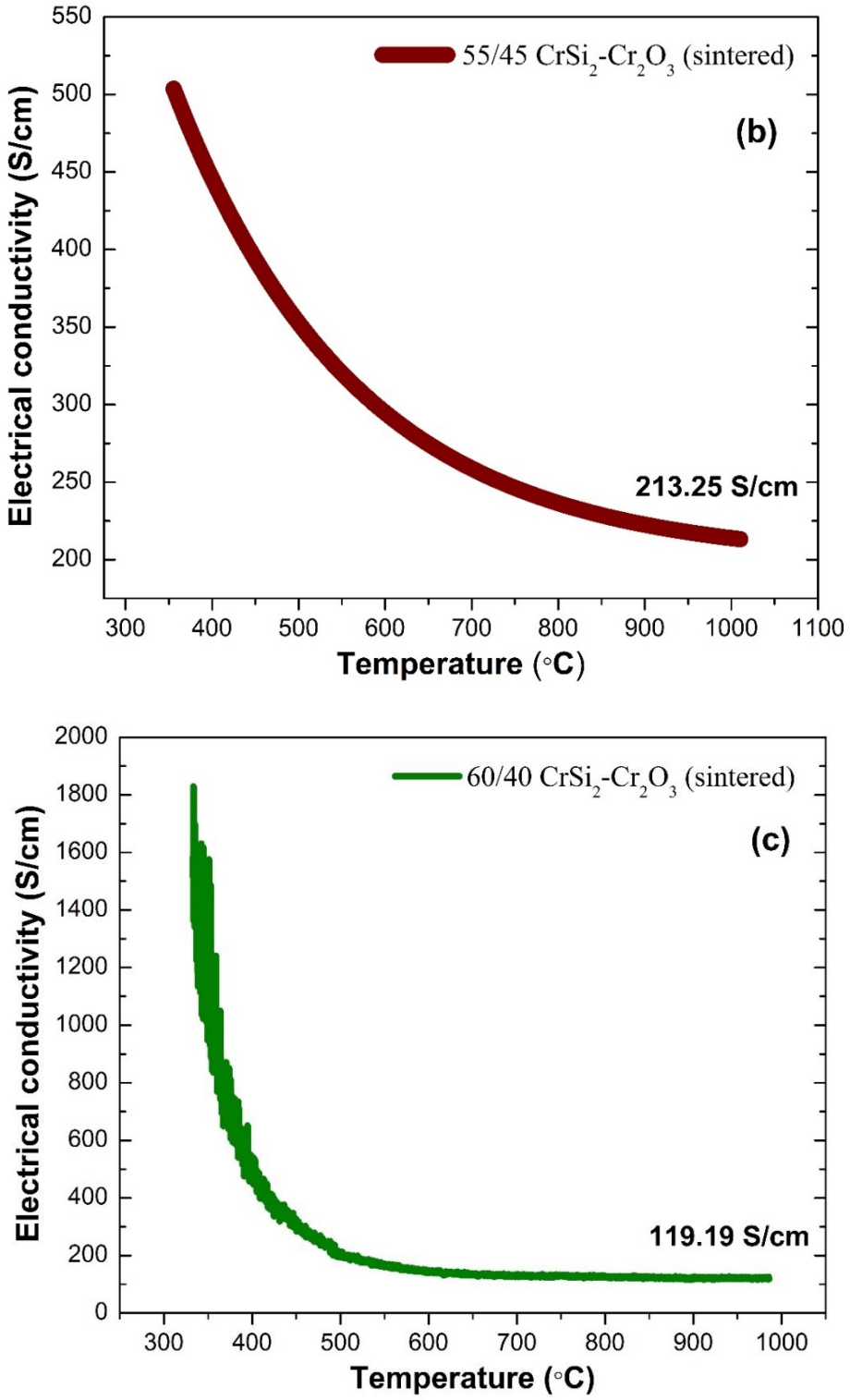

Figure 2.54. (continued) Electrical conductivity results of the (a) (50-50) vol% $CrSi_2$-Cr_2O_3, (b) (55-45) vol% $CrSi_2$-Cr_2O_3, and (c) (60-40) vol% $CrSi_2$-Cr_2O_3 composite samples sintered at 1400°C for 2 hours, as a function of temperature (100°-1000°C).

conductivity of Cr_5Si_3 phase compared to Cr_3Si. As a review of the electrical conductivity measurements of the (50-50), (55-45) and (60-40) vol% $CrSi_2$-Cr_2O_3 composites after sintering, it can be concluded that Cr_3Si and Cr_5Si_3 phases have high electrical conductivities at high temperatures, and therefore, the electrical conductivity of these composites can be successfully adjusted by slightly changing the initial chromium silicide fraction.

In addition to the measurements discussed above, their electrical conductivities were also measured after annealing at 1400°C for 24 and 48 hours, since some phase changes were observed for these composites as discussed in the XRD results. Figure 2.55a presents the electrical conductivity results of the (50-50) vol% $CrSi_2$-Cr_2O_3 composite samples after sintering and annealing at 1400°C. The electrical conductivities of the composite samples at around 1000°C after annealing for 24 and 48 hours were measured as 229.6 and 217.7 S/cm, respectively. It can be clearly seen that the high temperature electrical conductivity of the (50-50) vol% $CrSi_2$-Cr_2O_3 composite drastically increased with annealing at 1400°C, which may be related with further crystallization of the SiO_2 cristobalite phase and its potential effect on the percolation network. Also, it is important to point out that the high temperature electrical conductivities of the (50-50) vol% $CrSi_2$-Cr_2O_3 composite samples after annealing for 24 and 48 h are quite similar, which is an indication of its increased stability after annealing at 1400°C. The electrical conductivity results of the (55-45) vol% $CrSi_2$-Cr_2O_3 composite samples after sintering and annealing are presented in the Figure 2.55b. The electrical conductivity at 1000°C slightly increased from 213.7 to 234.7 S/cm with annealing at 1400°C for 24 h, but then relatively decreased from 234.7 to 174.7 S/cm with annealing for 48 h. This result may be explained by decreased amount of Cr_3Si and increased

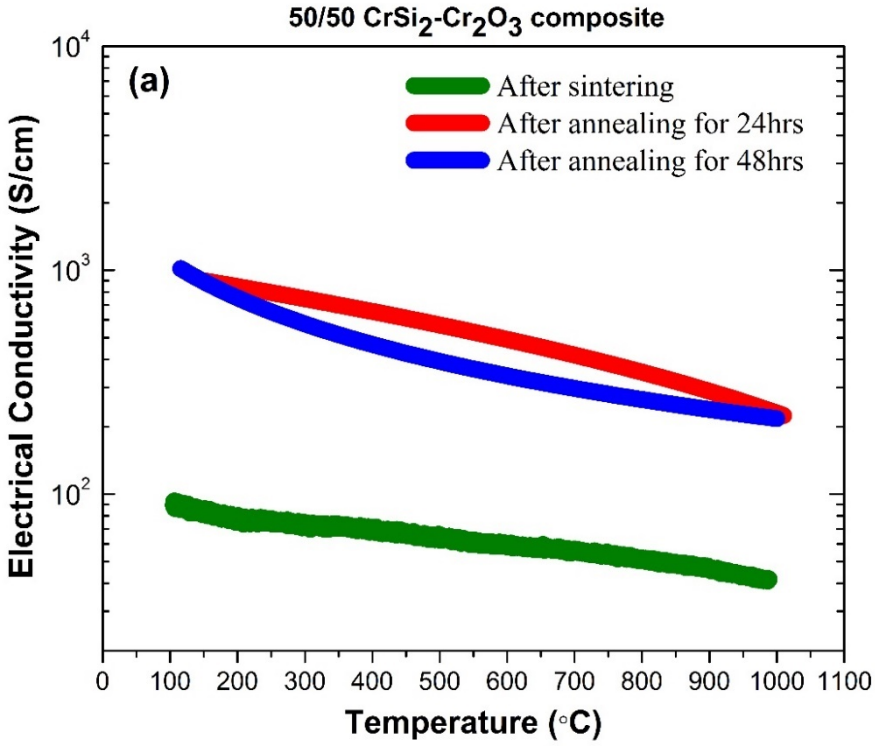

Figure 2.55. Electrical conductivity results of the (a) (50-50) vol% $CrSi_2$-Cr_2O_3, (b) (55-45) vol% $CrSi_2$-Cr_2O_3, and (c) (60-40) vol% $CrSi_2$-Cr_2O_3 composite samples after sintering at 1400°C for 2 h, and then annealing at 1400°C for 24-48 h, as a function of temperature (100°-1000°C).

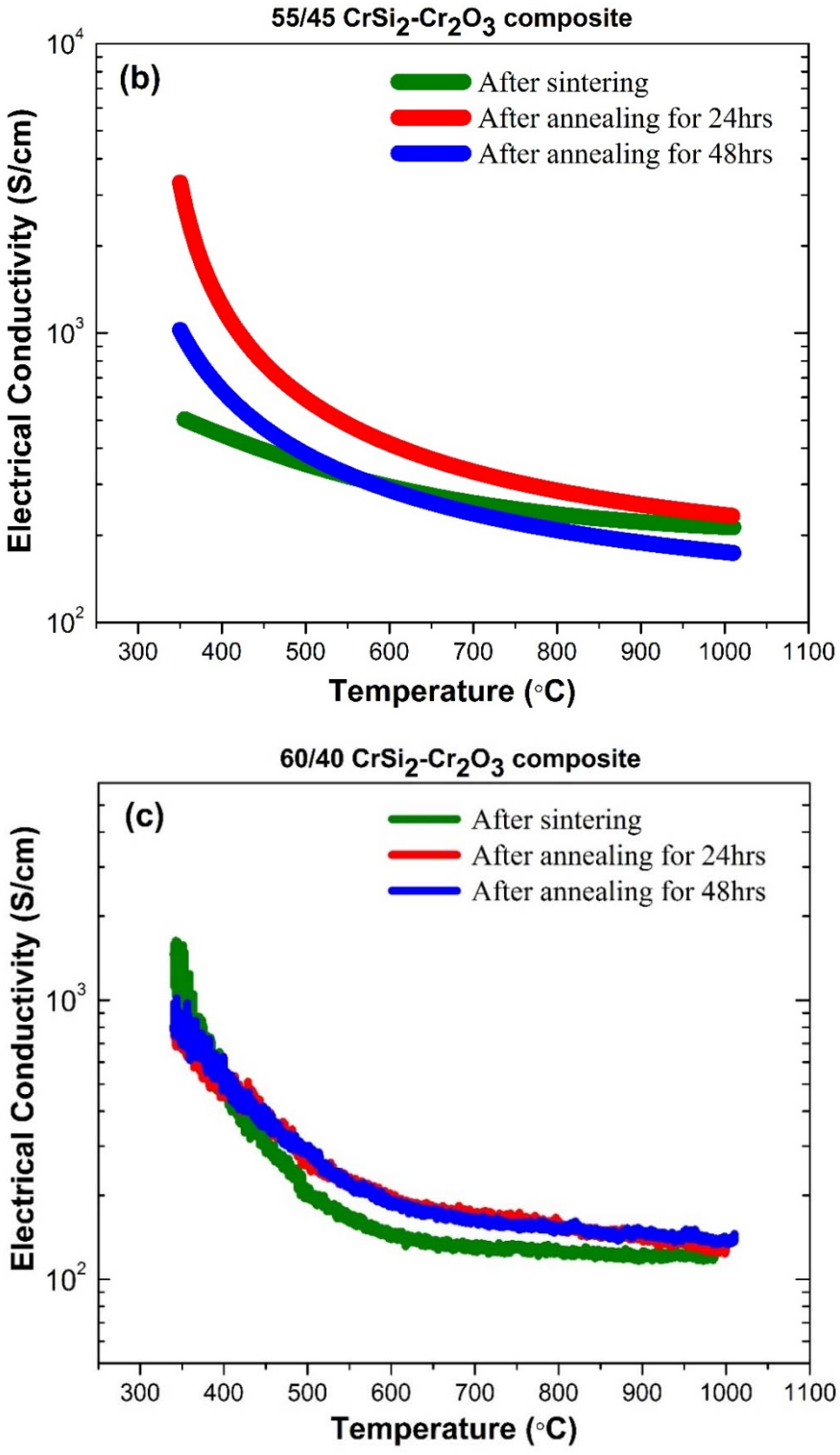

Figure 2.55. (continued) Electrical conductivity results of the (a) (50-50) vol% $CrSi_2$-Cr_2O_3, (b) (55-45) vol% $CrSi_2$-Cr_2O_3, and (c) (60-40) vol% $CrSi_2$-Cr_2O_3 composite samples after sintering at 1400°C for 2 h, and then annealing at 1400°C for 24-48 h, as a function of temperature (100°-1000°C).

amount of Cr_5Si_3. But it is also important to note that (55-45) vol% $CrSi_2$-Cr_2O_3 after annealing for 48 h can be accepted as more stable one, since there is no remaining $CrSi_2$ phase in the system and thus solid-state reaction is almost completed at this point. Figure 2.55c shows the electrical conductivity results of the (60-40) vol% $CrSi_2$-Cr_2O_3 composite samples after sintering and annealing at 1400°C. The electrical conductivity at around 990°C increased from 119.2 to 130.6 S/cm with annealing at 1400°C for 24 h, and then slightly increased from 130.6 to 134.6 S/cm with annealing for 48 h. It can be clearly seen from the Figure 2.55c that the electrical conductivities of the (60-40) vol% $CrSi_2$-Cr_2O_3 composite samples are almost same at the temperatures between 340°C and 1000°C, which clearly indicates that it becomes more stable after annealing at 1400°C. Based on the post-electrical conductivity measurements at high temperatures, it can be concluded that the (50-50) and (60-40) vol% $CrSi_2$-Cr_2O_3 composites are found more stable after annealing at 1400°C for 24 and 48 h. Among these composites annealed for 48 h, it is determined that the (50-50) vol% $CrSi_2$-Cr_2O_3 composite have higher electrical conductivity at high temperatures.

2.3.3.2 Coefficient of thermal expansion (CTE) measurements of the composites

Coefficients of thermal expansion (CTE) of the developed composites were measured by using a horizontal pushrod dilatometer up to 1000°C. Figure 2.56 shows the CTE results of the $MoSi_2$-Al_2O_3 composite samples with various $MoSi_2$ volume percentages, which were sintered at 1600°C for 2 h. It can be clearly seen that the thermal expansion coefficients of the $MoSi_2$-Al_2O_3 composite samples increased with increasing temperature from 100°C to 1000°C. The average thermal expansion coefficient of the 75 vol% $MoSi_2$-25 vol% Al_2O_3 between 100°C and 1000°C was higher ($9.87x10^{-6}K^{-1}$) in comparison to the other composites. However it is important to note that the average CTEs of the $MoSi_2$-Al_2O_3 composite samples, which range from $9.35x10^{-6}$ to $9.87x10^{-6}$, are quite similar to each other and hereby $MoSi_2$ volume percentage within the composite slightly influenced the CTEs of the composites.

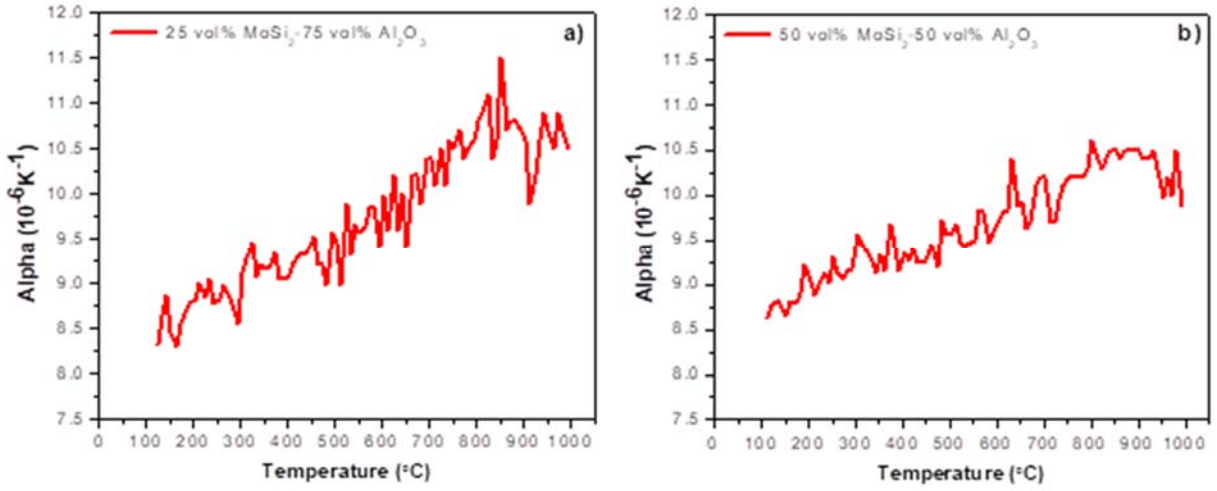

Figure 2.56. Coefficients of thermal expansion (CTEs) of the (a) 25 vol% $MoSi_2$-75 vol% Al_2O_3, (b) 50 vol% $MoSi_2$-50 vol% Al_2O_3, (c) 60 vol% $MoSi_2$-40 vol% Al_2O_3, and (d) 75 vol% $MoSi_2$-25 vol% Al_2O_3 composite samples sintered at 1600°C for 2 h.

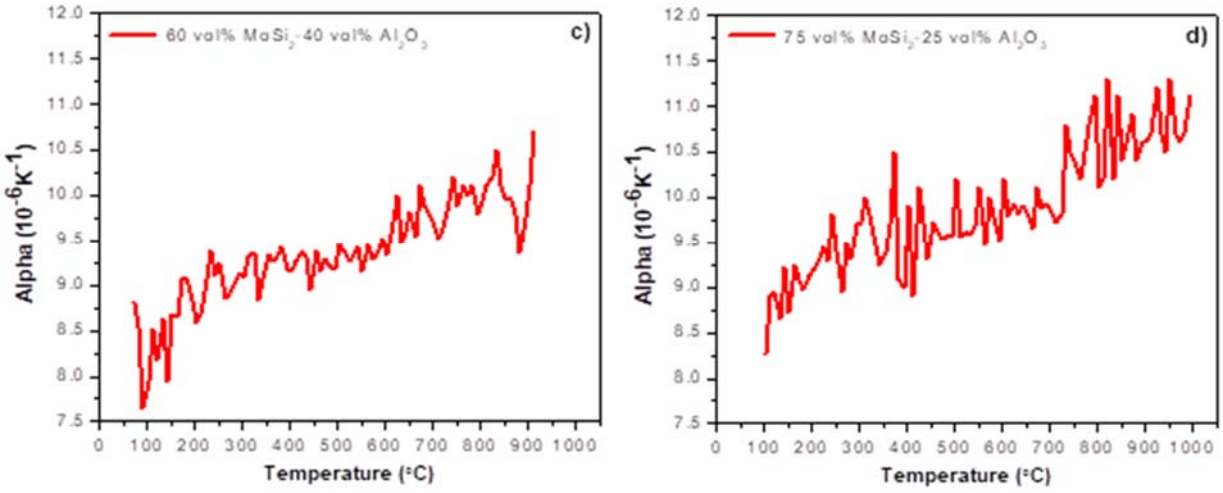

Figure 2.56. (continued) Coefficients of thermal expansion (CTEs) of the (a) 25 vol% $MoSi_2$-75 vol% Al_2O_3, (b) 50 vol% $MoSi_2$-50 vol% Al_2O_3, (c) 60 vol% $MoSi_2$-40 vol% Al_2O_3, and (d) 75 vol% $MoSi_2$-25 vol% Al_2O_3 composite samples sintered at 1600°C for 2 h.

As presented in Figure 2.57, similar results were also obtained for the WSi_2-Al_2O_3 composite samples with various WSi_2 volume percentages, which were sintered at 1600°C for 2 h. It is demonstrated that the average CTEs of the WSi_2-Al_2O_3 composite samples, which range from $9.31x10^{-6}$ to $9.56x10^{-6}$, are quite similar to each other and hereby do not depend on the WSi_2 content. As a result of the CTE measurements, it can be noted that the average thermal expansion coefficients (100°-1000°C) of the $MoSi_2$-Al_2O_3 and WSi_2-Al_2O_3 composites are $9.65x10^{-6}$ and $9.41x10^{-6}$, respectively (Figure 2.58). It is surprising that the average CTEs of the composites were higher than to that for reference $MoSi_2$, WSi_2, and Al_2O_3. The main reasons may be impurities such as SiO_2, formation of new phases during sintering such as W_5Si_3, and internal cracks existing in the pressed/measured sample.

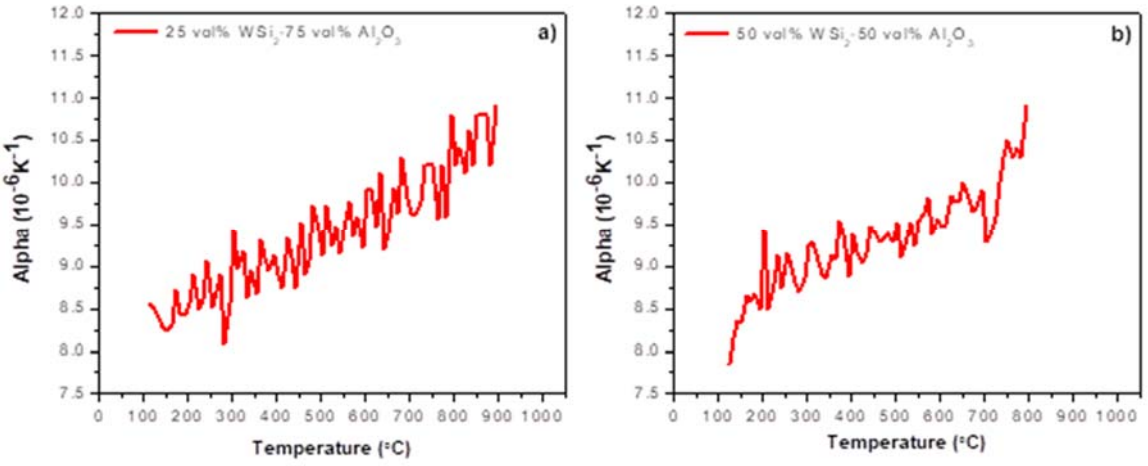

Figure 2.57. Coefficients of thermal expansion (CTEs) of the (a) 25 vol% WSi_2-75 vol% Al_2O_3, (b) 50 vol% WSi_2-50 vol% Al_2O_3, and (c) 60 vol% WSi_2-40 vol% Al_2O_3 composite samples sintered at 1600°C for 2 h.

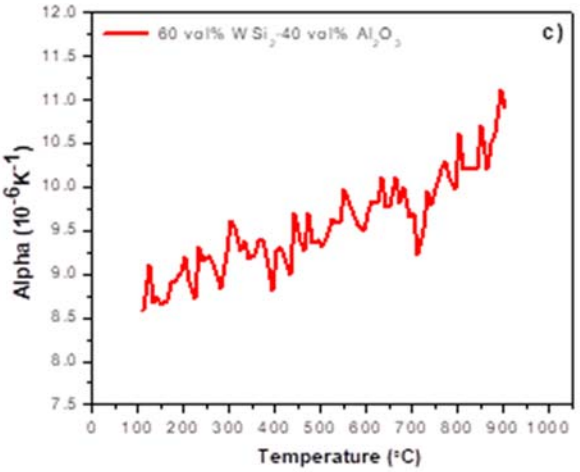

Figure 2.57. (continued) Coefficients of thermal expansion (CTEs) of the (a) 25 vol% WSi_2-75 vol% Al_2O_3, (b) 50 vol% WSi_2-50 vol% Al_2O_3, and (c) 60 vol% WSi_2-40 vol% Al_2O_3 composite samples sintered at 1600°C for 2 h.

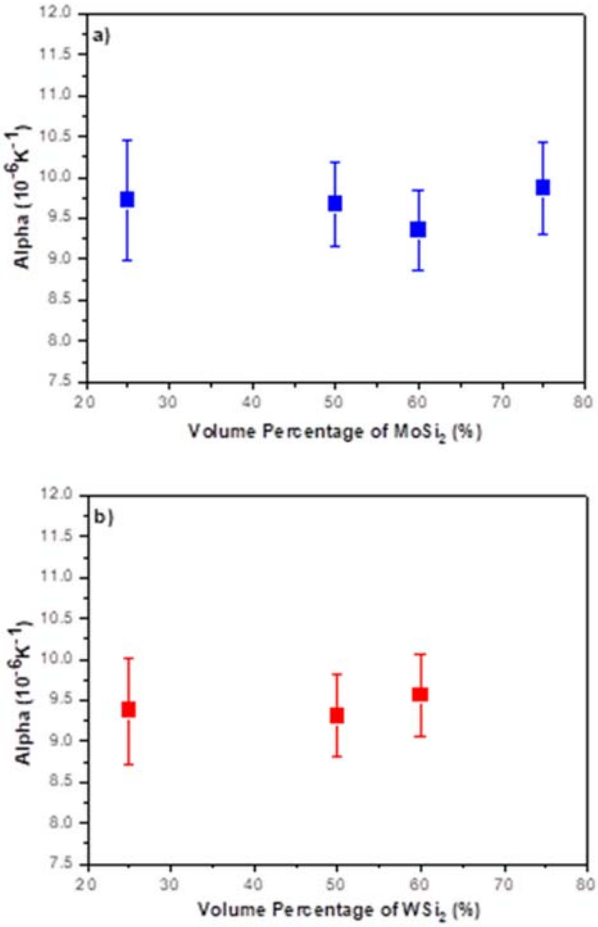

Figure 2.58. Coefficients of thermal expansion (CTEs) of the (a) $MoSi_2$-Al_2O_3 composite samples, and (b) WSi_2-Al_2O_3 composite samples sintered at 1600°C for 2 h as a function of the $MoSi_2$ and WSi_2 volume percentages.

2.3.3.3 High-temperature (pest) oxidation behavior of the composites

To understand the influence of the processing parameters and the addition of the refractory oxide phases on the pest oxidation, the thermogravimetric analyses (TGA) were conducted in an air atmosphere at the temperatures reaching 800°C on the as-sintered $NbSi_2$- and $TaSi_2$-based composites, as well as, the as-sintered metal silicides ($NbSi_2$, Nb_5Si_3, $TaSi_2$). Their oxidation-induced mass changes per unit surface area (mg/cm^2) are presented in the Figure 2.59, similarly as a function of the oxidation temperature. The pest oxidation of the $NbSi_2$ and Nb_5Si_3 was observed particularly at the temperatures ranging from 700° to 800°C. However, it was determined that the pest oxidation of the Nb_5Si_3 was more drastic than that of the $NbSi_2$. The oxidation-induced mass changes for the $NbSi_2$ and Nb_5Si_3 were measured at 800°C as 8.3 and 17.3 mg/cm^2, respectively, implying the negative influence of the Nb_5Si_3 phase formation on the pest oxidation of the composites. In addition, in the pest oxidation region, all $NbSi_2$-ZrO_2 composites and 60-40 $NbSi_2$-Al_2O_3 displayed lower mass changes than the Nb_5Si_3, but relatively higher than the $NbSi_2$ (Fig. 2.59a). The pest oxidation of the niobium silicide phases was highly eliminated by the 30-70 $NbSi_2$-Al_2O_3 composite, proving the positive influence of the refractory alumina addition on their oxidation behavior. In comparison to the $NbSi_2$ and Nb_5Si_3, the oxidation-induced mass change at 800°C was reduced by 85.8 and 93.2%, respectively, with the addition of 70 vol% alumina phase. Similarly, all the $TaSi_2$-based composites except for the 30-70 $TaSi_2$-Al_2O_3 oxidized relatively higher than the $TaSi_2$ at the temperatures of 650°-800°C. There was also a 24.4% reduction in the overall mass change at 800°C for the 30-70 $TaSi_2$-Al_2O_3 composite compared to the $TaSi_2$.

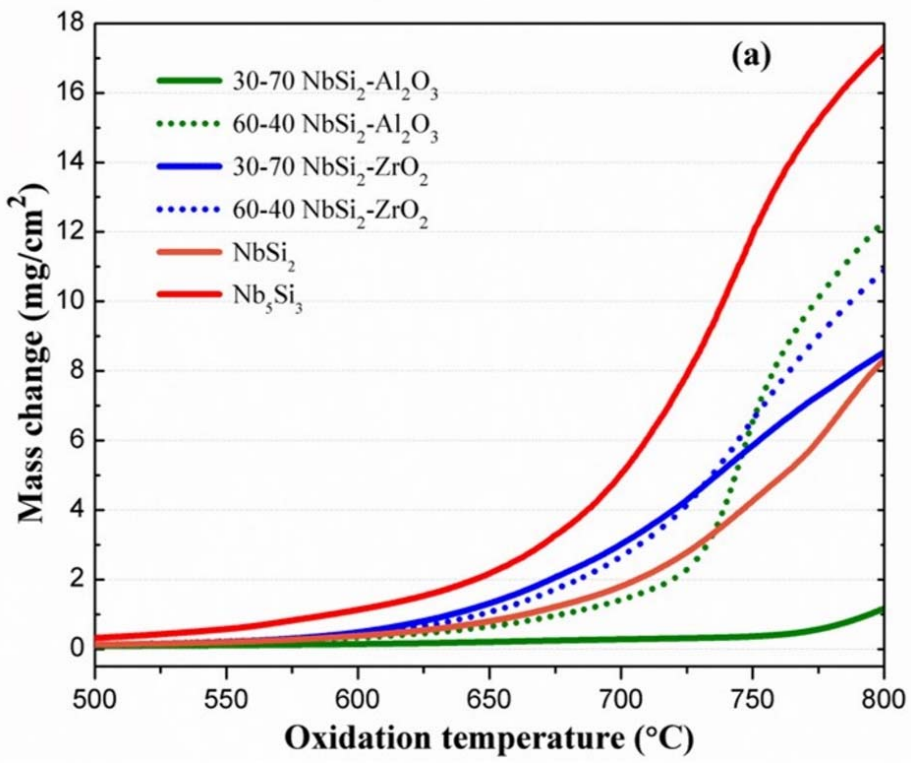

Figure 2.59. Comparison of the oxidation-induced mass changes (mg/cm^2) of the (a) $NbSi_2$-based composites with $NbSi_2$ and Nb_5Si_3, and (b) $TaSi_2$-based composites with $TaSi_2$, all sintered at 1600°C in argon, as a function of the oxidation temperature.

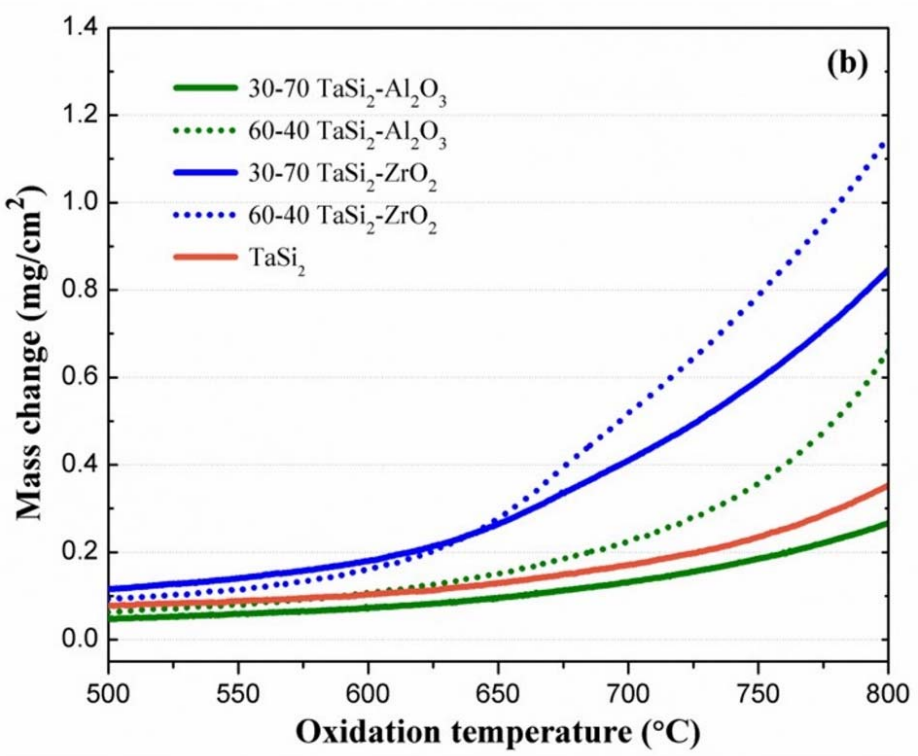

Figure 2.59 (continued). Comparison of the oxidation-induced mass changes (mg/cm^2) of the (a) $NbSi_2$-based composites with $NbSi_2$ and Nb_5Si_3, and (b) $TaSi_2$-based composites with $TaSi_2$, all sintered at 1600°C in argon, as a function of the oxidation temperature.

As a review of the oxidation studies, the lowest oxidation-induced mass changes were achieved by these composites sintered at 1600°C with 70 vol% alumina. The pest oxidation of these composites was also found to be lower than their dense monolithic metal silicides. This could be correlated to the lower porosity levels obtained for these composites (5.2-7.7%) and reduced oxygen diffusion rates due to the refractory oxide addition. However, this effect was more significant in the silicide-alumina composites, particularly at 30-70 volume percentages. Significant changes in the pest oxidation behavior of the silicide-zirconia composites were not similarly observed by adjusting the processing parameters. This could be explained with significantly higher porosity levels within these composites, since they all exhibited above 25.8% porosity at all sintering temperatures. These results clearly show that the key factor for reducing the pest oxidation rates is low porosity levels and improved densification, since it is apparent that the accelerated oxygen diffusion through the pores and/or across the pore surfaces is the main mechanism of the pest oxidation.

The oxidation-induced mass changes for the as-sintered silicides ($MoSi_2$, WSi_2) and their composites with the addition of 70 vol% alumina phase are presented in Figure 2.60 as a function of oxidation temperature ranging from 50°C to 870°C. A negligible mass gain ($\leq$ 0.12 mg/cm^2) was observed for the $MoSi_2$ and $MoSi_2$-Al_2O_3 composite samples up to around 400°C. It is apparent that there was a notable mass gain at the temperature region of 400°-780°C due to low-temperature oxidation of $MoSi_2$ leading to the formation of MoO_3 and SiO_2 as oxidation products.

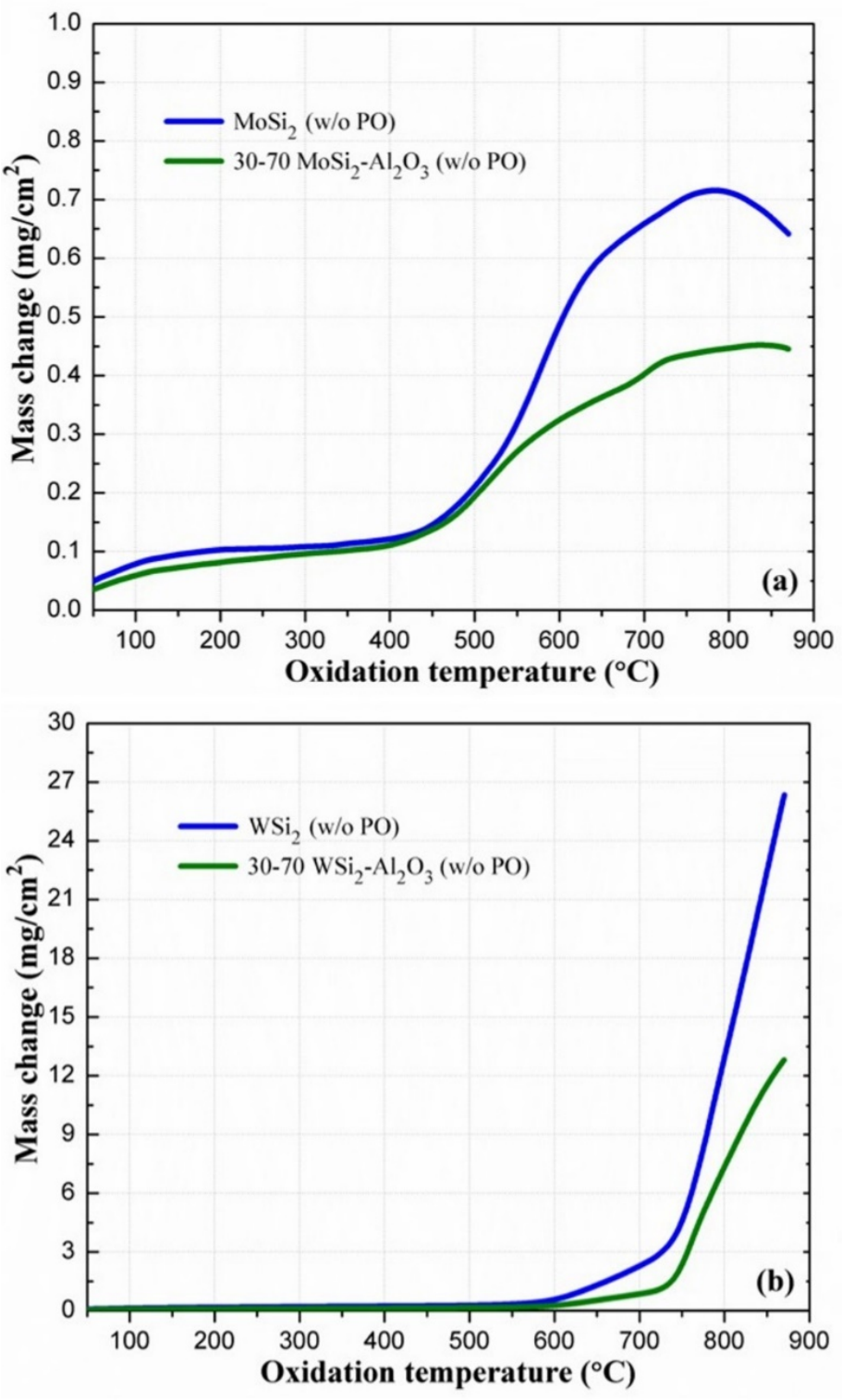

Figure 2.60. Mass change per unit surface area of the as-sintered (a) $MoSi_2$ and 30-70 vol% $MoSi_2$-Al_2O_3, and (b) WSi_2 and 30-70 vol% WSi_2-Al_2O_3 samples as a function of oxidation temperature in ambient air ("w/o" term refers to non-preoxidized or as-sintered samples).

The overall mass gain at 780°C for the $MoSi_2$-Al_2O_3 composite (0.44 mg/cm^2) was relatively lower than that for the $MoSi_2$ (0.72 mg/cm^2). The mass loss was detected above this temperature, which is related to the evaporation of the volatile MoO_3 phase. However, no pest oxidation was observed for both $MoSi_2$-based samples during non-isothermal oxidation, since pesting usually refers to the formation of volatile oxide species, followed by structural disintegration of the bulk samples. Similar to the $MoSi_2$-based materials, there was a very low mass gain (<0.27 mg/cm^2) for the as-sintered WSi_2 and WSi_2-Al_2O_3 composite samples at the temperature region of 50°-500°C (Figure 2.60b). The significant mass gain for both samples is apparent starting from 500°C, but it was found to be more drastic at the temperatures ranging from ~730°C to 870°C. However, the overall mass gain at 870°C for the WSi_2-Al_2O_3 composite (12.8 mg/cm^2) was substantially lower than that of the WSi_2 (26.3 mg/cm^2). Unlike the $MoSi_2$-based samples, these bulk samples completely disintegrated into a powder form owing to the poorer oxidation resistance of the WSi_2. In brief, the addition of the 70 vol% alumina highly reduced the mass gain, which could be attributed to the lower interaction of the metal silicide phases with the open environment owing to their coverage with the refractory oxide phase.

2.4 Conclusions:

As briefly stated in the introduction of this section, the main objectives of this task were to fabricate various composite compositions composed of transition metal silicides and refractory oxide ceramic particulates, and to characterize and test their high-temperature capabilities and properties as a function of different parameters such as temperature and composition. The main purpose behind these objectives was to understand and optimize the composite compositions and their properties, and finally to provide required information and data for more efficient sensor patterning and fabrication processes. In the Subtask 2.1, the starting metal silicide and refractory oxide powders were well-characterized, and then various silicide-oxide powders were synthesized using ball-milling technique. The initial phase and microstructural characterization of the commercial starting powders and as-synthesized composite powders by XRD and SEM provided important information for initial composition optimization. In the Subtask 2.2, thermal processing of the silicide-oxide composites was completed at different sintering conditions. Afterwards, their densification and sintering behavior, microstructures, phase development, chemical and thermal stability, homogeneity and grain growth behavior were investigated in detail at high-temperature regimes. The densification of the composites was highly improved with increasing sintering temperature, particularly with the addition of fine alumina particles at 80 vol% concentration. The silicide-alumina and silicide-zirconia composites were found to be highly stable up to 1600°C, with only formation of 5-3 metal silicide and silica as secondary phases. It was also demonstrated that the 5-3 secondary phase content increased with increasing annealing time at high-temperature. This knowledge is very crucial, since these silicide phases have significant influence on the physical properties of the composites, particularly when they present in certain amounts. The addition of micron-sized zirconia and alumina particles resulted in more homogeneous microstructures compared to the fine alumina addition. In addition, a new homogeneity analysis method was developed and it was proven to be highly effective on determination of homogeneity or distribution levels of the silicide-oxide composites. The results achieved in the Subtask 2.2 were then used as a supportive data and correlated with the physical properties of the composites for careful selection and optimization of the composite compositions for sensor fabrication. Subtask 2.3 discussed the electrical, thermal and oxidation measurements/tests of the silicide-oxide composites as a function of composition, processing and temperature. In the Subtask 2.3, M1 milestone was completed, since the results provided necessary data and information, which were

required for the selection of composite composition for the fabrication of thermocouple, thermistor and strain sensors. The silicide-oxide composites displayed sufficient electrical conductivity at high temperatures, and electrical percolation was achieved even at relatively low metal silicide contents (20-30 vol%). The high-temperature oxidation measurements also demonstrated that the addition of 40-70 vol% refractory oxide phase (particularly fine alumina) could highly reduce the oxidation-induced mass gain in the pest oxidation temperature regime, and thus, significantly enhance their oxidation resistance. Therefore, various silicide-oxide composite compositions showed promising results based on their high chemical and thermal stability, reduced grain growth rates, improved oxidation resistance and high electrical conductivities in a wide temperature range as a result of the studies completed in this task.

Task 3: Sensor Patterning and Embedding

3.1 Introduction:

The objective of this task was to define processes to pattern and embed the oxide-silicide composites within refractory ceramic monoliths (termed as a preform in this report) to incorporate temperature, strain/stress, and spallation sensors into ceramics that can be later embedded within the refractor bricks. The specific subtasks were as follows:

Subtask 3.1 Sensor Development and Patterning- embedding strategies (printed/laminated tape, fugitive carrier, and embedded composite tape) will be utilized to create the precursor sensor pattern.

Subtask 3.2 Thermal Processing Development and Structure Tailoring- Thermal schedules defined in Task 2 will used as the basis for the starting point for this task. Samples will be analyzed by SEM/EDS as a function of thermal processing. The propagation of defects and sintering mismatch will be carefully analyzed, and powder characteristics of the refractory matrix (reduction of aggregate size) and electrode composite will be tailored to remedy issues.

Subtask 3.3 Baseline Sensor Testing and Design Optimization- Sensor configurations will be designed that will focus on temperature and health measurements. Small refractory prototypes (preforms) will be fabricated, and electrical performance testing will be completed at high-temperature in varying atmospheres. Baseline electrical performance will be assessed, and the optimized designs for refractory cup and brick tests will be completed for Task 4.

3.2 Experimental Methods:

3.2.1 Fabrication of Substrates

All sensor designs and materials were patterned between either aluminum oxide (Al_2O_3, (99.8%, 8.6 m^2/g SSA; Almatis, Leetsdale, PA), or yttrium stabilized zirconia (YSZ, HSY – 8, Daiichi Kigenso Kagaku Kogyo Co., Ltd, Japan) substrates. The substrates were formed by tape casting slurry prepared by mixing desired substrate material with the polyvinyl butyral binder, poly-alkaline glycol and benzyl butyl phthalate plasticizers/modifiers (Tape Casting Warehouse, Morrisville, PA). The cast and dried tapes were ~20 μm thick. The dried tapes were cut into 18 x 18 cm thin sheets, stacked, and laminated at 93 °C and under 13 MPa to achieve 500 – 1000 μm substrate thickness. The laminates were cut into substrate shapes with and without holes for lead connections using a laser cutter (LS-1416, BOSS Laser, Sanford, FL).

3.2.2 Preparation of Silicide-based Sensor Materials

A number of different metal silicide powders were utilized for silicide-based sensors. Reagent grade (99.5% purity) powders, such as $MoSi_2$, WSi_2, $ZrSi_2$, $CrSi_2$, and $NbSi_2$ were all sourced from commercial vendor (Alfa Aesar, Tewksbury, MA). To control electrical responses and ensure adhesion to the substrate during co-sintering and operation processes, the silicide powders were combined with Al_2O_3(99.8%, 8.6 m^2/g SSA; Almatis, Leetsdale, PA), to form either composite inks or tapes and to be embedded in Al_2O_3 substrates. This study evaluated composite powder such as $MoSi_2$-Al_2O_3 and WSi_2-Al_2O_3 with 20-90 vol% of metal silicide content balanced with aluminum oxide. For simplicity, only the volume percentages were used to identify the composite compositions such as [50-50] and [90-10], since all the fractions for the composites were

determined based on volume percentages. The composite powders were prepared by ball milling silicide and alumina powder in isopropanol with zirconia media for 24 hrs. The ball milled suspensions were dried and sieved through 60-mesh screen.
The composite silicide tapes were produced using process described for substrate fabrication. To create sensor pattern, the composite tapes were laser cut into thermistors or thermocouple shapes. The sensing material was then embedded between precut green Al_2O_3 substrates and laminated at 93 °C and under 10 MPa and then co-sintered into sensor preforms at 1600 °C for 2 hrs.
The composite silicide inks were made by sonicating ball milled silicide-alumina powder with an organic vehicle (63-2 vehicle, Johnson Matthey, USA). The ratio of composite powders to organic vehicle was fixed at 70:30 by wt% in all ink formulations. The inks were used in fabrication of sensors by screenprinting or stenciling processes. In each case, the inks were screen printed using patterned 230-mesh screen or stenciled using masking tape onto Al_2O_3 substrates. At least two coats were applied with a drying step at 70 °C after each coat. The pattern was covered by another Al_2O_3 substrates and the stack was laminated together at 93 °C and under 10 MPa and then co-sintered into sensor preforms at 1600 °C for 2 hrs.

In case of thermocouples, the sensor materials were screen printed on alumina substrates with dimensions of 30 mm x 15 mm x 0.8 mm using an Aremco's Accu-Coat™ screen printer using a nylon screen (250 mesh). For $MoSi_2$-Al_2O_3//WSi_2-Al_2O_3 thermocouple, the left leg of the thermocouple was printed first with the $MoSi_2$-Al_2O_3 composite ink followed by a heat treatment for 5 min at 50°C in an oven to dry the ink. The screen printing and drying processes were repeated four times to achieve a 400 μm thick thermocouple leg. After screen printing and drying of the left leg of the thermocouple, the right leg was similarly printed with the WSi_2-Al_2O_3 composite ink or Pt ink. The screen printing of two legs of the thermocouples was completed separately only due to the ease of processing the multiple repeat sensor samples. The thermocouples were lastly sintered at 1500°C for 2 h under argon atmosphere. The // symbol represented in the report denotes a couple being formed with the compositions preceding and following the symbol. After optimization of the metal silicide-oxide composition, both 5.1 and 22.9 cm long thermocouples were fabricated and subsequently embedded into the as-prepared alumina preforms.

3.2.3 Preparation of Oxide-based Sensor Materials

The La_2NiO_4 (LNO) composition was selected for the oxide-based sensor material. LNO powder was synthesized using a conventional solid state reaction route. The stoichiometric amounts of high purity La_2O_3 and NiO powders (Alfa Aesar, USA) were uniformly mixed by roll mill (without any milling media) for 1 h followed by attrition-milling using zirconia media in ethanol for 4 h. The resultant slurry was dried overnight and sieved into a fine powder. The resulting powder was calcined at 1200°C for 4 h. X-ray diffraction (XRD) analysis was performed using Panalytical X-ray diffractometer having Cu Kα radiation. The X-ray analysis confirms single phase formation matching K_2NiO_4 crystal structure (JCPDF #01-089-3460). No additional phase formation was observed in the X-ray analysis.

The LNO thermistors were fabricated by screen printing LNO/Y-stabilized zirconia (YSZ) composites onto YSZ tapes. Two sets of LNO/YSZ inks were synthesized: [50-50] vol% LNO-YSZ and 100 vol% LNO or [70-30] vol% LNO-YSZ ink. The function of the [50-50] LNO-YSZ composite ink was to ensure adhesion with YSZ substrate, while LNO conductive core was formed with either 100 vol% LNO or [70-30] vol% LNO-YSZ ink. To limit grain growth of the LNO

during sensor application, LNO powders were further calcined at 1000 ºC, 1200 ºC, or 1400 ºC prior to ink preparation.

The sensor patterns were fabricated by a screen printing process. A 230 mesh screen was used for screen printing. The 50:50 LNO:YSZ ink was screen printed first onto green YSZ substrate and then the conductive core ink was screen printed on top making it one half of the sensor. The printed ink layers were dried at 70 °C. Two printed halves were laminated together to form YSZ embedded thermistor. The laminated thermistors were sintered into sensor preforms at 1450 °C for 2 h in air.

3.2.4 Characterization of Preforms

An X'Pert Pro Panalytical X-ray diffractometer (Westborough, MA) with CuK_α radiation source was used to investigate the phase development of the sintered thick-film thermocouples. Data was collected from 16 to 110° angles (2θ) with a step size of 0.02 increments at a rate of 1°/min. An X'Pert High Score software was used to identify the phases, lattice parameters and crystal structure. The microstructures of the sintered thermocouples were examined by a scanning electron microscopy (SEM, JEOL 7600F, Peabody, MA). In addition to the XRD analyses, quantitative phase analysis studies via Rietveld method were performed by using the MAUD software [12] to determine the volume fractions of secondary phases formed after sintering. X-ray photoelectron spectroscopy (XPS) measurements were also carried out using a Physical Electronics, PHI 5000 Versa Probe spectrometer with a monochromatic AlK_α source operated at 300 W and a base pressure of 5×10^{-8} Torr. As a reference, the C1s signal of the adventitious carbon was used which was fixed at 284.6 eV. Survey spectra were collected by 1.0 eV steps at an analyzer pass energy of 160 eV and the high-resolution analysis of small spectrum regions by 0.05 eV steps and pass energy of 20 eV. The composition and chemical states were determined from the charge-corrected high resolution scans with analyzer pass energy of 20 eV. The acquisition time of the sample was kept low to minimize any surface oxidation state changes under X-ray irradiation. All spectra were fitted with a Shirley background and a Voigt function was employed to simulate spectral lines with Gaussian component set to 40% for spectra collected with the Kratos instrument, and set to 70% for the PHI and SSX instruments. The best fits were determined by minimization of the summed root mean square value of the fit. The XPS analysis was performed to understand the changes in the valence state and binding energy of the constituent elements present in the samples.

Thermoelectric properties of the ceramic composite thermocouples were measured using an atmospheric controlled high-temperature furnace, where K- and S-type thermocouples were used to monitor the cold and hot junction temperatures, and a National Instruments thermocouple reader was digitally connected to the computer through a LabVIEW software.

In order to electrically evaluate the sintered preforms, platinum wire leads were threaded through holes that were laser cut into laminates prior to sintering. In order to ensure electrical connection between Pt wire and embedded sensing material additional sensing material or platinum ink was applied to fill the through holes. In case of LNO-based thermistor preforms, the lead connection was made with Pt wire and [70-30] vol% LNO-YSZ ink that was then heat treated to 1400°C. In case of silicide based preforms, the lead connection was made with Pt wire and Pt ink. The silicide- and oxide-based preforms were tested in a high temperature furnace up to 1500 °C in argon and air atmosphere, respectively.

3.3 Results and Discussion:

3.3.1 Silicide-based Thermistors:

The initial work on sensor development focused on fabrication of thermistors using metal silicides as the sensing material. Fig. 3.1 shows various patterns of the thermistors that were screen printed on laminated alumina substrates. The initial sensing material consisted of composite mixtures of molybdenum silicide, $MoSi_2$, and aluminum oxide, Al_2O_3. The volume percent of $MoSi_2$ in the composite ink ranged 20 – 90 vol%. The screen printed thermistor pattern was embedded between 600 micrometer thick alumina laminate and sintered at 1500°C for 2 hrs in argon forming a thermistor preform.

Figure 3.2 shows an example of sintered thermistor preform with electrical connections consisting of platinum wire and additional sensor ink. The preforms were tested to 1300°C in argon atmosphere. Figure 3.3 shows a typical silicide based thermistor, in this case 60 vol% $MoSi_2$ – 40 vol% Al_2O_3 (60-40 Mo-Al) composite sensing material, where there appears to be a linear relationship between resistance and temperature.

The initial preform design was used to identify and correct any co-sintering issues between metal silicide composite and alumina substrate as well as provide quick evaluation of electrical performance of the sensing material. These results were then used to prepare thermocouple, capacitance and spallation patterned preforms.

Figure 3.1. Optical pictures of various thermocouple designs with various leg thicknesses.

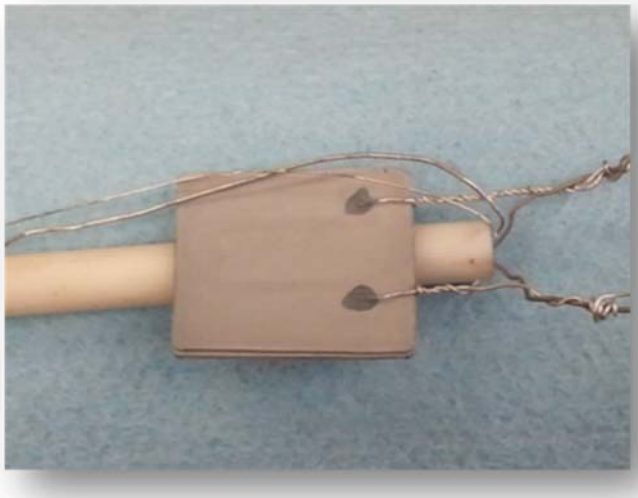

Figure 3.2. Optical picture of the first thermistor sensor embedded with alumina (with the Pt electrical connection shown).

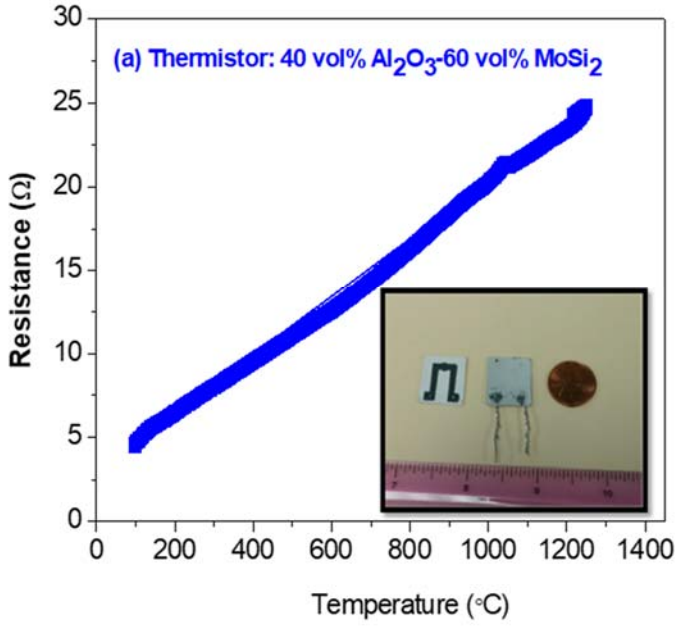

Figure 3.3. Resistance versus temperature of thermistor with composition 40 vol% Al_2O_3-60 vol% $MoSi_2$. Inset shows the photograph of thermistor.

To quickly evaluate other silicides, a set of thermistors was prepared including: [90-10] $NbSi_2$-Al_2O_3; [90-10] $TaSi_2$-Al_2O_3; [90-10] $ZrSi_2$-Al_2O_3; [90-10] WSi_2-Al_2O_3; [90-10] $MoSi_2$-Al_2O_3. The thermistors with composition [90-10] $NbSi_2$-Al_2O_3 and [90-10] $TaSi_2$-Al_2O_3 exhibited negative temperature coefficient of resistance as shown in Fig. 3.4. The resistance decreased with increasing temperature. The other three composition, [90-10] $ZrSi_2$-Al_2O_3, [90-10] WSi_2-Al_2O_3 , and [50-50] $MoSi_2$-Al_2O_3 exhibited positive temperature coefficient of resistance as shown in Figure 3.5. The resistance increased with increasing temperature. The values of the resistance at room temperature 1100 °C are given in the Table 3.1. Figure 3.6 shows the resistance of the thermistor with varying amount of $MoSi_2$ and Al_2O_3. The greatest amount of change in resistance with increasing temperature was recorded with [50-50] $MoSi_2$-Al_2O_3 sensor material. The analysis of the other three thermistor compositions ([60-40] $MoSi_2$-Al_2O_3; [75-25] $MoSi_2$-Al_2O_3 and [90-10] $MoSi_2$-Al_2O_3 showed that slope of resistance versus temperature diminishes with decreasing Al_2O_3 concentration. Since the $MoSi_2$ is the conductive species and as its percolation through the matrix becomes uninhibited at higher concentrations, these results show that the resistance is mainly effected by the formulation of the composite. These results also show that the resistance can be targeted just by changing the composition of the silicide and oxide mixture. The values of the resistance at room temperature 1100 °C is given in the Table 3.2.

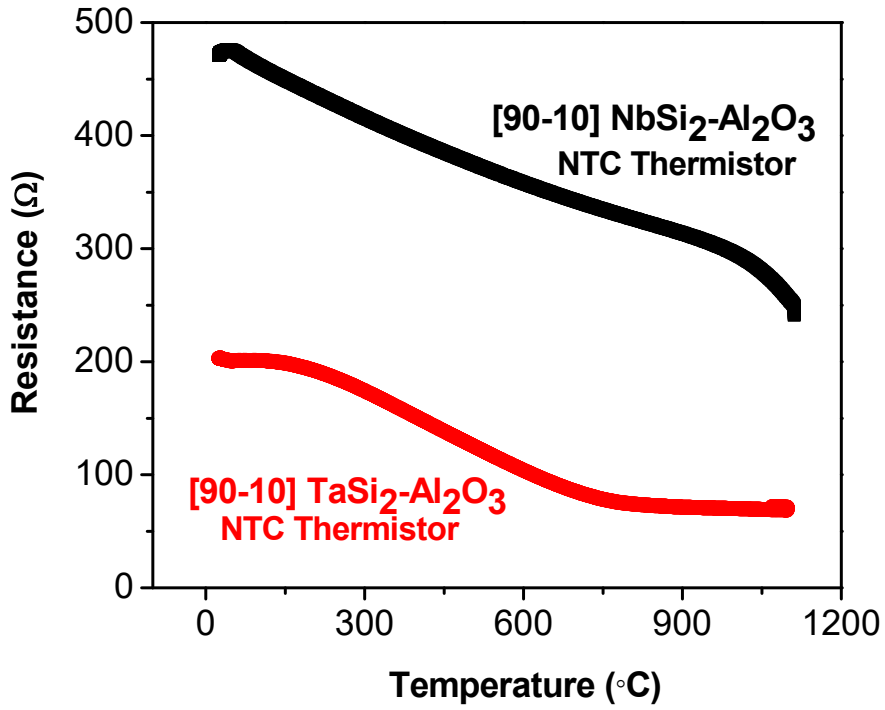

Figure 3.4. Performance analysis of thermistors [90-10] vol% $TaSi_2$-Al_2O_3 and [90-10] vol% $NbSi_2$-Al_2O_3.

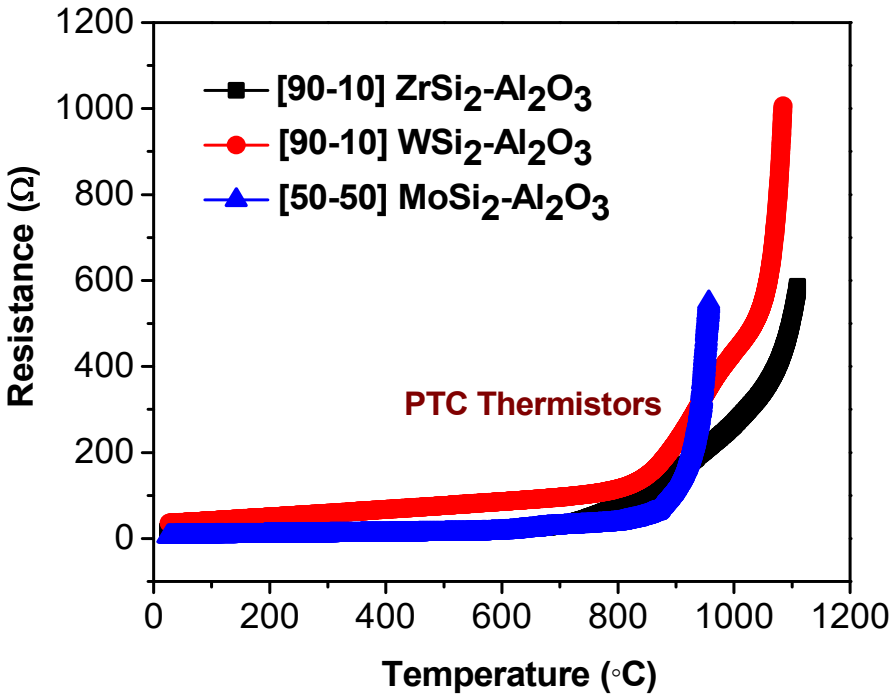

Figure 3.5. Performance analysis of thermistors [90-10] vol% $ZrSi_2$-Al_2O_3; [90-10] vol% WSi_2-Al_2O_3 and 90-10] vol% $MoSi_2$-Al_2O_3.

Table 3.1. Resistance of various metal-ceramic thermistors measured at RT and 1100 °C.

Thermistor s	Temperature	Resistance (Ω)
[90-10] $NbSi_2$-Al_2O_3	30	71.93
	1100	202.83
[90-10] $TaSi_2$-Al_2O_3	30	470.70
	1100	240.98
[90-10] $ZrSi_2$-Al_2O_3	30	17.41
	1100	586.15
[90-10] WSi_2-Al_2O_3	30	35.90
	1100	**1006.04**

[90-10] $MoSi_2$-Al_2O_3	30	6.32
	1100	**32.22**

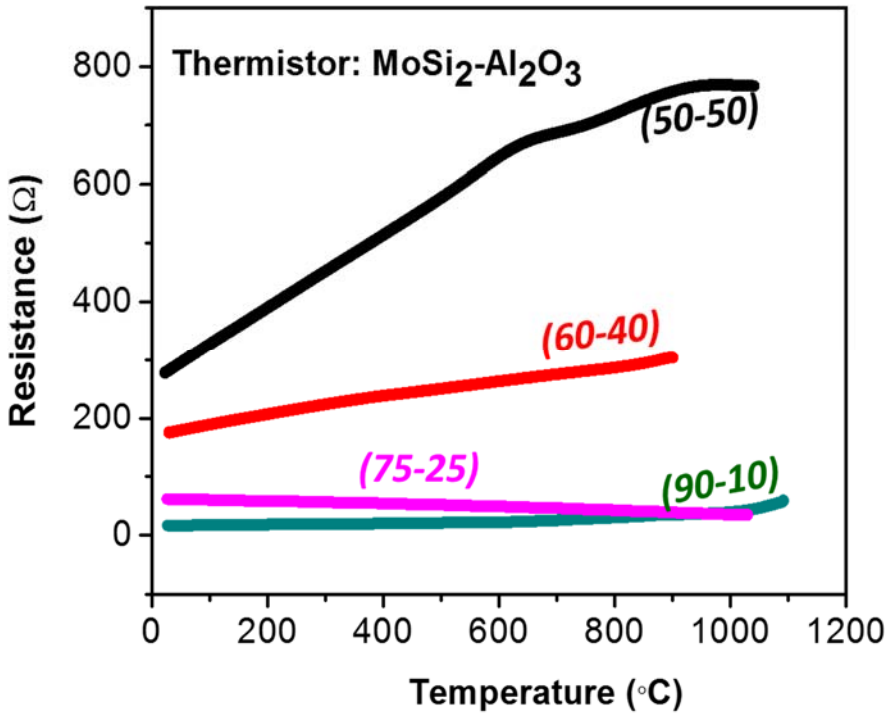

Figure 3.6. Resistance vs Temperature of four $MoSi_2$-Al_2O_3 thermostats with compositions (a) [50-50]vol% $MoSi_2$-Al_2O_3 (b) [60-40]vol% $MoSi_2$-Al_2O_3 (c) [75-25]vol% $MoSi_2$-Al_2O_3 (d) [90-10]vol% $MoSi_2$-Al_2O_3.

Table 3.2. Resistance of various $MoSi_2$-Al_2O_3 thermistors measured at RT and 1100 °C.

Thermistors	**Temperature (°C)**	**Resistance (Ω)**
[50-50] $MoSi_2$-Al_2O_3	100	325.81
	1100	768.50
[60-40] $MoSi_2$-Al_2O_3	100	189.74
	1100	323.26
	100	19.14

[75-25] $MoSi_2$-Al_2O_3	1100	41.45
[90-10] $MoSi_2$-Al_2O_3	100	8.79
	1100	10.76

In order to achieve the controlled grain growth, in this quarter we have switched the 80-20 wt. % coarse vs fine alumina into fine alumina to achieve small grains in fine grain matrix. For this purpose small thermistors were fabricated with appropriate amount of various silicide powders were mixed in a pre-milled fine alumina powder (SA: 8.6 m^2/g) and ball milled in isopropanol for 24 hours, vacuum dried and sieved into a fine powder using a 150 µm mesh. The resultant powder was casted into 100 µm thin tapes followed by lamination and laser cut into ~ 600 µm laminates. Fine alumina tapes were also casted and cut into 4" x 4" thermistor substrates and formed into embedded thermistors. Figure 3.4 shows the photographs of various stages of fabrication of embedded sensor preforms. The sensor tape laminates were embedded inside fine alumina filler and closed with fine alumina substrates, laminated and sintered at 1600 °C for 2h in argon.

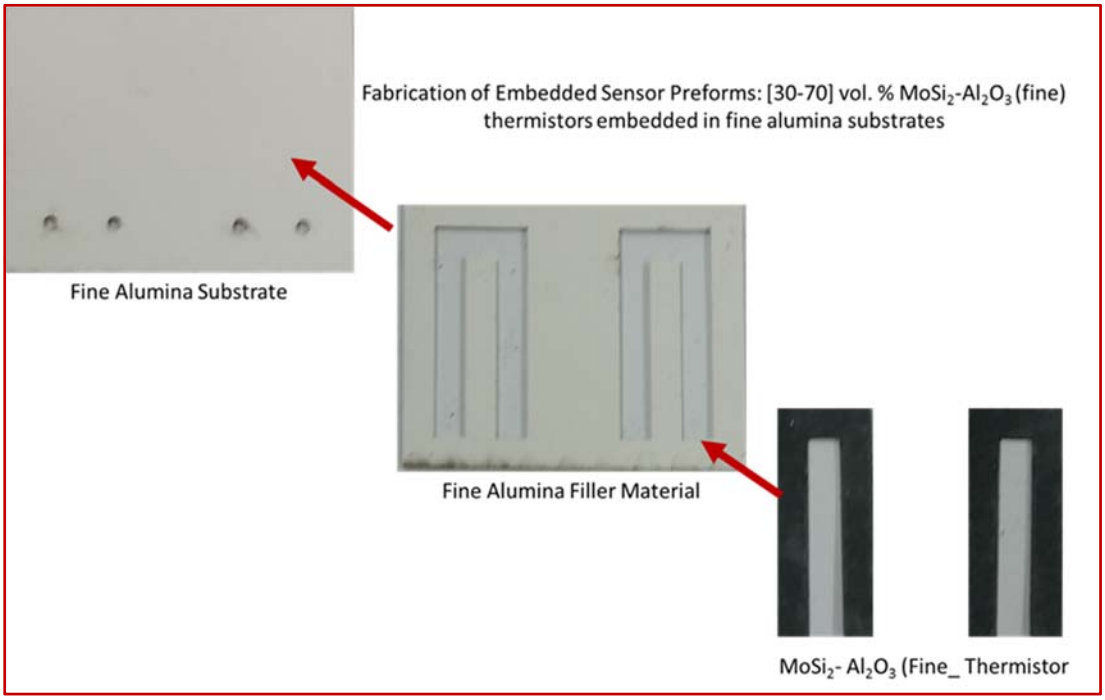

Figure 3.4. Photographs of various stages of fabrication of embedded sensor preforms.

Figure 3.5. Shows the photograph of [30-70] vol. % $MoSi_2$-Al_2O_3 (Fine) thermistor preform embedded inside a fine alumina substrate and sintered at 1600 °C for 2h in argon atmosphere. The thermoelectric properties of the sintered thermistor were tested at 1000 °C in argon atmosphere using a home- made furnace and the test results are showed in Figure 3.6. The thermistor was

performed excellently well and the resistance increased with increase in temperature and delivered 25Ω at 950 °C, for 2h in Argon atmosphere. The bulk density and theoretical density of the $MoSi_2$-Al_2O_3 (fine) and WSi_2-Al_2O_3 (fine) composites tape laminates (~ 800 μm) were measured using Archimedes principle and the results are showed in Table 3.3.

Figure 3.5. Photograph of [30-70] $MoSi_2$-Al_2O_3 thermistor (with material) embedded in fine alumina substrates and sintered at 1600 C for 2h in argon atmosphere.

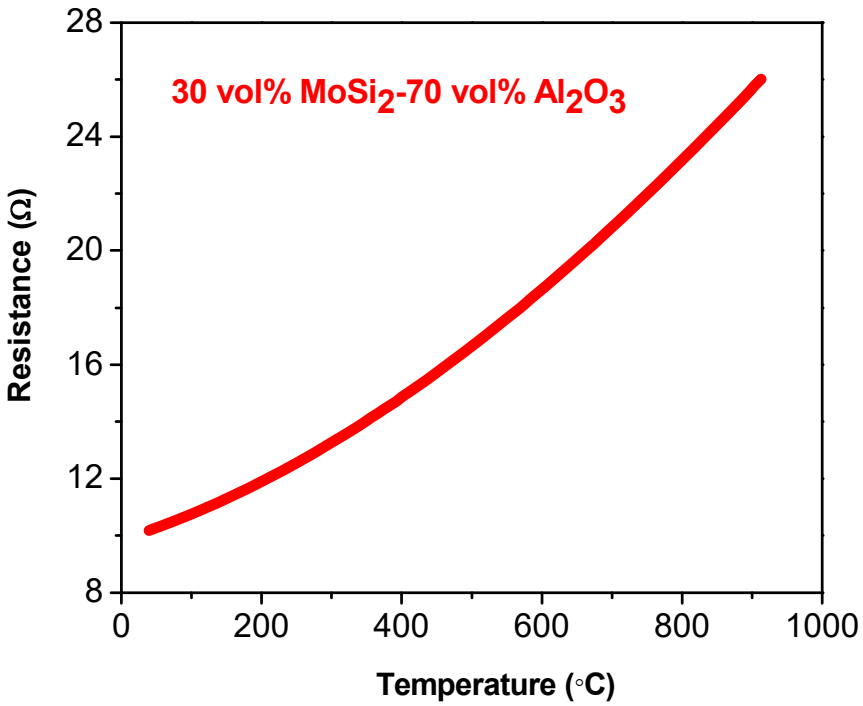

Figure 3.6. Resistance vs Temperature graph of [30-70] vol. % $MoSi_2$-Al_2O_3 thermistor, embedded in fine alumina substrates and sintered at 1600 °C, for 2h in Argon atmosphere.

It was observed that relative density of $MoSi_2$-Al_2O_3 and WSi_2-Al_2O_3 composite tapes decreases with increase in metal loading. The [20-80] vol. % $MoSi_2$-Al_2O_3 exhibited a theoretical density of 97.27% and [20-80] vol. % WSi_2-Al_2O_3 exhibited a theoretical density of 99.77% at 1600 °C in argon. Our studies show that by incorporating fine milled alumina in to the composite matrix along with a high temperature heat treatment we can increase the density maximum. This method will be continued in future to fabricate long thermocouples and thermistors with maximum density to get enhanced performance of the sensors.

Table 3.3. Density data of $MoSi_2$-Al_2O_3 (f) and WSi_2-Al_2O_3 (f) composites sintered at 1600 °C, 2h in argon.

Composite	Composition (mol%)	Rel Den. (%)	Bulk Den (gcm^{-3})	Teoretical Den.(gcm^{-3})
$MoSi_2$-Al_2O_3(fine)	20-80	97.27	4.3	4.4
$MoSi_2$-Al_2O_3(fine)	25-75	94.57	4.17	4.408
$MoSi_2$-Al_2O_3(fine)	30-70	94.38	4.16	4.4
$MoSi_2$-Al_2O_3(fine)	45-55	94.24	5.01	5.32
$MoSi_2$-Al_2O_3(fine)	50-50	94.13	4.79	5.09
$MoSi_2$-Al_2O_3(fine)	60-40	94.04	4.79	5.09
$MoSi_2$-Al_2O_3(fine)	75-25	93.53	4.98	5.324
$MoSi_2$-Al_2O_3(fine)	90-10	93.26	4.64	4.98
WSi_2-Al_2O_3(fine)	20-80	99.73	5.01	5.02
WSi_2-Al_2O_3(fine)	25-75	95.4	5.37	5.46
WSi_2-Al_2O_3(fine)	30-70	93.81	6.21	6.6
WSi_2-Al_2O_3(fine)	45-55	93.65	6.2	6.625
WSi_2-Al_2O_3(fine)	50-50	92.31	6.61	7.156
WSi_2-Al_2O_3(fine)	60-40	90.34	6.26	6.63
WSi_2-Al_2O_3(fine)	75-25	87.5	6.72	6.65
WSi_2-Al_2O_3(fine)	90-10	86.22	6.86	7.9625

3.3.2 Silicide-based Strain Sensors:

Figure 3.7 shows thermally processed strain sensors. (a) 60 vol% $MoSi_2$-40 vol% Al_2O_3; (b) 60 vol% WSi_2-40 vol% Al_2O_3; (c)75 vol% $ZrSi_2$-25 vol% Al_2O_3. The real time response of the strain sensor is measured by equibiaxial flexural strength test. The load fixtures and test specimens were prepared based on ASTM standard C 1499-03. Figure 3.8 shows section view of basic fixture and test specimen for equibiaxial testing. Although the temperature sensitivity may be significant, isothermal measurements or measurements using two gauges in adjacent arms of a wheatstone's bridge which can remove this effect. The resistance change is due to the mechanical strain induced in the sample under test. Figure 3.9 shows the response of the strain sensor with composition 60 vol% $MoSi_2$-40 vol% Al_2O_3 as a function of applied force and the inset shows the photograph of the sensor. The sensor showed linear response and the resistance varied from 228 to 229.6 Ω when the applied force is changed from 10-90 N. The response of the strain sensor with composition 60 vol% $MoSi_2$-40 vol% Al_2O_3 as a function of time is shown in Fig. 3.10.

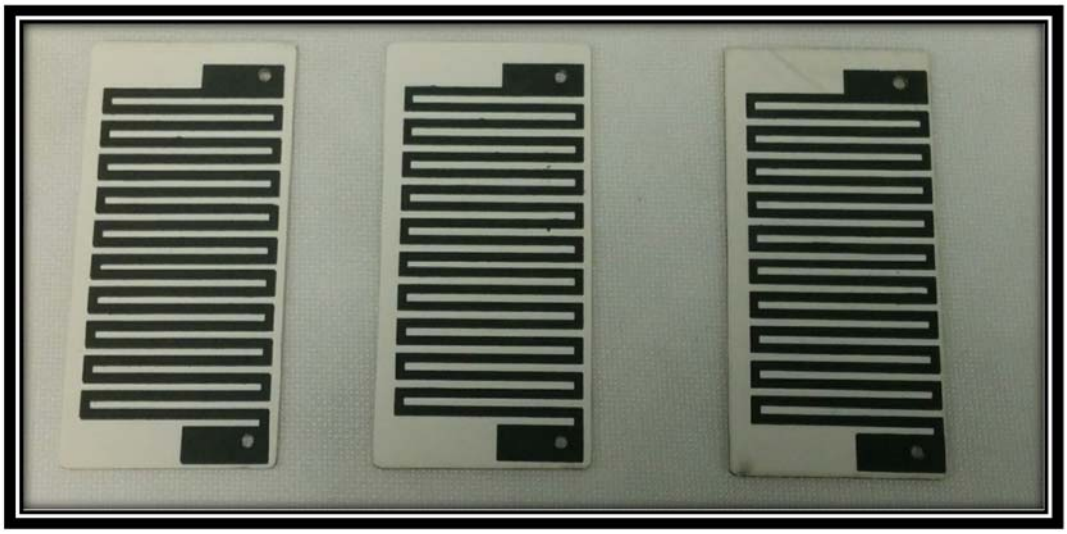

Figure 3.7. Thermal processed strain sensors. (a) 60vol% $MoSi_2$-40vol% Al_2O_3; (b) 60vol% WSi_2-40 vol% Al_2O_3; (c)75 vol% $ZrSi_2$-25 vol% Al_2O_3.

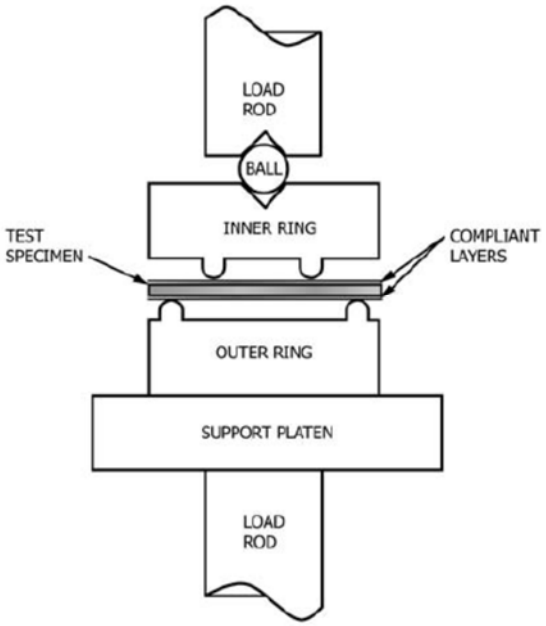

Figure 3.8. Section view of basic fixturing and test specimen for equibiaxial testing.

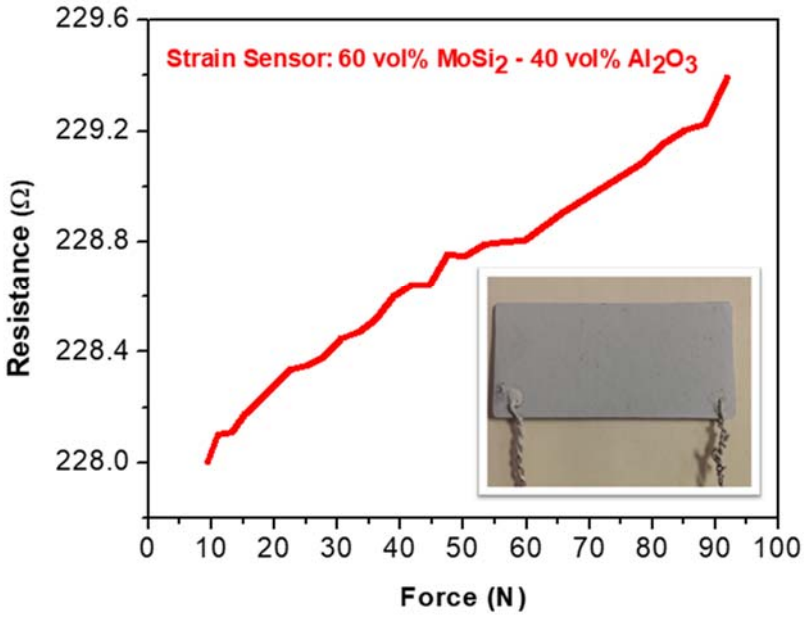

Figure 3.9. The response of the strain sensor with composition 60vol% $MoSi_2$-40vol% Al_2O_3 as a function of applied force and the inset shows the photograph of the sensor.

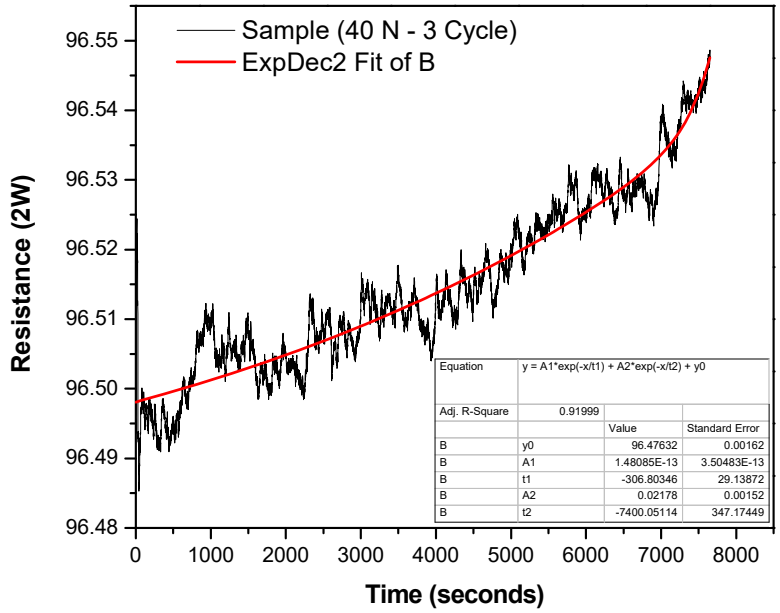

Figure 3.10. The response of the strain sensor with composition 60vol% $MoSi_2$-40vol% Al_2O_3 as a function of time.

3.3.3 Silicide-based Thermocouples:

3.3.3.1 Phase development in the composite thermocouples

XPS analyses were carried out to obtain information regarding chemical bonding and chemical state of the elements presented in the silicide-oxide composites. Figure 3.11a shows the XPS wide range survey spectra of the $MoSi_2$-Al_2O_3 composites with volume fractions of $MoSi_2$ varying from 50 to 90 vol% that were sintered at 1500°C for 2 h. The similar spectra and peaks corresponding to Mo, Si, Al, and O elements can be clearly seen for all the composites. In addition, high-resolution XPS spectra for the Mo3d, Si2p, Al2p and O1s collected from the $MoSi_2$-Al_2O_3 composite samples are presented in the Figure 3.11b. The Mo3d spectra consists of two doublet peaks arising from $Mo3d_{5/2}$ and $Mo3d_{3/2}$ at the binding energies of 227.9 and 231.1 eV, respectively, corresponding to Mo^4 [3.1]. It is clearly evident that both $Mo3d_{5/2}$ and $Mo3d_{3/2}$ peaks shifted towards lower binding energies with increasing $MoSi_2$ content in the composite. The peak observed at 98.7 eV, that is characteristic for the Si2p high-resolution spectra, refers to $MoSi_2$ phase [3.2]. Another high-intensity peak observed at 102.6 eV corresponds to SiO_2 phase, which indicated that $MoSi_2$ was oxidized to form SiO_2 and Mo_5Si_3 secondary phases based on its thermodynamically feasible oxidation reaction. In addition, the peaks appeared at 99.9 eV in the Si2p spectra were found to be a supportive data for the formation of Mo_5Si_3 phase in significant amounts particularly at the [75-25] and [90-10] $MoSi_2$-Al_2O_3 composites. For the Al2p spectra, the peaks observed at 75.0 eV presents the existence of Al_2O_3 phase in the composites after sintering [3.3]. It is important to note that several peak shifts observed in the high-resolution XPS spectra may be related to the changes in Fermi energy levels caused by variations in defect concentrations and changes in electron charge density [3.4]. The peaks observed at 532.2 eV in the O1s spectra indicate that SiO_2 may be in its amorphous state. In addition to the $MoSi_2$-Al_2O_3 composites, XPS survey spectra of the WSi_2-Al_2O_3 composites sintered at 1500°C for 2 h are shown in the Figure 3.12a. In the XPS spectra, the peaks corresponding to W, Al, Si and O were detected as expected for all the WSi_2-Al_2O_3 composite samples. Also, the high-resolution XPS spectra for the W4f, Si2p, Al2p and O1s peaks collected for these composites are presented in the Figure 3.12b. In the W4f spectra, two doublet peaks at the binding energies of 31.1 eV ($W4f_{7/2}$) and 33.5 eV ($W4f_{5/2}$) and a peak at 29.16 eV imply the presence of the WSi_2 phase. However, another single peak appeared at 35.4 eV, which represents WO_3 phase that might form on the surface in a very small amount due to high-temperature oxidation of the WSi_2 phase [3.5]. It is also found that the Si2p spectrum of the [50-50] WSi_2-Al_2O_3 composite displayed two peaks at 97.9 and 101.5 eV, which represent WSi_2 and W_5Si_3 phases, respectively [3.6]. The peak shifts to lower binding energy levels were clearly observed with increasing metal silicide fraction from 50 to 90 vol%. The peak detected at 73.3 eV in the Al2p spectra shows the presence of the Al_2O_3 phase. In addition, similar to the $MoSi_2$-Al_2O_3 composites, peaks detected at 530.4 eV in the O1s spectra reveal the presence of SiO_2 phase and its potential amorphous state [3.7]. The peak shifts to lower binding energy levels were also clear in Si2p, Al2p and O1s spectra with increasing WSi_2 fraction from 50 to 90 vol%. As a review of the XPS results, it was demonstrated that $MoSi_2$-Al_2O_3 composites having different volume fractions of metal silicide (50 to 90 vol%) consist of $MoSi_2$ and Al_2O_3 initial phases with Mo_5Si_3 and SiO_2 secondary phases formed during sintering. For all the WSi_2-Al_2O_3 composites, presence of WSi_2, W_5Si_3, Al_2O_3 and SiO_2 phases was similarly determined. However, the XPS results for the WSi_2-Al_2O_3 composite samples also revealed that

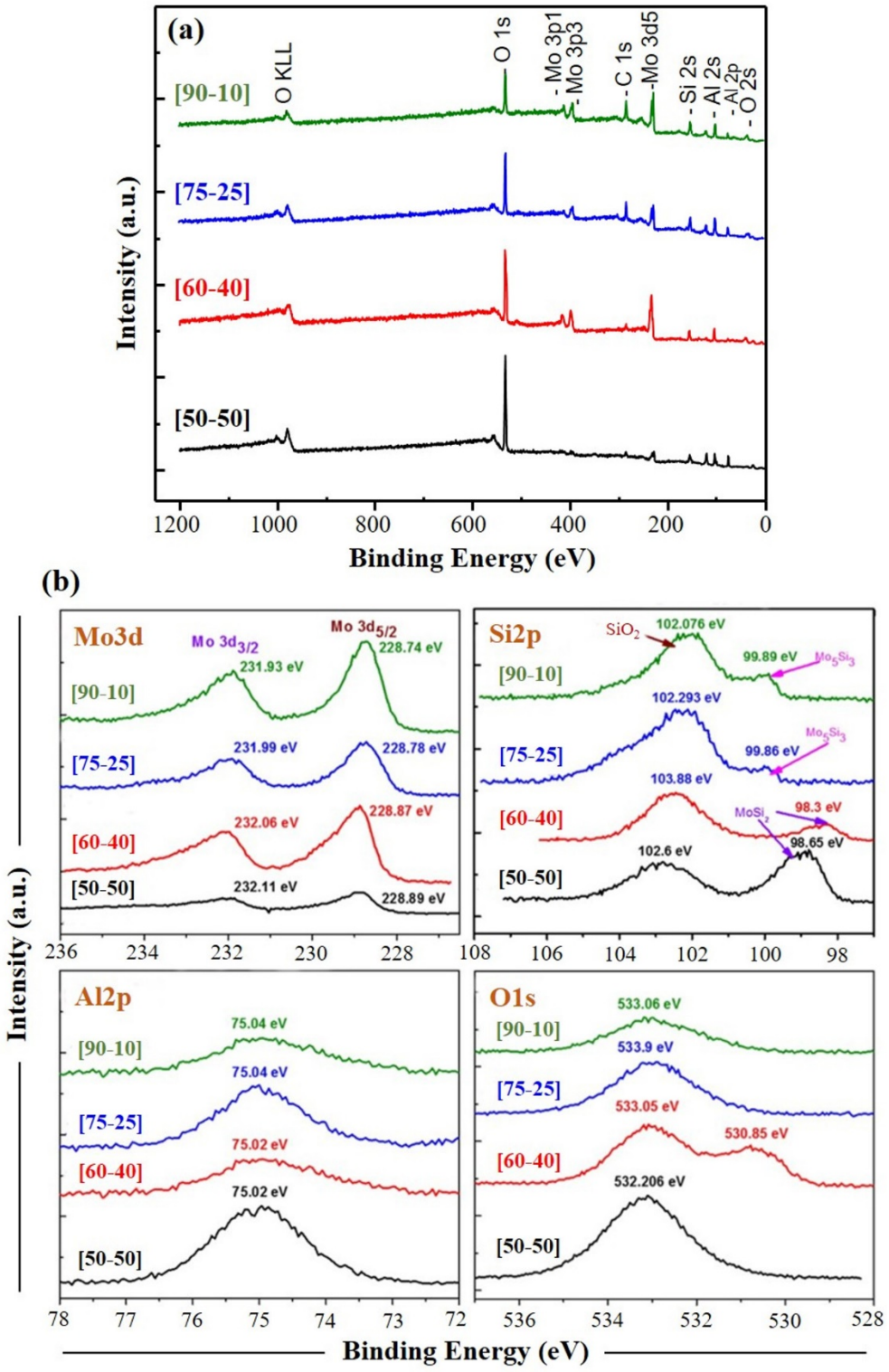

Figure 3.11 (a) XPS wide range survey spectra and (b) high-resolution XPS spectra (Mo3d, Si2p, Al2p, O1s) of the various $MoSi_2$-Al_2O_3 composites after sintering at 1500°C for 2 h.

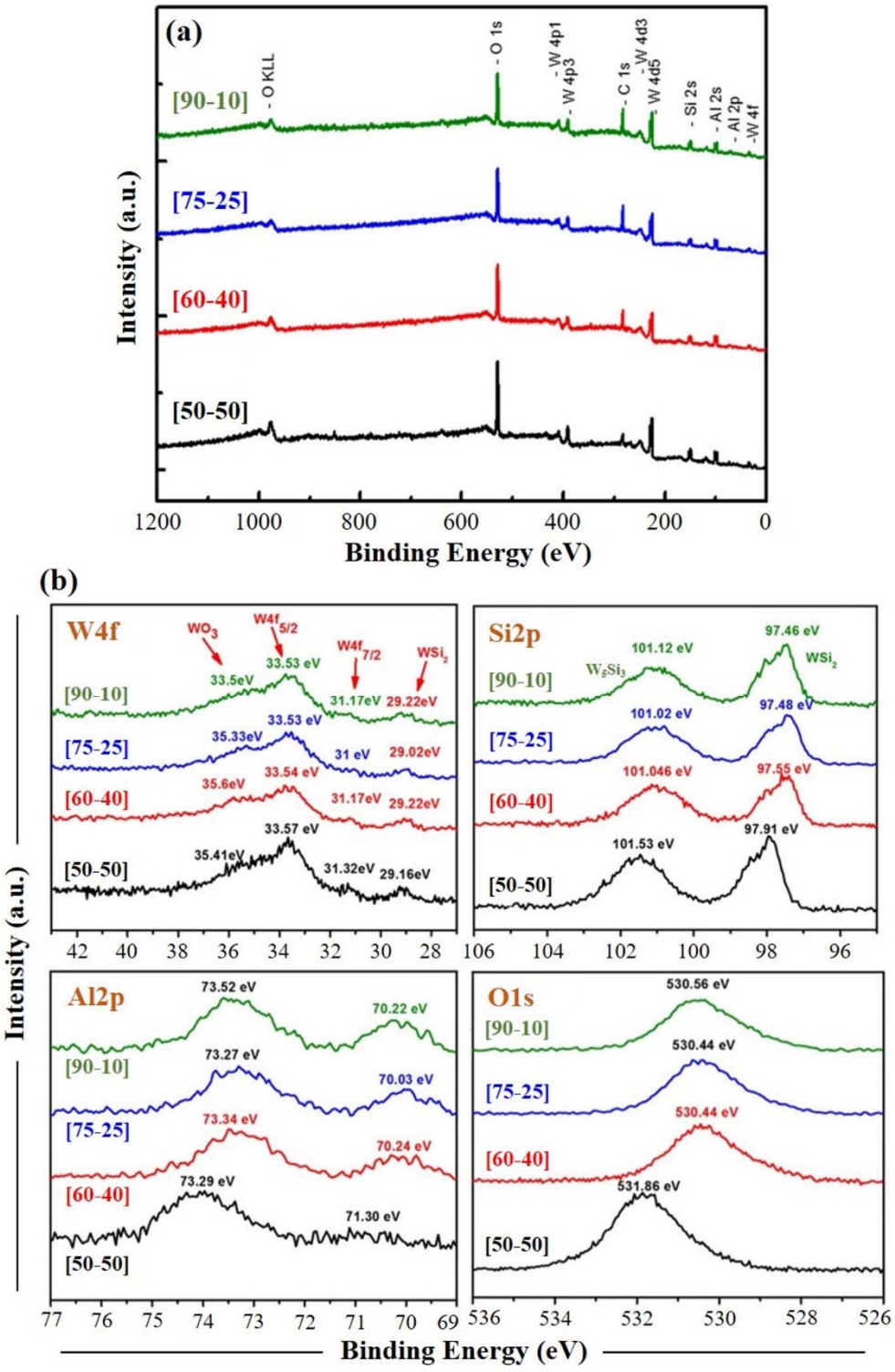

Figure 3.12 (a) XPS wide range survey spectra and (b) high-resolution XPS spectra (W4f, Si2p, Al2p, O1s) of the various WSi_2-Al_2O_3 composites after sintering at 1500°C for 2 h.

there may be a formation of WO_3 phase in a small amount on the sample surface due to the high-temperature oxidation of WSi_2. The formation of the 5-3 metal silicides (Mo_5Si_3, W_5Si_3) and SiO_2 as secondary phases could be related to the high-temperature oxidation of starting metal silicide phases and metal silicide-oxide interactions at high-temperatures [3.8, 3.9, 3.10].

The phase analysis studies were additionally performed by XRD to understand the phase development and secondary phase formation in the composite systems during sintering better. Therefore, two representative samples with the lowest and highest metal silicide content, which are [50-50] and [90-10] $MoSi_2$-Al_2O_3 composites, were selected for this study. Figure 3.13a shows the XRD patterns of these $MoSi_2$-Al_2O_3 composites after sintering at 1500°C for 2 h. $MoSi_2$, Mo_5Si_3 and Al_2O_3 phases were detected for these composites, since they revealed similar XRD patterns after sintering. The crystal structure of $MoSi_2$ is a body-centered tetragonal with a space group of I4/mmm and $C11_b$ type characterized by ABAB-type stacking along the c-axis, while Mo_5Si_3 has a tetragonal crystal structure with a space group of I-42m [3.2]. However, the silica phase could not be detected by XRD due to its very small amount on the surface and possibly its amorphous state based on the XPS data. The presence of Mo_5Si_3 as a secondary phase may not be disadvantageous, since it has a higher melting point, improved creep resistance and relatively low oxidation resistance [3.11]. Lin and Speyer also studied surface oxidation mechanisms of $MoSi_2$ in the high-temperature combustion environments, and their studies revealed that material stability could be reestablished after a transient period under oxidizing and reducing environments due to the formation of a stable Mo_5Si_3 layer [3.12]. It is important to point out that alumina addition as an oxidation-resistant refractory oxide could substantially lower the oxygen diffusion into the composite systems. Therefore, it may significantly lower the amount of Mo_5Si_3 secondary phase in the composite systems, particularly at [50-50] and [60-40] fractions due to a significant amount of alumina phase ($\geq$ 40 vol%). To determine the volume fractions of Mo_5Si_3 secondary phase and the changes in its fraction as a function of increasing metal silicide content, quantitative phase analysis studies were additionally performed by utilizing the Rietveld method on the XRD patterns of the [50-50] and [90-10] $MoSi_2$-Al_2O_3 composites. Figure 3.13(b-c) present the Rietveld refinement results of the [50-50] and [90-10] $MoSi_2$-Al_2O_3 composites, where solid red lines and black dots represent fitting curves and experimental XRD data, respectively. It is important to note that the quality of the Rietveld refinement was sufficient enough, since the goodness of fit (sig) and weighted profile R-factor (R_{wp}) values were 2.7-3.0 and 5.1-5.8, respectively. The amounts of Mo_5Si_3 phase for the [50-50] and [90-10] $MoSi_2$-Al_2O_3 composite samples were determined as 4.6 and 20.2 vol%, respectively. This result demonstrated that there was a 15.6 vol% increase in the volume fraction of Mo_5Si_3 secondary phase with increasing metal silicide fraction in the composite from 50 to 90 vol%. It was similarly reported in our previous study on the bulk $MoSi_2$- and WSi_2-oxide composites that amount of the Mo_5Si_3 and W_5Si_3 secondary phases substantially increased as a function of the refractory oxide material (fine/coarse Al_2O_3, ZrO_2) and the annealing time at 1400°C [3.13]. The XPS and XRD data in the current work shows that the $MoSi_2$- and WSi_2-based thick-film composites also undergo a similar transformation to the 5-3 metal silicide phase as shown for bulk samples; further work is currently being completed to better understand the effect of sample density, oxygen partial pressure, and metal silicide-alumina grain boundaries on the transformation kinetics.

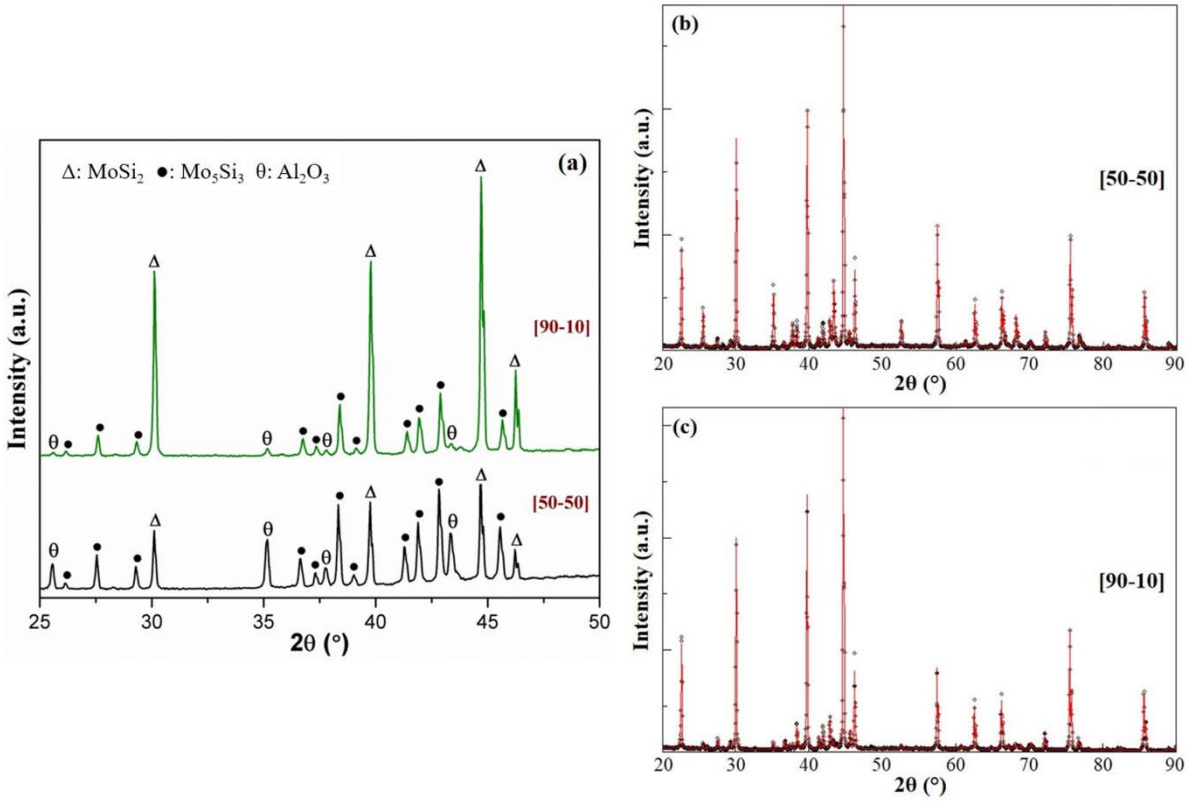

Figure 3.13 (a) XRD patterns of the [50-50] and [90-10] $MoSi_2$-Al_2O_3 composites after sintering at 1500°C for 2 h; (b-c) Rietveld refinement results of the [50-50] and [90-10] $MoSi_2$-Al_2O_3 composites, respectively [solid red lines = fitting curves; black dots = experimental XRD data].

3.3.3.2 Microstructures of the composite thermocouples

Figure 3.14(a-d) displays the SEM micrographs of the $MoSi_2$-Al_2O_3 composites after sintering at 1500°C for 2 h. The bright and dark regions within all microstructures correspond to the $MoSi_2$ and Al_2O_3 particles, respectively. It is clear that distribution of $MoSi_2$ and Al_2O_3 grains are relatively homogeneous within the composites. These results also demonstrated that the degree of percolation and $MoSi_2$ grain size increased by increasing $MoSi_2$ fraction from 50 to 90 vol%. Another feature observed in the microstructures of [60-40] and [75-25] $MoSi_2$-Al_2O_3 composites was agglomeration of the $MoSi_2$ grains in some regions. This may be due to the difference in wetting behavior and surface free energies of Al_2O_3 and $MoSi_2$ influencing the driving forces for sintering and grain growth. Further kinetic studies are currently being completed to understand the mechanisms of grain growth within the metal silicide-oxide composites. The SEM micrographs of the WSi_2-Al_2O_3 composites sintered at 1500°C are presented in the Figure 3.15(a-d). The bright and dark regions within these microstructures refer to the WSi_2 and Al_2O_3 particles, respectively. The microstructures were found to be highly similar to that of the $MoSi_2$-Al_2O_3 composites based on the homogeneity and grain sizes. The well-developed percolation paths of the conductive WSi_2 phase can be clearly seen for all WSi_2-Al_2O_3 composites. However, it is important to note that the

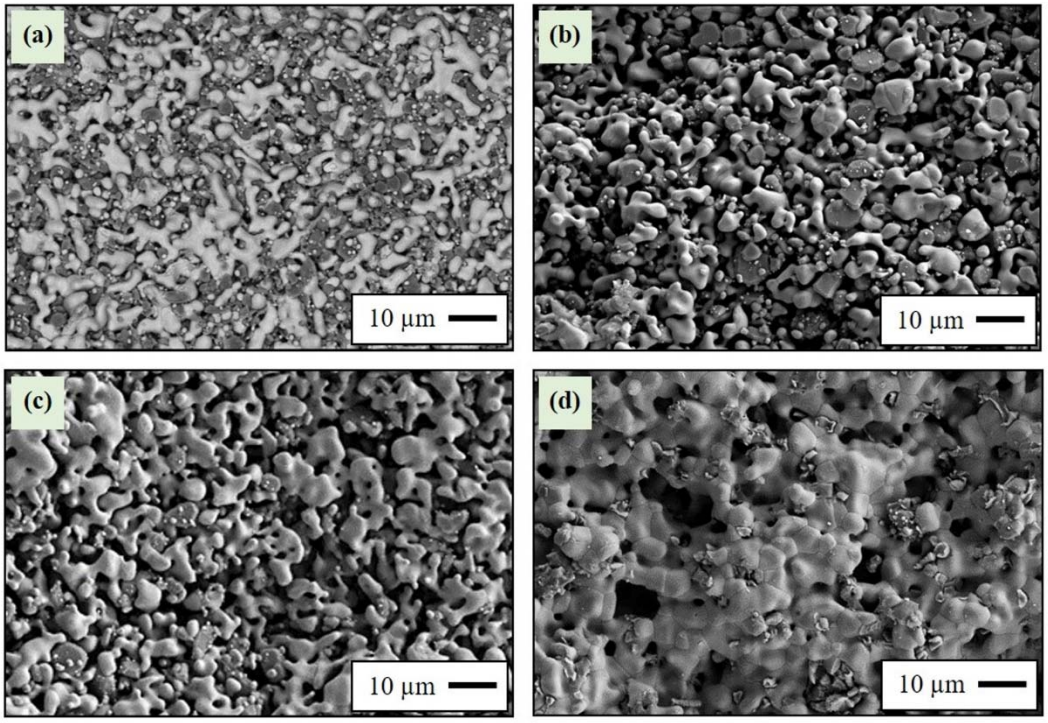

Figure 3.14 SEM micrographs of the (a) [50-50], (b) [60-40], (c) [75-25] and (d) [90-10] $MoSi_2$-Al_2O_3 composites after sintering at 1500°C for 2 h.

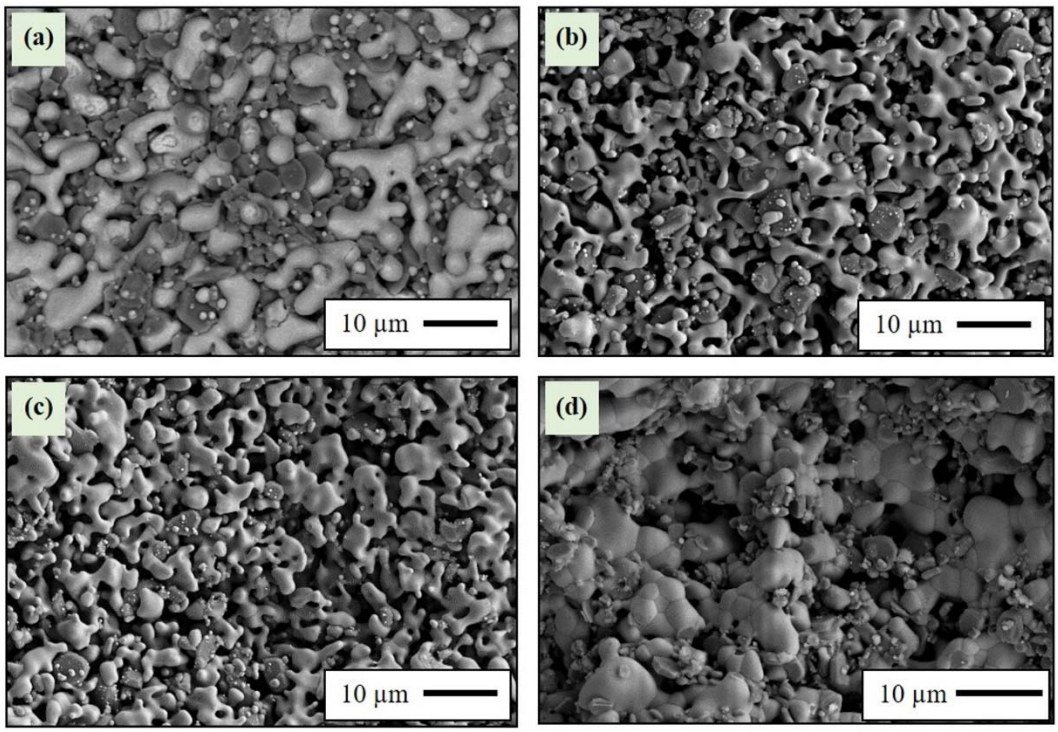

Figure 3.15 SEM micrographs of the (a) [50-50], (b) [60-40], (c) [75-25] and (d) [90-10] WSi_2-Al_2O_3 composites after sintering at 1500°C for 2 h.

5-3 metal silicide (Mo_5Si_3, W_5Si_3) secondary phases formed during sintering were not observable in the composite microstructures.

Figure 3.16 presents optical photographs and SEM micrographs of the [75-25] $MoSi_2$-Al_2O_3//Pt thermocouple screen printed on an alumina substrate and sintered at 1500ºC for 2 h in argon. The microstructures of the alumina substrate, left leg ($MoSi_2$-Al_2O_3), right leg (Pt) and thermocouple junction can be seen in detail. The average size of the $MoSi_2$ grains were measured as 3-5 µm, and they were found to be well-connected in such a way that the percolation path of $MoSi_2$ grains on the left leg of the thermocouple was continuous without any cracks or voids. However, Pt right leg, as well as, the thermocouple junction revealed a porous structure. Also, as-sintered alumina substrate showed a few large grains within a fine grain matrix. No cracks or voids were observed on the alumina substrate after sintering. In addition, the Pt right leg revealed a very fine grain microstructure having slightly more porosity than the $MoSi_2$-Al_2O_3 composite (left leg). As a review, all thermocouple lines made of $MoSi_2$-Al_2O_3 and WSi_2-Al_2O_3 composites in the present study showed a good adhesion on the alumina substrate. No evidence of degradation, blisters or coalesce was observed on the composite and platinum thermocouple lines even after high-temperature sintering in argon. It is well known for fabrication of the ceramic composites that occurrence of interfacial microcracks due to thermal expansion and sintering mismatch between substrate and composite films is an important issue that needs to be addressed [3.13, 3.14]. However, there was no evidence of interfacial microcracking in the presented composite microstructures. It must be noted that there is a close match between the coefficients of thermal expansion (CTEs) of metal silicides ($MoSi_2$, WSi_2) and alumina. Kobel et al. [3.15] studied thermal expansion behavior of the $MoSi_2$-Al_2O_3 composites with varying volume fractions of $MoSi_2$ in a wide temperature range. They reported that CTEs of the pure Al_2O_3 and $MoSi_2$ only differ by 4%, and CTE of the [75-25] $MoSi_2$-Al_2O_3 composite matches with that of the pure Al_2O_3 from room temperature to 900°C. Therefore, it can be pointed out that the possibility of interfacial cracking within the $MoSi_2$-Al_2O_3 and WSi_2-Al_2O_3 composites is expected to be very low after repeated thermal cycling. Lu et al. [3.16] also investigated the $MoSi_2$-based composites reinforced by alumina fibers and platelets, and they similarly reported that both types of reinforcement did not create any interfacial cracks between the fillers and matrix, which is highly beneficial for these silicide-oxide composite thermocouples screen printed on the alumina substrates.

3.3.3.3 Thermoelectric characterization of the composite thermocouples

The Seebeck coefficient is a material property that dictates the thermally-derived voltage generated within a material. This property may be measured for a material by evaluating the slope of thermoelectric voltage (E)-temperature difference (ΔT) graph. Thermocouple sensors are based upon the junction of two electrically dissimilar materials having dissimilar Seebeck coefficients (S_A and S_B). The generated thermoelectric voltage is defined by the difference in their Seebeck coefficients ($S_{AB} = S_A - S_B$), and this can be written as [3.17]:

$$S_{AB} = \lim_{\Delta T \to 0} \frac{\Delta V_{AB}}{\Delta T} \quad (1)$$

where ΔV_{AB} is the electric potential across the interface of two dissimilar conductors within a thermal gradient, ΔT. In the present study, intrinsic Seebeck coefficients of the $MoSi_2$-Al_2O_3 (S_{MA})

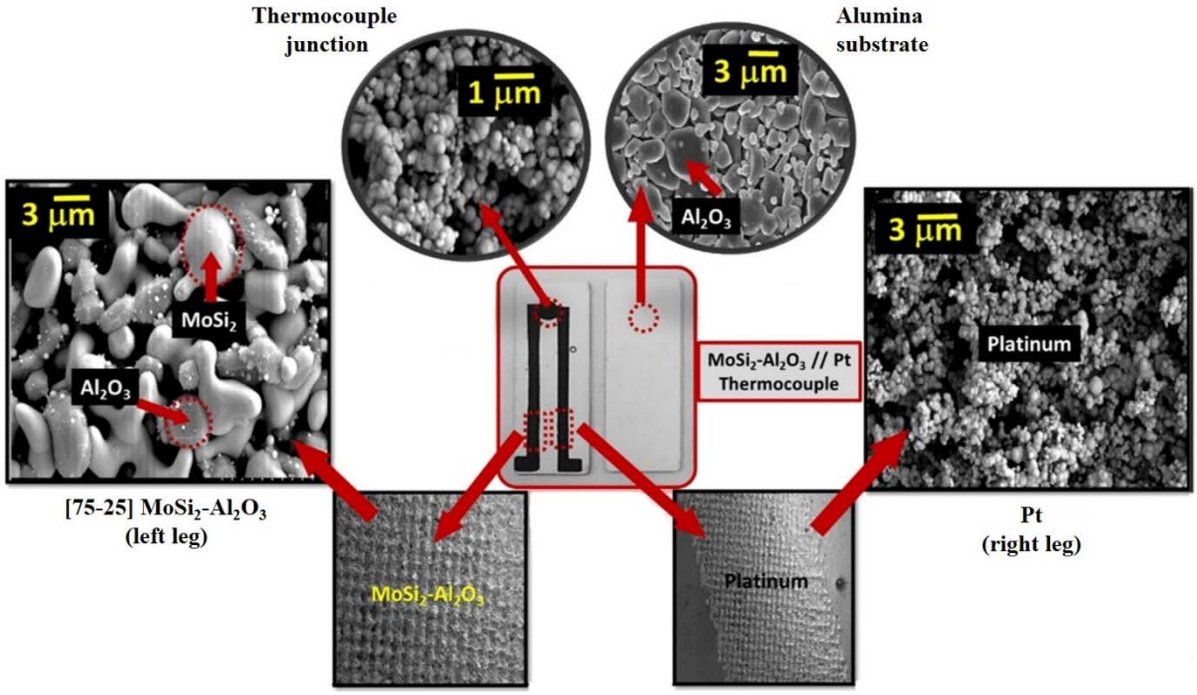

Figure 3.16 Optical photograph and SEM micrographs (alumina substrate, left leg, right leg, junction) of the [75-25] $MoSi_2$-Al_2O_3//Pt thermocouple screen printed on an alumina substrate and then sintered at 1500ºC for 2 h.

and WSi_2-Al_2O_3 (S_{WA}) composites were estimated from the effective Seebeck coefficients of the $MoSi_2$-Al_2O_3//Pt (S_{MAPt}) and WSi_2-Al_2O_3//Pt (S_{WAPt}) thermocouples tested up to 1000°C in argon. According to the equation (1), difference in the effective Seebeck coefficients of the thermocouples with configurations of the $MoSi_2$-Al_2O_3//Pt and WSi_2-Al_2O_3//Pt can be written as:

$$S_{MAPt} = S_{MA} - S_{Pt} \quad (2)$$

$$S_{WAPt} = S_{WA} - S_{Pt} \quad (3)$$

where S_{MAPt} is the difference in the intrinsic Seebeck coefficients of the $MoSi_2$-Al_2O_3 (S_{MA}) and Pt (S_{Pt}) legs of the thermocouple; and S_{WAPt} is the difference in the intrinsic Seebeck coefficients of the WSi_2-Al_2O_3//Pt (S_{WA}) and Pt (S_{Pt}) legs of the thermocouple. By using the equations (2-3), the effective Seebeck coefficient of a composite thermocouple with a configuration of the $MoSi_2$-Al_2O_3//WSi_2-Al_2O_3 (S_{MAWA}) could be estimated as:

$$S_{MAWA} = S_{MA} - S_{WA} \quad (4)$$

where ΔS_{MAWA} denotes the estimated effective Seebeck coefficient of the $MoSi_2$–Al_2O_3//WSi_2–Al_2O_3 thermocouple by using the data obtained from the thermocouples made of $MoSi_2$-Al_2O_3//Pt and WSi_2-Al_2O_3//Pt.

To evaluate this experimentally, standard thermocouples with configurations of [50-50], [60-40], [75-25] and [90-10] $MoSi_2$-Al_2O_3//Pt, and [50-50], [60-40], [75-25] and [90-10] WSi_2-Al_2O_3//Pt were fabricated, and their thermoelectric responses were recorded as a function of the

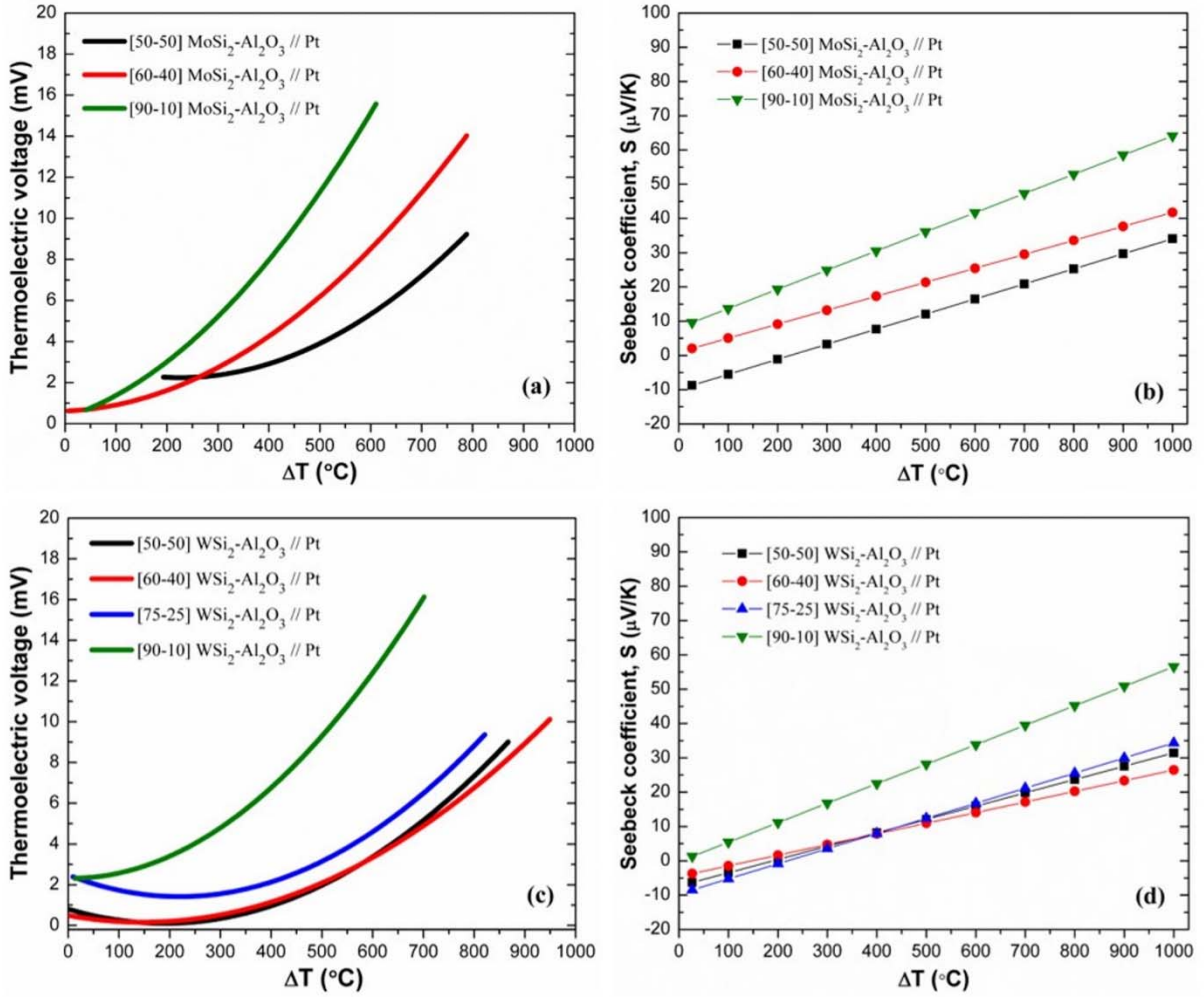

Figure 3.17 (a-c) Thermoelectric voltages (E) and (b-d) effective Seebeck coefficients (S) measured for the various $MoSi_2$-Al_2O_3//Pt and WSi_2-Al_2O_3//Pt thermocouples as a function of temperature difference.

temperature difference. It was reported that a Pt//Pd wire thermocouple (Pt-67 reference standard maintained by NIST) exhibited a Seebeck coefficient of 18.2 μV/K at 900ºC [3.18]. In the present study, thermocouples were tested by recording the voltage drop across the device with an acquisition system (DAQ, National Instruments) associated with a computer-based LabView software. The estimated Seebeck coefficients of the $MoSi_2$-Al_2O_3 and WSi_2-Al_2O_3 composites were determined by using the intrinsic Seebeck coefficient of Pt and effective Seebeck coefficients of $MoSi_2$-Al_2O_3//Pt and WSi_2-Al_2O_3//Pt thermocouples in the equations (2-3). Figure 3.17(a-d) presents the thermoelectric voltage and effective Seebeck coefficients of the various $MoSi_2$-Al_2O_3//Pt and WSi_2-Al_2O_3//Pt thermocouples as a function of temperature difference. The error margin in the thermoelectric characterization of [75-25] $MoSi_2$-Al_2O_3//Pt thermocouple was very high; therefore, the related data is not presented and not included in further Seebeck coefficient calculations. The thermoelectric voltages of the [50-50], [60-40], and [90-10] $MoSi_2$-Al_2O_3//Pt thermocouples were measured at 1000ºC as 15.4, 21.9 and 36.2 mV, respectively. In addition,

thermoelectric voltages of [50-50], [60-40], [75-25] and [90-10] WSi_2-Al_2O_3//Pt thermocouples measured at 1000ºC were 12.8, 11.5, 14.8 and 30.5 mV, respectively. The thermoelectric voltage increased with increasing temperature, as well as, increasing metal silicide content (from 50 to 90 vol%) in the $MoSi_2$-Al_2O_3//Pt and WSi_2-Al_2O_3//Pt thermocouples. However, [50-50] WSi_2-Al_2O_3//Pt showed relatively higher thermoelectric voltage than [60-40] WSi_2-Al_2O_3//Pt only at the temperature gradients above 570°C, which could be related to the differences in percolation, volume fraction of secondary W_5Si_3 phase and its overall effect on thermoelectric output with respect to platinum. At lower temperature differences up to ~200ºC, the thermoelectric voltages of all the $MoSi_2$-Al_2O_3//Pt and WSi_2-Al_2O_3//Pt thermocouples were found to be relatively low (<3 mV) (Figure 3.17a-c). It is also clear that the $MoSi_2$-Al_2O_3//Pt thermocouples exhibited higher thermoelectric voltages than the WSi_2-Al_2O_3//Pt thermocouples at [50-50] and [60-40] fractions. In addition, at [90-10] fraction, they displayed relatively similar thermoelectric performance (>12 mV) at the temperature gradient above 600°C. As presented in the Figure 3.17c, [50-50] and [60-40] WSi_2-Al_2O_3//Pt thermocouples also exhibited a very similar thermoelectric performance. However, a significant increase in the thermoelectric voltage was achieved by the [90-10] WSi_2-Al_2O_3//Pt thermocouple.

To determine the effective Seebeck coefficients of these thermocouples, thermoelectric responses were fit to a second-order or a third-order polynomial using a least square method. Based on the theory [3.19], thermoelectric voltage (E) and Seebeck coefficient (S) can be expressed as:

2^{nd} order: $E = A\Delta T + B\Delta T^2 + C$ $S = A + 2B\Delta T$ (5)

3^{rd} order: $E = A\Delta T + B\Delta T^2 + D\Delta T^3 + C$ $S = A + 2B\Delta T + 3D\Delta T^2$ (6)

where A, B , C and D are fitting coefficients, and ΔT is temperature gradient. In order to calculate the Seebeck coefficient in μV/K, the units of fitting coefficients were converted prior to these calculations. The effective Seebeck coefficients of the $MoSi_2$-Al_2O_3//Pt and WSi_2-Al_2O_3//Pt thermocouples are presented in the Figure 3.17(b-d) as a function of temperature difference (ΔT). At 500°C, the effective Seebeck coefficients (S_{500}) of [50-50], [60-40] and [90-10] $MoSi_2$-Al_2O_3//Pt thermocouples were measured as 12.1, 21.4 and 36.1 μV/K, respectively; while [50-50], [60-40], [75-25] and [90-10] WSi_2-Al_2O_3//Pt exhibited effective Seebeck coefficients of 12.0, 11.0, 12.4 and 28.2 μV/K, respectively. The effective Seebeck coefficients of all thermocouples increased with increasing temperature difference up to 1000°C. The [50-50] and [60-40] $MoSi_2$-Al_2O_3//Pt thermocouples exhibited similar behavior up to 200°C; however, [60-40] $MoSi_2$-Al_2O_3//Pt revealed higher effective Seebeck coefficients than [50-50] above that temperature. In the case of WSi_2-Al_2O_3//Pt thermocouples, relatively higher Seebeck coefficients were observed for the [75-25] fraction at the temperatures above 600°C, compared to the [50-50] and [60-40] thermocouples. Similar to their thermoelectric voltage data, [50-50] WSi_2-Al_2O_3//Pt thermocouple showed relatively higher Seebeck coefficient than [60-40] only at higher temperature gradients. However, a substantial increase in the Seebeck coefficient was observed at the 90 vol% metal silicide fraction both for $MoSi_2$-Al_2O_3//Pt and WSi_2-Al_2O_3//Pt thermocouples. These drastic increases in the effective Seebeck coefficients may be attributed to the interaction of charge carriers with non-equilibrium portion of the phonon distribution and the spatial redistribution of the charge carriers in the composite matrix that promotes the average energy of the charge carrier. In addition,

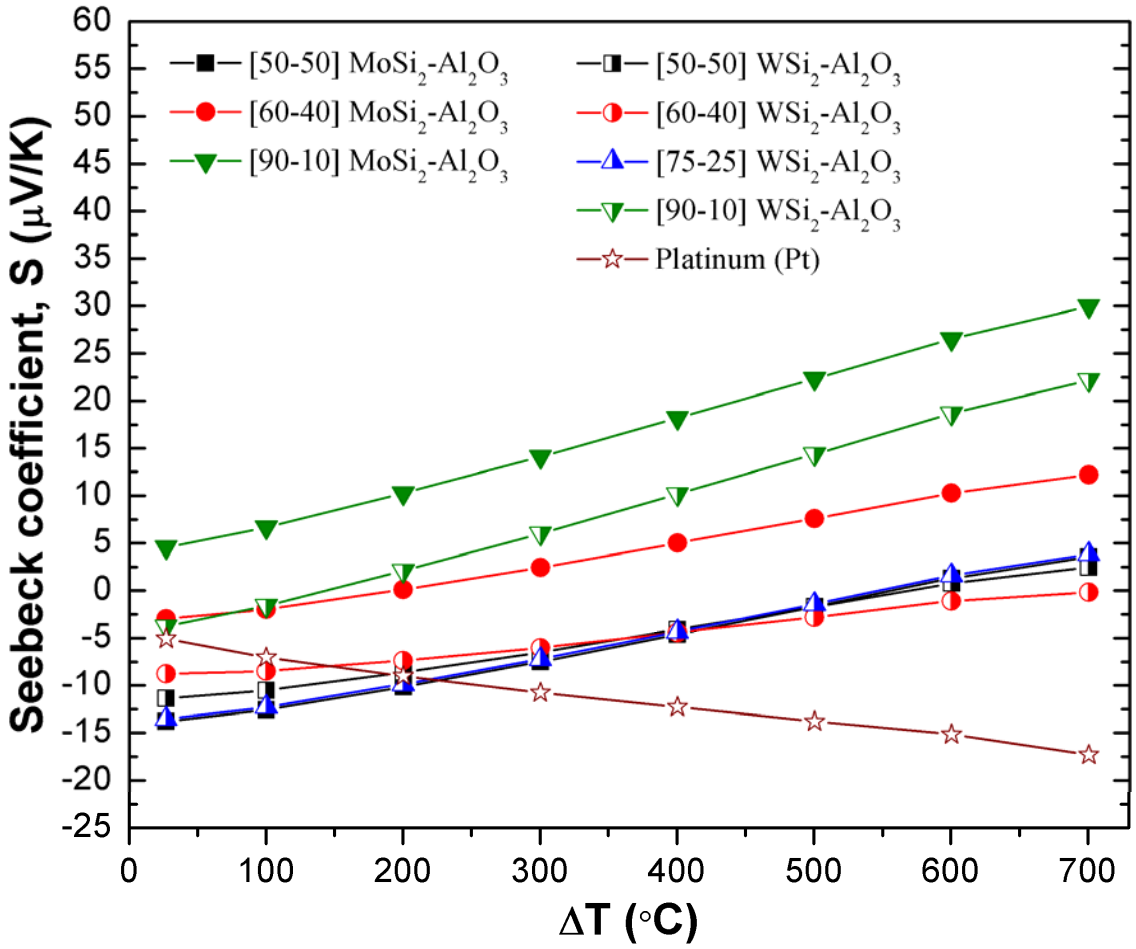

Figure 3.18 Estimated Seebeck coefficients (S) of the various $MoSi_2$-Al_2O_3 and WSi_2-Al_2O_3 composites as a function of temperature difference (S_{Pt} is also presented).

it can be seen that [50-50] $MoSi_2$-Al_2O_3//Pt and [50-50] WSi_2-Al_2O_3//Pt thermocouples revealed a similar trend for their effective Seebeck coefficients, whereas $MoSi_2$-Al_2O_3//Pt thermocouples always exhibited higher Seebeck coefficients than the WSi_2-Al_2O_3/Pt thermocouples with [60-40] and [90-10] fractions in a wide temperature range.

The experimental results of the $MoSi_2$-Al_2O_3//Pt and WSi_2-Al_2O_3//Pt thermocouples were initially used in this study to determine the estimated intrinsic Seebeck coefficients of the $MoSi_2$-Al_2O_3 and WSi_2-Al_2O_3 composites. Afterwards, these estimated values were utilized to calculate the estimated Seebeck coefficients of the various $MoSi_2$-Al_2O_3//WSi_2-Al_2O_3 composite thermocouples, which were then compared with the measured effective Seebeck coefficients of the equivalent $MoSi_2$-Al_2O_3//WSi_2-Al_2O_3 composite thermocouples. Figure 3.18 presents the estimated intrinsic Seebeck coefficients of various $MoSi_2$-Al_2O_3 and WSi_2-Al_2O_3 composites that were calculated by using the measured effective Seebeck coefficients of metal silicide-oxide//Pt thermocouples and reference intrinsic Seebeck coefficients of Pt [3.20] within the equations (2-3). At 500°C, intrinsic Seebeck coefficients of [50-50], [60-40] and [90-10] $MoSi_2$-Al_2O_3 composites

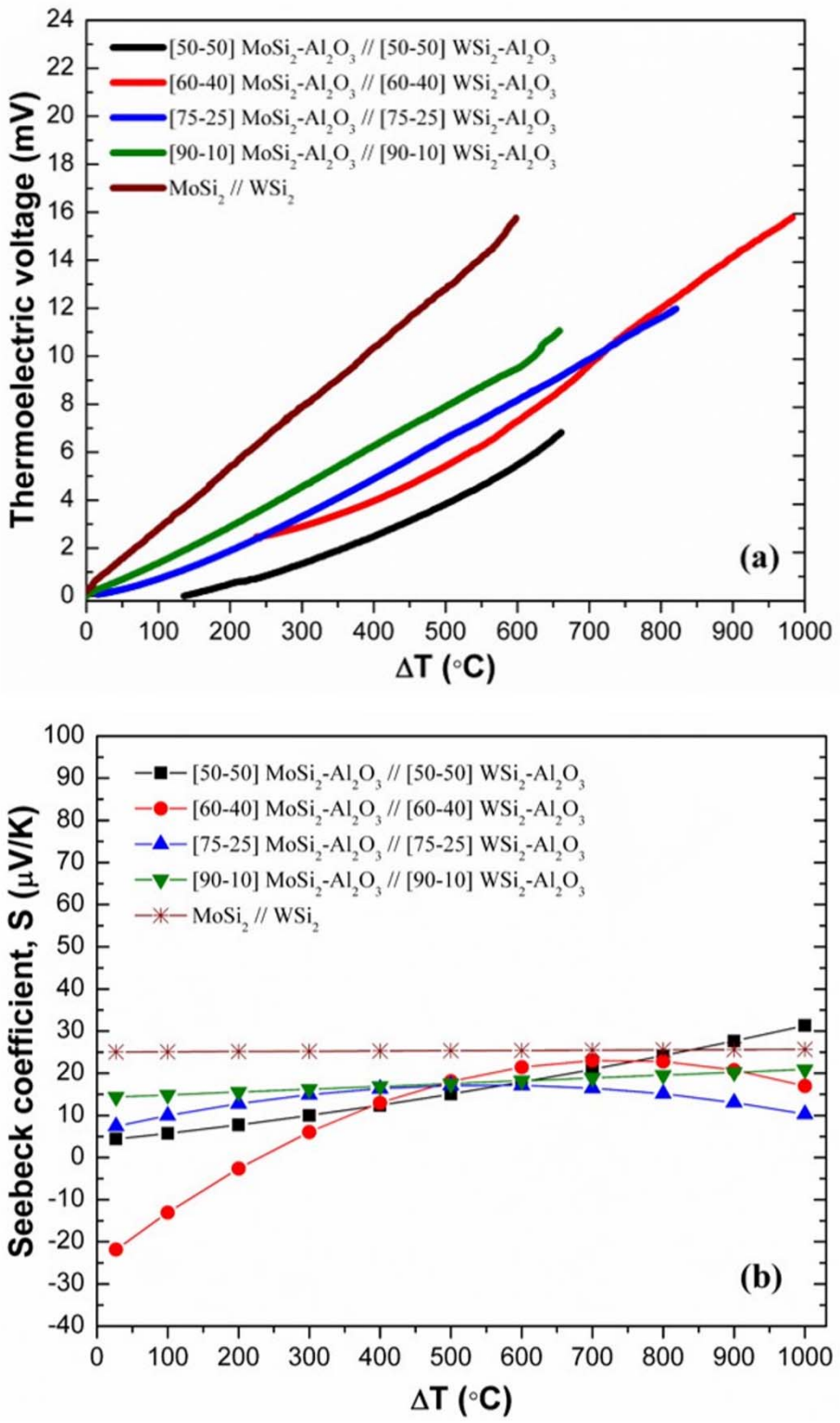

Figure 3.19 (a) Thermoelectric voltages (E) and (b) effective Seebeck coefficients (S) measured for the $MoSi_2$//WSi_2 and various $MoSi_2$-Al_2O_3//WSi_2-Al_2O_3 thermocouples as a function of temperature difference.

were calculated as -1.70, 7.59 and 22.3 μV/K, respectively. The intrinsic Seebeck coefficients of [50-50], [60-40], [75-25] and [90-10] WSi_2-Al_2O_3 composites were also determined at 500°C as -1.73, -2.82, -1.42 and 14.4 μV/K, respectively. Interestingly, the [60-40] $MoSi_2$-Al_2O_3, [90-10] $MoSi_2$-Al_2O_3 and [90-10] WSi_2-Al_2O_3 composites revealed mostly positive estimated Seebeck coefficients, all other composites displayed negative estimated Seebeck coefficients. In addition, the intrinsic Seebeck coefficients of the [50-50] $MoSi_2$-Al_2O_3 and [50-50], [60-40] and [75-25] WSi_2-Al_2O_3 composites decreased with increasing temperature gradient, since their intrinsic Seebeck coefficients were all higher as negative values (-13.8 to -4.11 μV/K) at the temperatures below 400°C. These composites displayed very low intrinsic Seebeck coefficients at the temperatures above that temperature. Also, [50-50] $MoSi_2$-Al_2O_3 and [75-25] WSi_2-Al_2O_3 composites showed almost identical intrinsic Seebeck coefficients at all temperatures (Figure 3.18). However, the intrinsic Seebeck coefficients of [90-10] $MoSi_2$-Al_2O_3 and [90-10] WSi_2-Al_2O_3 significantly increased with increasing temperature gradient, particularly above 200°C. These results indicated that the $MoSi_2$-Al_2O_3 and WSi_2-Al_2O_3 composites could have higher intrinsic Seebeck coefficients at [90-10] fraction based on the estimation using the data obtained by metal silicide-oxide//Pt thermocouples.

Their thermoelectric performance was analyzed under argon atmosphere and further compared with the estimated values. Pure $MoSi_2$//WSi_2 thermocouples were also fabricated to investigate the effect of alumina content on their thermoelectric performance. The thermoelectric voltages and effective Seebeck coefficients of these thermocouples are presented in the Figure 3.19(a-b) as a function of temperature difference (ΔT). The thermoelectric voltage of all $MoSi_2$-Al_2O_3//WSi_2-Al_2O_3 and $MoSi_2$//WSi_2 thermocouples increased significantly with increasing temperature up to 600°-1000°C. At 500°C, $MoSi_2$//WSi_2 thermocouple displayed a thermoelectric voltage of 12.9 mV; whereas, the [50-50], [60-40], [75-25], [90-10] $MoSi_2$-Al_2O_3//[50-50], [60-40], [75-25], [90-10] WSi_2-Al_2O_3 thermocouples showed 3.85, 5.41, 6.53 and 7.89 mV, respectively, at the same temperature. The thermoelectric voltage relatively increased with increasing metal silicide ($MoSi_2$, WSi_2) content on both legs of the thermocouple from 50 to 90 vol%. It was also demonstrated that the thermoelectric voltage decreased from 12.9 to 7.89 mV at 500°C with the addition of 10 vol% Al_2O_3 into both legs of the thermocouple. At 1000°C, [50-50], [60-40], [75-25], [90-10] $MoSi_2$-Al_2O_3//[50-50], [60-40], [75-25], [90-10] WSi_2-Al_2O_3 thermocouples exhibited 15.2, 16.0, 14.1 and 17.5 mV, respectively. It is clear that the [60-40] $MoSi_2$-Al_2O_3//[60-40] WSi_2-Al_2O_3 thermocouple could have relatively higher thermoelectric voltage than [50-50] and [75-25] at 1000°C based on the calculations. The [90-10] $MoSi_2$-Al_2O_3//[90-10] WSi_2-Al_2O_3 thermocouple performed better than the other composite thermocouples throughout the temperature range.

The effective Seebeck coefficients as a function of temperature difference for the composite thermocouples are presented in the Figure 3.19(b). The $MoSi_2$//WSi_2 thermocouple showed 25.4 and 25.7 μV/K at 500° and 1000ºC, respectively. The effective Seebeck coefficients of the [50-50], [60-40], [75-25], [90-10] $MoSi_2$-Al_2O_3//[50-50], [60-40], [75-25], [90-10] WSi_2-Al_2O_3 thermocouples measured at 500°C were 15.0, 18.1, 17.1 and 17.5 μV/K, respectively. Therefore, the [60-40] and [90-10] revealed slightly higher Seebeck coefficients than the other composite thermocouples at 500°C. In addition, the effective Seebeck coefficients of all the composite thermocouples were relatively lower than the pure $MoSi_2$//WSi_2 thermocouple at the same

temperature. At 1000°C, the effective Seebeck coefficients of the [50-50], [60-40], [75-25], [90-10] $MoSi_2$-Al_2O_3//[50-50], [60-40], [75-25], [90-10] WSi_2-Al_2O_3 thermocouples were measured as 31.3, 17.0, 10.3 and 20.9 μV/K, respectively. It is important to point out that [50-50] $MoSi_2$-Al_2O_3//[50-50] WSi_2-Al_2O_3 thermocouple exhibited relatively higher Seebeck coefficient than $MoSi_2$//WSi_2 and other composite thermocouples at 900° and 1000°C; although, it showed lower Seebeck coefficients than those thermocouples at the temperatures below ~200°C. This result may be related to the local compositional changes at the junction of the two composite legs of the [50-50] $MoSi_2$-Al_2O_3//[50-50] WSi_2-Al_2O_3 thermocouples. Furthermore, a non-linear thermoelectric response was observed for the [60-40] $MoSi_2$-Al_2O_3//[60-40] WSi_2-Al_2O_3 composite thermocouple as seen in the Figure 3.19(a-b). Multiple samples of this composition showed similar responses, and from the characterization previously presented, a significant difference in chemistry was not identified. This data was included in the paper to emphasize that there are some effects of phase formation and transformation at the junction that still require further characterization and understanding. In addition, the [90-10] $MoSi_2$-Al_2O_3//[90-10] WSi_2-Al_2O_3 composite thermocouple displayed a Seebeck coefficient of 20.9 μV/K at 1000°C, which is found to be highly comparable to that of the $MoSi_2$//WSi_2 thermocouple (25.7 μV/K) and also significantly higher than that of the high alumina containing composite thermocouples (10.3-17.0 μV/K). This result may be related to the high fraction of the 5-3 metal silicide (Mo_5Si_3, W_5Si_3) phases formed during sintering, since the XRD/Rietveld results proved that there was 15.6 vol% increase in the fraction of Mo_5Si_3 secondary phase with increasing metal silicide fraction in the composite from 50 to 90 vol%. Therefore, a significant increase in the thermoelectric voltage and Seebeck coefficient of the [90-10] $MoSi_2$-Al_2O_3//[90-10] WSi_2-Al_2O_3 thermocouple can be clearly seen at all temperatures, particularly at 1000°C. It also showed the most stable thermoelectric response in a wide temperature range in comparison to the other composite thermocouples, since its effective Seebeck coefficient increased only from 14.4 to 20.9 μV/K with increasing temperature gradient from 27°C to 1000°C. In addition, both $MoSi_2$//WSi_2 and [90-10] $MoSi_2$-Al_2O_3//[90-10] WSi_2-Al_2O_3 thermocouples revealed higher sensitivity (14.4-25.7 μV/K) than mostly used Pt-Rh//Pt high-temperature thermocouples; since it was reported that S-type (90% Pt-10% Rh//Pt) and R-type (87% Pt-13% Rh//Pt) thermocouples have sensitivity ranging from 5.5 to 13.0 μV/K throughout the temperature range from room temperature to 1000°C [3.21].

As a review, the above results indicated that higher silicide content positively affects thermoelectric response of the composite thermocouples in general, where the measured Seebeck coefficient was shown to generally increase with decreased alumina content. In addition, the results demonstrated that the $MoSi_2$//WSi_2 thermocouple (25.1-25.7 μV/K) showed nearly nine times higher performance compared to that predicted for the pure $MoSi_2$//WSi_2 couples estimated from previously reported Seebeck coefficient data. For example; the effective Seebeck coefficient for a $MoSi_2$//WSi_2 couple should be near 2.8 μV/°C, estimated from the data presented by Bennethum and Sherwood [3.22]. As briefly discussed above, the raw precursors and sintered composites used in the current study showed the additional 5-3 metal silicide phases (within both Mo and W compositions), as characterized by both XPS and XRD. It is believed that the addition of the 5-3 metal silicide phases within the thermocouple is enhancing the thermoelectric effect for the sensors above that predicted for the pure $MoSi_2$//WSi_2 compositions. As shown in this work, the amount of 5-3 metal silicide phase increases in both the $MoSi_2$ and WSi_2 compositions as the alumina

content is decreased, resulting in a significant increase in the Seebeck coefficient of the [90-10] $MoSi_2$-Al_2O_3//[90-10] WSi_2-Al_2O_3 thermocouple at 1000°C. Unfortunately, the Seebeck data for pure Mo_5Si_3 and W_5Si_3 phases are not available in literature, and further work is being completed by the current authors to investigate the intrinsic thermoelectric characteristics of various 5-3 metal silicide phases.

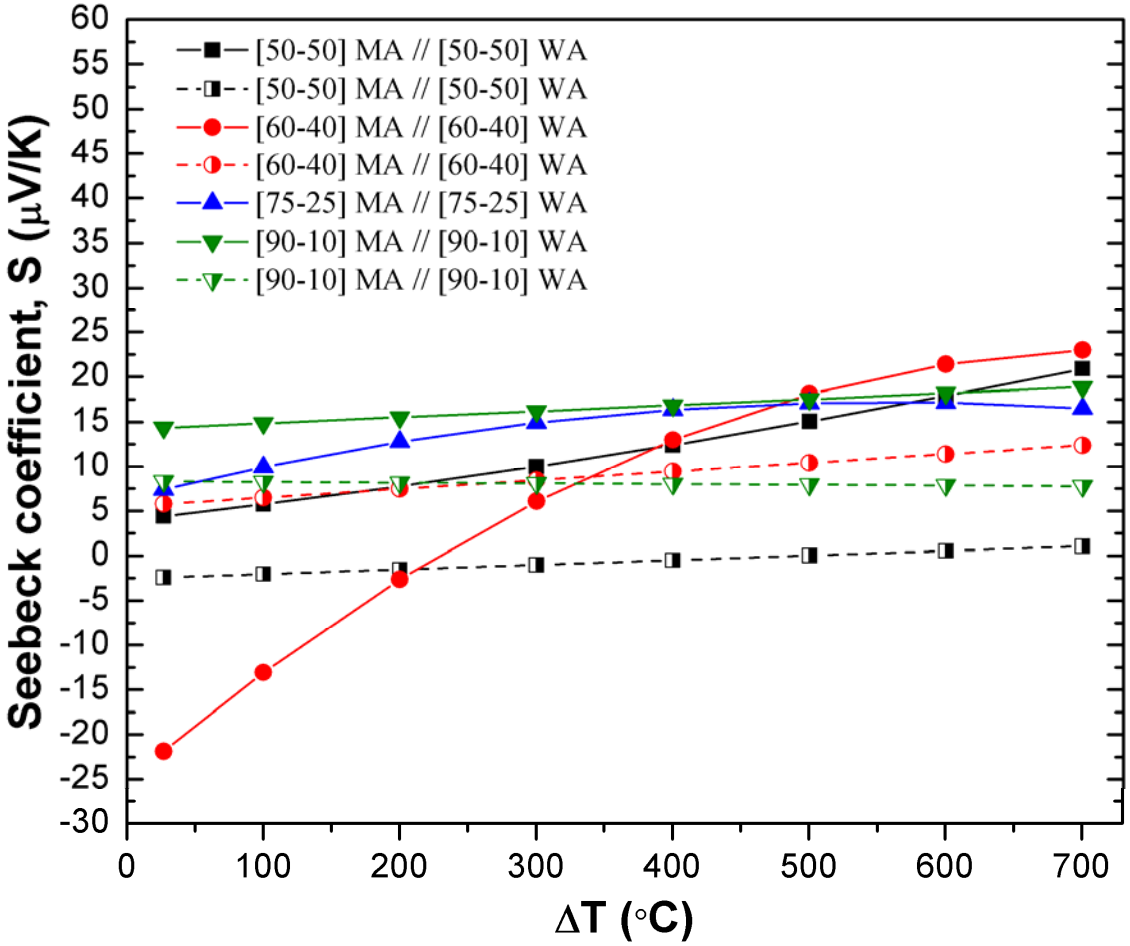

Figure 3.20 Comparison of the estimated (*dashed lines*) and measured effective (*solid lines*) Seebeck coefficients of the various $MoSi_2$-Al_2O_3//WSi_2-Al_2O_3 (*abbreviated as MA//WA*) composite thermocouples as a function of temperature difference.

In addition, Fig. 3.20 presents both estimated (*dashed lines*) and measured (*solid lines*) Seebeck coefficients of the various $MoSi_2$-Al_2O_3//WSi_2-Al_2O_3 composite thermocouples. The measured Seebeck coefficients of the $MoSi_2$-Al_2O_3//WSi_2-Al_2O_3 composite thermocouples were acquired directly from the experiments of the composite thermocouples. The estimated Seebeck coefficients were calculated by using the data obtained with the metal silicide-oxide//Pt thermocouples and utilizing the equations (2-4). It was demonstrated that the measured Seebeck coefficients from the actual $MoSi_2$-Al_2O_3//WSi_2-Al_2O_3 composite thermocouples were higher than those estimated from the data of metal silicide-oxide//Pt thermocouples and Pt reference. It can be also seen that the [50-

50], [60-40] $MoSi_2$-Al_2O_3//[50-50], [60-40] WSi_2-Al_2O_3 thermocouples exhibited relatively higher effective Seebeck coefficients than the [75-25] and [90-10] compositions only at 700°C; while they exhibited lower effective Seebeck coefficients at the temperatures ranging from 27° to ~480°C (*solid lines* in the Figure 3.20). In addition, the [60-40] $MoSi_2$-Al_2O_3//[60-40] WSi_2-Al_2O_3 thermocouple could display relatively higher Seebeck coefficients than the [90-10] at the temperatures above 400°C based on the estimated Seebeck coefficients (*dashed lines*). This estimated trend was clearly observed in the measured effective Seebeck coefficients of these composite thermocouples at the temperatures above 500°C, as seen in Figure 3.20. As a review, these results indicated that a difference in 5-3 metal silicide content may not be the only aspect influencing the thermocouple performance; local compositional changes at the junction of the two composite legs may also be enhancing the thermoelectric behavior. Further work must be completed in order to isolate the influence at this location, possibly through more compositionally controlled thin-film experiments.

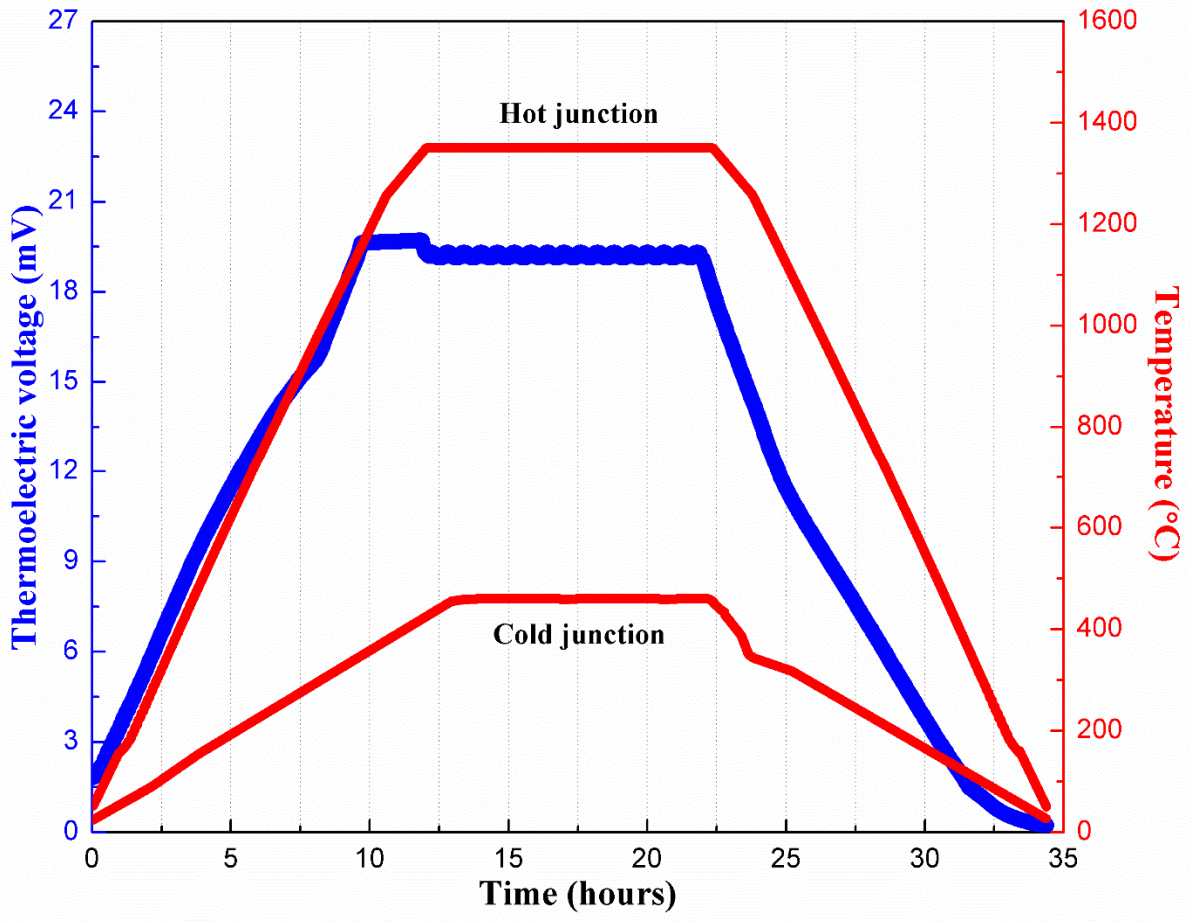

Figure 3.21 Thermoelectric performance of the [90-10] $MoSi_2$-Al_2O_3//[90-10] WSi_2-Al_2O_3 long composite thermocouple (22.9 cm length, 0.6 cm width) up to 1350°C, as a function of cold- and hot-junction temperature and time.

To investigate the thermoelectric performance of a long thermocouple (22.9 cm length, 0.6 cm width, ~400 µm thickness) at higher temperatures, a composite thermocouple with a configuration of [90-10] $MoSi_2$-Al_2O_3//[90-10] WSi_2-Al_2O_3 was selected for an extended demonstration of the thermoelectric performance at higher temperatures and durations (1350°C for 10 h in argon). The thermoelectric performance of a long [90-10] $MoSi_2$-Al_2O_3//[90-10] WSi_2-Al_2O_3 composite thermocouple is presented as a function of temperature and time in the Figure 3.21. A reference thermocouple was placed near the cold and hot junction of the sensor sample; the temperature versus measurement time data collected from both reference thermocouples was also included in Figure 3.21. A slightly different testing configuration (compared to the smaller thermocouples discussed in this work) was needed for testing at the higher operation temperature. The longer thermocouple was measured within a high-temperature tube furnace with alumina fiber-insulation placed around the cold-junction. Even with this insulation, the cold-junction reached a temperature of ~460ºC when the furnace 1350ºC isothermal was achieved. The thermoelectric voltage linearly increased with increasing temperature, and it exhibited a maximum thermoelectric voltage of 19.3 mV at 1350°C. It is also clear that its thermoelectric performance was adequately stable during the isothermal hold for 10 h. The slight changes in the thermoelectric voltage data during the isothermal hold were found to be caused by small temperature fluctuations (~0.02°C) of the high-temperature furnace; and therefore, it does not indicate any stability issue of the composite thermocouple. As a result, this thermoelectric response shows promise for future high-temperature applications for replacement of precious metal-based sensors.

The initial long thermocouples were fabricated by stenciling two different silicide-based inks on alumina substrates. These sensors were sintered and tested without enclosing the sensor materials inside an alumina shell. Four different thermocouple configurations were evaluated. Figure 3.22 shows nine inch long thermocouple and Fig. 3.23 shows the testing results for these thermocouples tested to 1300 °C. The composition selected for long thermocouples were (a) 90vol%WSi_2-10 vol% Al_2O_3// 90 vol%$TaSi_2$-10 vol%Al_2O_3; (b) 90vol% $MoSi_2$-10 vol% Al_2O_3// 90 vol%WSi_2-10 vol%Al_2O_3; (c) 90 vol% $MoSi_2$-10 vol% Al_2O_3// 90 vol%$NbSi_2$-10 vol%Al_2O_3; (d) 90 vol% $MoSi_2$-10 vol% Al_2O_3// 90 vol%$TiSi_2$-10 vol%Al_2O_3. The stenciled thermocouples were sintered at 1500 °C for 2 hours in argon inert gas atmosphere to obtain dense films without any delamination, warping or cracking. The films exhibited a good adhesion to the alumina substrates.

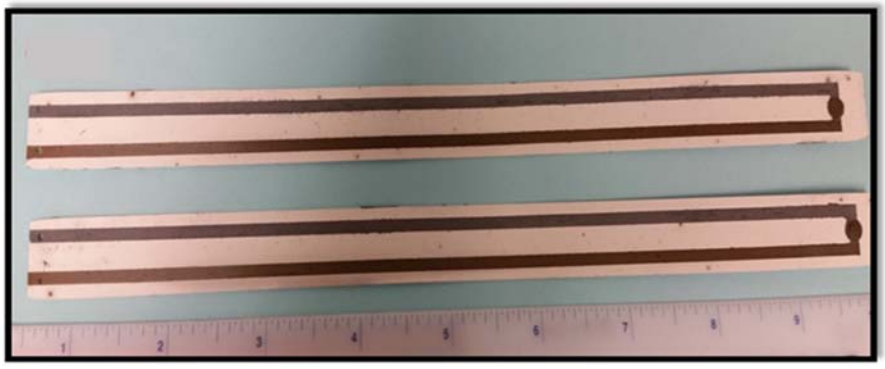

Figure 3.22. Nine inch long thermocouples.

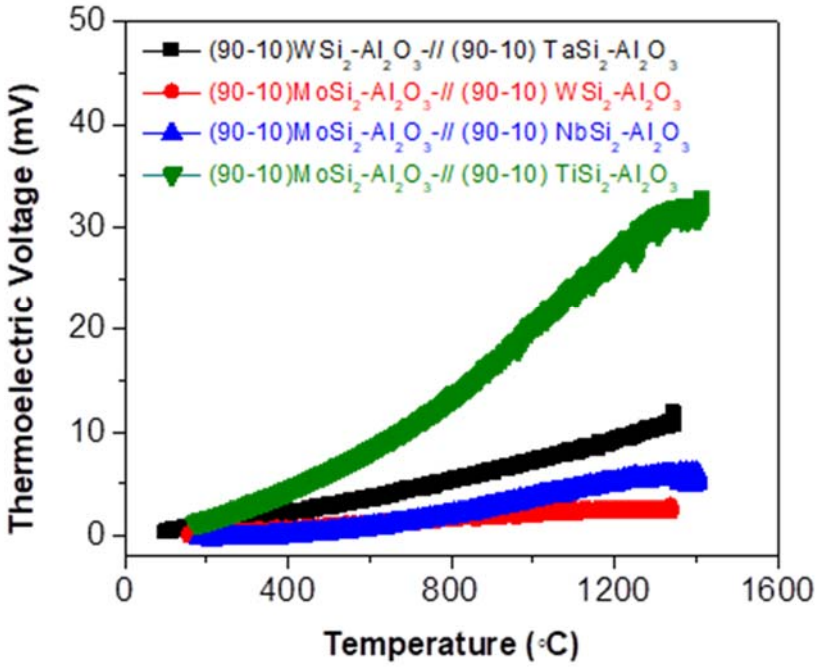

Figure 3.23. Performance of various silicide long length thermocouples.

In order to embed the thermocouple preforms in high chromia bricks, it was necessary to develop fabrication and co-sintering process for enclosed silicide-based sensors in alumina shell. Co-sintering of multiple materials with different porosity and sinterability levels while managing the oxidation and reacitivity of the materials has proven to be challenging. This study started with substrates that have been prepared by tape casting a bimodal alumina in 80/20 vol. % ratio of coarse alumina (SA: 1.2 m^2/g) vs fine alumina (SSA: 8.6 m^2/g) tapes that were laminated to achieve ~600 µm thickness. The substrates were cut into two pieces of 8'' x 1.5'' substrates. Masking tape (clean release blue masking tape with thickness~2'') was placed on one piece of the substrate. By adjusting the power of the laser cutter, a U-shaped profile used for either thermocouple or thermistor was cut in the masking tape without damaging the substrate underneath. The cut out masking tape was removed and the thermistor profile was revealed. The sensor ink [45-55] vol. % $MoSi_2$-Al_2O_3 was directly deposited into an effective mold. Several coats were deposited and dried in an oven at 70 °C to achieve 200 µm thick layer. The masking and stenciled thermistor is shown in Fig. 3.24. Once the entire thermistor was dried, then the stencil mask was peeled off and a second piece of 80/20 coarse/fine alumina was placed on top and the entire structure was laminated together. The laminated long thermistor was then sintered at 1500 °C for 2 h in argon. The green and sintered thermistors are shown in Fig. 3.25.

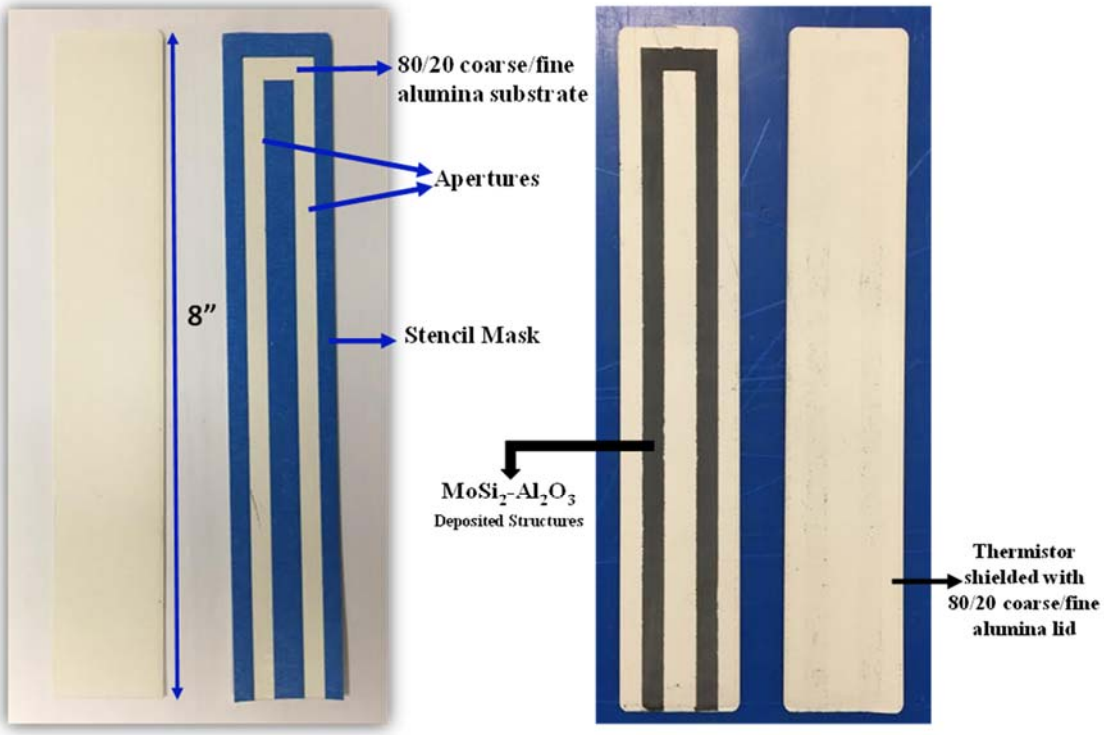

Figure. 3.24. Fabrication of Long Thermocouples (8” x 2” x 600 μm) using stencil lithography by using stencils as shadow masks for direct surface patterning without resist process.

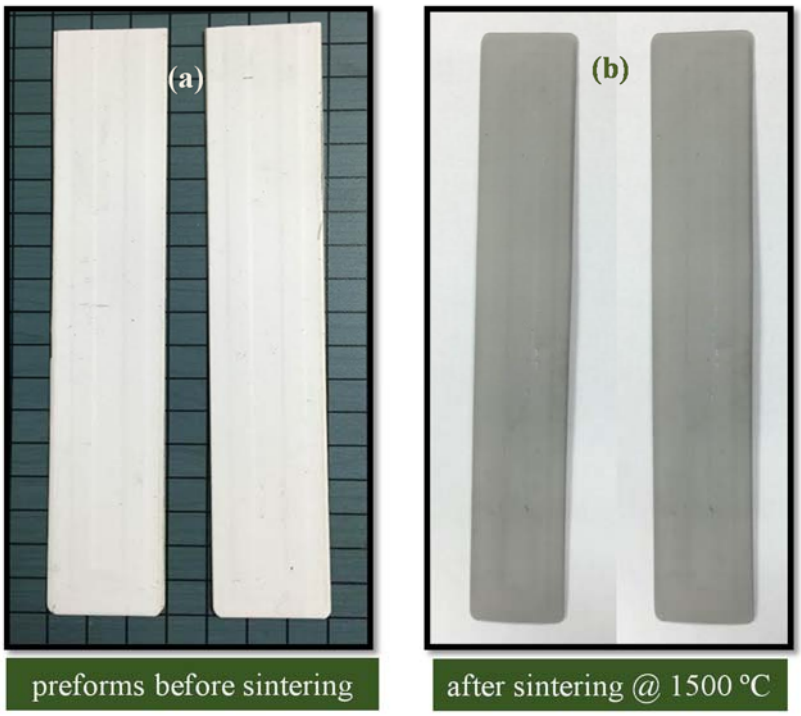

Figure 3.25. Long Thermistors (8" x 1.5" x 600 μm) fabricated through stencil writing. (a) Thermistor pre-forms laminated in between alumina substrates before sintering (b) Sensor preforms sintered at 1500 °C, 2h in argon atmosphere.

Long thermocouples were fabricated in a similar manner with the exception that each leg was applied separately while the other leg was masked off. For example, first the right leg of the thermocouple was masked with paper and [75-25] vol. % $MoSi_2$-Al_2O_3 (coarse alumina) ink was directly deposited in to the mold. Several layers were applied, again, to achieve 200 μm thick layer. Once the left leg was completed, the left leg was masked off and [75-25] vol. % WSi_2-Al_2O_3 was stenciled into the right side of the thermocouple mold. Once the entire thermocouple with appropriate thickness was finished and dried, then the stencil mask was peeled off and a second piece of 80/20 coarse/fine alumina substrate was placed on top and the entire structure was laminated together. The laminated long thermistor was then sintered at 1500 °C for 2 h in argon. The green and sintered thermistors are shown in Fig. 3.26.

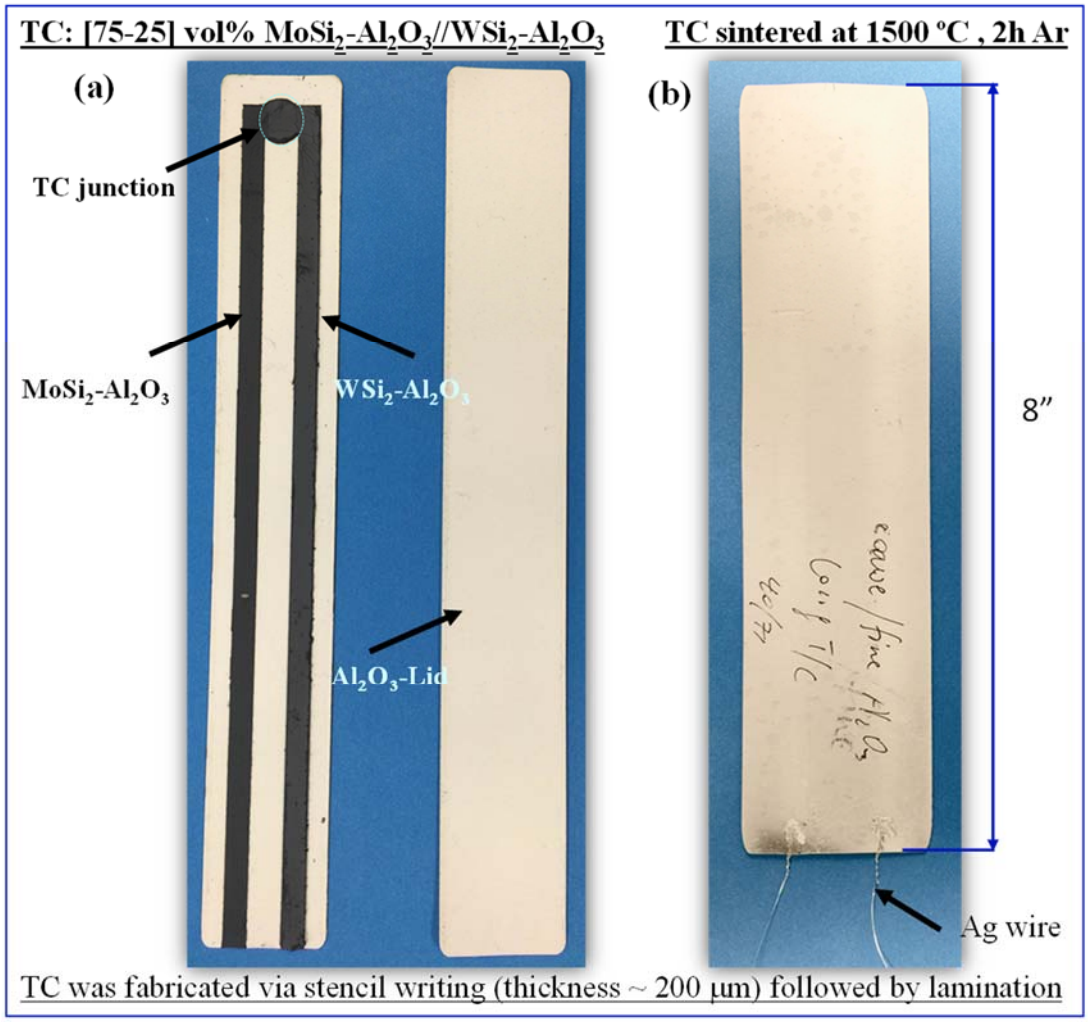

Figure 3.26. Long Thermocouple: [75-25] vol. % $MoSi_2$-Al_2O_3// [75-25] vol. % $MoSi_2$-Al_2O_3 fabricated through stencil writing. (a) Schematic showing long thermocouple fabricated via stencil lithography (b) Sensor preforms sintered at 1500 ºC, 2h in argon atmosphere.

The thermocouple was placed in an atmosphere controlled testing furnace and tested at 1350 °C for 5 hours at first cycle and for 10 hours at 2nd cycle under isothermal conditions in argon atmosphere. Figure 3.27, shows the performance analysis of [75-25] vol. % $MoSi_2$-Al_2O_3// [75-25] vol. % WSi_2-Al_2O_3thermocouple. The thermocouple performed stable for 15 hours by giving a thermoelectric voltage of 8.3 mV during the first cycle and 8.43 mV during the second cycle.

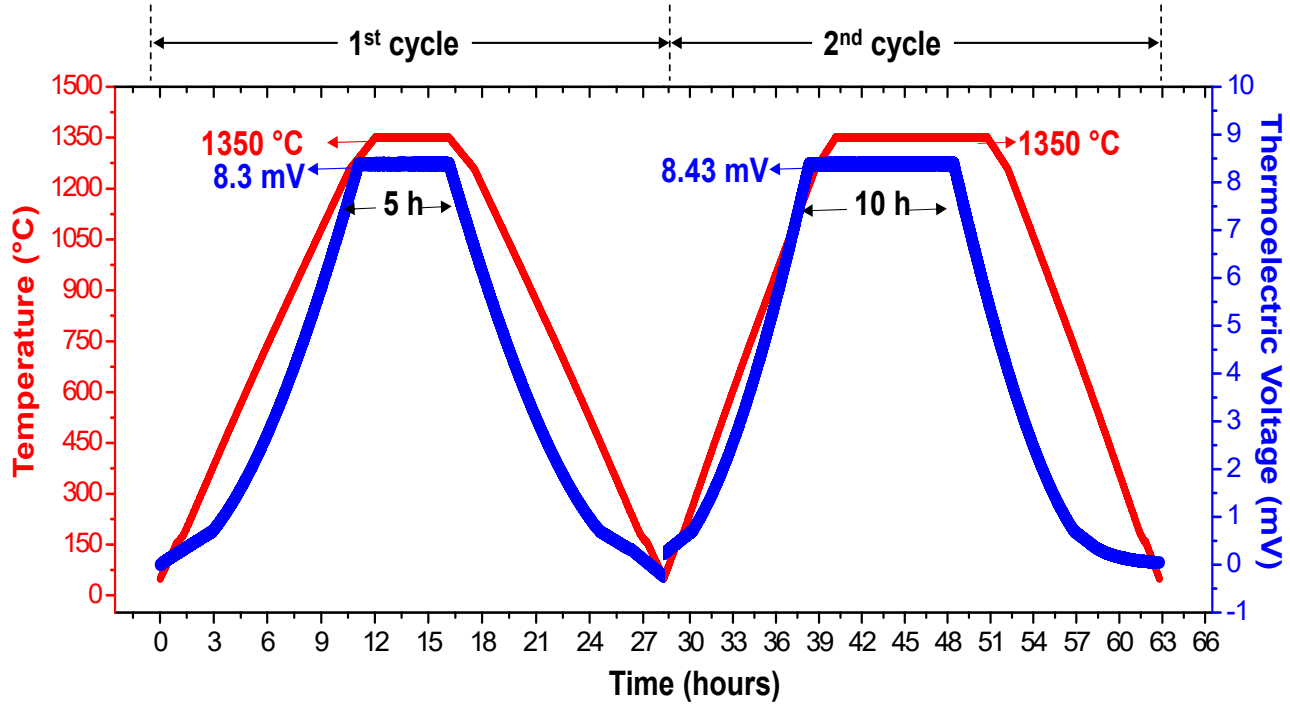

Figure 3.27. Performance analysis of [75-25] vol. % $MoSi_2$-Al_2O_3// [75-25] vol. % WSi_2-Al_2O_3 thermocouple fabricated through stencil lithography and laminated in between two 80/20 vol. % coarse/fine alumina laminated substrates. The thermocouple was tested at 1350 °C isothermally for 5h in 1st cycle and for 10h in 2nd cycle in argon atmosphere.

In an afford to improve structural stability and electrical continuity, the next set of thermocouples was fabricated using tape casted silicide-alumina composite sensors. In the first design, Fig. 3.28, the sensor tapes are carefully embedded inside a skeletal filler material and co laminated with a top and bottom shield of alumina substrate. The filler material was included to aid in lamination providing similar thickness between top and bottom alumina substrate around the sensing material. The sensor preform was sintered at 1550 °C for 2 h in argon. After sintering, the sensor legs were polished and exposed for electrical connection. Figure 3.29 shows sensor legs which are squished in between the filler material even though it has very good adhesion with the substrate. The preform, however, cracked along the sensor material due to differential shrinkage between silicide composite and alumina substrate.

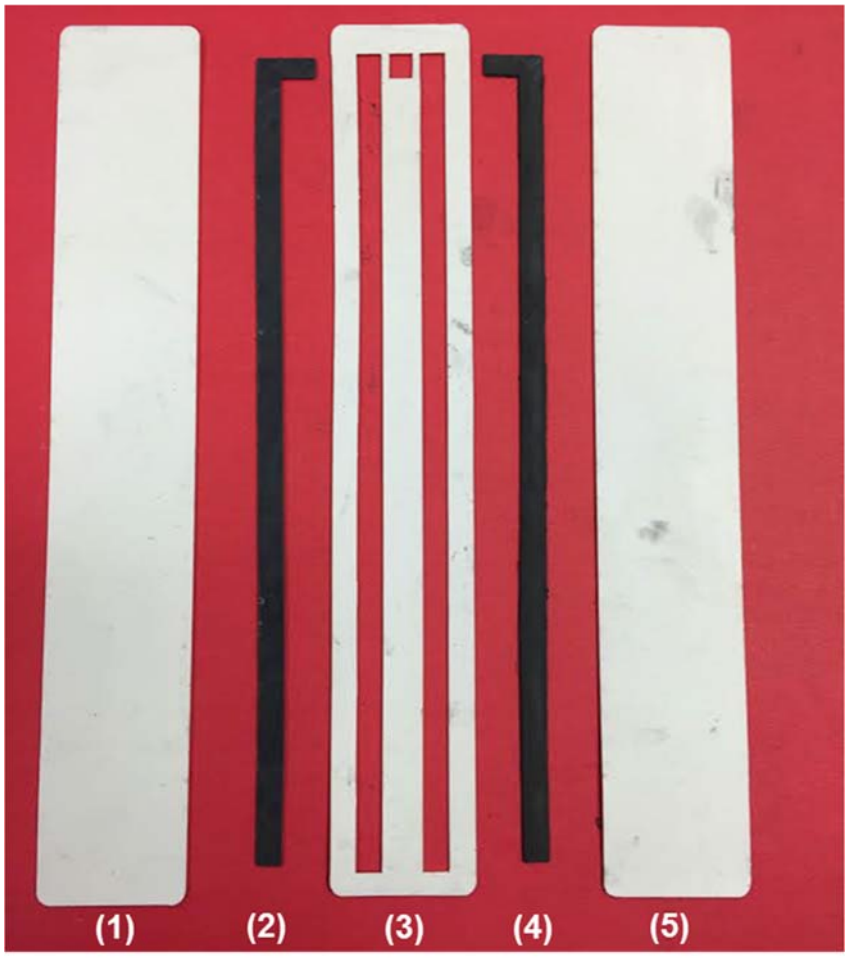

Figure 3.28. Fabrication of [75-25] $MoSi_2$-Al_2O_3//[75-25] WSi_2-Al_2O_3 thermocouple embedded in alumina substrates. The various components used are numbered as (1) (80-20) vol% coarse vs fine alumina substrate (2) [75-25] vol% $MoSi_2$-Al_2O_3 (3) (80-20) vol% coarse vs fine alumina filler material used to shape the sensor design (4) [75-25] vol% WSi_2-Al_2O_3 (5) (80-20) vol% coarse vs fine alumina substrate.

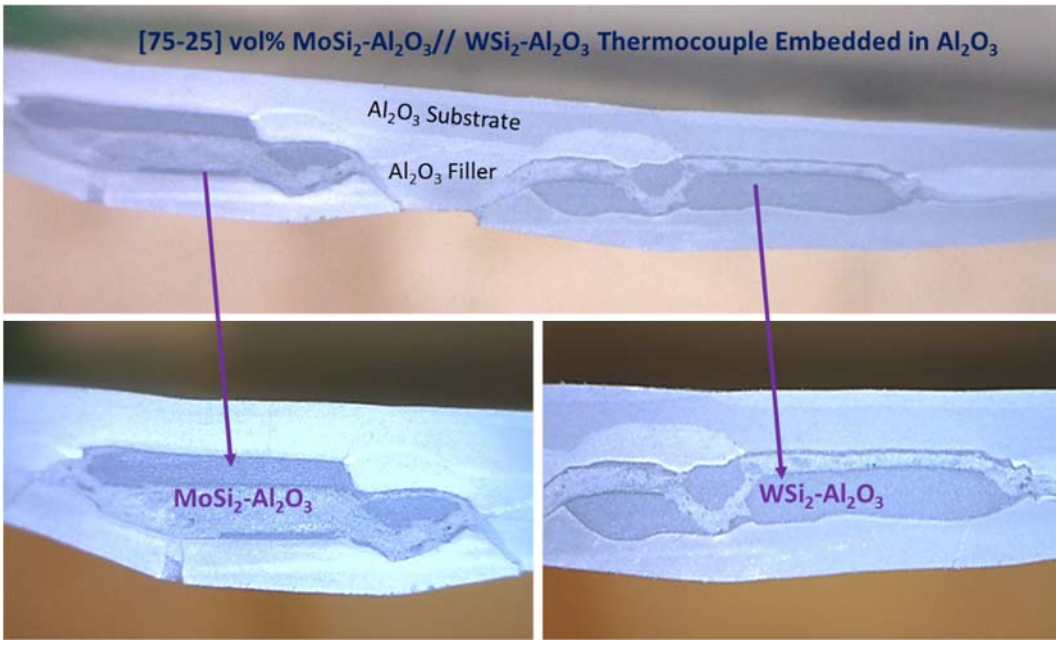

Figure 3.29. Photograph of [75-25] $MoSi_2$-Al_2O_3// [75-25] WSi_2-Al_2O_3 thermocouple (with full filler material as indicated by design I) embedded in alumina substrates.

In the second design. Fig. 3.30, only a center strip of composite alumina was used as a filler material to hold the sensor legs. The post sintering analysis of the sensor indicates that the adhesion between silicide-alumina composite sensor and composite alumina substrate appears to be intact even though some minor crack formed during the polishing of the sample. The photograph from the sensor-alumina substrate interface, Fig. 3.31, shows the sensor legs and its placement. The third design was made without filler material. Figure 3.32 shows a photograph of various components used in the fabrication of the thermocouple and temperature sensors. This design was simple but the space in between the sensor legs formed into a well on the sensor surface which resulted in cracking between the sensor and surrounding substrate wall.

Figure 3.30. Fabrication of [75-25] $MoSi_2$-Al_2O_3//WSi_2-Al_2O_3 thermocouple embedded in alumina substrates. The various components used are: (1) (80-20) vol% coarse vs fine alumina substrate (2) [75-25] vol% $MoSi_2$-Al_2O_3 (3) (80-20) vol% coarse vs fine alumina strip used as center filler (4) [75-25] vol% WSi_2-Al_2O_3 (5) (80-20) vol% coarse vs fine alumina substrate

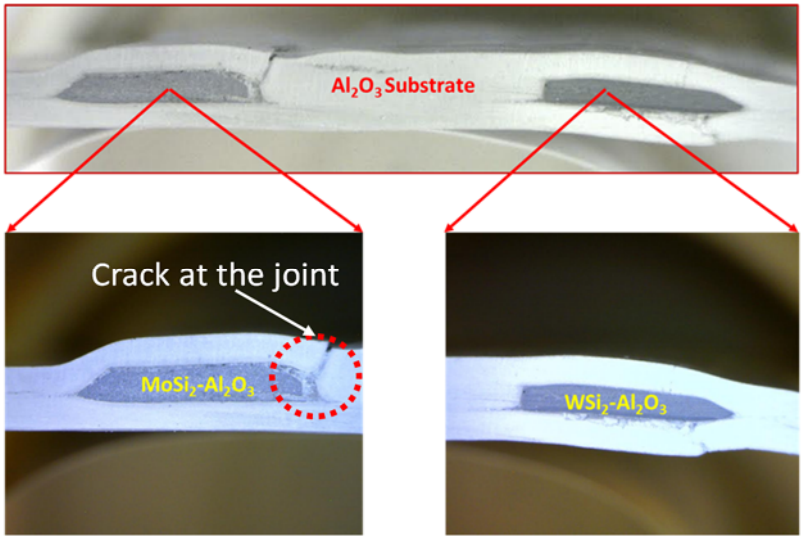

Figure 3.31. Photograph of [75-25] $MoSi_2$-Al_2O_3//[75-25] WSi_2-Al_2O_3 thermocouple (with center filler material) embedded in alumina substrates.

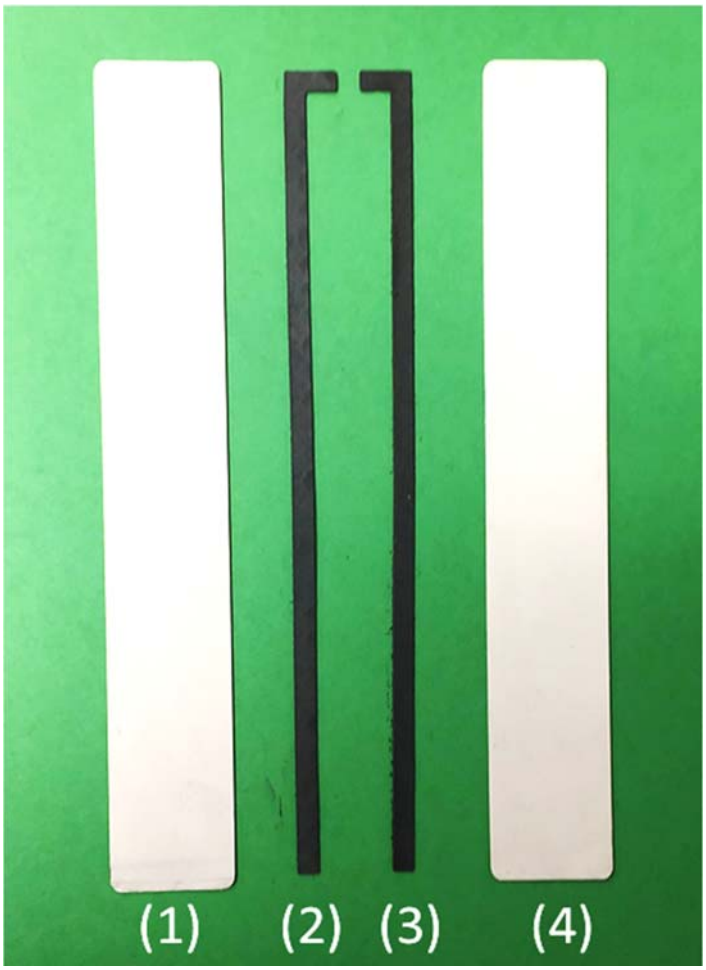

Figure 3.32. Fabrication of [75-25] $MoSi_2$-Al_2O_3// [75-25] WSi_2-Al_2O_3 thermocouple embedded in alumina substrates without filler material. The various components (1) (80-20) vol% coarse vs fine alumina substrate (2) [75-25] vol% $MoSi_2$-Al_2O_3 (3) [75-25] vol% WSi_2-Al_2O_3 (4) (80-20) vol% coarse vs fine alumina substrate.

Figure 3.33 shows green sensor preforms fabricated by all three designs described above. The laminated long thermocouple preforms were then sintered at 1550 ºC for 2 hours in argon atmosphere. Figure 3.34 shows the three thermocouples sintered at 1550 ºC for 2 hours in argon atmosphere. The sintered thermocouples are crack free except in the case of thermocouple made with full filler material, where cracks formed along the length of the alumina top cover.

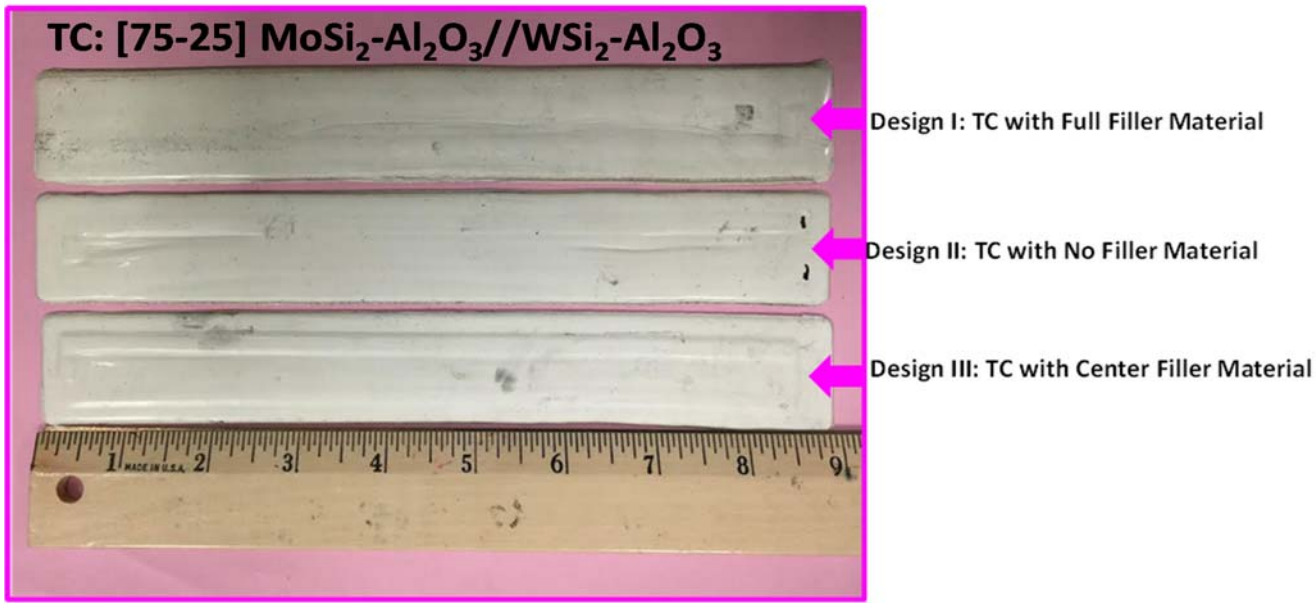

Figure 3.33. Photograph of [75-25] $MoSi_2$-Al_2O_3//[75-25] WSi_2-Al_2O_3 thermocouples embedded in alumina substrates (Green Sensors).

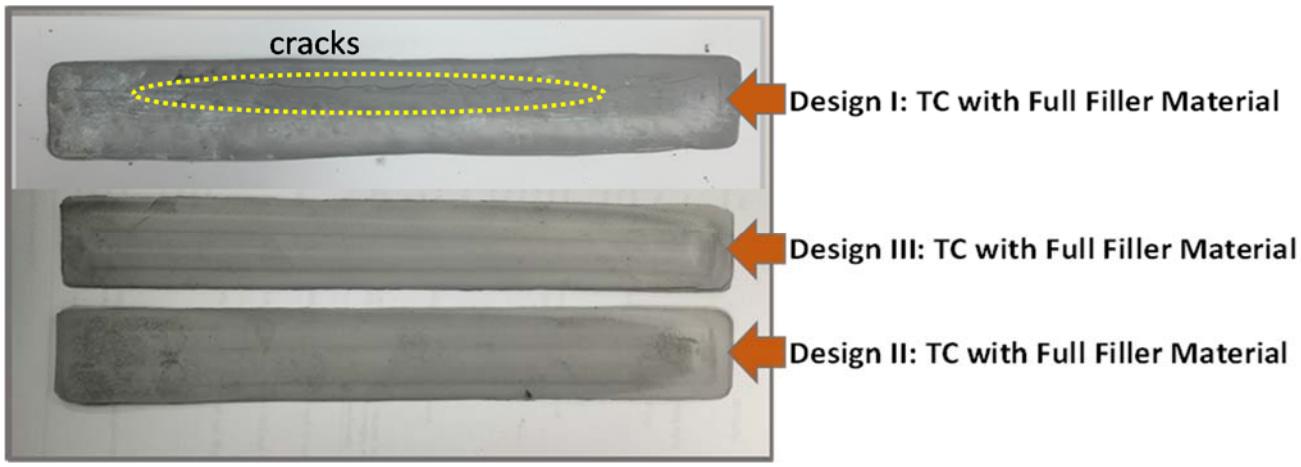

Figure 3.34. Photograph of [75-25] $MoSi_2$-Al_2O_3//[75-25] WSi_2-Al_2O_3 thermocouples embedded in alumina substrates and sintered at 1550 °C , 2h in argon.

The thermocouple with composition [75-25] $MoSi_2$-Al_2O_3//[75-25] WSi_2-Al_2O_3 embedded in a (80/20) wt% coarse/fine composite alumina substrate was tested at 1350 °C for 10h in argon. Figure 3.35(a) shows the post-test photograph of [75-25] vol% $MoSi_2$-Al_2O_3//WSi_2-Al_2O_3 thermocouple preform sintered at 1550 °C for 2 hours in argon atmosphere. Electrical contacts were made with Pt wire. Thermoelectric voltage of the thermocouple was measured in a high temperature tube furnace. Figure 3.35(b) shows the test set up. While the tip of the thermocouple was pointed towards the inside of the furnace, the legs were placed outside the furnace tube insulation to maintain a temperature gradient between the hot and cold junction as shown in Figure

3.35(c). The hot junction of the thermocouple was monitored by an independent B-Type thermocouple located at the tip of the test sample. A K-type thermocouple was located at the cold junction of the thermocouple to monitor cold junction temperature.

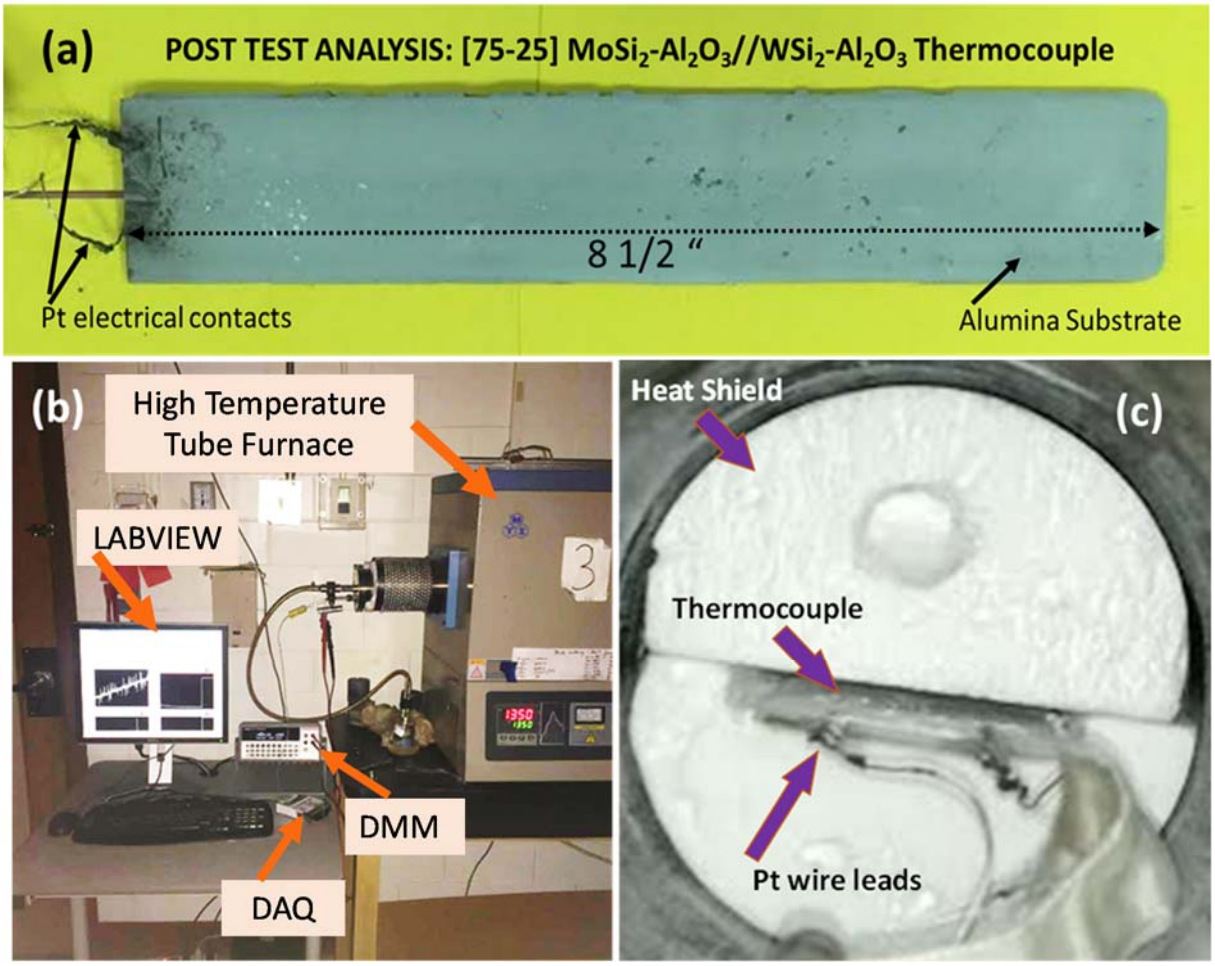

Figure 3.35 (a) Post-test photograph of [75-25] vol% $MoSi_2$-Al_2O_3//WSi_2-Al_2O_3 thermocouple sintered at 1550 °C for 2 hours in argon atmosphere. The thermocouple is embedded within 80/20 composite alumina substrate (b) Photograph of high temperature thermoelectric characterization facility for testing thermocouples/thermistors in argon atmospheres (c) Cold junction arrangement to test long thermocouples preforms.

Figure 3.36 shows the performance analysis of the thermocouple evaluated upto 1350 °C with 10 hours hold in argon atmosphere. The thermo- electric EMF of the [75-25] $MoSi_2$-Al_2O_3 // [75-25] WSi_2-Al_2O_3 thermocouple increased with increasing temperature and reaches a maximum of 25.8 mV at 1350 °C. The thermocouple delivered a maximum thermoelectric voltage of 25.8 mV at 1350 °C. However, a significant drift in voltage was observed during an isothermal hold of 10 h

at 1350 °C, where maximum EMF decreased from 25.8mV to 22.5 mV. Possible deterioration of sensing material was suspected in a form of oxidation of silicides.

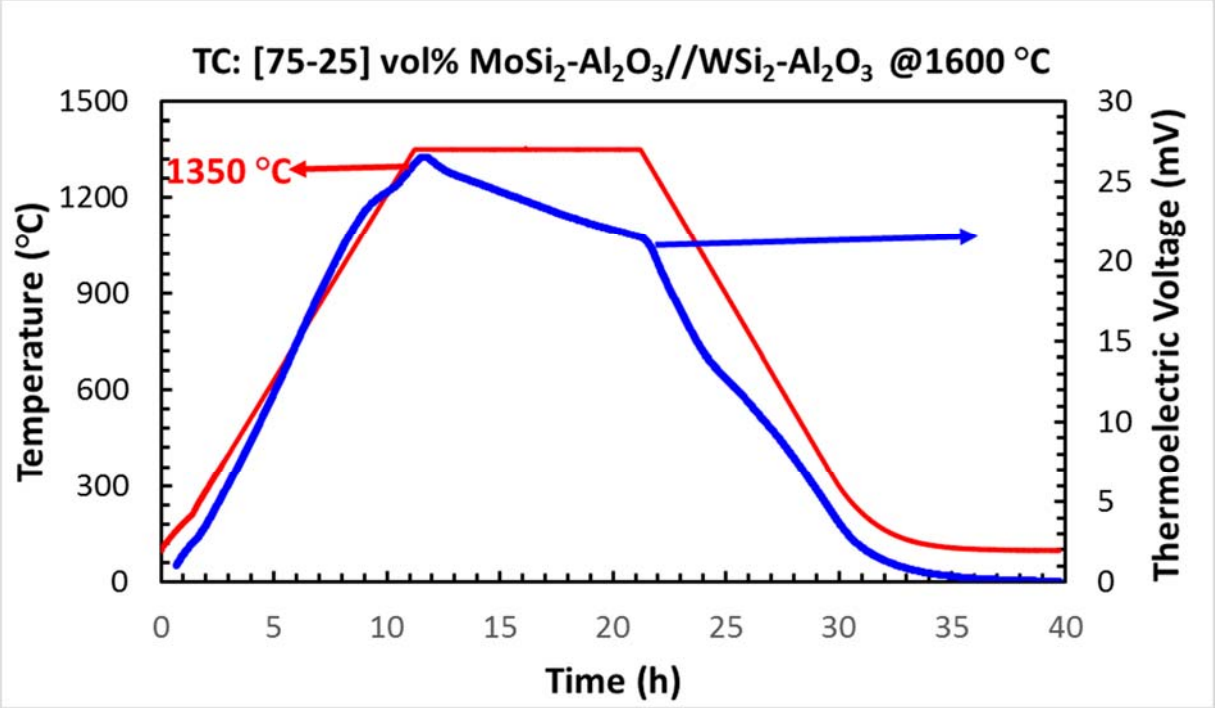

Figure 3.36. Thermoelectric voltage of [75-25] vol% $MoSi_2$-Al_2O_3 //WSi_2-Al_2O_3 thermocouple embedded in 80/20 alumina substrate and sintered at 1550 °C, 2 h and the preform was tested isothermally at 1350 °C, 10 h in argon atmosphere.

A thermocouple with composition [75-25] vol% $MoSi_2$-Al_2O_3//WSi_2-Al_2O_3, sintered at 1600 °C for 2 hours in argon atmosphere was used for the oxidation study. The oxidation test was conducted at an isothermal hold of 1350 °C for 10 hours in pure argon, 1 % O_2 and balance argon and 5 % O_2 and balance argon respectively in a high temperature tube furnace. The post-test thermocouple and oxidation test results are presented in Fig. 3.37 and Fig. 3.38. Initially, as expected, the thermoelectric voltage increases with increasing temperature linearly with a maximum thermoelectric voltage of 21.3 mV at 1350 °C, during the first run conducted in pure argon gas. Similarly, very little variation in the thermoelectric voltage was observed when the thermocouple was tested in 1 % O_2 and 99 % Ar gas, indicating a limited oxidation resistance to the formation of SiO_2 layer. However, the third run conducted in 5% O_2 balance argon mixture gas the thermocouple failed due to oxidation after 9 hours of operation at 950 °C which is clearly evident from the crack appeared along the length of the sensor which caused due to the disintegration of the 80-20 alumina substrate and subsequent oxidation of the sensor tapes.

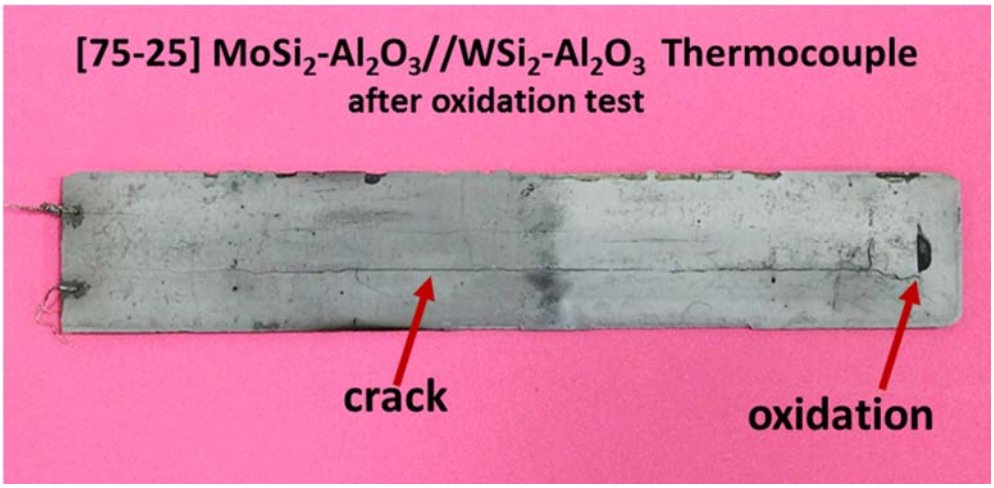

Figure 3.37. Post-oxidation test photograph of [75-25] vol. % $MoSi_2$-Al_2O_3//WSi_2-Al_2O_3 thermocouple sintered at 1600 °C for 2 hours in argon atmosphere. The thermocouple is embedded within 80/20 composite alumina substrate

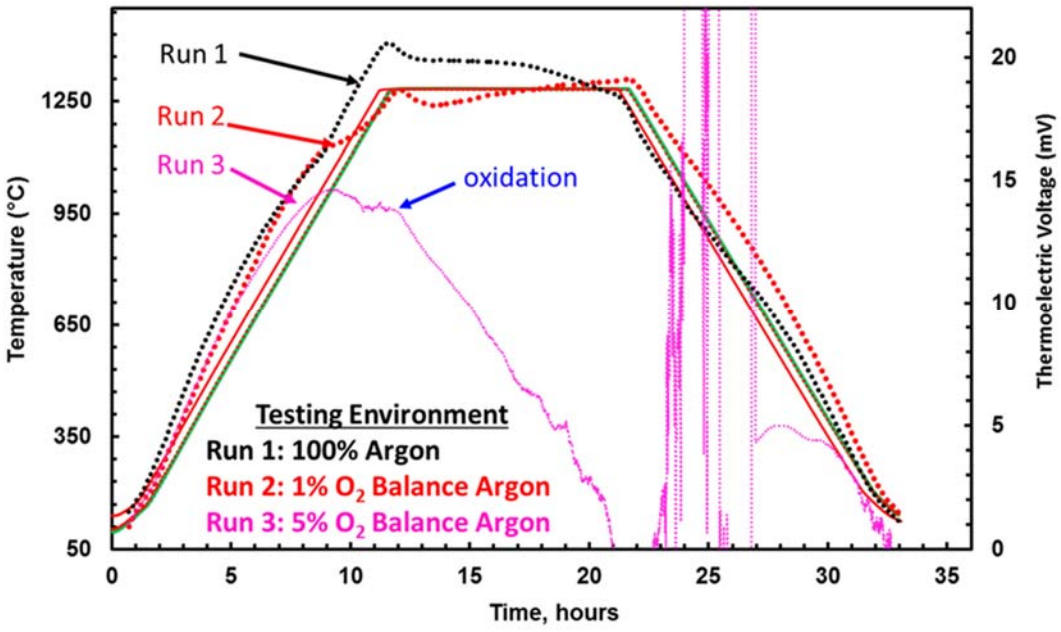

Figure 3.38. Oxidation study of the thermocouple with configuration [90-10] vol.% $MoSi_2$-Al_2O_3//WSi_2-Al_2O_3. The oxidation study was conducted as (a) Run1: 100% argon (b) 1% O_2 balance argon and (c) Run3: 5% O_2 balance argon.

Mitra et al. studied the oxidation behavior of $MoSi_2$ and WSi_2 and reported that both silicides exhibits similar oxidation behavior and distributed into four regimes, (a) 400-600 °C; (b) 600-

1000 °C; (c) 1000-1700 °C; (d) beyond 1700 °C. In the temperature range of 400-600 °C, these silicides undergo accelerated oxidation known as pesting, due to discontinuous formation of SiO_2 protection layer caused by the lower diffusivity of oxygen anions at these temperatures. Above 1000 °C, a continuous protective SiO_2 layer forms in the case of $MoSi_2$. However, in the case of WSi_2 loss of mass is reported at 1200 and 1500 °C due to the formation and volatilization of WO_3. Above 1700 °C oxidation resistance decreases due to the decrees of viscosity of SiO_2 which in turn produces large number of defects[3.23]. Our density study also reveals that WSi_2-Al_2O_3 composite is only 87.5 % dense which would effectively accelerate oxidation. All our studies pointing to the fact that the enhanced densification of the sensor as well as alumina substrate are very crucial for the long time operation and sustainability of our high temperature ceramic sensors and we will be continuing our efforts to densify the sensor components by using fine alumina powder as well as high temperature sintering for long time in argon atmosphere.

In order to reduce oxidation and improve densification of the silicide-based preforms, the long thermocouples and thermistors were fabricated with a pre-milled fine alumina powder (SA: 8.6 m^2/g). Figure 3.39 shows the photograph of [75-25] vol.% WSi_2-Al_2O_3 thermistor embedded in fine alumina substrates. The thermistors were sintered at 1600 °C for 2h in argon atmosphere and the photographs of the sintered thermistor is shown in Fig. 3.40. The sintered thermistor preform densified crack free.

Figure 3.39. Photograph of [75-25] vol% WSi_2-Al_2O_3 thermistor green preforms embedded in fine alumina (SA: 8.6 m^2/g) substrates (length 8 ¾" and thickness ~650 μm).

Figure 3.40. Photograph of [75-25] vol% WSi_2-Al_2O_3 thermistors embedded in fine alumina and sintered at 1600 °C for 5h in argon atmosphere.

Figure 3.41 shows the electrical response (Resistance vs Temperature) of the thermistor measured to 1350 °C with 5 hrs hold in argon atmosphere. in argon atmosphere. As we can see the resistance of the embedded thermistor increase with increase in temperature and delivered a maximum and stable resistance of 6 Ω at 1350 °C. There was no fluctuation of resistance observed throughout an isothermal hold for 10 hours under argon atmosphere. Figure 3.42 is a photograph of the [75-25] vol.% WSi_2-Al_2O_3 thermistor after testing at 1350 °C for 10h in argon atmosphere. The resistance measurements and post-test visual evaluation of the thermistor preform indicate that stable, oxidation free silicide-based sensor was successfully fabricated.

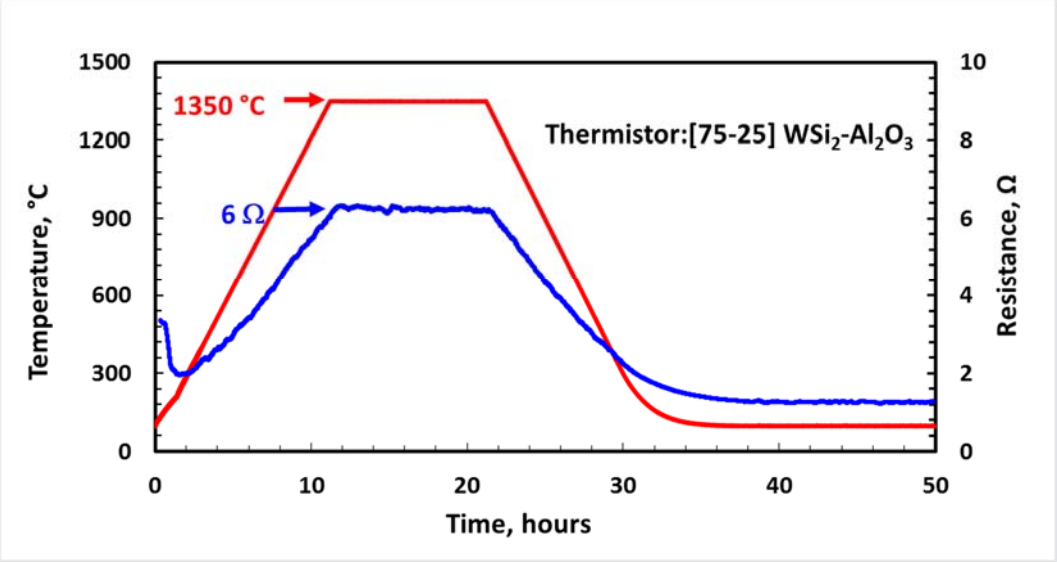

Figure 3.41. Temperature dependent resistance of [75-25] vol.% WSi_2-Al_2O_3 thermistor sintered at 1600 °C, 2h and tested at 1350 °C for 10h in argon atmosphere.

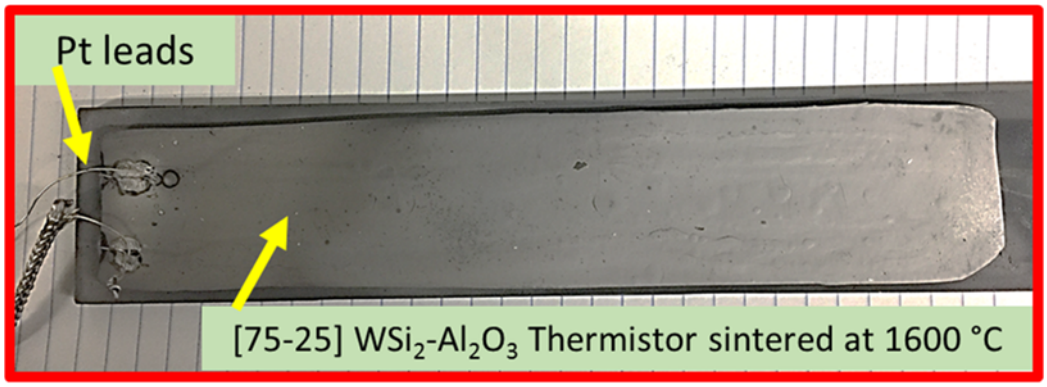

Figure 3.42. Post-test photograph of [75-25] vol% WSi_2-Al_2O_3 thermistor tested at 1350 °C, 10h.

3.3.4 Oxide-based Thermistors:

The La_2NiO_4 (LNO) composition was selected for the oxide-based sensor material. LNO powder was synthesized using a conventional solid state reaction route. Figure 3.43 show the XRD patterns of the calcined LNO powder sample. The X-ray analysis confirms single phase formation matching formation matching K_2NiO_4 crystal structure (JCPDF #01-089-3460). No additional phase formation was observed in the X-ray analysis.

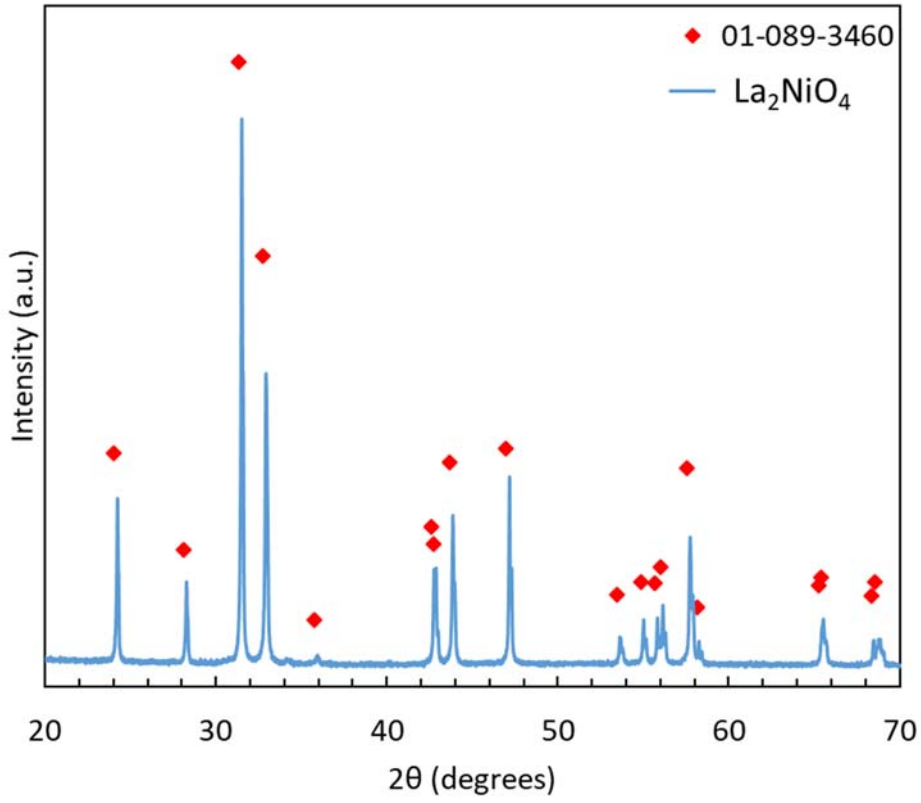

Figure 3.43. X-ray diffraction pattern for the La_2NiO_4 (LNO) calcined at 1200°C and matched with matching K_2NiO_4 crystal structure (JCPDF #01-089-3460).

Figure 3.44 shows the evolution of LNO thermistors from LNO inks screen printed on green YSZ substrates to co-sintered LNO thermistors inside the YSZ embedding layers. The initial LNO thermistors were fabricated with as- synthesized LNO powder, co-sintered at 1350 °C and tested to 1350 °C for 5 h. This initial thermistor was build using two LNO inks: 50 vol% LNO: 50 vol% YSZ (50:50 LNO:YSZ) composite ink and 100 vol% LNO ink. The function of the 50:50 LNO: YSZ composite ink was to ensure adhesion between YSZ substrate, while LNO conductive core was formed with 100 vol% LNO ink.

Figure 3.44 Images showing LNO thermistors: a) green, b) sintered, and c) sintered imaged on a light box to highlight embedded sensor material.

Figure 3.45 shows testing results for the initial sensor. The sensor showed promising results with a slight decrease in resistance over the high temperature hold. Following this result, a set of thermistors were fabricated and casted inside the chromia-based bricks. The brick fabrication protocol calls for a sintering temperature >1500 ºC. During sintering of the bricks, the LNO thermistors fabricated with fine LNO powder lost conductivity due to excessive coarsening of the sensor material at 1500°C.

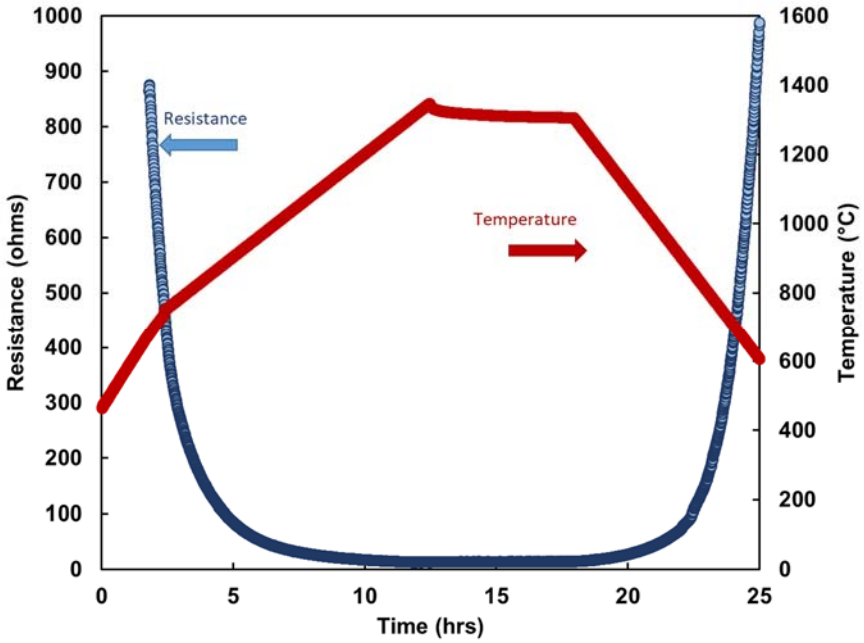

Figure 3.45 Resistance and temperature profile of LNO based thermistor co-sintered inside YSZ at 1350°C and tested to 1350°C. The thermistor material consisted of 100 vol% LNO core and 50:50 vol% LNO:YSZ intermediate layer inside YSZ shell.

In order to prevent coarsening of the sensor material at sintering temperature used for fabrication of chromia-based bricks, two new LNO-based inks were prepared and screen printed onto YSZ substrates. The inks were prepared with LNO powder calcined to 1000°C (LNO-1000). This coarser LNO powder was incorporated into 50 vol% LNO: 50 vol% YSZ composite ink for intermediate layer and 70 vol% LNO: 30 vol% YSZ composite ink for the conductive core layer. The inclusion of YSZ phase into the conductive core layer ink was expected to further limit coarsening of the material during brick sintering. The screen printed, laminated thermistors were sintered to 1450°C for 2 hrs in air.

Figure 3.46 shows secondary electron microscope (SEM) images of the evaluated thermistors and graphical layout of the layers and YSZ shell. SEM show that 100 vol% LNO core made with as-received LNO powder, sintered and separated from the intermediate 50:50 LNO:YSZ layer possibly resulting in the resistance increase. The core produced with the LNO-1000 material and consisting of 70:30 LNO:YSZ appears more porous, which indicates inhibited sintering most likely due to incorporation of YSZ phase inside the core layer. Additionally, the LNO-1000 did not separate from intermediate layers indicating microstructurally more stable system.

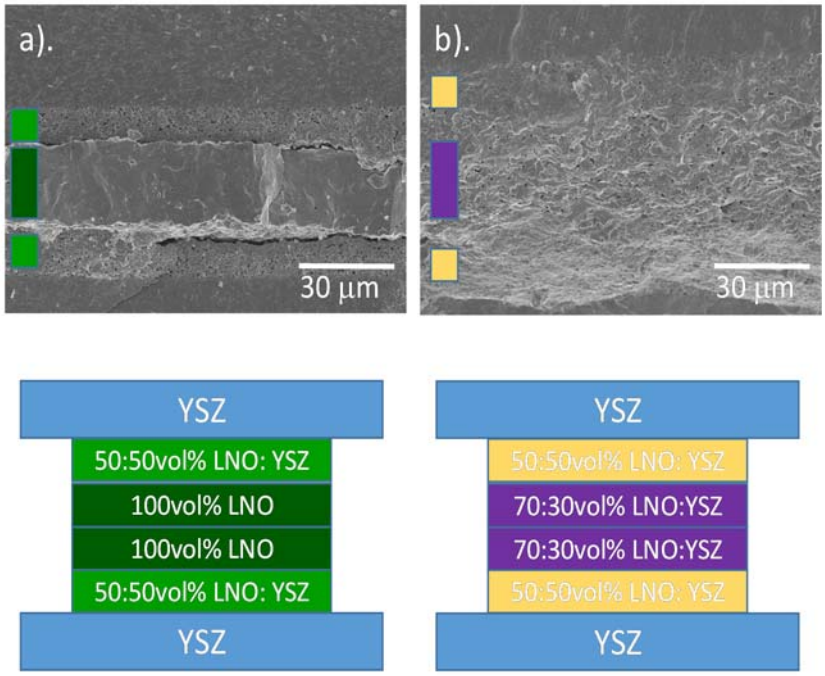

Figure 3.46 SEM images and graphic depiction of thermistors' construction showing the following thermistors: a). LNO (as-received) thermistor in YSZ sintered at 1350°C, and b). LNO-1000 thermistor in YSZ sintered at 1450°C.

In order to evaluate longer term stability of the sensor, the LNO-based thermistor was tested to nearly 100 hrs at 1400°C. At this point, the thought was that the sensor material is still undergoing coarsening. Figure 3.47 shows the resistance over 100 hours long high temperature hold for the LNO-based thermistor fabricated with LNO-1000 powder. This graph illustrates continuous decrease in resistance from 22.38 to 20.00 ohms (10.63% change) over the duration of the test. Based on these results, the next set of LNO-based inks will use powders calcined to 1200 and 1400°C to eliminate coarsening of the microstructure during testing as well as evaluate these thermistors at lower temperature of 1350°C.

The 1200°C and 1400 °C coarsen LNO powders were incorporated into two sets of 50 vol% LNO: 50 vol% YSZ composite ink for intermediate layer and 70 vol% LNO: 30 vol% YSZ composite ink for the conductive core layer. To differentiate, the sensors made with powders calcined either at 1200°C or 1400°C will be noted as LNO-1200 or LNO-1400 thermistors. The screen printed, laminated thermistors were sintered to 1450°C for 2 h in air. The sintered preforms were embedded into high-chromia bricks. The cast bricks were then sintered to 1450°C for 10 h in air.

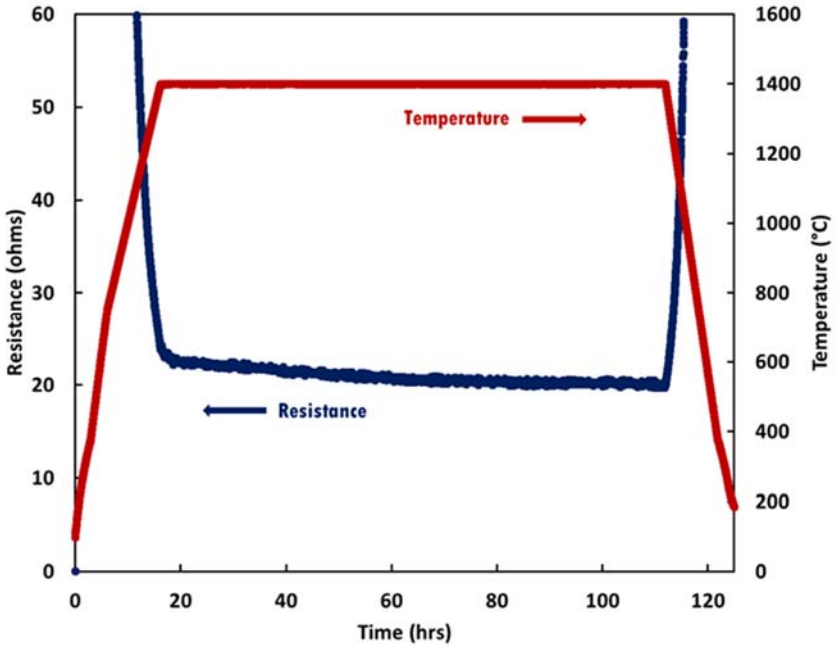

Figure 3.47 Resistance and temperature profile LNO-1000 based thermistor co-sintered inside YSZ at 1450°C and tested for 100 hrs at 1400°C. This graph illustrates continuous decrease in resistance from 22.38 to 20.00 ohms during the high temperature hold (10.63% change).

3.4 Conclusions:

The following is a list of accomplishments for the sensor patterning and embedding task.

1. All-ceramic thermocouple and thermistor preforms (and smart bricks) were fabricated and successfully tested, but issues with interconnection.
2. Silicide/oxide thermocouples and thermistors first reported in literature.
3. Methods to stabilize degradation in silicide composite sensors were developed, and implemented (but alternative compositions were transitioned to in August 2016).
4. Two new alternative oxide-based systems were investigated and preforms were developed (and embedded into smart bricks).

Task 4: Static and Dynamic Sensor Testing of Smart Refractory Specimens

4.1 Introduction:

The objective of this task was to incorporate the ceramic sensor preforms developed in Task 3 into the high-chromia bricks to form the proposed "smart refractory". Smaller prototypes of the smart refractory were then machined (or directly formed) into a cup structure, so that coal fly ash can be placed into the brick. After heating the ash to high temperature, a slag would be formed and penetrate down through the brick. This overall testing setup would provide an opportunity to test smart brick, electronics and communication, and initiate data that could be used within the modelling task. The specific subtasks were as follows:

Subtask 4.1 Cup Corrosion Testing of Smart Refractory- Prototype refractory brick and/or cup samples will be fabricated and tested within static slag conditions at 900-1450ºC extending over 24-250 hours. The sensor designs demonstrated in Task 3 will be initially utilized. Platinum hard lines will be used for sensor interconnection to DMM, impedance, and/or LCR meters. Post-mortem chemical and microstructural analysis will be compared to sensor output over the test, and electrical and refractory degradation data will be fed into Task 7.

Subtask 4.2 Dynamic Slag Testing of Smart Refractory- Similar tests completed in Subtask 4.1 will be completed in this task, but the tests will be completed in a WVU small-scale dynamic slag test stand. Larger-scale smart bricks will be incorporated into a furnace that rocks in order to provide slag movement within the cup-shaped bricks. This work will attempt to obtain electrical sensor performance during dynamic testing of the smart bricks at high-temperature. As in Subtask 4.1, electrical and degradation data (from chemical and microstructural analysis) maybe used in Task 5 and 6.

4.2 Experimental Methods:

4.2.1 Brick Fabrication

The thermistors/thermocouple preforms were embedded into high-chromia refractory brick at HarbisonWalker International (HWI, West Mifflin, PA, USA). The formulation of the brick composition is an intellectual property of HWI. The pre-sintered sensor preforms were embedded into brick material during casting of the high-chromia bricks. Several different brick designs were introduced throughout the program. There were 4 x 4 x 4 inch bricks for initial work for all material and sensor design systems as well as slagging experiments. Silicide-based thermistors and thermocouples also utilized long and narrow, 2 x 2 x 8 inch bricks for slag penetration experiments under argon atmospheres. In each case, the bricks were molded with cup-shaped cavity designed for slag testing mimicking infiltration and corrosion of the bricks during application. The design ensured that the tip of the thermistor was situated 1 cm below the bottom of the cavity. The cast bricks with silicide-based sensors were sintered to 1600 °C for 10 h in argon. The cast bricks with oxide-based thermistors were sintered to 1450 °C for 10 h in air.

4.2.2 Slag Preparation

Three slag compositions based on SiO_2-CaO-Fe_2O_3 ternary phase diagram were selected for this study to represents the slag used in coal gasifiers. Slag mimicking powders were synthesized using a conventional solid state reaction route. The stoichiometric amounts of high purity SiO_2, CaO, Fe_2O_3 and MgO powders (Alfa Aesar, USA) were uniformly mixed by roll mill using zirconia media in ethanol for 24 h. The resultant slurry was dried overnight and sieved into a fine powder. Eight grams of fine slag powders was die pressed into cylindrical pellets of dimension 1″ diameter and 1 cm thick. The slag pellets were biscuit fired at 800 °C for 1 h in order to reduce their volume.

4.2.3 Electrical Testing

In order to electrically evaluate the sintered high-chromia bricks with embedded preforms, it was necessary to expose the sensor material and connect it to platinum wire leads. After the bricks were sintered, a 5 mm slice was cut off the end of a brick to expose sensor leads. Two platinum wires were stretched across the exposed sensor material and cemented to the brick with Ceramabond™ 569 (Aremco Products Inc., Valley Cottage, NY) at two points without letting the cement touch the sensing material. Each wire was then attached to exposed sensor legs with Pt ink for silicide-based sensors and LNO-based ink for LNO-based sensor material. For LNO-based sensors, the Pt electrical connection was cured at 1350 °C for 2 h in and air. The electrical response versus temperature was continuously collected using a two-point DC measurement with a Keithley 2100 DMM using a National Instruments LabView™ program.

4.3 Results and Discussion:

4.3.1 Small Size Bricks with Silicide-based Thermistors

The initial silicide-based thermistors to be embedded in bricks were produced screen printing U-shaped sensor material unto pre-cut alumina substrates. Another alumina substrate was laminated on top to cover the sensor material and the entire piece was co-sintered to form silicide-based thermistor preform as showin in Fig. 4.1. The composition of the sensor material was [60-40] vol% $MoSi_2$-Al_2O_3.

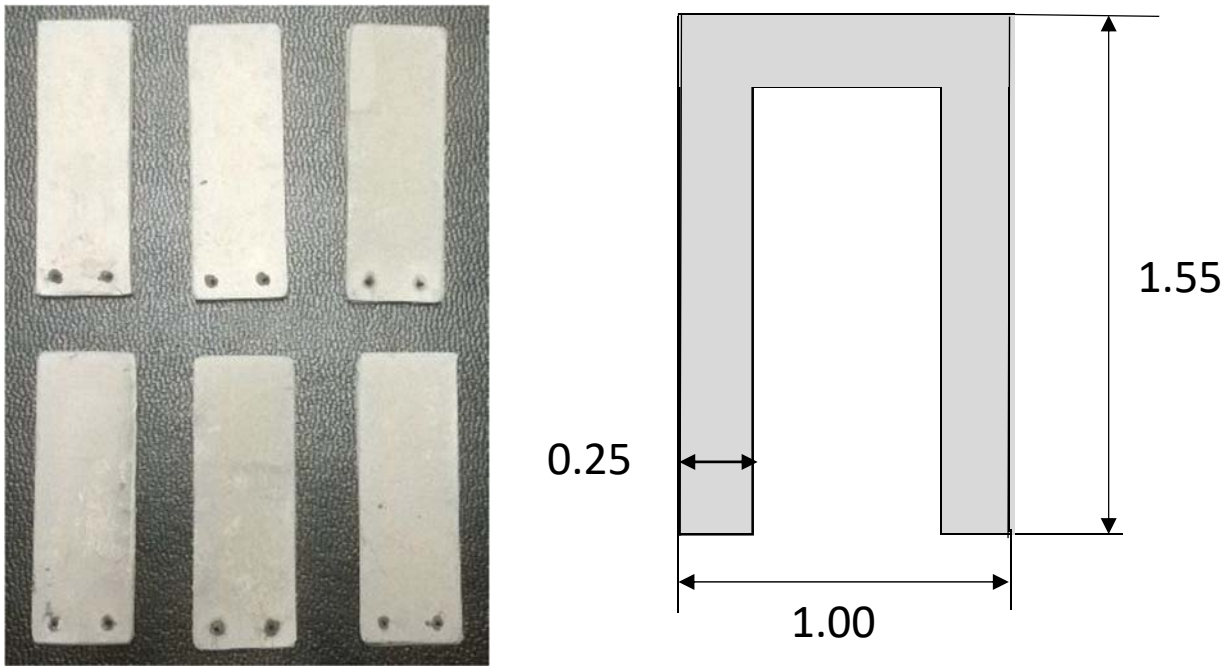

Figure 4.1. [60-40] vol% $MoSi_2$-Al_2O_3 thermistors screen printed on and laminated with Al_2O_3. The dimension of the thermistor is given on the right side.

Figure 4.2 shows the chromia refractory brick embedded with two separate temperature sensors before heat treatment. The experimental set up to measure the resistance of the temperature sensor as a function of temperature for extended hours (>250h) is shown in Fig. 4.3 which consists of Pt contact leads and Cu connecting wires. Figure 4.4 shows the performance analysis result of [60-40] vol% $MoSi_2$-Al_2O_3 temperature sensor for 250 hours at 1350 °C in Ar atmosphere. It is clearly evident from the figure that the embedded sensor exhibited stable behavior for 250 hours at a high temperature 1350 °C. The resistivity of the thermistor has been calculated from the resistance and found that resistivity increased with increase in temperature up to 1350 °C then it decreased which is the typical characteristic of PTC thermistors, as shown in Fig. 4.5.

Figure 4.2. Chromia brick showing the embedded sensor.

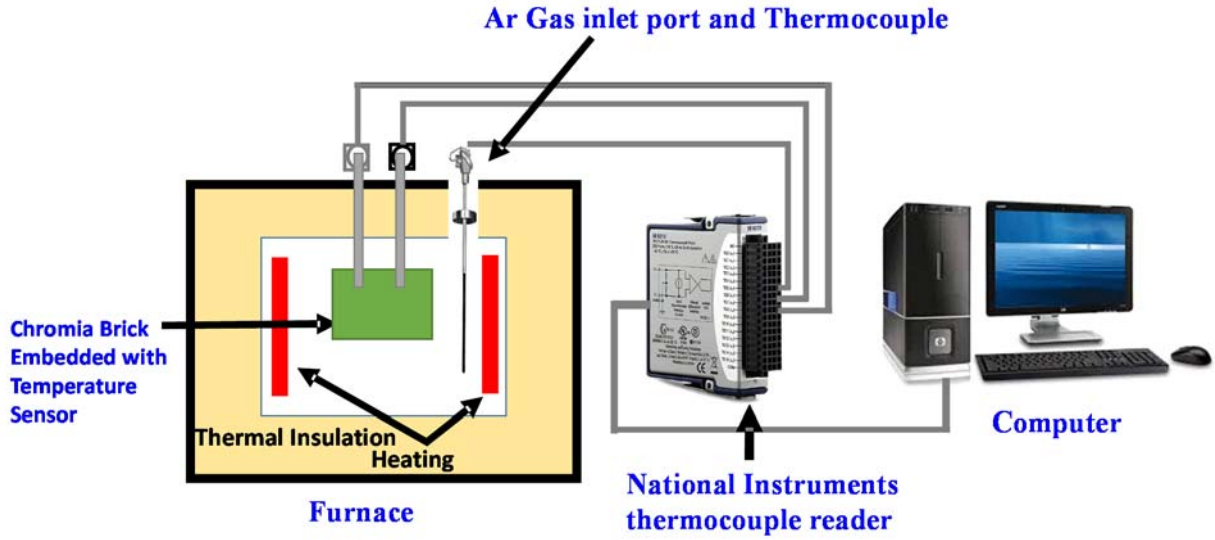

Figure 4.3. The schematic showing experimental set up used for the cup corrosion test.

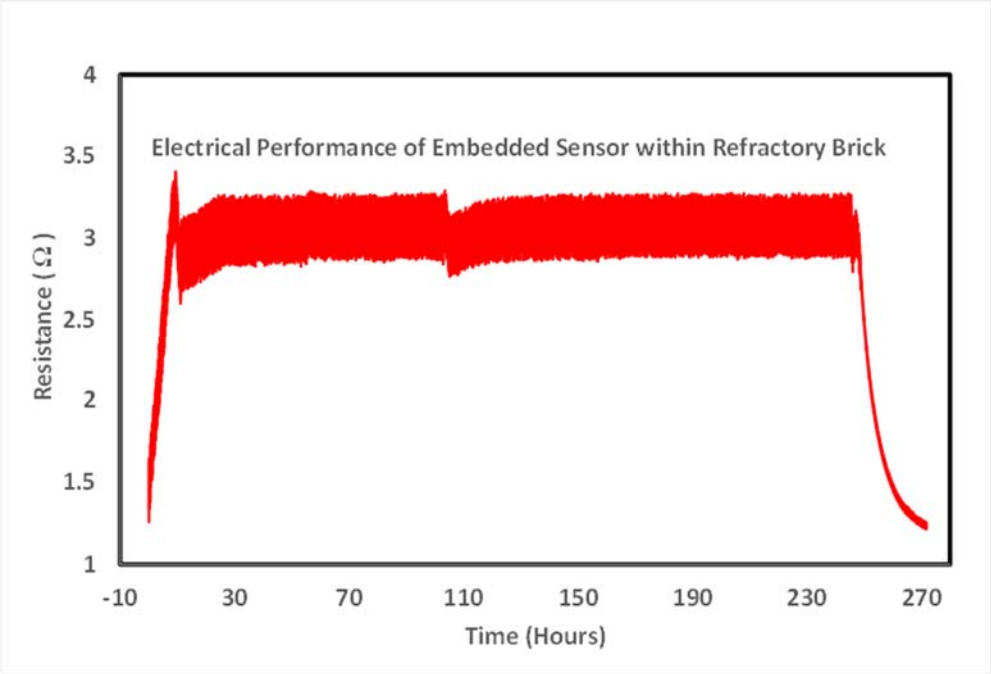

Figure 4.4. Performance analysis of [60-40] vol% $MoSi_2$-Al_2O_3 temperature sensor for 250 h.

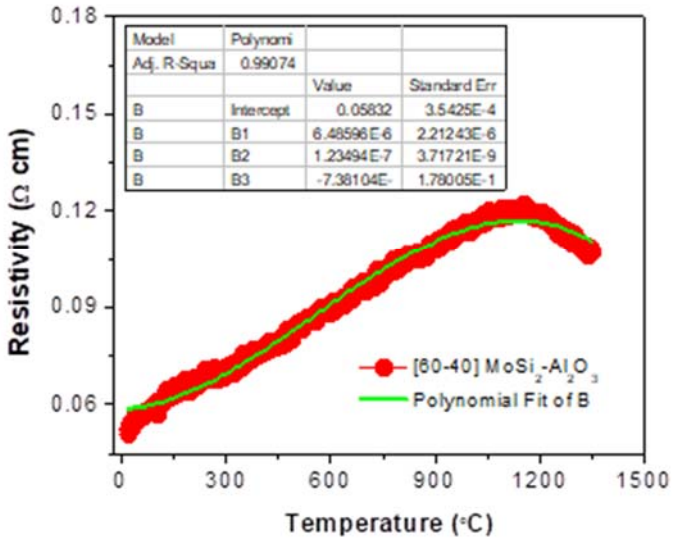

Figure 4.5. The resistivity of the thermistor increased with increase in temperature up to 1350°C then it decreased exhibiting a typical PTC thermistor characteristics.

4.3.2 Long Bricks with Silicide-based Thermocouples

In order to maintain hot junction and cold junction temperatures of the thermocouples and thereby to more accurately evaluate the performance of thermocouple under reducing conditions, the brick design was altered so that the bricks would fit inside 3-inch diameter tube furnace. The longer and more narrow bricks required a redesign of the sensor dimensions and preform microstructure. The substrate was fixed as 80/20 vol. % coarse/fine alumina laminates with thickness ~ 600 μm. These types of long thermistors and thermocouple green bodies were stenciled onto the alumina substrates, laminated to enclose sensor in alumina shell and then fired at 1500 °C, 2h in argon atmosphere. The sintered sensor preforms were embedded in long bricks. Figure 4.5 shows the green body of smart bricks embedded with sintered preforms of long thermistors/thermocouple sensors. These bricks were sintered at 1500 °C for 10 hours in argon atmosphere. After sintering, one end of the brick was trimmed to expose sensor material to make connections with Pt leads.

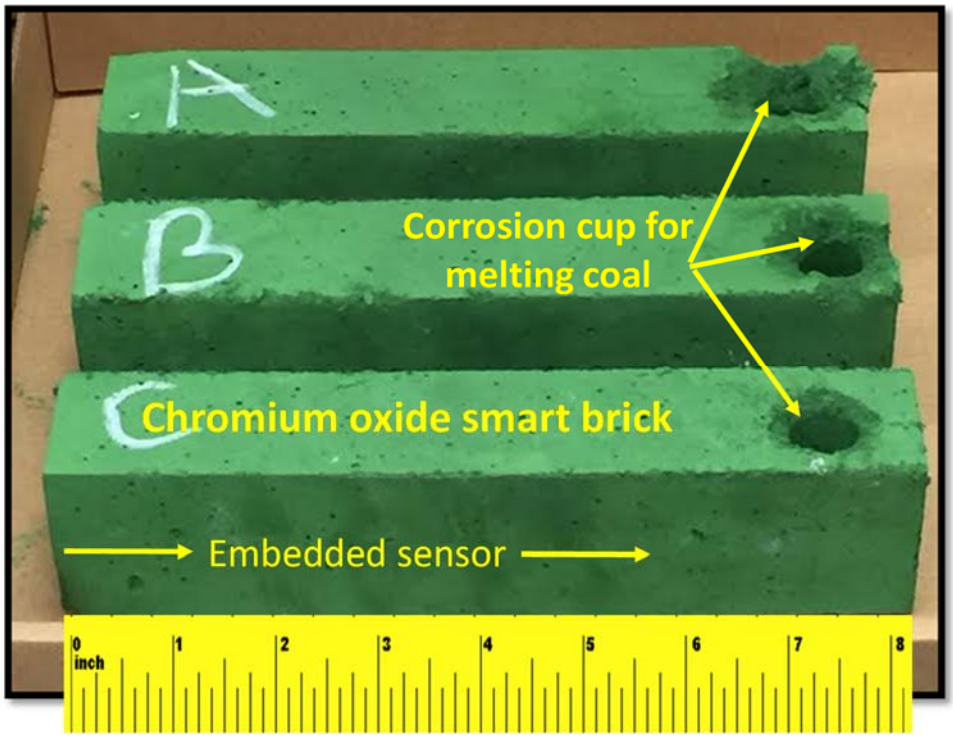

Figure 4.5. Photographs of green body of smart bricks embedded with sintered preforms of long thermistors/thermocouple sensors, slip casted at HWI (HarbisonWalker International).

Figure 4.6. shows the optical micrograph of the cross sectional interface of the smart brick sintered at 1500 °C for 10h in argon atmosphere. The sensor material appears to be well bonded with the alumina substrate as well as the chromium oxide refractory brick. No cracks or delamination occurred while trimming. The thickness of the sensor was measured as 120 μm. The exposed sensor legs were polished and connected to copper wire leads for electrical characterization. These embedded sensors were 8'' long and hence were placed in the furnace so that the electrical connections from the sensor leads were outside the hot zone of the furnace. This helped to maintain a cold junction temperature especially in the case if thermocouples and also allowed for the use of

silver wire and silver-based ink in place of expensive platinum ink and platinum wire as connection leads.

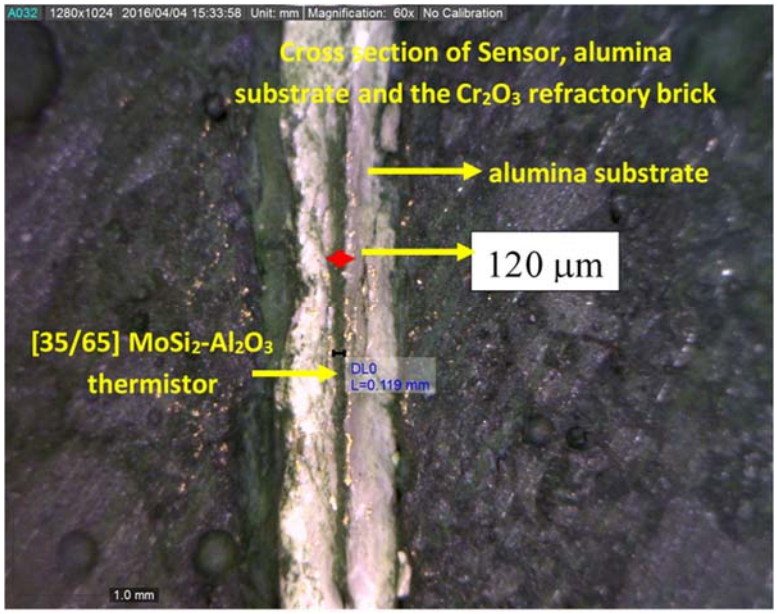

Figure 4.6. Optical micrograph of the cross sectional interface of the smart brick embedded with [35-65] vol. % $MoSi_2$-Al_2O_3 long thermistor.

Numerous smart bricks embedded with [75-25] vol. % $MoSi_2$-Al_2O_3 (coarse Al_2O_3)// [75-25] vol. % WSi_2-Al_2O_3 (coarse Al_2O_3) thermocouple were fabricated. All the bricks were sintered at 1500 °C for 10 h in argon atmosphere and the sensor legs were exposed by cutting and polishing one end of the brick. The exposed sensor legs were first coated with Ag/Cu nano ink and annealed at 800 °C for 1h in argon atmosphere and subsequently connected to Ag wire leads for electrical contacts. Figure 4.7(a). shows a [75-25] vol. % $MoSi_2$-Al_2O_3 (coarse Al_2O_3)//[75-25] vol. % WSi_2-Al_2O_3 (coarse Al_2O_3) thermocouple embedded smart brick connected to silver wire using Ag epoxy and ready to test. Figure 4.7(b). describes the way silver electrical wires are taken out from the sensor and Figure 4.7(c). shows the front view of the insulated testing arrangement of smart brick. We can clearly see the silver wire leads coming out of the brick. A K-type thermocouple was connected at the cold junction of the thermocouple to monitor cold junction temperature.

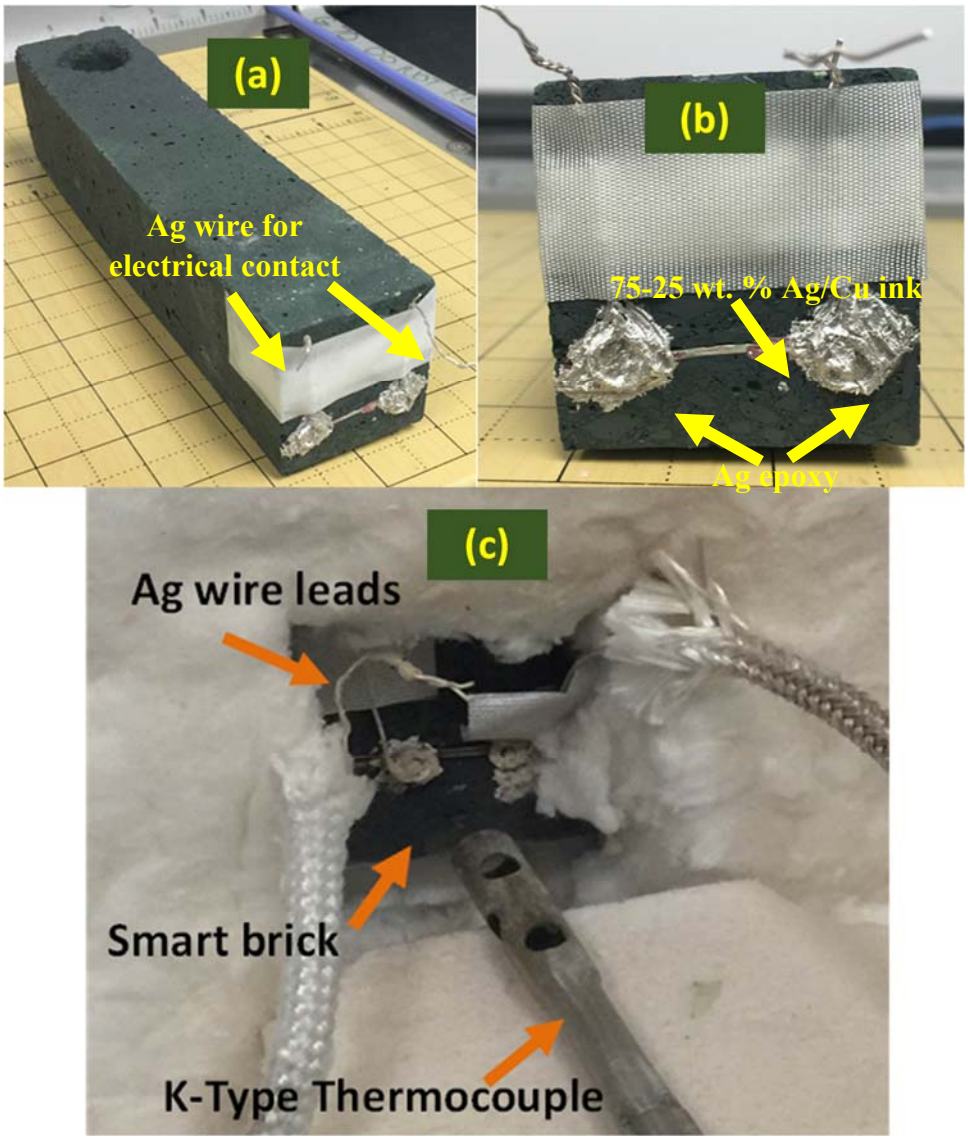

Figure 4.7. (a) Smart brick with embedded with TC : 34-79D[75-25] vol. % $MoSi_2$-Al_2O_3 (coarse Al_2O_3) // 34-79E[75-25] vol. % WSi_2-Al_2O_3 (coarse Al_2O_3) sintered at 1500 ºC, 2h in Argon; **(b)** Silver wire leads, connected to sensor using silver epoxy and Ag/Cu ink; **(c)** Thermoelectric testing arrangement of thermocouple embedded smart brick in an atmosphere controlled chamber furnace. The K-type thermocouple reads the cold junction temperature.

However, the thickness of the long embedded sensors, fabricated by stencil lithography was proven to be too thin (~ 110 μm). The stenciled thermocouples were too difficult to connect to the leads and the poor distribution of the matrix limited the percolation of conducting species. As a result, the embedded sensors were not conductive. In order to solve this issue, the stenciled sensors were replaced by tape cast thermocouples and temperature sensors. Figure 4.8 below shows photographs of various stages of fabrication for tape casted long temperature sensors. Figure 4.8. (1) shows the tape casted temperature sensor with no filler material, (2) shows the green laminated sensor preforms before firing and (3) Sensor preforms sintered at 1550 °C in argon. These sintered sensor

preforms were later used for embedding work which focused on testing thermistors in slagging experiments.

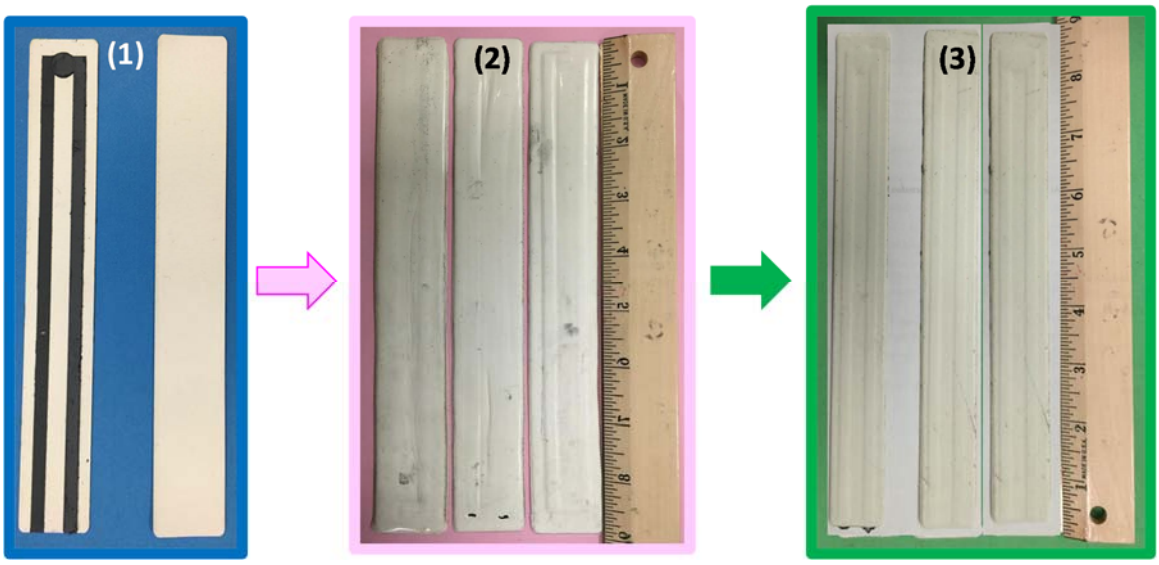

Figure.4.8. Photographs of tape casted long temperature sensors (1) Thermistor tapes laser cut and placed on composite alumina substrates with lid before lamination (2) Laminated sensor preforms before firing (3) Sensor preforms sintered at 1550 °C in argon.

4.3.3 Slag Testing of Embedded Silicide-based Sensors

It has been reported that accurately predicting the softening and melting temperature of coal compositions is very challenging due to variation in the constituents of the coal and its interactions during heating. For this study, the melting point of slag is found to be around 1350 °C. Jones and Buller characterized numerous compositions of coal ash and relate then to their softening temperature [4.1]. Based on their data and with an aid of SiO_2/Al_2O_3, Fe_2O_3, CaO ternary phase diagram, shown in Fig. 4.9, three different slag compositions have been identified with an addition of small amount of MgO to reduce the melting temperature. The compositions of the three slag compositions used in this study are presented in Table 4.1.

Table 4.1. Slag compositions used in melting and penetration experiments.

Name of the slag prepared	Compositions of the slag	Melting Temperature (°C)
Illinois # 6	$34.76SiO_2$-$23.38Fe_2O_3$-6.75CaO-1.12MgO	1500
Pocahontas	$60SiO_2$-$30Al_2O_3$-$4Fe_2O3$-0.6CaO-0.6MgO	1450
Lignite coal	$44.3SiO_2$-$5.26Fe_2O_3$-17.5CaO-6.64MgO	1300

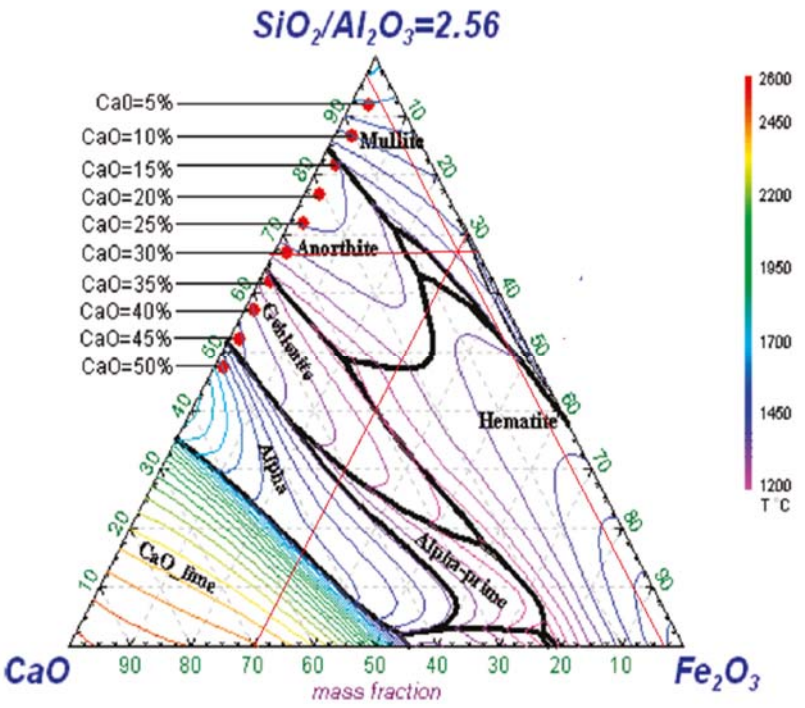

Figure 4.9. Phase diagram of CaO-Fe_2O_3-Al_2O_3/SiO_2.

The coal slag compositions have been prepared by solid route by mixing appropriate amounts of SiO_2/Al_2O_3, Fe_2O_3, CaO and MgO. The powder mixture was ball milled in ethanol, dried and sieved. Figure 4.10 shows the photographs of three slag compositions prepared (a) Illinois #6 (b) Pocahontas (c) Lignite coal. The well mixed powders were consolidated to pellets. Pellets' melting temperature was tested in 1300-1500 °C temperature range using shallow chromia crucibles. It was observed that the bituminous slag Illinois #6 was melted at 1500 °C, Pocahontas melted at 1450 °C and the lignite coal slag was melted 1300 °C. Figure 4.11 shows the melting behavior of the three slag compositions. From the experimental matrix, the lignite coal slag was selected for static/dynamic cup corrosion test.

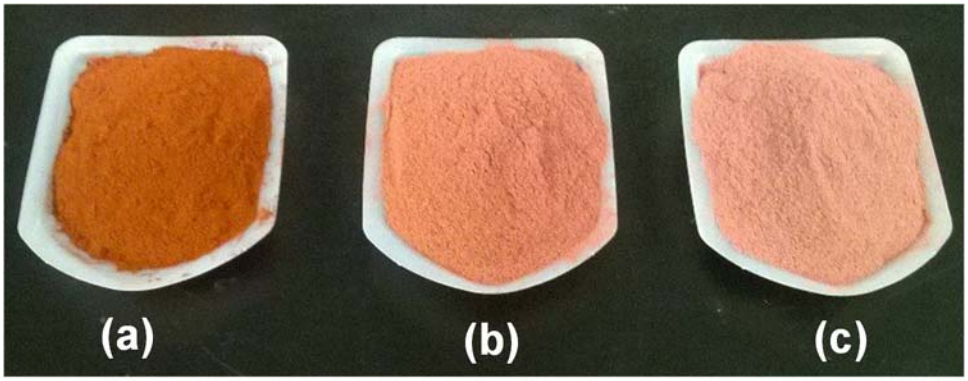

Figure 4.10. Photographs of three slag compositions prepare (a) Illinois #6 (b) Pocahontas (c) Lignite coal.

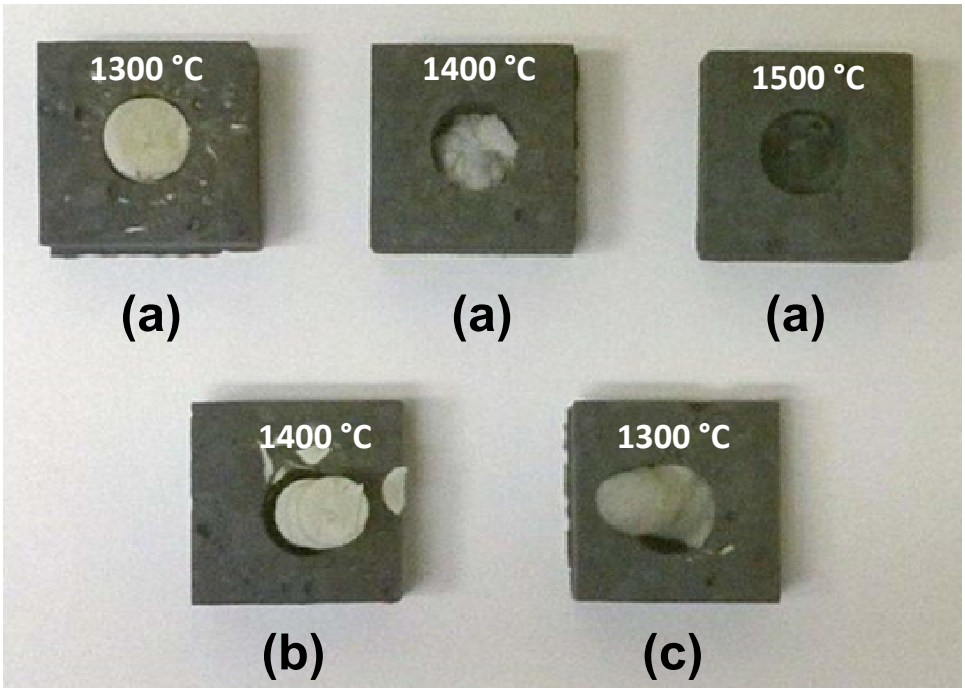

Figure 4.11. Photographs of three slag compositions melted in chromia refractory crucibles (a) Illinois #6 (b) Pocahontas (c) Lignite coal.

Slag composition mimicking lignite coal slag was used in penetration experiments in high-chromia bricks. The brick's cavity was filled with twenty eight-gram pellets. The brick was placed in a furnace and heated to 1350 °C. Figure 4.12 show a profile of a brick used in slag experiments and an internal cavity of the brick containing melted slag after heat treatment.

Figure 4.12. Images of a profile of a brick used in slag experiments and an internal cavity of the brick containing melted slag after heat treatment.

Post corrosion tests were performed using optical as well as scanning electron microscope. The bricks were cut into half and the fracture surface of the bricks were examined under optical microscope. The penetration depth of the slag was estimated from the difference in color as shown in Figure 4.13. The slag penetration depth increased with increase in hold time. The sample which hold at 1350 °C, 10 h exhibited slag penetration throughout the volume of the brick.

It is worth to mention here that the complete penetration of the slag through the brick made it difficult to conduct the static cup corrosion test with sensor embedded bricks for 250h. The lab scale experimental set up to study the cup and corrosion test does not provide a temperature difference across the refractory brick that is present when the bricks line the wall of gassifiers.

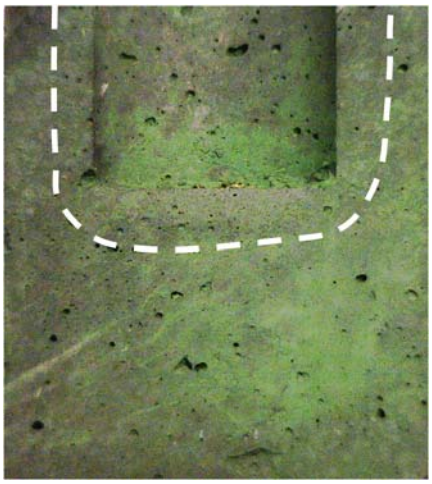

Figure 4.13. The optical micrograph showing the penetration of the slag. The marked (white dash lines) portion show the penetration of slag.

The thermocouples for static cup corrosion tests were fabricated through tape casting technique. The composition of the thermocouple was [90-10] $MoSi_2$-Al_2O_3//WSi_2-Al_2O_3. The $MoSi_2$-Al_2O_3 and WSi_2-Al_2O_3 powder were tape cast and laminated into 800 µm thick laminates. The two parts of the thermocouple were laser cut into L-shapes and then laminated in between two alumina substrates 100 µm thick, so that the two silicide tapes overlap in the center. The thermocouple laminate was laser cut into appropriate shape and size (4 cm X 1 cm). The thermocouples were embedded horizontally into the chromia refractory such a way that the legs of the thermocouple were exposed towards the side wall of the brick as shown in Fig. 4.14(a). The thermocouples laminated with alumina are shown in Fig. 4.14(b). The sensors were implanted at various locations along the direction of molten slag diffusion.

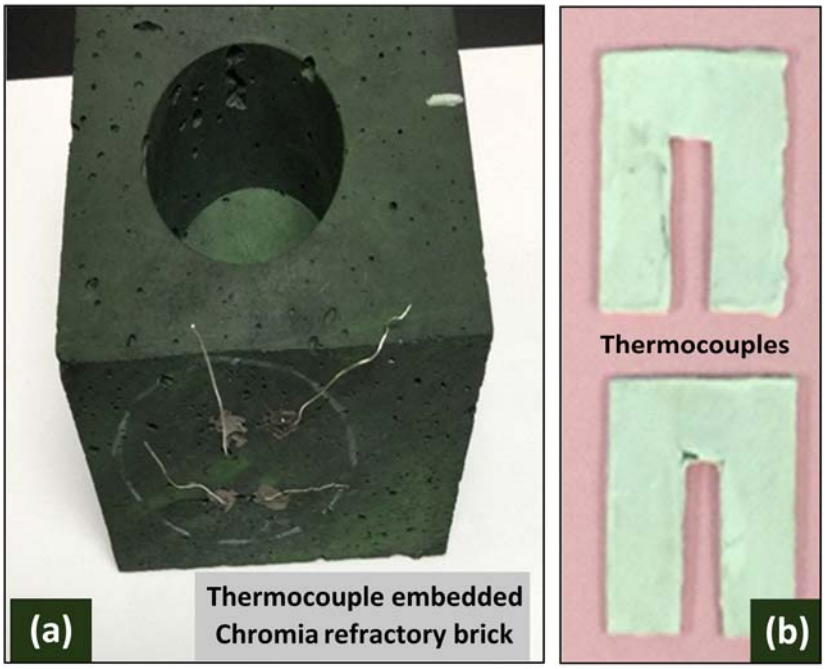

Figure 4.14. (a) Photograph of Cr_2O_3 refractory cup embedded with thermocouples for static cup corrosion test (b) screen printed thermocouples lamented with alumina tape.

In order to perform the static cup corrosion test, slag samples were prepared with chemical composition was similar to lignite coal slag. The slag powder was consolidated into pellets and biscuit fired at 800 °C for 1 h in order to make sure that a sufficient amount of slag is filled in to the refractory cup for corrosion test. The brick filled with slag pellets was heat treated to 1500 °C for 5 h heat treatment in Ar atmosphere and the melted slag diffused into Cr_2O_3 refractory brick. Figure 4.15(a) shows the interior of the brick cavity after heat treatment with small amount of melted slag that did not penetrate the brick. Optical microscopy was used to study penetration of slag into refractory brick. The refractory cup was cut centrally to expose the slag penetration profile. The fracture specimen was further polished to 1 μm level. It is clearly evident from the figure that the penetration depth of the slag along the length of the cup was ~3.41 cm. After completing the optical microscopy study, the refractory specimens were subsequently cut into small pieces for Scanning Electron Microscopy (SEM) study. Figure 4.15(b) and (c) show the electron microscopy images of refractory cup specimen. SEM analysis confirmed that molten slag penetrated into the refractory cup specimen up to depth of 3.41 cm. Beyond 3.41 cm only Cr_2O_3 grains were identified.

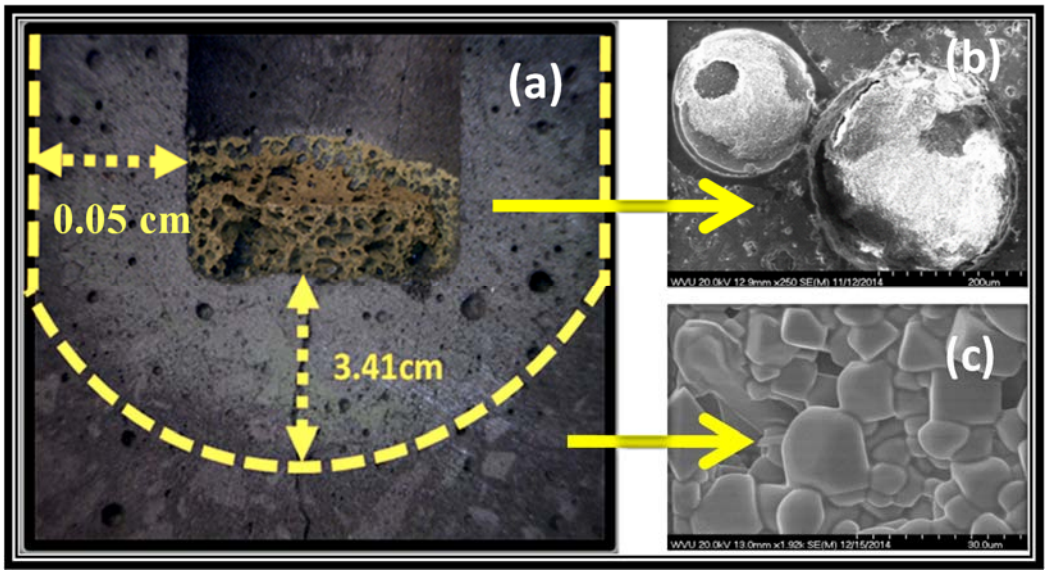

Figure 4.15. Optical and Scanning Electron Microscopy(SEM) images showing: (a) fracture surface of Cr_2O_3 refractory cup after 5 hours of slag corrosion test performed at 1500 °C; (b) slag particles in the refractory; (c) Cr_2O_3 grains without slag.

Figure 4.16(a) shows the optical microscopy image of the fracture surface of Cr_2O_3 refractory cup after 10 hours of slag corrosion test performed at 1500 °C in Ar atmosphere. After heat treatment, the refractory specimen was centrally cut into 7 small pieces for Scanning Electron Microscopy (SEM) study. Figure 4.16(1) through (7) show the electron microscopy images of refractory cup specimen indicating the slag penetration throughout the brick. SEM analysis showed that slag penetrated into the refractory cup specimen up to depth of 8.36 cm. Beyond that distance only Cr_2O_3 gains were identified.

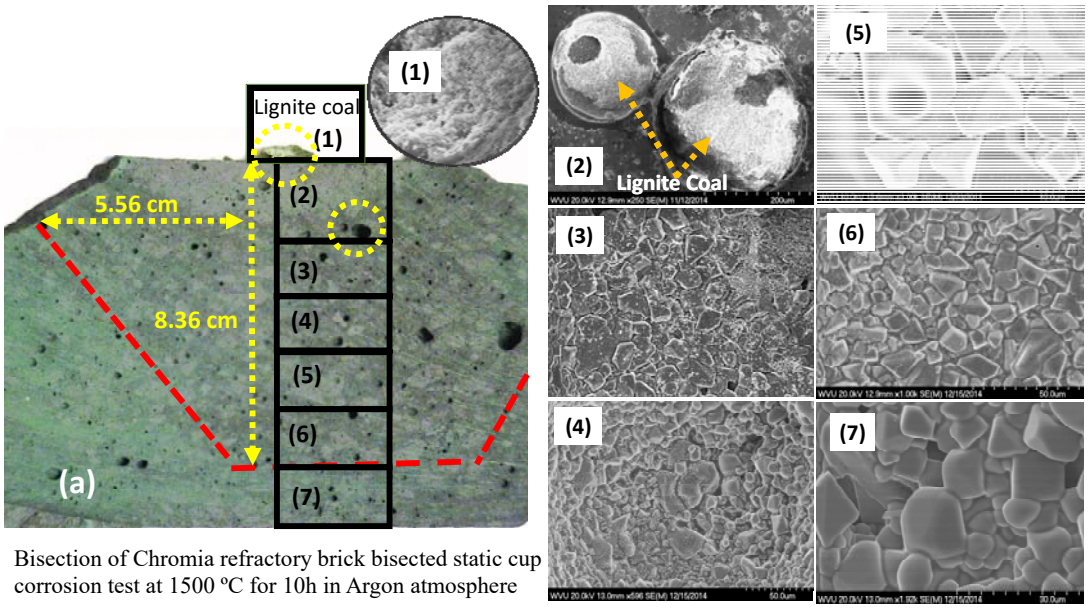

Figure 4.16. Optical and Scanning Electron Microscopy(SEM) images showing: (a) fracture surface of chromia refractory cup after 10 hours of slag corrosion test performed at 1500 °C; (1)-(7)SEM microstructure analysis of slag penetration inside the refractory.

In order to more accurately mimic the thermal gradient experienced by a brick in a gasifier application, the brick design was altered so that the bricks would fit inside 3-inch diameter tube furnace for atmosphere control and cold and hot junctions could be formed at the respective ends of the brick. The longer and more narrow bricks required a redesign of the sensor dimensions and preform microstructure. Figure 4.17(a) shows a 9" x 1 ½" x 1 ½" long chromia smart brick embedded with a [75-25] WSi_2-Al_2O_3 thermistor sensor. The smart brick was sintered at 1500°C for 10 hrs of isothermal hold at 1500°C in argon atmosphere. The electrical connections of the sensor leads were made by polishing the brick from sensor leg side using Buhler made diamond polishing machine. Figure 4.17(b) shows the original photograph of the interface exposing the sensor leads out. The polished sensor-brick interface shows the well sintered sensor material. However, cracks formed at the sensor-alumina joints which may have been introduced during the polishing of the smart brick. Figure 4.17 (d) shows photograph of the smart brick surface polished and wired using Pt wire, taken out from the sensor leads using Pt mesh and Pt ink. Once the Pt electrical connection was made, the brick was cured at 800 °C for 1 hour in argon atmosphere. Lignite coal slag samples (Figure 4.17 (c)) were prepared for slag test.

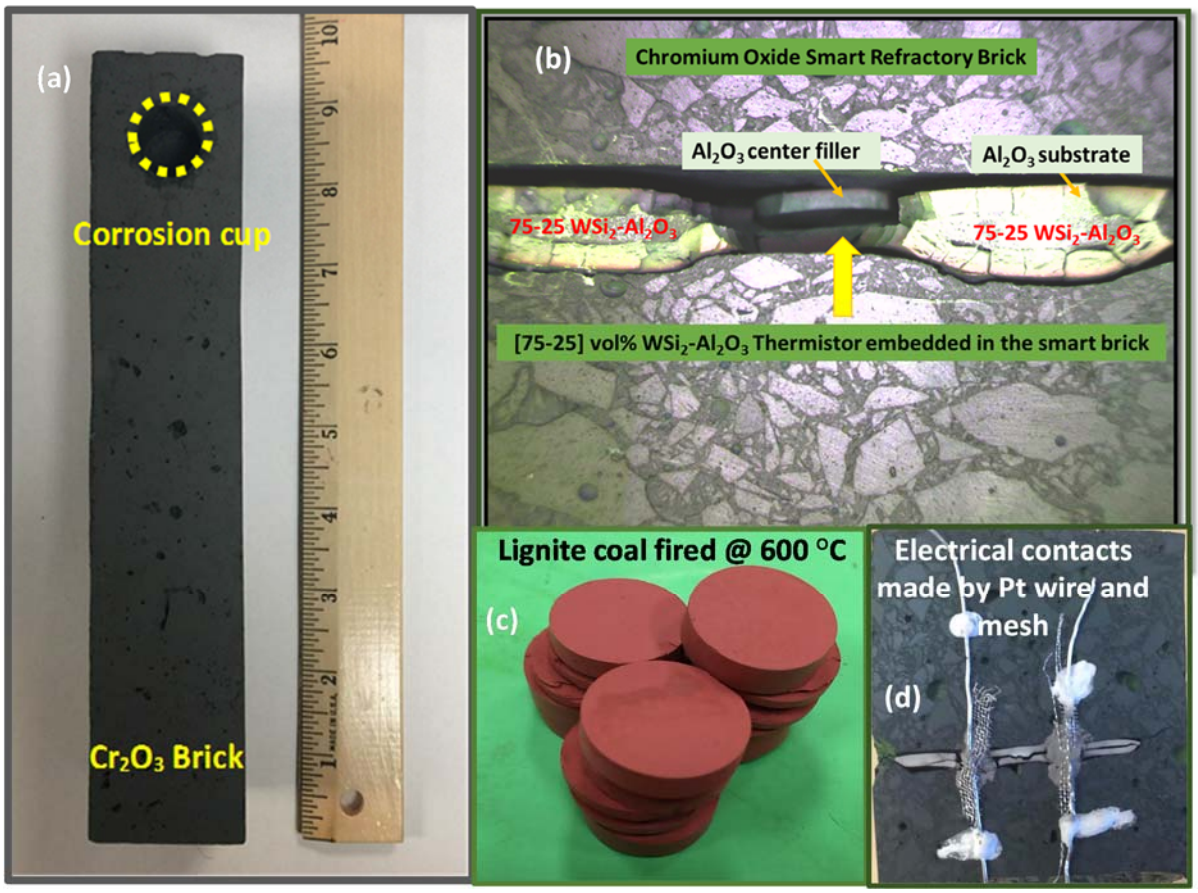

Figure 4.17. (a) Photographs of smart bricks embedded with long temperature sensors sintered 1550 °C in argon. (b) Photograph of the interface exposing the sensor leads out. (c) Lignite coal slag samples prepared for slag test (d) Photo graph of the smart brick surface polished and wired using Pt wire, Pt mesh and Pt ink.

Each brick was characterized twice with electrical property measurements. The first run was conducted as an empty run without loading the lignite coal and the second run was conducted at slagging conditions by loading biscuit fired lignite coal billets. Figure 4.18 shows an image of the smart brick after corrosion test with visible remains of molten slag in the refractory cup.

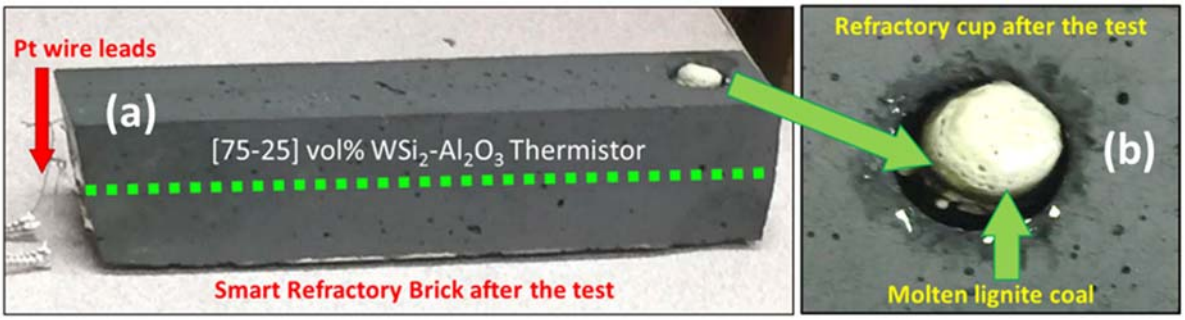

Figure 4.18. Post-test analysis of smart refractory brick embedded with [75-25] vol% Wsi_2-Al_2O_3 thermistor at 1350 °C in argon atmosphere.

Figure 4.19 shows the variation of resistance over time for a brick embedded with the [75-25] WSi_2-Al_2O_3 thermistor. The brick was cycled four times between room temperature and 1350 °C with a 5 hr hold for Runs 1-3, and 40 hr hold for Run 4. Runs 1 and 2 were without slag. Slag was added before Run 3, so that during Run 3 and 4 slag was present and infiltrating the brick. It was evident in all four Runs that the resistance of the [75-25] WSi_2-Al_2O_3 embedded thermistor increased with increasing temperature. A slight decrease in resistance was observed during the isothermal hold at 1350 °C, 5h in Runs 1 and 2 (without slag), possibly to microstructure coarsening. The abrupt change in resistance and resistance drift during hold in Run 3 may be attributed to the addition of slag. The fact that similar behavior is repeated and magnified in Run 4 further supports evidence of slag penetration effects the resistance measured by the thermistor. Further work is warranted to determine how slag addition increases the resistance.

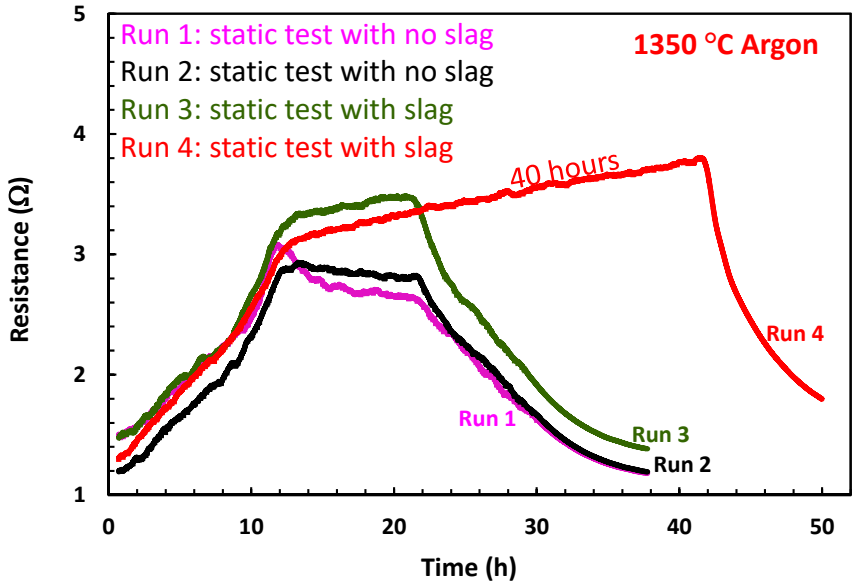

Figure 4.19. Static cup and corrosion test results of [75-25] WSi_2-Al_2O_3 thermistor embedded in chromia refractory tested with and without slag at 1350 °C in argon atmosphere.

4.3.4 Small Size Bricks with Oxide-based Thermistors

The first small size bricks with embedded oxide-based sensors contained LNO-1000 based thermistors, which means that the preform was formed with 50 vol% LNO: 50 vol% YSZ composite ink for intermediate layer and 70 vol% LNO: 30 vol% YSZ composite ink for the conductive core layer, where LNO powder was calcined at 1000°C prior to ink preparation. Since the LNO containing preforms were sintered to 1450°C, the bricks with the preforms were also sintered to 1450°C, Fig. 4.20. Figure 4.21 and 4.22 show the resistance and temperature profile and resistance versus temperature, respectively, for brick containing LNO-1000 thermistor tested to 1400°C for 10 hrs. The brick was cycled between room temperature and 1400°C two times without slag. Before third run, 32 grams of slag pellets were added. Figure 4. shows the melted slag after third cycle. With each thermal cycle, the resistance at each hold appears to increase, while it still shows slight decrease during the hold as shown with data collected with preforms.

At this point, the overall increase in resistance is thought to be generated at the connection between the brick and wire leads heading out of the furnace. For the preforms, the platinum wire is looped through a hole cored into the sensor material making a strong physical connection. That connection is further strengthen by addition of sensor material ink which is painted into the hole. For bricks, the electrical connection between the embedded thermistor and platinum leads depends only on adhesion of the painted sensor material ink. There is a strong possibility that due to thermal expansion mismatch between platinum and the sensor material some microcracking is occurring increasing the measured resistance.

Figure 4.20. Small bricks with embedded LNO-based thermistors.

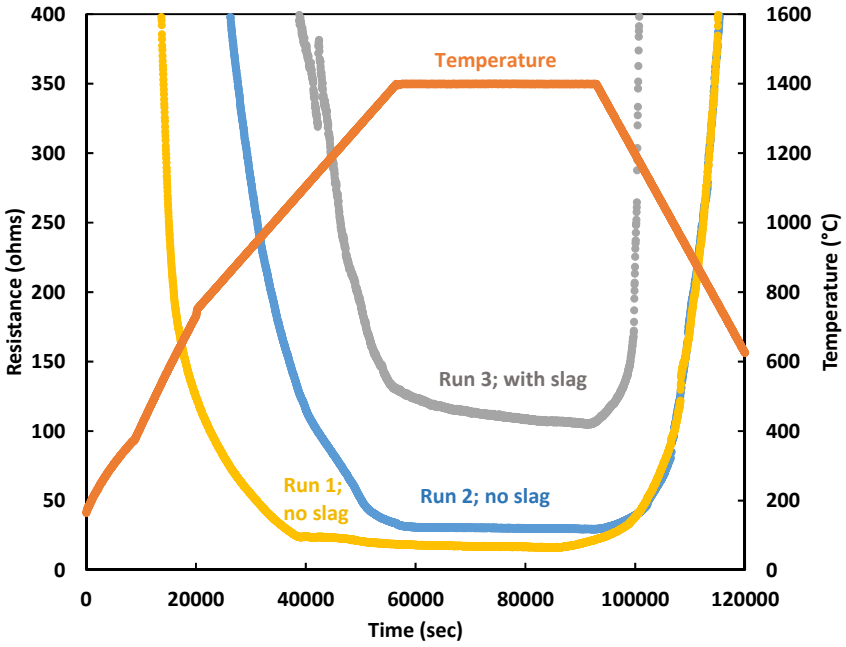

Figure 4.21. Slagging experiments with a brick containing LNO based sensor. The sensor consists of 70:30 vol% LNO-1000: YSZ core and 50:50 vol% LNO-1000: YSZ intermediate layer inside YSZ shell. The thermal cycle for each run was 25°C to 1400°C with 10 hrs hold at 1400°C and slag was added at room temperature before Run 3.

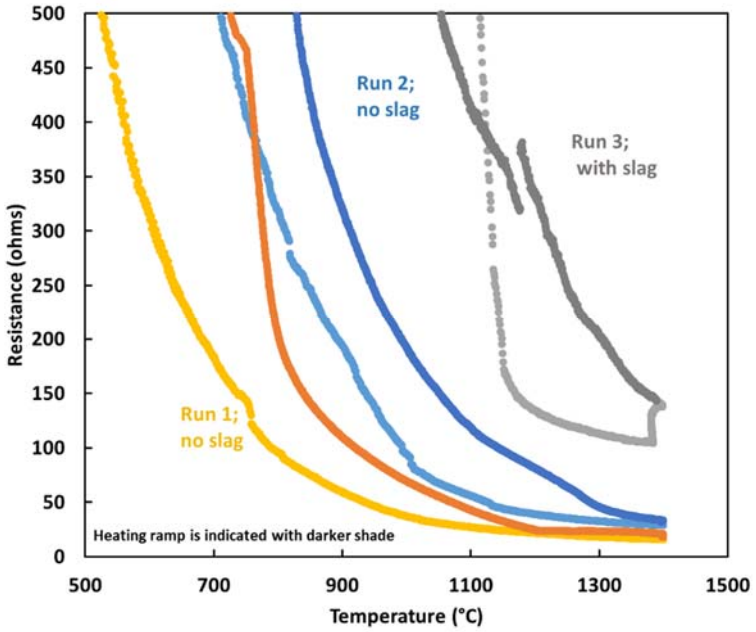

Figure 4.22. Resistance versus temperature curves for brick cycled two times without slag and once with slag. The graph highlights the difference in resistance measured during heating (darker color) and cooling ramps**.**

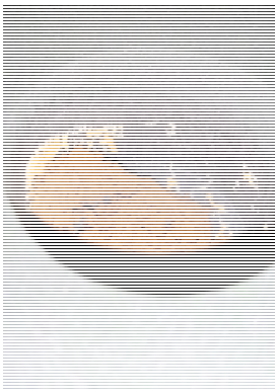

Figure 4.23. Remnants of re-solidified slag inside brick cavity after Run 3.

To determine the cause of the changes in resistance between cycles and during high temperature holds, new brick with LNO-1000 thermistor was cycled four times between 1400°C and 800°C. It was assumed that most of the damage to the contact between platinum lead and thermistor LNO material occurred during the cool down to room temperature. The data presented in Figure 4.24 shows that even with cooling only to 800°C, the resistance still drifts between cycles significantly and the high temperature resistance reflects drift observed at 800°C. For this brick, the minimum resistance observed between cycles 1-4 was 30, 26, 28, and 51 ohms.

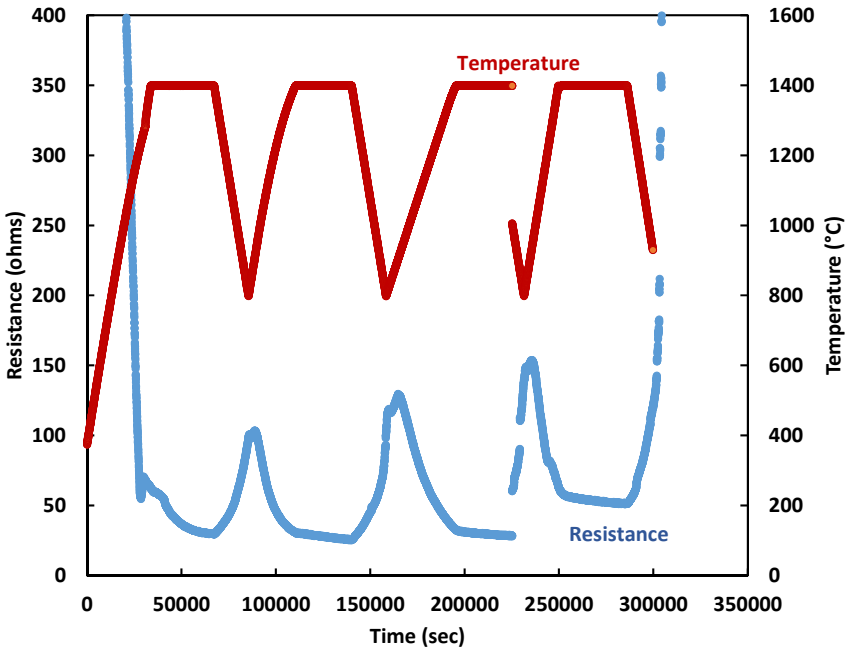

Figure 4.24. Thermal cycling of LNO-1000 based sensor embedded in a high-chromia brick. The sensor was sintered at 1450°C and tested between 800°C and 1400°C showing significant change in resistance between cycles at low temperature.

To confirm that most of the drift in resistance is due to contact between platinum and sensor material, the same brick that was thermally cycled was cooled to room temperature and more LNO-1000 ink was placed around the leads. The additional ink was expected to fill into cracks which might have formed during the thermal cycling and repair the electrical continuity between thermistor inside the brick and platinum leads. Figure 4.25 shows the data for the brick with additional conductive material around the leads tested again at 1400°C. The minimum resistance achieved by this brick was 28 ohms, which places it right in the middle of values obtained for the same brick during cycling experiment. This data confirms large changes in resistance were due to connection between platinum lead and LNO sensor material on the surface of the brick. This does not, however, address and eliminate lesser but still continuous decrease in resistance during high temperature hold seen both in LNO-based thermistors embedded in bricks and as preforms.

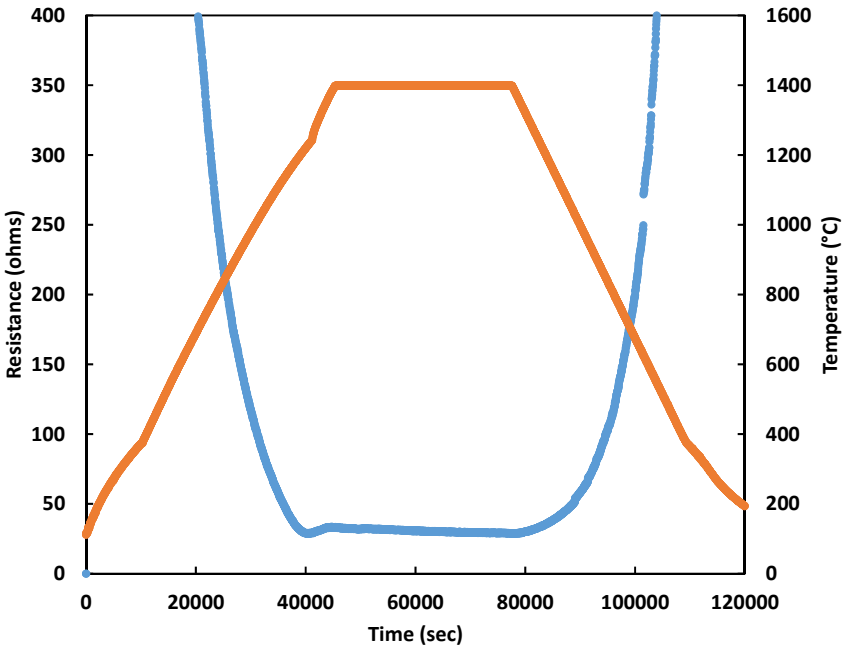

Figure 4.25. Resistance and temperature profile of LNO-1000 based sensor embedded in a high-chromia brick. This data was generated using the same brick shown in Fig. 4.24 after the electrodes were reapplied with extra 70:30 LNO(coarse):YSZ ink.

Figure 4.26 shows the resistance and temperature profile for brick containing LNO-1400 thermistor tested to 1350°C for 20 h. Platinum wire, platinum mesh, and additional 70 vol% LNO-1400: 30 vol% YSZ ink was used to make connection to the sensor embedded inside the brick. Prior to testing, the assembled leads were heat treated to 1400°C to pre-sinter the sensor to wire connection. To collect data for the Fig. 4.26, the sensor to wire connection was placed at the same level as high temperature refractory for the furnace door with additional insulation to mimic typical high temperature furnace refractory configuration. With this testing arrangement, the leads connection was exposed to only 132°C maximum temperature over the course of the test.

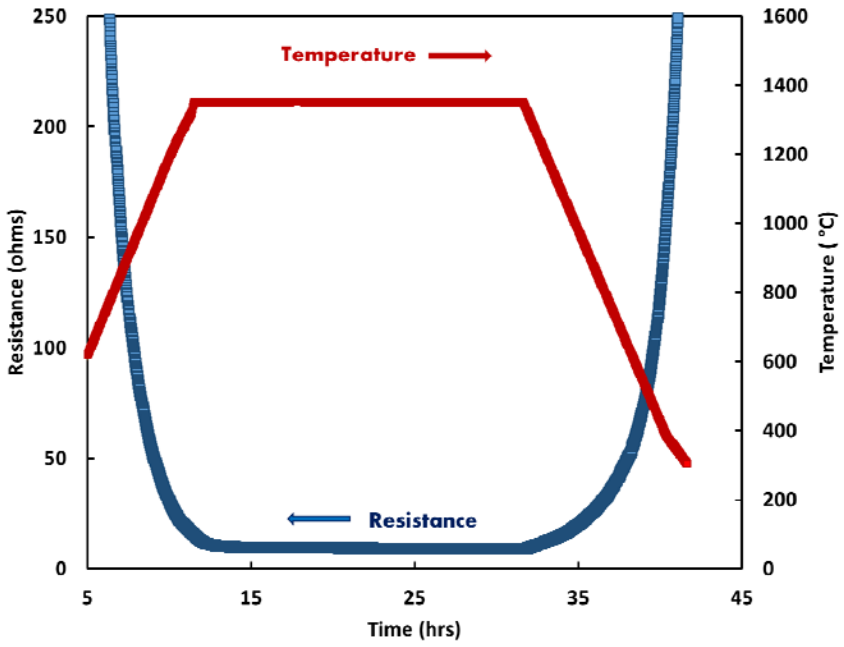

Figure 4.26. Resistance and temperature profile of the La_2NiO_4 (LNO-1400) based thermistor co-sintered inside YSZ and embedded in high-chromia brick at 1450°C and tested to 1350°C. During testing, the leads were placed outside hot zone of the furnace and were only exposed to 132°C maximum temperature.

With the leads outside the hot zone, the sensor recorded lowest resistance measured so far for the LNO based thermistor. The resistance drift during the temperature hold was recorded from 9.7 to 9.1 ohms over 20 hours. The stability of the sensor was further tested with thermal cycling between 1350°C and 500°C with only six hour hold at 1350°C. Figure 4.27 shows the results of the thermal cycling. There was small resistance increase at each 1350°C hold of 14.4, 15.7, 16.7, and 17.2 ohms for each consecutive thermal cycle with corresponding significant increase and measurement instability at 500°C. This change in resistance is believe to be due to lead to sensor connection, an issue which has been identified for significant developmental effort.

There was also a small drift within each high temperature hold. For example, in cycle 2, the resistance drifted from 16.4 ohms to 15.7 ohms. The magnitude of the drift hints at possibly something other than grain coarsening causing the resistance change. It is possible that the drift is caused by thermal gradients within the brick, especially since one face of the brick is at lower temperature at the face of the furnace. The cause of the drift will require further evaluation and testing specifically designed to resolve this particular issue.

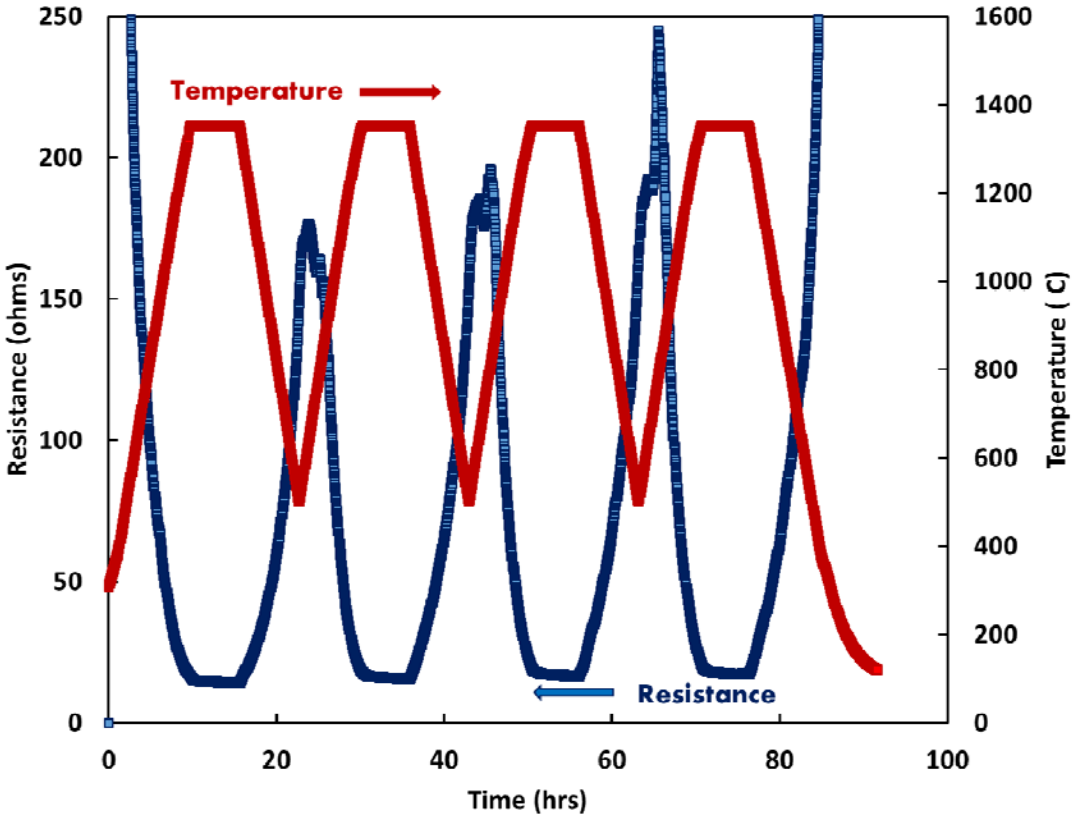

Figure 4.27. Resistance and temperature profile of the La_2NiO_4 (LNO-1400) based thermistor co-sintered inside YSZ and embedded in high-chromia brick at 1450°C and tested to 1350°C. During testing, the leads were placed outside hot zone of the furnace and were only exposed to 132°C maximum temperature.

To determine if the drift in the measurement will affect the necessary correlation between temperature and resistance, the brick was evaluated at different temperatures of 1350°C, 1300°C, 1250°C, and 1200°C, each with six hour hold. Figure 4.28 shows that the resistance drift within hold does not affect ability to clearly distinguish different temperatures. This is a promising result for the applicability of the sensor in the ability correlate temperature to resistance.

In summary, the lanthanum nickelate based thermistors are showing encouraging results with relatively predictable resistance to temperature response. Coarsening sensor material limits the resistance drift due to microstructural changes. Removal of the connection between platinum leads to sensors embedded in the brick sensor from furnace hot zone to outside the testing furnace significantly decreases resistance drift especially during thermal cycling. Future work will still need to address and improve the lead connection issues, but at this point the researcher feel confident to prepare samples for demonstration using the materials and techniques developed so far.

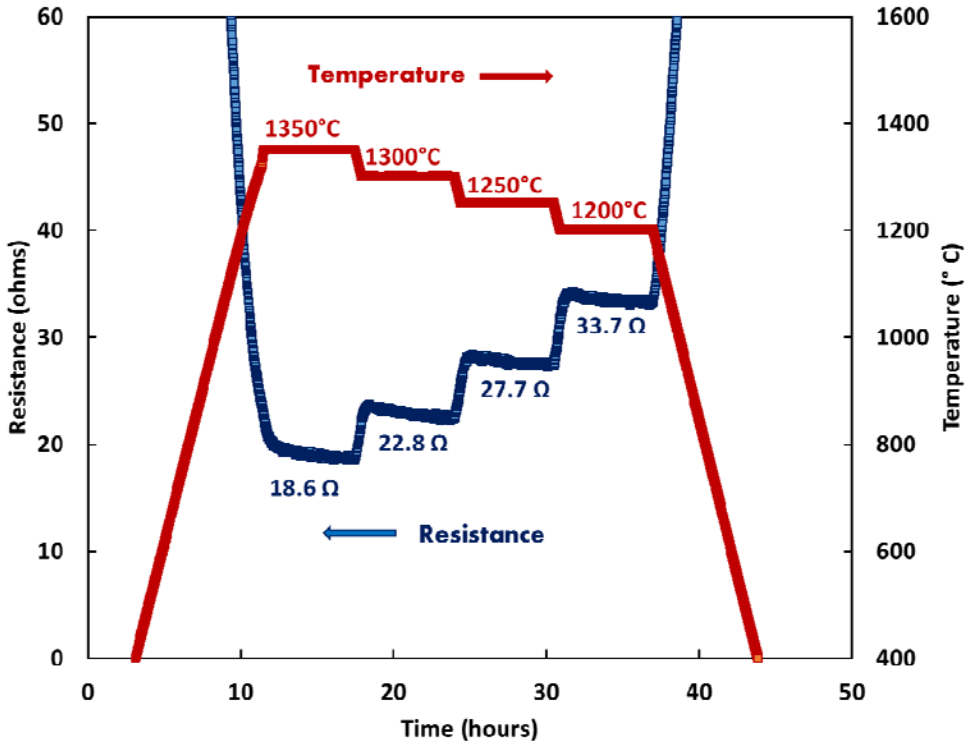

Figure 4.28. Resistance and temperature profile of the La_2NiO_4 (LNO-1400) based thermistor co-sintered inside YSZ and embedded in high-chromia brick at 1450°C and tested at 1350°C, 1300°C, 1250°C, and 1200°C, each with six hour hold.

4.4 Conclusions:

Milestone M2 "Demonstrated singular embedded temperature and strain sensor" was completed June 30, 2014.

Milestone M3 "Completed >250 hr static slagging cup test using temperature and strain sensor" was completed December 30, 2015 and April 5, 2017 for silicide and LNO systems, respectively.

The following is a list of accomplishments for the static and dynamic sensor testing task.

1. Thermistor, thermocouple, and strain sensors preforms fabricated and tested to 1300ºC.
2. Strain sensors were later down-selected from further work to focus on thermistor and thermocouples.
3. Embedded silicide-based thermistor into chromia brick, and completed slag cup test for >250 h at 1350ºC in argon (entire brick in hot zone).
4. Embedded oxide-based thermistor into chromia brick, and completed slag cup test for >250 h at 1350ºC in air (leads outside furnace).

Milestone M4 "Small scale dynamic slagging test completed using smart refractory at WVU" was not fully completed. WVU built dynamic slagging system, but system was destroyed in a lab fire in April 2015. Issues with interconnection to silicide bricks sitting in full hot-zone delayed refocus of this milestone (all focus was re-directed onto static testing).

Task 5: Data Ex-Filtration Using a Wireless Sensor Network

5.1 Introduction:

The objective of this task was to interface the electrical sensing outputs from the smart refractory for temperature and strain measurements with an embedded processor and to design a wireless sensor network to efficiently collect the data at a processing unit for further data analysis. Our performance goals in this task were to ensure that (i) the system is scalable to a large number of sensors, (ii) the system parameters can be reconfigured wirelessly post-deployment to avoid cumbersome maintenance procedures, and (iii) the software components are modularized to accommodate additional sensing modalities.

The specific subtasks were as follows:

Subtask 5.1: Interfacing Electrical Outputs to Motes- Initial interface circuitry will be designed using off-the-shelf components to obtain a working system and to allow for full system integration. These interface circuits will be used for monitoring the sensors within the smart bricks and providing the appropriate signals to the wireless motes. To provide longer lifetimes and better performance, custom integrated circuits will be designed using low-power circuit techniques. Energy harvesting using thermoelectric devices will be investigated to help power the sensor nodes and interface circuitry.

Subtask 5.2: Wireless Data Transport and Stand-alone Performance Evaluation with Simulated Electrical Signals- The aim of this sub-task will be to reliably transport the refractory sensing data from the individual motes to a data processing center over a wireless communication medium, and to allow convenient wireless configuration of sensor parameters from a remote processing center. We plan to develop in-network compression ideas to reduce the amount of data transmitted while preserving the information, so as to reduce the data volume and allow scalability to several hundreds of sensors. We also plan to install wireless data dissemination protocols to allow remote reprogramming of sensors after deployment. We also expect the software for the wireless sensing system to be plug and play with respect to addition and removal of sensing modalities. This will allow modification of underlying sensors convenient via a user interface as opposed to having to re-write several software components. The information delivery performance will be evaluated under different data sampling requirements, sensor density, number of sensors and sensor data correlation. This analysis is expected to enable the determination of optimal deployment configuration for data acquisition in the refractory system. The ability to of the system to reliably reconfigure parameters from a remote operating center will be also investigated.

Subtask 5.3: Performance Evaluation of Wireless Network with Static and Dynamic Smart Refractory- Once the wireless sensor network protocols for data acquisition and reconfiguration have been evaluated in stand-alone basis, they will then be integrated with an actual smart brick implementation. The integrated system will be tested in both a static and dynamic smart refractory system and the performance will be characterized. The expected outcome form Task 5.0 is a robust, reconfigurable wireless sensing system that is customized for the harsh operating conditions inside a refractory.

Our wireless sensor network architecture is summarized in Figure 5.32.

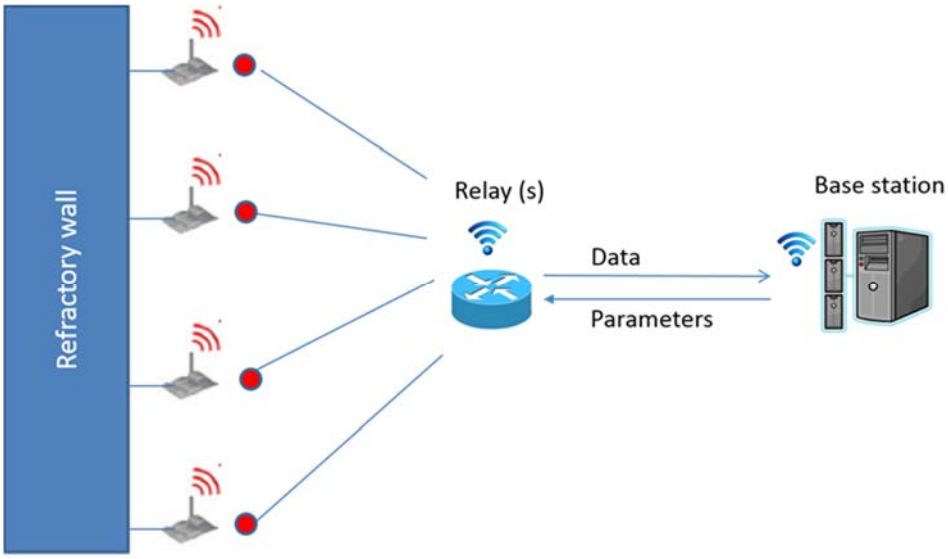

Figure 5.32. Wireless sensor network architecture for refractory monitoring

5.2 Experimental Methods:

5.2.1 Subtask 5.1: Interfacing Electrical Outputs to Motes:

Initial interface circuitry was designed using off-the-shelf components to obtain a working system and to allow for full system integration. These interface circuits are to be used for monitoring the sensors within the smart bricks and providing the appropriate signals to the wireless motes. To provide longer lifetimes and better performance, custom integrated circuits were designed using low-power circuit techniques. Energy harvesting using thermoelectric devices was investigated to help power the sensor nodes and interface circuitry. We will describe these activates in the following subsections.

5.2.1.1 Initial Sensor Node Prototype

In order to reliably collect data from the sensors embedded within the smart bricks and interface them to wireless sensor nodes for communication, we needed to develop circuitry that would allow us to verify the operation of the end-to-end system, even before the custom sensors had been finalized. To achieve this task, we initially developed circuits using off-the-shelf components. This work allowed us to achieve Milestone M5, which was to create initial sensor interface circuitry using off-the-shelf components (with correct measurements with at least 95% accuracy). We built sensor interface circuits for the two primary sensing modalities of this project, which are (1) resistive-based sensors and (2) thermocouples. To verify the operation of these circuits, we used commercial off-the-shelf (COTS) sensors; we used a COTS resistive temperature detector (RTD) and a COTS thermocouple. We also connected the output of the sensor interface circuits to wireless sensor network nodes (called motes) to verify that accuracy is maintained while interfacing to a network and transmitting the results wirelessly. The following discussion summarizes our results.

The first circuit that we developed was a circuit to measure changes in resistance, and it was based on a Wheatstone bridge circuit. Figure 5.33 shows the schematic of this circuit. Importantly, this circuit operates on a single power supply, which is essential for working with wireless sensor nodes that are typically powered by two AA batteries (3V supply). The following expression describes

the output voltage of the circuit.

$$V_{out} = V_{ref2} + \frac{R_2}{R_1}\delta\left(V_{ref1} - V_{ref2}\right)$$

This circuit has properties that are easily adjustable based upon the circuit parameters. For example, the temperature range (T_{min} to T_{max}) is set by R_1, R_2, and V_{ref1}, and the median of the temperature range is set by the value of R. As a result, this circuit is easily modifiable for developing and/or improving sensors.

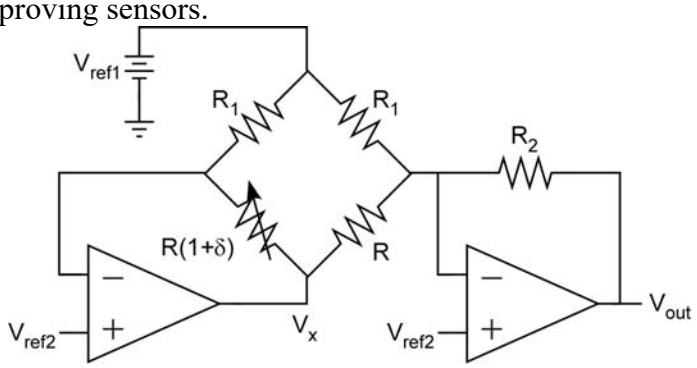

Figure 5.33. Circuit to measure resistance based upon a Wheatstone bridge.

To verify the operation of this circuit, we used a Pt100 K 2515 resistance temperature detector (RTD) as an exemplary resistance-based sensor (one of the highest temperature commercial RTDs, up to ~800°C). Figure 5.34 shows the output of this circuit over a range of temperatures. This circuit is able to maintain accuracy >95% over a wide range of temperatures.

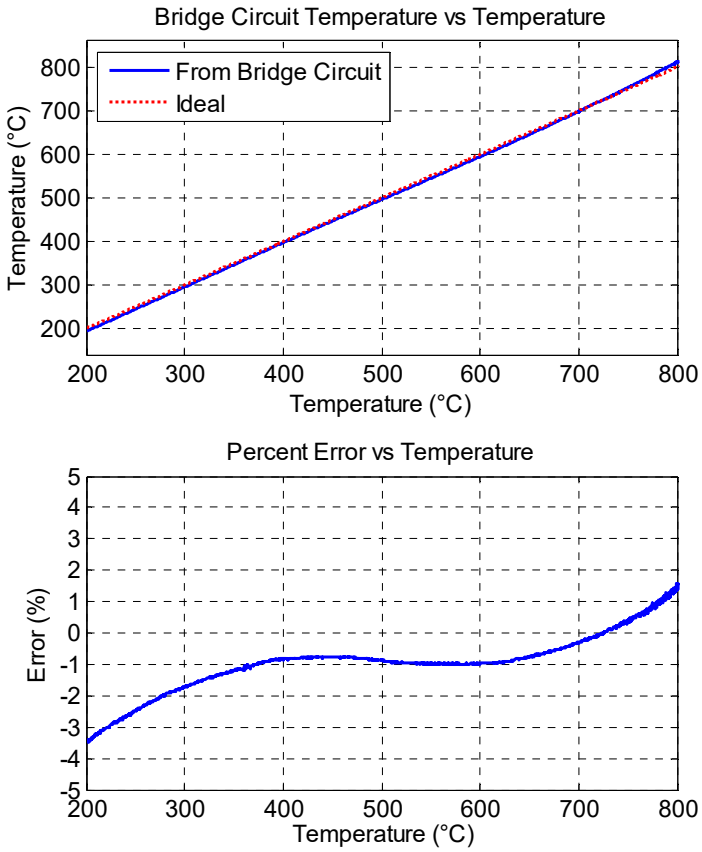

Figure 5.34. Output of the resistance-based sensor interface circuit, showing accuracy >95%.

The second circuit that we developed was for measuring the output of thermocouple-based sensors. Figure 5.35 shows the resulting circuit. This circuit leverages a COTS-based thermocouple circuit; the AD595 provides appropriate amplification and cold-junction compensation. The rest of this circuit adjusts the output reading to levels appropriate for a WSN mote. We verified the operation of this circuit using a commercially available K-type thermocouple, and the output of the circuit is shown in Figure 5.36. This circuit was connected to a COTS wireless sensor node, and its output was transmitted to a base station. As can be seen from these plots, the circuit is able to achieve accuracy >95% over a wide range of temperatures. This result verified that good accuracy can be maintained over a wireless sensor network.

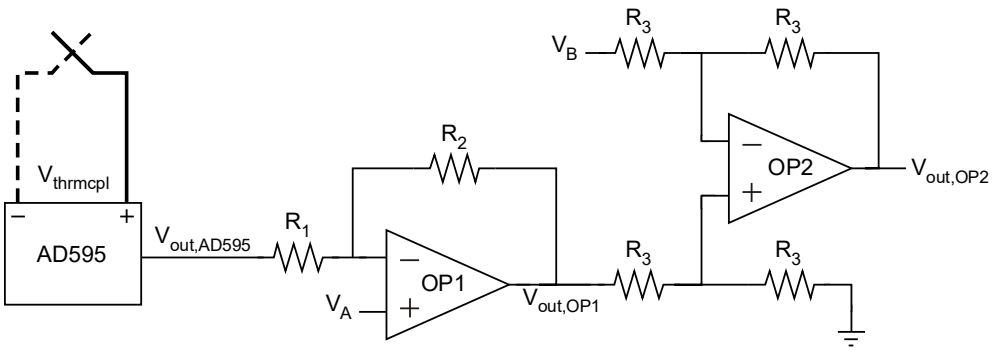

Figure 5.35. Schematic of a circuit to measure and amplify the output of thermocouple-based sensors.

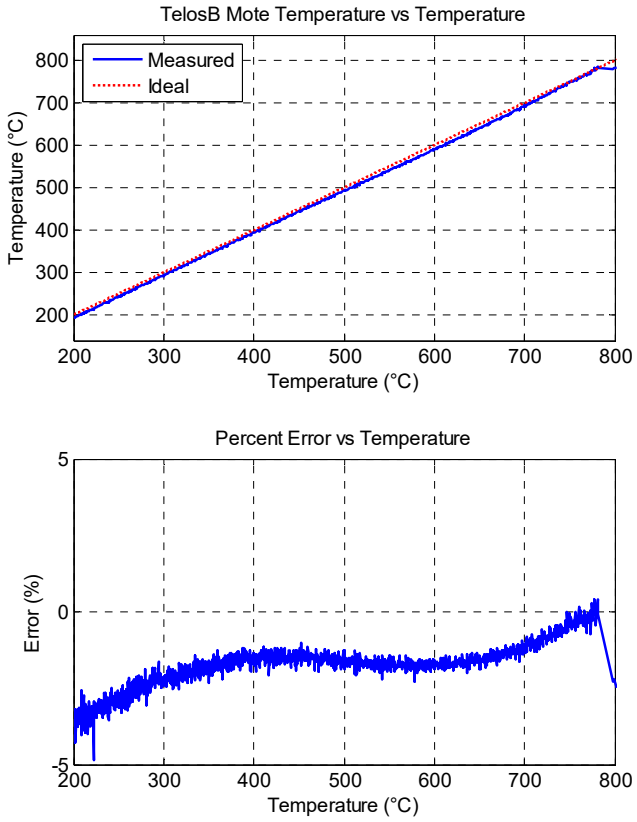

Figure 5.36. Output of the thermocouple amplifier circuit after being transmitted wirelessly over a wireless sensor network. The accuracy is >95%.

5.2.1.2 Custom Integrated Circuit Development

We designed an integrated circuit for lower-power sensor interface circuitry and verified its functionality to meet Milestone M6. This integrated circuit contained circuits for (1) resistance measurement using a Wheatstone bridge, (2) thermocouple amplifiers, (3) a bandgap temperature sensor for cold-junction compensation of the thermocouples, and (4) a capacitive sensor. Figure

5.37 shows a die photograph of the resulting integrated circuit.

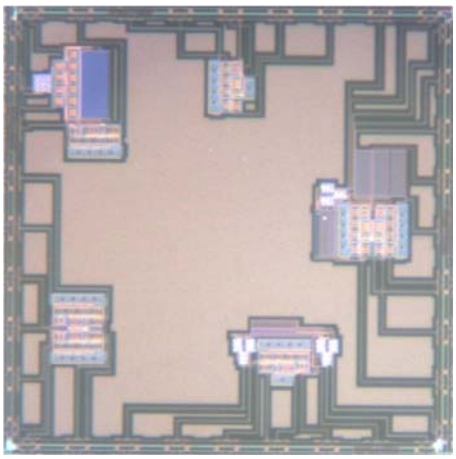

Figure 5.37. Die photograph of the integrated circuit prototype.

We designed a low-power Wheatstone bridge circuit by using only two amplifiers and no instrumentation amplifier. Additionally, this circuit uses a single voltage supply, which is important for connection to wireless sensor nodes that operate on a single battery. This circuit was based upon the design of Figure 5.33, and results of this circuit are shown in Figure 5.38. For testing, we utilized a commercial RTD, and this circuit can easily adapt to RTD/thermistors rated for higher temperature ranges. The Wheatstone-bridge correctly reports the temperature inside of the furnace to within a 3% margin of error, as is shown in Figure 5.38.

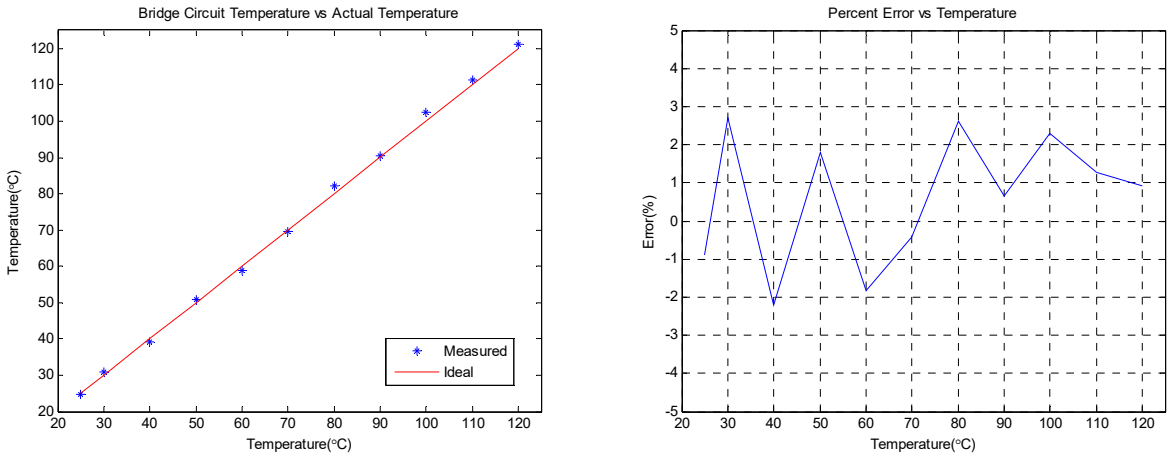

Figure 5.38. Wheatstone-bridge integrated circuit performance.

The second circuit tested was the thermocouple amplifier. This circuit is an integrated version of the circuit that was previously implemented using discrete, commercial components. The circuit was designed to operate over a range of input values based on the performance of the WVU-designed thermocouples. The following Figure shows a schematic of the design that was implemented on the integrated circuit.

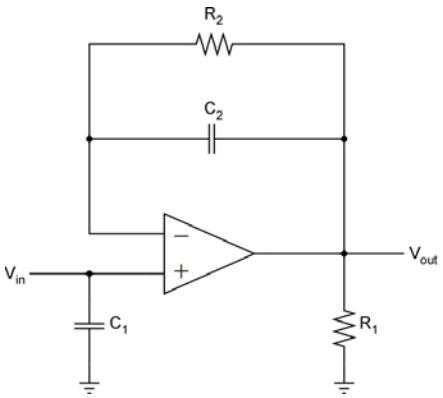

Figure 5.39. Thermocouple amplifier integrated circuit schematic.

This circuit was first tested without cold-junction compensation. The thermocouple amplifier received its input from the thermocouple, and reported furnace temperature without any measurement compensation. The results of the test are shown in the Figure 5.40. The solid red line corresponds to the actual temperature inside of the furnace. The dotted line shows the temperature reported by the thermocouple amplifier circuit. Without cold-junction compensation, the thermocouple amplifier reported the actual furnace temperature within a 4% margin of error over the temperature range of 1000°C–1450°C. The Figure below shows a percent error of the circuit's performance over the temperature range that it was tested.

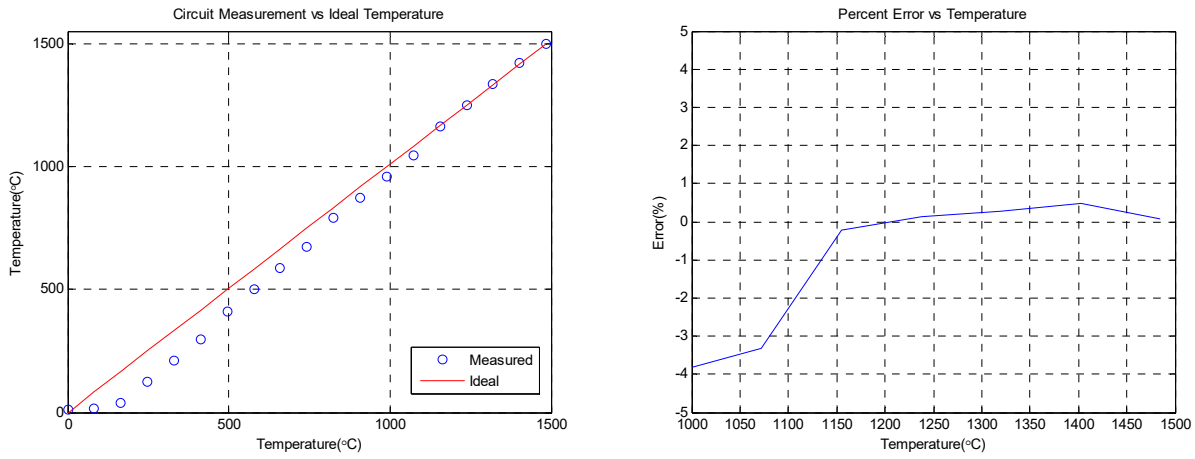

Figure 5.40. Thermocouple amplifier integrated circuit performance.

The third circuit to be tested was the cold-junction compensator (CJC). This circuit compensates for error at the measurement site. The temperature outside of the furnace, where the measurement takes place, must be taken into consideration for more accurate results. The CJC generates an offset voltage that is added to the thermocouple's negative terminal to allow for accurate measurements. The following Figure shows a schematic of the design that was implemented on the integrated circuit. This circuit was tested over a range of 0-120˚C, accounting for the full range

of temperatures that may be encountered when measuring the thermocouple outside of the furnace. The results of the test are shown in the Figure below. The dotted line corresponds to the output of the CJC at different temperatures. The output of this circuit was designed to correspond to the measurement compensation needed for the WVU-designed thermocouple.

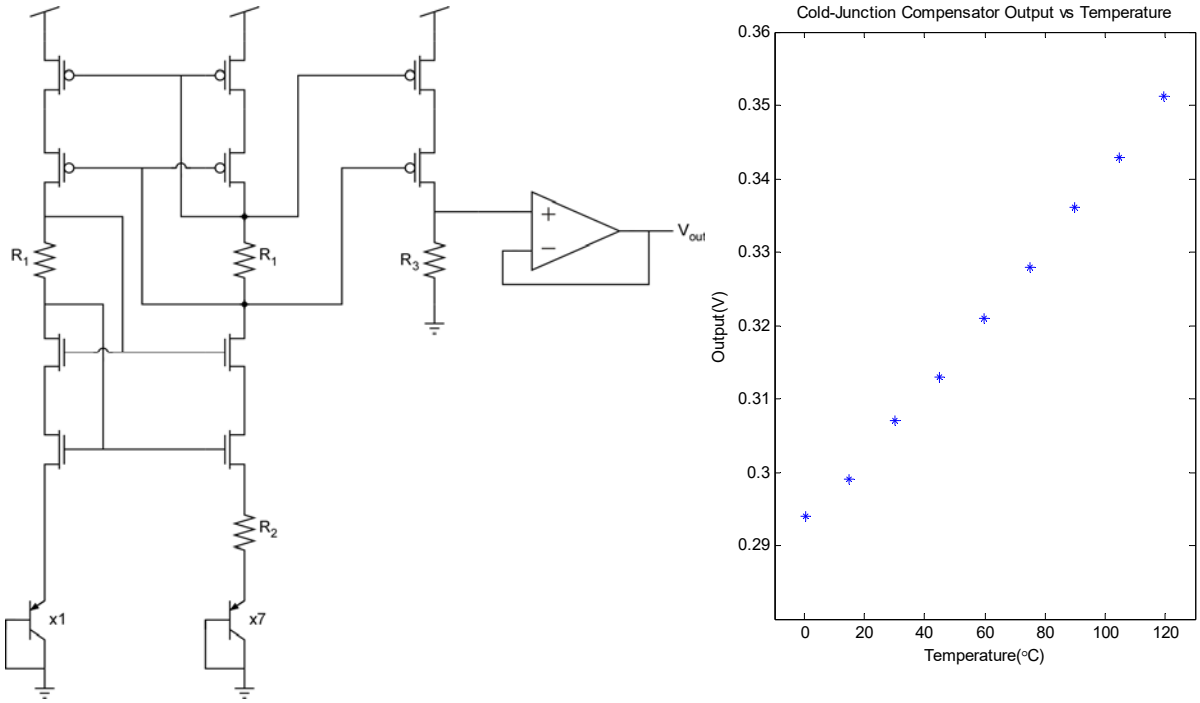

Figure 5.41. Cold-junction compensator integrated circuit schematic and measured performance.

The thermocouple amplifier and cold-junction compensator were then combined to more accurately report the temperature inside of the furnace. The following Figure shows how the CJC adds an offset to the thermocouple, allowing the thermocouple amplifier to report a more accurate temperature reading.

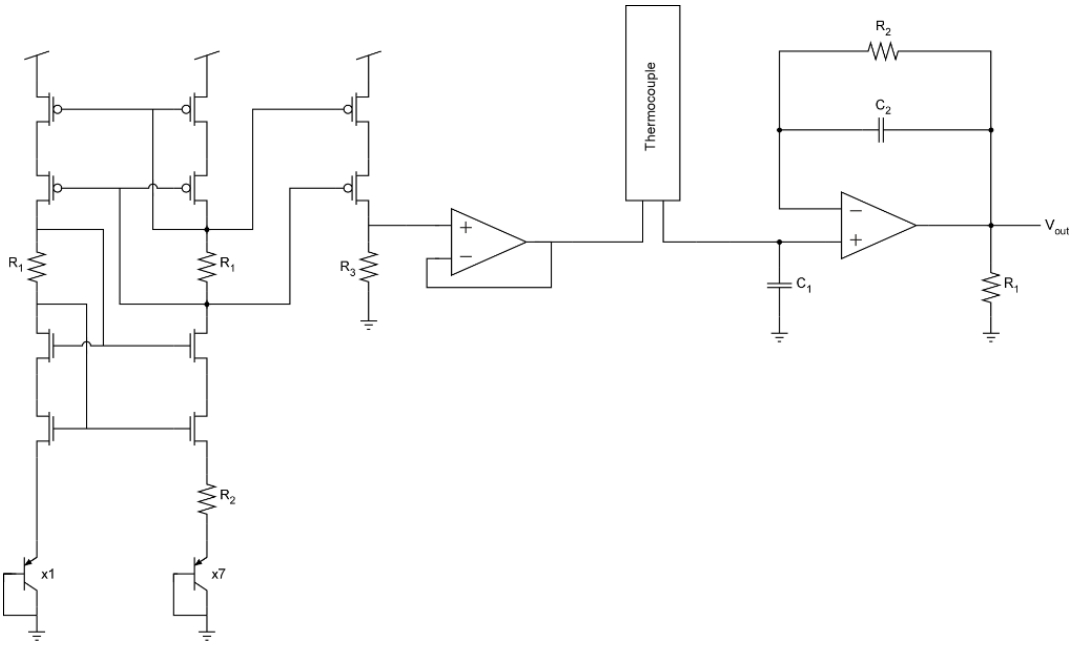

Figure 5.42. Schematic of cold-junction compensation being added to the thermocouple amplifier.

The CJC adds a static offset to the thermocouple depending on the temperature where the measurement is taking place. This offset is then seen by the thermocouple amplifier, allowing for a more accurate temperature reading. As stated above, without cold-junction compensation, the thermocouple amplifier reported the furnace temperature to within a 4% margin of error. With cold-junction compensation, the thermocouple amplifier reported the furnace temperature to within a 2% margin of error over a larger temperature range. The Figure below shows a percent error of the circuit's performance with cold-junction compensation.

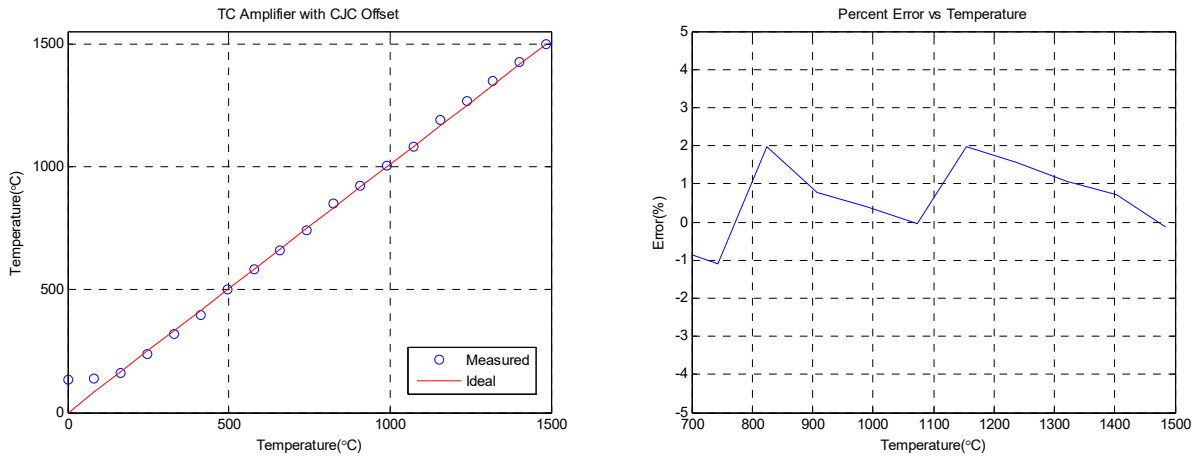

Figure 5.43. Thermocouple amplifier output without cold-junction compensation (left) and thermocouple amplifier output with cold-junction compensation (right).

The fourth design tested was the circuit for interfacing with capacitive-based sensors. The circuit was tested using a capacitor array to generate the output values of the capacitive sensor. The following Figure shows a schematic of the design that was implemented on the integrated circuit.

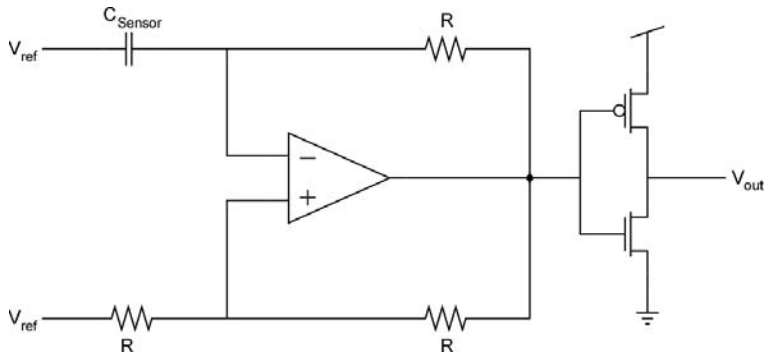

Figure 5.44. Schematic of circuit for interfacing with capacitive-based sensors.

This circuit converts a capacitance value to an oscillating signal with a set frequency. The frequency of the signal is measured by the wireless sensor and converted to a known temperature value. As the input capacitance increases, the output frequency decreases. The following Figure shows the output of the capacitive-based circuit.

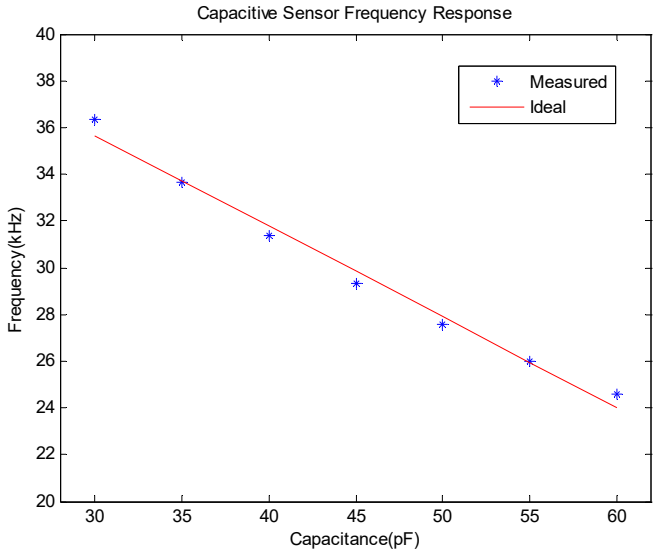

Figure 5.45. Capacitive-based sensor interfacing integrated circuit performance.

5.2.1.3 Reconfigurable Circuitry

To provide for flexibility in the operation of the sensor interfacing circuitry and to also permit adjustments to be made in the field to help improve performance in the case of environmental changes, we investigated implementing the sensor interfacing circuitry in a reconfigurable

framework. Specifically, we implemented the circuitry in our reconfigurable analog/mixed-signal processor (RAMP), which is a large integrated circuit composed of a wide variety of analog circuit building blocks that can be connected in any arbitrary fashion. As an example circuit that we implemented in the reconfigurable system, Figure 5.46 shows a resistive-based sensor-interface circuit that was synthesized. This circuit is the same circuit that was constructed from off-the – shelf components (Figure 5.33), but it was adapted to be synthesized in our reconfigurable system. We verified its operation with an off-the-shelf thermistor, but all other components were from our reconfigurable system on our reconfigurable integrated circuit. Figure 5.46 also shows the results of the sensor interface circuit as the temperature varied, showing that this circuit properly varied its response with the change in resistance. Since each of the circuit components shown in Figure 5.46 were connected together via a "switch matrix" that can connect any arbitrary circuit components together, there was some loss/inaccuracies due to parasitic effects. We expect that these non-idealities will be removed by more properly designing both the individual circuit components and also creating custom blocks that perform specific types of sensor interfacing tasks (i.e., circuit components at a higher level than just resistors and operational amplifiers).

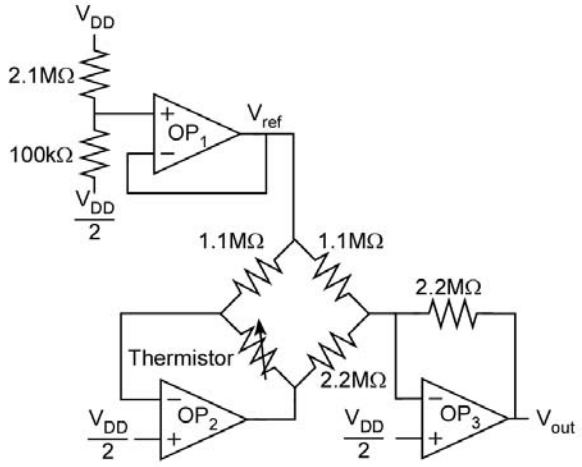

(a)

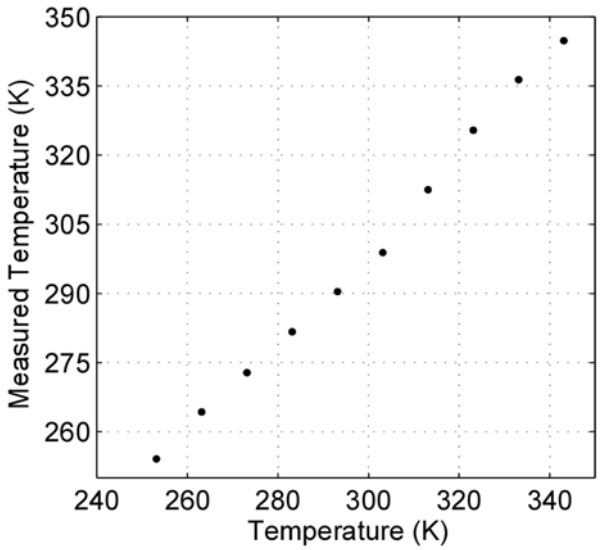

(b)

Figure 5.46. (a) Resistive-based sensor interface circuit implemented on our reconfigurable analog architecture. (b) Measured output across a 100K temperature range.

The RAMP system is built around the functionality of flash memory components referred to as floating-gate (FG) transistors. Like digital flash memory, FGs can be programmed to store information. In analog, an FG can store a continuum of values which can be used for computation. The direct application of analog FGs mainly takes the form of programmable current biases for circuits, which are highly sensitive to temperature. A schematic diagram of an FG operating as a current bias is displayed in Figure 5.47. The V_{tun} node is used for programming the FG, V_{cg} node is used for controlling the amount of current the FG is biasing, and I_{M1} is the current output.

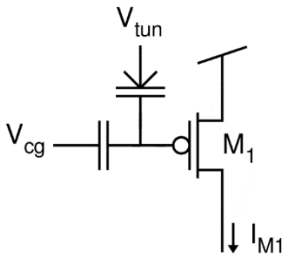

Figure 5.47. Floating Gate current source used to generate bias current on RAMP.

Before operating an FG device as a current source, it must first be programmed. There are two common programming mechanisms for modifying charge on an FG: Fowler-Nordheim (FN) tunneling and hot-electron injection. This is typically done at room temperature. By programming specific amounts of charge on the isolated gate, and thus programming the current to a specific value, the FG transistor becomes a tunable current source. The transistor's operational characteristics will have an inherent dependence on temperature. Figure 5. 48 shows the extent of temperature effects on an FG transistor experiencing ambient temperature changes from 0-120 °C. It can be seen that if a constant V_{cg} was chosen in the application region around 2V, then over a magnitude of change would be seen in its output bias current. Putting this result in the context of the furnace environment, the performance of the sensor interface circuit and/or event detection system would be drastically degraded in a system that relies on 10's of sensitive FGs for optimal performance.

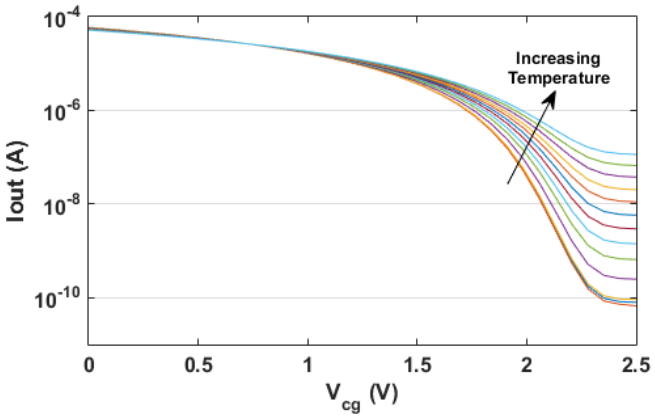

Figure 5. 48. Temperature dependence of an FG transistor from 0-120 °C ambient temperature. Vcg node is swept at every 10°C. A constant Vcg is usually chosen for the design.

It's clear a compensation scheme to modify V_{cg} in response to a change in temperature would be needed for furnace testing. The temperature compensation circuit is shown in the blue box of Figure 5. 49. M_{REF} is placed in diode-connection via the current mirrors comprised of transistors $M_{A\text{-}D}$. M_D mimics the behavior of M_{REF}, especially at the drain. The drain of M_D is then connected to the global V_{cg} node, allowing for the complete diode connection of M_{REF}. This configuration forms a feedback loop that automatically sets V_{cg} such that its output current is always I_{REF}, regardless of the temperature of the environment.

In the RAMP, there is a single, global V_{cg} to control all FGs like the ones in the red box of Figure 5. 49. Therefore, this compensation scheme must be effective in compensating multiple FGs with differing output currents. For example, to synthesize an event detection system would require multiple FGs that might have over a magnitude of difference from the smallest current to the largest current of the system.

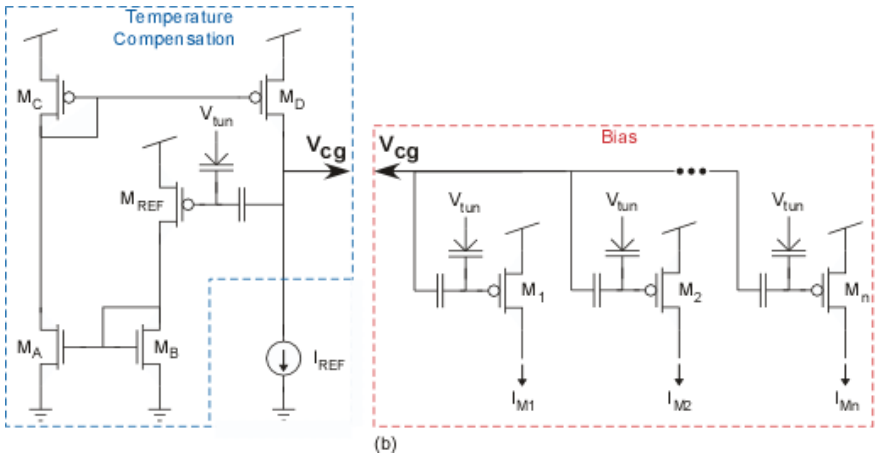

Figure 5. 49. Temperature compensation topology (blue) and multiple FGs within the FPAA.

The performance of the temperature compensation circuit is shown in Figure 5. 50. The left ratio number represents the integer multiple of the programmed I_{REF} value relative to the programmed bias current (e.g. like I_{M1} of Figure 5. 49). For example, the blue case shows that I_{REF} is a current that is ten times larger than its bias current. It is evident that the closer to unity that the current ratios are, the better the compensation performance. For all cases, the I_{REF} current was set to 10nA.

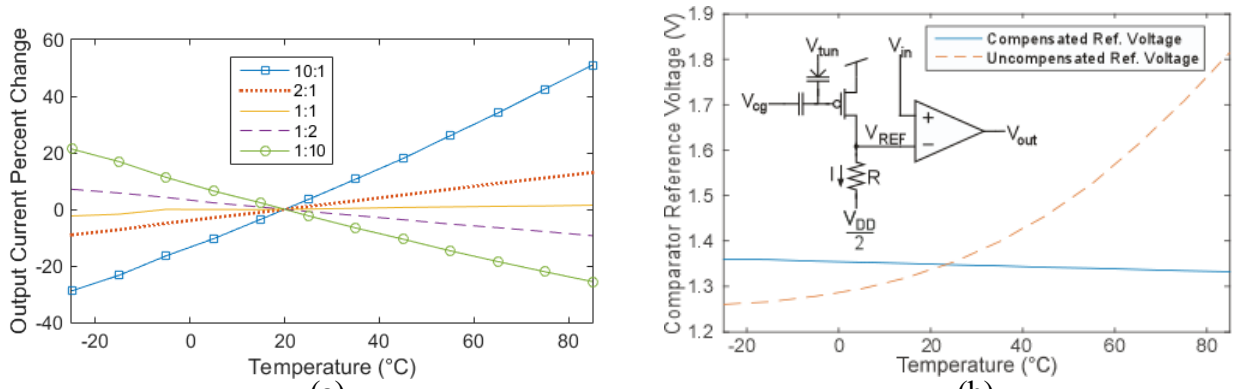

Figure 5. 50. (a) Temperature compensation performance over a range of programming biases. (b) Synthesized comparator circuit performance using a programmed reference value plotted against temperature for a compensated and uncompensated FG current bias.

For a more direct comparison of uncompensated and compensated FG currents, a comparator circuit was synthesized on the RAMP and is shown in Figure 5. 50b. The FG is programmed to draw a current across a resistor to set a desired reference voltage level, V_{REF}. The temperature

compensation ratio does not represent an ideal case, but greatly outperforms the uncompensated case.

5.2.1.4 Energy Harvesting

To supplement the power of the sensor nodes, we investigated an energy-harvesting system to transform some of the excess heat in the environment around the coal gasifier into energy to power the electronics. The energy-harvesting system was constructed using commercially available off-the-shelf components, such as the LTC3108-1 integrated circuit (IC). Based on the heated atmosphere of the targeted gasifier environment, a thermoelectric generator was chosen as the appropriate transducer to power the harvesting system. The following Figure shows a schematic of the circuit that was built.

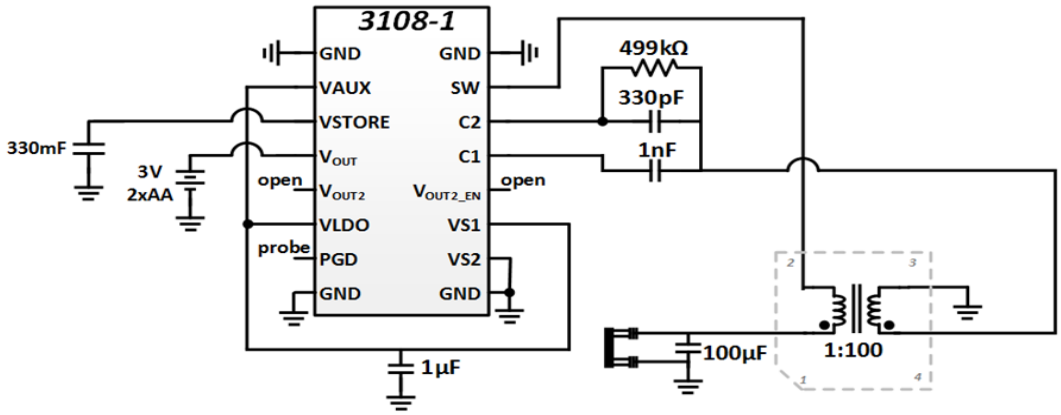

Figure 5. 51. Energy-harvesting circuitry.

To test system performance, a TelosB sensor node was powered solely by the harvested storage buffer, as shown in the Figure below. The blue trace represents the voltage produced by the thermoelectric generator (approximately 500mV). The yellow trace corresponds to the output of the energy buffer (the storage capacitor, where the energy is being collected). The pink trace corresponds to the VAUX pin on the energy harvesting IC. This pin outputs the voltage that is regulated from the charge pump. VAUX must regulate before the storage capacitor can begin to charge. The green trace represents the output voltage that is attached directly to the supply of the TelosB.

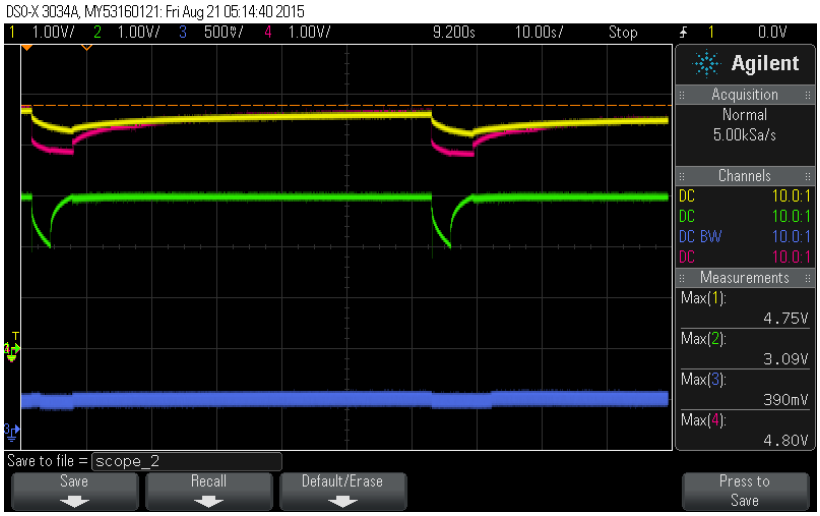

Figure 5. 52. Energy-harvesting system powering a TelosB wireless sensor node.

We also investigated the design of a custom energy-harvesting integrated circuit to replace the commercial prototype and to provide more efficient performance. A basic design for a power converter (i.e. charge pump) and control unit (perturb-and-observe frequency modification) was completed in simulation. The following Figure shows the schematic and the output of single-clock charge pump. The switching frequency of the charge pump is modified with feedback to ensure maximum output power. A single-clock charge pump is used to reduce power consumption. This charge pump can be used to step up the voltage output of a thermoelectric generator (often around 200mV) up to a voltage that can be used to power the whole system (approximately 3V).

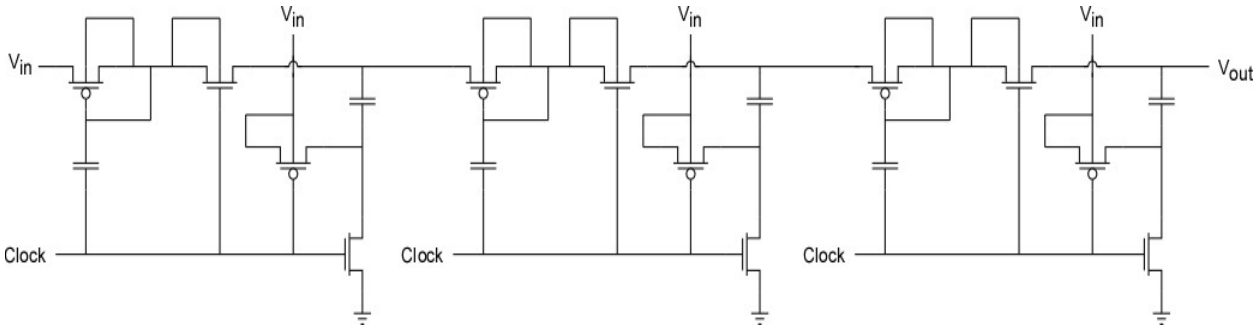

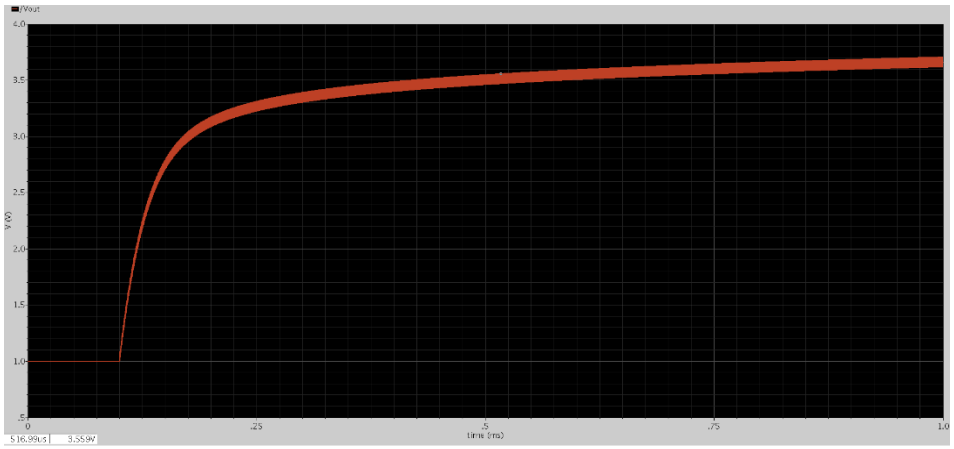

Figure 5. 53. Schematic and simulated results of the single-clock charge pump for a custom energy-harvesting system.

5.2.2 Subtask 5.2: Wireless data transport

5.2.2.1 Implementation of data collection and remote configuration protocols

The Collection Tree protocol (CTP) [1] was identified as a baseline technique for data collection. CTP is a distance-vector class of network routing protocols which dynamically establishes a data collection structure from all nodes to a single root (the base station). The key characteristics that distinguish CTP from other data collection protocols for sensor network are: (i) an agile link estimator which enables quick revision of routing paths when link quality changes and (ii) an adaptive beaconing strategy which increases the frequency of route discovery beacons when bad routes are detected and exponentially decreases the beaconing intervals when routes are relatively stable.

CTP has been evaluated before in different sensor network testbeds and good routing delivery performance has been demonstrated with a packet delivery ratio of over 90%. However, these tests were under low inter-packet intervals of approximately one packet every 16 – 25 seconds [1]. In this project, the goals were to study the routing delivery performance as a function of source packet generation rates and number of nodes. The aim was to understand the limit on source data rate that can be supported under different sensing parameters.

Based on our prior experience in working with multi-hop wireless sensor networks, we chose the Telosb as our primary platform for integrating the radio, processing and sensors. The Telosb has an 8MHz TI MSP430 processor and is integrated with an IEEE 802.15.4 Chipcon radio operating in the 2.4 GHz range. The mote offers several ADC pins for interfacing external sensors. It operates on 2AA batteries and is ideal for low power applications.

In order to be able to change the parameters on the mote remotely, a simple wireless flooding protocol was implemented. This enabled changing parameters such as sampling frequency and data transmission rate wirelessly from the base station in a post deployment phase.

5.2.2.2 Design and evaluation of a linear model based scheme for dynamic data compression

Model based information-centric ideas were explored to reduce the amount of data being transmitted, while still retaining the information being conveyed from the sensors to the base station or the controller. Such real-time data reduction ideas are important when the network scales to several hundreds to thousands of sensors. Transmitting raw data from each sensor over the network is infeasible. In this project, we designed a *dynamic linear model based scheme* for reducing the information being transmitted.

For any given sensor s it generates data d_s such that at any given time t, sensor data d_s has a value v_t. For example, a temperature sensor s would generate data d_s that is a tuple of values $\{v_0, v_1, ..., v_n\}$ corresponding to time $\{t_0, t_1.....t_n\}$. Instead of transmitting each data sample, the model based scheme aims to transmit only a subset of the data samples while still maintaining an acceptable error level at the receiver. The model runs synchronously on both ends of the communication; namely, source sensor and the base station within an application. Initially, sensor values corresponding to time t_0 and t_1 are communicated irrespective of the system state. Each sensor dynamically builds an estimation model m_s that estimates the value of the sensor s at time t using values at time $t - 1$ and $t - 2$. The model estimates the value e_t by using a linear equation represented by equation (1) over a sliding window with previous two time intervals. It achieves this by first solving m and c in equation (1) using the values at time $t - 1$ and $t - 2$.

$$v_t = m_t + c \quad \ldots\ldots\ldots\ldots\ldots\ldots\ldots\ldots(1)$$

Once it has determined m and c, the value e_t is estimated for time t. The value et at time t it is compared with the real value from sensor v_t; if the difference ratio $(v_t - e_t)/ v_t$, (represented as δt), falls within certain threshold T then the sensor does not communicate to the controller. When the difference δt doesn't fall within the threshold T, the sensor transmits the real value v_t and the new model parameters to update the receiver.

On the other hand, model at the controller m_c estimates the value e_t at time t and if no message is received from sensor s at the given interval, the controller reports estimated value e_t as the value from the sensor. It is important to note that e_t at both m_c and m_s are always expected to be identical at any given time t. The model m_c updates the equation (1) on receiving the control messages and reports the received value v_t as the value of sensor s.

Algorithm 1 Algorithm for sensor model m_s

1: **Initialize:**
   Transmit the values (v_0, v_1) for time (t_0, t_1)
2: **for** Each time t **do**
3: Solve for m, c in $e_t = m * t + c$ using (v_{t-1}, v_{t-2}) and $(t-1, t-2)$
4: Estimate sensor data value e_t at current time t
5: Calculate difference percentage $\delta_t \leftarrow |e_t - v_t|/v_t * 100$
6: **if** $\delta_t > th$ **then** ▷ If δ_t doesn't compare
7: Transmit v_t
8: Send control message
9: **end if**
10: **end for**

Algorithm 1 Algorithm for controller model m_c

1: **Initialize:**
   Receive the values (v_0, v_1) for time (t_0, t_1)
   Solve for m, c in $e_t = m * t + c$ using (v_0, v_1) and (t_0, t_1)
2: **for** Each time t **do**
3: Estimate sensor data value e_t at current time t
4: **if** control message is heard **then** ▷ If δ_t doesn't compare
5: **return** v_t
6: **end if**
7: **return** e_t
8: **end for**

Figure 5.54. Linear model based algorithm for data reduction.

Note that the model mc can introduce a small difference ***T*** (the threshold) but importantly it reduces traffic on the network. Also, in the presence of message losses, model inconsistencies may temporarily arise between the sensor and the controller. The difference is resolved upon receiving a subsequent message from the sensor.

5.3 Results and Discussion:

5.3.1 Subtask 5.1: Interfacing Electrical Outputs to Motes:

The final version of the wireless sensor node including the sensor interfacing circuitry and the wireless sensor mote is shown in Figure 5. 55. This structure consists of a vertical stack of three main components: the sensing circuit, the wireless sensor node (commonly referred to as motes) , and the battery pack. The sensing circuit interfaces the connection to the sensor via two banana connectors (red and black connectors of Figure 5. 55) to the leads of the embedded thermistor. The sensing circuit is designed to output a proportional voltage in a desired range of the thermistor resistance which was determined through characterization. This output voltage is pinned out below the circuit to the mote and measured by its analog-to-digital converter (ADC). The ADC resolves the output voltage of sensing circuit to a corresponding digital word which can then be transmitted

wirelessly to the base-station mote. These ADC measurements and transmissions are typically taken every thirty to sixty seconds.

In total, six wireless sensing nodes were constructed to enable a demonstration of the performance. All the components are modular and any battery pack, mote, and/or sensing circuit can be swapped out with one another. The design also has the capability of being programmed in the field to provide significant flexibility. All circuit components were selected with a low temperature dependence for robust operation in a furnace environment.

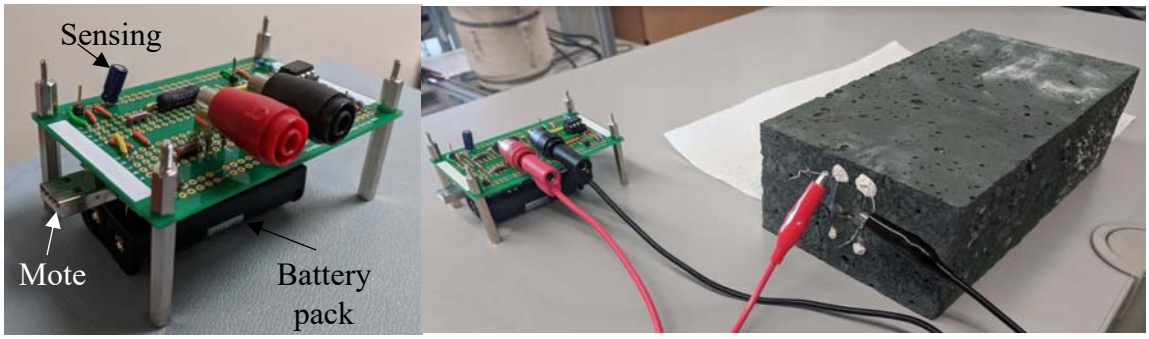

Figure 5. 55. Finalized design of wireless sensing node (left) and it interfaced with an embedded thermistor within a furnace brick.

Figure 5.56 shows the performance of the wireless sensing node during a furnace experiment that emulates the brick under a coal gasifier conditions. The experiment has the furnace holds the brick at 1350°C for 40 hours (from hours 10 to 50 in Figure 5.56) to place the brick in a thermally settled condition. The thermistor has a negative temperature coefficient and this effect is reflected in the output voltage since the output voltage is proportional to the effective sensor resistance. The furnace has difficulty keeping its internal temperature at the equilibrium hold temperature of 1350°C as evident in the 150mV variation in the output voltage during the hold period. In fact, as we'll see Figure 5.26, the internal temperature of furnace has difficulty achieving temperatures above 11250°C. However, Figure 5.25 shows the sensitivity of the circuit to detect changes in resistance via temperature. In this case, the temperature variations are around 15°C, which shows in practice if a sensor experiences a large temperature change, the resulting output voltage would be very evident.

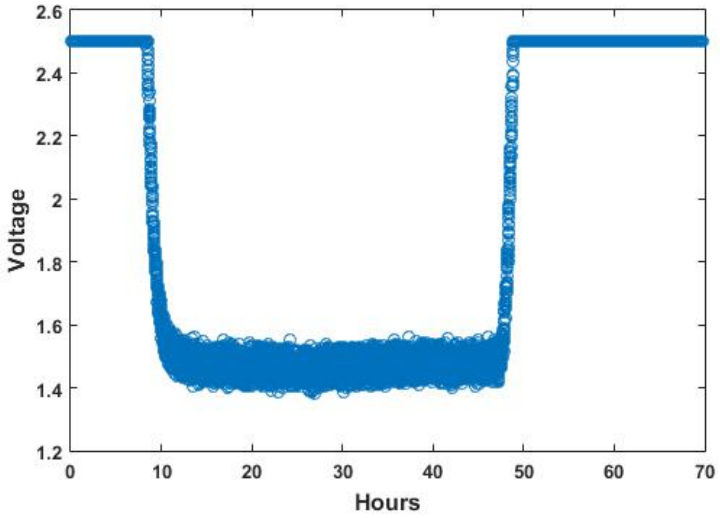

Figure 5.56. Sensing circuit output voltage over experimental furnace run with a measured temperature hold at 1200°C for 10 hours.

Figure 5.57 shows how an output voltage of the sensing circuit is mapped to a temperature via thermistor resistance. Note that for the right y-axis, "Furnace Temperature" is the independent variable and "Thermistor Resistance" is the dependent variable. Looking at the sensing circuit's output voltage, under normal furnace conditions the circuit's output voltage should largely be outputting in the range of 1.25V-2.5V. If the sensor experiences higher than normal temperature, the sensing circuit has enough operational room in the bottom half of its output to measure the intensity of the higher than normal temperature. In the graph, the thermistor resistance changes nonlinearly with respect to temperature which is largely due to the material's composition. An additional contributor to the nonlinearity is due to the heating process within the furnace when the internal temperature reaches the "hold temperature" and the time it takes for sensor to experience the "hold temperature" as the brick material acts as a buffer. Furthermore, the closer the internal furnace temperature is to the "hold temperature," the brick experiences smaller rates of change in temperature due to the temperature control system of the furnace. Comparing Figure 5.56 and Figure 5.57, the measured output voltage during the hold period of Figure 5.56 corresponds well to the mapping of Figure 5.57.

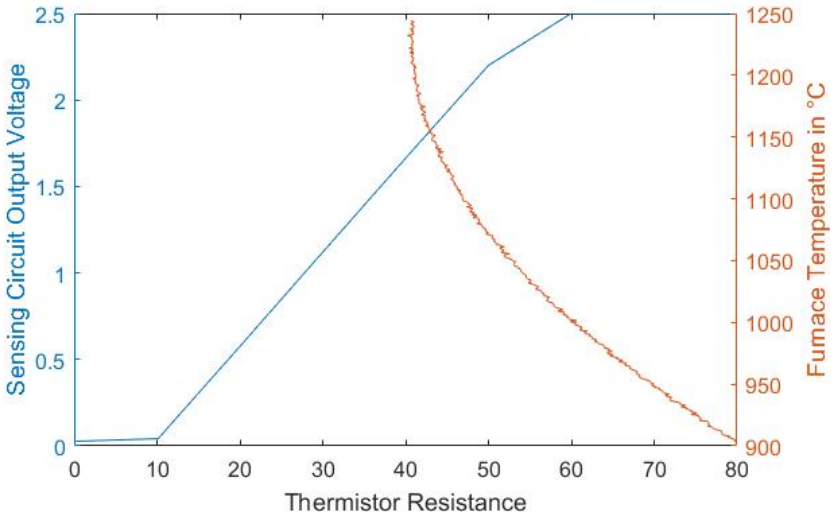

Figure 5.57. Output voltage and temperature versus thermistor resistance.

In summary, the completed wireless sensing node effectively measures the desired temperature range via an output voltage. It is highly module and can be easily reproduced and deployed as the number of sensors in a project increases.

5.3.2 Subtask 5.2: Evaluation of wireless data transport protocol

5.3.2.1 Evaluation of data collection performance

The data collection performance was evaluated under the following conditions

1. At room temperature
2. Inside a polycarbonate chamber adjacent to a furnace heated which is heated to 1400°C

A single hop network was considered where motes are in direct range of a base station. The results are summarized in the following two figures. The key observation is that the link quality is largely unaffected by the furnace temperature. For the common operating range of 1-20 Hz data rates, the performance was noted to be quite high.

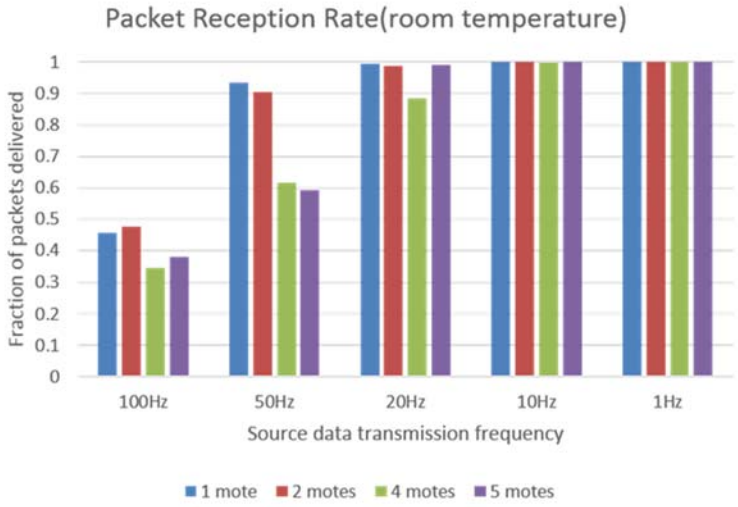

Figure 5.58. Percentage of packets received at the base station as a function of network size and source data transmission frequency (room temperature; no furnace).

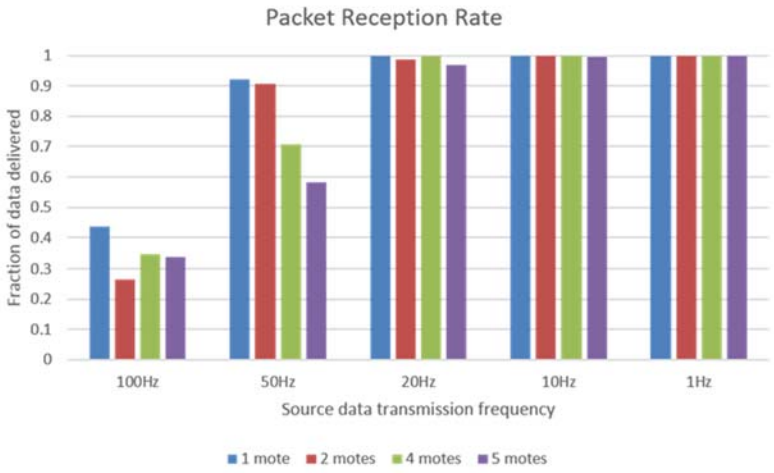

Figure 5.59. Percentage of packets received at the base station as a function of network size and source data transmission frequency (outside furnace at 1400c, inside an enclosed chamber).

5.3.2.2 Evaluation of model based data reduction

To validate the linear model based approach for dynamic data reduction, it was simulated using data from Mica2Dot sensors with weather boards deployed at Intel Berkeley Research Lab [5.y]. The data contains the time-stamped values of humidity, temperature, light, and voltage. The data is queried once every 31 secs and collected between February 28th and April 5th, 2004. The model is validated for three different threshold values i.e. T = {0.1, 0.5, 1} (values are denoted as percentage of difference between $\boldsymbol{v_t}$ and $\boldsymbol{e_t}$). In the following paragraph, the results generated from the experiment are presented.

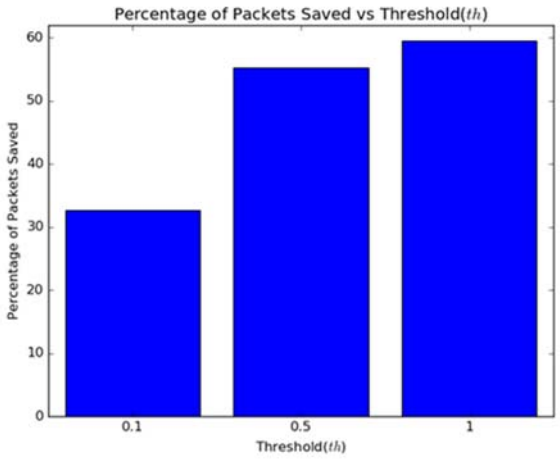

Figure 5.60. Percentage of packets saved as a function of preset threshold T.

First, the number of packets transmitted through the network with and without the piecewise linear estimation strategy are compared. In Figure 5.61, the percentage of packets that are saved from transmission as a function of the preset error threshold (T) is presented. The figure shows that when the threshold T is relaxed, the data transmitted increases. Further, it is important to note that even with the least allowed T=0.1, the model saves about 32.73% of the data packets.

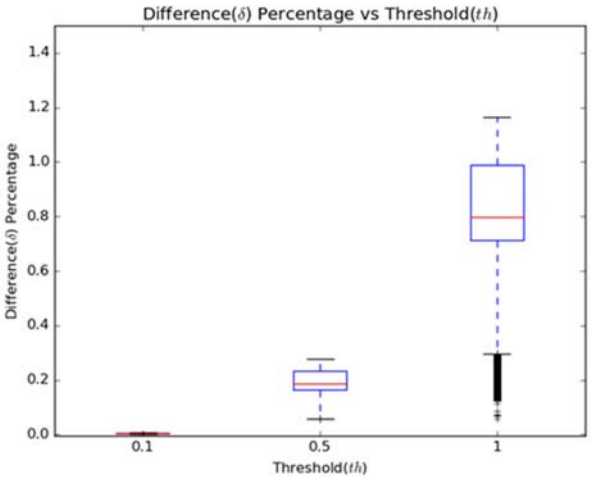

Figure 5.61. Actual error at the sensors as a function of the preset threshold T.

In Figure 5.61, the actual error in the controller with respect to each sensor is compared, as a function of the threshold T. It is observed that for most sensors, the actual errors are actually much smaller than the threshold T.

However, the analysis above assumed that there are no data drops when data is actually transmitted from sender to controller. If data is dropped, then it is likely that the estimate of error at sender and receiver are inaccurate. As a result, the base station may continue to use previous values when in reality the data has also deviated from the model at the sensor side and a new model is being used. This will be corrected only when the subsequent update arrives at the controller from the sensor. In the following figures, the impact of different levels of data drop rate on the accuracy of the linear model based system is presented.

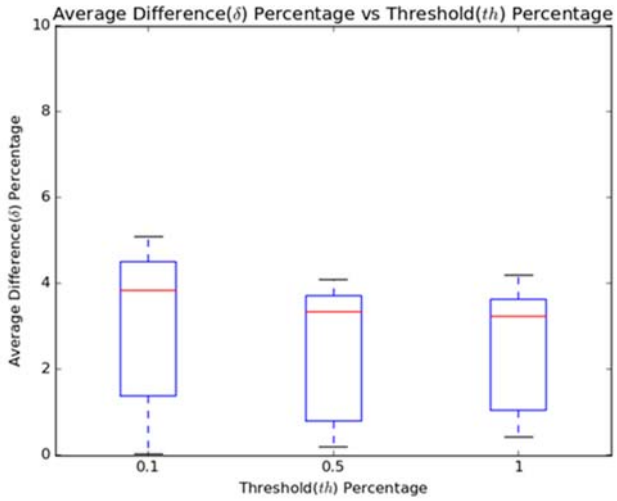

Figure 5.62- Impact of 5% data drops on the accuracy of the linear model based scheme

As seen in Figure 5.62, a median error of around 4% when 5% of the data is dropped. However, it should be noted that without data compression using the linear model the data reliability may actually decrease even more because of the higher interference in data transmission. Thus, the percentage of data drops in the system are likely to significantly decrease when we use such a model based scheme for data transmission.

5.4 Conclusions:

5.4.1 Sensor interface circuitry

Milestone M5 "Initial sensor interface circuitry using off-the-shelf components capable of correct measurements with 95% accuracy" was completed on September 30, 2014.

Milestone M6 "Integrated circuit design for lower-power sensor interface circuitry" was completed on December 31, 2015.

The following is a list of accomplishments for the sensor interfacing task.

1. Sensor interfacing circuits were developed both in discrete form and integrated form for the following sensing modalities:
    a. Resistive-based
    b. Thermocouple
    c. Capacitive-based
2. Inter-operation between sensor interface circuits and wireless sensor nodes were verified and did not degrade sensing performance.
3. Circuit measurement accuracy met at or above the 95% threshold for all sensing circuits.
4. Energy harvesting was investigated to supplement battery life of sensing nodes and was found to be viable source of energy in furnace environments.
5. A temperature compensation circuit was developed to explore reconfigurable sensor-interfacing circuits, which are temperature-sensitive, for furnace environments.

5.4.2 Wireless data transport

Milestone M7 “Establishing protocol for interfacing simulated sensor signals with mote” was completed on Mar 31 2015

The following is a list of accomplishments for the wireless data transport task.

1. Code for interfacing mote (radio + microcontroller) with the sensor circuits was designed and tested
2. The wireless system has been tested inside the furnace setup in lab to estimate link quality and packet loss.
3. Remote, wireless parameter change has been implemented.
    a. The base station sends data to a master mote on UART and the master broadcasts the commands wirelessly to the sensor motes
    b. Sampling intervals and broadcast rates can be changed dynamically
4. A user friendly Graphical Interface has been designed for data visualization and on the go parameter change.
5. A model based data reduction scheme was designed that allows reducing the volume of data being transmitted, while still maintaining the information at the base station within a predefined error rate.

Task 6: Model-Based Estimation of Temperature Profile and Extent of Refractory Degradation

6.1 Introduction:

The operating temperature of a gasifier is one of the key variables. [6.1] [6.2] Lower temperature can lead to lower carbon conversion and increase the viscosity of slag eventually leading to disruption in the slag flow. [6.3] Higher operating temperature can improve carbon conversion, but reduce the life of the refractory. [6.4] [6.5] The lifetime of the refractory lining of the gasifier is a major concern for both cost [6.6] and availability. If the gasifier is operated at the optimum temperature, the lifetime of the refractory can be prolonged to almost 2 years. [6.5] [6.7] Therefore, it is desired that the operating temperature of a gasifier is strictly monitored and controlled. Another key variable in the operation of the entrained-flow gasifiers is extent of slag penetration. Molten slag can penetrate into the refractory lining leading to chemical and physical degradation. [6.4] [6.8] [6.9] [6.10] Replacement of the liner costs significant money and time affecting the profitability of the IGCC plants. Thus a measure of the extent of slag penetration can be very useful not only for process monitoring, but also for developing effective mitigation strategies to reduce extent of slag penetration.

In this work, smart refractory is proposed to detect the temperature profile and extent of slag penetration. The key aspect of the proposed technology is that these sensors are made integral to the refractory by co-firing them. The materials for embedded sensors are carefully selected by matching their thermal properties with the host brick. Therefore, it is expected that the longevity of the brick will not be affected much by the embedded sensors. While smart refractory is a promising concept, several issues listed below need to be solved for their commercial application.

1. **Spatial Temperature Gradient**: The sensors embedded in the refractory lining of the gasifier need to withstand not only the harsh gasifier environment, [6.11] but also slag penetration. [6.4] [6.8] [6.9] [6.10] Unlike many other applications where spatial gradient in the temperature along the sensor length can be neglected, high temperature gradient does exist in the gasifiers [6.12] and therefore cannot be neglected. Spatial temperature gradient along the sensor length will lead to spatial gradient in the temperature-dependent refractory properties, such as the thermal conductivity, heat capacity, resistivity, and dielectric constant that affect the sensor response.

2. **Molten Slag**: As mentioned earlier, the molten slag that penetrates into the refractory lining and therefore, the thermal and electrical properties of the refractory material would change. [6.4] [6.8] [6.9] [6.10] Therefore, the typical approach to estimation of measured variables from the raw electrical response by using correlations that are developed based on the off-line experimental data would not yield satisfactory estimates. Rather, a model-based approach is appropriate for the gasifier application.

3. **Model Inaccuracy and Measurement Noise**: Inaccuracies are unavoidable for any model. In addition, the raw measurement data collected from the gasifier may be very noisy and inaccurate. By using the model and noisy measurements, filtering algorithms can be used to filter out the noises and estimate the variables accurately.

4. **Wireless Sensor Network**: The data collected from the embedded sensors are supposed to be transfer by using a wireless sensor network. These measurements are noisy and suffer from communication constraints, packet dropouts, and synchronization errors. Due to the limitations in the communication bandwidth, only limited packets can be transmitted at any instant. Measurements can be out of sequence. Out-of-sequence measurement data is used in this work to estimate temperature and slag penetration profile of a gasifier refractory wall.

In this task, the above issues are addressed. The assumptions made in this task are listed below:

1) Slag can only fill in the pores of the refractory brick. Chemical interaction between the slag and refractory are neglected.
2) The refractory material is homogenous and isotropic.
3) As the electrical conductivity of slag is much lower than the sensor material, slag penetration is not expected to affect the electric resistance of the slag-infiltrated brick.

The objective of this task was to develop algorithms for model-based estimation of temperature profile in the refractory, slag penetration depth, spallation thickness, and resultant health by using the data from the wireless sensor network. The specific subtasks were as follows:

Subtask 6.1 Modeling of the Smart Refractory with Embedded Sensors- A first-principles, dynamic model of the smart refractory will be developed. Experimental data collected at regular time intervals will be used to validate the model.

Subtask 6.2 Development of the Nonlinear Unknown Input Filter (UIF) for Measurements from a Wireless Network- For estimating the states and parameters, the algorithm for nonlinear UIF will be developed using unscented transformation. The measurements will be considered to be available from a wireless network with the following characteristics- random packet dropouts, communication constraints, and synchronization errors.

Subtask 6.3 Testing of the Developed Algorithms- The temperature profile and the extent of degradation (slag penetration and spalling) estimated by the nonlinear filter will be compared with the experimental data of temperature profile and extent of degradation (from the destructive tests). In addition, the algorithm will be tested for simulated data from an entrained-flow gasifier model that has been developed at WVU.

6.2 Experimental Methods:

Thermal Model:

It is anticipated that the smart brick will be placed on the hot face of an entrained-flow gasifier Therefore, a thermal model of the brick has been developed by considering heat transfer with the bulk of the gasifier and with other bricks on the wall. In addition, thermal models of other layers on the wall in the direction from hot face to cold face, namely the alumina castable layer, the silica fire brick layer, and steel shell layer have also been developed.

The dominant heat transfer mechanism through the gasifier wall is by conduction. Therefore, the same governing equation shown in Equation 3.1 is used for all the layers. The boundary condition on the hot face shown in Equation 3.2 is based off our earlier work and includes wall-gas, wall-

solid, and wall-wall heat transfer. [6.13] Effects of the radiative heat transfer, convective heat transfer, and heat loss from the outer shell are all considered in achieving this hot surface temperature profile. [6.13] Temperature and flux continuities are assumed at all interface boundaries. The governing equation is shown in Equation 6.1:

$$\frac{\partial T}{\partial t} = \frac{1}{\rho C_p}\left(\frac{1}{r}\frac{\partial}{\partial r}(rK\frac{\partial T}{\partial r}) + \frac{\partial}{\partial z}\left(K\frac{\partial T}{\partial Z}\right)\right) \quad (6.1)$$

where T is temperature, K is thermal conductivity, ρ is density, C_p is specific heat.

The boundary condition (BC) for the hot surface is given by:

$$T_{ch} = T_{gasifier} + mZ \quad (6.2)$$

where $T_{gasifier}$ is a constant temperature, m is the slope, which is set to be -28.6 $\frac{℃}{m}$.

The BCs on all interfaces are given by:

$$-K_1\frac{\partial T_1}{\partial r} = -K_2\frac{\partial T_2}{\partial r} \quad (6.3)$$

$$T_1 = T_2 \quad (6.4)$$

The BC on the cold surface is given by:

$$h_{air}(T_{st} - T_{air}) = -k_{st}\frac{\partial T}{\partial r} \quad (6.5)$$

where h_{air} denotes the convective heat transfer coefficient.

Slag Penetration Model:

The main driving force to be considered in the process of bulk slag intrusion is the capillary pressure. [6.14] In the gasifier application, the pore system of the refractory lining is oriented in horizontal direction. The velocity of capillary flow through the horizontal pores can be calculated by the Washburn equation. [6.15]

$$\varphi = \frac{\Delta P {R_p}^2}{8\eta l} \quad (6.6)$$

where φ is velocity of slag penetration, ΔP is the pressure drop across refractory lines, r is the refractory pore radius, η is slag viscosity, and l is infiltration length.

By accounting for the tortuosity of the refractory pore system, the following equation is used to evaluate the slag penetration length: [6.16]

$$\frac{dl}{dt} = \frac{\Delta P {R_p}^2}{8\eta\sigma^2 l} \quad (6.7)$$

where σ is the tortuosity of refractory pore system.

Table 6.1. shows the parameters for the penetration model. [6.10] The total pressure drop shown in the following table is the sum of the hydrostatic pressure, pressure drop across the wall, and the capillary pressure. The hydrostatic pressure is balanced by adhesion of slag to the wall of refractory. Due to the cracks and porosity of the refractory material, the pressure drop across the wall is considered to be very small. The capillary pressure is calculated by Young-Laplace equation and found to be 0.85 atm. [6.10] Based on above information, Williford et al. set the total pressure drop to be 1×10^5. [6.10]

Table 6.1. Parameters for the penetration model

Parameter	Value	Reference
Pore radius (m)	10×10^{-6}	[6.10]
Total pressure drop (Pa)	1×10^5	[6.10]
Tortuosity	7	[6.10]

Sensor Models:
In this task, five types of sensors, namely, thermocouple, thermistor, resistive circuit, interdigital capacitor, and strain gauge, are being considered. These sensor models will work as measurement models in the estimation algorithm. For all the results obtained by using IDCs, IDCs are considered to be placed perpendicular to the hot face, unless otherwise mentioned. For all the results by using resistive-type sensors (thermistor, resistive circuit, and strain gauge), they are also considered to be installed in the direction perpendicular to the hot face of gasifier.

Thermistor Model:

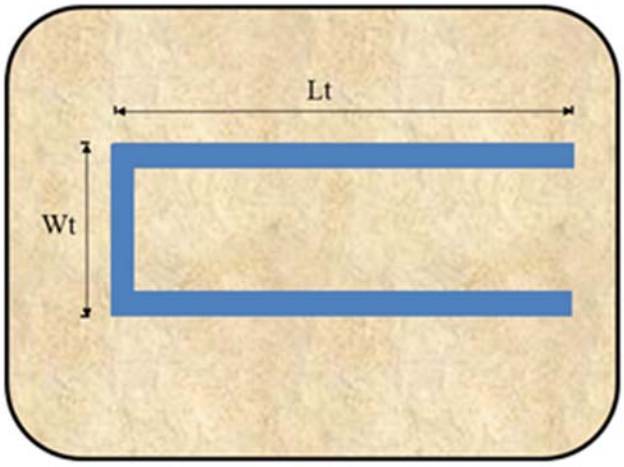

Figure 6.1. Schematic of the smart brick with layouts of thermistor.

The schematic of the embedded thermistor is shown in Fig. 6.1. Resistance of thermistors changes with the change in the temperature. The output electrical resistance of the thermistor depends on the electrical property of the sensor material. The expected electrical conductivities of slag is about 0.192 $\Omega^{-1}\text{cm}^{-1}$ at 1500 ℃, [6.17] while that of the sensor material is about 43.2 $\Omega^{-1}\text{cm}^{-1}$. As the electrical conductivity of slag is much lower than the sensor material, slag penetration is not expected to affect the electric resistance of the slag-infiltrated brick. The equivalent circuit method

is used to model the thermistor by considering spatially distributed temperature-dependent electrical conductivity of the sensor material. Thermistor was assumed to be a series connection of resistors. Resistances R_1 through R_n correspond to the resistances of each control volume where the sensor is located. Obviously, these resistances would differ depending on the local temperature. The electrical resistivity of the sensor material is calculated by Equation 6.8 based on our in-house data for WSi_2-Al_2O_3 thermistor:

$$\zeta = 1.1544 \times 10^{-6} T + 9.4155 \times 10^{-4} \tag{6.8}$$

where T is in ℃, and ζ is in Ω-cm.

The overall resistance of thermistor is the sum of the resistance of every control volume.

$$\bar{R} = \sum_{i=1}^{n} \bar{R}_i = \sum_{i=1}^{n} \frac{\zeta_i \Delta L}{S_i} \tag{6.9}$$

where ΔL is the length of the control volume, and S_i is the cross-sectional area of the thermistor for control volume i.

Interdigital Capacitor (IDC) Model:
IDC is a comb-like capacitor with wide applications, such as in integrated circuits, [6.18] [6.19] for dielectric property studies, [6.20] and as temperature sensors. [6.21] [6.22] The schematic of the layouts of IDC embedded in smart brick is shown in Fig. 6.2.

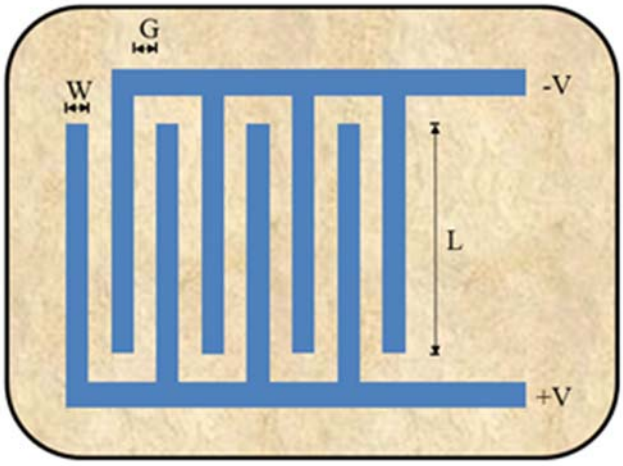

Figure 6.2. Schematic of the smart brick with layouts of the IDC.

Both the physical dimensions of the sensor and the permittivity of the refractory impact the capacitance. Therefore, overall change in the capacitance of the IDC sensor is expected to occur due to the following three reasons:

1) change in the dielectric constant due to temperature change;
2) thermal expansion of the sensor materials, which will change the size of the sensor and the distance between the fingers;

3) change in the dielectric constant due to slag infiltration.

Fig. 6.2 shows the geometry of the IDC sensor. Using conformal mapping, an analytical model of the IDC has been proposed by Igreja and Dias. [6.23] The conformal mapping technique can convert the capacitance of an IDC to the capacitance of an equivalent easily-calculated plate capacitor in a new coordinate. Due to the 2-D temperature distribution considered in this work, the approach proposed by Igreja and Dias [6.23] is slightly modified. The total capacitance of an IDC can be evaluated as a function of interior electrode capacitance C_I and exterior electrode capacitance C_E as shown in Fig. 6.3. Using equivalent circuit analysis, the total capacitance for an IDC sensor shown in Fig. 6.3 is obtained by:

$$C = \frac{C_I^2 C_E^1}{C_I^2 + C_E^1} + \frac{C_I^{2N-3} C_E^{2N-2}}{C_I^{2N-3} + C_E^{2N-2}} + \sum_{i=2}^{N-2} \frac{C_I^{2i-1} C_I^{2i}}{C_I^{2i-1} + C_I^{2i}} \qquad N > 3 \tag{6.10}$$

where N is the number of electrodes.

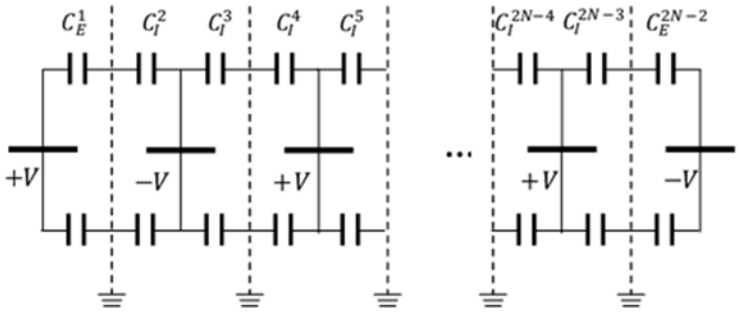

Figure 6.3. Equivalent circuit for an IDC with N electrodes.

As the interdigital capacitor will be embedded in the smart refractory, the temperature distributions both above and under the electrodes of the sensor will affect the dielectric constant of refractory. The partial capacitance technique is used to account for this spatial variation of dielectric constants. For each layer above the sensor plane as shown in Fig. 6.4, $C_{Ia,i}$ and $C_{Ea,i}$ can be obtained by the conformal mapping technique with partial capacitance technique as shown in Equation 6.11 and 6.12. [6.23]

$$C_{Ia,i} = \varepsilon_0 L(\varepsilon_{i,a} - \varepsilon_{i+1,a}) \frac{K_e(k_I)}{K_e(k_I')} \tag{6.11}$$

$$C_{Ea,i} = \varepsilon_0 L(\varepsilon_{i,a} - \varepsilon_{i+1,a}) \frac{K_e(k_E)}{K_e(k_E')} \tag{6.12}$$

In Equations 6.11 and 6.12, ε_0 is vacuum permittivity; $\varepsilon_{i,a}$ and $\varepsilon_{i+1,a}$ are the relative dielectric constants of layer i and layer $i+1$ above the sensor plate respectively; $C_{Ia,i}$ is the interior half-capacitance of layer i above the electrode plane. $K_e(.)$ is the complete elliptic integral of first kind with modulus k_I, k_I', k_E, and k_E'. These moduli are dependent on the key design parameters of IDC (i.e. W and G as shown in Fig. 6.2)) and the thickness of dielectric layer τ. More details on how these moduli are calculated by W, G and τ can be found in reference [6.23].

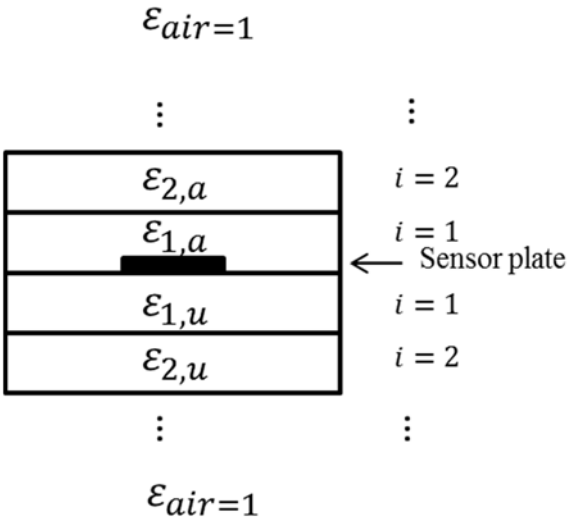

Figure 6.4. Schematic showing the partial capacitance technique.

The same approach is used to obtain $C_{Iu,i}$, the capacitances of layers under the electrode plane. Then, using the partial capacitance technique, [6.23] the total interior electrode capacitance C_I^i as shown in Fig. 6.3 can be calculated by summing the interior layer capacitances above and under the sensor plane.

$$C_{I,a} = C_{I,a\infty} + \sum_{i=1}^{Ns} C_{Ia,i} \quad (6.13)$$

$$C_{I,u} = C_{I,u\infty} + \sum_{i=1}^{Ns} C_{Iu,i} \quad (6.14)$$

$$C_I^i = C_{I,a} + C_{I,u} \quad (6.15)$$

where Ns is the number of sensitive layers; $C_{I,a\infty} = C_{I,u\infty} = \varepsilon_0 L \frac{K_e(k_{I\infty})}{K_e(k'_{I\infty})}$. Equations used to calculate $k_{I\infty}$ and $k'_{I\infty}$ can be found in reference [6.23].

The same approach is used to obtain the total exterior capacitance C_E^1 and C_E^{2N-2}. Then, the output capacitance is obtained by Equation 6.10.

The change in temperature can not only affect the refractory dielectric constant but also the dimensions of the IDC. Both of them affect the capacitance. The coefficient of linear thermal expansion of high chromia brick is $8.154 \times 10^{-6}\ ^{\circ}\mathrm{C}^{-1}$. A temperature dependent sensor dimension is used to deal with the effect of the thermal expansion.

The dielectric constant of high chromia brick would change due to slag penetration, which results in a change in the output of embedded IDC as well. To evaluate this impact, the effective dielectric constant of slag-penetrated refractory needs to be calculated. Assuming that the slag can only fill the pores of refractory brick and neglecting effect of any other physical or chemical interaction between slag and refractory, a phenomenological mixing rule is used to calculate the effective dielectric constant. Using the spatially distributed effective dielectric constant, the output capacitance of an IDC sensor for varying extent of slag penetration can be obtained by the same approach as described before.

Resistive Circuit Model:
The embedded resistive circuit can be useful for detecting the temperature difference as well as the refractory spallation. Fig. 6.5 shows the layout of the embedded resistive circuit considered in our study:

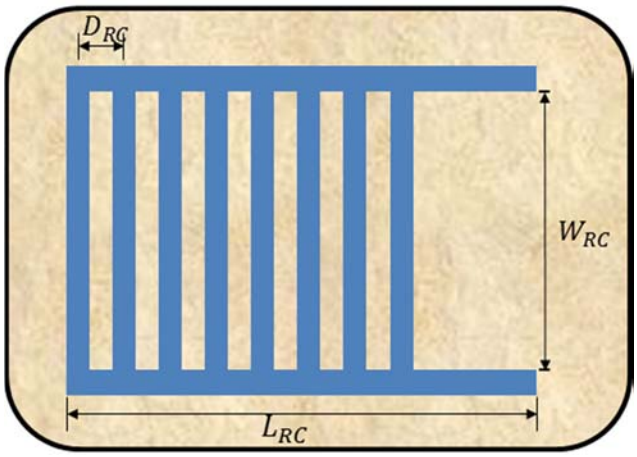

Figure 6.5. Schematic of smart brick with layouts of the resistive circuit.

The output resistance of the resistive circuit depends on both the temperature-dependent electrical conductivity of the sensor material and the physical dimensions of the sensor. The temperature-dependent electrical conductivity is calculated by Equation 6.8. Assuming that the sensor is installed in the center of the brick and using the equivalent circuit method as discussed in thermistor model section, the model for the embedded resistive circuit has been developed.

Thermocouple Model:
The voltage produced by a thermocouple is completely depends on the sensor material. The data available in the literature [6.24] for R-type thermocouple (platinum vs. platinum plus 13% rhodium, reference T=32°F) have been used in this study.

Strain Gauge Model:
When the refractory is subjected to a stress, the sensor embedded in it will be stretched or compressed and the sensor deformation caused by the stress will result in the change of the electrical resistance. The change in the electrical resistance of the sensor depends on the deformation of the sensor while the extent of deformation due to a given stress strongly depends on the material properties. The following Fig. 6.6 shows the schematic of the embedded strain gauge that has been modeled.

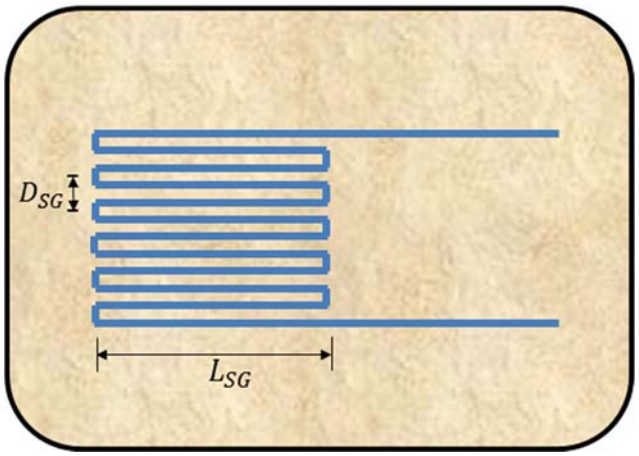

Figure 6.6. Schematic of smart brick with layouts of strain gauge.

The strain and stress will be related by Hooke's law:

$$\sigma = E\varepsilon \tag{6.16}$$

where σ represents stress, and ε represents strain.
Using the definition of strain and the equivalent circuit method, a first-principle model for the embedded strain gauge was previously developed in Matlab.

Estimation:
Traditional Kalman Filter:
For estimating the temperature and extent of slag penetration, the traditional Kalman filter (TKF) is evaluated first in this work. The thermal model (process) employed in the estimator is a non-linear model including both the differential governing equations and the algebraic boundary and constitutive relations. The system of equations is of the form shown below:

$$\dot{x} = \bar{F}(x, z, u) + \gamma \tag{6.17}$$
$$\bar{0} = \bar{G}(x, z, u) \tag{6.18}$$
$$Y = \bar{H}(x, z) + \omega \tag{6.19}$$

where x, z, u, γ, ω, and Y represent differential variables, algebraic variables, system inputs, process noise, measurement noise, and measurements, respectively.

In order to apply the TKF to the nonlinear system shown above, the above system is linearized first. For a linear system shown below:

$$\dot{x} = A\,x + B\,z + E\,u \tag{6.20}$$
$$0 = C\,x + D\,z + Fu \tag{6.21}$$
$$Y = Gx + Hz \tag{6.22}$$

The approach proposed by Mandela et al. [6.25] is used to convert the DAE system into an ODE system. This method treated the system as augmented system with both the algebraic and the differential variables. The matrix form of the system is given by:

$$\begin{bmatrix}\dot{x}\\ \dot{z}\end{bmatrix} = \begin{bmatrix} A & B \\ -D^{-1}CA & -D^{-1}CB \end{bmatrix}\begin{bmatrix}x\\ z\end{bmatrix} + \begin{bmatrix} E & 0 \\ -D^{-1}CE & -D^{-1}F \end{bmatrix}\begin{bmatrix}u\\ \dot{u}\end{bmatrix} \quad (6.23)$$

$$Y = [G \quad H]\begin{bmatrix}x\\ z\end{bmatrix} \quad (6.24)$$

The augmented form shown below is generated:

$$\dot{x}^{aug} = A^{aug}\, x^{aug} + B^{aug}\, u^{aug} \quad (6.25)$$

$$Y = H^{aug} x^{aug} \quad (6.26)$$

where

$$A^{aug} = \begin{bmatrix} A & B \\ -D^{-1}CA & -D^{-1}CB \end{bmatrix}$$

$$B^{aug} = \begin{bmatrix} E & 0 \\ -D^{-1}CE & -D^{-1}F \end{bmatrix}$$

$$H^{aug} = [G \quad H]$$

Then, the standard traditional KF algorithm [6.26] is applied to the modified system shown above.

Extended Kalman Filter:
The extended Kalman filter (EKF), which is widely used for nonlinear dynamic systems, is also evaluated. In this study, performance of the TKF is found to be unsatisfactory for estimating the slag penetration. Standard algorithms available in the literature for the EKF have been used. [6.27]

Unscented Kalman Filter:
The nonlinear unscented Kalman filter (UKF) is also studied in this task. If the noise of process and measurement are additive, the UKF algorithm can be simplified. As discussed in the previous section, the process model employed in the estimator includes both the differential governing equations and algebraic boundary and initial equations. The system is a differential algebraic equation (DAE) system. Therefore, the unaugmented algorithm of the additive noise UKF for DAE system is explored firstly.

For a DAE system shown in Equation 6.25 and 6.26, the UKF algorithm is explained below: [6.27]

The initial conditions:
$\hat{x}_0 = E[x_0]$ with error covariance P_0

Pick sigma points:

$$X_{k-1} = [\hat{x}_{k-1} \;\; \hat{x}_{k-1} \pm \sqrt{(L+\lambda)\hat{P}_{k-1}}] \quad (6.27)$$

Calculate Z_{k-1} by $\bar{0} = \bar{G}(X_{k-1}, Z_{k-1}, u)$.

Time update:

$$X_k = \bar{F}(X_{k-1}, Z_{k-1}, u) \quad (6.28)$$

$$x_k^- = \sum_{i=0}^{2L} W_i^{(m)} X_{i,k} \quad (6.29)$$

$$P_k^- = \sum_{i=0}^{2L} W_i^{(c)} \{X_{i,k} - x_k^-\}\{X_{i,k} - x_k^-\}^T + Q \quad (6.30)$$

Recalculate Z_k by $\bar{0} = \bar{G}(X_k, Z_k, u)$.

$$X_k^{aug} = [X_k{}^T \ , Z_k{}^T]^T \tag{6.31}$$
$$x_k^{aug-} = \sum_{i=0}^{2L} W_i^{(m)} X_{i,k}^{aug} \tag{6.32}$$
$$Y_k = H(X_k^{aug}) \tag{6.33}$$
$$y_k^- = \sum_{i=0}^{2L} W_i^{(m)} Y_{i,k} \tag{6.34}$$

Measurement correction:

$$P_{\tilde{y}_k\tilde{y}_k} = \sum_{i=0}^{2L} W_i^{(c)} \{Y_{i,k} - y_k^-\}\{Y_{i,k} - y_k^-\}^T + \mathrm{R} \tag{6.35}$$
$$P_{x_k y_k} = \sum_{i=0}^{2L} W_i^{(c)} \{X_{i,k}^{aug} - x_k^{aug-}\}\{Y_{i,k} - y_k^-\}^T \tag{6.36}$$
$$K = P_{x_k y_k} P_{\tilde{y}_k\tilde{y}_k}^{-1} \tag{6.37}$$
$$\hat{x}_k = x_k^- + K^{diff}(y_k - y_k^-) \tag{6.38}$$
$$P_k = P_k^- - K^{diff} P_{\tilde{y}_k\tilde{y}_k} K^{diff^T} \tag{6.39}$$

Where

K^{diff} is the Kalman gain corresponding to differential states

$$\lambda = \alpha^2(L + k) - L, \tag{6.40}$$
$$W_0^{(m)} = \frac{\lambda}{L+\lambda} \tag{6.41}$$
$$W_0^{(c)} = \frac{\lambda}{L+\lambda} + (1 - \alpha^2 + \beta), \tag{6.42}$$
$$W_i^{(m)} = W_i^{(c)} = \frac{1}{2(L+\lambda)} \quad i = 1, \ldots, 2L, \tag{6.43}$$

Q is process noise and R is measurement noise.

If the non-additive noise is considered, the simplified UKF algorithm cannot be used. The augmented UKF algorithm for DAE system has also been implemented. The major difference between the augmented UKF and unaugmented UKF is that the process and measurement noises are considered to be state variables and are estimated in the augmented UKF. The proposed approach is explained below: [6.27]

The initial conditions:

$\hat{x}_0 = E[x_0]$ with error covariance P_0

$\hat{x}_0^{aug} = E[x^{aug}] = [\hat{x}_0^T \ 0 \ 0]^T$

$$P_0^{aug} = E\left[\left(x_0^{aug} - \hat{x}_0^{aug}\right)\left(x_0^{aug} - \hat{x}_0^{aug}\right)^T\right] = \begin{bmatrix} P_0 & 0 & 0 \\ 0 & \mathrm{Q} & 0 \\ 0 & 0 & \mathrm{R} \end{bmatrix}$$

Pick sigma points:

$$X_{k-1}^{aug} = [\hat{x}_{k-1}^{aug} \ \ \hat{x}_0^{aug} \pm \sqrt{(L + \lambda)P_{k-1}^{aug}}] \tag{6.44}$$

Calculate Z_{k-1} by $\bar{0} = \bar{G}(X_k^x, Z_{k-1}, u)$.

Time update:

$$X_k^x = \bar{F}(X_{k-1}^x, Z_{k-1}, u, X_{k-1}^v) \tag{6.45}$$
$$\hat{x}_k^- = \sum_{i=0}^{2L} W_i^{(m)} X_{i,k}^x \tag{6.46}$$

$$P_k^- = \sum_{i=0}^{2L} W_i^{(c)} \{X_k^x - x_k^-\}\{X_k^x - x_k^-\}^T \quad (6.47)$$

Recalculate Z_k by $\bar{0} = \bar{G}(X_k^x, Z_k, u)$.

$$X_k^{aug} = [X_k^{x^T}, Z_k{}^T]^T \quad (6.48)$$

$$\hat{x}_k^{aug-} = \sum_{i=0}^{2L} W_i^{(m)} X_{i,k}^{aug} \quad (6.49)$$

$$Y_k = H(X_k^{aug}) \quad (6.50)$$

$$\hat{y}_k^- = \sum_{i=0}^{2L} W_i^{(m)} Y_{i,k} \quad (6.51)$$

Measurement correction:

$$P_{\tilde{y}_k \tilde{y}_k} = \sum_{i=0}^{2L} W_i^{(c)} \{Y_{i,k} - y_k^-\}\{Y_{i,k} - y_k^-\}^T + \mathrm{R} \quad (6.52)$$

$$P_{x_k y_k} = \sum_{i=0}^{2L} W_i^{(c)} \{X_{i,k}^{aug} - \hat{x}_k^{aug-}\}\{Y_{i,k} - y_k^-\}^T \quad (6.53)$$

$$K = P_{x_k y_k} P_{\tilde{y}_k \tilde{y}_k}^{-1} \quad (6.54)$$

$$\hat{x}_k = \hat{x}_k^- + K^{diff}(y_k - \hat{y}_k^-) \quad (6.55)$$

$$P_k = P_k^- - K^{diff} P_{\tilde{y}_k \tilde{y}_k} K^{diff^T} \quad (6.56)$$

Where

K^{diff} is the Kalman gain corresponding to differential states

$$\lambda = \alpha^2(L + \beta) - L, \quad (6.57)$$

$$W_0^{(m)} = \frac{\lambda}{L+\lambda} \quad (6.58)$$

$$W_0^{(c)} = \frac{\lambda}{L+\lambda} + (1 - \alpha^2 + \beta), \quad (6.59)$$

$$W_i^{(m)} = W_i^{(c)} = \frac{1}{2(L+\lambda)} \quad i = 1, \ldots, 2L, \quad (6.60)$$

Q is process noise and R is measurement noise.

Multi-Scale Dual Kalman Filter:

The extent of slag penetration has great impact on the temperature profile across the gasifier wall. At the same time, extent of slag penetration strongly depends on the temperature history of the gasifier wall. Therefore, it is necessary to estimate both the temperature and the extent of slag penetration simultaneously. However, compared to the temperature, slag penetration is a relatively slow time-varying mechanism. While the time scale of temperature is in minutes, time scale of slag penetration is in hours or days. If estimation of slag penetration is considered in the time scale of temperature, it will result in an unnecessary high computational expense. In order to address this difficulty, the multi-scale extended Kalman filter has been used. [6.28] Based on the results obtained from the heat transfer and slag penetration models, time steps for estimating temperature and slag penetration profiles are set to be 1 min and 30 min, respectively. Two different multiscale extended Kalman filter algorithms have been considered. In the first algorithm, the slag penetration length is considered to be a constant value during the whole 'macro' scale time step (30 min). In the second algorithm, the time update for slag penetration estimation is implemented on a 'micro' time scale (1 min), while the predicted length of slag penetration is corrected by measurements on a macro scale (30 min).

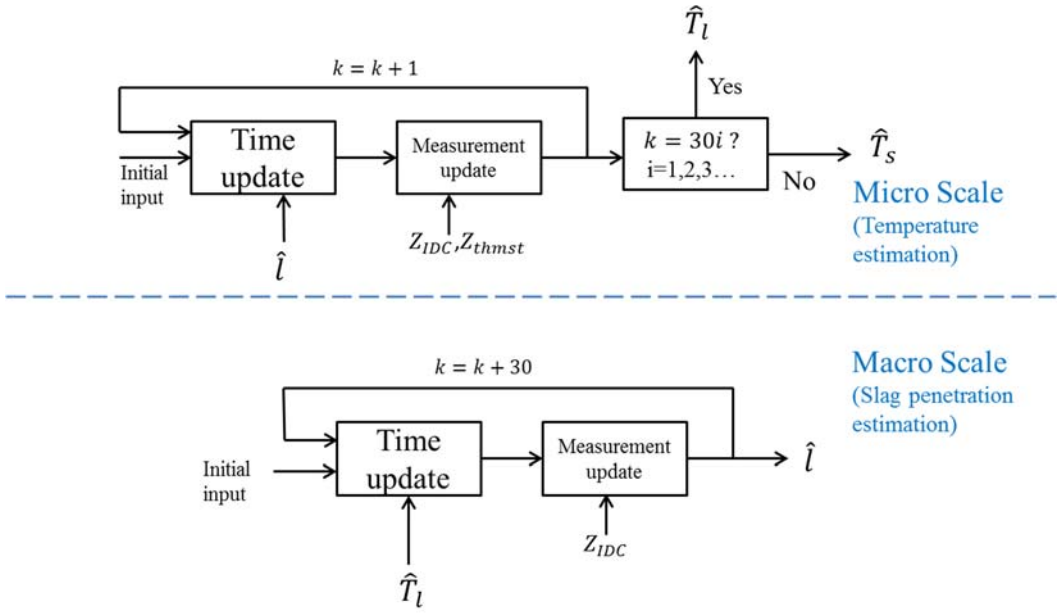

Figure 6.7. Schematic description for multi-scale Kalman filter algorithm 1.

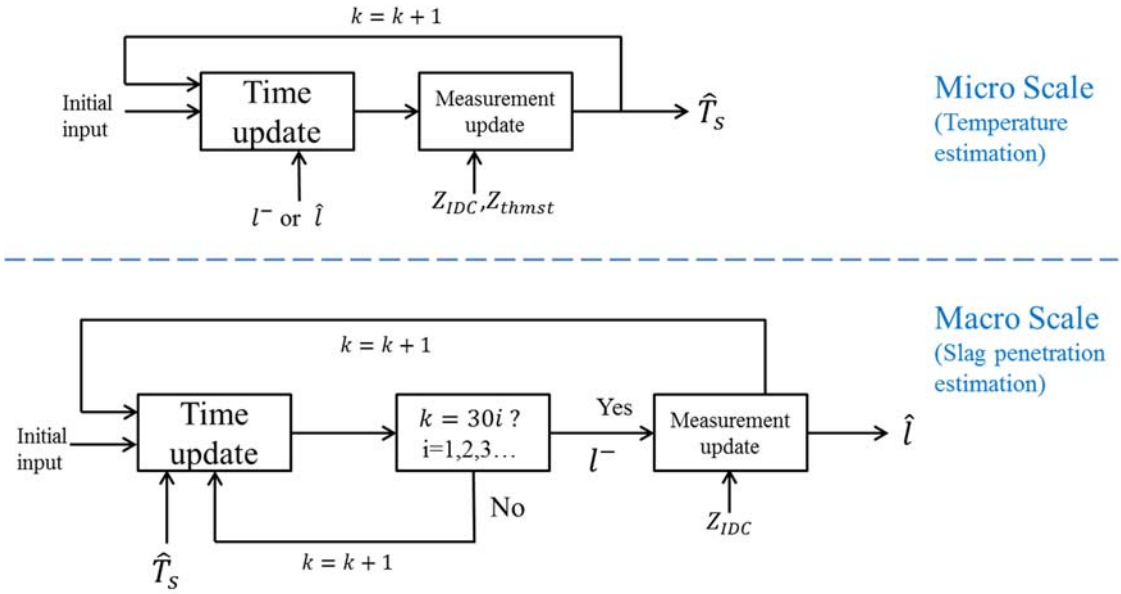

Figure 6.8. Schematic description for multi-scale Kalman filter algorithm 2.

Kalman Filter with Out-of-Sequence Measurements:

The data collected by embedded sensors is supposed to be transferred through a wireless transmitter installed on the surface of the gasifer outer wall. These data are expected to be sent to fusion center for further processing. This transmission process usually suffers from a random time delay due to communication delay, and as a result that measurements for the same target may arrive out-of-sequence (OOSM). The one-step lag (measurements delay within one sampling interval) OOSM problem is well studied by Bar-shalom [6.29] and Zhang [6.30].

For a system shown below:

$$x(k) = A(k, k-1)x(k-1) + v(k, k-1) \quad (6.61)$$
$$z(k) = H(k)x(k) + w(k) \quad (6.62)$$

The problem is to update the state estimates at k step with the "older" measurement collected at step κ ($k\text{-}1 < \kappa < k$). The main difference between Bar-shalom and other's studies is that $v(k, k-1|k)$ is considered to have a non-zero mean in his work. The proposed approach by Bar-shalom is explained below [6.29]:

Time update (retrodict from step k to κ)

$$\hat{x}(\kappa|k) = A(\kappa, k)[\hat{x}(k|k) - Q(k, \kappa)H(k)^T S(k)^{-1} O(k)] \quad (6.63)$$
$$P_{vv}(k, \kappa|k) = Q(k, \kappa) - Q(k, \kappa)H(k)^T S(k)^{-1} H(k)Q(k, \kappa) \quad (6.64)$$
$$P_{xv}(k, \kappa|k) = Q(k, \kappa) - P(k|k-1)H(k)^T S(k)^{-1} H(k)Q(k, \kappa) \quad (6.65)$$
$$P(k|k) = P(k|k-1) - P(k|k-1)H(k)^T S(k)^{-1} H(k)P(k|k-1) \quad (6.66)$$
$$P(\kappa|k) = A(\kappa, k)[P(k|k) + P_{vv}(k, \kappa|k) - P_{xv}(k, \kappa|k) - P_{xv}(k, \kappa|k)^T]A(\kappa, k)^T \quad (6.67)$$
$$S(\kappa) = H(\kappa)P(\kappa|k)H(\kappa)^T + R(\kappa) \quad (6.68)$$

Measurement correction (correct the current states with "older" measurements)

$$P_{xz}(k, \kappa|k) = [P(k|k) - P_{xv}(k, \kappa|k)]\, A(\kappa, k)^T H(\kappa)^T \quad (6.69)$$
$$K(k, \kappa) = P_{xz}(k, \kappa|k) S(\kappa)^{-1} \quad (6.70)$$
$$\hat{x}(k|\kappa) = \hat{x}(k|k) + K(k, \kappa)[z(\kappa) - H(\kappa)\hat{x}(\kappa|k)] \quad (6.71)$$
$$P(k|\kappa) = P(k|k) - P_{xz}(k, \kappa|k) S(\kappa)^{-1} P_{xz}(k, \kappa|k)^T \quad (6.72)$$

where $A(\kappa, k)$ is backward transition matrix

$$O(k) = z(k) - \hat{z}(k|k-1) \quad (6.73)$$
$$S(\kappa) = cov[z(k)|k-1] \quad (6.74)$$

Following Fig. 6.9 shows the algorithm of the Kalman filter with OOSM measurements. In this study, modified traditional Kalman filter (TKF) for DAE system was used to estimate the temperature profile across the refractory wall. Due to the high nonlinearity of the slag penetration model, extended Kalman filter (EKF) was employed to estimate the extent of slag penetration. The augmented transition matrix is used as process transition matrix employed in TKF and the process noise covariance matrix Q is the augment noise covariance matrix with setting the noise corresponding to algebraic states to be 0. This augmented form of the system is also used in negative-time measurement update (OOSM) step as shown in Fig. 6.9.

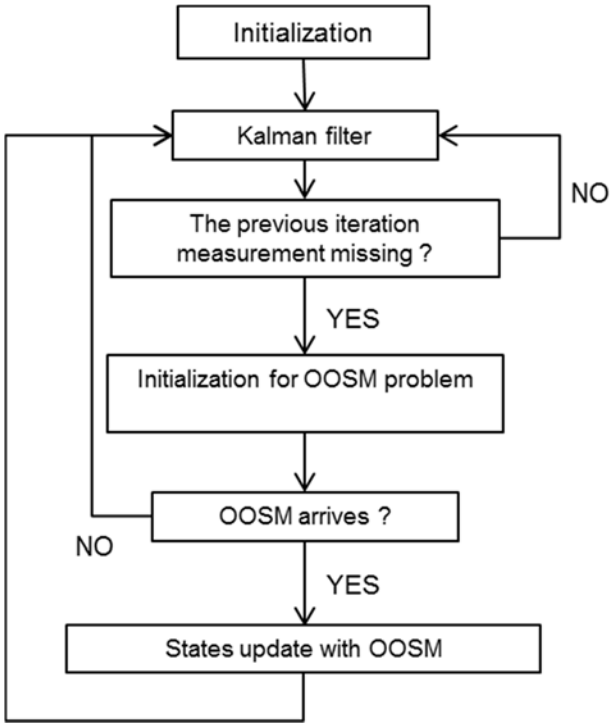

Figure 6.9. Flowchart for the Kalman filter with out-of-sequence measurements.

6.3 Results and Discussion:

Model Validation:

A series of in-house experiments have been conducted to test the embedded sensors. The thermistor made from 75 vol% WSi_2 and 25 vol% Al_2O_3 is embedded into alumina substrates, and then a substrate (with sensor on it) is embedded into a long thin high-chromia brick slice with the dimension of 21.6 cm× 5 cm× 5cm. The length and width of the embedded thermistor is shown in Fig. 6.10. The cross-sectional area of the thermistor is 4×10^{-2} cm^2. Please note that the thermistor of this size is only used for the experimental evaluation. A smaller size is considered for the gasifier application.

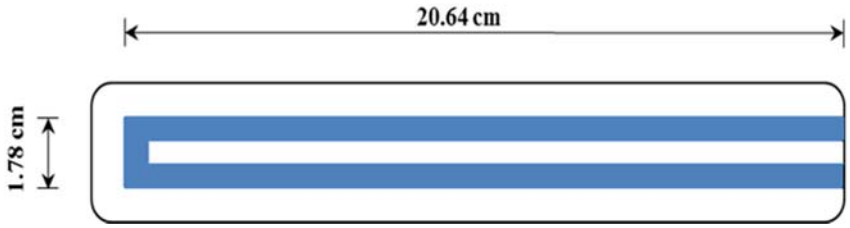

Fig. 6.10. Schematic of the thermistor printed on the Al2O3 substrate.

The brick slice with the thermistor embedded was heated from 100 ℃ to 1350 ℃ at the constant heating rate of 1.9 ℃/min. Then it was tested at 1350 ℃ for 10 hour. Finally, it was cooled to 99 ℃ with the cooling rate of 1.9 ℃/min. In order to validate the model with the experimental data, a modified thermal model is necessary to mimic the heat transfer process of the brick slice heated

up in the furnace. Convection is usually considered as the dominant heat transfer mechanism between a solid and a fluid (the high chromia brick slice and the furnace environment for this case). However, due to the small size of the test brick, temperature is assumed to be uniform and equal to the furnace environmental temperature. The result from the model is compared with the in-house experimental data as shown in Fig. 6.11. Discrepancies between the model and the experimental data are noticeable in Fig. 6.11 at certain ranges. Since the brick was maintained at a temperature of 1350 ℃ , it is expected that the electrical resistance would be constant, but it is noticed that the resistance overshoots and then slowly slides down closer to the value estimated by the model. The reason for this behavior is not well understood and is being currently investigated.

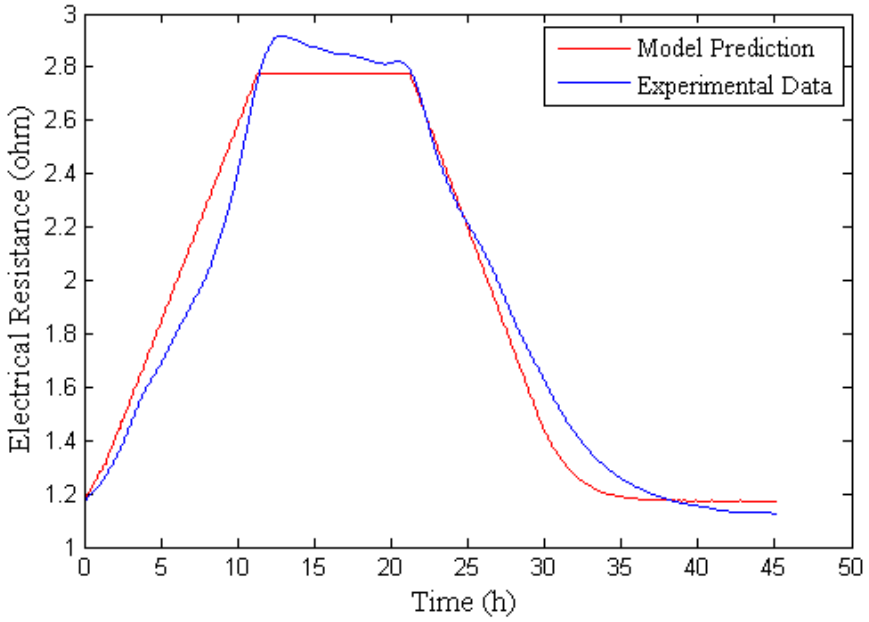

Figure 6.11. Validation of thermistor response to the change of the temperature.

As observed in Fig. 6.11, the temperature sensitivity for the embedded WSi_2-Al_2O_3 thermistor is relatively lower than the commercial thermistor. It should be noted that the temperature sensitivity is a material-specific property. A higher sensitivity can be achieved by using different materials some of which are currently being evaluated.

Results from the Refractory and Sensor Models:

Thermal Profile:

By considering the nominal operating temperature on the hot face (i.e. $T_{gasifier}$=1400ºC) the steady-state temperature profile along the radial direction of the gasifier wall is shown in Fig. 6.12. As the rate of temperature decrease depends on the thermal diffusivity, the alumina castable layer is found to have the steepest drop in temperature. As mentioned earlier, Fig. 6.12 shows the steep drop in the radial direction, and why an assumption of constant temperature through the length of the sensor, which is oriented in the radial direction, would not be appropriate.

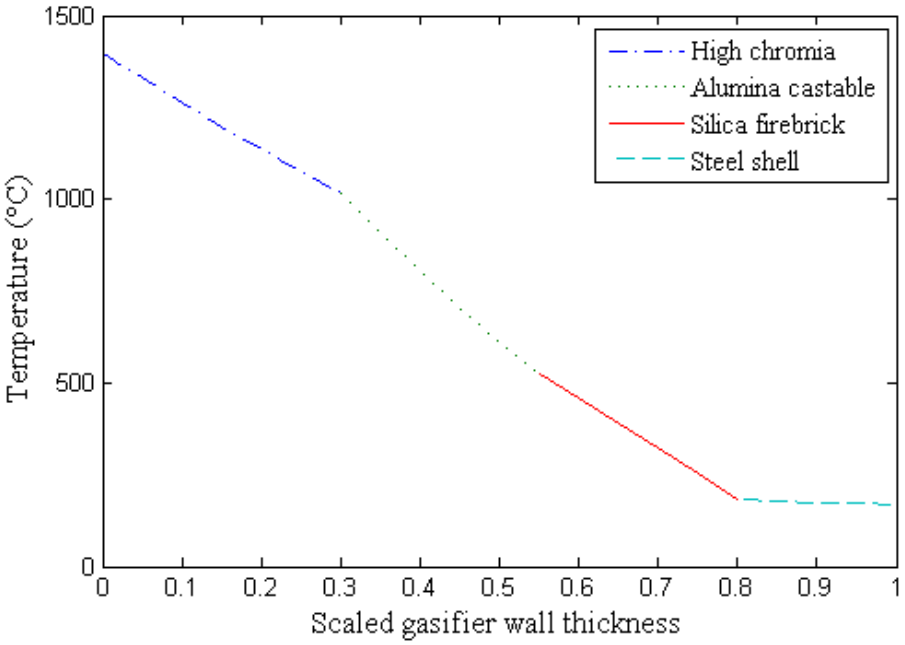

Figure 6.12. Temperature distribution in the gasifier wall at steady-state.

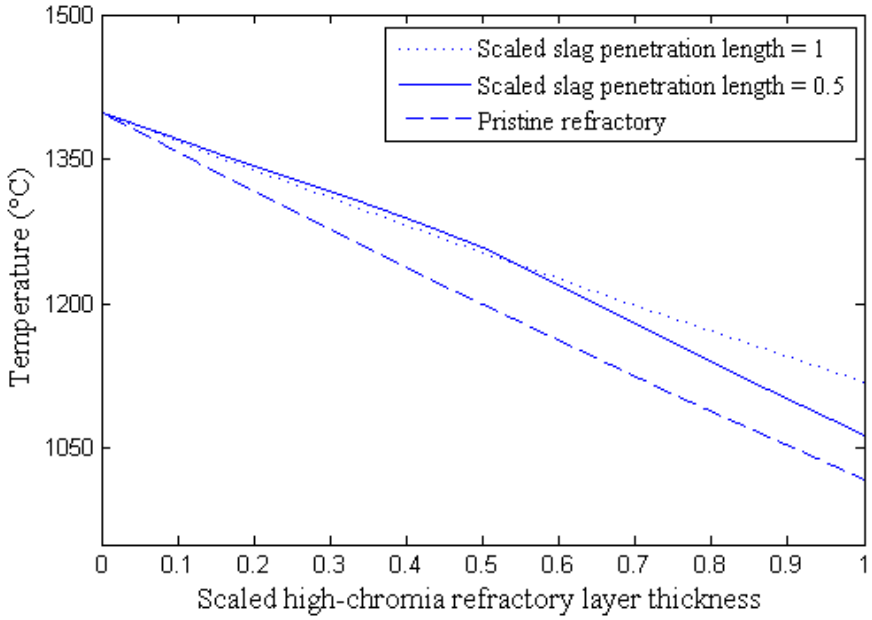

Figure 6.13. Effect of slag penetration on the steady-state temperature profile in the high-chromia refractory brick.

Besides the change in the hot face temperature, slag penetration can also result in a change in the temperature profile of the gasifier wall. Fig. 6.13 compares the temperature profile of the high-chromia refractory layer for the pristine brick, for the slag-infiltrated brick when the slag penetration length is 50% of the high-chromia refractory layer thickness, and for the slag-infiltrated brick when the slag has penetrated up to the interface between the high-chromia brick

and the alumina castable layer. As the thermal conductivity of the slag-infiltrated brick keeps increasing with increasing extent of slag penetration, the temperature of the brick keeps increasing as the slag penetrates further.

Slag Penetration Profile:
Fig. 6.14 shows the slag penetration lengths along the radial direction of the gasifier wall when $T_{gasifier}$ is specified to be 1300, 1400, and 1500 ℃. It is observed that the rate of slag penetration sharply decreases as the viscosity of the slag increases significantly due to the decrease in the temperature. As expected, the slag penetrates further as the hot face temperature is increased. For the highest temperature case studied here, the slag penetration length is 118.5 mm in 1000 hour, which is still lower than the thickness of the high-chromia layer.

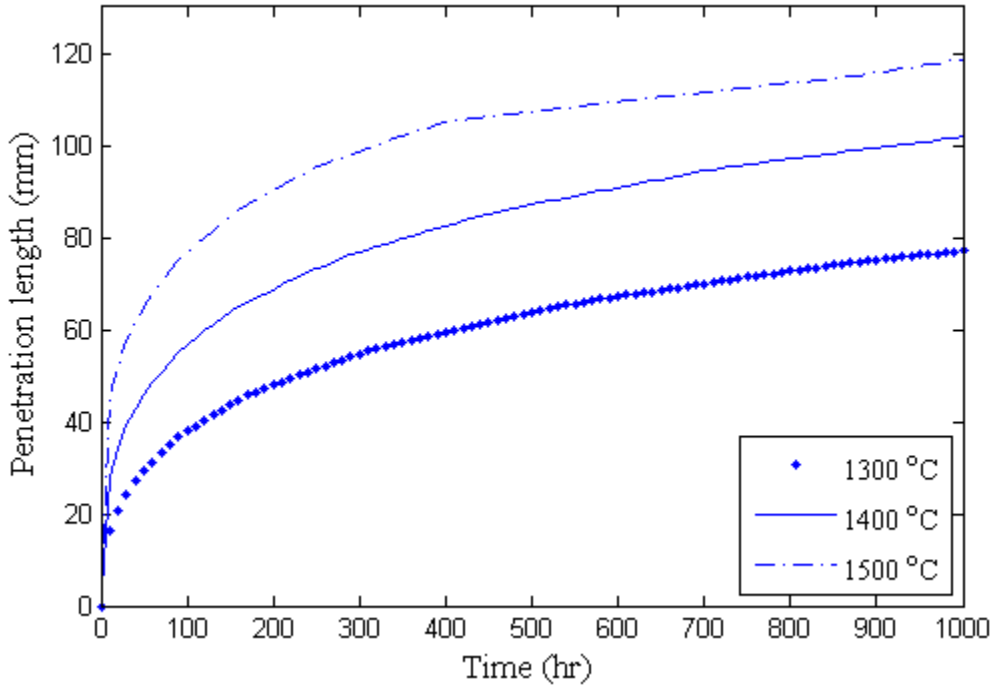

Figure 6.14. Slag penetration length with time.

Thermistor Response to Change in Temperature and Slag Penetration:
The thermistor is assumed to be embedded in the center of the high-chromia refractory brick. Due to the geometry limitation of the high chromia lining thickness and the harsh gasifier environment, a thermistor of smaller dimensions than what was considered in model validation is considered for the gasifier application. Therefore, in the results presented in the following sections, the length, width and cross-sectional area of the thermistor are set to be 1.6 cm, 0.27 cm and 4×10^{-2} cm^2, respectively. Fig. 6.15 shows the output electrical resistances of the thermistor at different values of $T_{gasifier}$. As expected, the electrical resistance of the thermistor keeps increasing as the temperature increases. It should be noted that even though an almost linear change in the electrical resistance is observed in this temperature range, it may be nonlinear if the temperature is increased further.

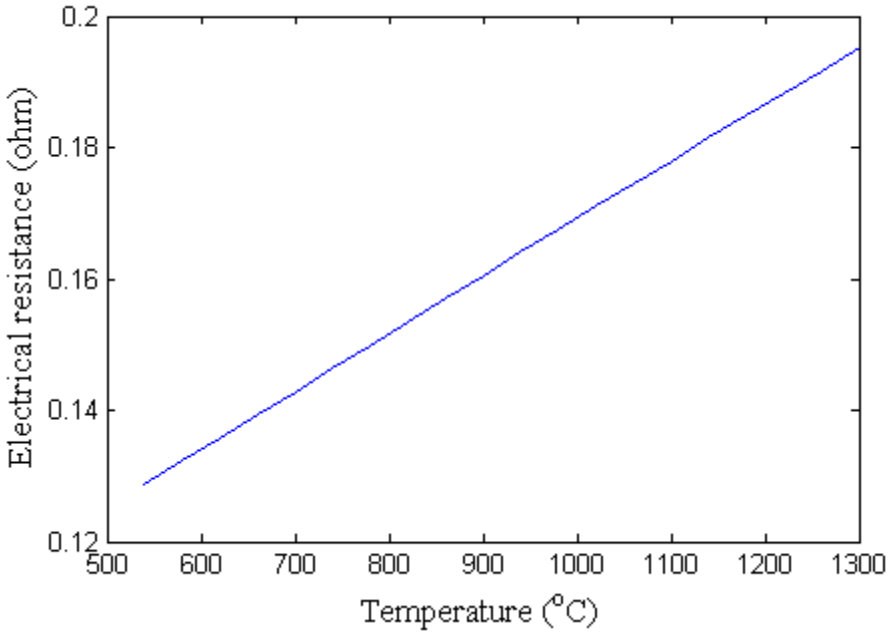

Figure 6.15. Sensitivity of the thermistor to the hot face temperature.

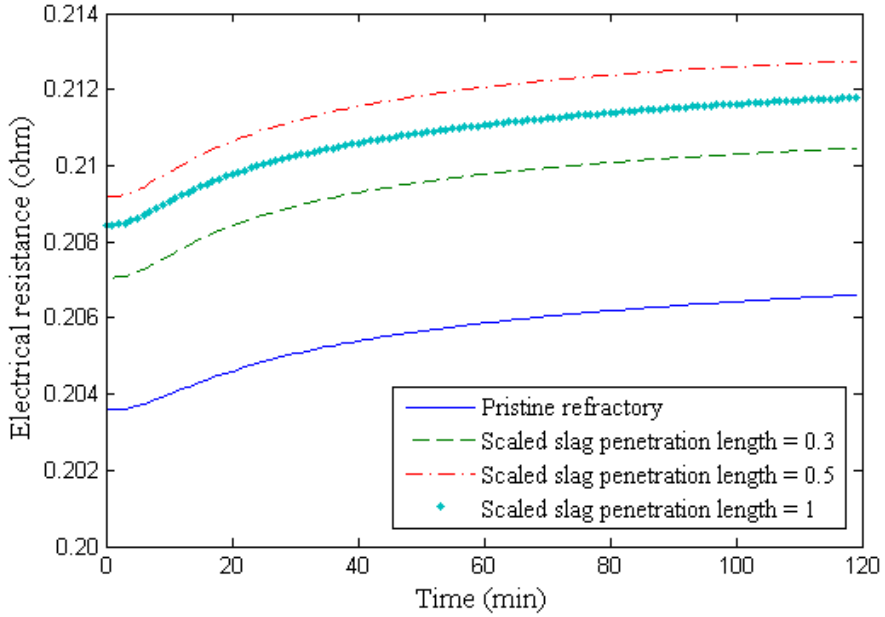

Figure 6.16. Thermistor responses following a step increase in the hot face temperature at different extents of slag penetration.

As discussed earlier, temperature profile of the gasifier wall can also be affected by slag penetration. Fig. 6.16 shows the change in the thermistor output for different extent of slag penetration following a 50 ℃ step increase in $T_{gasifier}$. It is observed that the sensor response takes nearly 2 hours to reach its new steady state. The resistance for the case when the scaled slag penetration length is 0.5 is observed to be higher than the full slag penetrated case. It is because

the case of 0.5 slag penetration has a higher temperature at the center of the high chromia brick. It should be noted that the response of the thermistor depends not only on the slag penetration length but also the location where it is embedded. This study shows that as the change in the local temperature can occur due to the change in the extent of slag penetration, change in the hot face temperature, or both, it is hard, if not impossible, to correctly estimate the temperature profile or extent of slag penetration by simply using a correlation between the thermistor output and temperature or slag penetration. Once again, the study presented in this section points to the requirement of a model-based approach as discussed earlier.

Interdigital Capacitor (IDC) Response to Change in Temperature and Slag Penetration:
Similar to the thermistor, the IDC is also considered to be installed in the center of the high-chromia layer with 20% porosity. It is assumed to have 8 electrodes. As compared to the spatial temperature variation in the radial direction, the temperature variance in the azimuth direction is supposed to be relatively small. Therefore, length of the fingers (L as shown in Fig. 6.2) is assumed to be independent of temperature and equal to 0.3758 cm. The temperature-dependent geometric parameters W and G are expressed by using the following equations:

$$W = e^{(8.154\times10^{-6}T-7.4088)} \quad (6.75)$$

$$G = e^{(8.154\times10^{-6}T-6.3437)} \quad (6.76)$$

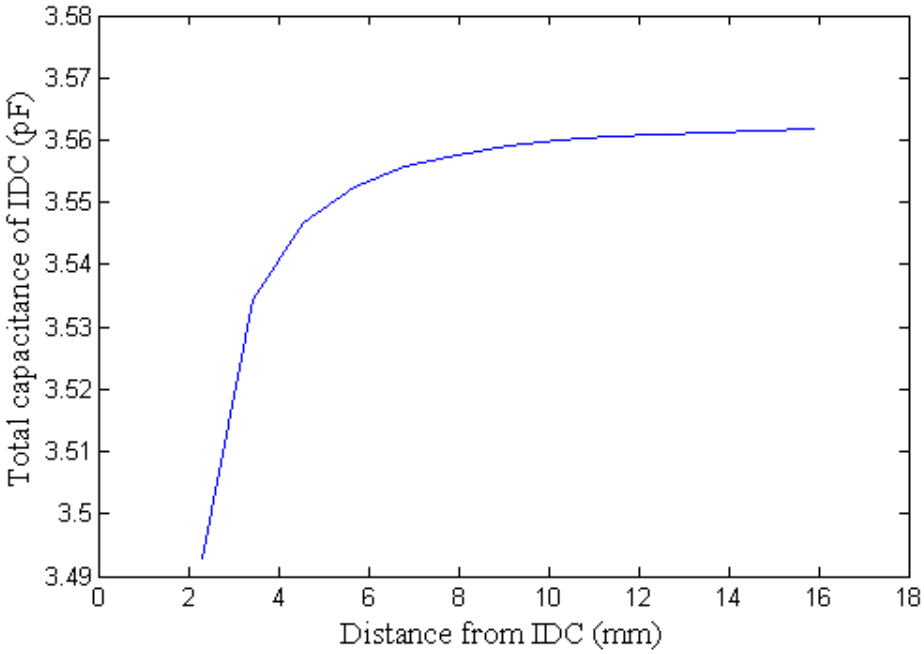

Figure 6.17. Change in the total capacitance of the IDC with distance from the electrode plane under nominal operating temperature.

Fig. 6.17 shows that the capacitance of the IDC sensor is not sensitive to the plane beyond a distance from the electrode plane greater than about 10 mm. This distance depends on the temperature distribution as well as the geometric parameters (W, G, and L) of IDC.
Sensitivity of the embedded IDC sensor to temperature and extent of slag penetration is also

analyzed to evaluate the feasibility of the IDC sensors for estimating the temperature profile and extent of slag penetration. Fig. 6.18 shows how the capacitance of the IDC sensor changes with the hot face temperature. Fig. 6.19 shows the sensor response after a 50 ℃ step increase in the hot face temperature. As expected, an increase in the temperature would be registered by a change in the capacitance. Similar to before, the capacitance measurement takes about 2 hours to settle following a 50°C step increase in the hot face temperature.

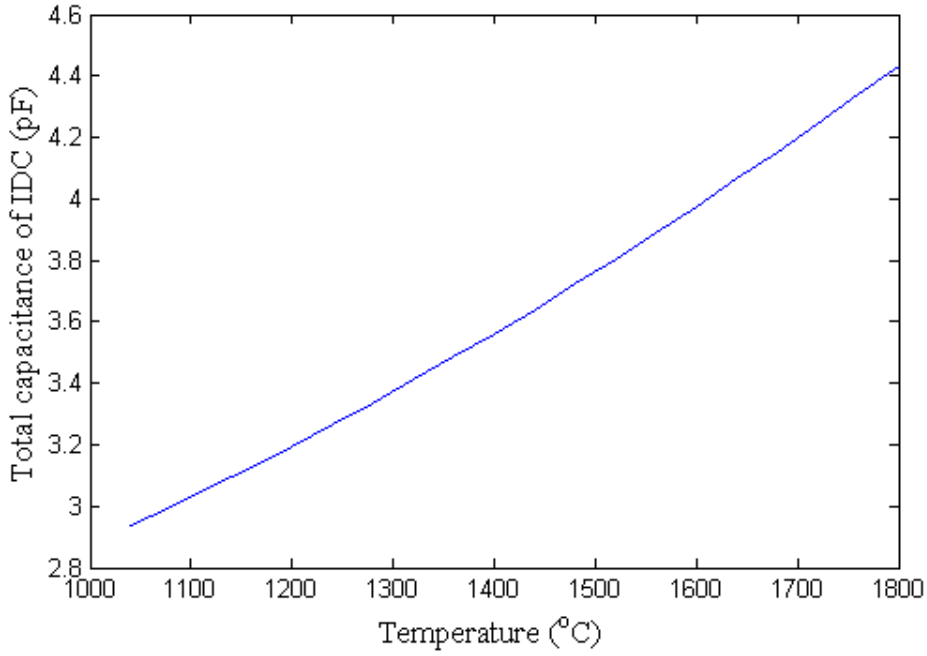

Figure 6.18. Change in the capacitance due to temperature change.

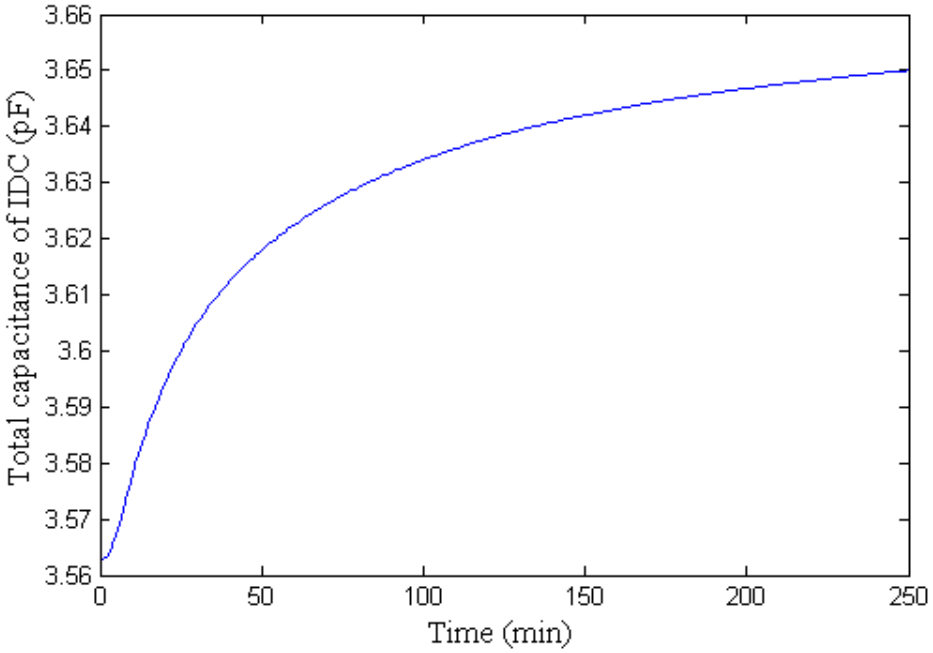

Figure 6.19. Change in the capacitance due to temperature change.

Fig. 6.20 shows the effect of slag penetration on capacitance and how it changes with the distance from the electrode planes. It can be found that the capacitance increases by about 0.26 pF from the pristine brick to the brick with the 0.5 scaled penetration length. It then drops by about 0.05 pF for the fully-penetrated brick. Even though the change in the capacitance is small, it can be measured by the widely-used low capacitance measurement techniques, such as RC oscillation method, AC bridges, and charge /discharge method. [6.31] For an example, the AC bridges method has the highest resolution of about 3.5×10^{-5} pF. [6.32] It should also be noted that the range of output capacitance can be easily adjusted by carefully choosing the values of W, G, and L of the IDC. [6.23] Therefore, the IDC sensor is expected to be feasible for detecting the extent of slag penetration.

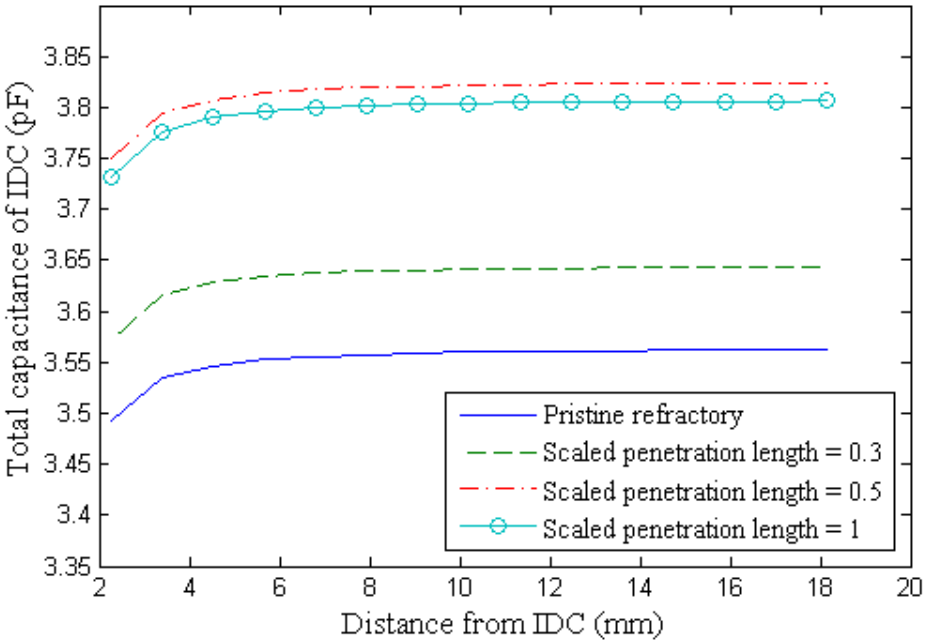

Figure 6.20. Change in the capacitance due to slag penetration at the nominal operating temperature.

Fig. 6.19 and 6.20 show that both the temperature increase and slag penetration can result in an increase of the output capacitance. For example, for a slag-free brick, a 0.07 pF increase in the capacitance can occur due to a temperature increase of 35 °C or due to change in the scaled slag penetration length from 0 to 0.3. Therefore, similar to the thermistor, it is hard, if not impossible, to correctly estimate the temperature profile or extent of slag penetration by using a correlation based approach. In the following section, results from the filtering approach are presented to estimate these variables by using the simulated noisy data from the thermistor and IDC sensor models.

Resistive Circuit Response to Change in Temperature and Slag Penetration:

For the results presented in this section, the resistive circuit sensor is embedded in the center of the high-chromia refractory brick. The geometric parameters of resistive circuit sensor, D_{RC}, L_{RC}, W_{RC} as shown in Fig. 6.5 are set to be 0.1758 cm, 1.503 cm, and 0.8 cm, respectively. The cross-sectional area and number of electrodes for resistive circuit are chosen to be 4×10^{-2} cm^2 and 8. Fig. 6.21 describes how the output electrical resistance of the embedded resistive circuit sensor

changes as $T_{gasifier}$ increases. An almost-linear increase in electrical resistance is observed in this temperature range.

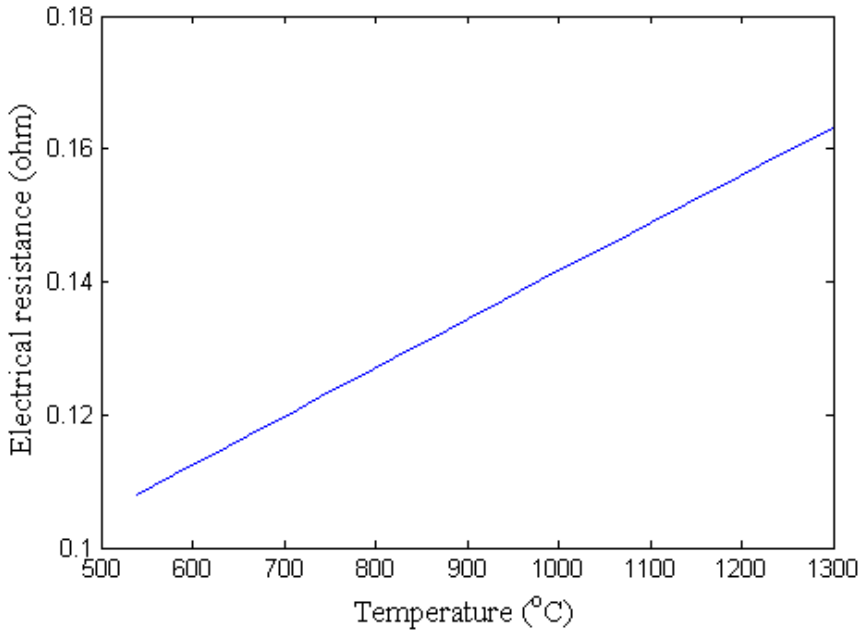

Figure 6.21. Change in the electrical resistance due to change in hot face temperature.

Figure 6.22 shows the response of resistive circuit to different slag penetration length following a 50 ℃ step increase in hot face temperature. Due to the face that the change in the electrical resistance of resistive circuit is a result of temperature changes caused by slag penetration, similar results as those obtained by the thermistor is obtained here.

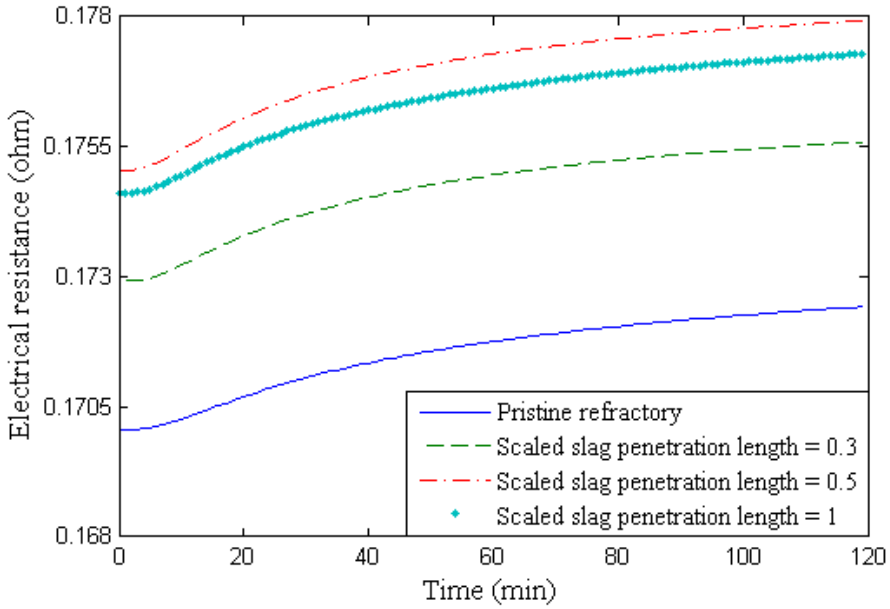

Figure 6.22. Resistive circuit responses following a step increase in the hot face temperature at different extents of slag penetration.

Strain Gauge Response to Change in Stress, Temperature, and Slag Penetration:
The strain gauge is also assumed to be placed in the center of the smart brick. The dimensions of the strain gauge, D_{SG}, L_{SG}, shown in Fig. 6.6 are assumed be 0.55 cm and 2 cm respectively. The cross-sectional area and number of turns for strain gauge are set to be 4×10^{-2} cm^2 and 6. With consideration of nominal operating temperature on hot face, Fig. 6.23 shows how the output electrical resistance of strain gauge changes with stress.

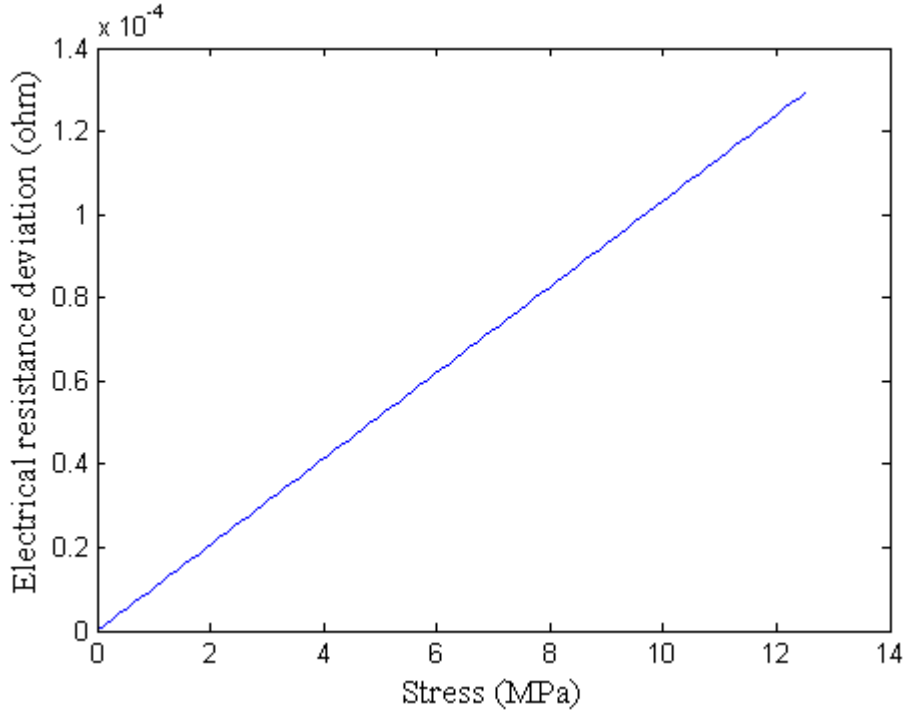

Figure 6.23. Change in the electrical resistance due to stress.

As shown in Fig. 6.23, the change in electric resistance is about 1.3×10^{-4} ohm as stress increases from 0 to 12.5 MPa. It should be noted that this change can be increased by increasing number of electrode turns.

Sensitivity of the embedded strain gauge sensor to temperature is analyzed. A change in the temperature can impact the output electrical resistance of the sensor due to thermal stress that leads to deformation, and due to change in the resistivity of the sensor material. To study this effect, stress is kept to be 6.25 MPa. Fig. 6.24 shows how the responses of the strain gauge due to the changes in hot face temperature. Fig. 6.25 shows the dynamic response of the sensor after a 50 ℃ step increase is introduced to hot face.

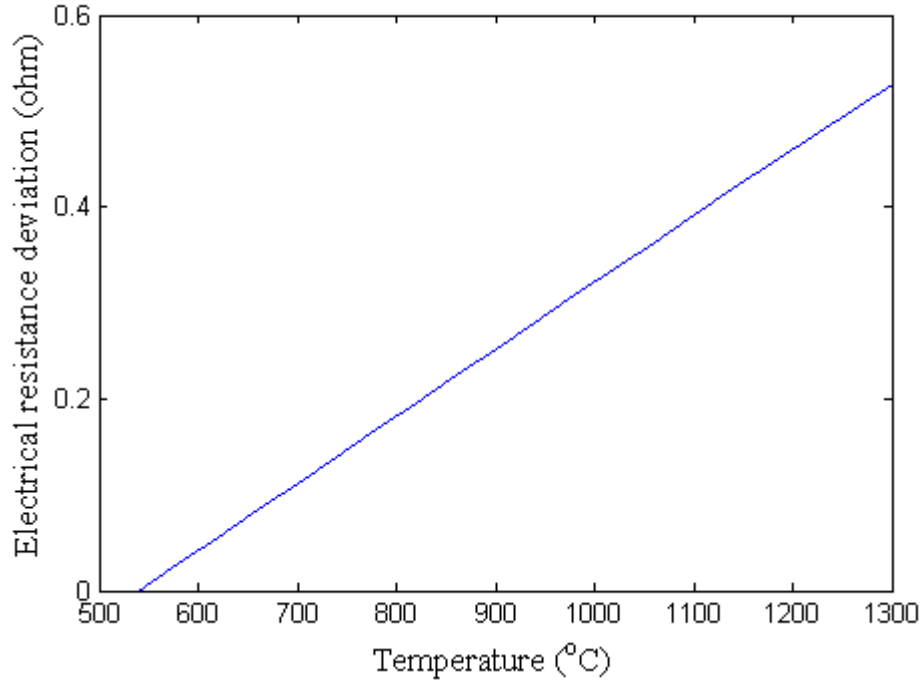

Figure 6.24. Change in the electric resistance due to hot face temperature change.

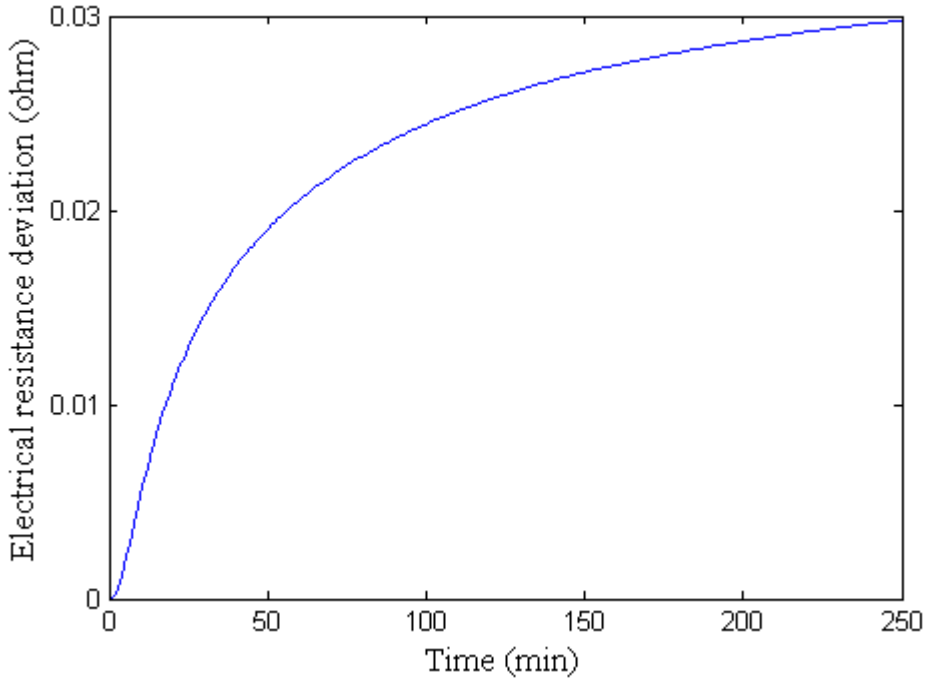

Figure 6.25. Change in the electrical resistance after introducing a 50 ℃ step increase to hot face.

As Fig. 6.24 and 6.25 show, the output resistance increases as the temperature increases. Interestingly, the relative change in resistance is more significant than the relative change in

resistance due to deformation.

Sensitivity of the embedded strain gauge sensor to extent of slag penetration is also analyzed. Similar as before, stress is considered to be 6.25 MPa. Fig. 6.26 shows the change in the strain gauge output for different extent of slag penetration following a 50 ℃ step increase in $T_{gasifier}$.

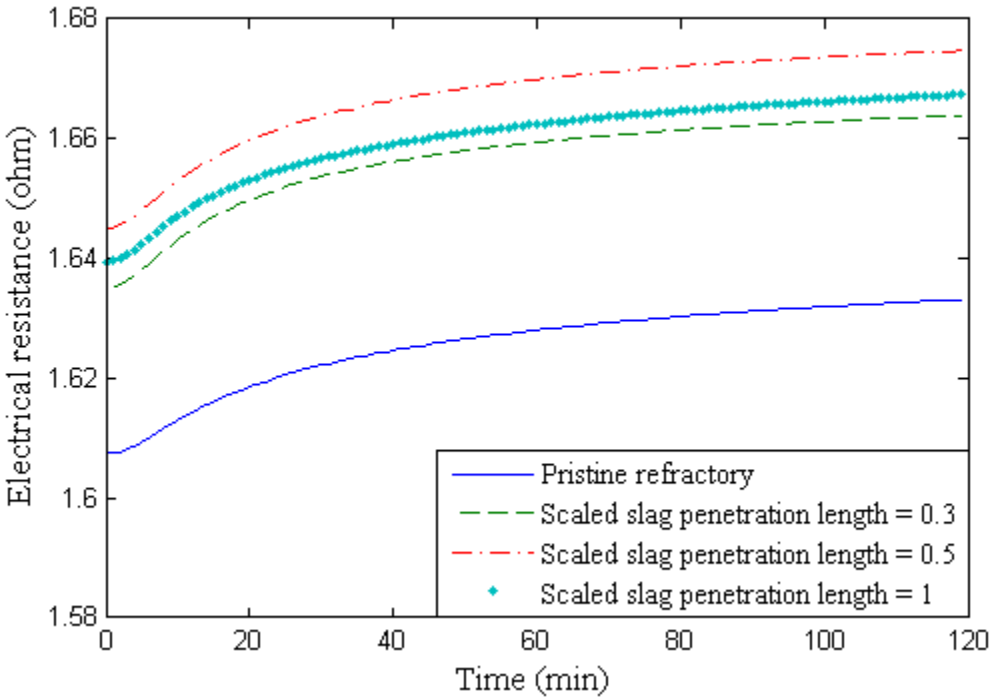

Figure 6.26. Change in the electrical resistance for different extent of slag penetration after introducing a 50 ℃ step increase to hot face.

Estimation Results:
The TKF, EKF, UKF, and multi-scale dual Kalman filter are used to estimate both the temperature profile and the extent of slag penetration. However, while the time scale of temperature is in minutes, time scale of slag penetration is in hundreds of hours. Therefore, different time steps are used while simulating the slag penetration model vs the thermal model. For the implementations of TKF, EKF, and UKF, extent of slag penetration is considered to be at the value obtained at the previous time instant while estimating the temperature profile and the hot face temperature is held constant and the energy conservation equation is solved to obtain the steady-state temperature profile for various extents of slag penetration when simulating the extent of slag penetration. Based on the results obtained from the heat transfer and slag penetration models, time steps for estimating temperature and slag penetration profiles are set to be 1 min and 10 hr, respectively.

TKF Estimation of Temperature with Embedded Thermistors:
Five thermistors are considered to be embedded diagonally in the high-chromia refractory brick as shown in Fig. 6.27. These sensors are numbered from 1 to 5 from the left to the right. The TKF is used to estimate the temperature with the measurements from these five embedded thermistors.

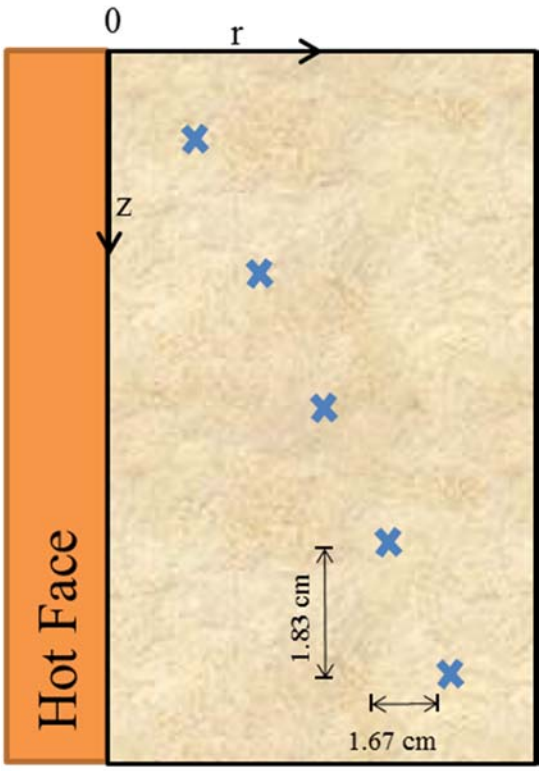

Figure 6.27. Schematic of the high-chromia refractory lining with sensors embedded (blue cross represents the center point of sensor).

A 50 ℃ step increase in the hot face temperature is introduced. Fig. 6.28 shows the resistance and temperature estimation for the complete slag-infiltrated brick at the location of Sensor #3. The TKF not only filters the noisy resistance measurements, but also provides satisfactory estimates for the temperature profile even in the presence of model mismatch. The TKF can also be used to estimate the temperature profile in the locations where there is no sensor. Fig. 6.29 shows the temperature estimation of the right-bottom corner of the high-chromia brick where there is no sensor.

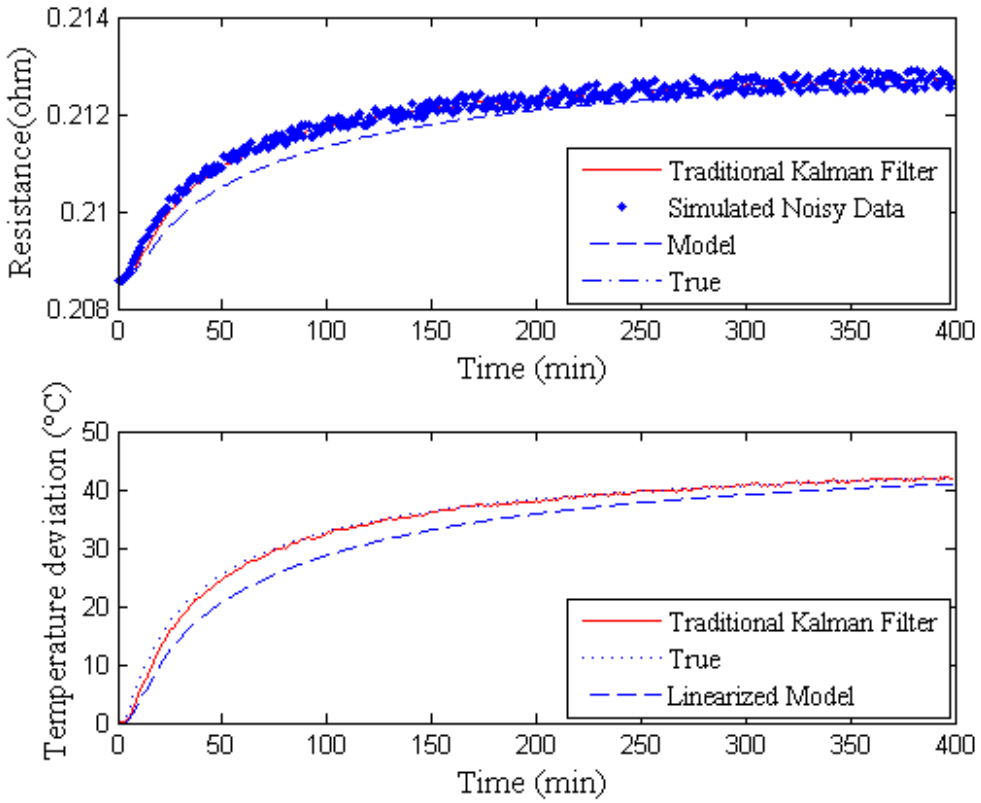

Figure 6.28. Estimations using the TKF with the measurements from embedded thermistors.

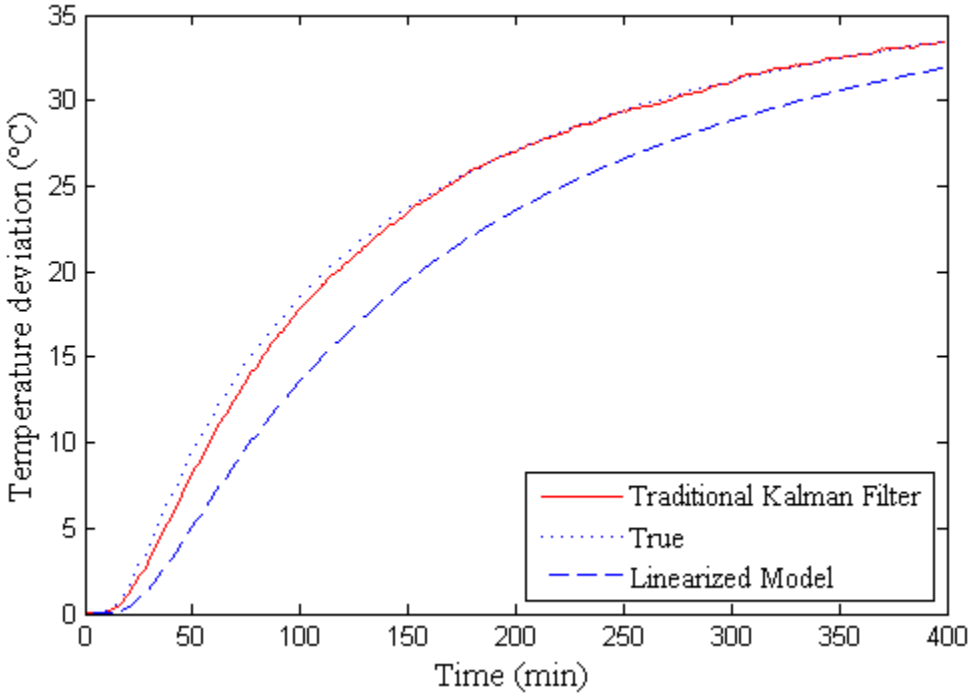

Figure 6.29. Estimation of temperature using the TKF for a location where there is no sensor.

TKF Estimation of Temperature with Embedded IDC Sensors:
The TKF is also applied for the case with five IDC sensors installed similar to Fig. 6.27. Fig. 6.30 shows the estimations results from the TKF for the completely slag-infiltrated brick for the location where Sensor#3 is located.

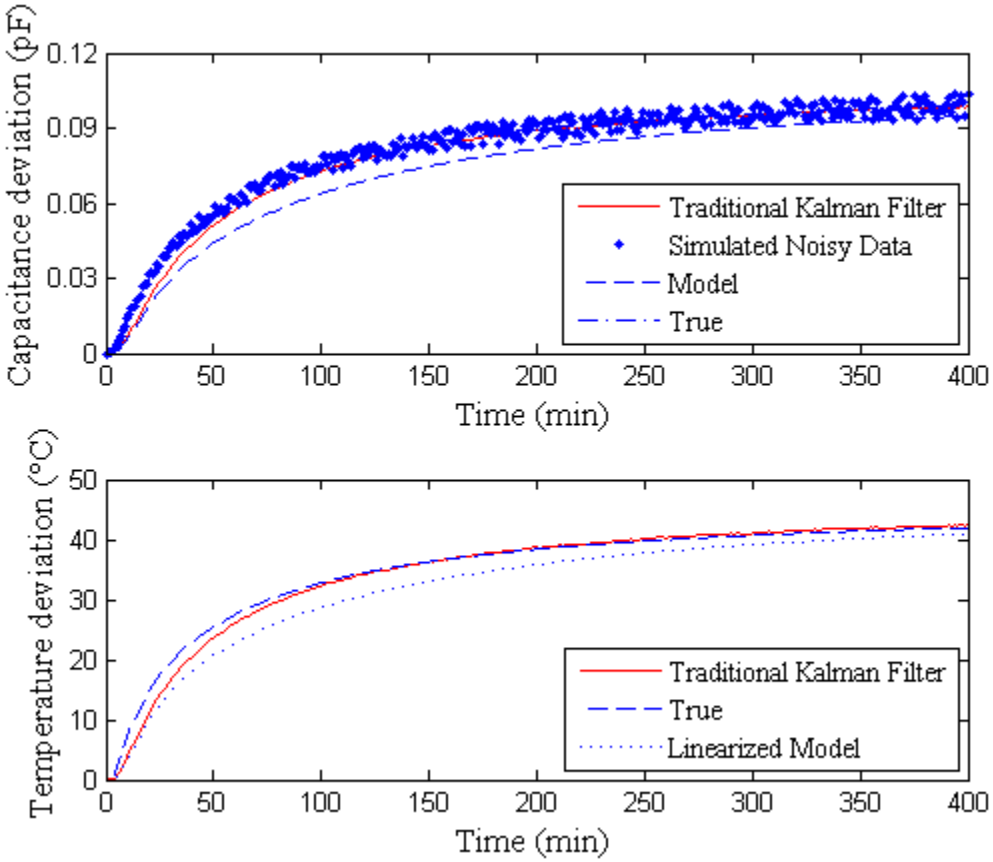

Figure 6.30. Estimations using TKF with the measurements from embedded IDCs.

As shown in Fig. 6.28 and 6.30, the embedded IDC sensors and thermistors result in similar performance for temperature estimation using the TKF. Estimations of temperature using TKF has also been done for other type of sensors. All types of sensors result in similar performance for temperature estimation by using TKF. Since the thermistor is expected to be the cheaper than the other kinds of sensor not only due to the sensor itself but also due to the measurement technique required, thermistor is the preferred type if estimation of temperature profile is of interest only.

EKF Estimation of Temperature with Embedded Thermistors:
Since the thermal model developed in this study is nonlinear, EKF is implemented to check whether temperature estimation will be improved significantly by using a nonlinear estimator. The thermistors are assumed to be installed as shown in Fig. 6.27. A 50 ℃ step increase is introduced to the hot face. Fig. 6.31 shows the resistance and temperature estimation for the complete slag-infiltrated brick at the location of Sensor #3.

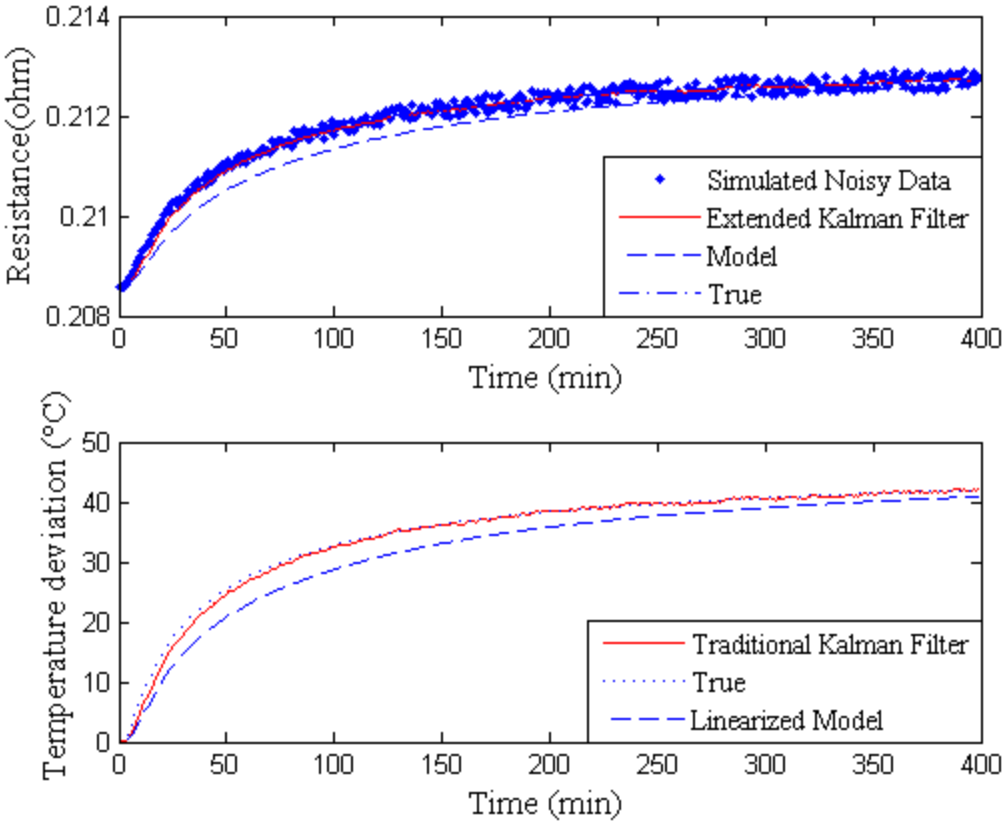

Figure 6.31. Estimations using EKF with the measurements from embedded thermistors.

As observed in Fig. 6.28 and 6.30, the performances for temperature estimation by using TKF and EKF are similar. Similar performances are observed for temperature estimation with the measurements from the other types of sensors by using EKF. However, the computational expense of EKF is much higher than TKF. Therefore, if the temperature is the only variable of interest, the TKF is preferred.

EKF Estimation of Slag Penetration with Embedded IDC Sensors:
First, the TKF is used to estimate the extent of slag penetration with the simulated measurements from the IDC sensors. It is assumed that all states (extent of slag penetration) are measured. It should be noted that measurement of all states is not feasible for this case, but considered here only to investigate the best case scenario. Fig. 6.32 shows the best estimate that we could obtain using the TKF.

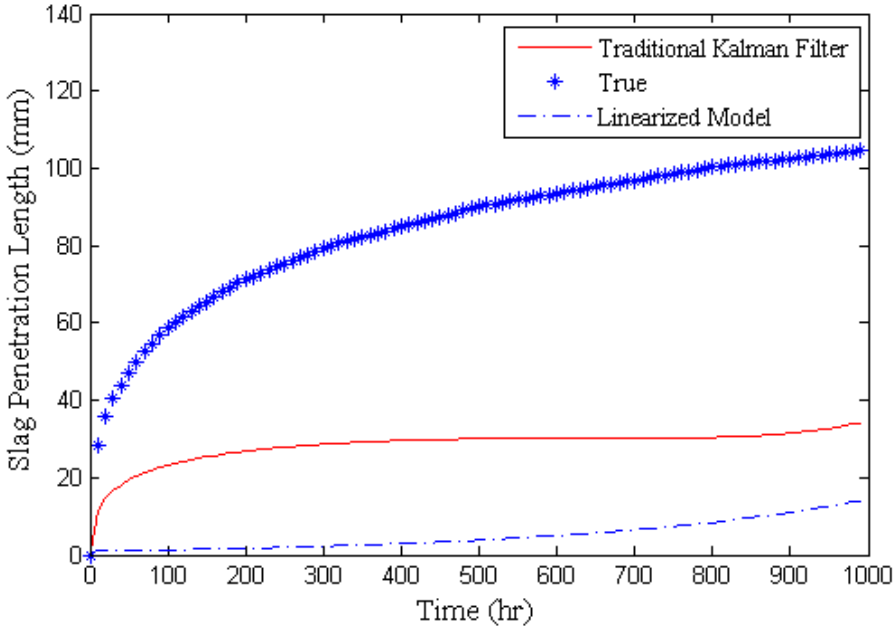

Figure 6.32. Estimation of slag penetration length with TKF (Asterisk represents the nonlinear process; red solid line represents the TKF estimates; dash-dot line represents the linearized model).

The slag penetration length is also estimated using the EKF. A full-state measurement case is considered. Fig. 6.33 shows that the EKF successfully filters the noise in the simulated measurement data and very accurately estimates the slag penetration length.

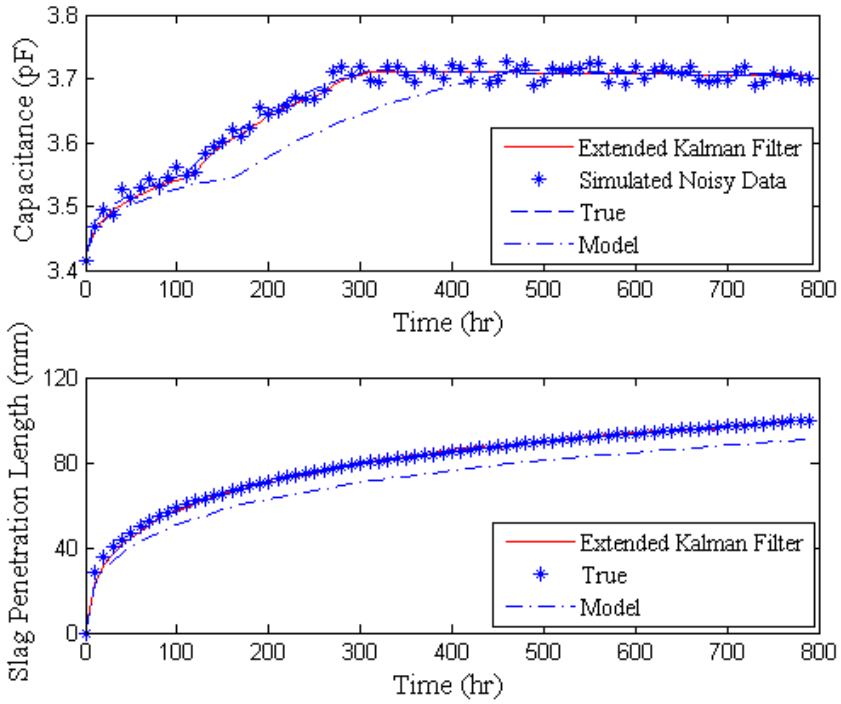

Figure 6.33. Estimation using the EKF with measurements from IDCs.

Fig. 6.33 shows that the slope of the plot increases around 120 hr for the actual process. This phenomenon occurs as the front of slag penetration reaches the center of the refractory lining (the location of the sensor) at 120 hr. As discussed in the previous section, slag penetration leads to a change in the temperature profile at a given hot face temperature. The change in the capacitance from 0 to 120 hr is due to the change in the temperature only, while the change in the capacitance from 120 hr to 300 hr is due to the complex effect that the slag penetration has on the temperature profile as well as the refractory and sensor properties.

EKF Estimation of Slag Penetration with Embedded Thermistors:
As discussed in the previous section, slag penetration leads to a change in the temperature profile at a given hot face temperature. Therefore, the change of the temperature in the radial direction can be used to estimate the extent of slag penetration at a given hot face. The EKF has also been implemented to estimate the extent of slag penetration with the measurements from the embedded thermistors. A full-state measurement case has been considered in this study. The hot face temperature is held constant. The energy conservation equation is considered to be at steady state and solved together with the slag penetration equation. Fig. 6.34 shows the EKF estimates with the simulated measurements from the thermistors for the center line of the brick along the radial direction.

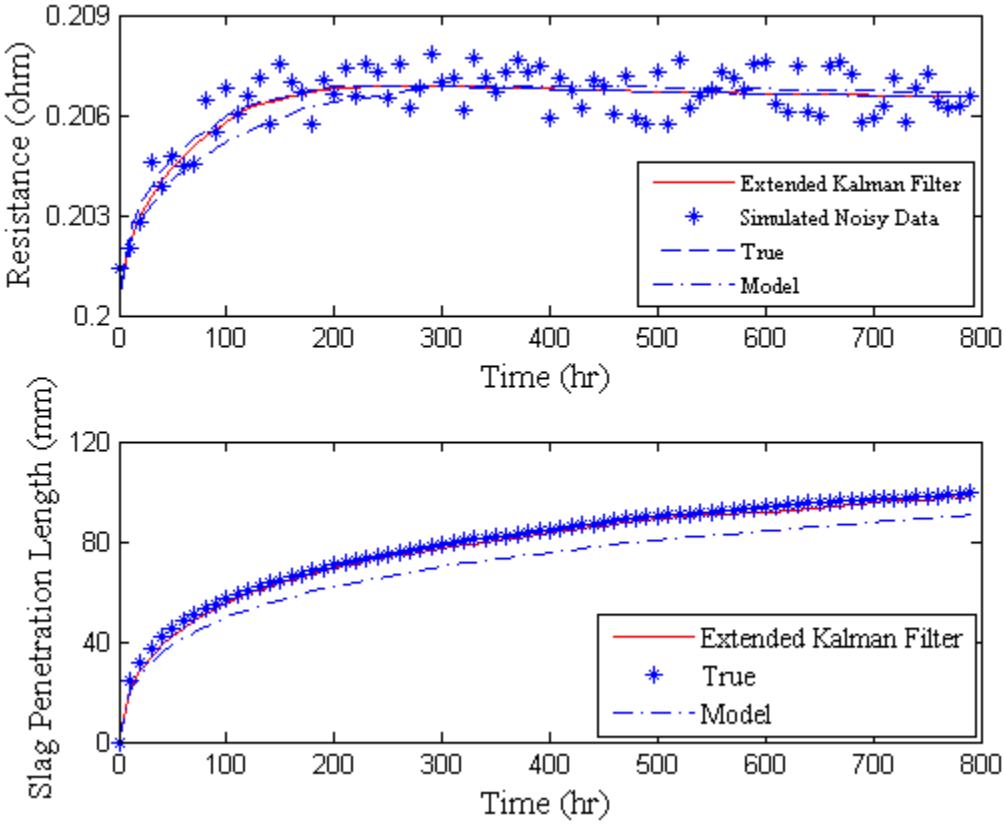

Figure 6.34. Estimation using the EKF with measurements from thermistors.

The other resistive types of sensors are also used to estimate extent of slag penetration by using EKF. Similar results as Fig. 6.34 are observed.

UKF Estimation of Temperature with Embedded IDCs:

By using noise capacitance measurements from the interdigital capacitors (IDC), estimation of wall temperature is completed. Five IDCs are considered to be installed as shown in Fig. 6.27 and the parameters $\alpha, \beta,$ and k used in the unscented transformation are chosen to be 1, 2, and 0, respectively. Fig. 6.35 and 6.36 show the estimation of temperature in the location for the 2nd embedded sensor and the estimation of capacitance in the location of the 5th embedded sensor, respectively.

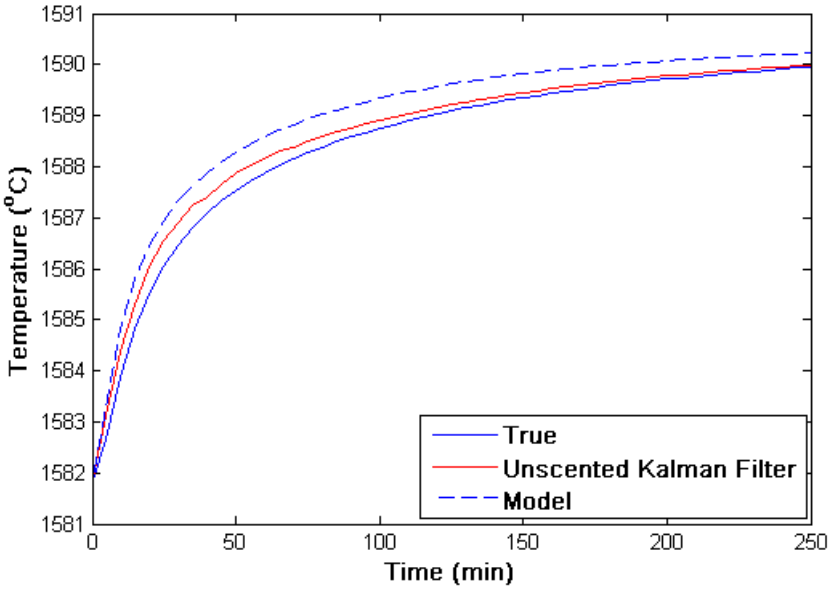

Fig. 6.35. Temperature estimation using UKF with measurements from IDCs

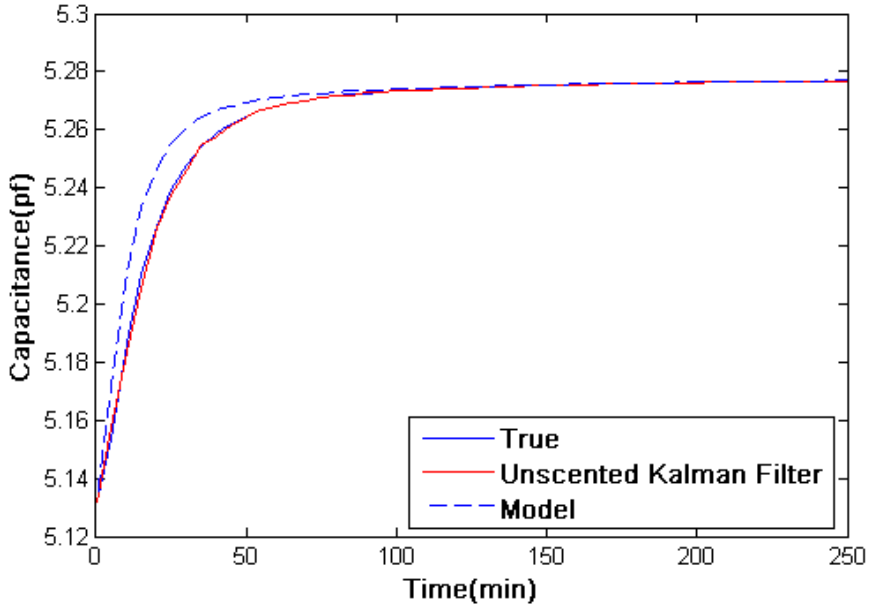

Figure 6.36. Capacitance estimation using UKF with measurements from IDCs.

UKF Estimation of Slag Penetration with Embedded IDCs:
Measurements from the embedded interdigital capacitors are used to estimate the extent of slag penetration. Full-state measurement has been assumed. It should be noted that the measurement of all states is not feasible for this case, but considered here only to investigate the best case scenario. The hot face temperature is held constant. Estimation results are shown in Fig. 6.37 and 6.38.

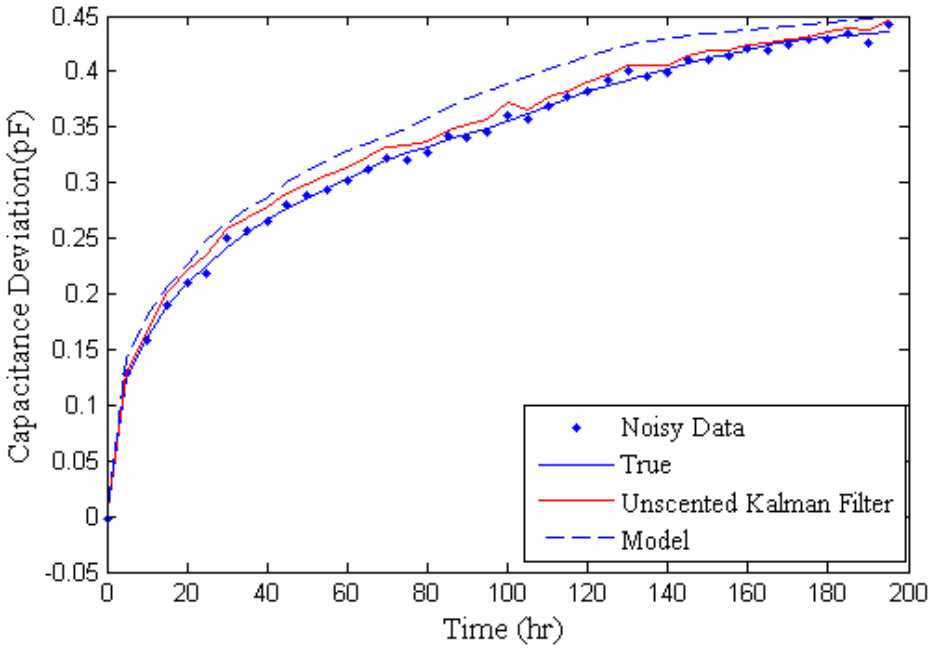

Figure 6.37. Estimation of capacitance using UKF with measurements from IDCs.

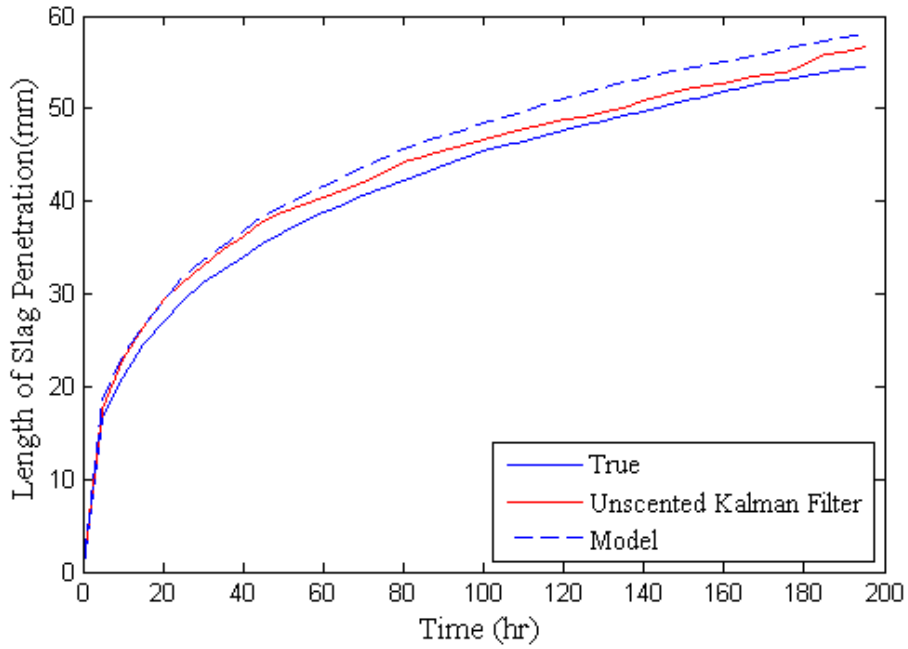

Figure 6.38. Estimation of slag penetration length using UKF with measurements from IDCs.

UKF Estimation of Temperature with Embedded Resistive Circuit Sensors:
Estimation of the gasifier wall temperature by using the unscented Kalman filter (UKF) with measurements from embedded resistive circuit sensors is also studied in this task. Following cases studied are performed:

1) No process noise, additive measurement noise, exact R;
2) Additive process noise, additive measurement noise, exact R and Q;
3) Additive process noise , additive measurement noise, ineaxct Q while exact R;
4) Additive process noise, additive measurement noise, inexact Q and R;
5) Non-additive process noise.

Cases 1 to 4 are studied using the simplified UKF algorithm provided in the previous report. For case 5, the white Gaussian noise is added to the thermal conductivity of high-chromia refractory as shown below:

$$K = 5.6541 + \gamma - 1.1981 \times 10^{-3}T + 3.6673 \times 10^{-7}T^2 - 2.2522 \times 10^{-10}T^3 \quad (6.77)$$

where γ is the process noise.

As the thermal conductivity appears in the argument of the derivative, the simplified UKF algorithm for additive noise cannot be used for Case 5. The augmented UKF algorithm for DAE system has been implemented. The only difference between the simplified UKF and augmented UKF is that the process and measurements noises are treated as state variables and are estimated in augmented UKF. Interested reader are referred to [27] for more details about augmented UKF. Noisy measurements from the embedded resistive circuits have been used to estimate the temperature profile across the gasifier wall. Five resistive circuit sensors are considered to be evenly embedded in the diagonal of the high-chromia refractory brick as shown in Fig. 6.27. Estimation results for the location where the 4th Sensor is located are shown in Fig. 6.39 through 6.44, for Cases 1 through 5, respectively.

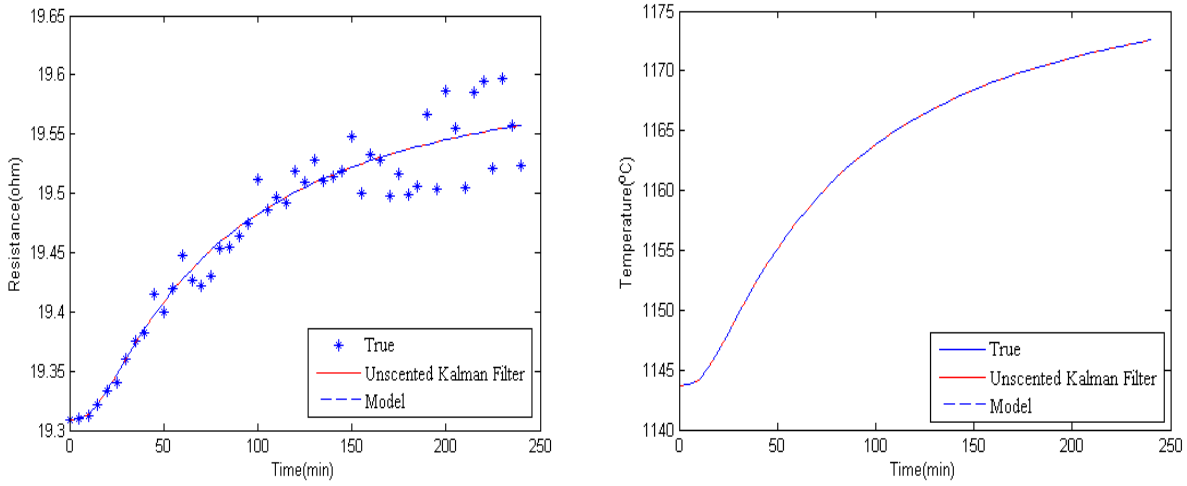

Figure 6.39. Estimation results for Case 1.

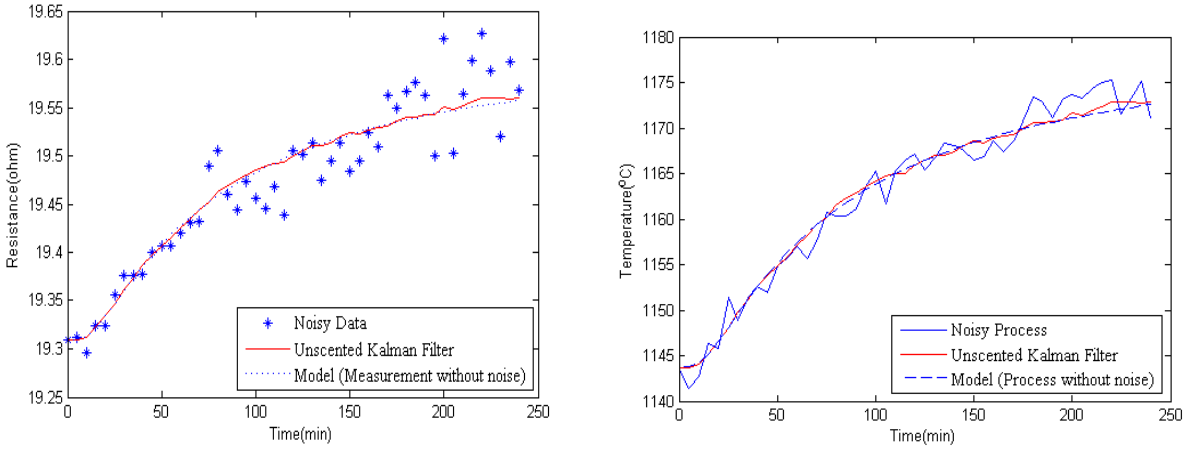

Figure 6.40. Estimation results for Case 2.

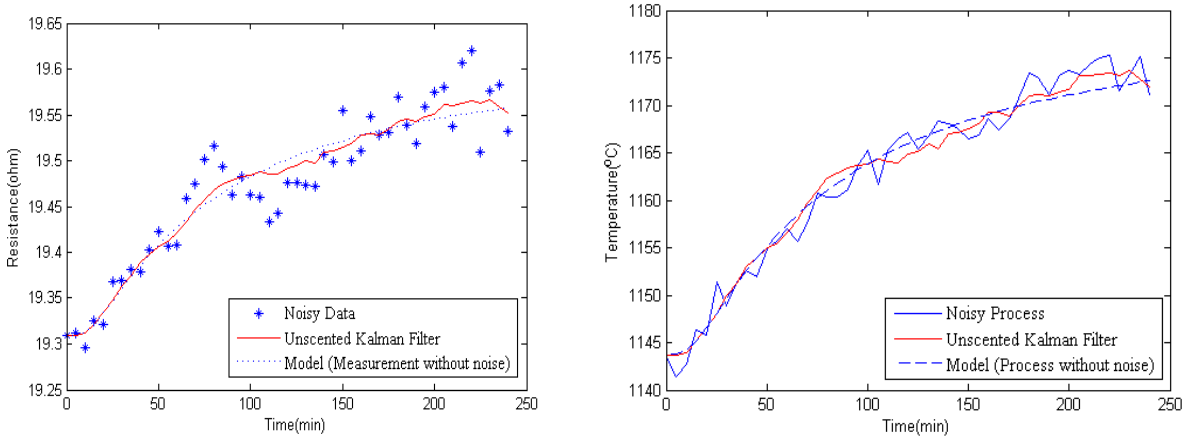

Figure 6.41. Estimation results for Case 3.

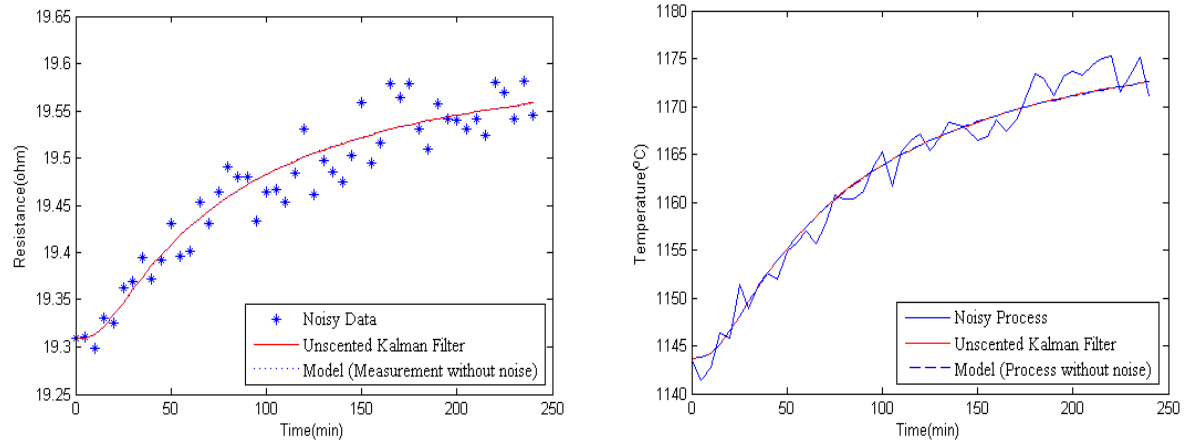

Figure 6.42. Estimation results for Case 4.

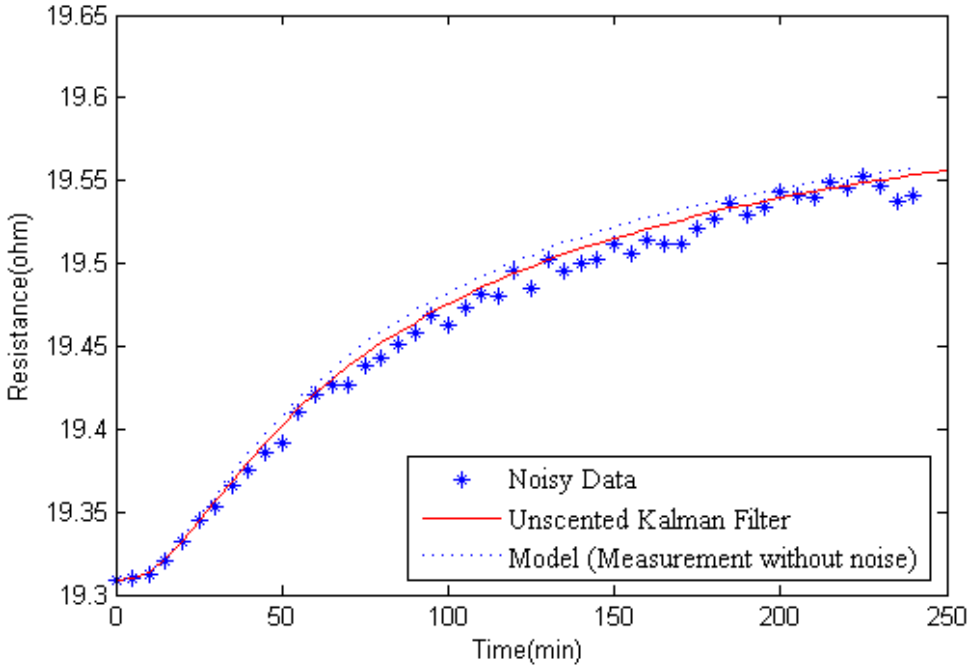

Figure 6.43. Estimation of resistance for Case 5.

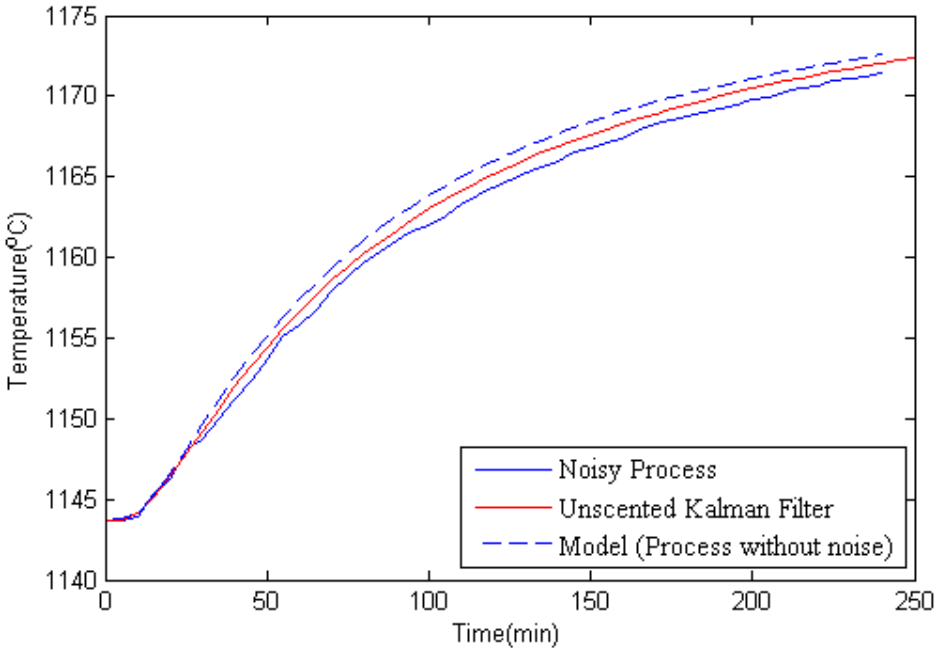

Figure 6.44. Estimation of temperature for Case 5.

As shown in Fig 6.43 and 6.44, a process-model mismatch is observed. These results show that UKF can successfully filter out both the nonlinear process noise and additive measurement noise.

Estimations Using Multi-Scale Dual Kalman Filter:

In the previous sections, resistance-type sensors show the feasibility in estimating slag when hot face temperature is held constant. However, in the real life, the change of temperature in refractory lining can be because of slag penetration, change in hot face temperature or both. In this section, thermistor is used as an example of resistance-type thermistor to analyze the possibility of using them in the real application. A 50 ℃ step increase in the hot face temperature was introduced. Full state measurement case is considered. Fig. 6.45 shows the estimation results at the center of brick by using multi-scale dual Kalman filter Algorithm 1 (shown in Fig. 6.7) with simulated measurements from embedded thermistors.

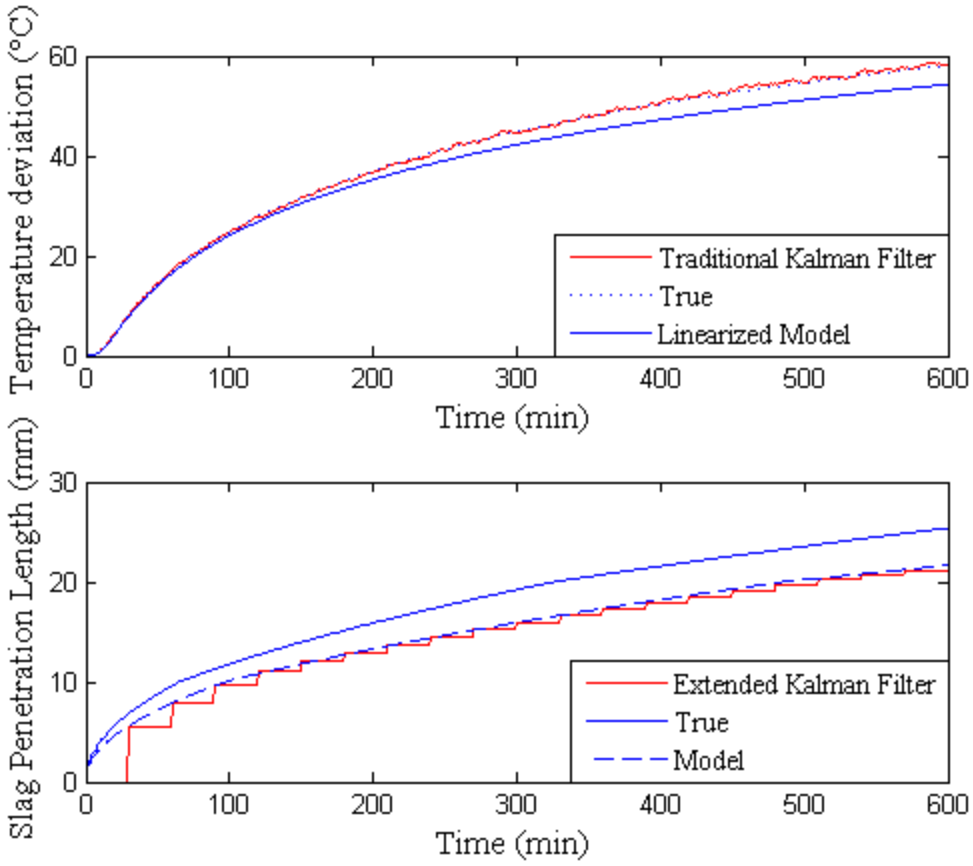

Figure 6.45. Estimations by using Multi-scale EKF algorithm 1 with measurements from thermistors

As expected, good estimates for temperature is observed in Fig. 6.45. However, the performance of dual Kalman filter for slag estimation is very poor. It appears that thermistors are preferred for temperature estimation and IDC can be used to detect the extent of slag penetration. Therefore, both the IDC and thermistor are used in these multi-scale extended Kalman filters to estimate extent of slag penetration and temperature simultaneously. A 50℃ step increase in the hot face temperature is introduced. Both the measurement and process noises are considered. Fig. 6.46 and 6.47 show the estimation results by using Algorithm 1 shown in Fig. 6.7. Fig. 6.48 and 6.49 show the estimation results by using Algorithm 2 given in Fig. 6.8.

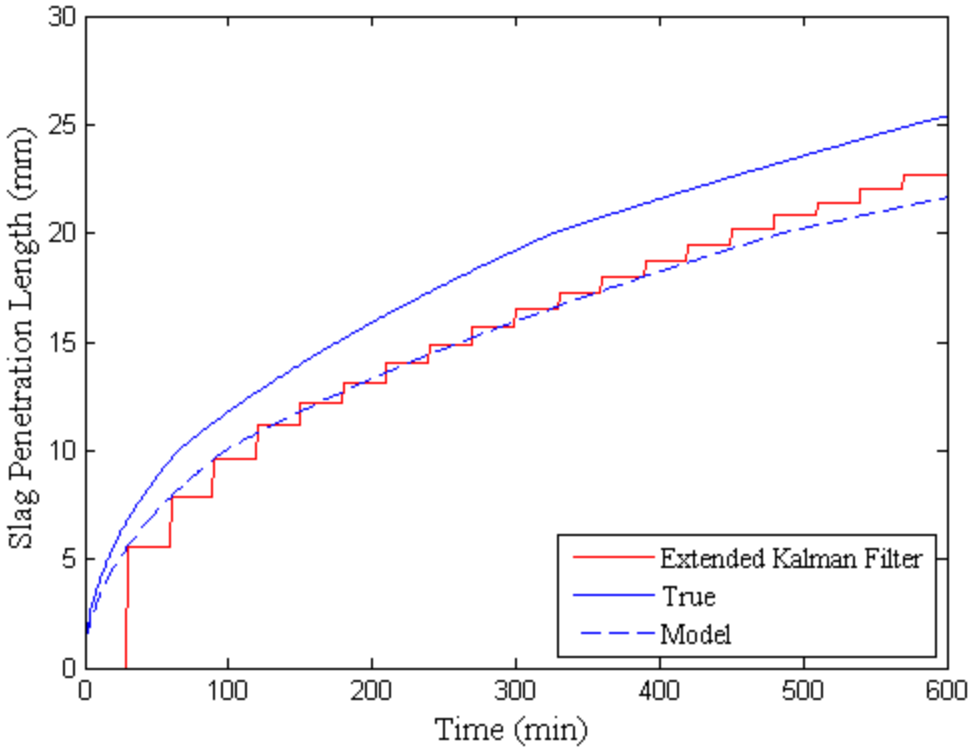

Figure 6.46. Estimation of slag penetration with Multi-scale EKF algorithm 1 for the centerline of brick.

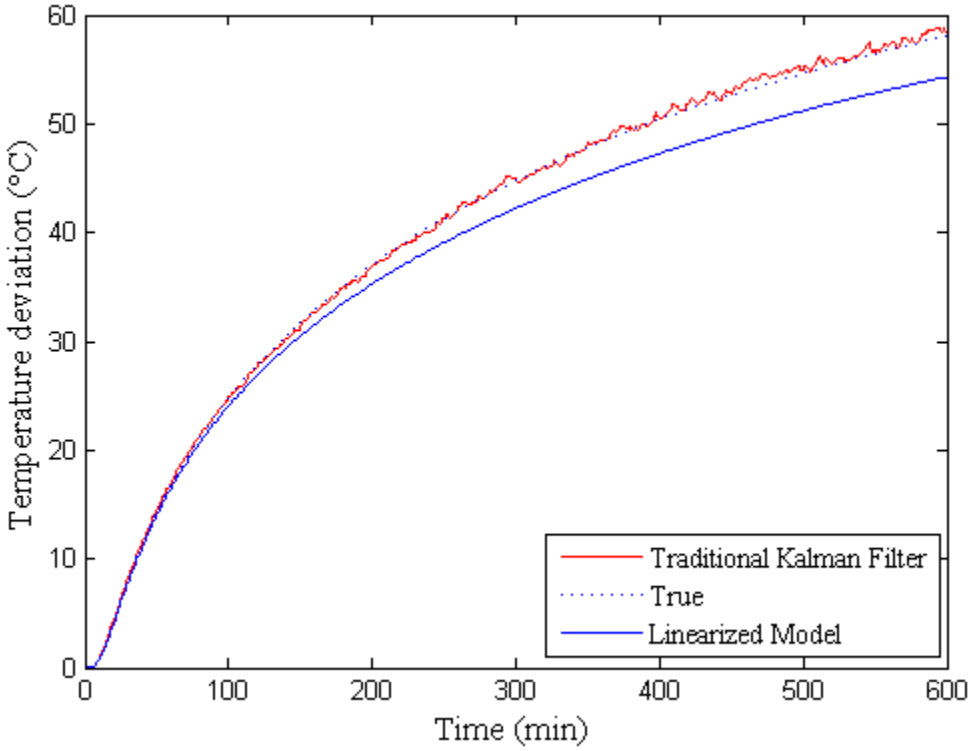

Figure 6.47. Estimation of temperature with multi-scale EKF algorithm 1 for the center of brick.

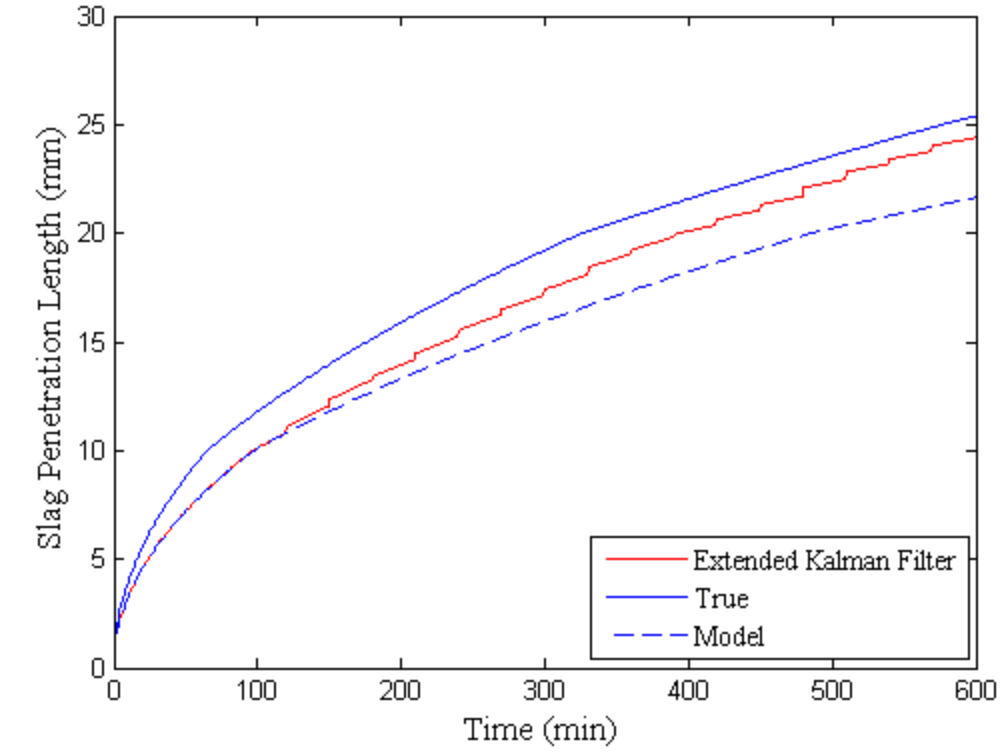

Figure 6.48. Estimation of slag penetration with multi-scale EKF algorithm 2 for the centerline of brick.

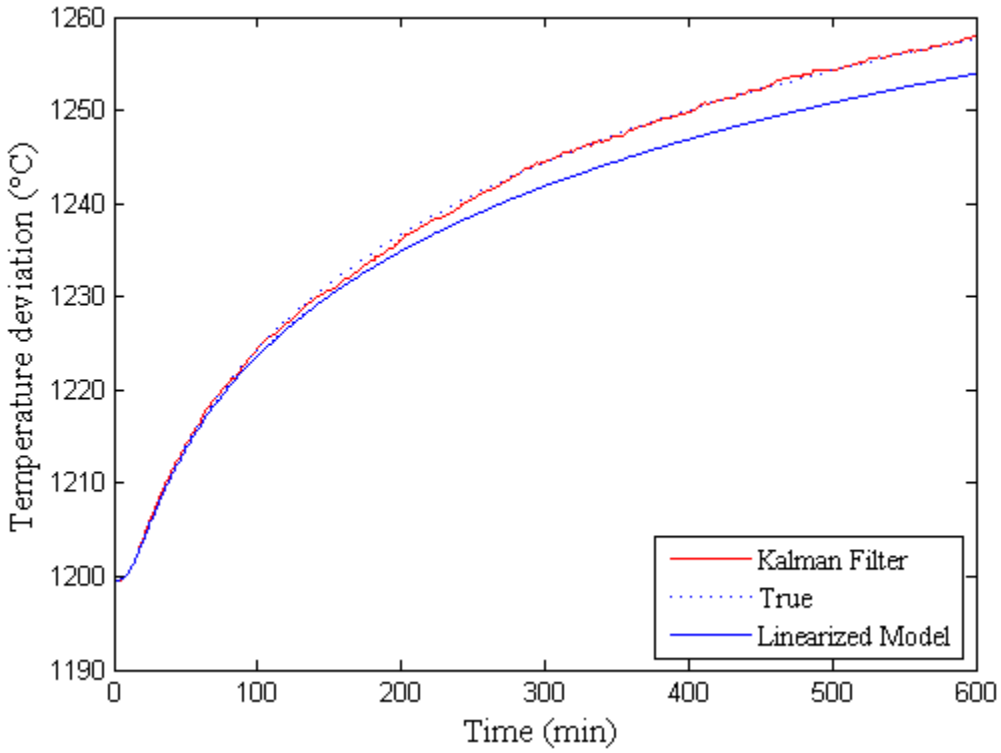

Figure 6.49. Estimation of temperature with multi-scale EKF algorithm 2 for the center of brick.

It is observed in Fig. 6.46-6.49 that, similar accuracies have been obtained for the temperature estimates by both algorithms, while for the estimation of slag penetration, Algorithm 2 converges to the true states much quicker than Algorithm 1. It is because the velocity of slag penetration is relatively high during the first several hours. Therefore, the constant slag penetration length assumption used in Algorithm 1 tends to introduce larger estimation error than Algorithm 2, in which the time update is considered to be implemented on the microscale.

Estimation of Temperature Profile with Out-of-Sequence Measurements (OOSM) from Embedded Thermistors:

The goal of this study is to estimate temperature profile with out-of-sequence measurements (OOSM) from embedded thermistors. Clearly, the OOSM problem becomes important when the information provided by the measurements is not redundant for the state estimation. Therefore, before implementing the algorithm discussed in the previous section, it is necessary to analyze the sensitivity of Kalman filter (KF) estimation accuracy to the number of sensors.

For temperature profile estimation, a 50℃ step increase in the hot face temperature was introduced and the temperature was estimated using the traditional Kalman filter (TKF). Thermistors are considered to be embedded evenly spaced on diagonal of the smart refractory brick. Number of thermistors is varied from 1 to 10. The estimation quality was evaluated by using the average integral squared error (ISE) and the average mean squared error (MSE). The average ISE for the discrete time system is defined as:

$$average\ ISE = \frac{1}{N\Delta t}\left(\sum_{i=1}^{N}(\hat{x}_i - x_i)^2\Delta t\right) \tag{6.78}$$

The average MSE for the discrete time system is defined as:

$$MSE = \frac{1}{N}\left(\sum_{i=1}^{N}(\hat{x}_i - x_i)^2\right) \tag{6.79}$$

where N is the number of state estimates; $\hat{x}_i$ is the state estimate; and x_i is the true value of state corresponding to $\hat{x}_i$; Δt is the sampling time. The estimates of temperature were correctly initialized. The sensitivity of TKF performance on temperature estimation to the number of thermistors is shown in the following Fig. 6.50:

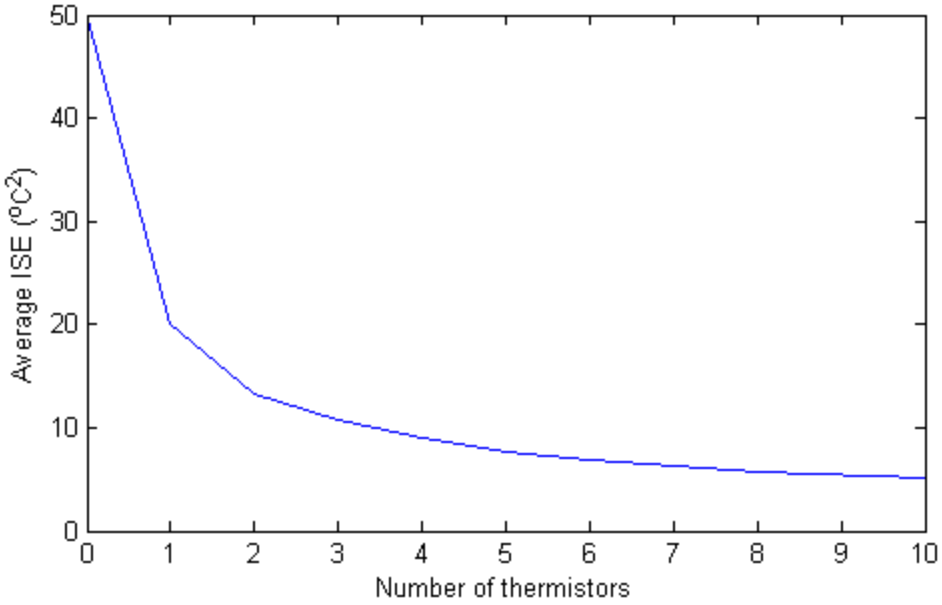

Figure 6.50. Estimation accuracy of temperature with respect to the number of thermistors.

By analyzing results presented in Fig. 6.50 and computational expense, three thermistors are considered for further analysis. These are embedded diagonally in high chromia brick as shown in Fig. 6.51. These thermistors are numbered from left to right as Sensor 1, 2, and 3. The Kalman filter is used to estimate the temperature profile as shown in Fig. 6.52. It shows how the estimation accuracy changes as some of the measurements are lost.

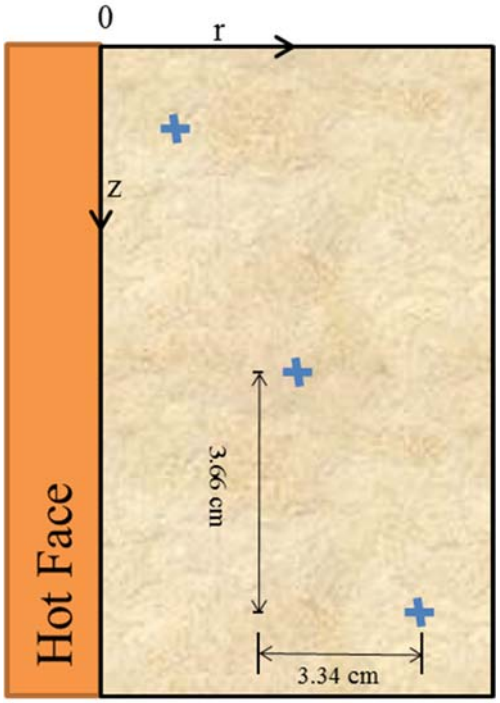

Figure 6.51. Schematic of the high-chromia refractory lining embedded with three thermistors (blue cross represents the center point of sensor).

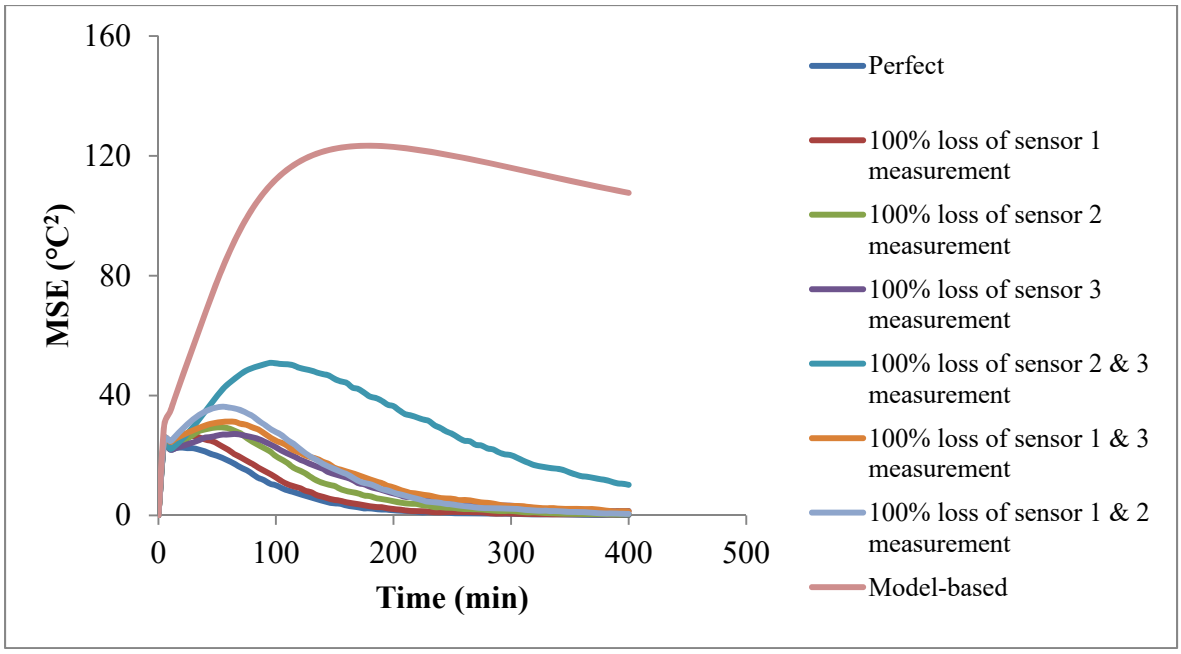

Figure 6.52. Estimation accuracy with lossy sensor network.

It is observed in Fig. 6.52 that the loss of measurements from both Sensor 2 and 3 causes the largest decrease in the estimation accuracy.

For implementing the OOSM algorithm, it is assumed that all the measurements from Sensor 1 arrive on time. Out-of-sequence measurements and measurement loss randomly happen for measurements from Sensors 2 and 3. The OOSM algorithm is used to estimate temperature profile using measurements from these 3 embedded sensors. Two parameters, data loss rate (represented as Loss in Fig. 6.53 and 6.54) and data late arrival rate (represented as OOSM in Fig. 6.53 and 6.45) have been used to characterize the measurements received in this system. The data loss rate is defined as the ratio of data that is never received (completely lost). The data late arrival rate is defined as the percentage of data that arrives late but the delay is still within one sampling interval. The average MSE is used to evaluate the estimation accuracy.

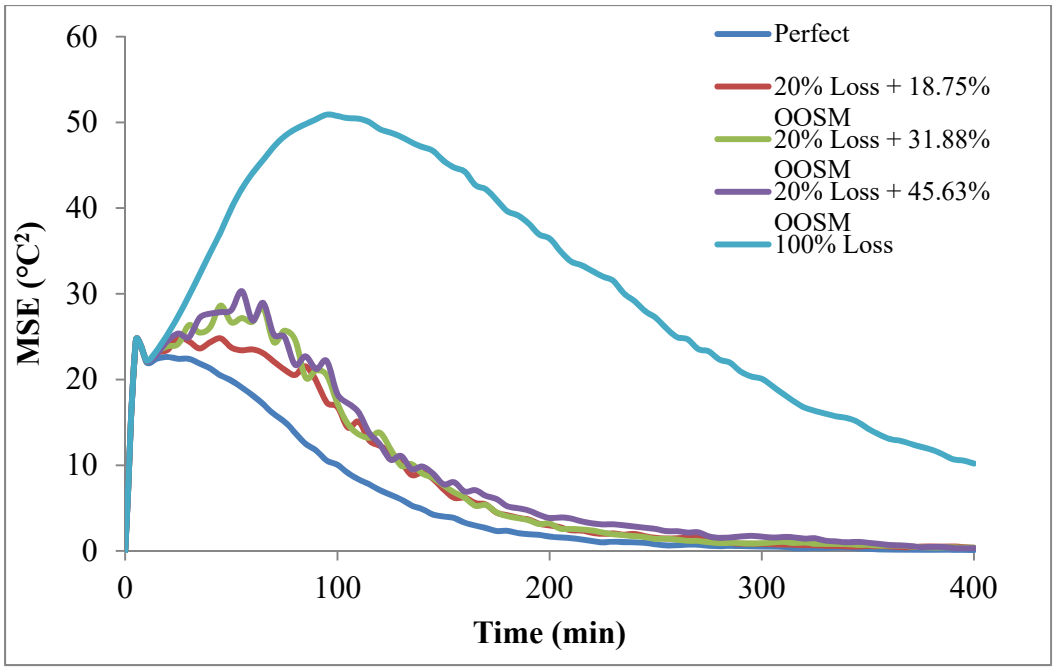

Figure 6.53. Estimation accuracy versus the data late arrival rate (OOSM).

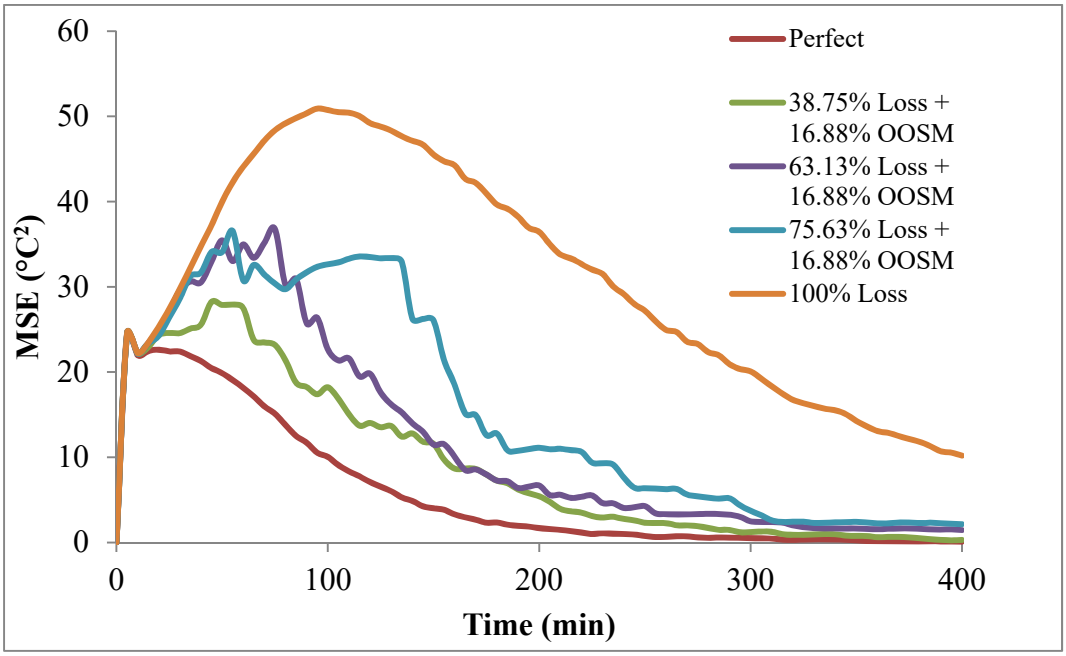

Figure 6.54. Estimation accuracy versus the data loss rate.

Figure 6.53 shows that the temperature profile by using the algorithm shown in Fig. 6.9. Compared to the process of slag penetration, the process of heat transfer is much faster. While the time scale of heat transfer is in minutes, time scale for the slag penetration is in days. Therefore, when estimating the temperature profile, the extent of slag penetration was set to be a constant. The completely slag penetrated case is considered. Fig. 6.55 shows the temperature estimates at the

center of the smart brick, and the resistance estimates for the second sensor along the diagonal of brick.

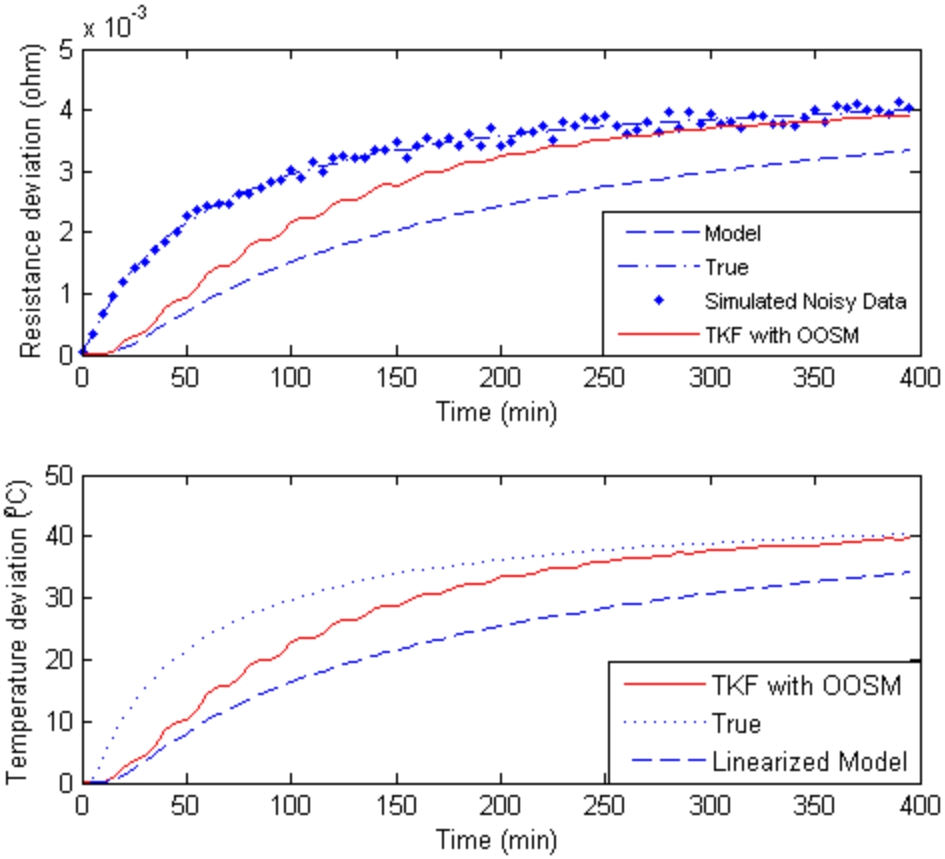

Figure 6.55. TKF estimation with OOSM measurements from embedded thermistors.

As observed in Fig. 6.55, a satisfactory estimation accuracy is obtained. The ISE for this case is about 11 $℃^2$. This value is obtained using 3 sensors shown in Fig. 6.50.

Estimation of Extent of Slag Penetration with OOSM from Embedded IDCs:
Since the slag penetration model employed in this study is a 1-D model and the IDC's sensitivity distance is limited, the estimation sensitivity problem can be simplified as a 1-D problem. The sensitivity of the extended Kalman filter (EKF) estimation accuracy to the number of the IDCs on the horizontal centerline of the smart brick was studied. It is found that the estimation accuracy decreases rapidly as the sensor number is reduced from 6 to 0. Therefore, the OOSM algorithm is implemented based on the case which 6 IDCs are evenly spaced embedded on centerline of the high-chromia brick.

An extreme case is considered in estimating the extent of slag penetration by using the OOSM measurements from IDCs with EKF. In this extreme case, all the measurements from the 6 IDCs are considered to be received one sampling time later. While estimating the length of the slag penetration, the hot face temperature is set to be constant. Fig 6.56 shows the estimate of slag penetration length along the centerline of brick and the capacitance estimate of the 3^{th} IDC, for the extreme case.

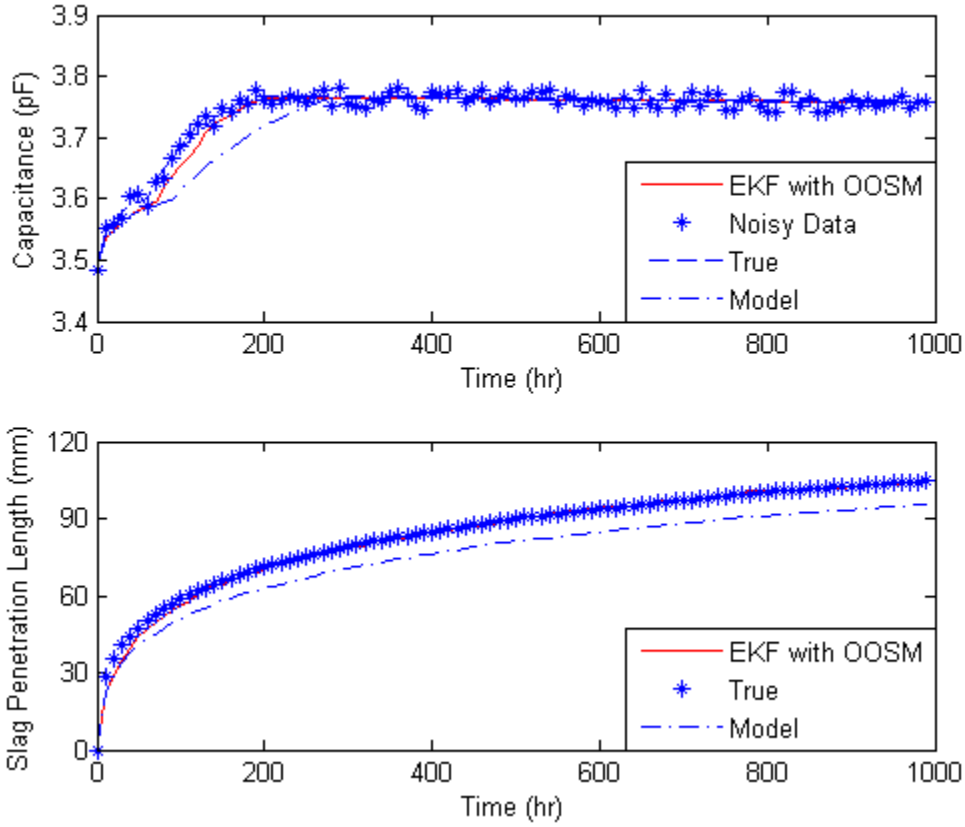

Figure 6.56. EKF estimation with OOSM measurements from embedded IDCs.

As observed in the Fig. 6.56, good estimates are achieved using the OOSM algorithm when the IDC measurements that arrive late are utilized.

6.4 Conclusions:

In this task, a rigorous, first-principles, dynamic model of the smart refractory brick has been developed. The thermal model for multi-layer gasifier wall has been developed by considering properties of the pristine smart refractory brick as well as that of the slag-infiltrated brick. Models of the sensors, namely thermistor, IDC, thermocouple, resistive circuit and strain gauge, have been developed by considering the installation direction and the geometries of the embedded sensors. The sensitivities of embedded sensors to the temperature as well as extent of slag penetration are analyzed.

The TKF is first applied to estimate the gasifier wall temperature profile using measurements from four types of sensors (thermistor, IDC, resistive circuit, strain gauge). All of them are found to provide satisfactory estimates of the temperature profile for pristine and slag-infiltrated bricks despite high model mismatch. Our results show that satisfactory estimation of temperature profile can be obtained even for locations where there is no sensor by utilizing measurements from sensors placed elsewhere. Due to the fact that thermal model is nonlinear, EKF is implemented with the

simulated measurement data from these four types of sensors to check if a better performance of temperature estimation can be achieved. Similar temperature estimates as using TKF are observed.

The TKF is found to result in poor estimation of the slag penetration length. But the EKF yields superior estimates even though the rate of change of the capacitance becomes higher when the slag reaches the sensor. Since slag penetration leads to a change in the temperature profile at a given hot face temperature, the EKF can also provide good estimates by measuring the change of temperature with the measurements from embedded resistance-type sensors (thermistor, resistive circuit, and strain gauge).

The extent of slag penetration has great impact on the gasifier temperature profile, and vice versa, extent of slag penetration strongly depends on the temperature history of the gasifier wall. Therefore, it is necessary to estimate both the temperature and the extent of slag penetration simultaneously. However, compared to the temperature, slag penetration is a relatively slow time-varying mechanism. While the time scale of temperature is in minutes, time scale of slag penetration is in hundreds of hours. The multi-scale EKF has been developed to estimate temperature and slag penetration depth simultaneously using measurements from embedded thermistors and IDCs. Two different multi-scale dual Kalman filter algorithms are compared. Similar estimation accuracies have been obtained for the temperature estimates for both algorithms. While for the estimation of slag penetration, algorithm with time update for slag penetration estimation on a ‘micro’ time scale has been observed to provide superior estimates.

In addition, measurements that arrive late have been utilized in KF-estimation frame work. Based on the estimator performance, a series of sensitivity studies have been conducted. OOSM algorithm is proved to be able to take use of the out-of-sequence measurements and provide good estimates in a wide range of the data arrival rate.

This study shows the promise of a model-based approach for estimating the temperature profile and the slag penetration profile in the gasifier wall by using ‘smart’ refractory bricks. Therefore, the ‘smart’ refractory bricks can play a strong role in health monitoring of the refractory linings.

Task 7: Full Wireless Concept Demonstration

7.1 Introduction:

The goal of the entire work plan was to produce a suite of hardware and software that would culminate into a smart brick system that could be implemented for actual health and process monitoring of a slagging gasifier. The work from Tasks 2-6 would result in all the parts of a complete sensor system proposed for this application. In order to demonstrate this, a full wireless concept demonstration was proposed with the commercial partner, which included the insertion of the smart bricks within a static and dynamic erosion brick test system that would mimic a basic high-temperature reactor. The specific subtasks were as follows:

Subtask 7.1 Scale-up of Smart Refractory Production- WVU will fabricate the sensor preforms and deliver to the commercial partner HWI. Development of interconnect bricks (with embedded electrodes) and connection pins (and potentially conductive cement or high-temperature brazes) will be completed to insure reliable "through-brick" sensor connection to the outer reactor wall (without hard lines and access ports).

Subtask 7.2 Larger-Scale Slag Testing and Wireless Concept Demonstration- Smart refractory bricks will be incorporated into HWI testing kilns. Five or more wireless sensor nodes will be incorporated into the demonstration utilizing the optimal electronic interface, power configuration, and wireless network developed in Task 5. The data will be collected at a singular hub, and the performance during dynamic testing of the smart bricks at high-temperature will be *in situ* monitored.

7.2 Experimental Methods:

7.2.1 Preform Fabrication

The LNO thermistors were fabricated by screen printing LNO/Y-stabilized zirconia (YSZ) composite inks onto YSZ tapes. Two sets of LNO/YSZ inks were synthesized: [50-50] vol% LNO-YSZ and [70-30] vol% LNO-YSZ ink. The function of the [50-50] LNO-YSZ composite ink was to ensure adhesion with YSZ substrate, while LNO conductive core was formed [70-30] vol% LNO-YSZ ink. To limit grain growth of the LNO during sensor application, LNO powders were calcined at 1400 ºC prior to ink preparation.

The sensor patterns were fabricated by a screen printing process. A 230 mesh screen was used for screen printing. The 50:50 LNO:YSZ ink was screen printed first onto green YSZ substrate and then the conductive core ink, [70-30] vol% LNO-YSZ, was screen printed on top, making it one half of the sensor. Every printed ink layer was dried at 70 °C. Two printed halves were laminated together to form YSZ embedded thermistor. The laminated thermistors were sintered into sensor preforms at 1450 °C for 2 h in air.

7.2.2 Brick Fabrication

The thermistors/thermocouple preforms were embedded into high-chromia refractory brick at HarbisonWalker International (HWI, West Mifflin, PA, USA). The formulation of the brick composition is an intellectual property of HWI. The pre-sintered sensor preforms were embedded into brick material during casting of the high-chromia bricks. For the demonstration, a full-size

bricks were cast. The full size brick is 4 x 4 x 9 inch. The cast bricks with oxide-based thermistors were sintered to 1450 °C for 10 h in air.

7.2.3 Electrical Testing

In order to electrically evaluate the sintered high-chromia bricks with embedded preforms, it was necessary to expose the sensor material and connect it to platinum wire leads. After the bricks were sintered, a 5 mm slice was cut off the end of a brick to expose sensor leads. Two platinum wires were stretched across the exposed sensor material and cemented to the brick with Ceramabond™ 569 (Aremco Products Inc., Valley Cottage, NY) at two points without letting the cement touch the sensing material. Each wire was then attached to exposed sensor legs with Pt ink for silicide-based sensors and LNO-based ink for LNO-based sensor material. For LNO-based sensors, the Pt electrical connection was cured at 1350 °C for 2 h in and air. The electrical response versus temperature was continuously collected using a two-point DC measurement with a Keithley 2100 DMM using a National Instruments LabView™ program.

7.3 Results and Discussion:

At the end of the program, the lanthanum nickelate based thermistors were selected to demonstrate the feasibility of the technology. LNO-1400 sensor material was showing encouraging results with relatively predictable resistance to temperature response. Work in Task 5 showed that coarsening of the sensor material limitted the resistance drift due to microstructural changes. Removal of the connection between platinum leads to sensors embedded in the brick sensor from furnace hot zone to outside the testing furnace significantly decreased resistance drift especially during thermal cycling. Future work will need to address and improve the lead connection issues, but nevertheless the researcher felt confident to prepare samples for demonstration using the materials and techniques developed in Task 5.

The preparations for the final demonstration started with a planning session on dimensions and sensor positioning at Harbison Walker International (HWI). An agreement was reached to utilize an existing brick sintering furnace at HWI. Figure 7.1 shows the front door of the furnace that was selected for the demonstration. The front door is lined with three layers of 9 x 4 x 4 inch bricks. Figure 7.1b shows the door assembled with indicated locations for the sensor bricks. The sensor bricks will be placed length wise, perpendicular to current arrangement of the wall, and spanning thickness of layer 1 and 2 as shown in the Figure 7.1a. This arrangement will move the leads from maximum application temperature (1400°C) to estimated 500°C, which will limit the resistance drift due to leads connection.

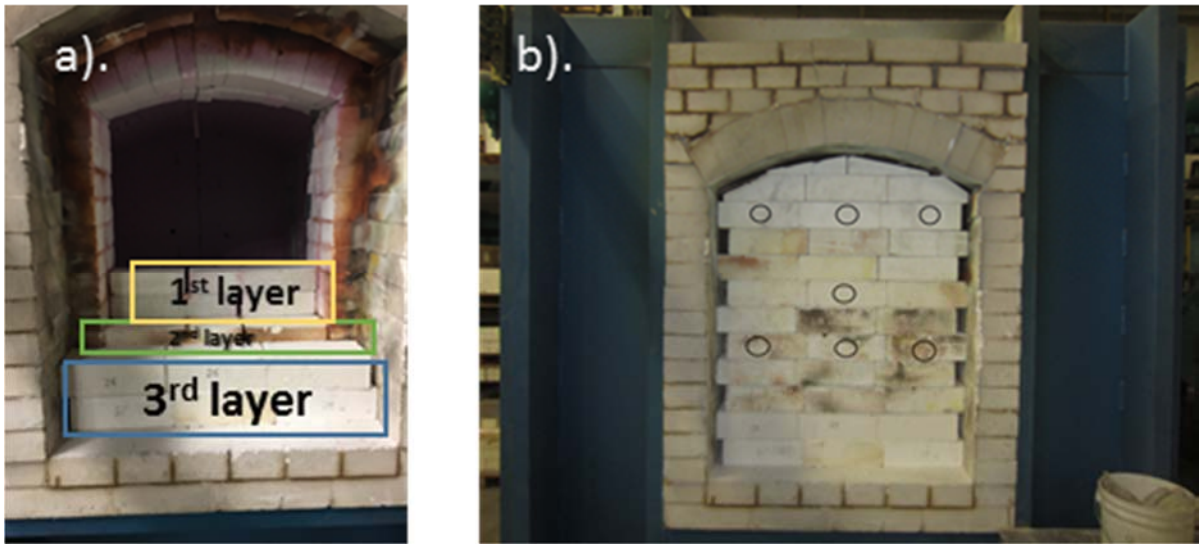

Figure 7.1 Images of the furnace selected for sensor brick demonstrations (Fig. 7.1a shows the door construction of three layers of bricks and Fig. 7.1b the selected locations for the sensors).

During the meeting between Harbison Walker International team and Dr. Sabolsky's group, it was decided to make the sensor match the size of the currently used bricks. Since the bricks used in the demonstration furnace are 9 x 4 x 4 inch, the target length of the sensor was determined to be just under nine inches. However, due to processing equipment limitations, the maximum sensor length was established at 7.13". Based on this limited dimension, couple options were proposed for the arrangement of the sensor within the 9-inch long brick, as illustrated in Figure 7.2. The proposed options were:

Option 1: The sensor is positioned towards the rear of the brick. Allowing for 1.85" of brick wall between sensor and hot zone. It should provide cooler temperatures for the connections, but delayed or less accurate reflection of internal furnace conditions.

Option 2: The sensor is positioned about 0.5" from the face of the brick and the brick is cut short to expose connections. This arrangement is more similar to how we test embedded sensors now. This arrangement will have higher temperatures at connections, but reflect more accurate hot zone conditions.

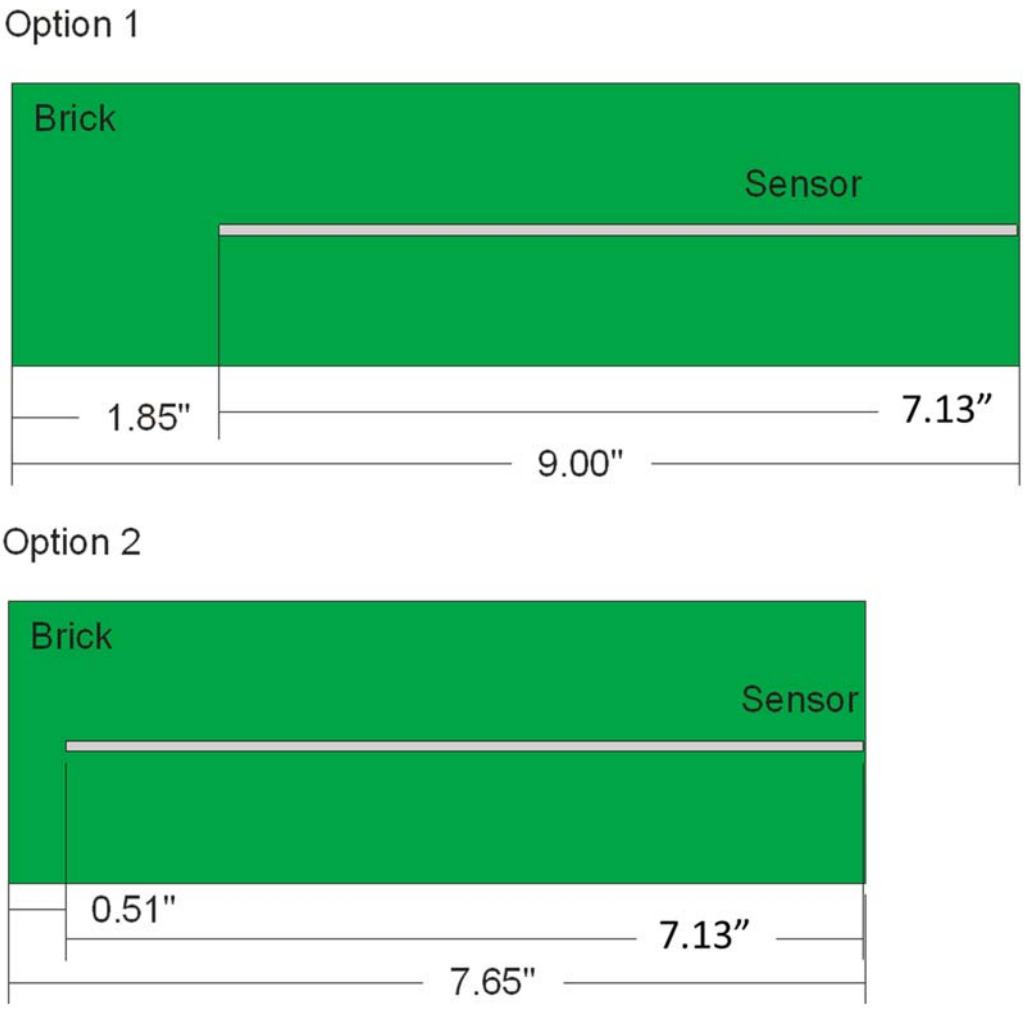

Figure 7.2 Schematic illustration of the two options for the placement of 7.13” long sensors inside 9” long brick.

With the sintered length of the sensor established and the width matched to previously fabricated short sensors, the green dimensions of the sensor were determined at 9.5 x 1.25 “. Due to the size of the green sensor and limited size of the screen printer used to deposit the conductive sensor material, the screen art work required the pattern to be printed into two steps per layer with layers overlapping by about an inch in the center of the sensor.

In review, the thermistors were build using two LNO inks: 50 vol% LNO: 50 vol% YSZ and 70 vol% LNO: 30 vol% YSZ composite inks. In both inks, the LNO was calcined to 1400°C to improve thermal stability of the sensor material. The LNO inks were printed on green YSZ substrates, laminated into green preform, and then sintered to 1400°C. The fabrication scale-up from 2 inch long preform to 7.13 inch preforms was more problematic than expected due to multiple factors. The most significant were binder burnout and lamination. Due to multiple overlapped layers of LNO ink, the initial binder burnout was inadequate in eliminating all organics resulting in splitting and/or pillowing of sensor materials during sintering. The size of the preforms was also problematic during lamination. The equipment available at WVU was inadequate to reliably laminate long preforms. The problem was exacerbated with the change in YSZ powder

lot used in substrate fabrication. This change required change in tape casting formulation and most significantly change in lamination force for initial tape lamination and lamination of the green preforms. Figure 7.3 shows the evolution of the preforms as each problem was individually identified and corrected. The final processing parameters for preform lamination, binder burnout, and sintering are listed in Table 7.1.

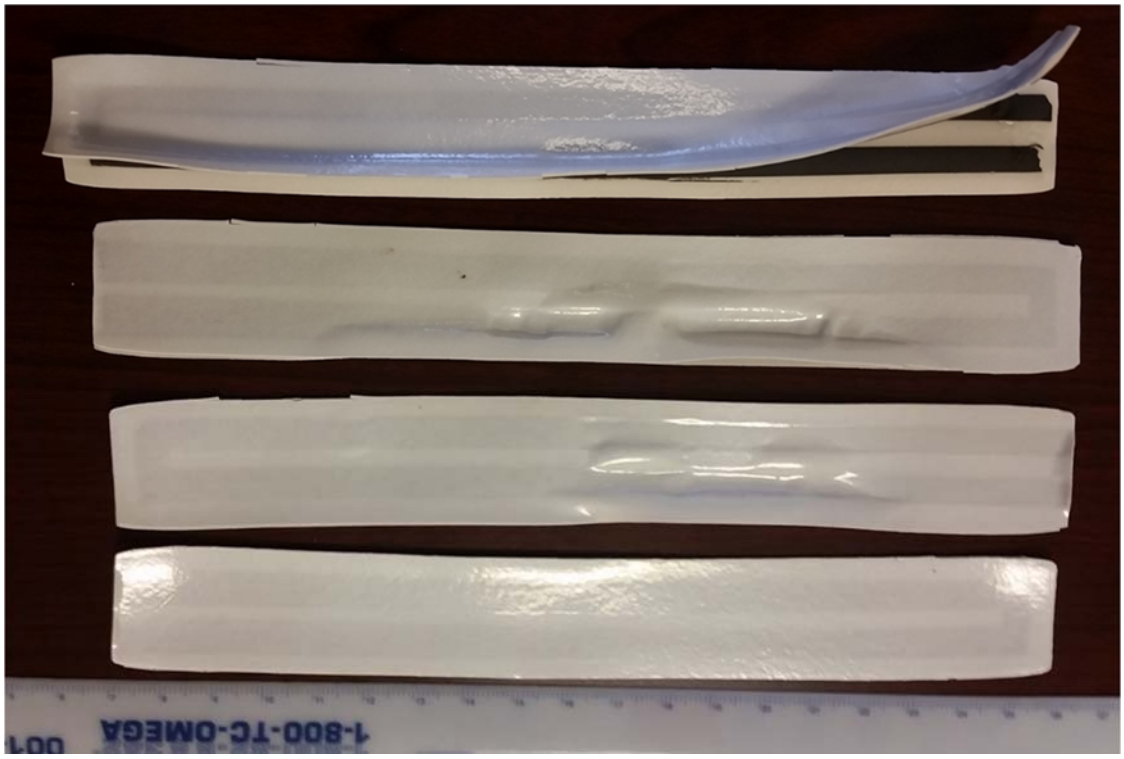

Figure 7.3 The evolution of the preforms from earliest to latest as each processing problem was individually identified and corrected.

Table 7.1 The final processing parameters for preform lamination, binder burnout and sintering.

Preform Lamination	Binder Burnout Schedule	Sintering Schedule
20 min at 1.5 klbs and 40 min at 55 klbs at 100°C	1°C/min to 150°C for 240 min; 1°C/min to 200°C for 240 min; 1°C/min to 400°C for 240 min; 1°C/min to 600°C for 120 min; 1°C/min to 1000°C for 120 min; 5°C/min to RT	2°C/min to 1000°C; 1°C/min to 1400°C for 120 min

Throughout the fabrication process of the long preforms, the yield of successfully formed sensors hovered around 20%. The size of the preforms illuminated the processing limitation of the lamination and sintering equipment available at the West Virginia University (WVU). In order to ensure that plenty of bricks are available for the demonstration, multiple sets of long sensor preforms was produced. Alongside the long preforms, a decision was made to fabricate half-size,

4-inch long, preforms in order to provide greater number of samples. The fabrication yield for the 4-inch preforms was 100%. The long and half-size preforms were cast into 4 x 4 x 9 inch bricks, but the half-size preforms were placed along the short side of the brick. The bricks were then sintered at 1450°C using the standard furnace and heating schedule employed at the HarbisonWalker International (HWI).

Eight full-side bricks, Fig. 7.4, were prepared for testing following the procedures established in Task 5 and then tested to 1400°C. The bricks were initially tested at the WVU, where calibration curves were collected for each individual brick, Fig. 7.5 in expectation that the bricks will be taken to the HWI for the final demonstration. The data also shows the readout for the hot-junction and cold-junction thermocouples. The hot-junction thermocouple was placed inside the furnace. The cold-junction thermocouple was placed near the connection between leads and embedded sensor. Multiple bricks were tested each showing similar resistance results and also using the wireless system. See Task 5 for further discussion of the wireless testing results.

Figure 7.4. Full-size bricks with embedded LNO-1400 preforms and attached platinum wire leads.

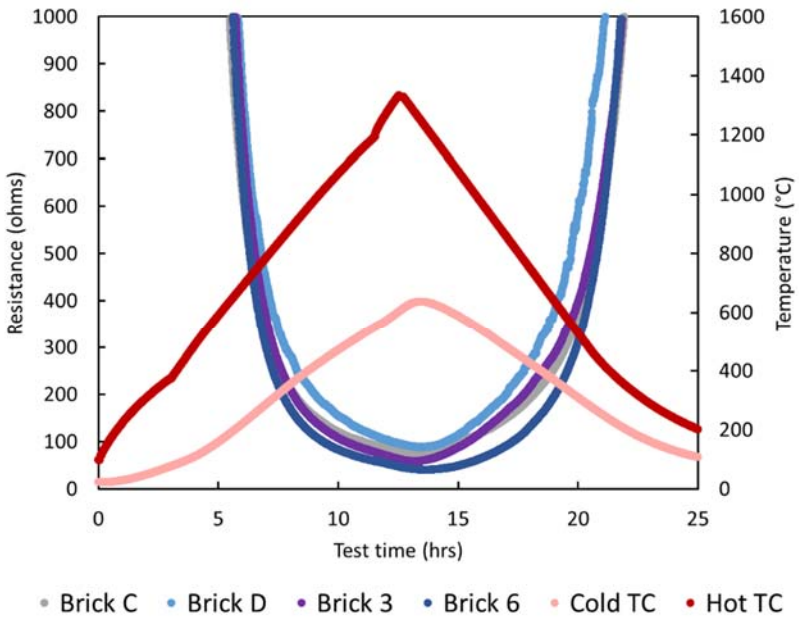

Figure 7.5. Resistance data for full-size bricks showing reproducible results for multiple bricks. The graph includes hot- and cold-junction thermocouples read out.

7.4 Conclusions:

Milestone M12 "HWI fabricated full size smart refractory bricks for erosion/corrosion testing" was completed with the initial silicide system December 31, 2015 and with the final LNO system November 30, 2017.

The following is a list of accomplishments for the full wireless concept demonstration task.

1. Fabricated 8 full size smart bricks with LNO thermistors.
2. Verified reproducible performance between 5 bricks.
3. Verified complete operation of smart brick system and successfully measured data wirelessly.

GRAPHICAL MATERIALS LIST(S)

None

REFERENCES

Task 1 References

None

Task 2 References

[2.1] L. Lutterotti, S. Matthies, H.R. Wenk, MAUD: A friendly Java program for material analysis using diffraction, IUCR Newsletter of the CPD 21 (1999) 14-15.

[2.2] C.A. Schneider, W.S. Rasband, K.W. Eliceiri, NIH image to ImageJ: 25 years of image analysis, Nature Methods 9 (2012) 671-675.

[2.3] L. Hui, R.C. Smith, X. Wang, J.K. Nelson, L.S. Schadler, Quantification of particulate mixing in nanocomposites, Annual Report Conference on Electrical Insulation Dielectric Phenomena (2008).

[2.4] ASTM B193-16, Standard test method for resistivity of electrical conductor materials, ASTM International (2016) West Conshohocken, PA.

[2.5] Crystallography Open Database website: *http://www.crystallography.net/cod*.

[2.6] P.A. Karnezis, G. Durrant, B. Cantor, Characterization of reinforcement distribution in cast Al-Alloy/SiC_p composites, Materials Characterization 40 (1998) 97-109.

[2.7] M. Besterci, O. Velgosova, I. Kohutek, Microstructural parameters of dispersion strengthened Al-Al_4C_3 material by image analysis, Iranian Journal of Science & Technology, Transaction B 28 (2004) 233-238.

[2.8] U. Gottlieb, F. Nava, M. Affronte, O. Laborde, R. Madar, Electrical transport in metallic TM silicides, in: K. Maex, M.V. Rossum (Eds.), Properties of Metal Silicides, Inspec/Iee, London (1995) pp. 189-204.

[2.9] S. Madhukar, S. Aggarwal, A.M. Dhote, R. Ramesh, S.B. Samavedam, S. Choopun, R.P. Sharma, Pulsed laser-ablation deposition of thin films of molybdenum silicide and its properties as a conducting barrier for ferroelectric random-access memory technology, J. Mater. Res. 14 (1999) 940-947.

[2.10] Y. Ito, M. Sato, K. Wakisaka, S. Yoshikado, Improvement of heating characteristics of molybdenum silicide thin film electric heaters, Electr. Eng. Jpn. 168 (2009) 11-19.

[2.11] S. Kobel, J. Pluschke, U. Vogt, T.J. Greuel, $MoSi_2$-Al_2O_3 electroconductive ceramic composites, Ceram. Int. 30 (2004) 2105-2110.

Task 3 References

[3.1] T. Tabaru, K. Shobu, M. Sakamoto, S. Hanada, Effects of substitution of Al for Si on the lattice variations and thermal expansion of Mo $(Si, Al)_2$, Intermetallics. 12 (2004) 33-41.

[3.2] J. Xu, Z.Y. Li, P. Munroe, Z.H. Xie, Oxidation resistance of $Mo(Si_{1-x}Al_x)_2$ nanocrystalline films and characterization of their oxide scales by electrochemical impedance spectroscopy, RSC Adv. 4 (2014) 55696–55708.

[3.3] J. Xua, Z. Li, Z.H. Xiec, P. Munroed, X.L. Lua, X.F. Lana, Novel high damage-tolerant, wear resistant $MoSi_2$ based nanocomposite coatings, Applied Surface Science. 270 (2013) 418-427.

[3.4] E.N. Kaufmann, Characterization of Materials, vol. 2, John Wiley & Sons, Hoboken, New Jersey, 2003.

[3.5] Z. Liu, Y. Kawashima, A. Komatsu, T. Hamada, H. Kawano, K. Shiotani, Formation mechanism of metal-oxides on plasma-exposed WSix/ poly Si gate stacks, Jpn. J. Appl. Phys. 38 (1999) 209-211.

[3.6] J.K. Yoon, K.W. Lee, S.J. Chung, I.J. Shon, J.M. Doh, G.H. Kim, Growth kinetics and oxidation behavior of WSi_2 coating formed by chemical vapor deposition of Si on W substrate, Journal of Alloys and Compounds. 420 (2006) 199–206.

[3.7] T.M. Christensen, Surface studies of amorphous $W_{75}Si_{25}$ oxidation, J. Vac. Sci. Technol. A. 7 (1989) 1689-1693.

[3.8] Z. Yao, J. Stiglich, T.S. Sudarshan, Molybdenum silicide based materials and their properties, J. Mater. Eng. Perform. 8 (1999) 291-304.

[3.9] G. Jiang, S. Bai, L. Chen, W. Li, H. Zhuang, Fabrication and microstructure of $MoSi_2/Al_2O_3$ functionally graded material, Mater. Sci. Forum. 423-425 (2003) 195-198.

[3.10] C.D. Wirkus, D.R. Wilder, High-temperature oxidation of molybdenum disilicide, J. Am. Ceram. Soc. 49 (1966) 173-177.

[3.11] J.J. Petrovic, A.K. Vasudevan, Key developments in high temperature structural silicides, Mater. Sci. Eng. A. 261 (1999) 1-5.

[3.12] W-Y. Lin, R.F. Speyer, Stability of molybdenum disilicide in combustion gas environments, J. Am. Ceram. Soc. 77 (1994) 1162-1168.

[3.13] G.A. Yakaboylu, R.C. Pillai, K. Sabolsky, E.M. Sabolsky, Stability and electrical properties of $MoSi_2$- and WSi_2-oxide electroconductive composites, J. Am. Ceram. Soc. 100 (2017) 4461-4475.

[3.14] A. Chakraborty, S.V. Kamat, R. Mitra, K.K. Ray, Effect of $MoSi_2$ and Nb reinforcements on mechanical properties of Al_2O_3 matrix composites, J. Mater. Sci. 35 (2000) 3827-3835.

[3.15] S. Kobel, J. Pluschke, U. Vogt, T.J. Graule, $MoSi_2$–Al_2O_3 electroconductive ceramic composites, Ceram. Int. 30 (2004) 2105-2110.

[3.16] T.C. Lu, J. Yang, Z. Suo, A.G. Evans, R. Hecht, R. Mehrabian, Matrix cracking in intermetallic composites caused by thermal-expansion mismatch, Acta Metall. Mater. 39 (1991) 1883-1890.

[3.17] J. Martin, T. Tritt, C. Uher, High temperature Seebeck coefficient metrology, J. Appl. Phys. 108 (2010) 121101-1-12.

[3.18] K.G. Kreider, G. Gillen, High temperature materials for thin-film thermocouples on silicon wafers, Thin Solid Films. 376 (2000) 32-37.

[3.19] K.G. Kreider, Thin film high temperature silicide thermocouples, U.S. Patent, No. 5474619 (1995).

[3.20] M. Gunes, M. Parlak, M. Ozenbas, An instrument for the high temperature measurement of the Seebeck coefficient and electrical resistivity, Meas. Sci. Technol. 25 (2014) 055901.

[3.21] E. Committee, Ed., Manual on the use of thermocouples in temperature measurement, STP470B-EB, ASTM International, West Conshohocken, PA, 1981.

[3.22] W.H. Bennethum, L.T. Sherwood, Sensors for ceramic components in advanced propulsion systems, NASA Contractor Report. NASA-CR-180900 (1988) August.

[3.23] R. Mitra, Mechanical behavior and oxidation resistance of structural silicides, International Materials Reviews, 51 (2006) 13-64.

Task 4 References

[4.1] D.J. Jones and E.L. Buller, Analyses and softening temperatures of coal ash: From coals in the northern anthracite field., Ind. Eng. Chem. Anal. Ed., 8 (1936) 25–27.

Task 5 References

None

Task 6 References

[6.1] Y. Jiang and D. Bhattacharyya, Plant-wide modeling of an indirect coal-biomass to liquids (CBTL) plant with CO_2 capture and storage (CCS), Int. J. Greenh. Gas Con. 31 (2014) 1-15.

[6.2] T. Parameswaran, R. Hughes, P. Gogolek and P. Hughes, Gasification temperature measurement with flame emission spectroscopy, Fuel 134 (2014) 579-587.

[6.3] P. Wang and M. Massoudi, Slag behavior in gasifiers. part I: influence of coal properties and gasification conditions, Energies 6 (2013) 784-806.

[6.4] K. Kwong, A. Petty, J. Bennett, R. Krabbe and H. Thomas, Wear mechanisms of chromia refractories in slagging gasifiers, Int. J. Appl. Ceram. Tec. 4 (2007) 503-513.

[6.5] R.E. Williford, K.I. Johnson and S.K. Sundaram, Modelling of high-chromia refractory spalling in slagging coal gasifiers, Ceram. Int. 34 (2008) 2085-2089.

[6.6] S.J. Clayton, G.J. Siegel and J.G. Wimer, DOE/FE-0447, U.S. Department of Energy Report (2002).

[6.7] Z.Q. Guo, B.Q. Han and H. Dong, Effect of coal slag on the wear rate and microstructure of the ZrO_2-bearing chromia refractories, Ceram. Int. 23 (1997) 489-496.

[6.8] J. Nakano, S. Sridhar, J. Bennett, K.S. Kwong and T. Moss, Interactions of refractory materials with molten gasifier slags, Int. J. Hydrogen Energy 36 (2011) 4595-4604.

[6.9] J.P. Bennett and K.S. Kwong, Failure mechanisms in high chrome oxide gasifier refractories, Metall. Mater. Trans. A 42 (2011) 888-904.

[6.10] R.E. Williford, K.I. Johnson, S.K. Sundaram and S. Pilli, Effective diffusivity and spalling models for slagging coal gasifiers, J. Am. Ceram. Soc. 91 (2008) 4016-4022.

[6.11] I. Ye and C. Ryu, Numerical modeling of slag flow and heat transfer on the wall of an entrained coal gasifier, Fuel 150 (2015) 64-74.

[6.12] S. Chakraborty, S. Sarkar, S. Gupta and A. Ray, Damage monitoring of refractory wall in a generic entrained-bed slagging gasification system, P. I. Mech. Eng. A-J. Pow. Energy 222 (2008) 791-807.

[6.13] J.S. Kasule, R. Turton, D. Bhattacharyya and S.E. Zitney, Mathematical modeling of a single-stage, downward-firing, entrained-flow gasifier, Ind. Eng. Chem. Res. 51 (2012) 6429-6440.

[6.14] R. Krishnaswamy, T.K. Kaneko, B.M. Mazumdar, P. Rozelle, S. Sridhar and J.M. Kuhlman, Infiltration velocity and thickness of flowing slag film on porous refractory of slagging gasifiers, J. Energy Resour. Technol. 136 (2014) 032203.

[6.15] E.W. Washburn, the dynamics of capillary flow, Phys. Rev. 17 (1921) 273.

[6.16] S. Carbonell, M.J. Hey, J.R. Mitchell, C.J. Roberts, J. Hipkiss and J. Vercauteren, Capillary flow and rheology measurements on chocolate crumb/ sunflower oil mixtures, J. Food Sci. 69 (2004) 465-470.

[6.17] G.H. Zhang and K.C. Chou, Simple method for estimating the electrical conductivity of oxide melts with optical basicity, Metall. Mater. Trans. B 41 (2010) 131-136.

[6.18] G.D. Alley, Interdigital capacitors and their application to lumped-element microwave integrated circuits, IEEE Trans. Microwave Theory Tech. 18 (1970) 1028-1033.

[6.19] R.K. Hoffmann, Handbook of Microwave Integrated Circuits, Norwood: Artech House, 1987.

[6.20] K.Kotani, I. Kawayama and M. Tonouchi, Dielectric response of co-oriented $SrBi_2Ta_2O_9$ thin films observed with interdigital electrodes, Jpn. J. Appl. Phys. 41 (2002) 6790-6792

[6.21] W.P. Shih, L.C. Tsao, C.W. Lee, M.Y. Cheng, C. Chang, Y.J. Yang and K.C. Fan, Flexible temperature sensor array based on a graphite-polydimethylsiloxane composite, Sensors 10 (2010) 3597-3610.

[6.22] M.R.R. Khan and S.W. Kang, Highly sensitive temperature sensors based on fiber-optic PWM and capacitance variation using thermochromic sensing membrane, Sensors 16 (2016) 1064.

[6.23] R. Igreja and C.J. Dias, Analytical evaluation of the interdigital electrodes capacitance for a multi-layered structure, Sens. Actuators, A: Phys. 112 (2004) 291-301.

[6.24] B.G. Lipták, Process Measurement and Analysis, London: CRC Press, 2003.

[6.25] R.K. Mandela, R. Rengaswamy, S. Narasimhan and L.N. Sridhar, Recursive state estimation techniques for nonlinear differential algebraic systems, Chem. Eng. Sci. 65 (2010) 4548-4556.

[6.26] P.S. Maybeck and G.M. Siouris, Stochastic models, estimation, and control, IEEE Trans. Syst. Man Cybern. Syst. 10 (1980) 282.

[6.27] S.S. Haykin, Kalman Filtering and Neural Networks, New York: Wiley, 2001.
[6.28] C. Hu, B.D. Youn and J. Chung, A multiscale framework with extended Kalman filter for lithium-ion battery SOC and capacity estimation, Appl. Energy 92 (2012) 694-704.

[6.29] Y. Bar-Shalom, Update with out-of-sequence measurements in tracking: exact solution, IEEE Trans. Aerosp. Electron. Syst. 38 (2002) 769-777.

[6.30] K. Zhang, X.R. Li and Y. Zhu, Optimal update with out-of-sequence measurements, IEEE Trans. Signal Process. 53 (2005)1992-2004.

[6.31] S.M. Huang, A.L. Stott, R.G. Green and M.S. Beck, Electronic transducers for industrial measurement of low value capacitances**,** J. Phys. E 21 (1988) 242.

[6.32] W.Q. Yang, A.L. Stott and M.S. Beck, High frequency and high resolution capacitance measuring circuit for process tomography, IEE P. - Circ. Dev. Syst.141 (1994) 215-219.

Task 7 References

None

BIBLIOGRAPHY

None

LIST OF ACRONYMS AND ABBREVIATIONS

XRD	X-ray Diffraction
FE-SEM	Field Emission Scanning Electron Microscopy
SEM	Scanning Electron Microscopy
CTE	Coefficients of Thermal Expansion
TGA	Thermogravimetric Analyzer
EDS	Energy Dispersive Spectroscopy
YSZ	Yttrium Stabilized Zirconia
SSA	Specific Surface Area
LNO	La_2NiO_4
XPS	X-ray Photoelectron Spectroscopy
S_{AB}	Seebeck Coefficient
DMM	Digital Multimeter
ε	Dielectric Constant
ε_0	Permittivity of Free Space
T	Temperature
n_d	Carrier Concentration
d	Grain Size
L	Thickness of Sensing Layer
COTS	Commercial Off-the-Shelf
RTD	Resistive Temperature Detector
WSN	Wireless Sensor Network
CJC	Cold-Junction Compensator
RAMP	Reconfigurable Analog/Mixed-Signal Processor
FG	Floating-Gate Transistor
IC	Integrated Circuit
CTP	Collection Tree Protocol
ADC	Analog-to-Digital Converter

C_p	Heat Capacity ($J/g \cdot ℃$)
K	Thermal Conductivity ($W/m \cdot ℃$)
T	Temperature (℃)
m	Slope of Temperature Profile on Hot Face ($℃/m$)
h	Convective Heat Transfer Coefficient ($W/m \cdot ℃$)
φ	Velocity of Capillary Flow (m/s)
η	Slag Viscosity ($Pa.s$)
σ	Tortuosity of Refractory Pore System
R_p	Pore Radius (m)
l	Infiltration Depth (m)
ΔP	Pressure Difference across Refractory Lines
ζ	Electrical Resistivity (Ω-cm)
$\bar{R}$	Resistance (Ω)
ΔL	Length of Control Volume
S_i	Cross-sectional Area for Control Volume i
N	Number of Electrodes
Ns	Number of Sensitive Layers
k	Modulus
k'	Complementary Modulus
ε_0	Vacuum Permittivity (F/m)
ε	Relative Dielectric Constant
τ	Thickness of a Dielectric Layer(m)
C	Capacitance (pF)
x	Vector of Differential Variables
z	Vector of Algebraic Variables
u	Vector of System Inputs
γ	Process Noise
ω	Measurement Noise
Y	Measurements
A^{aug}	Augmented Process Transition Matrix

B^{aug}	Augmented Input Matrix
H^{aug}	Augmented Measurement Matrix
x^{aug}	Vector of Augmented State Variables
u^{aug}	Vector of Augmented System Inputs
Q	Covariance of the Process Noise
R	Covariance of the Measurement noise
P	Error Covariance Matrix

APPENDICES

List of Publications:

1. B. Rumberg, D. Graham, S. Clites, B. Kelly, M. Navidi, A. Dilello, V. Kulathumani, "RAMP: Accelerating Wireless Sensor Design with a Reconfigurable Analog/Mixed-Signal Platform", *Proceedings of the ACM/IEEE Conference on Information Processing in Sensor Networks (ISPN'15)*, pp. 47-58, Seattle, WA, April 13-16, (2015).
2. E. M. Sabolsky, R. C. Pillai, K. Sabolsky, G. A. Yakaboylu, B. Armour, A. Teter, M. Palmisiano and T. Close, "Refractory Ceramic Sensors for Process and Health Monitoring of Slagging Gasifiers", *ECS Trans.*, Vol 66 (37), pp. 43-53 (2015).
3. Q. Huang, D. Bhattacharyya, E.M. Sabolsky, "Estimation of Gasifier Wall Profile Using Measurements from a Wireless Sensor Network", Paper 247i, *AIChE Annual Meeting*, San Francisco, CA, USA, November 13-18, (2016).
4. Q. Huang, P. Paul, D. Bhattacharyya, R.C. Pillai, K. Sabolsky, E.M. Sabolsky, "Model-Based Estimation in Gasifiers Using a Smart Refractory Brick with Embedded Sensors", *To be published in the Proceedings of 11th International Workshop on Structural Health Monitoring*, (2017).
5. Q. Huang, P. Paul, D. Bhattacharyya, R.C. Pillai, K. Sabolsky, E.M. Sabolsky, "Estimations of Gasifier Wall Temperature and Extent of Slag Penetration Using a Refractory Brick with Embedded Sensors", 56, 9858-9867, *Industrial and Engineering Chemistry Research*, (2017).
6. Q. Huang, D. Bhattacharyya, "Optimal Sensor Network Design for Multi-scale Smart Refractory Brick System in Gasifier Applications", *To be submitted to Chemical Engineering Research and Design*, (2018).
7. A. Dilello, S. Andryzcik, B. Kelly, B. Rumberg, D. Graham, "Temperature compensation of floating-gate transistors in field-programmable analog arrays", *Proceedings of the IEEE Symposium on Circuits and Systems*, pp. 262-265, Baltimore, MD, May (2017).
8. G.A. Yakaboylu, E.M. Sabolsky, "Determination of a homogeneity factor for composite materials by a microstructural image analysis method", *Journal of Microscopy*, Vol 266 (3), pp. 263-272 (2017).
9. G.A. Yakaboylu, R.C. Pillai, K. Sabolsky, E.M. Sabolsky, "Stability and Electrical Properties of $MoSi_2$- and WSi_2-oxide Electroconductive Composites", *Journal of the American Ceramic Society*, Vol 100 (10), pp. 4461-4475 (2017).
10. G.A. Yakaboylu, R.C. Pillai, K. Sabolsky, E.M. Sabolsky, "$MoSi_2$- and WSi_2-based embedded ceramic composite thermocouples for high-temperature and harsh-environment sensing", *Sensors and Actuators A: Physical*, Vol 272, pp. 139-152 (2018).

11. G.A. Yakaboylu, K. Sabolsky, E.M. Sabolsky, "Phase stability, microstructure and high-temperature properties of $NbSi_2$- and $TaSi_2$-oxide conducting ceramic composites", *Journal of Materials Science*, Vol 53 (14), pp. 9958-9977 (2018).
12. G.A. Yakaboylu, K. Sabolsky, E.M. Sabolsky, "Chromium silicide-based composites fabricated via solid-state reactions: Phase development, oxidation behavior and electrical properties at high-temperatures", Submitted on 3-16-2018 (*currently under review*).
13. G.A. Yakaboylu, T. Yumak, K. Sabolsky, E.M. Sabolsky, "Understanding the effect of alumina phase and high-temperature preoxidation treatment on the oxidation (pest) behavior of $MoSi_2$- and WSi_2-based composites", Submitted on 3-27-2018 (*currently under review*).

List of Presentations:

1. G.A. Yakaboylu, E.M. Sabolsky, K. Sabolsky, R.C. Pillai, S. Chockalingam, M. Palmisiano, "Electrical and Thermomechanical Characterization of Silicide/Oxide Composites", *Materials Science and Technology MS&T2014, Pittsburgh, PA, USA, October 12-16, (2014).*
2. Q. Huang, D. Bhattacharyya, E.M. Sabolsky, "Dynamic Model of a Smart Refractory Brick for Gasifier Applications", Paper 126c, *AIChE Annual Meeting*, Atlanta, GA, USA, November 16-21, (2014).
3. G.A. Yakaboylu, R.C. Pillai, S. Chockalingam, B. Armour, M. Palmisiano, K. Sabolsky, E.M. Sabolsky, "Thermal Processing and Properties of Conductive Refractory Composites for High-Temperature Electrical Applications", *International Conference and Exposition on Advanced Ceramics and Composites*, Daytona Beach, FL, USA, January 25-30, (2015).
4. E.M. Sabolsky, R. Chockalingam, K. Sabolsky, G.A. Yakaboylu, O. Ozmen, B. Armour, A. Teter, D. Bhattacharyya , David Graham , Vinod Kulathumani, Close Timothy and Marc Palmisiano, "Refractory Ceramic Sensors for Process and Health Monitoring of Slagging Gasifiers", *227th ECS Meeting*, Chicago, Illinois, USA, May 28th, (2015).
5. E.M. Sabolsky , R. Chockalingam, K. Sabolsky, G.A. Yakaboylu, O. Ozmen, B. Armour, A. Teter, D. Bhattacharyya, David Graham, Vinod Kulathumani, Close Timothy and Marc Palmisiano, "Conductive Ceramic Composites Used to Fabricate Embedded Sensors for Monitoring the Temperature and Health of Refractory Brick in Slagging Gasifiers," *XIVth International Conference European Ceramic Society*, Toledo, Espana, 24th June, (2015).
6. R. C. Pillai, E.M. Sabolsky, K. Sabolsky, G.A. Yakaboylu, B. Armour, J. Mayer, J. Bogan, M. Raughley and J. Sayre, "Performance of high temperature ceramic-ceramic thermocouples embedded within chromia refractory bricks to monitor the health and

stability of industrial gasifiers", *Materials Science and Technology MS&T2015*, Columbus, OH, USA, October 4-8, (2015).

7. G.A. Yakaboylu, R.C. Pillai, B. Armour, K. Sabolsky, E.M. Sabolsky, "Development of Refractory Oxide/Metal Silicide Composites for High Temperature Harsh-Environment Sensor Applications", *Materials Science and Technology MS&T2015*, Columbus, OH, USA October 4-8, (2015).
8. Q. Huang, P. Paul, D. Bhattacharyya, E.M. Sabolsky, "Dynamic Model and Estimator Development for a Smart Refractory Brick with Embedded Sensors for Gasifier Applications", *AIChE Annual Meeting*, Salt Lake City, UT, USA, November 8-13, (2015).
9. R.C. Pillai, G.A. Yakaboylu, K. Sabolsky and E. M. Sabolsky, J. Bogan, J. Sayre, "Composite Ceramic Thermocouples for Harsh-Environment Temperature Measurements", *International Conference and Exposition on Advanced Ceramics and Composites*, Daytona Beach, FL, USA, January 24-29, (2016).
10. G.A. Yakaboylu, R. C. Pillai, B. Armour, K. Sabolsky and E. M. Sabolsky, "Conductive Ceramic Composites for Fabricating High Temperature and Harsh Environment Sensors: Thermal Processing, Stability and Properties", *International Conference and Exposition on Advanced Ceramics and Composites*, Daytona Beach, FL, USA, January 24-29, (2016).
11. G.A. Yakaboylu, R.C. Pillai, K. Sabolsky, J. Meyer, E.M. Sabolsky, J. Bogan, M. Raughley, J. Sayre, "Electroceramic Composite Sensors for Monitoring Harsh-Environment Energy Systems", *Materials Science and Technology MS&T2016*, Salt Lake City, UT, USA, October 23-27, (2016).
12. G.A. Yakaboylu, R.C. Pillai, K. Sabolsky, E.M. Sabolsky, "Processing of Metal Silicide/Refractory Oxide Composites for High-Temperature and Harsh-Environment Sensing Applications", *Gordon Research Conference (GRC), Ceramics, Solid State Studies in*, South Hadley, MA, USA, July 31-August 5, (2016).
13. Q. Huang, D. Bhattacharyya, E. M. Sabolsky E, "Estimation of Gasifier Wall Profile Using Measurements from a Wireless Sensor Network", AIChE Annual Meeting, San Francisco, CA, November 13-18 (2016)
14. Q. Huang, E.M. Sabolsky, R. Pillai, K. D. Sabolsky, D. Bhattacharyya, , "Health-Monitoring of Multiscale Systems Using an Optimal Multi-Rate Wireless Sensor Network", *AIChE Annual Meeting*, Minneapolis, MN, USA, October 29-November 3, (2017).
15. G.A. Yakaboylu, R.C. Pillai, K. Sabolsky, E.M. Sabolsky, "Metal Silicide-Refractory Oxide Electroconductive Ceramic Composites for High-Temperature and Harsh-Environment Sensing Applications", *Materials Science and Technology MS&T'17*, Pittsburgh, PA, USA, October 8-12 (2017).

16. G.A. Yakaboylu, R.C. Pillai, K. Sabolsky, D.J. Haynes, E.M. Sabolsky, “Metal Silicide-Refractory Oxide Ceramic Composites for High-Temperature and Harsh-Environment Sensing: Processing, Stability and Thermoelectric Properties”, *233rd ECS Meeting*, Seattle, WA, USA, May 13-17 (2018).
17. G.A. Yakaboylu, R.C. Pillai, K. Sabolsky, T. Yumak, E.M. Sabolsky, “Transition Metal Silicide-Based Ceramic Composites for High Temperature and Harsh Environment Sensing”, To be presented at the *Materials Science and Technology MS&T’18*, Columbus OH, October 14-18 (2018).

List of Students and Post-docs Supported:

Rajalekshmi C. Pillai (Post-doc)

Gunes A. Yakaboylu (PhD)

Qiao Huang (PhD)

Alexander Dilello (PhD)

Spencer Clites (MSc)

Steven Andryzcik (MSc)

Priyashraba Misra (MSc)

Brian Armour (Undergraduate)

James Meyer (Undergraduate)

Aaron Teter (Undergraduate)